Springer Series in Materials Science 188

Konstantinos I. Tserpes
Nuno Silvestre *Editors*

Modeling of Carbon Nanotubes, Graphene and their Composites

Springer

Springer Series in Materials Science

Volume 188

For further volumes:
http://www.springer.com/series/856

The Springer Series in Materials Science covers the complete spectrum of materials physics, including fundamental principles, physical properties, materials theory and design. Recognizing the increasing importance of materials science in future device technologies, the book titles in this series reflect the state-of-the-art in understanding and controlling the structure and properties of all important classes of materials.

Konstantinos I. Tserpes · Nuno Silvestre
Editors

Modeling of Carbon Nanotubes, Graphene and their Composites

Springer

Editors
Konstantinos I. Tserpes
Department of Mechanical Engineering and Aeronautics
University of Patras
Patras
Greece

Nuno Silvestre
Department of Mechanical Engineering, IDMEC
University of Lisbon
Lisbon
Portugal

ISSN 0933-033X
ISSN 2196-2812 (electronic)
ISBN 978-3-319-01200-1
ISBN 978-3-319-01201-8 (eBook)
DOI 10.1007/978-3-319-01201-8
Springer Cham Heidelberg New York Dordrecht London

Library of Congress Control Number: 2013950371

Printed on acid-free paper

Springer is part of Springer Science+Business Media (www.springer.com)

Preface

Materials science has always played an important role in the evolution of humankind. Over dozens of centuries, the knowledge about materials has paved the way for our modern technologies. Nowadays, technology is crossing a new age, in which materials at the atomic scale are being developed. Thus, nanotechnology is partly revolutionizing the way we live, learn, and organize our lives.

From the total of 118 chemical elements existing in the periodic table, one of the most intriguing elements is definitely carbon. The several hybridization states of carbon (sp, sp2, and sp3) can lead to numerous carbon allotropes, such as diamond (sp3), graphite (sp2), fullerene (sp2), carbon nanotubes (sp2), and graphene (sp2). The supreme properties and potential applications of synthetic carbon-based materials, particularly nanotubes and graphene, demonstrate their exceptional scientific and technological relevance and have attracted huge amount of funding for scientific projects as well as driven extensive research efforts. Due to their very interesting mechanical, optical, and electrical properties, carbon nanotubes (CNTs) and graphene could be established as cornerstones for tomorrow's technology. These carbon-based materials are associated with superlative mechanical strength. In the nanometer scale, the vast knowledge gained so far has established graphene and CNTs as two of the strongest materials ever tested. Ultrahigh elastic stiffness (about 1.0 TPa from computational predictions and experimental measurements) and tensile strength (about 100 GPa from computational predictions and about 130 GPa from experimental measurements) have been reported for graphene and CNTs. Extensive research studies on the mechanical properties of CNTs and graphene have been carried out via varieties of experimental, theoretical, and computer simulation approaches. One of the striking features of CNTs and graphene is the enormous potential to use them in nanoscale devices and also as reinforcement of structural materials. Either in nanoscale devices or carbon-based materials, excessive strains and localization phenomena can occur due to thermal, kinematical, or lattice mismatch between different materials. Therefore, the reliability of many devices and the effectiveness of strengthening of several carbon-based materials depend critically on the understanding of the response of CNTs and graphene to mechanical loading. Consequently, a proper understanding of the mechanics of CNTs and graphene is crucial to engineer novel nanoscale devices and materials.

Since the effects of single atoms can dominate the materials behavior at nanoscale, the atomistic viewpoint becomes a very critical issue not only for scientists but also for engineers. However, the experimental measurement of mechanical properties at nanoscale is difficult because the straightforward manipulation of the nanostructure is rather complex to achieve. Currently, there are still few appropriate measuring techniques at the nanoscale and it is really difficult to obtain some reliable data from indirect measurements. Thus, the computational techniques play an important role in investigating the mechanical properties of nanostructures. In this view, computer modeling will become more and more important in the development of new technologies. There are two main groups of methods: (i) dynamic and (ii) static. While the former consider the interaction between atoms purely dynamic, the latter simplify this interaction to static behavior. The dynamic methods are subdivided into three main types: (i) ab initio methods, (ii) tight-binding methods, and (iii) classical molecular dynamics (MD) simulations. Ab initio method treats separately the electronic and ionic degrees of freedom, thus needing a wave function description for the electrons. Since the ab initio method is too expensive and time-consuming, it is common practice to incorporate some approximations such as the density functional theory (DFT), which is based on the fact that the ground-state electronic energy is a unique function of the electronic density, instead of many-body interacting wave functions. In tight-binding methods, the electrons should be tightly bound to the atom to which they belong and they should have limited interaction with states and potentials on surrounding atoms of the solid. The advantage of the tight-binding method is that it can handle a much larger system than the ab initio methods. Molecular dynamics (MD) methods treat the atoms as classical entities (position and momentum). They are based on Newton's second law or the equation of motion, depending on the force exerted on the atom, its mass, and its acceleration. From this trajectory, the average values of properties can be determined. Once the positions and velocities of each atom are known, the state of the system can be predicted at any time. Interatomic potentials are the core of classical MD methods. During the past decades, numerous potentials describing atomic interaction in various materials with different levels of accuracy have been proposed. For covalently-bonded materials like carbon, bond-order multi-body potentials have been developed. These multi-body potentials capture not only pairwise interactions, but also additional contributions from the local geometric configuration of the neighboring atoms. MD simulations can be time-consuming and computationally expensive if a high number of atoms is involved, but they are much faster than either *ab inito* or tight-binding methods. The static methods are subdivided into two main types: (i) molecular mechanics (MM) methods and (ii) continuum shell methods. MM methods consider massless carbon atoms and treat the several carbon–carbon bonds as nonlinear elastic springs, with different terms accounting for bond stretching, twisting, and bending, as well as non-bonded van der Waals forces and cross interactions between these variables. In MM methods, the equilibrium configuration of the model system is sought by minimizing the energy, which consists of the sum of the interatomic potentials minus any work by external

forces. Unlike MD simulations, MM methods imply a temperature of 0 K and cannot account for the effects of temperature.

Continuum methods are divided into shell models and beam models. In continuum shell models, the atomic structures of the CNTs and graphene are treated as continuous and homogeneous macrostructures, and their material microstructures, such as the lattice spacing between individual carbon atoms, are ignored. The two-dimensional hexagonal lattice of carbon atoms is replaced by a continuous thin sheet, either plan (graphene) or cylindrical (CNT). On the other hand, in continuum beam models, the exact atomic lattice of the nanomaterials is represented by replacing the bonds with beams whose behavior is derived from interatomic potentials. Continuum models have been widely used to assess the strength and stability of structural systems at macroscale, try to mimic the solutions of discrete methods (ab initio, tight-binding, MD, and MM). Continuum shell models have several disadvantages compared to beam models, such as (i) the neglecting, or at least approximating, the discrete nature of hexagonal lattice and (ii) the consideration of a shell thickness that does not correspond to the nanoscale value. However, continuum models are tremendous efficient from the computational viewpoint. The drawback of dynamic methods (*ab inito*, tight-binding, or MD methods) is that a large computing power is needed, especially when dealing with a large number of atoms. This prompted researchers to develop reliable and efficient continuum models for characterizing and predicting the mechanical behavior of graphene and CNTs.

In resume, several computational methods exist to model and simulate the behavior of nanostructures. All of them present advantages and drawbacks; none of them is the perfect method. This book presents a survey on the computational modeling of the mechanical behavior of CNTs, graphene, and their composites by including different modeling approaches, such as MD simulations, continuum shell methods, atomistic-based finite element models, nonlocal elastic models, and stochastic models applied in a variety of geometries and load-cases.

Each chapter is an independent contribution by scientists with worldwide expertise and international reputation in the technological area treated by this book.

McCarthy, Byrne, O'Brien, and Murmu discuss in "Improved Mechanical Performance of CNTs and CNT Fibres in Nanocomposites Through Inter-Wall and Inter-Tube Coupling" the potential for addressing the problem of easy sliding between CNT walls and between CNTs in bundles, which drastically reduces their effective shear, bending, tensile, and compressive properties, through creation of inter-wall and/or inter-tube covalent bonds via irradiation with electrons or ions. The topic is addressed through an extensive series of MD simulations as well as an analytical shear-lag model.

"A Review on the Application of Nonlocal Elastic Models in Modeling of Carbon Nanotubes and Graphenes" by Arash and Wang, presents a review on the application of nonlocal continuum theory in the modeling of CNTs and graphene sheets, discusses the advantages of nonlocal continuum theory compared to its local counterpart and the necessity of calibration of the small-scale parameter as

the key parameter, describes nonlocal beam, plate, and shell models, and recommends potential areas for future research. Besides surveying the different nonlocal continuum models, the chapter presents further applications of the nonlocal continuum theory to model nanomaterials.

Georgantzinos, Giannopoulos, Spanos, and Anifantis present in "A Heterogeneous Discrete Approach of Interfacial Effects on Multi-Scale Modelling of Carbon Nanotube and Graphene Based Composites" a multi-scale finite element formulation, combining nanoscopic and macroscopic considerations for the modeling of the elastic mechanical response of single-walled CNTs and graphene-based composites. Emphasis is given on interfacial region modeling, where the interactions between the two phases are implemented by utilizing appropriate stiffness variations describing a heterogeneous interfacial region. Using the proposed technique, predictions on mechanical properties and load transfer conditions are performed.

"Effect of Covalent Functionalization on Young's Modulus of a Single-Wall Carbon Nanotube" authored by Shah and Batra, presents a study on the effect of hydrogen (–H), hydroxyl (–OH), carboxyl (–COOH), and amine (–NH2) functionalization on Young's modulus of a single-walled CNT using MM simulations with the MM3 potential and the software TINKER. The chapter shows that functionalization localizes deformations of the CNT at the functionalized sites, which decreases the modulus of elasticity. The type of functional group is found to have negligible effect on the value of Young's modulus of the functionalized SWCNT.

"Multiscale Modeling of Multifunctional Fuzzy Fibers Based on Multi-Walled Carbon Nanotubes" written by Seidel, Chatzigeorgiou, Ren and Lagoudas, presents an introduction to a novel class of multifunctional scale-bridging materials known as fuzzy fibers, which consist of multi-walled CNTs grown directly on the surface of structural carbon and glass fibers. The chapter identifies some of the key challenges in the modeling of the mechanical, electrical, and thermal properties of fuzzy fibers and the composites in which they are embedded, and reviews some of the recent efforts to model these materials available in the literature.

In "Geometry–Property Relation in Corrugated Nanocarbon Cylinders" Shima provides an overview of the geometry–property relation in cylindrical nanocarbon materials. The first half of the chapter is devoted to axially corrugated nanocarbon cylinders in which axial corrugation induces drastic changes in electronic and optical properties that are distinct from the case of straight, noncorrugated cylinders. In the second half, the application of hydrostatic pressure to CNTs that yields another class of corrugation, i.e., flowershaped cross-sectional deformation is seen. Molecular dynamics simulations of such radial corrugation and its consequences to physicochemical properties of multi-walled CNTs are also discussed.

In "Prediction of Mechanical Properties of CNT Based Composites Using Multi-Scale Modeling and Stochastic Analysis" Rafiee and Shokrieh compute the Young's modulus and Poisson's ratio of CNT-reinforced polymer by a full-range multi-scale modeling technique covering all scales of nano, micro, meso, and macro. This modeling strategy is analyzing the material at each scale and obtained

results are fed to the upper scale as input information. Due to uncertainties arisen from processing of CNT-reinforced polymers, a full stochastic implementation of modeling is employed treating length, orientation, agglomeration, waviness, and volume fraction of CNTs as random parameters.

Wang, Chowdhury, Koh, and Zhang present in "Molecular Dynamics Simulation and Continuum Shell Model for Buckling Analysis of Carbon Nanotubes" extensive sets of MD critical buckling loads/strains for single-walled CNTs and double-walled CNTs with various aspect ratios less than 10. The adaptive intermolecular reactive bond order (AIREBO) potential was adopted for MD simulations. Based on the MD results, the Young's modulus, Poisson's ratio, and thickness for an equivalent continuum cylindrical shell model of CNTs are calibrated. The equivalent continuum shell model may be used to calculate the buckling loads of CNTs, in-lieu of MD simulations.

"Influence of Bond Kinematics on the Rupture of Non-Chiral CNTs under Stretching–Twisting" written by Faria, Silvestre, and Canongia Lopes, focuses on the role played by bond kinematics in the collapse behavior of armchair and zigzag CNTs under combined stretching-twisting. The analyses are performed through MD simulations using LAMMPS code with the in-built potential AIREBO for C–C bonds. It is concluded that two kinematic mechanisms influence the failure of CNTs: (i) the bond elongation for meaningless to moderate twisting-to-stretching rate and (ii) the hexagonal cell distortion for moderate to high twisting-to-stretching rate.

Finally, "Finite Element Modeling of the Tensile Behavior of Carbon Nanotubes, Graphene and Their Composites" is authored by Tserpes and Papanikos and reviews the continuum beam models that have been developed in order to predict the elastic properties of isolated defect-free CNTs, to simulate the tensile behavior of defected CNTs and graphene, and to evaluate parametrically the effective elastic properties of nano-reinforced polymers. The methodologies and results presented in this chapter verify that continuum modeling has been proved efficient and effective in the modeling of nanomaterials and can be considered as a very strong alternative to atomistic simulation methods.

Patras, Greece — Konstantinos I. Tserpes
Lisbon, Portugal — Nuno Silvestre

Contents

Improved Mechanical Performance of CNTs and CNT Fibres in Nanocomposites Through Inter-Wall and Inter-Tube Coupling

Michael A. McCarthy, Emmett M. Byrne, Nathan P. O'Brien and Tony Murmu

Abstract The exceptional mechanical properties of carbon nanotubes (CNTs) make them highly attractive as potential reinforcing constituents in next generation composites. CNTs can be used individually or in small bundles as toughening agents in matrices, or large, aligned bundles can be twisted into fibres (Cheng 2007; Zhang et al. 2007). However, in both applications a major drawback is the weak van der Waals forces between the walls of multi-walled CNTs (MWCNTs) and between individual tubes in CNT bundles. This makes for easy sliding between CNT walls and between CNTs in bundles, which drastically reduces their effective shear, bending, tensile and compressive properties. In this chapter we discuss the potential for addressing this deficiency through creation of inter-wall and/or inter-tube covalent bonds via irradiation with electrons or ions. The topic is addressed through an extensive series of Molecular Dynamics simulations as well as an analytical shear-lag model. We show that both inter-wall and inter-tube bonding can have highly beneficial effects on the mechanical properties of CNT-based nanocomposites. The benefits can significantly outweigh the detrimental effects of induced defects from the irradiation process.

M. A. McCarthy (✉) · E. M. Byrne · N. P. O'Brien · T. Murmu
Department of Mechanical, Aeronautical and Biomedical Engineering, University of Limerick, Limerick, Ireland
e-mail: michael.mccarthy@ul.ie

E. M. Byrne
e-mail: emmett.byrne@ul.ie

N. P. O'Brien
e-mail: nathan.obrien@ul.ie

T. Murmu
e-mail: tony.murmu@ul.ie

K. I. Tserpes and N. Silvestre (eds.), *Modeling of Carbon Nanotubes, Graphene and their Composites*, Springer Series in Materials Science 188,
DOI: 10.1007/978-3-319-01201-8_1,

Keywords Multi-wall carbon nanotube · Nanotube fibre, nanocomposite · Inter-wall and inter-tube bonding · Load transfer · Structural properties · Molecular dynamics

1 Introduction

The outstanding mechanical properties of carbon nanotubes (CNTs) make them highly attractive as potential reinforcing constituents in structural composites (Barber et al. 2005a, b; Byrne et al. 2009; Locascio et al. 2009; Ogata and Shibutani 2003; Pantano et al. 2008; Peng et al. 2008; Pregler and Sinnott 2006; Sammalkorpi et al. 2004, 2005; Troya et al. 2003; Xia and Curtin 2004; Xia et al. 2007; Yu et al. 2000a, b; Zhang et al. 2005). However, achievement of high performance materials using CNTs requires major advances in processing methods and a fundamental understanding of the mechanics of nanoscale reinforcement. CNTs can be used individually or in small bundles as toughening agents in polymers, or large, aligned bundles can be twisted into fibres (Cheng and Hsu 2007; Zhang et al. 2007). In both applications one of the key drawbacks is the weak van der Waals forces between the walls of multi-walled CNTs (MWCNTs) and between individual tubes in CNT bundles. This makes for easy sliding between CNT walls and between CNTs in bundles, which drastically reduces their effective shear, bending, tensile and compressive properties. In this chapter we discuss the potential for addressing this deficiency through creation of inter-wall and/or inter-tube covalent bonds via irradiation with electrons or ions. The topic is addressed through an extensive series of Molecular Dynamics simulations as well as an analytical shear-lag model. The chapter is arranged as follows. Section 2 deals with MWCNTs and shows how with quite limited amounts of inter-wall bonding they can be stronger and tougher than single-wall nanotubes (SWCNTs); it also discusses the implications of this for nanocomposite design. Section 3 then addresses how such inter-wall bonding could be achieved in an optimal way. Section 4 discusses simulations of the irradiation process itself and the resulting effects on CNT bundles in terms of inter-*tube* bonding, as well as the side effect of increased defect levels. Section 5 then relates the inter-tube bonding and defects created to the mechanical properties of the resulting CNT bundles.

2 Strengthening and Toughening Effects of Inter-Wall Bonding on Multi-Walled Carbon Nanotubes and the Implications for Nanocomposite Design

The use of carbon nanotubes to reinforce polymer, ceramic, and metal matrices to achieve enhanced stiffness, strength, and toughness, in a wide array of applications has been the topic of intense research in recent years. Single-wall carbon

nanotubes (SWCNTs) appear ideal, with theoretical tensile strengths approaching 100 GPa (Ogata and Shibutani 2003; Sammalkorpi et al. 2004; Troya et al. 2003). But, like most brittle materials, SWCNTs contain fabrication defects that lower their strengths below the ideal level (Hashimoto et al. 2004; Suenaga et al. 2007). In many applications, multi-wall CNTs (MWCNTs) have been used due to their lower cost, availability, and ease of fabrication (Pantano et al. 2008; Xia et al. 2004; Shimizu et al. 2008; Pasupuleti et al. 2008; Yu et al. 2008; Zhou et al. 2008; Kuan et al. 2008). MWCNT structures can vary widely depending on the fabrication process, and so MWCNTs are considered to be defective and disordered relative to SWCNTs, and to have lower strengths.

MWCNTs have the possibility of inter-wall coupling between the graphitic CNT walls, via the growth process (e.g. CVD) or controlled irradiation or sputtering (Seldin and Nezbeda 1970; Tanabe 1996; Salonen et al. 2002; Krasheninnikov and Nordlund 2004; Kis et al. 2004). Molecular dynamics (MD) models show that inter-wall coupling improves inter-wall shear strength and load-transfer to the inner shells (Pregler and Sinnott 2006; Xia et al. 2007; Kis et al. 2004; Huhtala et al. 2004) and compression buckling resistance (Xia et al. 2007). Calculations also predict the presence of strength-reducing intra-wall defects, with vacancies as likely candidates (Sammalkorpi et al. 2004; Zhang et al. 2005; Hirai et al. 2003; Xiao and Hou 2006; Ashrafi and Hubert 2006). However, MWCNTs grown by Chemical CVD, which should contain a high level of defects, have strengths greater than either SWCNTs or MWCNTs grown by arc-discharge, and the strengthening is attributed to inter-wall coupling (Barber et al. 2005a, b). Experiments by Peng et al. (2008) clearly showed that the outer wall of an uncoupled MWCNT can have similar strength to that of a SWCNT with small defects and that irradiating MWCNTs induces inter-wall coupling that leads to much higher load-carrying capacity with little loss of strength. In spite of significant experimental efforts to measure strengths of MWCNTs (Barber et al. 2005; Yu et al. 2000a, b) and various hypotheses on the influence of inter-wall coupling on mechanical behaviour, little modelling work to date has investigated MWCNT tensile strength, perhaps the most important property for most mechanical applications.

In this section, we show via simulation that MWCNTs with sp^3 inter-wall bonding have strengths exceeding those of SWCNTs containing the same size initial intra-wall defect. Increasing inter-wall bonding also causes planar fracture rather than "sword-and-sheath" fracture. We further argue that MWCNTs with sufficient inter-wall bonding should have a minimum strength of 35–45 GPa. These results are consistent with the experimental data in (Peng et al. 2008). The strengthening effects of inter-wall bonding can compensate for the creation of defects during irradiation, so that MWCNTs with inter-wall bonding can be preferable to even the smallest and strongest SWCNTs for use as mechanical reinforcements in composites.

2.1 Methodology

Molecular dynamics (MD) was used to simulate the failure of nanotubes, a widely used approach (Pregler and Sinnott 2006; Sammalkorpi et al. 2004; Troya et al. 2003; Xia et al. 2007; Zhang et al. 2005; Kis et al. 2004; Huhtala et al. 2004). We present results for (50,0) single-wall CNTs (diameter = 4 nm), (50,0)/(41,0) double-wall CNTs (DWCNT), and (59,0)/(50,0)/(41,0) triple-wall CNTs (TWCNT), all of length 11.8 nm, which is sufficient to preclude end effects influencing fracture. DWCNTs and TWCNTs were populated with randomly-distributed inter-wall sp^3 bonding of variable density, defined as the number of sp^3 bonds between any two walls divided by the average number of atoms in each of the two walls. Crack-like defects were introduced at the middle cross-section of the (50,0) wall by removing hexagonal units of carbon in a horizontal line, as in Zhang et al. (2005). Defect length is defined as the distance between the intact C–C bonds on either end of the defect. Hydrogen atoms saturate the dangling bonds, which is likely to occur for MWCNTs grown by CVD. Figure 1 shows one DWCNT.

The widely-studied Tersoff-Brenner reactive empirical bond-order (REBO) potential (Brenner et al. 2002) was used for all interactions in this section. To better predict bond breaking forces, we proceed similarly to Shenderova et al. (2000) by changing the range of the cut-off function from 1.7–2.0 to 1.995–2.0 Å. This precludes formation of new bonds, but this is not a limitation for this study (it *is* for studies in later sections of this chapter). Non-bonded inter-wall interactions use a Lennard-Jones potential $E(r) = 4e\left[(r_0/r)^{12} - (r_0/r)^6\right]$ with $r_0 = 3.468$ Å and $e = 2.86$ meV (Xia and Curtin 2004) connected to the REBO potentials via cubic

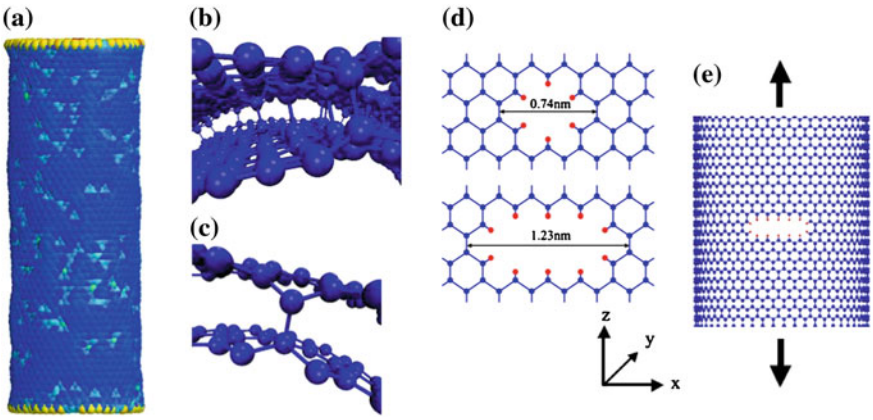

Fig. 1 Schematic of computational models: **a** Entire DWCNT with inter-wall sp^3 bonding, showing distortions of the wall surface and the atomic energy variations due to sp^3 bonds; **b, c** Views of the DWCNT along the tube axis, showing the inter-wall bonding and local distortion in the CNT structure; **d** Examples of small defects placed into the outerwall; **e** SWCNT (50,0) with a 1.72 nm defect perpendicular to the loading axis

splines with no discontinuities. Zhang et al. (2005) showed that this MD potential underestimates nanotube strength compared to quantum mechanical calculations, but here we perform a *comparative* study so that absolute strengths are not of great importance. Furthermore, the size scales needed for our calculations completely preclude the use of quantum methods. The nanotubes were relaxed via MD for 18.75 ps at temperature $T = 0.5$ K using a Berendsen thermostat (Berendsen et al. 1984) and a time step of 0.25 fs. Loading was then applied by fixing the z displacements of the two rings of C atoms at the bottom of the nanotube and displacing the two rings at the top vertically by 0.025 Å every 0.25 ps. The total force at the end of each displacement step was divided by the CNT cross-sectional area $A_{cnt} = \pi\left[(r_0 + 0.5t)^2 - (r_i - 0.5t)^2\right]$ to obtain the stress, where r_o and r_i are the outer and inner radii, respectively, and $t = 0.335$ nm is the inter-wall spacing. Use of A_{cnt} for SWCNTs allows for consistency in stress and elastic modulus computations among SWCNTs and MWCNTs. For each crack size, 5–10 randomly-arranged sp^3 bond distributions were simulated.

2.2 Results

Figure 2 shows all our results for strength versus defect size and nanotube structure. For SWCNTs, we obtain a defect-free strength of 82 GPa (similarly to (Zhang et al. 2005)) and decreasing strength with increasing defect size, scaling as $\sigma \propto c^{-\beta}$, $\beta \approx 0.4$ (Fig. 2, inset). This is close to the value $\beta \approx 0.5$ predicted by fracture mechanics for a sharp crack in a brittle material, differing slightly due to the blunt crack shape and discrete lattice effects. DWCNTs with no inter-wall bonding have strengths equal to those of SWCNTs, as expected. DWCNTs with 2.5 % sp^3 inter-wall bonding show an entirely different strength scaling (Fig. 2 and inset). With no defects, these tubes are weaker than SWCNTs due to the disorder induced by sp^3 bonds (Fig. 1). However, with defects larger than 1 nm, the strength is equal to or larger than that for a SWCNT with a similar sized defect. The strength decreases slowly with increasing defect size, scaling as $\sigma \propto c^{-\beta}$, $\beta \approx 0.14$. This weak scaling shows that DWCNTs are *toughened* by sp^3 bonding, which stems from the inner wall constraining the opening of the crack in the outer wall through stretching of inter-wall bonds. The constraint decreases the crack-tip stresses and is more effective for larger defects, thus decreasing the scaling exponent. This phenomenon is similar to the strengthening of a thin brittle film on a tough elastic substrate (Hutchinson and Suo 1992); here the cracked CNT wall plays the role of the film while the other wall(s) play the role of the substrate bonded to the film. Strengths of TWCNTs with 2.5 % sp^3 bonds are even larger than for DWCNTs because the outer wall provides additional constraint. Figure 2 also shows the strengths for DWCNTs with 0.5 and 1.5 % sp^3 bond fractions; strengths are reduced relative to the 2.5 % case because of the weaker mechanical constraint imposed by the bonding to the inner wall. In all cases, however, the DWCNT strength is larger than the SWCNT

strength. With this mechanistic insight, we conclude that the MWCNT strength always remains higher than that for SWCNTs, and can be *insensitive* to defect size for sizes beyond one or two vacancies.

Simple considerations of load transfer among walls lead to an estimated lower bound for strengths of MWCNTs with inter-wall bonding. For sufficiently high inter-wall bonding in a many-walled CNT, failure of the outer wall at $\bar{\sigma}$ increases the stress on the inner neighbour to $1.5\bar{\sigma}$ (Weibull 1951). This suggests a minimum MWCNT strength of $\sigma_{\min} \approx \sigma_o/1.5$ where σ_o is the defect-free strength. With $\sigma_o \approx 63$ GPa (Fig. 2), we find the value $\sigma_{\min} \approx 42GPa$ that is within 5 % of our simulation data on TWCNTs and 5–10 % of our data for 1.5 and 2.5 % DWCNTs. This estimate ignores small statistical and "weak-link" size effects (Curtin 2000; Mahesh et al. 1999; Mahesh and Phoenix 2004) but shows that strengths for MWCNTs with many walls should exceed those of SWCNTs with defects larger than 1.7 nm.

The fracture mode changes with sp^3 density. For high sp^3 bonding in a DWCNT (2.5 %; Fig. 3a), the sp^3 bonding induces a high stress concentration in the neighbouring wall, resulting in near-planar fracture. Low sp^3 bonding (0.5 %; Fig. 3b) increases the length over which stress is transferred among walls, such that the inner wall fails at a slightly weaker location away from the outer wall fracture plane, leading to the "sword and sheath" failure mode. For intermediate sp^3 bonding (1.5 %), the failure mode varies between planar and limited "sword and sheath" mode depending on the sp^3 bond distribution. A TWCNT can show features of both modes as well (Fig. 3c). This transition in fracture mode is consistent with experimental observations (Barber et al. 2005a, b; Peng et al. 2008).

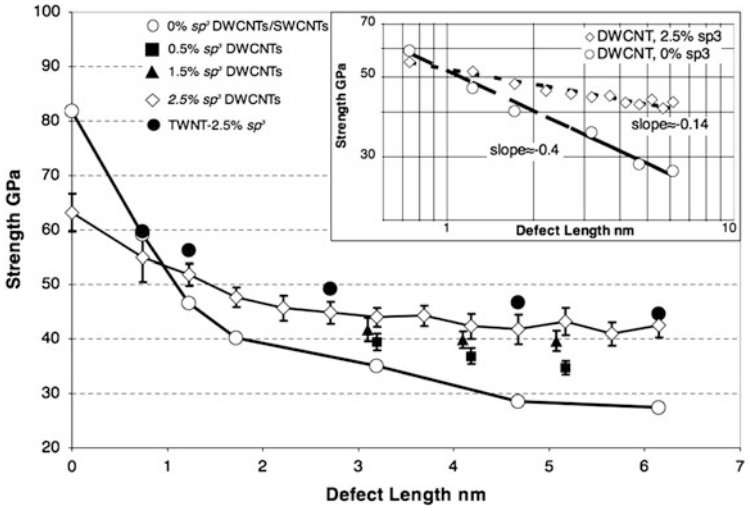

Fig. 2 SWCNT and MWCNT strengths versus initial defect (crack) length, for varying densities of inter-wall sp^3 bonding. For defects longer than ≈1 nm, the MWCNTs with inter-wall sp^3 bonding are stronger than SWCNTs or MWCNTs with no inter-wall bonding. Inset shows approximate power-law scaling of strength versus length, $\sigma \propto c^{-\beta}$, with MWCNTs with inter-wall bonding showing weak scaling (small β)

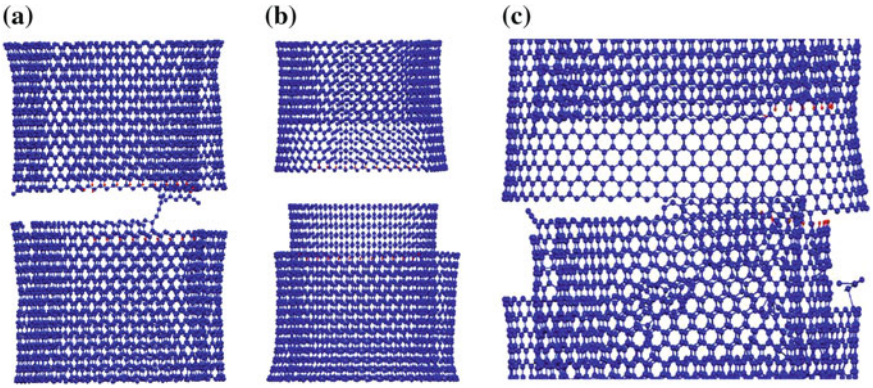

Fig. 3 Fracture mode transition **a** Flat fracture mode in a DWCNT with 2.5 % sp^3 inter-wall bonding; Carbon "chains" can often be seen linking the structure after failure; **b** Sword-and-sheath fracture mode in a DWCNT with 0.5 % sp^3 bonding; **c** Mixed fracture in a TWCNT with 2.5 % sp^3 bonding

We now compare our results to experimental data in (Peng et al. 2008). Peng et al. (2008) use the observed "sword-and-sheath" fracture mode to deduce the number of CNT walls bearing load in a given MWCNT. The first six columns in Table 1 present the data published by Peng et al. on six specific MWCNTs of varying diameters, exposed to varying degrees of irradiation, including the deduced number of walls coupled by inter-wall bonding. The number of load-bearing walls increases with increasing irradiation dose, consistent with the idea that increased irradiation creates more inter-wall bonding and at increasing depths into the MWCNT. The un-irradiated samples (1, 2, 3) have no inter-wall bonding and thus fracture *as if* they were SWCNTs, and this data thus serves as "reference data". The average strength of 102 GPa also corresponds reasonably to first-principles calculations of SWCNTs with single vacancies. The strength of an

Table 1 Observed and predicted tensile strengths for six individual MWCNTs subjected to irradiation

Sample	Outer Diam. (nm)[a]	# Walls Coupled[a]	Dose (C cm^{-2})[a]	Measure Strength (GPa)[a]	Measured Strength Ratio[a]	Predicted Strength (GPa)	Predicted Strength Ratio
1,2,3	14.7–26.0	1	0	102 (ave)	1	≈ 65[b]	1
4	39.48	3	3.1	82	0.8	45–55	0.69–0.85
5	25.87	18	31	58	0.57	43	0.66
6	49.01	52	558	35	0.34	43	0.66

[a] Ref. (Peng et al. 2008)
[b] Ref. (Zhang et al. 2005; Brenner et al. 2002)
Also shown is the strength ratio defined as the strength normalized to the strength of a SWCNT with a single vacancy defect; this scales out the absolute difference arising from the use of the REBO potential in the predictions. Samples 1–3 are essentially SWCNTs and thus serve as reference cases

SWCNT with such a defect, calculated using the semi-empirical REBO potential, is 65 GPa (Zhang et al. 2005; Fonseca et al. 2011). Since the nanotube deformation is essentially elastic, the most useful comparison between experiments and MD simulations is obtained by considering strength *ratios* rather than absolute values. These ratios are thus calculated in Table 1 by dividing the experimental data by 102 GPa, and our MD data by 65 GPa (i.e. both sets of data are normalized with respect to the corresponding single vacancy SWCNT value). For Sample 4 in (Peng et al. 2008), three walls fail and the strength ratio is 0.8. Sample 4 is similar to our TWCNT, for which we find, over a wide range of defect sizes, strengths in the range 45–55 GPa and thus a strength ratio of 0.69–0.85. For Sample 5, 18 walls fail (Peng et al. 2008) and the strength ratio is 0.57. Our lower-bound analysis gives a strength ratio of 0.66. For Sample 6, 52 walls fail (Peng et al. 2008) and the strength ratio is 0.34 while our analysis still gives a strength ratio of 0.66. This discrepancy suggests that the high irradiation dose for Sample 6 induced large defects that were correlated between successive walls, which is consistent with the experimental findings of a greatly-reduced elastic modulus and evidence of amorphous carbon (Peng et al. 2008). Our results are thus largely consistent with the quantitative data of Peng et al. (2008).

We now examine some basic design concepts for use of MWCNTs in composites that are essential for making decisions on fundamental material design of nanocomposites. In a composite with aligned CNTs of outer diameter D, consider a volume fraction V_{cnt} of n-walled CNTs having nominal area $\frac{\pi}{4}(D+t)^2$. The composite ultimate tensile strength σ_{uts} is proportional to the *actual* load-bearing area fraction $V'_{cnt} = \left[\frac{2t}{D}\left(\frac{1+n+(n^2-1)t/2D}{(1+t/D)^2}\right)\right]V_{cnt}$. For CNTs having a Weibull strength distribution with Weibull modulus m (Weibull 1951) and coupled to a matrix via interfacial shear strength τ, σ_{uts} can be accurately estimated using the "Global-Load-Sharing" model (Curtin 1999) as

$$\sigma_{uts} = V'_{cnt}\phi(m)\left[\frac{2\tau L}{\sigma_{cnt}D}\right]^{\frac{1}{m+1}}\sigma_{cnt} \tag{1}$$

where $\phi(m) = \left(\frac{2}{m+2}\right)^{\frac{1}{m+1}}\frac{m+1}{m+2}$ is a statistical "bundle" factor, $\left[\frac{2\tau L}{\sigma_{cnt}D}\right]^{\frac{1}{m+1}}$ is a statistical length scaling factor, and σ_{cnt} is the reinforcement strength measured at gauge length L (Curtin 1999). Equation 1 neglects the strength contribution of the matrix, which is small for polymers, ceramics, and most metals. The Weibull modulus, related to the coefficient of variation ($c.o.v.$) as $m \approx 1.2/c.o.v.$, arises from a combination of the underlying Weibull distribution of defect sizes having Weibull modulus m' and the defect size-scaling exponent β, with $m = m'/\beta$. Thus, the low β for DWCNTs with inter-wall bonding increases the Weibull modulus by a factor of $0.4/0.14 \approx 3$ over SWCNTs with the same underlying defect distribution.

Within the above framework, the design trade-off is then between SWCNTs of very small diameter and larger MWCNTs with inter-wall coupling between n walls, but with the same V_{cnt} (i.e. the same total amount of carbon material or the same load-bearing area of carbon), the same interface τ, and the same underlying

statistical defect distribution m'. To make comparisons as favourable as possible for SWCNTs, we compare MWCNT materials to SWCNTs of the *smallest* feasible diameters of $D_{SW} = 1.1$ and 1.8 nm and the *highest* feasible strength of $\sigma_{SW} = 100$ GPa. For specific results, we use the strengths from Peng et al. (2008) at $L = 2000$ nm, a value $\tau = 50$ MPa typical of polymer, metal, and ceramic matrices (Curtin 1999), and $m = 7$ typical of good-quality carbon fibers. Then, $\phi(3m)/\phi(m) = 1.16$ and $(2\tau L/\sigma_{MW}D_{MW})^{\frac{1}{3m+1}}/(2\tau L/\sigma_{SW}D_{SW})^{\frac{1}{m+1}} \sim 0.8 - 0.9$ for a wide range of σ_{MW} and D_{MW}. Hence, the ratio of MWCNT and SWCNT composite strengths, $\sigma_{uts,MW}/\sigma_{uts,SW}$, is controlled mainly by V'_{cnt}/V_{cnt}, favouring MWCNTs, and $\sigma_{cnt,MW}/\sigma_{cnt,SW}$, favouring SWCNTs. Assuming that a given radiation dosage effectively couples n walls (e.g. Table 1), we can maximise $\sigma_{uts,MW}/\sigma_{uts,SW}$ by using a fully dense MWCNT of diameter $D_{MW} \sim 2(n+1)t$. For a dosage coupling $n = 3$ walls with $\sigma_{MW} = 82$ GPa (e.g. Sample 4), $D_{MW} = 2.4$nm is optimal and yields $\sigma_{uts,MW}/\sigma_{uts,SW}$ = 0.92–1.32, i.e. the MWCNT composite has 92–132 % of the strength of an equal nominal area of small, strong SWCNTs. For a dosage coupling $n = 18$ walls with $\sigma_{MW} =$ 58 GPa (e.g. Sample 5), $D_{MW} = 12.5$ nm is optimal and yields $\sigma_{uts,MW}/\sigma_{uts,SW}$ = 0.61–0.87. For a dosage coupling $n = 52$ walls with $\sigma_{MW} =$ 35 GPa (e.g. Sample 6), $D_{MW} = 35$ nm is optimal and yields $\sigma_{uts,MW}/\sigma_{uts,SW}$ = 0.37–0.53. MWCNT-based composites are thus competitive with the *best possible* SWCNT systems.

SWCNTs are brittle, defect-sensitive materials (Fig. 2) and so as-processed SWCNT strengths could be lower than 100 GPa. Functionalisation of SWCNTs to achieve coupling to a matrix material is also accompanied by strength decreases (Coleman et al. 2006; Garg and Sinnott 1998). In contrast, our simulation results demonstrate that MWCNTs with inter-wall coupling are damage-tolerant (strength weakly dependent on defect size) with high retained strengths ($\approx$35–50 GPa) unless exposed to harsh conditions. From the standpoints of reliability and robust design (as well as cost and manufacturability, issues not discussed here), we conclude that MWCNTs suitably designed using Eq. 1 are preferable to SWCNTs for high-performance materials.

2.3 Concluding Remarks

In summary, we have shown that MWCNTs with inter-wall coupling are inherently stronger than SWCNTs with the same size initial intra-wall defect, a result understood through basic mechanics considerations. We find that the measured and simulated strength ratios between irradiated MWCNTs and un-irradiated SWCNTs are in reasonable agreement. We have then also shown that composites composed of MWCNTs can be as strong as composites composed of the highest-strength, smallest diameter SWCNTs, and conclude that composites with suitably-designed MWCNTs (diameter, number of walls, and irradiation dosage) can perform better

than most SWCNT-based composites. In totality, our results provide a framework for guiding the creation of high-performance composites based on MWCNTs through carefully-controlled inter-wall bonding.

3 Optimising Inter-Wall Coupling for Load Transfer in Multiwall Nanotubes

3.1 Introduction

As described in Sect. 2, multi-wall CNTs (MWCNTs) are an appealing option for reinforcement of nanocomposites, since if all the walls can be made to share the load, more load can be carried per unit area than with single-wall CNTs (SWCNTs). However, if only van der Waals forces exist between the walls of MWCNTs, then the walls slide over each other relatively easily and load applied to the outside wall (e.g. by a surrounding matrix) cannot be transferred to the inner walls, rendering them structurally ineffective.

Experiments have shown that controlled sputtering and irradiation of graphite and pristine MWCNTs can enhance inter-wall coupling and sliding resistance via the formation of inter-wall sp^3 bonds (Seldin and Nezbeda 1970; Tanabe 1996; Pregler and Sinnott 2006). Inter-wall coupling can also occur with standard CNT fabrication techniques (Barber et al. 2005a, b; Yu et al. 2000b). As noted in Sect. 2, Peng et al. (2008) induced variable degrees of inter-wall coupling in MWCNTs, via controlled electron irradiation dosages, and tested the resulting specimens in tension up to failure. With increasing irradiation dosage, the fracture load and number of walls sharing the load was increased due to inter-wall bonding. Quantitatively, the failure load was up to $\sim$11.6 times the load expected if only their outermost wall had been loaded. This is particularly impressive given the fact that numerous defects were induced by the irradiation process. Irradiation thus appears to be a promising route to producing MWCNTs with controlled levels of inter-wall coupling, although considerable scope exists for optimizing the process.

Computational modelling via e.g. Molecular Dynamics simulation is too time-consuming for optimisation studies. Analytical models of load transfer in MWCNTs having only van der Waals coupling between walls have recently been presented by Zalamea et al. (2007) and Tsai and Lu (2009). Zalamea et al. (2007) present a shear transfer model involving a "shear transfer efficiency" factor which varies between zero and one, as well as a shear lag model, with the shear strain at the interface obtained by assuming a linear strain distribution between the walls. They compare the two models and use them to predict the dependence of elastic modulus of MWCNTs on tube length. Tsai and Lu (2009) presented a similar shear lag model and examined a composite unit cell consisting of a MWCNT surrounded by a matrix. They incorrectly claim reduced efficiency of load transfer in MWCNTs compared to SWCNTs due to an error in boundary conditions. They

assume that the far-field equilibrated stress in the walls of a MWCNT is the same as that in a SWCNT of the same outer diameter, while in fact the load is shared by multiple walls in the MWCNT. Correcting this boundary condition leads to results that contradict many of their main conclusions.

In this section, we present an analytical model to capture the stress transfer between walls of MWCNTs with explicit inter-wall bonding and study the same problem using direct MD simulations. Our analytical model is a shear lag model, but differs from (Zalamea et al. 2007; Tsai and Lu 2009) in that the walls are assumed of zero thickness, while the interface is of thickness equal to the wall spacing, with a $1/r$ variation in shear stress. Our simulations show that the detailed variations in inter-wall bonding from wall to wall, and along the tube length, are important for the precise load transfer from outer to inner walls. Good agreement between the analytical model and the simulations is obtained when such variations are minimized. Optimal load transfer is also achieved for a spatially homogeneous distribution of inter-wall bonds. We further investigate inter-wall bond distributions that might be reasonably obtained through irradiation processes, involving decreasing inter-wall bond density from outer to inner walls, for which the load transfer is found to be close to optimal provided the density variations are not too large. The validated model is a valuable tool for estimation of load transfer in MWCNTs with varying degrees of inter-wall coupling of any type (inter-wall bonding or interstitial defects (Locascio et al. 2009; Peng et al. 2008)), and can help guide future experimental efforts to optimise load transfer efficiency in MWCNT-based nanocomposites.

3.2 Analytical Model

We consider n cylindrical, concentric carbon nanotubes separated by the graphitic spacing t, with limited amounts of sp^3 bonds forming links between the walls, forming a MWCNT. A load F is applied on the top surface of the outer wall, which is then transferred into the internal walls through shear of the inter-wall bonds. To obtain an analytical solution for the load transfer, the MWCNT system is treated similarly to the "shear lag" model of a micro-scale fibre composite in (Hutchinson and Jensen 1993; Aveston 1971; Sutcu and Hillig 1990), where the walls of the MWCNT act as the "fibers" that carry only axial stress, while load transfer is facilitated by a "matrix" (the inter-wall bonds) that carries only shear stress. As shown in Fig. 4, the walls ($i = 1,\ldots n$, with $i = 1$ the inner-most wall) have radii r_i and zero thickness (so that the distance between walls is $r_{i+1} - r_i = t$). However, to convert axial wall forces to stresses, an effective thickness t equal to the graphitic plane spacing is used to determine the effective wall cross-sectional area $A_i = 2\pi r_i t$. All walls have identical axial stiffness corresponding to a Young's modulus E. The matrices ($i = 1,\ldots n$-1) have thickness t and individual shear moduli μ_i that depend on the density of inter-wall sp^3 bonds between walls i and $i + 1$. With z being the coordinate along the axis of the walls, a load F is applied to

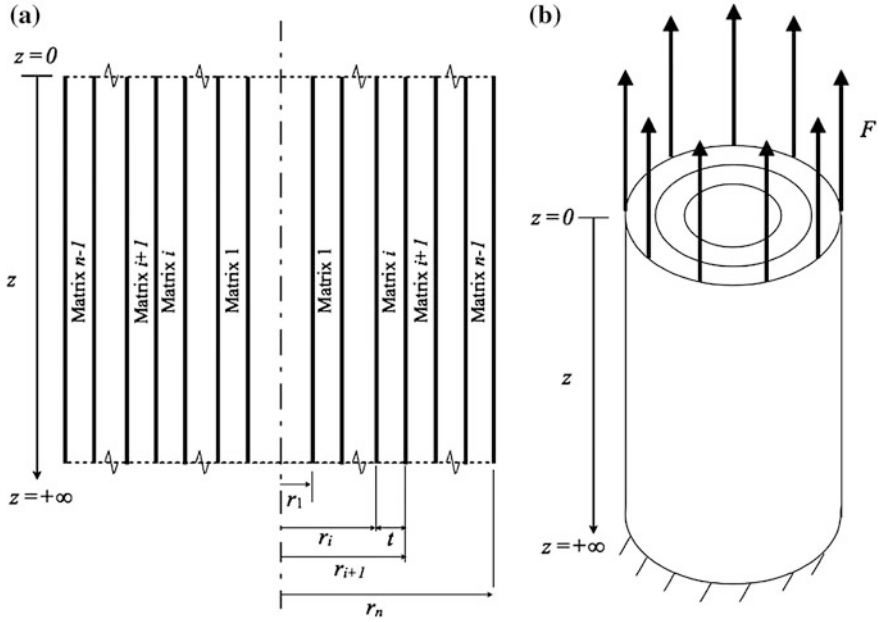

Fig. 4 MWCNT load transfer model: **a** 2D elevation view showing the matrix regions, matrix thickness, and fiber radii; **b** 3D view of the model boundary conditions

the outermost wall only, at $z = 0$. At $z = +\infty$ the strains and stresses in all walls are equal. The displacement, strain, and stress in wall i are functions of z, and denoted $w_i(z)$, $\varepsilon_i(z)$ and $\sigma_i(z)$ respectively, while the displacement, strain and stress in matrix i are functions of r and z, for r varying between r_i and r_{i+1}, and denoted $w(r, z)$, $\gamma_i(r, z)$ and $\tau_i(r, z)$ respectively.

To derive an analytical shear lag model, we determine the equilibrium equations for the one-dimensional walls and matrices as a special case of the three-dimensional model of Mikata and Taya (1985). We then assume elastic constitutive behaviour for all walls and matrices, and use strain–displacement relations to produce a set of coupled differential equations for the stresses in each wall.

Figure 5 shows an infinitesimal element of matrix i, at position z, with axial thickness dz and radial thickness dr. Equilibrium of an infinitesimal element of matrix i, at position z, of radial thickness dr and axial thickness dz is expressed as $\tau_i(r + dr, z)(2\pi(r + dr))dz = \tau_i(r, z)(2\pi\, rdz)$, which can be rearranged to give

$$\frac{\partial \tau_i(r, z)}{\partial r} = \frac{-\tau_i(r, z)}{r} \tag{2}$$

with the general solution

$$\tau_i(r, z) = \frac{a}{r} f(z) \tag{3}$$

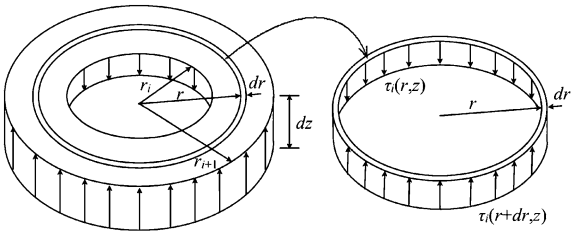

Fig. 5 Elemental matrix element

where a is a constant and $f(z)$ is an unknown function of z. The matrix constitutive behavior is simple linear elasticity, so the engineering shear strain is

$$\gamma_i(r,z) = \frac{a}{\mu_i r} f(z) \tag{4}$$

Assuming small deformations, the strain–displacement relation for the matrix is$\gamma_i = \partial w(r,z)/\delta r$. Using (4) and integrating leads to $w(r,z) = -(a/\mu_i)f(z)\ln r + g(z) + c$ where c is another constant and $g(z)$ another unknown function of z. Applying the boundary conditions for matrix i, $w(r_i,z) = w_i(z)$ and $w(r_{i+1},z) = w_{i+1}(z)$, where $w_i(z)$ and $w_{i+1}(z)$ are the displacements of walls i and $i+1$ respectively, leads to an expression for a which when inserted in (2) leads to

$$\tau_i(r,z) = \mu_i \frac{w_i(z) - w_{i+1}(z)}{r \ln \frac{r_{i+1}}{r_i}} \tag{5}$$

Next we consider wall (nanotube) equilibrium, for walls $1 < i < n$. Equilibrium of an infinitesimal section of wall i of length dz yields

$$[\sigma_i(z+dz) - \sigma_i(z)](2\pi r_i; t) + \tau_{i-1}(r_i,z)(2\pi r_i dz\ ) - \tau_i(r_i,z)(2\pi r_i dz\ ) = 0 \tag{6}$$

recalling that the walls are considered to be of thickness t in converting between wall force and stress. Rearranging leads to

$$\frac{d\sigma_i(z)}{dz} = \frac{\tau_i(r_i,z) - \tau_{i-1}(r_i,z)}{t} \tag{7}$$

Using (5) in (7) yields

$$\frac{d\sigma_i(z)}{dz} = \frac{1}{t}\left(\mu_i \frac{w_i(z) - w_{i+1}(z)}{r_i \ln \frac{r_{i+1}}{r_i}} - \mu_{i-1} \frac{w_{i-1}(z) - w_i(z)}{r_i \ln \frac{r_i}{r_{i-1}}}\right) \tag{8}$$

Assuming a linear elastic constitutive relation for the wall, $\sigma_i(z) = E\varepsilon_i(z)$, and strain–displacement relationship $\varepsilon_i(z) = dw_i(z)/dz$ leads to a differential equation for the axial stress in wall i as a function of axial position z

$$\frac{d^2\sigma_i(z)}{dz^2} - \frac{1}{tEr_i}\left(\left[\frac{\mu_i}{\ln \frac{r_{i+1}}{r_i}} + \frac{\mu_{i-1}}{\ln \frac{r_i}{r_{i-1}}}\right]\sigma_i(z) - \frac{\mu_i}{\ln \frac{r_{i+1}}{r_i}}\sigma_{i+1}(z) - \frac{\mu_{i-1}}{\ln \frac{r_i}{r_{i-1}}}\sigma_{i-1}(z)\right) = 0 \tag{9}$$

Consideration of equilibrium of walls 1 and n differ slightly because they are connected to matrix on only one side, but the analysis follows a similar procedure, producing two more differential equations given below.

We define a non-dimensional length $\tilde{z} = z/l$, where $l = t\sqrt{E/\bar{\mu}}$ and $\bar{\mu}$ is the average shear modulus for all the matrices in the MWCNT. Non-dimensional shear moduli are also defined as $\tilde{\mu}_i = \mu_i/\bar{\mu}$. Hence, the equations can be re-written finally as:

$$\text{for } i = 1\,(\text{innerwall}), \frac{d^2\sigma_1(\tilde{z})}{d\tilde{z}^2} - \frac{t\tilde{\mu}_1}{r_1 \ln\frac{r_2}{r_1}}(\sigma_1(\tilde{z}) - \sigma_2(\tilde{z})) = 0 \tag{10}$$

$$\text{for} 2 \le i \le n, \frac{d^2\sigma_i(\tilde{z})}{d\tilde{z}^2} - \frac{t}{r_i}\left(\left[\frac{\tilde{\mu}_i}{\ln\frac{r_{i+1}}{r_i}} + \frac{\tilde{\mu}_{i-1}}{\ln\frac{r_i}{r_{i-1}}}\right]\sigma_i(\tilde{z}) - \frac{\tilde{\mu}_i}{\ln\frac{r_{i+1}}{r_i}}\sigma_{i+1}(\tilde{z}) - \frac{\tilde{\mu}_{i-1}}{\ln\frac{r_i}{r_{i-1}}}\sigma_{i-1}(\tilde{z})\right) = 0 \tag{11}$$

$$\text{for } i = n\ (\text{outerwall}), \frac{d^2\sigma_n(\tilde{z})}{d\tilde{z}^2} + \frac{t\tilde{\mu}_{n-1}}{r_n \ln\frac{r_n}{r_{n-1}}}(\sigma_{n-1}(\tilde{z}) - \sigma_n(\tilde{z})) = 0 \tag{12}$$

The boundary conditions are $\sigma_i(\tilde{z} = 0) = 0$ for $1 \le i \le n-1$, $\sigma_n(\tilde{z} = 0) = F/2\pi r_n t$, and $d\sigma_i(\tilde{z} = +\infty)/dz = 0$ for $1 \le i \le n$. The above equations can be solved analytically but the analysis (and resulting solution) becomes extremely cumbersome as n increases. Simplification of these equations is possible in the limit $r_i >> t$, but this conveys no advantage in obtaining analytical solutions. Numerical solutions for any value of n can be obtained easily using numerical analysis tools such as MATLAB, and this is the approach used here.

3.3 Molecular Dynamics Model

To investigate the validity of the analytical model and uncover any atomic-scale features not contained in the continuum model, various MWCNT configurations were studied using the analytical model and MD simulations. For the MD simulations, the Tersoff-Brenner Reactive Bond Order (REBO) potential (Brenner et al. 2002) was used, with a Lennard-Jones model for non-bonded inter-wall interactions (Byrne et al. 2009; Girifalco et al. 2000; Xia et al. 2007) connected to the bonding potential via cubic splines. We studied two, three, four, five and six wall MWCNTs made up of nested CNTs with the following chirality and radii: (12,12) ($r_1 = 0.79$ nm), (17,17) ($r_2 = 1.12$ nm), (22,22) ($r_3 = 1.45$ nm), (27,27) ($r_4 = 1.78$ nm), (32,32) ($r_5 = 2.11$ nm) and (37,37) ($r_6 = 2.44$ nm). These MWCNTs were created with controlled overall densities λ_{CNT} of inter-wall sp^3 bonding, defined as the total number of inter-wall bonds divided by the total number of atoms in the MWCNT. Samples were generated starting from an ideal MWCNT

of the desired length L and inner diameter d. The inter-wall sp^3 bonds were added at random locations with the caveat that they were prevented from forming where a first or second neighbour atom was already sp^3 bonded, as described in Xia et al. (2007). The "random" process of introducing inter-wall bonds actually produced approximately the same *number* of inter-wall bonds between each pair of walls in a MWCNT. So, we define an inter-wall bond density λ_i between any pair of walls as the total number of inter-wall bonds between walls i and $i + 1$ divided by the total number of atoms in walls i and $i + 1$. The models described above thus have decreasing values of λ_i, corresponding to decreasing shear moduli μ_i, from the inner walls to the outer walls (see Fig. 6). To allow all wall stresses to attain their equilibrium far-field value, $\sigma_i(\tilde{z} = +\infty) = F \Big/ \left(2\pi t \sum_{i=1}^{i=n} r_i \right)$, an MWCNT length of 40 nm was used. For every geometric and inter-wall bond density configuration studied, three statistical realizations of the spatial inter-wall bond distribution were simulated.

After adding the desired fraction of sp^3 bonds, the entire nanotube was relaxed to equilibrium under zero applied load for 150 ps at temperature $T = 0.01$ K using a Berendsen thermostat (Berendsen et al. 1984) and a 1 fs time step. All MD calculations were performed using the open source software LAMMPS (Plimpton 1995). Loading was then applied by fixing the z displacements of the bottom two

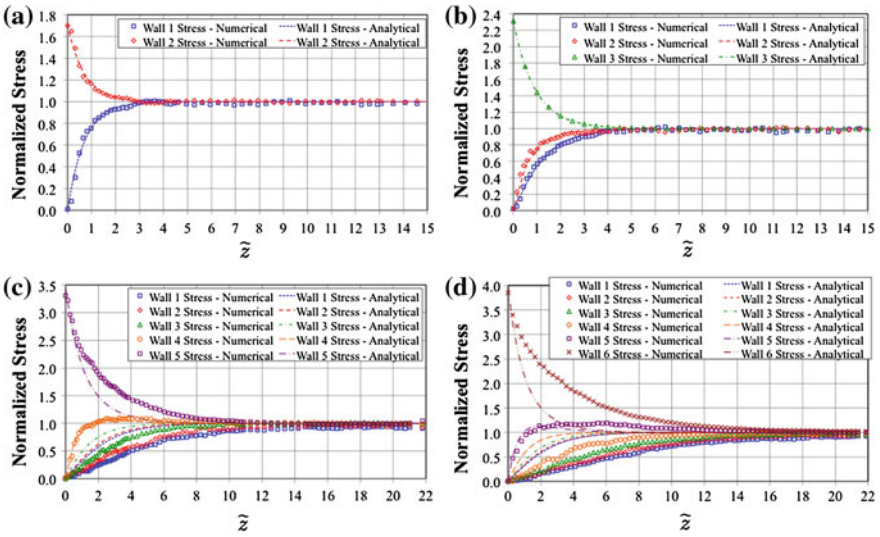

Fig. 6 Analytical and MD results for *two, three, five* and *six* wall MWCNTs with 2.5 % inter-wall bond density. Stress is normalized with respect to the far field stress in the nth wall,. Range of shown is less than full length of tube to highlight load transfer region. **a** *Two wall*: E = 886 GPa, = 44 GPa, = 1. **b** *Three wall*: E = 867 GPa, = 34.11 GPa, = 1.15, = 0.85. **c** *Five wall*: E = 844.5 GPa, = 29.8 GPa, = 1.45, = 1.045, = 0.802, = 0.704. **d** *Six wall*: E = 827 GPa, = 29.5 GPa, = 1.56, = 1.146, = 0.927, = 0.74, = 0.62

rings of C atoms and displacing the top two rings of the outermost wall vertically by 0.05 Å every 1 ps. All other atoms were free to move subject to the empirical potential and the thermostat. To minimize end effects due to the imposed boundary conditions and CNT splaying effects at the ends of the tubes, no inter-wall bonding was introduced in the top 4 rings of C atoms. Hence, the $\tilde{z} = 0$ position, where load transfer begins, corresponds to ring 5 of the total MWCNT structure.

Displacement was stopped when the applied stress reached approximately 45–55 GPa on the outer wall at $\tilde{z} = 0$, which was within the elastic range of deformation for these nanotubes, with no C–C bond failures observed. The internal degrees of freedom in the CNTs were then relaxed for an additional 100 ps. At each axial ring position z_j we computed the cross-sectional force by determining the forces exerted on all C atoms with axial coordinate $z \geq z_j$ due to all atoms with axial coordinate $z < z_j$. This calculation required a special-purpose subroutine that was developed and integrated into LAMMPS.

In the analytical model, the effective shear modulus μ_i between walls i and $i + 1$ was determined from the actual inter-wall bond density λ_i between each pair of walls in the MD simulations using $\mu_i = (1760\ GPa)\lambda_i$ previously derived for DWCNTs (Troya et al. 2003).[1] The average shear modulus $\bar{\mu}$ for all the matrices in the MWCNT was then found and used to determine the non-dimensional $\tilde{\mu}_i$. The values used in the analytical models for $\tilde{\mu}_i$ and E were the averages from the MD simulations on three MWCNT structures. It was found that the value of E decreases as more inter-wall bonds are added: for the four-wall CNT we measure $E = 860.1$ GPa for 1.0 % sp^3 density, $E = 857$ GPa for 2.5 % sp^3 density, and $E = 792$ GPa for 4.0 % sp^3 density. The decrease in axial stiffness is due to increased out of plane deformation in the initial structures caused by the inter-wall bonding, which reduces the graphitic wall stiffness.

3.4 Results and Discussion

3.4.1 Inter-wall Stress Transfer

Figures 6 and 7 show the normalized stresses in each wall for various nanotubes as obtained from the numerical and analytical models. Figure 6 shows two-wall, three-wall, five-wall and six-wall cases with an overall sp^3 bond density of $\lambda_{CNT} = 2.5$ %, while Fig. 7 shows four-wall cases with bond densities of 1.0, 2.5 and 4.0 %. The wall stresses are normalized with respect to the far-field stress. Each MD result is an average value from simulations performed on three MWCNTs, with identical number of walls and average inter-wall bond density but

[1] In (Troya et al. 2003) this equation is given as $\mu_i = (880\ \text{GPa})\lambda_i$ because the number of sp^3 bonds was taken as the number of atoms involved in an sp^3 bond, which is in fact twice the number of sp^3 bonds.

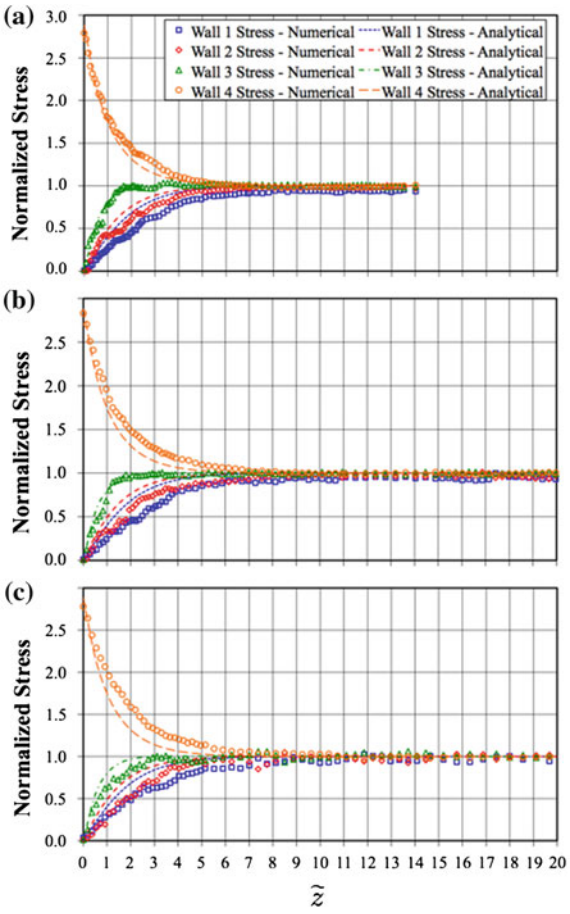

Fig. 7 Analytical and MD results for *four wall* MWCNTs with varying inter-wall bond density. Stress is normalized with respect to the far field stress in the nth wall. **a** 1.0 % density: E = 860.1 GPa, = 12.5 GPa, = 1.33, = 0.925, = 0.75. **b** 2.5 % density: E = 857 GPa, = 31 GPa, = 1.29, = 0.96, = 0.75. **c** 4.0 % density: E = 792 GPa, = 49.9 GPa, = 1.31, = 0.946, = 0.74

different randomly distributed inter-wall bond locations. In all cases studied, the results show stress transfer from the outer wall to the inner walls, in accordance with the prescribed boundary conditions, with full transfer taking place well within the length of the tubes studied, at these inter-wall bond densities.

We observe that the analytical and MD results are in excellent agreement for the two-wall and three-wall cases along the entire length of the tube. With no adjustable parameters, the analytic model thus captures the fundamental mechanics of load transfer between walls of a MWCNT. The agreement for the four-wall case is not as good (Fig. 7), but the length required for full stress transfer is quite similar for the numerical and analytical models. This demonstrates that the characteristic length $l = t\sqrt{E/\bar{\mu}}$ captures the dominant trend in the load transfer. It also demonstrates that the relationship $\mu = \lambda \times (1760\,\text{GPa})$ originally derived for double wall nanotubes, is valid over a wide range of MWCNT configurations.

Agreement between the analytical model and the simulation is not nearly as good for the five and six-wall cases however, with the analytic model predicting much faster load transfer into the inner walls than found in the MD simulations.

3.4.2 Effect of Inter-wall Bond Distribution

The agreement between the model and the simulations for two and three wall cases is strong evidence for the applicability of the analytic model. The disparities observed for the five and six-wall cases must thus lie in detailed differences between the modelling assumptions and the actual simulations. The analytical model assumes a uniform shear modulus between each pair of walls throughout the length of the tube whereas the MD models have sp^3 bonds added randomly, which leads to stochastic variations in the local sp^3 bond density along the length of the tube as well as around the circumference. To examine how these effects can influence the load transfer, we have (i) created simulation samples with very controlled regular distributions of inter-wall bonds and (ii) examined the actual distribution of sp^3 bonds and the load transfer more closely. These studies are described in more detail below.

A five-wall MWCNT was created with inter-wall bonds distributed as evenly as possible along the axial direction and with bond densities in each matrix region such that the values of $\tilde{\mu}_i$ were approximately the same. This required an increasing number of inter-wall bonds for increasingly exterior walls. The precise distribution was achieved as follows. Let $\{\tilde{z}_k\}$ be the dimensionless discrete set of coordinates for rings of C atoms in an undeformed MWCNT. Dividing the MWCNT axially into groups of four rings of atoms, we denote the inter-wall bonds within those rings as (*ijkl*). In the innermost matrix (matrix 1), one inter-wall bond was placed at each $\tilde{z}_k$, i.e. (1111). In matrix 2, an additional inter-wall bond was placed at every fourth $\tilde{z}_k$, i.e. (2111). For matrix 3, yet another inter-wall bond was added to give (2211). Finally for the outermost matrix (matrix 4) two inter-wall bonds were placed at each $\tilde{z}_k$, i.e. (2222). The inter-wall bonds were distributed evenly around the circumference of the MWCNT but with the constraint that nearby inter-wall bonded atoms be separated by at least two other atoms, because if a bond between walls i-1 and i is placed too close to one between walls i and $i + 1$, bonds can break and defects can result.

The results from the MD simulation and analytical model for the specially designed 5-wall MWCNT are shown, alongside the random-bond five-wall CNT results in Fig. 8. Agreement between the simulation and the analytical model is much better for all walls. This supports the notion that spatial randomness in the sp^3 bonding leads to the discrepancies found in Figs. 6 and 7. The minor remaining discrepancies in Fig. 8 are believed to be mainly due to the non-linear stiffness of the REBO potential as a function of bond distance which cannot be accounted for using constant values of E and μ. Comparison of the analytical model results in Fig. 8a, b also reveals that load transfer occurs slightly more rapidly in Fig. 8. This difference arises because the inter-wall shear stiffnesses are more-evenly

distributed in the carefully controlled case (Fig. 8b: $\tilde{\mu}_1 = 1.052$, $\tilde{\mu}_2 = 0.979$, $\tilde{\mu}_3 = 0.934$, $\tilde{\mu}_4 = 1.034$) as compared to the "random case" (Fig. 8a: $\tilde{\mu}_1 = 1.45$, $\tilde{\mu}_2 = 1.045$, $\tilde{\mu}_3 = 0.802$, $\tilde{\mu}_4 = 0.704$). This point will be discussed below.

Since random inter-wall bonding is expected in realistic materials, we now examine one random distribution in more detail to understand why the load transfer lengths are increased when bonding is not evenly distributed along the tube length. Figure 9 shows the number of inter-wall bonds in each "matrix" at each $\tilde{z}_k$ location together with the normalized stress in the wall just inside that matrix, as obtained from simulation and as predicted for *one* random-bond five-wall MWCNT and only over the initial load transfer region ($0 \leq \tilde{z} \leq 3$). The average number of inter-wall bonds over the full length of the tube is shown as a dashed line. The figure does not show effects due to randomness in the circumferential distribution of inter-wall bonds, which are believed to be secondary.

Figure 9a shows that the *rate* of stress transfer into Wall 4 between locations $\tilde{z}_k$ and $\tilde{z}_{k+1}$ is strongly correlated with the number of inter-wall bonds in matrix 4 at location $\tilde{z}_k$. When the number of inter-wall bonds is below the average (e.g. at $\tilde{z}_1$ and $\tilde{z}_2$), the stress transfer is below the analytical result, and hence the stress is also below the analytical result. The low number of inter-wall bonds is compensated for further along the CNT (e.g. $\tilde{z}_3$, $\tilde{z}_4$,$\tilde{z}_7$) by above-average numbers of inter-wall bonds, which leads to increased rates of stress transfer that are larger than the analytical prediction. This allows the simulated stress to approach the predicted stress. This situation is generally expected. However, stress transfer to wall i, $i < 4$, is more complex as it depends on bonds in multiple walls ($\forall j, j \geq i$). In particular, an above average number of bonds in an inside matrix (such as in matrix 2 for $\tilde{z}_k$, $k = 1,2,3$) is not effective in transferring stress if it coincides with a below average number of bonds in a matrix further out at the same $\tilde{z}_k$ (matrix 4 in this case). Thus no stress is transferred to wall 2 until distance $\tilde{z}_4$, and the above average number of bonds in matrix 2 at $\tilde{z}_k$, $k = 1,2,3$ cannot compensate for below average values further along the z-axis in matrix 2. In general, regions of above average inter-wall bonding cannot always compensate for other locations of below average inter-wall bonding in the same matrix (for matrices $i < n - 2$), and hence delays in the stress transfer accumulate. With increasing number of walls in the CNT, there are more

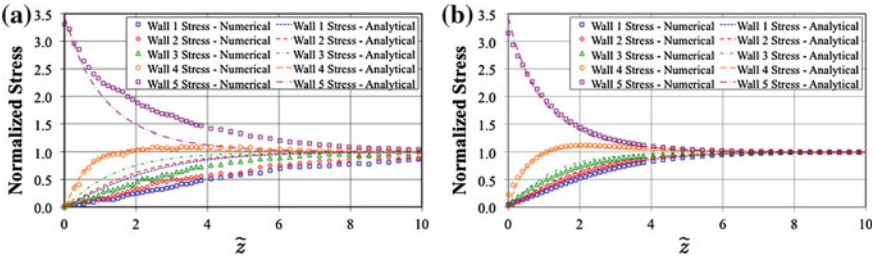

Fig. 8 Load transfer in five-wall CNT with **a** randomly distributed inter-wall bonds (reproduced from Fig. 6c) and **b** evenly distributed inter-wall bonds

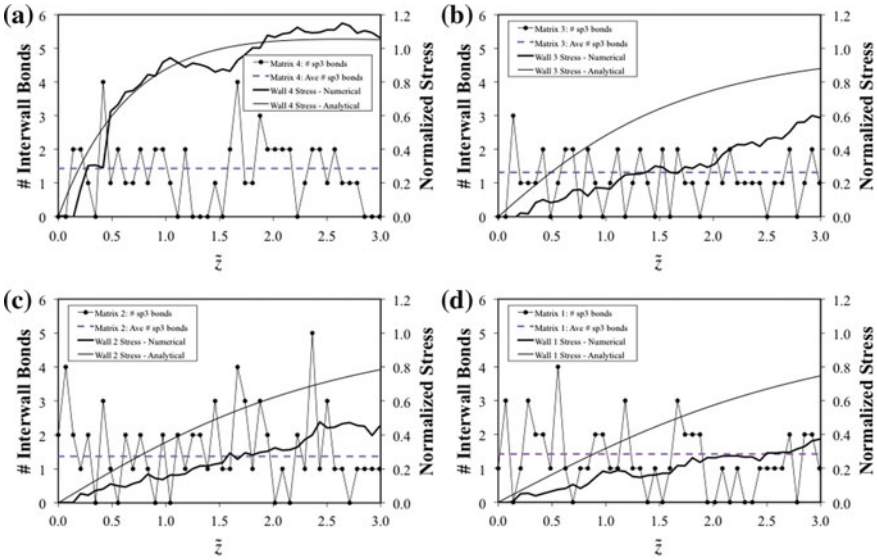

Fig. 9 Analytical and single MD simulation of the *five-wall* CNT with random inter-wall bond distribution. Shown, for each matrix, are number of inter-wall bonds and normalized stress as a function of $\tilde{z}$ over first three characteristic lengths, together with average number of inter-wall bonds in each matrix over the full length of the tube. **a** Matrix 4. **b** Matrix 3. **c** Matrix 2. **d** Matrix 1

locations with below average bond density in at least one of the matrices outside wall 1, which is the reason why the stress transfer into wall 1 is delayed more and more, relative to the analytical result, as walls are added. The more homogenous the axial distribution of inter-wall bonds, the less such fluctuations occur, and the load transfer can thus occur faster, as we saw for the specially designed 5-wall tube in Fig. 8b. The analytical shear-lag model above could be generalized to account for axial variations in the inter-wall bonding. In essence, the shear moduli would become functions of axial position, $\mu_i = \mu_i(z)$, and the analysis would otherwise be identical. However, $\mu_i(z)$ would need to be a continuous function and would need to be determined for each specific realization of inter-wall bonding of interest. Thus, while possible, the feasibility and utility of such an approach is greatly limited and it is not pursued further here.

The simulations above have, for computational feasibility, used relatively small diameter MWCNTs. However, the fluctuations in bonding are exacerbated in small systems and should be smaller in larger systems. Specifically, assuming circumferential fluctuations in inter-wall bonding are not important, the axial fluctuations become smaller, relative to the mean, for larger diameter MWCNTs. For N possible circumferential bonding locations at any location $\tilde{z}_k$, the variance in the number of bonds scales with $N^{-1/2}$. Thus, larger MWCNTs should have more uniform axial inter-wall bond distributions and exhibit load transfer that is closer to the analytical model.

3.5 Design of MWCNTs for Optimal Load Transfer

Turning to practical considerations, although it may appear that enhanced inter-wall bonding near the ends of a MWCNT can enhance load transfer, in fact inter-wall bonding must be distributed along the entire length of the MWCNTs to accommodate the fracturing of MWCNTs during loading. During tensile failure of composites, fibers break many times along their length and stress is transferred back into the remaining fragments through load transfer. In addition, fiber pull out from the matrix absorbs considerable energy but also requires load transfer. Thus composite strength and toughness depend on being able to transfer stress not only to intact fibers, but also to broken fibers. The optimum strategy for achieving maximum composite strength and toughness is thus to aim for a constant number of inter-wall bonds along the entire length of the MWCNTs.

We now examine how to achieve the most rapid load transfer for a given overall average density of inter-wall bonds. Data in Fig. 8 suggested that faster load transfer occurs when $\tilde{\mu}_i$ is approximately the same from matrix to matrix. To investigate this more broadly, we examine MWCNTs with 3, 5, 10 and 25 walls and varying degrees of wall-to-wall non-uniformity in the $\tilde{\mu}_i$. Specifically, we assign $\tilde{\mu}_i$ values to each matrix region randomly in the range $0 < \mu_i < 2\bar{\mu}$ around a target mean $\bar{\mu} = 25$ GPa and rescale the selected random values so that their *actual* mean equals $\bar{\mu}$. For each MWCNT created, we calculate the coefficient of variation $CV_{\tilde{\mu}}$ of the actual inter-wall bond distribution and use the model to predict the distance L_{LT} required for "full" load transfer. Here L_{LT} is defined as the distance at which the load in the innermost ($n = 1$) nanotube has reached 99 % of its far-field equilibrium value. For perfectly uniform MWCNTs (i.e. $\mu_i = \bar{\mu}$; $CV_{\tilde{\mu}} = 0$), we label the load transfer length as L_{LT}^{uniform}. Figure 10 shows the predicted load transfer distance L_{LT} normalized by L_{LT}^{uniform} as a function of the coefficient of variation $CV_{\tilde{\mu}}$ within the MWCNT. We observe that $L_{LT}/L_{LT}^{\text{uniform}} \geq 1$ for all values of $CV_{\tilde{\mu}}$, demonstrating that a uniform distribution of shear moduli across all walls leads to the fastest load transfer. In terms of inter-wall bond density, since the number of atoms in the walls of a commensurate MWCNT increases linearly from wall 1 to wall n, optimal load transfer should occur when the number of inter-wall bonds increase linearly from the inside to the outside walls. The data in Fig. 10

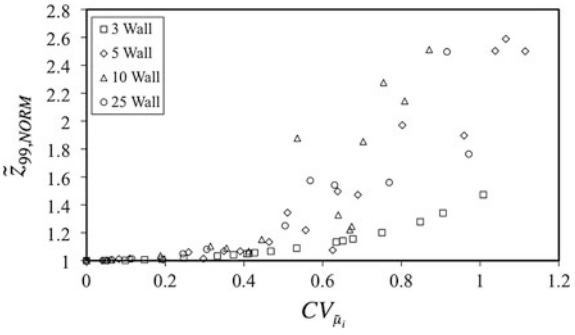

Fig. 10 Effect of variations in shear modulus from matrix to matrix on the length for full load transfer (99 % of far field stress) normalized by the full load transfer length for a perfectly uniform distribution ($CV_{\mu} = 0$)

further shows that moderate wall-to-wall variations, e.g. $CV_{\tilde{\mu}} < 0.5$, do not significantly increase the load transfer length. Even for high variations the deviations remain only a few times larger than L_{LT}^{uniform}.

In practice, the creation of inter-wall bonding by irradiation seems likely to create more inter-wall bonds in the outer walls as compared to the inner walls (Pregler and Sinnott 2006). This is consistent with the data of Peng et al. (2008) who found increasing irradiation dose to correlate with increasing depth of inter-wall coupling, as measured by examining fractured MWCNTs. Fortunately, if a gradient in inter-wall bonding is to occur, load transfer favours decreasing inter-wall bonding from the outside to the inside. Table 2 illustrates the load transfer in five 26-wall cases: a uniform case (case 1: all $\tilde{\mu}_i = 1$), two cases with small $CV_{\tilde{\mu}}$ (cases 2, 3) but with $\tilde{\mu}_i$ *decreasing* from outside to inside (case 2) and $\tilde{\mu}_i$ *increasing* from outside to inside (case 3), and two cases with larger $CV_{\tilde{\mu}}$ (cases 4, 5) and again with $\tilde{\mu}_i$ *decreasing* from outside to inside (case 4) and $\tilde{\mu}_i$ *increasing* from outside to inside (case 5). L_{LT} in case 2 is slightly faster than in case 3, and only 2 % larger than L_{LT}^{uniform}, while load transfer in case 4 is also faster than in case 5. Thus, decreasing moduli from outside to inside is preferable.

Peng et al. (2008) also showed that high irradiation could lead to excessive damage in the MWCNTs. Our results combined with those of Peng et al. (2008) suggest irradiation strategies that can most-effectively cause load transfer. Specifically, subjecting MWCNTs to an initial dose of high energy radiation to penetrate into the inner walls and create inter-wall bonds in the interior followed by lower energy radiation to form more inter-wall bonds in the outer walls might lead to relatively uniform inter-wall shear moduli, and hence good load transfer.

Finally, Fig. 11 shows that the load transfer length L_{LT}^{uniform}, normalized by the characteristic length ℓ, depends linearly on the number of walls n in the MWCNT,

$$L_{LT}^{\text{uniform}}/\ell \approx 1.5\, n \tag{13}$$

This remarkably simple equation demonstrates that when inter-wall bonds are distributed evenly throughout the structure, or with modest variations (viz. as in Fig. 10), the characteristic length for load transfer for an n-wall MWCNT scales as

$$L_{LT} \sim 1.5nt\sqrt{E/\bar{\mu}} \tag{14}$$

Table 2 Normalized load transfer length $L_{LT}/L_{LT}^{\text{uniform}}$ as a function of the gradient in shear modulus for an $n = 26$ wall MWCNT

Case	$\tilde{\mu}_i$	L_{LT}	$CV_{\tilde{\mu}}$
1	$\tilde{\mu}_i = 1, \forall i$	39.27 ($= L_{LT}^{uniform}$)	0
2	$\tilde{\mu}_i = 0.52 + 0.04(i-1),\ 1 \le i \le 25$	40.06	0.294
3	$\tilde{\mu}_i = 1.48 - 0.04(i-1),\ 1 \le i \le 25$	40.86	0.294
4	$\tilde{\mu}_i = 0.04 + 0.08(i-1),\ 1 \le i \le 25$	48.47	0.589
5	$\tilde{\mu}_i = 1.96 - 0.08(i-1),\ 1 \le i \le 25$	51.37	0.589

Decreasing modulus from outside to inside ($n = 25$ to $n = 1$) provides faster load transfer than increasing modulus from outside to inside

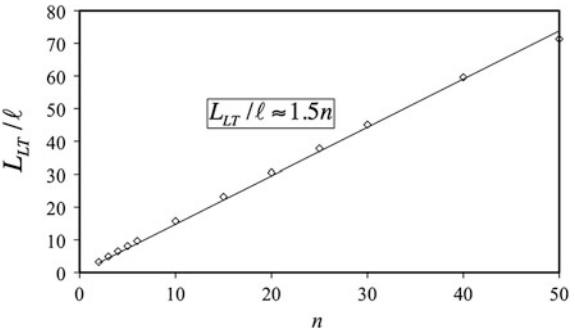

Fig. 11 Non-dimensional length to 99 % stress transfer, with equal shear moduli in each inter-wall space, versus number of walls in MWCNT

where t is the CNT wall spacing, E the effective Young's modulus, and $\bar{\mu}$ the overall average inter-wall shear modulus due to inter-wall coupling. This equation can thus be used to predict a good lower bound for load transfer, given a relationship between $\bar{\mu}$ and the inter-wall bond density λ, which depends on the type of inter-wall coupling. Here we have studied direct inter-wall sp^3 bonding such that $\mu = \lambda \times (1760\ \text{GPa})$. The lower bound arises due to the neglect of the statistical fluctuations that tend to increase the load transfer length, but that may be less influential in larger-diameter MWCNTs. Equation 13 is a major broad outcome of our study.

3.6 Concluding Remarks

We have presented an analytical shear-lag model that is a useful tool for predicting load transfer in MWCNTs as a function of the degree of inter-wall bonding between pairs of walls in the structure. Molecular dynamics simulations generally validate the model, showing it to be most accurate when the inter-wall bond density is uniform axially within each matrix region. Via numerical tests, we have shown that deviations between the model and the simulations arise due to statistical fluctuations in the bonding. Exercising the model over a range of parameters, optimal load transfer has been shown to occur when the inter-wall shear modulus is uniform from wall to wall in the MWCNT, and axially along the tube length. For more realistic scenarios of inter-wall bond formation via irradiation, where the inter-wall bond density likely decreases from the outer to inner walls, the deviations in load transfer length from the ideal case are relatively small if the inter-wall bond density variation is not too large. We conclude that the general scaling for load transfer in an n-wall MWCNT can be estimated as $\sim 1.5\, nt\sqrt{E/\bar{\mu}}$, which captures the dominant trends with respect to number of walls, Young's modulus, and average shear modulus due to inter-wall bonding. These guidelines should assist in design of engineered MWCNTs, where inter-wall coupling is introduced to enhance load transfer, energy dissipation, and thus composite strength and toughness in ceramic- and polymer-matrix composite materials.

4 Improved Inter-Tube Coupling in CNT Bundles Through Carbon Beam Irradiation

4.1 Introduction

The ultra-high stiffness and strength of carbon nanotubes (CNTs), of the order of 1 TPa and 100 GPa respectively (Yu et al. 2000a; Yakobson and Avouris 2001), has stimulated intense interest in CNT-based composites, including the development of super strong fibres from CNT bundles. However, the mechanical properties of such fibres are generally far lower than that of individual CNTs, due to the weak van der Waals shear interactions between neighbouring shells and tubes (Peng et al. 2008; Xia and Curtin 2004; Salvetat et al. 1999; Filleter et al. 2011), which severely limits load transfer. This deficiency affects not just shear and bending properties, but also the tensile strength and toughness when such fibres are used in composite materials, since load is generally introduced by the matrix to the outer tubes in the fibre, and must be transferred through inter-tube shear if the inner tubes are to share the load. Additionally CNTs generally do not run the full length of the fibre so inter-tube shear load transfer is essential if the fibre is to behave as a coherent entity. Without it, sword-in-sheath type fibre failure occurs in which only a few of the CNTs are actually fractured, with the rest pulled out with minimal resistance.

A number of researchers have investigated the use of irradiation, either via electrons or ions, to promote covalent bonds or cross-links between neighbouring walls in multi-wall CNTs (MWCNTs) (Byrne et al. 2009; Peng et al. 2008; Pregler and Sinnott 2006; Byrne et al. 2010; Pavia and Curtin 2011; Fonseca et al. 2010; Li et al. 2009) or tubes (Kis et al. 2004; Ni et al. 2001; Federizzi et al. 2006; Cornwell and Welch 2011) in CNT bundles. It has been shown computationally that only a small amount of cross-links can dramatically increase inter-wall or inter-tube stiffness (Xia et al. 2007; Kis et al. 2004). Recently experimental evidence has been presented of a three-fold increase in tensile strength in MWCNTs (Peng et al. 2008) and an order of magnitude increase in tensile strength and modulus in CNT bundles (Filleter et al. 2011), achieved through promotion of cross-links via irradiation. These studies provide strong motivation for further investigation of this topic, with the aim of understanding and optimising the irradiation process.

The dilemma when using irradiation for this purpose is that the intended inter-tube or inter-wall cross-links can only be achieved with the generally unwanted side effect of other kinds of defects, such as vacancies, adatoms, and Stone–Wales defects, which have a detrimental effect on mechanical properties (Pregler and Sinnott 2006; Sammalkorpi et al. 2005; Kis et al. 2004). Thus a delicate balance has to be struck. The formation of defects (including cross-links) is influenced by many factors including CNT size, the number of walls, the number of tubes in the bundle, incident particle mass, energy, dosage and whether or not the particle forms chemical bonds with C atoms (Xu et al. 2009), so there are too many

variables involved to optimise this process experimentally. It is thus crucial to increase understanding of the deposition process and the formation of defects through computational and theoretical study. To date, molecular dynamics studies have been performed on CNT deposition with ions of noble gases (Pregler and Sinnott 2006; Salonen et al. 2002; Pomoell et al. 2004; Pregler et al. 2008), CH_3 (Ni et al. 2001; Ni and Sinnott 2000), CF_3 (Pregler and Sinnott 2006), potassium (Kotakoski et al. 2005), boron and nitrogen (Kotakoski et al. 2005). Electron irradiation has also been mimicked via a primary knock-on atom method, whereby high kinetic energies are assigned to random CNT atoms (Pregler and Sinnott 2006). To the best of our knowledge, deposition of carbon ions has only been considered for irradiation of CNT bundles in (Federizzi et al. 2006) and irradiation of single tubes in (Xu et al. 2009). It has also recently been considered for graphene (Compagnini et al. 2009). Carbon ion deposition is an interesting option since it introduces no impurities into the system, provides additional carbon interstitial atoms to mediate cross-links, and enables efficient momentum transfer due to the match between the mass of the deposition and target atoms.

In this section, we provide a detailed study of the carbon ion deposition process on bundles of single-wall CNTs (SWCNTs) using molecular dynamics simulations. Our study differs from that in (Federizzi et al. 2006) in that we consider specific irradiation strategies aimed at improvement of mechanical properties, and use a recently-developed reactive bond-order potential with environment-dependent first nearest-neighbour definition (Pastewka et al. 2008) which accurately simulates bond-forming and bond-breaking processes in carbon-based systems. The ideal result for our purposes would be a uniform level of inter-tube covalent bonding between all adjacent tubes (with the ability to somehow control that level) with a minimum level of defects in the CNT walls. This would allow transfer of load between CNTs, enabling all of them to engage in loading, with the least loss in strength due to intra-wall defects. The ability to control the *level* of cross-linking would allow design of fibres to give the desired balance between strength and toughness. We find that for 7-tube bundles, the level of cross-linking can be reliably controlled through varying the irradiation parameters. Many different types of cross-links and defects are formed and characterised here. We also examine 19-tube bundles and find bigger challenges in terms of controlling cross-link density. For yet larger bundles, we propose some alternative approaches.

4.2 Simulation Method

4.2.1 Interatomic Interactions

For realistic Molecular Dynamics (MD) simulations of the deposition process, accurate inter-atomic potentials, capable of representing bond breaking and forming, are required. Molecular mechanics calculations using the well-established REBO potential (Brenner et al. 2002) show inappropriate fracture

mechanisms and grossly overestimate the stress for C–C bond breaking, as compared with values predicted by quantum mechanics calculations (Hirai et al. 2003; Shenderova et al. 2000; Yakobson et al. 1997; Pastewka et al. 2010). The inaccuracy stems from the functional form for a cut-off function used in the original REBO potential that greatly increases the bond force for distances between 0.17 and 0.20 nm (Belytschko et al. 2002). For studies only concerned with bond breaking some authors have avoided the non-physical fracture mechanisms by removing the cut-off function (Byrne et al. 2009; Zhang et al. 2005; Shenderova et al. 2000), which then leads to an underestimate of the stresses for bond breaking relative to quantum mechanics calculations (Byrne et al. 2009; Zhang et al. 2005; Hirai et al. 2003; Shenderova et al. 2000; Li et al. 2009; Yakobson et al. 1997) and, moreover, precludes a consideration of bond formation. To rectify these problems we used a modified REBO potential recently presented in (Pastewka et al. 2008), where a local environment-dependent cut-off function based on screening concepts (Baskes et al. 1994) allows a bond between two atoms to persist over long distances provided that no third atom moves into the bonding region. This leads to smooth changes in forces and a much better description of bond breaking and reforming compared with first principles calculations.

Concerning the deposition process, our simulations mimic the pulsed laser deposition process in (Schittenhelm et al. 2002; Sorescu et al. 2003) which produced both C^+ ions and neutral carbon atoms (as well as slower C_2 and C_3 molecules). Since classical MD does not include charge effects or electron excitation, we are constrained, like previous authors (Pregler and Sinnott 2006; Sammalkorpi et al. 2005; Salonen et al. 2002; Federizzi et al. 2006; Pomoell et al. 2004; Pregler et al. 2008), to only treating the incident particles as neutral carbon atoms. While we recognise that particle charge will affect the chemical reactions that occur, we expect that MD simulation can provide results on the degree of cross-linking and damage that occurs which are qualitatively correct and useful for comparing different irradiation strategies. Our simulations consider nuclear stopping only, ignoring electron stopping, which is justified based on the low energies involved in our study (Federizzi et al. 2006; Krasheninnikov and Nordlund 2010). The public domain parallelized program LAMMPS (Plimpton 1995) was used for all simulations.

4.2.2 Geometry

Our simulation models comprised bundles of seven or 19 hexagonally arranged (26,0) SWCNTs (see Fig. 12). Each tube had radius 10.18 Å, length 59.6 Å, contained 1456 carbon atoms and was initially defect-free. Periodic boundary conditions (PBCs) were applied in the z direction to simulate an 'infinitely' long bundle. A number of "rings" (in most cases five) of 50 carbon atoms each in the 7-tube case (85 each for the 19-tube case to maintain the same fluence, see below), were initially placed around the CNT bundle, as shown in Fig. 12a. A gap of 4 Å between each ring, and each atom within each ring, was ensured to avoid initial

interactions. Within these constraints, the atoms in each ring were distributed randomly circumferentially and also along the length of the bundle.

4.2.3 Deposition Simulation

Random incident trajectories within the angle ±28°, illustrated in Fig. 12b for the 7-tube case, were assigned to each deposition atom. The strategy behind such a wide angle is to produce inter-tube links which connect the CNTs not just radially, but also circumferentially, which is desirable from the viewpoint of bundle mechanical properties. The deposition strategy simulated is somewhat idealised, but should be achievable through modification of the pulsed laser deposition procedure used in (Sorescu et al. 2003). In the 7-tube simulations the kinetic energy was the same for all incident atoms, and cases of 50, 100, 150, 200 and 300 eV/ion were examined. For the 19-tube simulations, variable energy strategies were considered in an attempt to achieve as uniform level of cross-linking within the bundle as possible.

Throughout the simulations free boundary conditions were applied in the x and y directions. An initial relaxation phase of 3.125 ps was applied to equilibrate the bundle, while the rings of C atoms were held fixed. An NVE ensemble was used with velocity rescaling at 0.5 K, while the velocity verlet algorithm was used to integrate the equations of motion with a time step of 0.25 fs. The innermost ring was then deposited without a thermostat so the energy of the impinging atoms was added to the CNT bundle. A time step of 0.0625 fs was used during the deposition which allowed the atomic interactions to be determined with sufficient accuracy

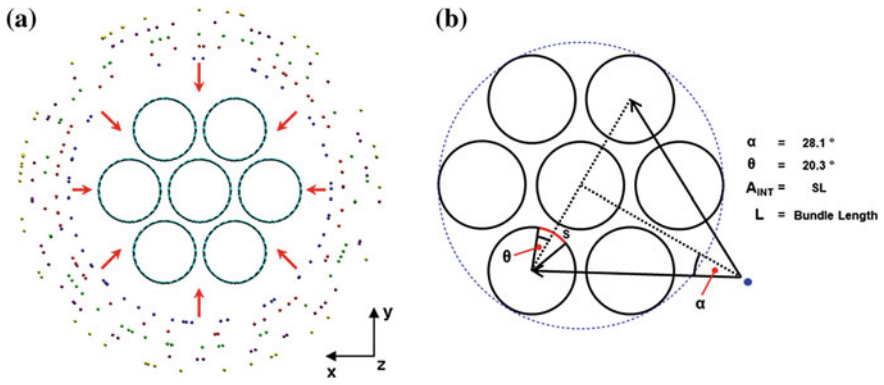

Fig. 12 **a** Hexagonally arranged 7-tube (26 0) SWCNT bundle model with five "rings" of deposition atoms; the atoms in each ring are distributed randomly in the axial and circumferential directions. **b** Random deposition atom trajectory parameters and reference area A_{INT} used to determine the number of bonds per area at each interface; the curve segment S is defined to include all atoms in the outer CNT which are within the interaction distance of centre CNT, for the potential function used

for all deposition energies. This was followed by a relaxation phase and a cooling phase. During the relaxation phase, the CNT bundle reached a new equilibrium state as evidenced by the levelling out of the potential energy. In the cooling phase, the bundle was cooled back down to 0.5 K, to facilitate analysis of defects (as done in (Xu et al. 2009; Pomoell et al. 2004)). This process was then repeated for the remaining rings.

The irradiation area for the CNT bundle was taken to be the circumference of the circle circumscribing the bundle multiplied by the bundle height, which is 125×10^{-14} cm^2 for the 7-tube bundle and 211×10^{-14} cm^2 for the 19-tube bundle. For the majority of our simulations, five rings of atoms were deposited, so the fluence (particles per unit area) ranged from 4.0×10^{13} cm^{-2} for one ring, up to 2.0×10^{14} cm^{-2} for five rings; in a few cases extra rings (higher fluence) were considered to extrapolate observed trends, as will be outlined later. According to (Pomoell et al. 2004), for Ar ions at 1 keV energy, the number of coordination defect numbers (signifying all kinds of defects, including inter-tube links) increases with fluence up to around 2×10^{14} cm^{-2} and then levels off. Our fluence values are at or below this level and would be classed as "low dosage" in (Krasheninnikov and Nordlund 2010). We define "dosage" differently here though as the total incident energy—which is the energy/ion multiplied by the number of incident ions—divided by the mass of the CNT bundle. This differs from fluence in that the energy of the incident ions, not just their number, is accounted for. Apart from the few extra cases mentioned above, our dosages ranged from 2 MGy (or J/kg) for one ring of 50 eV ions to 60 MGy for five rings of 300 eV ions. Any deposition atoms that rebounded off the CNT bundle and strayed outside a set radius (65 Å) of the CNT bundle were frozen in space to stop them from exiting and re-entering the periodic simulation box. This caused a small but negligible drop in the total system energy. For the 7-tube bundle, for all incident energies, five runs with varying initial random trajectories of the incident C atoms were performed in order to assess statistical variation. For the 19-tube bundle, due to the computational time required, only a small number of simulations were performed to evaluate strategies suggested by the 7-tube study.

4.3 Results and Discussion

4.3.1 Single-Atom Deposition

To validate the use of the modified REBO potential (Pastewka et al. 2008) in our problem, we first consider a direct impact of a single C atom on a CNT lattice atom (see Fig. 13a) Our simulations indicate that the deposition atom needs a threshold kinetic energy of $E_{th} = 21.9\,eV$ to fully displace an atom from the CNT lattice. At this energy, the displaced atom travels to the far wall of the impacted CNT and deposits there as an adatom, while the deposition atom takes its place in the lattice. Unlike most solids, the open structure of nanotubes allows this type of large

interstitial-vacancy Frenkel pair separation, so instant recombination does not necessarily occur (Krasheninnikov and Nordlund 2010). To knock out an atom from the lattice, a displacement threshold energy T_d must be transferred to the atom (Krasheninnikov and Nordlund 2010). For most types of deposition ions, the energy of the impinging ion needs to be substantially larger than this, e.g. classical binary collision theory gives (Krasheninnikov and Nordlund 2010):

$$E_{th} = \frac{(m_c + m_I)^2}{4m_c m_I} T_d \tag{15}$$

where m_I is the mass of the ion and m_c is the mass of the carbon atom. However from (15), when the impinging ion is carbon, $E_{th} = T_d$, i.e. complete energy transfer occurs, and the velocity of the ion after the impact is zero (regardless of the initial energy of the ion). In comparison, for Ar ions, $E_{th} = 1.4T_d$ and for electrons $E_{th} = 5469\ T_d$. Our simulations confirm that for direct impact with energies from 21.9 to 300 eV, no damage occurs at the impact site, and the impinging ion simply replaces the impacted ion in the lattice. Studies using molecular dynamics with the non-orthogonal density functional based tight binding (DFTB) force model (Krasheninnikov et al. 2005; Banhart et al. 2005) give $T_d \cong 20\,eV$for "dynamic" simulations (initial kinetic energy that needs to be given to a lattice atom for it to escape the system) and $T_d \cong 13$ eV for "static" simulations (energy to create a vacancy and an adatom—i.e. a widely separated vacancy-interstitial Frenkel-pair—from a perfect CNT lattice) for zigzag CNTs with diameter 2 nm. According to (Krasheninnikov and Nordlund 2010) the true value lies between these values, probably closest to the dynamic value. Thus our value of $E_{th} = 21.9$ eV, being just above the dynamic DFTB value for T_d in (Krasheninnikov et al. 2005; Banhart et al. 2005), is a very reasonable one, considering that binary collision theory is only an approximation so that E_{th} is likely to be somewhat above T_d.

We next consider a "penetrating" impact, i.e. a deposition atom aimed directly at the centre of a CNT hexagon, Fig. 13b. Our simulations indicate that the kinetic energy of the deposition atom decreases when it gets within the interaction distance of the CNT atoms, attains a minimum as it passes through the hexagon and then increases slightly thereafter until it leaves the interaction region and continues on. The net energy loss after passing through varied from ~22 eV for 50 eV initial energy to ~ 16 eV for 300 eV initial energy. To explain the occurrence of a minimum we note that while the deposition atom interacts with the lattice atoms, their coordination number increases giving an equilibrium bond distance greater than 1.42 Å. To squeeze through the hexagon, the deposition atom must pass within 1.42 Å of all the hexagon atoms, resulting in a repulsive force which gives the atom a kick once it passes through; hence the small recovery of kinetic energy. The energy lost by the deposition atom is transferred to the lattice (setting up vibrations and potentially forming defects) and has been termed "chemical erosion" in (Xu et al. 2009); this process obviously does not occur for non-bonding ions like He, Ar, and Ne. This observation for non-direct impacts, combined with

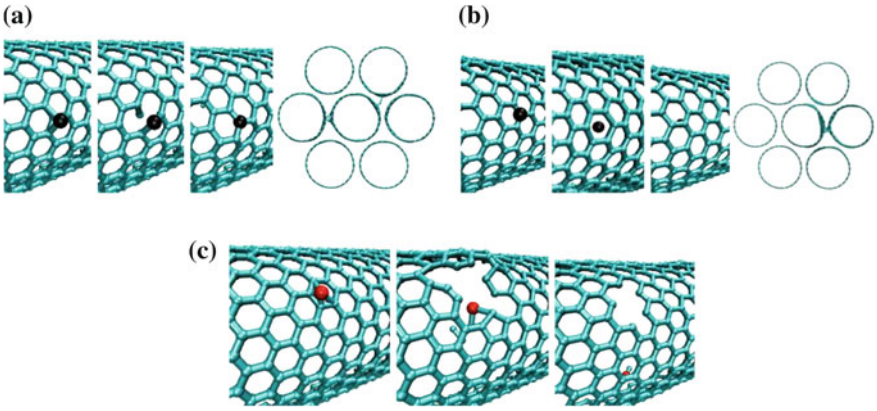

Fig. 13 Single C atom impacts. **a** Direct impact sequence, and cross-links formed for 200 eV case. **b** Penetrating impact sequence, and cross-links formed for 200 eV case. **c** Oblique impact sequence for 200 eV case

consideration of Eq. (1) for direct impacts, explains results in the literature wherein considerably higher deposition energies (around 50 eV) were required to effect modification of the CNT lattice using noble gas ions such as Ar (Pregler and Sinnott 2006; Salonen et al. 2002; Xu et al. 2009; Krasheninnikov and Nordlund 2010; Tolvanen et al. 2007) than for the C ions studied here.

The final single atom impact we consider is an oblique impact, 20° from the normal direction, (Fig. 13c). In this case, significant damage occurs, in keeping with (Krasheninnikov and Nordlund 2010) which stated that multi-vacancies normally appear for tangential hits. The unique ability of CNTs to "self-heal" themselves (Krasheninnikov and Nordlund 2010) by saturating dangling bonds is clearly visible in this figure, and is certainly an advantageous feature for our current purpose. Inter-tube links occur when atoms are knocked from the inside wall of the impacted CNT, either by a displaced lattice atom in the case of a direct impact, or by the deposition atom in the case of a penetrating impact—see Fig. 13a, b. No inter-tube links were formed for 20° oblique impacts.

4.3.2 Multi-Atom Deposition: Inter-Tube Links and Defects Formed

Figure 14 illustrates the level of inter-tube cross-link formation from multi-atom depositions on 7-tube bundles for a variety of energies and fluences. We see that very few bonds with the centre CNT are created at 50 eV/ion, Fig. 14a, and none involve deposition atoms (coloured red), even at a fluence of 2×10^{14} cm^{-2} (5 rings of 50 atoms). The number of such bonds increases for 100 eV/ion, Fig. 14b, and 150 eV/ion, Fig. 14c, and some deposition atoms make it to the centre of the bundle. At 200 eV/ion, significant bonding with the centre CNT can be achieved with a lower fluence of 1.21×0^{14} cm^{-2}, Fig. 14d, although because

of the random positioning and trajectories of the deposition atoms, the bonding is unevenly distributed; for a higher fluence of 2×10^{14} cm^{-2} at this energy, Fig. 14e, a high level of inter-tube bonding is achieved. Similar observations can be made for 300 eV, Fig. 14f, where significant inter-tube bonding occurs for a fluence of just 4×10^{13} cm^{-2} (just 50 atoms). At a fluence of 1.2×14 cm^{-2}, Fig. 14g, the damage to the CNTs is becoming excessive, and at 300 eV, 2×10^{14} cm^{-2}, the centre CNT is virtually amorphised, which is obviously undesirable for structural applications.

Figure 15 shows the large variety of inter-tube link types formed. The bonds involved in the cross-link are labelled according to the hybridisation of the participating carbon atoms, e.g. a bond between two four-coordinated C atoms is labelled an sp^3-sp^3 bond and so on. The bond lengths and angles are given in Table 3. Link types (c)-(f) were relatively common, so an average and a range over five different instances of each type is given in Table 3. Link types (a), (b) and (g-j) were very rare (less than five instances) so a range is not given. Even more complex links involving more than three interstitials were also found; the more complex links were mostly found at high dosages, perhaps through amalgamation of adjacent simpler links. We see that the bond lengths and angles differ somewhat from the equilibrium distances for pure sp, sp^2, and sp^3 bonds, indicating the bonds are stretched and distorted. Overall, bond type (d), in which a single interstitial atom is bonded to one atom in one CNT and two atoms in another CNT, was the most common type of cross-link. Bond types (a), (b), (d) and (f) were reported for C atom deposition on CNT bundles in (Federizzi et al. 2006), but the other types have not been reported before. Bond lengths, angles and frequency of occurrence are quite different from (Federizzi et al. 2006), e.g. direct bonding

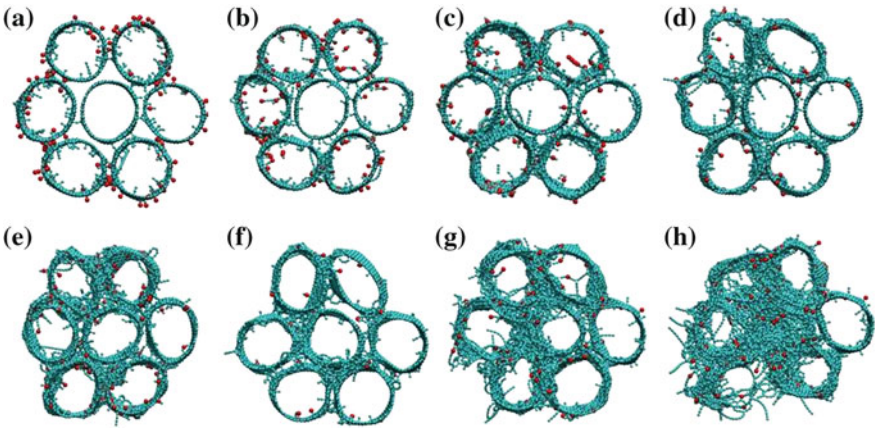

Fig. 14 Irradiated SWCNT bundles for: **a** 50 eV/ion, fluence $= 2 \times 10^{14}$ cm^{-2}, **b** 100 eV, fluence $= 2 \times 10^{14}$ cm^{-2}, **c** 150 eV, fluence $= 2 \times 10^{14}$ cm^{-2}, **d** 200 eV, fluence $= 1.2 \times 10^{14}$ cm^{-2}, **e** 200 eV, fluence $= 2 \times 10^{14}$ cm^{-2}, **f** 300 eV, fluence $= 4 \times 10^{13}$ cm^{-2}, **g** 300 eV, fluence $= 1.2 \times 10^{14}$ cm^{-2}, **h** 300 eV, fluence $= 2 \times 10^{14}$ cm^{-2}, (Original deposition atoms = *Red*; Original CNT rope atoms = *Blue*)

without an interstitial (bond type (a)) was found to be rare here, but more common in (Federizzi et al. 2006). The potential function used in (Federizzi et al. 2006) was a relatively old Tersoff potential (Tersoff 1988), which helps to explain these differences. Chainlike crosslinks of sp-hybridized atoms, like bond type (f), have been reported before between MWCNT walls in (Pregler and Sinnott 2006) following CH_3^+ ion irradiation. The cross-links formed will provide inter-tube mechanical coupling as desired. The stiffness and strength of each of these types of cross-link are likely to vary, although should be governed by the the weakest bond in the link. For example, bond type (f) contains a high-strength triple C–C bond, but the other bonds in the chain will determine the strength of the cross-link. The effects of these inter-tube bonds on mechanical properties of the bundle will be quantified in Sect. 5.

The side effect of irradiation is the formation of defects which weaken the structure. Figure 16 shows the variety of defects formed during our simulations which include single atom vacancies, two-atom vacancies, larger vacancies, Stone–Wales defects and a pentagon-hexagon (5665) defect that we have not seen before in the literature. Stone–Wales defects are thought to be responsible for the release of excessive strain under axial mechanical load of nanotubes (Krasheninnikov and Nordlund 2010), with ties in with an observation that after deposition, the CNT bundle was in a state of tension due to the geometric changes caused by defects and cross-links.

4.3.3 Effects of Deposition Parameters on Inter-Tube Cross-Link and Defect Characteristics

Figure 17 shows the number of "centre links", i.e. links formed between the centre CNT and the surrounding CNTs, and the number of "circumferential links", i.e. the links between the outer CNTs only, as a function of dosage, for 50–300 eV/ion energy levels. The results are presented per interface area, where the interface area for one CNT–CNT interface, A_{INT}, is defined in Fig. 12b. There are six interfaces involved in both the centre links and the circumferential links so the number of bonds is divided by $6A_{INT}$ in each case. To enable comparison of different energy levels at similar dosages, additional rings of deposition atoms (beyond five) were examined for the 50 and 100 eV cases (total 15 rings for 50 eV, 10 for 100 eV). The error bars demonstrate the variation obtained from the five different random trajectories applied for each data point. For 300 eV deposition, it was only possible to count the cross-links after one ring of atoms were deposited—after that the bundle became nearly amophous. We see that for energies in the range 100–200 eV, both the number of centre links and the number of circumferential links increase almost linearly with dosage, with only a slight dependency on energy. Thus within this energy range, a given percentage increase in either energy/ion or fluence has the same effect on cross-link density, giving us two ways to control the level of cross-linking. Below this energy range, i.e. for 50 eV/ion,

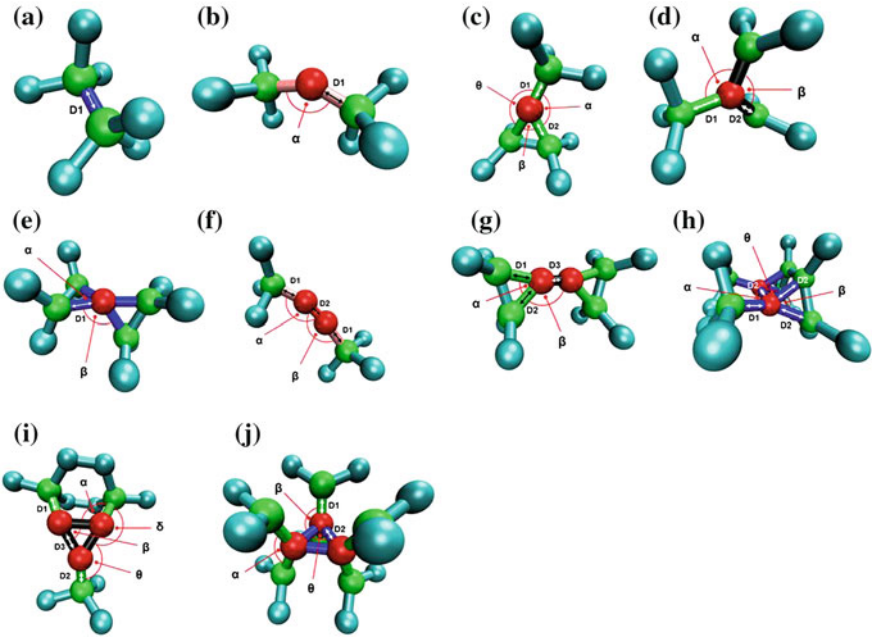

Fig. 15 Inter-tube cross-link types **a** direct sp^3-sp^3 bond, **b** two sp^3-sp bonds with one interstitial atom, **c** three sp^3-sp^2 bonds with one interstitial atom, **d** one sp^3-sp^2 and two sp^2-sp^2 bonds with one interstitial atom, **e** four sp^3-sp^3 bonds with one interstitial atom, **f** one sp–sp and two sp^3-sp bonds with two interstitial atoms, **g** one sp^2-sp^2 and four sp^3-sp^2 bonds with two interstitial atoms, **h** seven sp^3-sp^3 bonds, and two interstitial atoms, **i** three sp^3-sp^2 and three sp^2-sp^2 bonds, and three interstitial atoms, **j** six sp^3-sp^2 and three sp^3-sp^3 bonds, and three interstitial atoms. Atoms: *Red* = interstitial, *Green*: CNT atom involved in cross-link, *Blue*: CNT atom not involved in cross-link. Bonds: *Blue* = sp^3-sp^3, *Pink* = sp^3-sp, *Green* = sp^3-sp^2, *Black* = sp^2-sp^2, *Red* = sp–sp

the efficiency of bond formation with the centre CNT is significantly less. We found, for all our simulations, that the number of deposition atoms staying in the system ("trapped atoms") was approximately constant at 80 %, with the remainder being deflected out on first impact during oblique impacts. Thus we see that within the 100–200 eV energy range, as the incident energy increases, a higher percentage of the trapped atoms result in inter-tube links, whereas at lower energy, many trapped atoms merely "stick" (as adatoms) to the bundle, but do not cause inter-tube links.

We also observe that the number of circumferential links is approximately double the number of centre links. It is anticipated the distribution could be made more uniform by decreasing αin Fig. 12b. The single data points for 300 eV show a dramatic variation from the trends shown at lower energy levels. At 300 eV ~ 2 nm^{-2} links can be achieved radially and circumferentially with a fluence of just 4×10^{13} cm^{-2} or 50 deposition atoms. However, the fluence would have to be very carefully controlled at this energy level to avoid excessive damage

Table 3 Inter-tube cross-link bond lengths and angles

Cross link type*	$N_I^\dagger$	Bond types (no. of)	D1 (Å)	D2 (Å)	D3 (Å)	α (°)	β (°)	θ (°)	δ (°)
(a)	0	sp^3-sp^3 (1)	1.63						
(b)	1	sp^3-sp (2)	1.56			147			
(c)	1	sp^3-sp^2 (3)	1.51 ± 0.05	1.67 ± 0.07		128	58	163	
(d)	1	sp^3-sp^2 (1) sp^2-sp^2 (2)	1.55 ± 0.07	1.42 ± 0.02		126	109		
(e)	1	sp^3-sp^3 (4)	1.67 ± 0.08			58	117		
(f)	2	sp–sp (1) sp^3-sp (2)	1.57 ± 0.07	1.22 ± 0.01		150	168		
(g)	2	sp^2-sp^2 (1) sp^3-sp^2 (4)	1.68	1.65	1.25	58.4	135		
(h)	2	sp^3-sp^3 (7)	1.54	1.69		110	57	86	
(i)	3	sp^3-sp^2 (3) sp^2-sp^2 (3)	1.57	1.49	1.61	112	60	147	152
(j)	3	sp^3-sp^2 (6) sp^3-sp^3 (3)	1.49	1.65		128	112	60	

* Refer to Fig. 15, † N_I = number of interstitial atoms

to the bundle (Fig. 14). As noted in (Pomoell et al. 2004), this continuing increase in defect numbers (considering cross-links to be a type of defect) with irradiation energy is a result of the deposition atoms being primarily trapped in the system. Above 300 eV we expect the level of defects produced to level off as deposition atoms would start to pass right through the bundle, limiting the number of recoils. Our results are also in accord with (Xu et al. 2009), where for C ion deposition on a single SWCNT, the number of coordination defects increased linearly with ion energy up to 200 eV/ion and then started to level off as the ions started to pass through the CNT.

We also analysed the defects produced and found that as energy/ion increases from 50 to 200 eV, the number of single atom vacancies decreases sharply (by a factor of ~4), the number two atom vacancies stays relatively constant, the number of larger (more than two-atom) vacancies increases sharply (by a factor of ~4), and the number of Stone–Wales and pentagon-hexagon defects (small at all energies) stays constant. The overall conclusion is that at higher energy, larger holes are formed either from the first impact or through hole enlargement via subsequent impacts which overwhelm the self-healing ability of the CNTs. These findings are in line with the findings in (Krasheninnikov et al. 2005) that the transformation of single atom vacancies to double vacancies has quite a low energy cost relative to formation of single atom vacancies from pristine tubes, because only two bonds need to be broken instead of three, and the double vacancy reconstruction, Fig. 16b, is more stable than the one vacancy reconstruction, Fig. 16a, due to the absence of dangling bonds.

A feature that is likely to strongly influence bundle tensile strength is the largest hole in the bundle. Figure 18 shows the largest hole size (measured as the largest

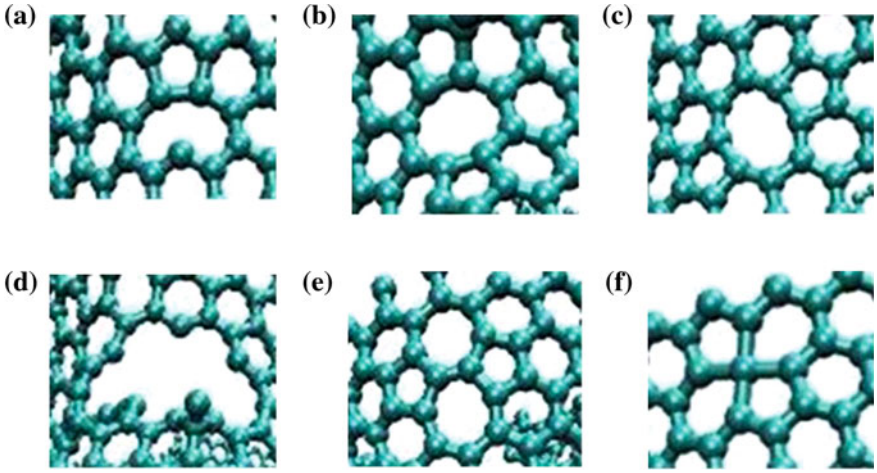

Fig. 16 Vacancies/defects formed for irradiated CNT rope models **a** one atom vacancy (symmetric reconstruction), **b** two atom vacancy (symmetric reconstruction), **c** two atom vacancy (asymmetric reconstruction), **d** greater than two atom vacancy, **e** Stone–Wales (5775) defect, **f** pentagon-hexagon (5665) defect

distance across the hole) as a function of dosage for various energies. We see that largest hole size increases with dosage, but there is also a dependency on energy with lower energies producing smaller holes for the same dosage and thus being preferable.

4.3.4 Irradiation Strategies to Improve Mechanical Performance in 7-Tube Bundles

As stated at the start, the ideal result for our purposes would be a controllable, uniform level of inter-tube cross-links between all adjacent tubes with a minimum level of defects in the CNT walls. This would allow transfer of load between CNTs, enabling all of them to engage in loading, with the least loss in strength due to intra-wall defects. From the previous section, we conclude that for seven-tube bundles, the achievement of a uniform and controllable level of inter-tube cross-links via C ion irradiation is possible within the energy range of 100–200 eV/ion. To keep the largest hole size to a minimum, which is likely to be the key parameter for tensile strength, lower energy is best, so the optimum strategy is to use energy/ion of $\sim$100 eV, and to control the cross-link density through the fluence. The desirable level of cross-link density will be discussed in the next section, but in general terms higher density will give higher interface shear stiffness and strength, and based on results in (Pavia and Curtin 2011) for CNT-diamond matrix composites, is likely to produce higher sliding stress during pull-out of a CNT from the bundle, which increases toughness. Too high a level however could lead to CNT

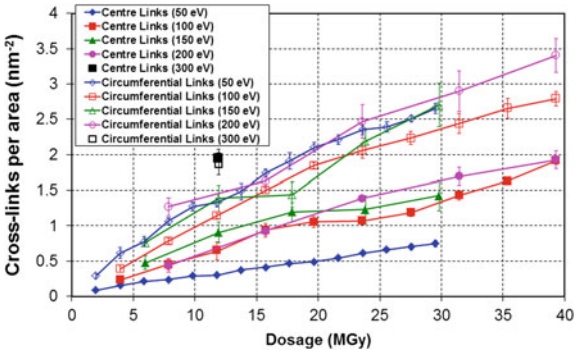

Fig. 17 Number of inter-tube links per area (A_{INT} in Fig. 12b), between centre CNT and outer CNTs ("Centre Links"), and between outer CNTs only ("Circumferential Links") as a function of dosage, with incident beam energies of 50–300 eV; error bars show standard error or $\sigma/\sqrt{N}$ where N is the number of repeats with different random trajectories

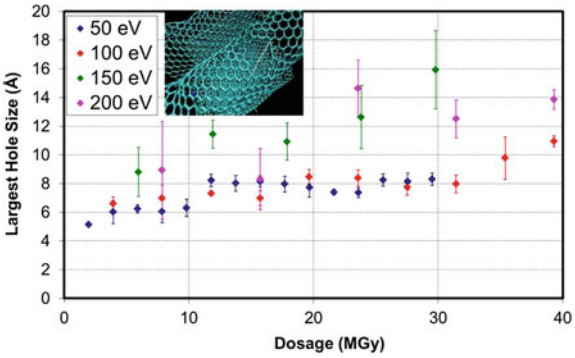

Fig. 18 Largest hole size as a function of dosage, with incident beam energies of 50–200 eV; error bars show standard error or $\sigma/\sqrt{N}$ where N is the number of repeats with different random trajectories

breakage during pull-out giving a brittle response. Our results show that for 7-tube bundles it is possible to engineer the interface to achieve the desired response.

4.3.5 Extension to Larger Bundles

To examine if a satisfactory irradiation strategy can also be found for larger bundles, we now consider the next largest hexagonally-packed bundle arrangement which consists of 19 tubes. Six different irradiation strategies, all involving the same overall dosage (24.6 MGy) are considered. The final state of the bundle and the number of inter-tube links per interface area at each interface are shown in Fig. 19. Note that there does seem to be some bias towards more cross-links on the left, suggesting the positions of the irradiating atoms were not truly random, but the effect of this on the results is of minor importance. The first strategy involved irradiation at a constant energy level of 100 eV/ion and we see from the results in

Fig. 19a that the two outer layers of the bundle are very well-connected both circumferentially and radially, but the centre CNT remains almost completely unconnected. In the second strategy the energy level is doubled to 200 eV/ion (while the fluence is halved), and Fig. 19b shows that the resulting level of cross-linking is very similar to the first strategy. This is quite an interesting result as it shows that within the range 100–200 eV/ion, the cross-link density between the outer CNTs and the next innermost layer of CNTs is a function of dosage and thus can be controlled either through fluence or energy/ion; this is the same result as we found for 7-tube bundles.

In the third strategy, we attempt a variable energy approach, applying a 8×10^{13} cm^{-2} fluence at 300 eV/ion, then 8×10^{13} cm^{-2} fluence at 150 eV/ion, then 4×10^{13} cm^{-2} fluence at 100 eV/ion. Given the results for 7-tube bundles, in which 300 eV/ion was deemed to be too high an energy level due to the excessive damage caused, we expected this strategy to be successful in forming cross-links with the centre CNT. However over the six interfaces with the centre CNT we see from Fig. 19c that the average number of cross-links per interface area is only 0.42 nm^{-2}, which is very low in comparison to the results for 7-tube bundles (see Fig. 17). In the fourth strategy we increase the initial energy to 400 eV/ion (4×10^{13} cm^{-2} fluence) followed by 8×10^{13} cm^{-2} fluence at 200 eV/ion, then 8×10^{13} cm^{-2} fluence at 100 eV/ion, but this gives just 0.31 nm^{-2} links to the centre CNT (Fig. 19d).

The best results are found with the fifth strategy of 500 eV/ion (4×10^{13} cm^{-2} fluence), followed by 150 eV/ion (8×10^{13} cm^{-2} fluence) and then 100 eV/ion (8×10^{13} cm^{-2} fluence), which gives 0.70 nm^{-2} links to the centre CNT (Fig. 19e). However damage to some of the outer tubes is becoming excessive, and a few interfaces are so amorphous that counting links is impossible (signified by "M" for "multiple links"). In the last strategy the initial energy is increased to 600 eV/ion (4×10^{13} cm^{-2} fluence), followed by 1.6×10^{14} cm^{-2} fluence at 100 eV/ion. This again gives 0.70 nm^{-2} links with the centre CNT (Fig. 19f), but in a less desirable way in that 16 of them are with just two of the surrounding CNTs, with no links at all to two adjacent CNTs. In this last case, the centre CNT has moved off-centre to the left, making links with CNTs from further irradiation impossible, and the level of damage is also clearly excessive. Further improvements could be obtained through variations on the fifth strategy, but the overall trends are clear, and given the long computation time for the 19-tube simulations, it was decided not to optimise further.

Our results are in line with those in (Federizzi et al. 2006) and (Salonen et al. 2002). In (Federizzi et al. 2006) C ion irradiation on CNT bundles, with energies up to 200 eV/ion, produced only a few cross-links with the third CNT layer. In (Salonen et al. 2002), Ar ion irradiation on CNT bundles with energies up to 250 eV/ion caused no cross-links beyond the first interface layer, and iradiation at 500 eV/ion produced very few links beyond the third CNT layer. Neither (Federizzi et al. 2006) nor (Salonen et al. 2002) presented explicit information on the damage produced by irradiation though, as has been done here.

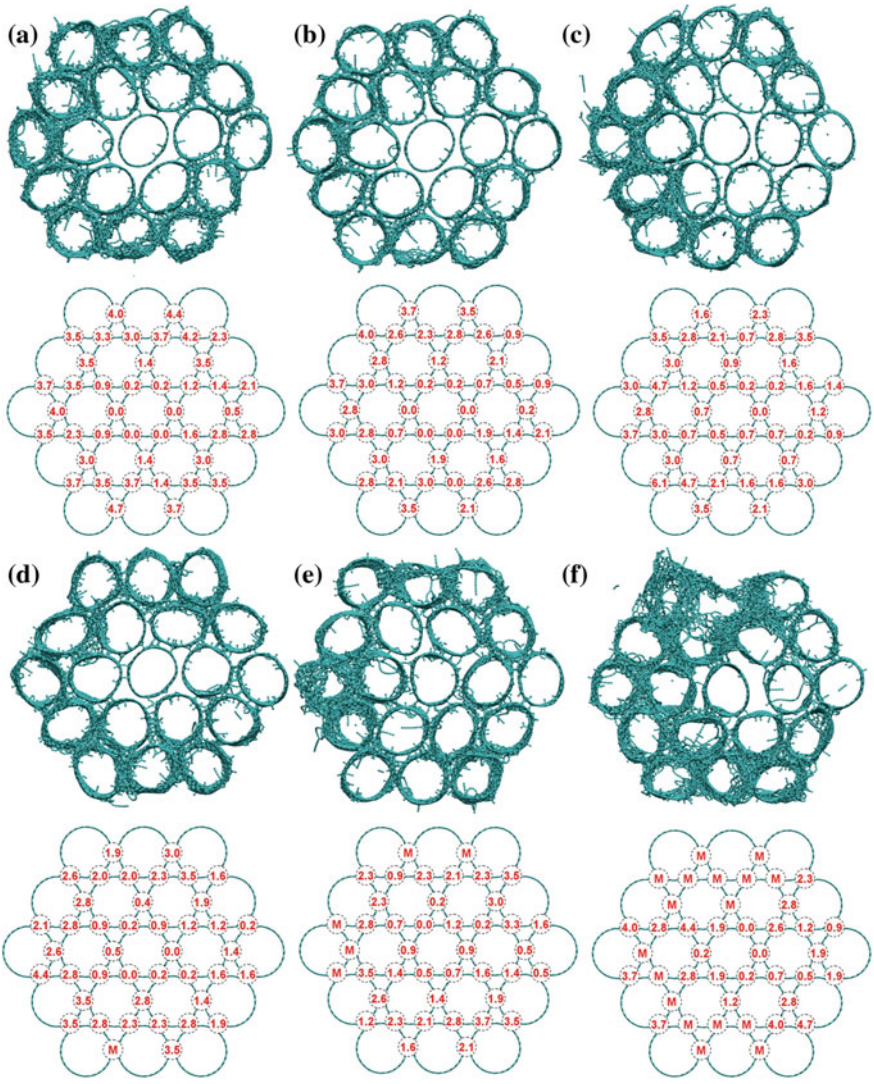

Fig. 19 Final state and number of inter-tube cross-links per area (A_{INT} in Fig. 12b) at each CNT–CNT interface for various irradiation strategies with same overall dosage **a** 4×10^{14} cm^{-2} fluence, 100 eV/ion, **b** 2×10^{14} cm^{-2} fluence, 200 eV/ion, **c** 8×10^{13} cm^{-2} fluence at 300 eV/ion, then 8×10^{13} cm^{-2} fluence at 150 eV/ion, then 4×10^{13} cm^{-2} fluence at 100 eV/ion, **d** 4×10^{13} cm^{-2} fluence at 400 eV/ion, then 8×10^{13} cm^{-2} fluence at 200 eV/ion, then 8×10^{13} cm^{-2} fluence at 100 eV/ion, **e** 4×10^{13} cm^{-2} fluence at 500 eV/ion, then 8×10^{13} cm^{-2} fluence at 150 eV/ion, then 8×10^{13} cm^{-2} fluence at 100 eV/ion, **f** 4×10^{13} cm^{-2} fluence at 600 eV/ion, then 1.6×10^{14} cm^{-2} fluence at 100 eV/ion. "M" stands for multiple in cases where the interface is too amorphous to allow counting of links

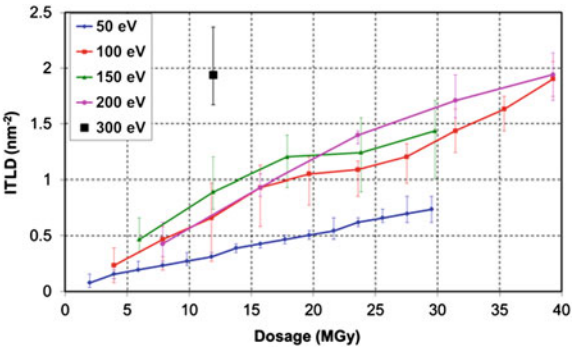

Fig. 20 Areal inter-tube link density (ITLD or ρ), as a function of dosage, with incident beam energies of 50–300 eV (only links to centre CNT included)

It is clear from the results that controlling the cross-link density in bundles containing more than seven tubes, while simultaneously limiting the damage to acceptable levels is a much more difficult task as the bundle size increases. One can imagine that for the next size bundle up (37 tubes) it will be extremely difficult to reach the centre CNT without destroying the outer layer of CNTs completely. Electron irradiation will be more successful in penetrating to the centre of large bundles, and the most successful experimental demonstrations of inter-wall and inter-tube cross-linking to date have involved electron irradiation (Peng et al. 2008; Filleter et al. 2011). However, in electron irradiation all the interstitial C atoms in the cross-links must come from the CNT lattice, so the level of damage is likely to be high, e.g. in the CNT bundles in (Filleter et al. 2011) the highest tensile strength achieved was 17 GPa, which while impressive is well below achievable CNT strengths (Peng et al. 2008).

One possible future scenario to achieve highly cross-linked CNT fibres through C ion irradiation is through a modification of the method in (Zhang et al. 2004; Sears et al. 2010; Ghemes et al. 2012) in which CNT yarns are created by drawing multiple small bundles of CNTs simultaneously from a CNT forest and then twisting them into a rope. Significantly the small bundles are described in (Zhang et al. 2004) as containing just "a few" CNTs and prior to twisting are laid out parallel to each other (Fig. 1 in (Zhang et al. 2004)). Irradiation at that point in the process with C ions at 100–200 eV/ion could produce excellent results due to the small size of the bundles being pulled off. The extra C adatoms deposited might also lead to cross-links between the bundles as they are brought into intimate contact through the twisting process. However, it needs to be pointed out that the CNTs in (Zhang et al. 2004; Sears et al. 2010; Ghemes et al. 2012) are MWCNTs unlike the SWCNTs studied here. The optimal irradiation parameters for MWCNT bundles would be quite different from those found here for two reasons. Firstly the objective would be different for MWCNT bundles in that not only inter-tube but also inter-wall cross-links would be desired for optimal mechanical performance,

making the overall problem significantly more complex. Secondly, MWCNTs perform differently to SWCNTs under irradiation, being generally more stable because the atoms sputtered from inner shells remain in the MWCNT and Frenkel pairs created inside the MWCNT can easily recombine (Krasheninnikov and Nordlund 2010). Thus further study is needed to establish suitable irradiation parameters for MWCNT bundles, and to determine if the suggested method of irradiating CNTs prior to twisting into a yarn would produce useful results.

4.4 Concluding Remarks

Carbon ion irradiation of single wall carbon nanotube bundles, for the purpose of achieving inter-tube cross-links to enhance mechanical performance, has been investigated using classical molecular dynamics. For 7-tube bundles, within the range 100–200 eV/ion, the level of cross-linking is directly proportional to dosage and therefore controllable. Lower energy irradiation produces smaller-sized defects so $\sim$100 eV/ion is the preferred energy level. More than 10 different types of cross-link are formed, and a variety of defects are created including single atom and multi-atom vacancies, adatoms, Stone–Wales defects, and 5665 defects. The defect level becomes excessive if either the energy or the fluence is set too high, with amorphisation occurring at the highest level of energy and fluence considered. Extension to larger bundles however is significantly more challenging. In 19-tube bundles, irradiation within the same 100–200 eV/ion range used for 7-tube bundles produces satisfactory cross-linking in the first two layers of CNTs, but almost none with the centre CNT. An energy level of $\sim$500 eV/ion is required to form significant numbers of cross-links with the centre CNT, and at this energy level careful control of fluence is required to avoid excessive damage to the outer layer of CNTs. Larger bundles are likely to prove even more problematic. Thus ion irradiation is likely to be of practical value for improving mechanical properties only for small bundles. However, a scenario whereby small bundles are irradiated prior to twisting into ropes is suggested as a possible future method for producing macro-scale cross-linked CNT fibres.

5 Quantification of the Potential Improvement in the Mechanical Properties of Carbon Nanotube Bundles by Carbon Ion Irradiation

In Sect. 4 we presented a molecular dynamics study of the carbon-ion irradiation of SWCNT bundles, with carbon ions. We demonstrated that carbon-ion irradiation induces CNT cross-links but also causes defects. The ability to control the level of cross-linking through adjusting the energy/ion or the fluence was demonstrated in principle for small bundles. The cross-links formed were found to be

of several different types, from simple direct bonds between CNTs, to complex links involving one or more interstitial atoms. In the present section, we study the relationship between the cross-links and defects induced by carbon ion irradiation of SWCNT bundles, and the resulting mechanical properties. We quantify the improved inter-tube shear and toughness properties through pull-out tests of individual CNTs from the bundle. This also gives us the opportunity to examine the applicability of standard "friction laws" to nano-scale sliding interfaces, building on the work in (Pavia and Curtin 2011) on sliding between CNTs and diamond matrices. We also measure the reduction in tensile properties due to induced defects. Our study uses a recently-developed reactive bond-order potential with environment-dependent first nearest-neighbour definition (Pastewka et al. 2008) which accurately simulates bond-forming and bond-breaking processes in carbon-based systems. Our simulations reveal that with careful control of irradiation parameters, shear and toughness parameters are greatly increased, with only modest reductions in tensile properties. Interstitial C atoms are found to play a key role in sliding behaviour. Within a certain range of cross-link density, the interface shear modulus, shear stress at onset of debonding, and frictional sliding stress after debonding are all linearly related to cross-link density making controlled design of fibre shear properties feasible.

5.1 Simulation Method

5.1.1 Interatomic Interactions

To study the pull-out of CNTs from a bundle and tensile strength of bundles, an accurate interatomic potential capable of representing bond breaking and bond forming is essential. Thus, as in Sect. 4, we use the modified REBO potential recently presented in (Pastewka et al. 2008).

5.1.2 Geometry and Irradiation Simulations

Full details of the irradiation simulations are given in Sect. 4. In this section we focus on the 7-tube bundle in Fig. 12.

5.1.3 Mechanical Test Simulations

The mechanical properties of the pristine and irradiated SWCNT bundles were evaluated through MD simulations of tensile tests and "pull-out" tests involving drawing out of the centre CNT. The bundles tested were those for which one, three, and five rings of atoms had been deposited, giving 15 tensile tests and 15 pull-out tests at each deposition energy. As in the deposition simulations, periodic

boundary conditions were applied for both tests in order to simulate an 'infinitely' long bundle and to avoid end effects. The MD time step was set to 0.25 fs and a velocity re-scaling thermostat was used to maintain the temperature of the CNT rope models at 0.5 K throughout each test. During the initial relaxation phase which lasted 12.5 ps for the tensile test and 18.75 ps for the pull-out test, both ends of the CNT bundle were fixed in z and free to move in x and y for both tests. After relaxation, the tensile and pull-out tests were performed. An NVE microcanonical ensemble was used for the pull-out tests, whereas an NPT ensemble was used for the tension tests to allow the volume of the simulation box to vary as it is deformed in the z direction.

For the tensile test, the top face of the periodic box was displaced 0.025 Å in the z direction every 0.25 ps, while the bottom face was kept fixed in z, until the bundle failed. The applied stress was measured on the top face. For the pull-out test, the bottom two rings of atoms for the outer CNTs were fixed in the z direction, and the centre CNT was drawn out by displacing its upper two rings of atoms 0.025 Å every 0.25 ps, across the periodic box boundaries. The pull-out force was obtained as the force on these two rings of atoms. Relaxation was performed between displacements. For both test series, the displacement rate was 10 m/s and all CNTs were free to move in the x and y directions throughout.

5.2 Results and Discussion

5.2.1 Irradiation Effects on Inter-Tube Shearing

The irradiation simulations resulted in inter-tube cross-links (Fig. 14). More than ten different types of cross-link were observed, including direct sp^3 bonded links with no interstitial C atom, and links mediated by one or more interstitial C atoms. For full details see Sect. 4. The cross-links relevant to the pull-out tests are those between the outer tubes and the centre tube, hereafter referred to as "centre links". We define a reference area for shear resistance as A_{SH}, see Fig. 12. This area includes all atoms in the outer CNTs which are within the interaction distance of the centre CNT atoms for the potential (Pastewka et al. 2008) used here (prior to irradiation) and includes all centre links post-irradiation. We divide the number of centre links by A_{SH} to get an areal inter-tube link density (ITLD or ρ). Figure 20 shows ρ as a function of dosage for energy/ion of 50–300 eV. We see that in the range 100–200 eV/ion, ρ is proportional to dosage, and thus can be controlled by varying either the fluence or the energy/ion. Lower energy irradiation (50 eV/ion) was relatively ineffective in forming centre links. Higher energy irradiation (300 eV/ion) was highly effective in forming centre links, but production of defects was excessive (see Sect. 4).

The average interfacial shear stress is calculated as the pull-out force divided by A_{SH}. Figure 21 shows the pull-out stress versus pull-out distance for the irradiated SWCNT bundles; only the result which is most representative of the five random

trajectory instances is shown for clarity. For comparison, the result for the pristine case is shown in Fig. 21a. We see that the nano-scale interface response resembles that of traditional micro-scale composites: pull-out is characterized by an elastic stretching region at small displacements ($x < 1$–2 Å), followed by the onset of debonding, in which inter-tube bonds are broken, up to a displacement of 2–3.5 Å and then a drop to a lower oscillating sliding stress ("pull-out sliding" regime). The only exception to this behaviour is the highest dosage case (39.3 MGy) where the shear stress reaches a peak of 10.1 GPa and then drops to zero. In this case, the centre CNT did not pull out and instead failed in tension. Both the elastic and sliding response vary with dosage, which as mentioned above is directly related to ρ. Notably, the effective frictional stresses at the interface after debonding are quite high (several GPa) for higher cross-link densities.

The nano-scale pull-out behaviour shown in Fig. 21, resembles micro-scale composite response, and can be understood by analysing the atomic deformation mechanisms at the interface. As noted above, more than ten different types of inter-tube cross-link were found post-irradiation. Figure 22 shows snapshots in time of the pull-out behaviour of three of them: a direct link, a link involving one interstitial carbon atom, and a link involving two interstitial carbon atoms. The key finding from this figure is that when cross-links involving an interstitial atom (Fig. 22b, c) break (at the end of the elastic region of pull-out), new links are formed and broken several times subsequently. On the other hand, direct links in which no interstitial is present (Fig. 22a), once broken, do not reform, and so do

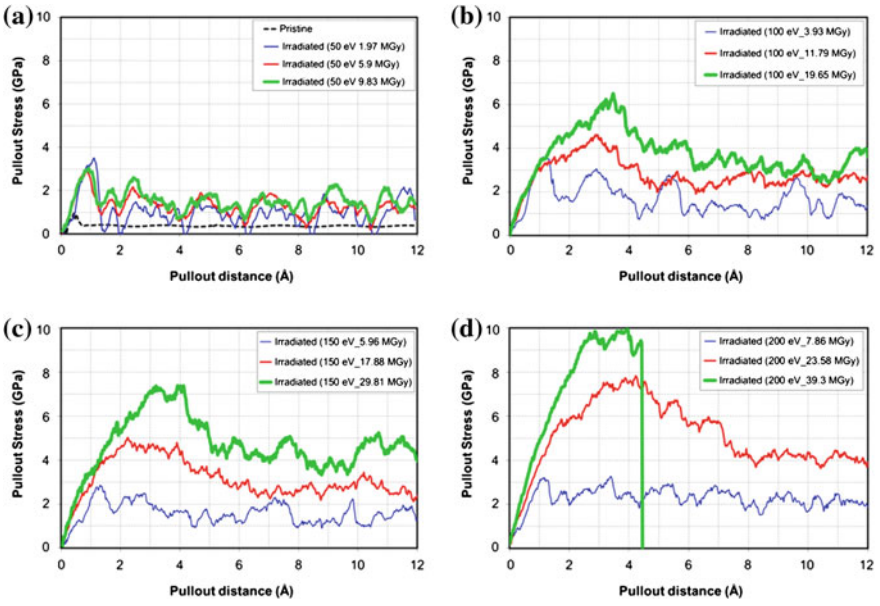

Fig. 21 Pull-out stress versus pull-out distance for irradiated CNT bundles with incident energies of **a** 50 eV, **b** 100 eV, **c** 150 eV, and **d** 200 eV

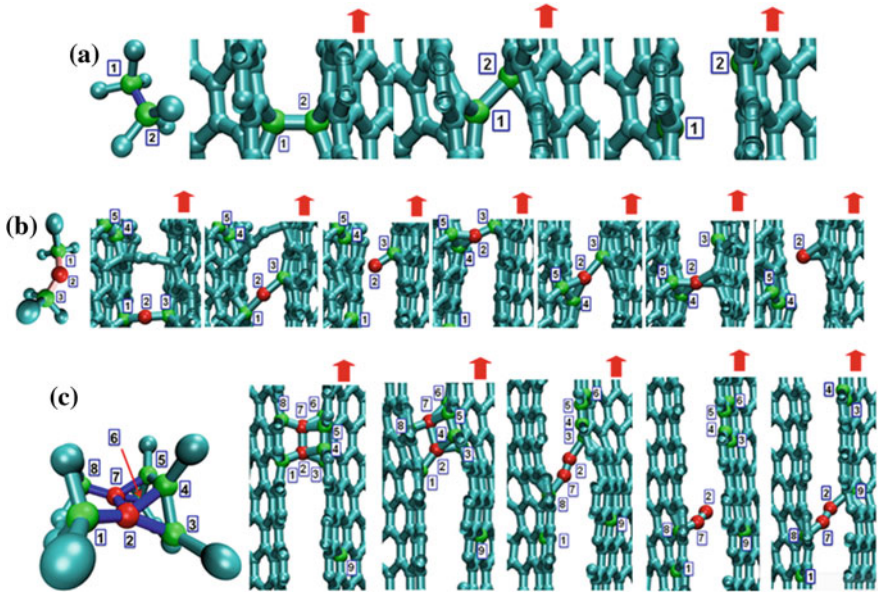

Fig. 22 Bond breaking and re-forming during pull out of centre CNT. Snapshots in time, time increasing from *left to right*, numbers are to guide eye in following individual atoms over time **a** direct sp^3-sp^3 bond, **b** cross-link with one interstitial and two sp^3-sp bonds, **c** cross-link with two interstitials and seven sp^3-sp^3 bonds

not contribute to the pull-out force in the sliding regime. The bond breaking and reforming processes for interstitial-mediated cross-links are responsible for the overall '*stick and slip*' behaviour observed. The directly bonded cross-links contribute to the initial elastic behaviour but not to the sliding stress. We can conclude that to produce tough CNT-fibres, in which significant energy is absorbed during CNT pull-out from the fibre, it is desirable to have C interstitials at CNT interfaces, since inter-tube links will spontaneously form and break during sliding. This makes C ion deposition an attractive option over irradiation by electrons or other types of ions, since extra C atoms are added to the system, so not all interstitials have to come from knocking out atoms from the CNT lattice (thereby reducing tensile strength).

The pull-out force was divided by the number of centre links to give the pull-out force per centre link, which is plotted against pull-out distance in Fig. 23, for energies ranging from 50–200 eV; only representative instances among the five random trajectories for each case are shown for clarity. The ITLD (ρ) is also shown in the legend. In (Pavia and Curtin 2011) the pull-out force per cross-link involving a single interstitial carbon atom between a CNT and a diamond matrix was found to collapse all the data for different interstitial densities onto nearly a single universal curve for interstitial C atom densities of 0.73–2.18 nm^{-2}. The system studied here differs from that in (Pavia and Curtin 2011) in that the cross-

links are between two CNTs rather than between a CNT and diamond matrix, and there are several different types of cross-link, some of which are direct links and some of which involve one or multiple interstitials. We see from Fig. 23 that for low cross-link densities, $\rho < 0.7$ nm^{-2}, the force per cross-link is high and oscillates erratically. This is due to the small number of inter-tube links at this density, given the short length of the tubes studied. With just a few links distributed randomly axially and circumferentially very unsymmetrical loads on the centre CNT occur, with large relative force oscillations as individual cross-links break and re-form. However, as ρ increases into the range considered in (Pavia and Curtin 2011), i.e. $\rho > 0.7$ nm^{-2} (which corresponds to > 18 centre links in total in the system) the curves collapse quite well onto a single curve, as in (Pavia and Curtin 2011). We can thus say that the varying strength of the different cross-link types averages out if enough of them are present, and we can directly relate the shear mechanical properties to the number of cross-links present orρ. Unlike (Pavia and Curtin 2011) however, we find an upper limit to this, since above $\rho = 1.7$ nm^{-2}, we see from Fig. 23d that failure of the centre CNT during pull-out can occur since the interfacial shear stress is too large. It needs to be borne in mind that, unlike in (Pavia and Curtin 2011), the centre CNT, like all the CNTs in the bundle, contains defects such as vacancies and Stone–Wales defects due to the irradiation process, so the value of ρ needed to cause pull-out CNT failure would vary somewhat depending on the damage level in the pull-out CNT.

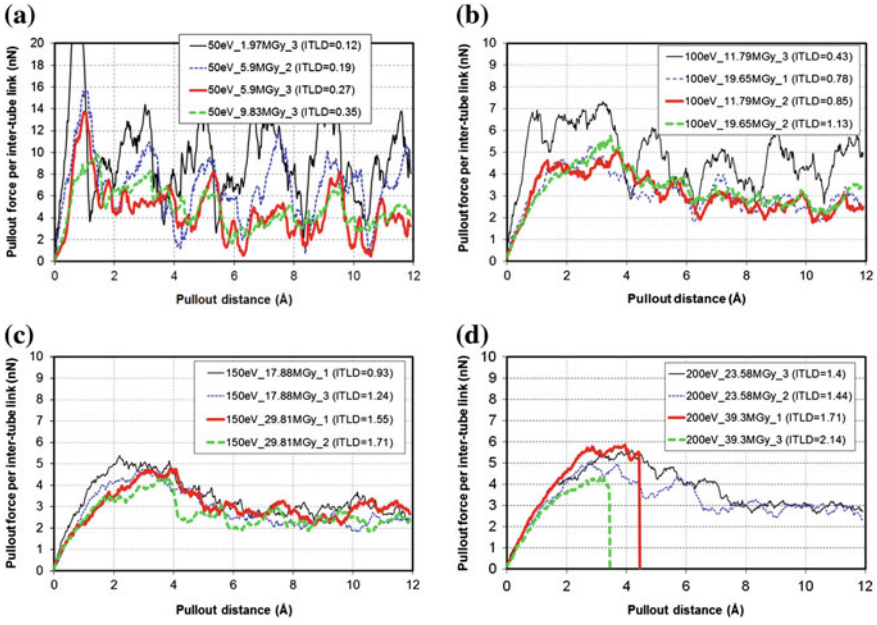

Fig. 23 Pull-out force per inter-tube cross-link with the centre CNT versus pull-out distance for irradiated CNT bundles with incident energies of **a** 50 eV, **b** 100 eV, **c** 150 eV, and **d** 200 eV (ITLD = inter-tube link density or $\boldsymbol{\rho}$ in) $1/nm^2$

In Fig. 24, we plot some key parameters against ρ, for $\rho > 0.7\ \text{nm}^{-2}$. Figure 24a shows the "interface shear modulus" μ prior to debonding. Here we have defined the interface shear strain γ_{xy}as the applied displacement divided by the inter-tube gap. From the graph we see that μ scales linearly with ρ, in the range $\rho = 0.7 - 1.7\ \text{nm}^{-2}$,

$$\mu \cong 10\rho\ \text{GPa nm}^2 \tag{16}$$

This is more than double the value $\mu \cong 4.6\rho$ GPa nm^2, found in (Pavia and Curtin 2011) for CNT sliding in a diamond matrix with interstitial carbon atoms. On the other hand, in (Xia et al. 2007) an effective shear modulus for the interface between walls of a DWNT directly bonded with sp^3-bonds was found that scales with the bond fraction f. Converting their bond fraction f to an areal density of bonds ρ, their result is

$$\mu \cong 12\rho\ \text{GPa nm}^2 \tag{17}$$

Since in our system, both direct bonds and bonds mediated by interstitial C atoms are present, it is reasonable that our result should be between the values found in (Pavia and Curtin 2011) and (Xia et al. 2007). Furthermore, the bonds in (Pavia and Curtin 2011) involved one interstitial C atom initially bonded to just one CNT atom and one diamond matrix atom. As described in (O'Brien et al.

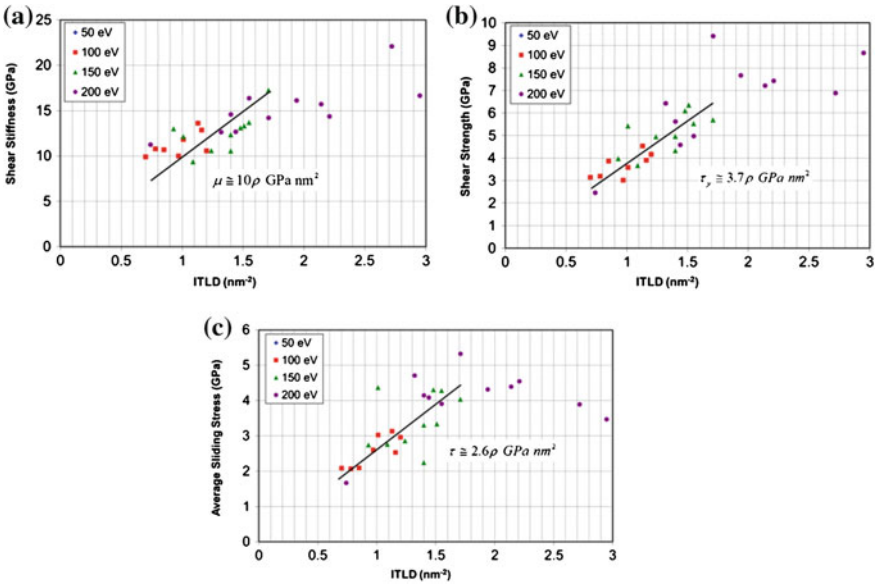

Fig. 24 Elastic and sliding parameters for pull-out versus ITLD (or $\boldsymbol{\rho}$) for irradiated CNT bundles **a** interface shear modulus, **b** interface shear strength, and **c** interface sliding stress. *Lines* show linear relationships in the range $\rho = \mathbf{0.7 - 1.7 nm^{-2}}$

2013) many of the interstitial atoms in our system were initially bonded to more than one atom in each CNT—an example can be seen in Fig. 22c—which is a stiffer arrangement, so the interstitial-mediated bonds here are on average stiffer than in (Pavia and Curtin 2011). We see that with an areal density of cross-links, $\rho = 1.7$ nm^{-2}, we get an interface shear modulus 17 GPa. This is more than three times the value of 5 GPa found from our simulations of CNT bundles without cross-linking.

In Fig. 24b, c we see that in the range $\rho = 0.7 - 1.7$ nm^{-2}, the interface shear stress at the onset of debonding or yield stress, τ_y (note this is not the maximum shear stress during pull-out, it is the stress at the end of the linear region of the load–displacement curve), and the frictional sliding stress after debonding, τ (calculated for pull-out distance $x > 8$ Å) are both linearly dependent on ρ, scaling as

$$\tau_y \cong 3.7\rho \,\text{GPa nm}^2 \tag{18}$$

$$\tau \cong 2.6\rho \,\text{GPa nm}^2 \tag{19}$$

Concerning the interface shear strength τ_y, we see that with $\rho = 1.7$ nm^{-2}, we get an interface shear strength of 6.3 GPa. This is seven times larger than the value of 0.9 GPa we found for CNT bundles without cross-linking. The equation for τ is slightly below the value found in (Pavia and Curtin 2011) ($\tau \cong 3\rho \,\text{GPa nm}^2$), which contrasts with the finding on modulus above. The reason for this becomes clear from examining Fig. 22c and other similar cases, from which we see that while original cross-links may be quite complex and initially stiffer than those in (Pavia and Curtin 2011), re-bonds after failure tend to be chain-like, resembling the cross-links involving a single interstitial in (Pavia and Curtin 2011). In addition, unlike (Pavia and Curtin 2011) there are some direct bonds between CNTs in our system, which as noted above do not reform once broken and thus do not contribute to the sliding stress. Our results provide further evidence to that in (Pavia and Curtin 2011) that a friction-like sliding stress emerges at the atomistic scale, thus conforming to the standard constant sliding stress used in the majority of models to predict composite performance.

An important issue in composite behaviour is toughness, which is dominated by the energy dissipated by frictional sliding during fibre pull-out. The energy dissipated due to "friction" generated by breaking and re-forming of interstitial-mediated inter-tube bonds can be computed as the work done during pull-out, corresponding to the area under the applied force versus displacement curve. Typically the pull-out work is converted into a fracture toughness by division by the composite cross-sectional area; here we take the "composite" cross-sectional area to be the area of the circle enclosing the 7-tube bundle. For a density of $\rho = 1.46$ nm^{-2}, we obtain a toughness of $\sim$2.8 J m^{-2} for just 1 nm of pull out. Such a value far exceeds the work done by weak van der Waals bonding between perfect nanotubes (0.2 J m^{-2} for 1 nm of pull out in our simulations).

5.2.2 Tensile Test Simulations

The trade-off for the above greatly enhanced shear properties is reduced tensile strength due to irradiation-produced defects. For our tensile tests, the tensile stress was defined as the tensile force divided by the cross-sectional area of the CNT bundle (~ 15 nm^2), which was computed as seven times the area of a single CNT, as given in Eq. (20),

$$A = 7\pi\left[\left(r + \frac{t}{2}\right)^2 - \left(r - \frac{t}{2}\right)^2\right] \tag{20}$$

where r is the CNT radius and $t = 0.335$ nm is the graphitic layer thickness. The strain was calculated by dividing the change in length by the original length of the CNT bundle. Figure 25a shows the tensile stress versus strain for the bundles irradiated with energies of 100 eV/ion (for all random trajectories)—the curves from other irradiation energies are similar in form. For comparison, our result for the pristine (unirradiated) bundle is also shown. For the pristine case, the Young's modulus, tensile strength and maximum strain are 860 GPa, 91 GPa and 17.2 % respectively, which is at the low end of theoretical values in the literature for individual CNTs (Ogata and Shibutani 2003; Peng et al. 2008; Mielke et al. 2004). MD simulations tend to underestimate tensile strength compared to more accurate quantum mechanics calculations (Hirai et al. 2003; Shenderova et al. 2000; Yakobson et al. 1997; Pastewka et al. 2010). However our interest is in changes due to irradiation, not exact theoretical values, so the fact that these values are in the correct range is sufficient for our purposes.

We see from Fig. 25a that carbon atom irradiation causes a significant decrease in stiffness, strength and maximum strain relative to the pristine case. However, while pristine CNTs are the ultimate baseline, their existence in practical macro-scale composites can be considered rare. Thus we performed a tensile test simulation on a bundle with just one single-atom vacancy in one CNT and from Fig. 25a we find a tensile strength of 81 GPa and a tensile strain of 11.9 %, representing drops of 11 and 31 % respectively from the pristine case. This level of reduction is in line with previous studies on single CNTs with single vacancies (Belytschko et al. 2002). We see that the reduction in tensile properties due to irradiation is much milder when considered against this less stringent baseline.

Clean planar fracture was exhibited for the pristine bundle, with the stress dropping to zero after failure. The irradiated bundles exhibited a less clean fracture, with crack propagation between CNTs at sites where inter-tube bonds had formed, and the stress does not reduce to zero as bonds still remain between CNTs after failure occurs. Another feature evident in Fig. 25a is that the irradiated bundles were already under slight tensile load before they were tensile tested, particularly at higher energies. This is because damage and inter-tube linking caused the equilibrium length of the CNT bundle to reduce during irradiation.

Figure 25b, c provide a statistical analysis of the results from all tensile test simulations for strength and maximum strain respectively. We see that for the

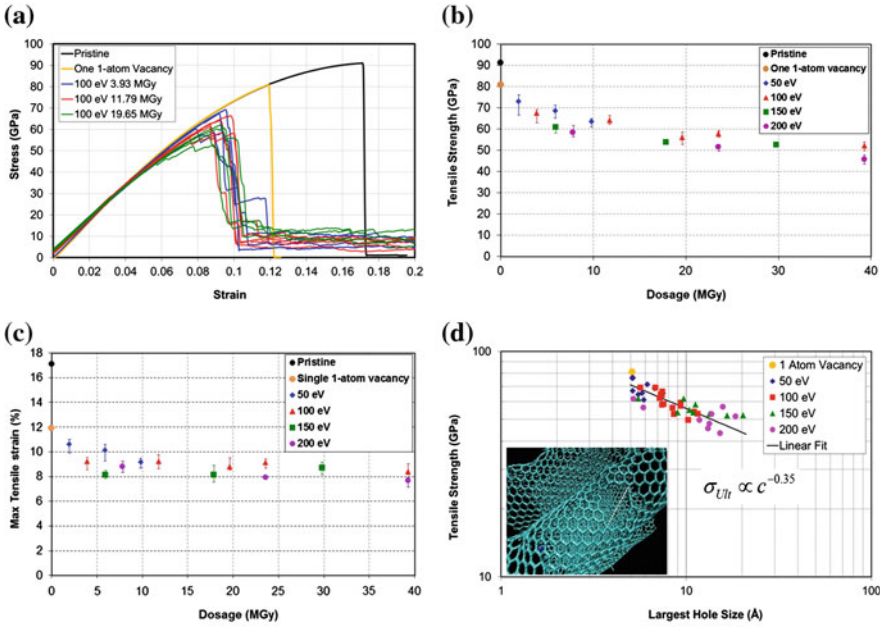

Fig. 25 Tensile test result on 7-tube bundles **a** stress versus strain for incident energy of 100 eV, **b** tensile strength, **c** maximum strain, **d** strength versus maximum hole size

maximum dosage considered here (40 MGy), the tensile strength reduces to $\sim$50 GPa and the maximum strain reduces to $\sim$8 %, representing 38 and 33 % drops respectively from the single 1-atom vacancy case. It is also noticeable that at similar dosages, lower energy irradiation produces less of a reduction. In the previous section, we found that within the inter-tube link density range $\rho = 0.7 - 1.7$ nm^{-2}, the shear properties are predictable and improve by an order of magnitude over non-irradiated bundles. Thus we see a very large benefit, for a relatively small cost. In fact the reduction in tensile strength considered here is greater than would occur in practical CNT-fibre reinforced composites. In macro-scale CNT fibres, individual CNTs would be unlikely to run along the full length of the fibre, and when embedded in a matrix, load would generally be transferred from the matrix to the outer CNTs and then inwards through shear load transfer between CNTs. Highly imperfect bonding to the matrix would exist at the fibre ends, in contrast with the end conditions here. Inter-tube cross-links would facilitate the transfer of load to all CNTs in the fibre, and so would have major beneficial effects on the tensile strength of macro-scale fibres in composites, which would offset the reductions described above.

As noted above we found many different types of defects (O'Brien et al. 2013) post-irradiation, at random locations within the bundle. Under tensile load, the load transfer within the cross-linked, defective CNT bundles is highly complex. However, Fig. 25d shows that there is still a strong correlation between the

reduction in tensile strength and the largest hole size in the bundle after irradiation (measured as the largest distance across the hole, as illustrated in the figure), as one would expect for a single CNT. We find that $\sigma_{Ult} \propto c^{-m}$, with $m \cong 0.35$, where c is the largest hole size. This is close to the value $m \cong 0.4$ that we found in (Byrne et al. 2009) for pristine MWCNTs. There is scatter in Fig. 25d because tensile strength is also affected by other defects found such as Stone–Wales defects and adatoms. For example, we performed a tensile test simulation with just one adatom on one CNT and found the bundle strength decreases to 85.9 GPa and the maximum strain diminishes to 13.5 %, which are reductions from the pristine case of 5.6 and 22 % respectively. This is because the bonding at the attachment point changes from sp^2 to sp^3, with consequent increase of bond length from 1.42 to 1.54 Å, which weakens the CNT structure.

In considering an optimal strategy for irradiation then, one should consider the effect on maximum hole size. In (O'Brien et al. 2013) we found that for the same dosage, irradiation with 100 eV irradiation led to smaller holes than 200 eV irradiation, and this ties in with the tensile strength values seen in Fig. 25b, d. An advantage of C ion deposition is that it provides extra C atoms to the system, which on subsequent annealing have the potential to migrate to vacancy locations, causing healing of the CNT lattice. A further observation related to this issue is that irradiation at very low energy ($\sim$1 eV/ion) can actually result in filling in or healing of pre-existing holes as deposition atoms latch onto dangling bonds on the hole perimeter. This process is illustrated in Fig. 26a, b. This results in an increase in tensile strength of the bundle with negligible change in pull-out stress—see Fig. 27 for the beneficial effect of 1250 additional "healing" C atoms deposited at 1 eV/ion energy. Thus a potential strategy would be to apply low energy deposition, *after* irradiation at the energies needed to produce cross-links. The limitation on this is that as well as filling in holes, the low energy atoms also adsorb as adatoms. As noted above, adatoms reduce tensile strength, though the effect is masked by vacancy defects which have a greater impact on tensile strength. However, if enough adatoms are deposited during low energy irradiation they will eventually line up somewhere in the bundle, perpendicular to the CNT axial

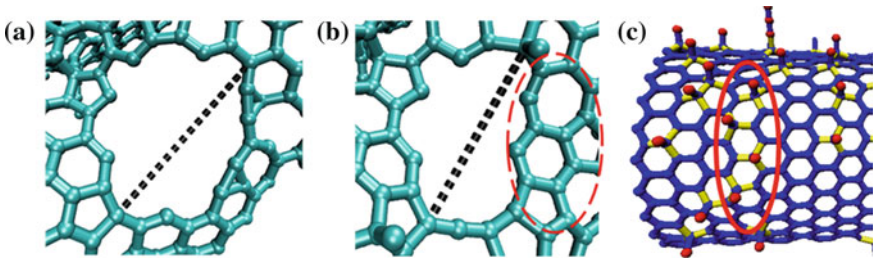

Fig. 26 Largest hole size for 150 eV, 17.88 MGy **a** pre-healing, **b** after depositing 3 additional rings of 250 atoms at 1 eV (red dashed ring highlights area where hole healing has taken place), **c** line up of adatoms providing weak point in structure; yellow bonds are $\sim$1.54 Å in length, blue bonds are $\sim$1.42 Å in length

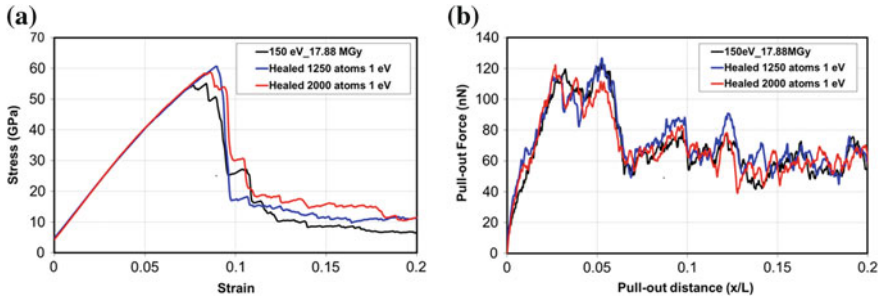

Fig. 27 Effect of "healing" 1 eV C ion irradiation on **a** tensile strength and **b** pull-out stress

direction, forming a crack-like weakening of the structure. The highlighted area in Fig. 26c shows one such example after 2000 "healing" atoms were applied, and the CNT bundle failed at this location when tensile loading was applied resulting in a reduction in tensile strength (see Fig. 27a).

5.3 Concluding Remarks

In summary, we have investigated the improvement of the mechanical properties of single wall carbon nanotube bundles through carbon ion irradiation using classical molecular dynamics simulations. These studies were made possible through the use of a recently developed modified REBO potential that introduces an environmental screening coefficient to accurately capture bond breaking and reforming processes. With careful control of irradiation parameters, we find that shear and toughness properties are increased by an order of magnitude, while tensile properties are reduced by only $\sim$30–40 % relative to a bundle with a single defect. In fact in real CNT fibres containing discontinuous CNT filaments the increased load transfer between CNTs would result in an increase in tensile strength that would significantly offset or even negate such a reduction. We find that the nano-scale interface response resembles that of traditional micro-scale composites: pull-out is characterized by an elastic stretching region at small displacements followed by the onset of debonding, in which inter-tube bonds are broken, and then a drop to a lower sliding stress, in which inter-tube links involving interstitial C atoms are continuously re-formed and broken. In contrast direct bonds between CNTs, once broken do not reform and thus do not contribute to the sliding stress. For energy absorption during pull-out it is thus desirable to have C interstitials at CNT interfaces, which makes C ion deposition an attractive option over irradiation by electrons or other types of ions, since extra C atoms are added to the system. Another advantage of adding C atoms to the system is that they may migrate on annealing to partially heal vacancies caused by irradiation. Within a certain range of cross-link density, the interface shear modulus, shear

stress at onset of debonding, and frictional sliding stress after debonding are all linearly related to cross-link density making controlled design of fibre shear properties feasible. Despite the variety of defects formed the tensile strength of irradiated bundles depends strongly on one parameter, viz: largest hole size in the bundle. A possible post-irradiation treatment with very low energy irradiation is proposed for healing such holes and therefore partially restoring tensile strength. The relationships found here between cross-link/defect density and mechanical properties should hold for larger bundles than considered here, although as noted in Sect. 4 the irradiation strategies for achieving such cross-link densities will be more complex.

Acknowledgments The authors gratefully acknowledge support of this work by Kildare County Council, the University of Limerick Research Office, the INSPIRE project under the Programme for Research in Third Level Institutions, Higher Education Authority of Ireland, the Irish Research Council for Science and Engineering Technology (IRCSET), and the Irish Centre for High End Computing facilities (ICHEC).

References

Ashrafi B, Hubert P (2006) Modeling the elastic properties of carbon nanotube array/polymer composites. Compos Sci Technol 66(3–4):387–396

Aveston J, Cooper G, Kelly A (1971) Single and multiple fracture: the properties of fiber composites. In: Proceedings of the national physical laboratory, Surrey: IPC Science and Technology Press Ltd., pp 15–26

Banhart F, Li JX, Krasheninnikov AV (2005) Carbon nanotubes under electron irradiation: stability of the tubes and their action as pipes for atom transport. Phys Rev B 71(24)

Barber AH, Andrews R, Schadler LS, Wagner HD (2005a) On the tensile strength distribution of multiwalled carbon nanotubes. Appl Phys Lett 87(20):106–203

Barber AH, Kaplan-Ashiri I, Cohen SR, Tenne R, Wagner HD (2005b) Stochastic strength of nanotubes: an appraisal of available data. Compos Sci Technol 65(15–16):2380–2384

Baskes MI, Angelo JE, Bisson CL (1994) Atomistic calculations of composite interfaces. Modell Simul Mater Sci Eng 2(3A):505–518

Belytschko T, Xiao SP, Schatz GC, Ruoff RS (2002) Atomistic simulations of nanotube fracture. Phys Rev B 65(23):235430-1–8

Berendsen HJC, Postma JPM, Vangunsteren WF, Dinola A, Haak JR (1984) Molecular-dynamics with coupling to an external bath. J Chem Phys 81(8):3684–3690

Brenner DW, Shenderova OA, Harrison JA, Stuart SJ, Ni B, Sinnott SB (2002) A second-generation reactive empirical bond order (REBO) potential energy expression for hydrocarbons. J Phys: Condens Matter 14(4):783–802

Byrne EM, Letertre A, McCarthy MA, Curtin WA, Xia Z (2010) Optimizing load transfer in multiwall nanotubes through interwall coupling: theory and simulation. Acta Mater 58(19):6324–6333

Byrne EM, McCarthy MA, Xia Z, Curtin WA (2009) Multiwall nanotubes can be stronger than single wall nanotubes and implications for nanocomposite design. Phys Rev Lett 103(4): 045502-1–4

Cheng TW, Hsu WK (2007) Winding of single-walled carbon nanotube ropes: an effective load transfer. Appl Phys Lett 90(12):123120-1–3

Coleman JN, Khan U, Blau WJ, Gun'ko YK (2006) Small but strong: a review of the mechanical properties of carbon nanotube-polymer composites. Carbon 44(9):1624–1652
Compagnini G, Giannazzo F, Sonde S, Raineri V, Rimini E (2009) Ion irradiation and defect formation in single layer graphene. Carbon 47(14):3201–3207
Cornwell CF, Welch CR (2011) Very-high-strength (60-GPa) carbon nanotube fiber design based on molecular dynamics simulations. J Chem Phys 134(20):204708-1–8
Curtin WA (2000) Dimensionality and size effects on the strength of fiber-reinforced composites. Compos Sci Technol 60(4):543–551
Curtin WA (1999) Stochastic damage evolution and failure in fiber-reinforced composites. Adv Appl Mech 36:163–253
Federizzi RL, Moura CS, Amaral L (2006) Polymerization of carbon nanotubes through self-irradiation. J Phys Chem B. 110(46):23215–23220
Filleter T, Bernal R, Li S, Espinosa HD (2011) Ultrahigh strength and stiffness in cross-linked hierarchical carbon nanotube bundles. Adv Mater 23(25):2855–2860
Fonseca AF, Borders T, Baughman RH, Cho KJ (2010) Load transfer between cross-linked walls of a carbon nanotube. Phys Rev B 81(4):045429-1–7
Fonseca AF, Lee G, Borders TL, Zhang HJ, Kemper TW, Shan TR, et al (2011) Reparameterization of the REBO-CHO potential for graphene oxide molecular dynamics simulations. Phys Rev B 84(7):075460-1–9
Garg A, Sinnott SB (1998) Effect of chemical functionalization on the mechanical properties of carbon nanotubes. Chem Phys Lett 295(4):273–278
Ghemes A, Minami Y, Muramatsu J, Okada M, Mimura H, Inoue Y (2012) Fabrication and mechanical properties of carbon nanotube yarns spun from ultra-long multi-walled carbon nanotube arrays. Carbon 50(12):4579–4587
Girifalco LA, Hodak M, Lee RS (2000) Carbon nanotubes, buckyballs, ropes, and a universal graphitic potential. Phys Rev B. 62(19):13104–13110
Hashimoto A, Suenaga K, Gloter A, Urita K, Iijima S (2004) Direct evidence for atomic defects in graphene layers. Nature 430(7002):870–873
Hirai Y, Nishimaki S, Mori H, Kimoto Y, Akita S, Nakayama Y et al. (2003) Molecular dynamics studies on mechanical properties of carbon nano tubes with Pinhole defects. Jpn J Appl Phys (Copyright (C) 2003 The Japan Society of Applied Physics) 42:4120
Huhtala M, Krasheninnikov AV, Aittoniemi J, Stuart SJ, Nordlund K, Kaski K (2004) Improved mechanical load transfer between shells of multiwalled carbon nanotubes. Phys Rev B 70(4):045404-1–8
Hutchinson JW, Jensen HM (1993) Models of fiber debonding and pullout in brittle composites with friction (Vol 9, P 139, 1990). Mech Mater 14(3):221
Hutchinson JW, Suo Z (1992) Mixed-mode cracking in layered materials. Adv Appl Mech 29(29):63–191
Kis A, Csanyi G, Salvetat JP, Lee TN, Couteau E, Kulik AJ et al (2004) Reinforcement of single-walled carbon nanotube bundles by intertube bridging. Nat Mater 3(3):153–157
Kotakoski J, Krasheninnikov A, Nordlund K (2005a) A molecular dynamics study of the clustering of implanted potassium in multiwalled carbon nanotubes. Nucl Instrum Methods Phys Res Sect B-Beam Interact Mater Atoms 240(4):810–818
Kotakoski J, Krasheninnikov AV, Ma YC, Foster AS, Nordlund K, Nieminen RM (2005) B and N ion implantation into carbon nanotubes: insight from atomistic simulations. Phys Rev B 71(20):205408-1–6
Krasheninnikov AV, Banhart F, Li JX, Foster AS, Nieminen RM (2005) Stability of carbon nanotubes under electron irradiation: role of tube diameter and chirality. Phys Rev B 72(12):125428-1–6
Krasheninnikov AV, Nordlund K (2010) Ion and electron irradiation-induced effects in nanostructured materials. J Appl Phys 107(7):071301-1–70
Krasheninnikov AV, Nordlund K (2004) Irradiation effects in carbon nanotubes. Nucl Instrum Methods Phys Res Sect B-Beam Interact Mater Atoms 216:355–366

Kuan C-F, Kuan H-C, Ma C-CM, Chen C-H (2008) Mechanical and electrical properties of multi-wall carbon nanotube/poly(lactic acid) composites. J Phys Chem Solids 69(5–6):1395–1398
Li L, Xia ZH, Curtin WA, Yang YQ (2009) Molecular dynamics simulations of interfacial sliding in carbon-nanotube/diamond nanocomposites. J Am Ceram Soc 92(10):2331–2336
Locascio M, Peng B, Zapol P, Zhu Y, Li S, Belytschko T et al (2009) Tailoring the load carrying capacity of MWCNTs through inter-shell atomic bridging. Exp Mech 49(2):169–182
Mahesh S, Beyerlein IJ, Phoenix SL (1999) Size and heterogeneity effects on the strength of fibrous composites. Physica D 133(1–4):371–389
Mahesh S, Phoenix SL (2004) Lifetime distributions for unidirectional fibrous composites under creep-rupture loading. Int J Fract 127(4):303–360
Mielke SL, Troya D, Zhang S, Li JL, Xiao SP, Car R et al (2004) The role of vacancy defects and holes in the fracture of carbon nanotubes. Chem Phys Lett 390(4–6):413–420
Mikata Y, Taya M (1985) Stress-field in a coated continuous fiber composite subjected to thermomechanical loadings. J Compos Mater 19(6):554–578
Ni B, Andrews R, Jacques D, Qian D, Wijesundara MBJ, Choi YS et al (2001) A combined computational and experimental study of ion-beam modification of carbon nanotube bundles. J Phys Chem B. 105(51):12719–12725
Ni B, Sinnott SB (2000) Chemical functionalization of carbon nanotubes through energetic radical collisions. Phys Rev B. 61(24):16343–16346
O'Brien NP, McCarthy MA, Curtin WA (2013) Improved inter-tube coupling in CNT bundles through carbon ion irradiation. Carbon 51:173–184
Ogata S, Shibutani Y (2003) Ideal tensile strength and band gap of single-walled carbon nanotubes. Phys Rev B. 68(16):165409-1–4
Pantano A, Modica G, Cappello E (2008) Multiwalled carbon nanotube reinforced polymer composites. Mater Sci Eng A-Struct Mater Prop Microstruct Process 486(1–2):222–227
Pastewka L, Moser S, Moseler M (2010) Atomistic insights into the running-in, lubrication, and failure of hydrogenated diamond-like carbon coatings. Tribol Lett 39(1):49–61
Pastewka L, Pou P, Perez R, Gumbsch P, Moseler M (2008) Describing bond-breaking processes by reactive potentials: Importance of an environment-dependent interaction range. Phys Rev B 78(16):161402-1–4
Pasupuleti S, Peddetti R, Santhanarn S, Jen K-P, Wing ZN, Hecht M et al (2008) Toughening behavior in a carbon nanotube reinforced silicon nitride composite. Mater Sci Eng A-Struct Mater Prop Microstruct Process 491(1–2):224–229
Pavia F, Curtin WA (2011) Interfacial sliding in carbon nanotube/diamond matrix composites. Acta Mater 59(17):6700–6709
Peng B, Locascio M, Zapol P, Li SY, Mielke SL, Schatz GC et al (2008) Measurements of near-ultimate strength for multiwalled carbon nanotubes and irradiation-induced crosslinking improvements. Nat Nanotechnol 3(10):626–631
Plimpton SJ (1995) Fast parallel algorithms for short-range molecular dynamics. J Comp Phys 117:1–19
Pomoell JAV, Krasheninnikov AV, Nordlund K, Keinonen J (2004) Ion ranges and irradiation-induced defects in multiwalled carbon nanotubes. J Appl Phys 96(5):2864–2871
Pregler SK, Jeong B-W, Sinnott SB (2008) Ar beam modification of nanotube based composites using molecular dynamics simulations. Compos Sci Technol 68(9):2049–2055
Pregler SK, Sinnott SB (2006) Molecular dynamics simulations of electron and ion beam irradiation of multiwalled carbon nanotubes: the effects on failure by inner tube sliding. Phys Rev B. 73(22):224106-1–9
Salonen E, Krasheninnikov AV, Nordlund K (2002) Ion-irradiation-induced defects in bundles of carbon nanotubes. Nucl Instrum Methods Phys Res Sect B-Beam Interact Mater Atoms 193:603–608
Salvetat JP, Briggs GAD, Bonard JM, Bacsa RR, Kulik AJ, Stockli T et al (1999) Elastic and shear moduli of single-walled carbon nanotube ropes. Phys Rev Lett 82(5):944–947

Sammalkorpi M, Krasheninnikov A, Kuronen A, Nordlund K, Kaski K (2004) Mechanical properties of carbon nanotubes with vacancies and related defects. Phys Rev B 70(24):245416-1–8

Sammalkorpi M, Krasheninnikov AV, Kuronen A, Nordlund K, Kaski K (2005) Irradiation-induced stiffening of carbon nanotube bundles. Nucl Instrum Methods Phys Res Sect B-Beam Interact Mater Atoms 228:142–145

Schittenhelm H, Geohegan DB, Jellison GE, Puretzky AA, Lance MJ, Britt PF (2002) Synthesis and characterization of single-wall carbon nanotube-amorphous diamond thin-film composites. Appl Phys Lett 81(11):2097–2099

Sears K, Skourtis C, Atkinson K, Finn N, Humphries W (2010) Focused ion beam milling of carbon nanotube yarns to study the relationship between structure and strength. Carbon 48(15):4450–4456

Seldin EJ, Nezbeda CW (1970) Elastic constants and electron-microscope observations of neutron-irradiated compression-annealed pyrolytic and single-crystal graphite. J Appl Phys 41(8):3389–3400

Shenderova OA, Brenner DW, Omeltchenko A, Su X, Yang LH (2000) Atomistic modeling of the fracture of polycrystalline diamond. Phys Rev B. 61(6):3877–3888

Shimizu Y, Miki S, Soga T, Itoh I, Todoroki H, Hosono T et al (2008) Multi-walled carbon nanotube-reinforced magnesium alloy composites. Scripta Mater 58(4):267–270

Sorescu M, Grabias A, Tarabasanu-Mihaila D, Diamandescu L (2003) Bulk versus surface effects in magnetic thin films obtained by pulsed laser deposition. Appl Surf Sci 217(1–4):233–238

Suenaga K, Wakabayashi H, Koshino M, Sato Y, Urita K, Iijima S (2007) Imaging active topological defects in carbon nanotubes. Nat Nanotechnol 2(6):358–360

Sutcu M, Hillig WB (1990) The effect of fiber-matrix debond energy on the matrix cracking strength and the debond shear-strength. Acta Metall Mater 38(12):2653–2662

Tanabe T (1996) Radiation damage of graphite—Degradation of material parameters and defect structures. Phys Scr T64:7–16

Tersoff J (1988) Empirical interatomic potential for carbon, with applications to amorphous-carbon. Phys Rev Lett 61(25):2879–2882

Tolvanen A, Kotakoski J, Krasheninnikov AV, Nordlund K (2007) Relative abundance of single and double vacancies in irradiated single-walled carbon nanotubes. Appl Phys Lett 91(17):173109-1–3

Troya D, Mielke SL, Schatz GC (2003) Carbon nanotube fracture—differences between quantum mechanical mechanisms and those of empirical potentials. Chem Phys Lett 382(1–2):133–141

Tsai J-L, Lu T-C (2009) Investigating the load transfer efficiency in carbon nanotubes reinforced nanocomposites. Compos Struct 90(2):172–179

Weibull W (1951) A statistical distribution function of wide applicability. J Appl Mech Trans Asme 18(3):293–297

Xia Z, Curtin WA (2004) Pullout forces and friction in multiwall carbon nanotubes. Phys Rev B 69(23):233408-1–4

Xia Z, Riester L, Curtin WA, Li H, Sheldon BW, Liang J et al (2004) Direct observation of toughening mechanisms in carbon nanotube ceramic matrix composites. Acta Mater 52(4):931–944

Xia ZH, Guduru PR, Curtin WA (2007) Enhancing mechanical properties of multiwall carbon nanotubes via sp(3) interwall bridging. Phys Rev Lett 98(24):245501-1–4

Xiao S, Hou WY (2006) Fracture of vacancy-defected carbon nanotubes and their embedded nanocomposites. Phys Rev B. 73(11):115406-1–7

Xu ZJ, Zhang W, Zhu ZY, Huai P (2009) Molecular dynamics study of damage production in single-walled carbon nanotubes irradiated by various ion species. Nanotechnology 20(12):125706-1–11

Yakobson BI, Campbell MP, Brabec CJ, Bernholc J (1997) High strain rate fracture and C-chain unraveling in carbon nanotubes. Comput Mater Sci 8(4):341–348

Yakobson BI, Avouris P (2001) Medical properties of nanotubes. Carbon Nanotubes. Book: Topics in Applied Physics 80:287–327

Yu MF, Files BS, Arepalli S, Ruoff RS (2000a) Tensile loading of ropes of single wall carbon nanotubes and their mechanical properties. Phys Rev Lett 84(24):5552–5555

Yu MF, Lourie O, Dyer MJ, Moloni K, Kelly TF, Ruoff RS (2000b) Strength and breaking mechanism of multiwalled carbon nanotubes under tensile load. Science 287(5453):637–640

Yu N, Zhang ZH, He SY (2008) Fracture toughness and fatigue life of MWCNT/epoxy composites. Mater Sci Eng A-Struct Mater Prop Microstruct Process 494(1–2):380–384

Zalamea L, Kim H, Pipes RB (2007) Stress transfer in multi-walled carbon nanotubes. Compos Sci Technol 67(15–16):3425–3433

Zhang M, Atkinson KR, Baughman RH (2004) Multifunctional carbon nanotube yarns by downsizing an ancient technology. Science 306(5700):1358–1361

Zhang SL, Mielke SL, Khare R, Troya D, Ruoff RS, Schatz GC et al (2005) Mechanics of defects in carbon nanotubes: atomistic and multiscale simulations. Phys Rev B. 71(11):115403-1–12

Zhang XF, Li QW, Tu Y, Li YA, Coulter JY, Zheng LX et al (2007) Strong carbon-nanotube fibers spun from long carbon-nanotube arrays. Small 3(2):244–248

Zhou Z, Wang S, Lu L, Zhang Y, Zhang Y (2008) Functionalization of multi-wall carbon nanotubes with silane and its reinforcement on polypropylene composites. Compos Sci Technol 68(7–8):1727–1733

A Review on the Application of Nonlocal Elastic Models in Modeling of Carbon Nanotubes and Graphenes

Behrouz Arash and Quan Wang

Abstract Recent research studies on the application of the nonlocal continuum theory in modeling of carbon nanotubes and graphene sheets are reviewed, and substantial nonlocal continuum models proposed for static and dynamic analyses of the nano-materials are introduced. The superiority of the nonlocal continuum theory to its local counterpart, and the necessity of calibration of the small-scale parameter as the key parameter revealing small-scale effects are discussed. The nonlocal beam, plate, and shell models are briefly presented and potential areas for future research are recommended. It is intended to provide an introduction to the development of the nonlocal continuum theory in modeling the nano-materials, survey the different nonlocal continuum models, and motivate further applications of the nonlocal continuum theory to nano-material modeling.

Keywords Carbon nanotubes · Graphene sheets · Nonlocal continuum theory · Modeling and simulations · Small scale effect

1 Introduction

Nanoscience and nanotechnology have opened a new area of research in many fields of science and technology such as materials science, engineering, medicine, biomaterials and energy production. Among different nano-materials, carbon nanotubes (CNTs) (Iijima 1991) and graphene sheets (GSs) (Novoselov et al. 2004)

B. Arash (✉) · Q. Wang
Department of Mechanical and Manufacturing Engineering, University of Manitoba, Winnipeg, MB R3T 5V6, Canada
e-mail: umarash@cc.umanitoba

Q. Wang
e-mail: Q.Wang@ad.umanitoba.ca

K. I. Tserpes and N. Silvestre (eds.), *Modeling of Carbon Nanotubes, Graphene and their Composites*, Springer Series in Materials Science 188,
DOI: 10.1007/978-3-319-01201-8_2,

are of great potential applications due to their unparallel mechanical, electronic and thermal properties. The superior properties make the two nano-materials instrumental for developing and innovating new nanodevices in a wide range of applications including gas detection, graphene transistors, solar cells, ultra-capacitors, diagnosis devices and ultra-strength composite materials (Wagner et al. 1998; Thostenson et al. 2001; Qian et al. 2002; Sirtori 2002; Antonelli et al. 2002; Brauns et al. 2002; Lau K-t and Hui 2006; Stankovich et al. 2006; Bunch et al. 2007; Schedin et al. 2007; Chiu et al. 2008).

In addition to formidable experimental methods (Chaste et al. 2012; Falvo et al. 1997), there are three main approaches for theoretically modeling of the nano-materials: (a) atomistic modeling, (b) hybrid atomistic-continuum mechanics and (c) continuum mechanics. Atomic modeling includes techniques such as classical molecular dynamics (MD), tight-binding molecular dynamics (TBMD) and the density functional theory (DFT) (Hernández et al. 1998; Iijima et al. 1996; Sánchez-Portal et al. 1999; Yakobson et al. 1997; Li and Chou 2006; Liew et al. 2004). Hybrid atomistic-continuum mechanics allows one to directly incorporate interatomic potential into the continuum analysis by equating the molecular potential energy of a nano-structured material with the mechanical strain energy of a continuum model (Bodily CTS 2003; Li and Chou 2003a, b). Continuum mechanics includes classical (or local) beam, plate and shell theories that are practical for analyzing nanostructures at large scale sizes (Yakobson et al. 1996; Krishnan et al. 1998; Parnes and Chiskis 2002). Continuum mechanics approach is less computationally expensive than the former two approaches and their formulations are relatively simple. These advantages make continuum modeling as an alternative way to simulate some phenomena in nanostructures such as buckling (Duan et al. 2010; Wang et al. 2005), wave propagation (Liew and Wang 2007; Wang and Varadan 2006a, b) and free vibration (Kitipornchai et al. 2005; Sun and Liu 2007; Behfar and Naghdabadi 2005; He et al. 2005; Liew et al. 2006). Since the continuum mechanics theory is based on the continuous assumption in modeling, verification of results obtained from the theory with those of molecular dynamics simulations or experiments are indispensable.

Based on classical or local continuum theory, CNTs and GSs are modeled as continuous and homogenous macrostructures, while the lattice spacing between individual carbon atoms in the nano-materials is ignored. In local continuum models, the stress at a given point is defined as the function of the strain at that point. Despite the research efforts have been conducted on the basis of classical or local continuum theory, their applicability at very small scales is questionable. The limited applicability is due to the fact that at nanoscale sizes the lattice spacing between individual atoms becomes increasingly important and the discrete structure of the nano-materials can no longer be homogenized into a continuum (Peddieson et al. 2003; Sudak 2003; Zhang et al. 2004; Wang 2005; Ansari and Arash 2013; Gibson et al. 2007). Therefore, the application of continuum mechanics by considering the size dependence in nano-materials became another topic of major concern that led to the application of nonlocal continuum mechanics, allowing for taking into account of the small-scale effects in analysis of nano-materials.

On the basis of the nonlocal continuum theory developed by Eringen (1976, 1983) the stress state at a given reference point is a function of the strain field at every point in the body. The assumption enables the theory to account for information about the long range forces between atoms and the scale effect. Peddieson et al. (2003) showed that nonlocal continuum mechanics could be employed in nanotechnology applications. Wang (2005) indicated that nonlocal elasticity theory should be used for an accurate prediction of wave propagation in CNTs, and estimated a range of the small-scale parameter. Applications of nonlocal continuum mechanics have been also investigated by many researchers in topics of static (Sudak 2003; Wang and Liew 2007; Yang et al. 2008; Wang et al. 2006a, b,c; Murmu and Pradhan 2009a, b, c, d; Zhang et al. 2004, 2006, 2009a, b, 2010; Xie et al. 2006; Shen 2010a, b; Li and Kardomateas 2007; Yan et al. 2010; Amara et al. 2010; Hao et al. 2010; Mohammadimehr et al. 2010; Khademolhosseini et al. 2010; Shen and Zhang 2010; Pradhan 2009; Pradhan and Murmu 2009, 2010, 2011) and dynamic analysis (Zhang et al. 2005; Wang and Varadan 2006a, b; Wang et al. 2007; Aydogdu 2009; Filiz and Aydogdu 2010; Murmu and Adhikari 2010; Yang et al. 2010; Duan et al. 2007; Arash and Ansari 2010; Li and Kardomateas 2007; Murmu and Pradhan 2009a, b, c, d; Lee and Chang 2009; Wang 2009; Pradhan and Murmu 2010; Kiani and Mehri 2010; Kiani 2010; Zhen and Fang 2010; Soltani et al. 2010; Şimşek 2010; Lee et al. 2010; Aydogdu and Filiz 2011; Wang and Hu 2005; Wang and Varadan 2007; Hu et al. 2008; Narendar and Gopalakrishnan 2009; Heireche et al. 2008; Song et al. 2010; Pradhan and Phadikar 2009; Murmu and Pradhan 2009a, b, c, d; Pradhan and Kumar 2010, 2011a, b; Shen et al. 2010; Ansari et al. 2010a, b, 2011; Arash and Wang 2011; Arash et al. 2012).

According to the aforementioned studies on the basis of Eringen's nonlocal elasticity theory, a consensus has been reached that the refined nonlocal models are superior to their local counterparts. However, since the theory also belongs to the category of continuum mechanics, verification of nonlocal continuum models is essential to identify the magnitude of the small-scale parameter, $e_0 a$, which is the key in revealing scale effect in models.

After the nonlocal elastic theory was introduced, many studies started applying the theory in modeling of CNTs and GSs. The static analysis (Sudak 2003; Zhang et al. 2004, 2006, 2009a, b, 2010; Wang and Liew 2007; Yang et al. 2008; Wang et al. 2006a, b, c; Murmu and Pradhan2009a, b, c, d; Xie et al. 2006; Shen 2010a, b; Li and Kardomateas 2007; Yan et al. 2010; Amara et al. 2010; Wang et al. 2010a, b, c; Hao et al. 2010; Mohammadimehr et al. 2010; Khademolhosseini et al. 2010; Shen and Zhang 2010; Murmu and Pradhan 2009a, b, c, d; Pradhan 2009; Pradhan and Murmu 2009; 2010, Pradhan and Kumar 2011a, b), free vibration (Zhang et al. 2005, 2009a, b; Wang and Varadan 2006; Wang et al. 2007; Aydogdu 2009; Filiz and Aydogdu 2010; Murmu and Adhikari 2010; Yang et al. 2010; Duan et al. 2007; Arash and Ansari 2010; Li and Kardomateas 2007; Murmu and Pradhan 2009a, b, c, d; Lee and Chang 2009; Wang 2009; Pradhan and Murmu 2010; Kiani and Mehri 2010; Kiani 2010; Zhen and Fang 2010; Soltani et al. 2010; Şimşek 2010; Lee et al. 2010; Aydogdu and Filiz 2011; Pradhan and Phadikar

2009; Pradhan and Kumar 2010, 2011a, b; Ansari et al. 2010a, b, 2011; Shen et al. 2010; Arash and Wang 2011) of and wave propagation (Wang 2005; Wang and Hu 2005; Wang et al. 2006a, b, c, 2010a, b, c; Wang and Varadan 2007; Hu et al. 2008; Narendar and Gopalakrishnan 2009; Heireche et al. 2008; Song et al. 2010; Arash et al. 2012) in the nano-materials were widely studied and the continuum models were reformulated based on the nonlocal continuum theory. This paper aims to provide a brief review on enormous studies invested on the application of nonlocal elastic models in modeling of CNTs and GSs to (1) present a summary of the state-of-the-art findings (2) introduce major challenges in the modeling based on the nonlocal continuum theory, and (3) clarify the key issues of future research studies. To this end, Sect. 2 focuses on applications of nonlocal continuum models in static analysis of CNTs and GSs. Section 3 surveys applications of nonlocal continuum models in dynamic analysis of CNTs and GSs. Section 4 presents a summarization of elastic models. Section 5 gives a summary and recommendations for future research studies.

2 Application in Static Analysis of CNTs and GSs

Since static loadings in transverse direction may lead to bending of nano-materials, the development and application of nonlocal continuum mechanics in studying scale effects on static responses of nano-materials are of great significance (Wang and Liew 2007). In addition, CNTs are susceptible to buckling or structural instability due to their long and hollow tubular structures (Chaste et al. 2012; Hernández et al. 1998). This can significantly influence their performance as structural or functional elements in CNT-based nano-composites and nano-electromechanical systems (Wagner et al. 1998; Thostenson et al. 2001; Qian et al. 2002; Lau K-t and Hui 2006; Stankovich et al. 2006). Therefore, tremendous efforts have also been devoted to buckling of CNTs under diverse loading conditions such as axial loading (Sudak 2003; Zhang et al. 2004; Wang et al. 2006a, b, c; Murmu and Pradhan 2009a, b, c, d; Zhang et al. 2009a, b), radial and bending loading (Zhang et al. 2006, 2010; Xie et al. 2006; Shen 2010a, b), thermal loading (Li and Kardomateas 2007; Yan et al. 2010; Amara et al. 2010; Wang et al. 2010a, b, c) and torsion (Hao et al. 2010; Mohammadimehr et al. 2010; Khademolhosseini et al. 2010; Shen and Zhang 2010).

2.1 Bending of CNTs Under Static Transverse Loadings

Wang and Liew (Wang and Liew 2007) investigated the scale effect on static deformation of micro- and nano-rods or tubes subjected to transverse loadings by

using the nonlocal Euler-Bernoulli and Timoshenko beam theories. The major finding on cantilever nano-rods is reviewed below.

The transverse deformation of cantilever nano-rod with length L subjected to a concentrated force P at $x = l$ via the nonlocal Euler-Bernoulli and Timoshenko beam theories are provided to be (Wang and Liew 2007).

$$w_E(x) = \frac{1}{EI}\left(\frac{P(x-l)^3}{6}H(x-l) - P(e_0a)^2(x-l)H(x-l) - \frac{Px^3}{6} + \frac{Plx^2}{2}\right) \quad (1)$$

$$\begin{aligned} w_T(x) = &\frac{1}{EI}\left(\frac{P(x-l)^3}{6}H(x-l) - P(e_0a)^2(x-l)H(x-l) - \frac{Px^3}{6} + \frac{Plx^2}{2}\right) \\ &+ \frac{\Omega L^2}{EI}(Px - P(l-x)H(x-l)) \end{aligned} \quad (2)$$

where subscripts E and T denote Euler-Bernoulli and Timoshenko beam theories, respectively. $H(x-l)$ is the Heaviside function, $\Omega = \frac{EI}{GA\kappa L^2} = \frac{1+\upsilon}{8\kappa}\left(\frac{d}{L}\right)^2$ is the shear parameter, υ is Poisson's ratio, and d is the diameter of the rod or tube under investigation. The coefficient, d/L, represents the slenderness of the structure.

Equations (1) and (2) reveal that the small-scale term, $P(e_0a)^2(x-l)H(x-l)$, affects the response of the cantilevered rod only for the space domain $x \geq l$. Moreover, Eq. (2) shows that the nonlocal Timoshenko beam theory does not induce additional scale effect compared to the nonlocal Euler-Bernoulli beam theory for the cantilevered rod.

They further investigated an additional example on the deformation profiles along the length of a cantilevered rod or tube subjected to a concentrated force at the middle as shown in Fig. 1. In Fig. 1, the scale effect and the diameter-to-length ratio have been given as $e_0a/L = 0.2$ and $d/L = 0.2$, respectively. A noticeable observation is that there is no scale effect on the deformation at all locations on the left side of the point force, and such effect initiates immediately after the location of the point force. Their results also showed that the small-scale effect is noticeable for nano-structures in their static responses. On the other hand, the scale effect is obscure when the length of the structure is over 20 nm. Therefore, they concluded that scale effects would not manifest for typical micro-systems such as micro-electromechanical systems (MEMS) which have lengths of the order $rm\mu$m. In addition, the shear effect is evident for nano-structures indicating the importance of applying the Timoshenko beam theory in static analysis of shorter nano-structures. Nano-beams as potential nano-switches subjected to a transverse electrostatic force within the framework of nonlocal elasticity theory to account for the small-scale effect were studied by Yang et al. (2008). The transverse electrostatic force from an applied voltage and intermolecular force was approximated as a linear distributed load model and closed-form solutions were obtained for cantilever and fixed–fixed nano-beams.

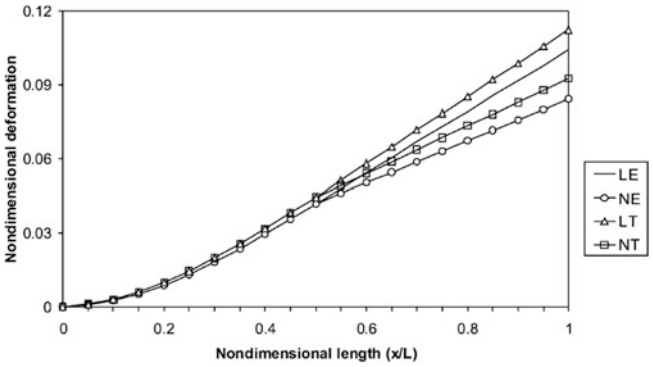

Fig. 1 Static deformation of a cantilever structure subjected to a force at the middle by using local and nonlocal models: local Euler-Bernoulli beam model (LE), nonlocal Euler-Bernoulli beam model (NE), local Timoshenko beam model (LT) and nonlocal Timoshenko beam model (NT) (Wang and Liew 2007)

2.2 Buckling of CNTs and GSs

Sudak (2003) investigated the buckling of CNTs subjected to axial loading using the nonlocal continuum theory. In the study, the nonlocal Euler- Bernoulli beam model for the buckling of multi-walled carbon nanotubes (MWCNTs) was presented which clearly demonstrated that small-scale effects significantly contribute to buckling solution of MWCNTs. Explicit expressions for the critical buckling load and strain were derived for axially loaded rods/tubes based on the nonlocal Timoshenko beam theory (Zhang et al. 2004; Wang et al. 2006a, b, c). Wang et al. (2006a, b, c) developed nonlocal elastic beam and shell models to investigate the small-scale effect on buckling analysis of CNTs under compression. They derived a general buckling solution for CNTs with a length of L and various boundary conditions via the nonlocal beam model as

$$\frac{P}{P_l} = \frac{1}{1 + (e_0 a)^2 \left(\frac{\beta\pi}{L}\right)^2} \tag{3}$$

where $P_l = EI(\beta\pi/L)^2$ is the buckling solution for a beam structure via the local elastic beam theory and EI is the bending rigidity. β has different values given for different boundary conditions. For example, the buckling solutions for the first three modes are: $\beta = 1, 2, 3$ for a pinned-pinned CNT, $\beta = 1/2, 3/2, 5/2$ for a cantilevered CNT, and $\beta = 2, 4, 6$ for a fixed-fixed CNT. From Eq. (3), it is obvious that the scale effect is indispensable in providing more accurate results for mechanical behaviors of CNTs with lengths of the order nm via continuum mechanics. On the other hand, the small-scale effect is negligible for CNTs with lengths of the order μm. The explicit solutions for CNTs buckling analysis via nonlocal continuum mechanics provided benchmark for scale effect studies of

CNTs mechanical analyses. The nonlocal Timoshenko beam model was implemented (Murmu and Pradhan 2009a, b, c, d) to investigate an axial buckling of single-walled CNTs (SWCNTs) embedded in an elastic medium, and the influence of the small-scale effect and stiffness of the surrounding medium was investigated. Zhang et al. (2009a, b) presented an assessment of nonlocal beam and shell models in the prediction of critical buckling strains of axially loaded SWCNTs by use of MD simulation results for SWCNTs.

A nonlocal multiple-shell model was developed for the elastic buckling of MWCNTs under uniform external radial pressure (Zhang et al. 2006; Xie et al. 2006). To investigate the bending, buckling and vibration responses of CNTs, Zhang et al. (2010) employed the hybrid nonlocal beam model. The radial and bending buckling behaviors of microtubules were also studied based on the nonlocal elasticity theory (Shen 2010a, b). Since there are insufficient results by MD simulations or experiments for radial and bending buckling, the use of the small-scale parameter calibrated for vibration and axial buckling to radial and bending buckling analysis was recommended. Such a recommendation was not justified. It is pointed out here that the parameter calibrated in vibration or axial buckling analysis may not be applicable to another type of motion of CNTs. It is hence recommended that a nonlocal model is confirmed to be applicable to a nanomaterial for a type of motion only after the scale parameter is carefully calibrated for the material with the type of motion.

In order to study the thermal buckling behavior of MWCNTs, a nonlocal elastic shell model was developed (Li and Kardomateas 2007). Buckling governing equations of CNTs were formulated on the basis of the nonlocal elastic theory and the small-scale effect on CNTs buckling results under the temperature field was investigated (Yan et al. 2010; Amara et al. 2010). Wang et al. (2010a, b, c) studied the thermal buckling properties of CNTs based on the nonlocal continuum theory and the Timoshenko beam model. They concluded that small-scale effects should be considered for thermal buckling behaviors, especially for higher mode numbers and short CNTs.

Nonlocal elasticity shell models were presented to study torsional buckling of CNTs in Refs. (Hao et al. 2010; Mohammadimehr et al. 2010; Khademolhosseini et al. 2010; Shen and Zhang 2010). The scale coefficient was estimated by matching the buckling torque of CNTs observed from MD simulation results with the numerical results obtained from the nonlocal shear deformable shell model (Khademolhosseini et al. 2010). Khademolhosseini et al. (Shen and Zhang 2010) performed torsional buckling of SWCNTs using MD simulations and nonlocal shell models. To match the results obtained from nonlocal continuum models to those of MD simulations, different values of effective thickness of CNTs were manually enforced in local and nonlocal continuum models. Enforcing different values of the effective thickness in continuum models to match the atomistic results may not be a feasible way as the physical properties of materials should not be manually set to justify any proposed models.

The buckling analysis of single-layered GSs (SLGSs) under biaxial and uniaxial compression was studied using the nonlocal continuum mechanics (Murmu and Pradhan 2009a, b, c, d; Pradhan 2009; Pradhan and Murmu 2009, 2010; Pradhan and Kumar 2011a, b). GSs have been acknowledged to be a membrane structure among researches in nano-community. In structural mechanics, a membrane is a structure with negligible bending rigidity (Gao and Hao 2009; Lu and Huang 2009). Because of this, a membrane structure is unable to be subjected to any notable compression loading and bending, or the capacity of buckling load of such a structure is almost zero. However, it is pointed out here that GSs can be subjected to in-plane shear leading to another type of local buckling state, wrinkles (Duan et al. 2011). Wrinkles are observed in GSs due to their relatively small bending rigidity. A continuum model was developed for the characteristics of the wrinkles which show that the wrinkle wavelength decreases with an increase in shear loading, while the amplitude of the wrinkles is found to initially increase and then become stable (Duan et al. 2011). So far, there have been few studies on ripples (Fasolino et al. 2007) GSs and failure of GSs and graphene nanoribbons (GNRs) under tensile loadings using the nonlocal continuum theory. Therefore, future studies are required to evaluate nonlocal models in simulation of ripples in GSs and failure of GSs and GNRs under tensile loadings.

3 Application in Dynamic Analysis of CNTs and GSs

Now we turn our attention to applications of nonlocal models in vibration and wave propagation of CNTs and GSs. The vibration of nanotubes and graphenes is an important subject in nanotechnology since it is related to the electronic and optical properties of nanostructures (Sirtori 2002; Antonelli et al. 2002; Brauns et al. 2002). Furthermore, growing interests in design of terahertz devices at nanoscale sizes (Bunch et al. 2007; Schedin et al. 2007; Chiu et al. 2008) have drawn more attention to CNTs and GSs phonon dispersion relation, especially in the terahertz frequency range. Therefore, the study of vibration of and wave propagation in CNTs and GSs has technological significance in gaining a more in-depth understanding of dynamic behaviors of CNTs and GSs. The factors that influence dynamic behaviors of CNTs and GSs such as geometry of CNTs (radius, length, and number of tubes), geometry of GSs (width, length, and number of layers), surrounding medium, temperature and boundary conditions are investigated.

3.1 Free Vibration of CNT

A nonlocal double-elastic beam model for free transverse vibrations of double-walled CNTs (DWCNTs) was developed by Zhang et al. (2005). They studied the small-scale effect on vibrational properties of CNTs. Wang and Varadan (2006)

investigated vibration of SWCNTs and DWCNTs based on nonlocal beam theories and explicitly derived small-scale effects on vibration characteristics of CNTs. They showed that the results based on nonlocal continuum mechanics are in agreement with a published experimental report. They derived resonant frequency for mode n, ω_n, of an SWNT with a length of L and simply supported boundary condition as follows

$$\frac{\omega_n}{\omega'_n} = \frac{1}{\sqrt{1 + \frac{n^2\pi^2}{L^2}(e_0 a)^2}} \tag{4}$$

where $\omega'_n = \frac{n^2\pi^2}{L^2}\sqrt{\frac{EI}{\rho A}}$ is the resonant frequency of the CNT obtained on the basis of the classical or local Euler-Bernoulli beam theory; $EI$is the bending rigidity; ρ is the mass density; and A is the cross sectional area of the CNT. From Eq. (4), the small-scale effects decrease by an increase in the length of a CNT. The governing equations were solved analytically for the vibration frequencies of beams with various end conditions (Wang et al. 2007). The axial vibration frequencies were shown to be highly over estimated by the local rod model, which ignores the effect of small length scale (Aydogdu 2009; Filiz and Aydogdu 2010; Murmu and Adhikari 2010). A nonlocal Timoshenko beam model was reformulated to study nonlinear free vibration of SWCNTs based on von Karman geometric nonlinearity and Eringen's nonlocal elasticity theory (Yang et al. 2010). Duan et al. (2007) calibrated the scale coefficient of the nonlocal Timoshenko beam theory for a free vibration of SWCNTs by using vibration frequencies generated from MD simulations at room temperature. They showed that the calibrated e_0 ranges between 0 and 4 for a (5, 5) SWCNT with clamped-clamped boundary condition versus length-to-diameter ratio from 1 to 14. It is worth mentioning that adopting various e_0 at every distinct length-to-diameter ratio may be inconvenient in applying the nonlocal model. In view of this problem, Arash and Ansari (2010) assessed a nonlocal shell model to analyze vibration characteristics of SWCNTs with different boundary conditions subjected to initial strain. They calibrated the small-scale parameter for a wide range of length-to-diameter ratios from 5 to 35 by use of MD simulations as a benchmark of good accuracy and showed that the small-scale parameter, $e_0 a$, only depends on boundary condition. The small-scale parameter, $e_0 a$, was respectively justified to range from 1.7 to 2 nm for clamped-clamped and clamped-free SWCNTs. The use of a unique small-scale parameter, $e_0 a$, for a wide range of length-to-diameter ratio is more practical. Li and Kardomateas (2007) formulated a nonlocal shell model for free vibrations of MWCNTs. They found that resonant frequencies decrease due to the van der Waals (vdW) interaction between two adjacent nanotubes. The effectiveness of local and nonlocal Timoshenko beam models in the vibration analysis of SWCNTs with different boundary conditions was assessed by Zhang et al. (2009a, b). The scale coefficient,e_0, was derived to be 1.25 for a range of length-to-diameter ratio from around 5 to around 35. Murmu and Pradhan (2009a, b, c, d) analyzed a thermal vibration analysis of SWCNTs based on the nonlocal elasticity theory.

Lee and Chang (2009) developed a nonlocal Euler-Bernoulli elastic beam model for the vibration of nanotubes conveying fluid using the theory of nonlocal elasticity. They observed that the nonlocal effect on the fundamental frequency becomes significant as the flow velocity of viscous fluid decreases. In addition, the viscosity effect on the frequency of SWCNTs becomes significant as the flow velocity of viscous fluid increases. Wang (2009) obtained the resonant frequencies and critical flow velocities of tubular nano- and micro-beams conveying fluid using nonlocal elastic theory. Results showed that the small-scale effect on the critical flow velocities is visible for fluid-conveying nanotubes with nano-scale length; however, and this effect may be neglected for micro-scale length. Pradhan and Murmu (2010) developed a single nonlocal beam model to investigate the flapwise bending-vibration characteristics of a rotating nanocantilever. Dynamic analysis of nanotube structures under excitation of a moving nanoparticle was carried out using nonlocal continuum theory (Kiani and Mehri 2010; Kiani 2010). Based on the nonlocal elasticity theory, elastic beam models were developed for analysis of dynamical behavior of fluid conveying SWCNTs embedded in an elastic medium (Zhen and Fang 2010; Soltani et al. 2010). Vibration analysis of a simply-supported SWCNT subjected to a moving harmonic load was investigated by using the nonlocal Euler-Bernoulli beam theory (Şimşek 2010). The potential of SWCNTs as mass sensors via a vibration analysis was investigated using nonlocal elasticity theory (Lee et al. 2010; Aydogdu and Filiz 2011). Frequency shifts of the nanotubes caused by attached mass were examined to measure the sensitivity of the sensors. It is suggested again that the verification of results obtained by nonlocal continuum models and calibration of the small-scale parameter are indispensable for applicability and justification of the models.

3.2 Wave Propagation in CNT

Wang (2005) first investigated wave propagation in CNTs with nonlocal elastic Euler-Bernoulli and Timoshenko beam models. The work revealed the significance of the small-scale effect and the limitation of the applicability of local continuum models in analysis of wave propagation in CNTs. It was also found that the experimental results are qualitatively in agreement with the simulations derived from nonlocal continuum models. Further, a conservative evaluation on the small-scale parameter of $e_0 a < 2.1\,nm$ was suggested for wave propagation in SWCNTs. Wang and Hu (2005) studied on the flexural wave propagation in armchair (5, 5) and (10, 10) SWCNTs for a wide range of wave numbers by use of the nonlocal beam models and the MD simulations. Their simulation results showed that the nonlocal Timoshenko beam model provides a better prediction for the dispersion of flexural waves in the two SWCNTs than the nonlocal Euler beam. They proposed the scale coefficient $e_0 = 0.288$ for a wide range of wave length from ~ 0.2 to ~ 70 nm for the flexural wave propagation in an SWCNT through the comparison results of nonlocal Timoshenko beam model and MD simulations. Such a

speculation of a unique coefficient may not be practical as pointed out by later studies from other scholars. The nonlocal Euler-Bernoulli and Timoshenko beam models were proposed by Wang et al. (2006a, b, c) to study the small-scale effect on wave dispersion results for DWNTs with respect to the variation of DWNT's wavenumbers and diameters. Wang and Varadan (2007) showed that the nonlocal shell theory is indispensable in predicting CNT phonon dispersion relations at larger longitudinal and circumferential wavenumbers and smaller wavelength in the circumferential direction. Hu et al. (2008) modeled SWCNTs and DWCNTs as nonlocal single and double elastic cylindrical shells. It was indicated that the wave dispersion predicted by the nonlocal elastic cylindrical shell theory is in good agreement with that of the MD simulations in a wide frequency range up to the terahertz region. They also reported that nonlocal shell models are required when the wavelengths are approximately less than 2.36 nm and 0.95 nm for transverse wave in an armchair (15, 15) SWCNT and torsional wave in an armchair (10, 10) SWCNT, respectively. The MD-based estimation of the scale coefficient e_0 for the nonlocal elastic cylindrical shell model was suggested to be 0.6 and 0.2 for transverse wave and torsional wave in CNTs, respectively. The small-scale parameter introduces certain band gap region in both flexural and shear wave mode where no wave propagation occurs when the wavenumber tends to infinite (Narendar and Gopalakrishnan 2009). The frequency at which this phenomenon occurs is called the "Escape frequency" and it is proportional to the nonlocal scaling parameter.

3.3 Free Vibration of GSs

On the basis of the nonlocal constitutive relations of Eringen, Pradhan and Phadikar (2009) reformulated the classical plate theory (CLPT) and the first-order shear deformation theory (FSDT) to study free vibrations of GSs. The difference in the frequencies predicted by CLPT and FSDT is significantly smaller for double layered plate than that for single layered plate (Wang et al. 2010a, b, c). Murmu and Pradhan (2009a, b, c, d) studied small-scale effect on the free in-plane vibration of nano plates by a nonlocal continuum model. A vibration analysis of orthotropic GSs was also conducted (Pradhan and Kumar 2010, 2011a, b). A nonlocal plate model based on FSDT was developed to study free vibrations of embedded multi-layered GSs (MLGSs) (Ansari et al. 2010a, b, 2011). A nonlocal plate model for the nonlinear vibration of SLGSs with simply supported boundary conditions in thermal environments was presented and the small-scale parameter was estimated by matching the natural frequencies of SLGSs observed from the MD simulation results with those of the nonlocal plate model (Shen et al. 2010). There has been no evidence on necessity of using third order shear deformation theory to model GSs. Ansari et al. (2010a, b) evaluated a nonlocal plate model to predict the resonant frequency of SLGSs. They calibrated the small-scale parameter (e_0a) for the free vibration of squared shaped SLGSs with simply-supported and clamped boundary

conditions for a wide range of sizes from 10 nm to 50 nm by use of MD simulation results as a benchmark. Their simulation results showed that the values of e_0a are 1.41 and 0.87 nm for simply-supported and clamped SLGSs. Arash and Wang (2011) investigated free vibrations of single-layered graphene sheets (SLGSs) and double-layered GSs (DLGSs) with different boundary conditions by employing the nonlocal continuum theory and MD simulations. The vibrations of DLGS with different combinations of boundary conditions between two layers were studied. The dependence of boundary conditions and vibrational modes on calibration of the scale coefficient for a range of sizes of GSs was also investigated. They showed that the classical elastic model overestimated the resonant frequencies of the sheets by a percentage as high as 62 % at sizes of 2.47 nm. The nonlocal plate model is found to be indispensable in vibration analysis of GSs with a length less than 8 nm on their sides (Arash and Wang 2011). Their results showed that the difference between local plate model and nonlocal counterpart remains significant for all ranges of GS aspect ratios, and the overestimation is found to be around 50 % at GS aspect ratio of $a/b = 4$.

3.4 Wave Propagation in GSs

Wave propagation in GS was studied in Refs. (Wang et al. 2010a, b, c; Arash et al. 2012). It was shown that the scale coefficient introduces certain band gap region in in-plane and flexural wave modes where no wave propagation occurs (Wang et al. 2010a, b, c). This is manifested as the region where the wavenumber tends to infinite or wave speed tends to zero. Arash et al. (2012) developed a finite element (FE) model from the weak-form of the nonlocal elastic plate model and fulfilled a comprehensive study on wave propagation in GSs. They showed that the nonlocal FE plate model is indispensable in predicting graphene phonon dispersion relations, especially at wavelengths less than 1 nm, when the small-scale effect becomes dominant. Moreover, the small-scale parameter, e_0a, was calibrated through the verification process with results of MD simulations and a calibrated nonlocal parameter $e_0a = 0.18$ nm was recommended for a GS with a size of for wavenumber ranging from 2.55×10^9 to 9.17×10^9 1/m. From Fig. 2, it is found that as wavenumber increases from 2.55×10^9 to 9.17×10^9 1/m, the phase velocity tends to increase from $1.32 \times 10^3$to 3.44×10^3 m/s and the small length scale effects become dominant indicating a high scale effect in wave propagation in the GS.

4 A Re-Visit on Nonlocal Elastic Models

Nonlocal continuum mechanics models have been found to successfully describe mechanical behaviors of nano-materials. The results obtained by the nonlocal continuum models have been compared with those from MD simulations (Duan

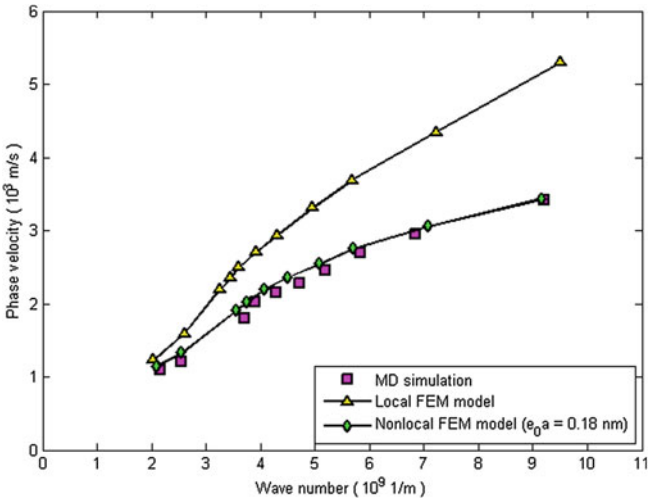

Fig. 2 Dispersion relations of a GS with a size of 3.62 × 15.03 *nm* obtained from MD simulations, the local FEM plate model, and the nonlocal FEM model (Arash et al. 2012)

et al. 2007; Arash and Ansari 2010; Hu et al. 2008; Ansari et al. 2010a, b; Arash and Wang 2011). Inspired by the pioneering works, many continuum models, including beam models, cylindrical shell models, and plate models based on the nonlocal continuum theory, have been developed and applied in studying static and dynamic analysis of CNTs and GSs. In the following section, we provide a general introduction of the elastic beam, shell, and plate models for analysis of CNTs and GSs.

4.1 General Theory

According to the nonlocal theory by Eringen (1976, 1983), the stress at a reference point x in an elastic continuum not only depends on the strain at the point but also on strains at every point of the body. The basic equations for linear homogenous and isotropic elastic solids neglecting the body forces are

$$\begin{aligned} \sigma_{ij,j} &= 0 \\ \sigma_{ij}(x) &= \int \lambda(|x - x'|, \alpha) C_{ijkl} \varepsilon_{kl}(x') dV(x'), \ \forall x \in V \\ \varepsilon_{ij} &= \frac{1}{2}\left(u_{i,j} + u_{j,i}\right) \end{aligned} \tag{5}$$

where σ_{ij} and ε_{ij} are the stress and strain tensors, respectively; C_{ijkl} is the elastic modulus tensor in classical isotropic elasticity; and $u_i$is the displacement vector.

Eq. (1) shows that stress (σ) at a reference point depends on local strain at the source x'induced by deformation within a finite volume, V, surrounding the material point, by means of a nonlocal kernel $\lambda(|x-x'|, \alpha)$ that weights the classical strains around point x. λ is the nonlocal modulus or attenuation function which is a function of the distance in Euclidean form, $|x-x'|$, and a material constant α. Material constant α defined as $e_0 a/l$ depends on the internal characteristics lengths, a (lattice parameter, granular size, distance between C–C bonds), external characteristics lengths l (crack length, wave length) and e_0 is a constant appropriate to each material. The parameter $e_0 a$ is the small-scale parameter revealing the small-scale effect on the responses of structures of nano-size. Generally, a conservative estimate of the small-scale parameter is $e_0 a < 2\,nm$ for an SWCNT (Wang 2005) for wave propagation. Note that this value is both chirality and size dependent, as the material properties of CNTs are widely acknowledged to be chirality dependent. So far, there is no rigorous study made on estimating the scale coefficient. It is suggested that the coefficient be determined by conducting a comparison of dispersion curves from nonlocal continuum mechanics and lattice dynamics of nano-material crystal structure (Eringen 1976, 1983).

The kernel function $\lambda(|x-x'|, \alpha)$ is given by Eringen as

$$\lambda(|x|, \alpha) = \left(2\pi l^2 \alpha^2\right)^{-1} K_0\left(\frac{\sqrt{x \cdot x}}{l\alpha}\right) \tag{6}$$

where K_0 is the modified Bessel function. By combining Eqs. (5) and (6), the constitutive relation may be obtained as

$$\left(1 - (e_0 a)^2 \nabla^2\right)\sigma = C : \varepsilon \tag{7}$$

where ∇^2 is the Laplacian operator.

4.2 Elastic Beam Model

It is well known that CNTs are slender tube like hollow structures with high aspect ratios. A slender CNT behaves like an elastic beam during motions, in which the central axis of the beam deforms sideways and the deformation pattern can thus be described as a single deflection. The simplest beam theory is the Euler-Bernoulli beam theory (EBT) (Sudak 2003; Wang and Liew 2007; Wang and Varadan 2006; Wang et al. 2006a, b, c; Reddy 2007; Adali 2008; Aydogdu 2009), in which Hook's law for one-dimensional stress state can be determined by

$$\sigma(x) - (e_0 a)^2 \frac{\partial^2 \sigma(x)}{\partial x^2} = E\varepsilon(x) \tag{8}$$

where E is the Young's modulus of the material. The resultant bending moment and the kinematics relation in a beam structure are given as

$$M = \int_A y\sigma dA, \ \varepsilon = -y\frac{\partial^2 w}{\partial x^2} \tag{9}$$

where y is the coordinate measured from the mid-plane in the height direction of the beam and $w(x, t)$ is the flexural deflection of the beam. The equilibrium equations of a vibrating beam structure subjected to an axial loading, P, and transverse loading, q, can be easily provided below:

$$\frac{\partial V}{\partial x} - \rho A\frac{\partial^2 w}{\partial t^2} + q(x) = 0 \tag{10a}$$

$$V - \frac{\partial M}{\partial x} + P\frac{\partial w}{\partial x} = 0 \tag{10b}$$

where $V(x,t)$ and $M(x,t)$ are the resultant shear force and bending moment on the beam; ρ is the mass density of the material, and A is the cross sectional area of the beam. Substituting Eq. (10b) into (10a) leads to the nonlocal Euler-Bernoulli beam model,

$$\begin{aligned} EI\frac{\partial^4 w}{\partial x^4} + P\frac{\partial^2}{\partial x^2}\left(w - (e_0 a)^2\frac{\partial^2 w}{\partial x^2}\right) + \rho A\frac{\partial^2}{\partial t^2}\left(w - (e_0 a)^2\frac{\partial^2 w}{\partial x^2}\right) \\ - \left(q(x) - (e_0 a)^2\frac{\partial^2 q(x)}{\partial x^2}\right) = 0 \end{aligned} \tag{11}$$

from which it is easily seen that the local or classical Euler-Bernoulli beam model is recovered when the parameter e_0 is identically zero.

Modeling of applications of CNTs can be extended from the above fundamental modeling. For example, the analysis of the vibration and stability of an SWCNT conveying fluid can be theoretically studied with a model provided below:

$$\begin{aligned} EI\frac{\partial^4 w}{\partial x^4} + P\frac{\partial^2}{\partial x^2}\left(w - (e_0 a)^2\frac{\partial^2 w}{\partial x^2}\right) + \rho A\frac{\partial^2}{\partial t^2}\left(w - (e_0 a)^2\frac{\partial^2 w}{\partial x^2}\right) \\ - \left(q(x) - (e_0 a)^2\frac{\partial^2 q(x)}{\partial x^2}\right) + m_f\left(1 - (e_0 a)^2\frac{\partial^2}{\partial x^2}\right) \\ \times \left(2v_f\frac{\partial^2 w}{\partial x \partial t} + v_f^2\frac{\partial^2 w}{\partial x^2} + \frac{\partial^2 w}{\partial t^2}\right) = 0 \end{aligned} \tag{12}$$

where m_f the mass of fluid per unit length in the carbon nanotube.

The Euler beam model is adequate for the static and dynamic analysis of CNTs with high aspect ratios. However, it is well known that the model neglects the transverse shear deformation. Thus, the nonlocal Timoshenko beam model was developed in analysis of static and analysis of CNTs by considering the effects of transverse shear deformation and rotary inertia (Wang and Liew 2007; Murmu and Pradhan 2009a, b, c, d; Wang et al. 2006a, b, c, 2007; Wang and Wang 2007; Reddy 2007).

Two nonlocal Timoshenko beam models have been presented in literature. In both models, small scale effect was well modeled in constitutive relation of normal stress and strain as shown in Eq. (8). The only difference is on the necessity of including the scale effect in shear force and strain relation. When the small-scale effect is considered in shear force term (Reddy 2007), the equilibrium equation in terms of displacement, w, and rotation, φ, is given as

$$K_sAG\frac{\partial}{\partial x}\left(\varphi+\frac{\partial w}{\partial x}\right)+(e_0a)^2\left(P\frac{\partial^4 w}{\partial x^4}+\rho A\frac{\partial^4 w}{\partial x^2\partial t^2}+\frac{\partial^2 q(x)}{\partial x^2}\right) - P\frac{\partial^2 w}{\partial x^2}-\rho A\frac{\partial^2 w}{\partial t^2}-q(x)=0 \tag{13a}$$

$$EI\frac{\partial^2\varphi}{\partial x^2}-K_sAG\left(\varphi+\frac{\partial w}{\partial x}\right)-\rho I\frac{\partial^2\varphi}{\partial t^2}+(e_0a)^2\rho I\frac{\partial^4\varphi}{\partial x^2\partial t^2}=0 \tag{13b}$$

Different from the model, Wang and Wang (2007) suggested a nonlocal Timoshenko model in which the small-scale effect is not exerted on the shear force term. The reasoning is provided hereinafter. In the Timoshenko theory, $\gamma_0=\frac{\partial w}{\partial x}-\varphi$ is defined as the shear strain at the centroidal axis, and the relation of the shear force and the shear strain is directly defined as $V=K_sAG\left(\frac{\partial w}{\partial x}-\varphi\right)$ where K_s is the shear correction factor, G is the shear modulus and A is the cross-sectional area. Therefore, the relation of the shear force and shear strain suggested in the Timoshenko beam theory is applied to the entire straight cross section, and not to a single point on the section. The assumed relation makes the local Timoshenko beam somewhat different from the local Euler-Bernoulli beam theory in which the shear stress at a certain point is related to the strain at the point. Hence, the shear stress at a cross section in the Timoshenko theory has already been considered to be a function of the strain of the cross section as a whole, the nature of a nonlocal variable. In view of this, in the nonlocal Timoshenko model, the consideration of the scale effect on the shear force may not be necessary.

In Fig. 3, we compare the fundamental resonant frequency of SWCNTs obtained from the two nonlocal Timoshenko beam models to show that modeling of scale effect in shear force is not a key consideration in the beam models. The scale effect is only indispensible in normal stress and strain relation, as shown in Eq. (8). The variation of resonant frequency of an SWCNT with length (L) ranging from 5 to 50 nm, diameter (d) 1 and 2 nm and simply-supported boundary condition modeled by the two nonlocal Timoshenko beam models is presented in Fig. 3. The mechanical parameters are set as follows: the Young's modulus $E=1\,TPa$, the Poisson's ratio $v=0.19$, the mass density $\rho=2.3\,g/\mathrm{cm}^3$, the effective thickness $t=0.34\,\mathrm{nm}$ the small-scale parameter $e_0a=2\,\mathrm{nm}$ and the shear correction factor $K_s=10/9$. The difference percentage of fundamental resonant frequency obtained by the two nonlocal Timoshenko models for an SWCNT with a diameter of 2 nm decreases from 8 % at the length of 5 nm

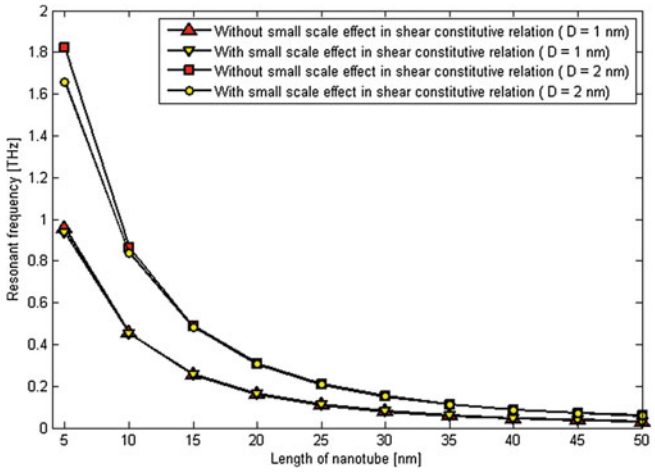

Fig. 3 Influence of the small-scale effect in shear constitutive relation oresonant frequency of an SWCNT with length ranging 5 and 50 nm, diameter 1 and 2 nm, simply-supported boundary condition and $e_0 a = 2\,nm$ modeled by two nonlocal Timoshenko beam models

($L/d = 2.5$) to only 2.5 % at the length of 10 nm ($L/d = 5$). As it is shown, the modeling of the small-scale effect in shear relation on resonant frequency is not necessary.

4.3 Elastic Shell Model

In addition to nonlocal beam models, CNTs with lower length-to-diameter ratios have been models with elastic shell models for their shell-like motions in which these CNTs move sideways while maintaining their straight axes. Hence, nonlocal shell models become indispensable especially when the length-to-radius ratio of CNTs decreases.

Two shell theories, i.e. the classical shell theory (Li and Kardomateas 2007; Wang and Varadan 2007; Hu et al. 2008) and FSDT (Arash and Ansari 2010), have been widely considered in literature for static and dynamic analysis of nanotubes.

In the classical shell theory, the three-dimensional displacement components u_x, u_y and u_z in the x, θ and z directions respectively are assumed to be

$$\begin{aligned} u_x(x,\,\theta,\,z,\,t) &= u(x,\,\theta,\,t) - z\frac{\partial w(x,\,\theta,\,t)}{\partial x} \\ u_y(x,\,\theta,\,z,\,t) &= v(x,\,\theta,\,t) - z\frac{\partial w(x,\,\theta,\,t)}{\partial x} \\ u_z(x,\,\theta,\,z,\,t) &= w(x,\,\theta,\,t) \end{aligned} \tag{14}$$

where u, v and w are the reference surface displacements. For a CNT with a radius R, length L and thickness h, the governing equations of a nanotube subjected to axial load, $\bar{N}_{xx}$,orsional force, $\bar{N}_{x\theta}$, and external pressure, $\bar{N}_{\theta\theta}$, on the basis of Flugge's shell theory are given as (Wang and Varadan 2007; Hu et al. 2008)

$$\begin{aligned}
&\frac{\partial N_{xx}}{\partial x}+\frac{1}{R}\frac{\partial N_{\theta x}}{\partial \theta}+\bar{N}_{xx}\frac{\partial^2 u}{\partial x^2}+\bar{N}_{\theta\theta}\left(\frac{1}{R}\frac{\partial^2 u}{\partial \theta^2}-\frac{\partial w}{\partial x}\right)+\frac{2}{R}\bar{N}_{x\theta}\frac{\partial^2 u}{\partial x\partial \theta}=\rho h\frac{\partial^2 u}{\partial t^2}\\
&\frac{1}{R}\frac{\partial N_{\theta\theta}}{\partial \theta}+\frac{\partial N_{x\theta}}{\partial x}+\frac{1}{R^2}\frac{\partial M_{\theta\theta}}{\partial \theta}+\frac{1}{R}\frac{\partial M_{x\theta}}{\partial x}+\bar{N}_{xx}\frac{\partial^2 v}{\partial x^2}+\frac{1}{R}\bar{N}_{\theta\theta}\left(\frac{\partial w}{\partial \theta}-\frac{\partial^2 v}{\partial \theta^2}\right)\\
&\qquad+\frac{2}{R}\bar{N}_{x\theta}\left(\frac{\partial w}{\partial \theta}-\frac{\partial^2 v}{\partial x\partial \theta}\right)=\rho h\frac{\partial^2 v}{\partial t^2} \qquad (15)\\
&\frac{\partial^2 M_{xx}}{\partial x^2}+\frac{1}{R^2}\frac{\partial^2 M_{\theta\theta}}{\partial \theta^2}+\frac{2}{R}\frac{\partial^2 M_{x\theta}}{\partial x\partial \theta}-\frac{N_{\theta\theta}}{R}+\bar{N}_{xx}\frac{\partial^2 w}{\partial x^2}\\
&+\bar{N}_{\theta\theta}\left(\frac{\partial u}{\partial x}-\frac{1}{R}\frac{\partial v}{\partial \theta}+\frac{1}{R}\frac{\partial^2 w}{\partial \theta^2}\right)+\frac{2}{R}\bar{N}_{x\theta}\left(\frac{\partial^2 w}{\partial x\partial \theta}-\frac{\partial v}{\partial x}\right)=\rho h\frac{\partial^2 w}{\partial t^2}
\end{aligned}$$

where N_{xx}, $N_{\theta\theta}$, $N_{x\theta}$; M_{xx}, $M_{\theta\theta}$, $M_{x\theta}$ are the components of internal force and the internal moments into which the small-scale effect has been incorporated (Wang and Varadan 2007). x and θ denote the longitudinal and circumferential coordinates, respectively. Equation (15) in terms of the three field variables (u, v and w) are given in Ref. (Arash and Wang 2012).

In the FSDT, the three-dimensional displacement components u_x, $u_y$and u_z in the x, θ and z directions respectively are assumed to be

$$\begin{aligned}
u_x(x,\,\theta,\,z,\,t)&=u(x,\,\theta,\,t)-z\psi_x\\
u_y(x,\,\theta,\,z,\,t)&=v(x,\,\theta,\,t)-z\psi_\theta\\
u_z(x,\,\theta,\,z,\,t)&=w(x,\,\theta,\,t)
\end{aligned} \qquad (16)$$

where u, v and $w$are the reference surface displacements and ψ_x, ψ_θ re the rotations of transverse normal about the x-axis and y-axis, respectively. The governing equations of a shell subjected to a axial force, $\overline{N}_{xx}$, torsional force, $\overline{N}_{x\theta}$, and external pressure, $\overline{N}_{\theta\theta}$, on the basis of the Donnell shell theory are given as (Arash and Ansari 2010).

$$\begin{aligned}
&\frac{\partial N_{xx}}{\partial x}+\frac{1}{R}\frac{\partial N_{x\theta}}{\partial \theta}=I_0\ddot{u}+I_1\ddot{\psi}_x\\
&\frac{\partial N_{x\theta}}{\partial x}+\frac{1}{R}\frac{\partial N_{\theta\theta}}{\partial \theta}=I_0\ddot{v}+I_1\ddot{\psi}_\theta\\
&\frac{\partial Q_{xx}}{\partial x}+\frac{1}{R}\frac{\partial Q_{\theta\theta}}{\partial \theta}-\frac{N_{\theta\theta}}{R}+\bar{N}_{xx}\frac{\partial^2 w}{\partial x^2}+\bar{N}_{xx}\frac{\partial^2 w}{\partial x^2}+\frac{1}{R}\bar{N}_{x\theta}\frac{\partial^2 w}{\partial x\partial \theta}+\frac{1}{R^2}\bar{N}_{\theta\theta}\frac{\partial^2 w}{\partial \theta^2}=I_0\ddot{w}
\end{aligned}$$

$$\frac{\partial M_{xx}}{\partial x}+\frac{1}{R}\frac{\partial M_{x\theta}}{\partial \theta}-Q_{xx}=I_1\ddot{u}+I_2\ddot{\psi}_x$$
$$\frac{\partial M_{x\theta}}{\partial x}+\frac{1}{R}\frac{\partial M_{\theta\theta}}{\partial \theta}-Q_{\theta\theta}=I_1\ddot{v}+I_2\ddot{\psi}_\theta \tag{17}$$

where N_{xx}, $N_{\theta\theta}$, $N_{x\theta}$; $Q_{xx}, Q_{\theta\theta}$; M_{xx}, $M_{\theta\theta}$, $M_{x\theta}$ are the components of internal force and the internal moments into which the small-scale effect has been incorporated (Arash and Ansari 2010). $I_i=\int_{-h/2}^{h/2}\rho z^i dz$ $(i=0,\ 1,\ 2)$ is the mass moment of inertia where ρ is the mass density. The nonlocal first order shell model in terms of displacements and rotations is provided in Ref. (Arash and Wang 2012).

4.4 Elastic Plate Model

GSs have been modeled by nonlocal continuum theories as two-dimensional nanoplates (Pradhan and Phadikar 2009; Murmu and Pradhan 2009a, b, c, d; Pradhan and Kumar 2010, 2011a, b; Ansari et al. 2010a, b; 2011; Shen et al. 2010; Arash and Wang 2011). In continuum plate models, the classical plate theory (CLPT) (Pradhan and Phadikar 2009; Murmu and Pradhan 2009a, b, c, d; Arash and Wang 2011) and FSDT (or Mindlin plate theory) (Pradhan and Phadikar 2009; Pradhan and Kumar 2010; Ansari et al. 2010a, b) have been incorporated in modeling the nanoplates.

In CLPT, transverse shear strains are neglected. Based on the CLPT, the three-dimensional displacement components u_x, u_y and u_z in the x, y and z directions respectively are assumed to be

$$\begin{aligned}u_x(x,\ y,\ z,\ t)&=u(x,\ y,\ t)-z\frac{\partial w(x,\ y,\ t)}{\partial x}\\ u_y(x,\ y,\ z,\ t)&=v(x,\ y,\ t)-z\frac{\partial w(x,\ y,\ t)}{\partial x}\\ u_z(x,\ y,\ z,\ t)&=w(x,\ y,\ t)\end{aligned} \tag{18}$$

where u, v and w are the reference surface displacements. The dynamic equilibrium equations of the stress and moment resultants are given as (Pradhan and Phadikar 2009; Pradhan and Kumar 2010; Ansari et al. 2010a, b)

$$\frac{\partial^2 M_{xx}}{\partial x^2}+2\frac{\partial^2 M_{xy}}{\partial x\partial y}+\frac{\partial^2 M_{yy}}{\partial y^2}=I_0\frac{\partial^2 w}{\partial t^2}-I_2\frac{\partial^4 w}{\partial x^2\partial t^2} \tag{19}$$

The nonlocal plate model of a single-layered graphene sheet in terms of the displacements is given below when the rotary inertia is considered:

$$D\nabla^4 w=\left(1-(e_0a)^2\nabla^2\right)\left[-I_0\frac{\partial^2 w}{\partial t^2}+I_2\left(\frac{\partial^4 w}{\partial x^2\partial t^2}+\frac{\partial^4 w}{\partial y^2\partial t^2}\right)\right] \tag{20}$$

In FSDT, the three-dimensional displacement components u_x, u_y and u_z in the x, $y$and z directions respectively are assumed to be

$$\begin{aligned} u_x(x, y, z, t) &= u(x, y, t) - z\psi_x \\ u_y(x, y, z, t) &= v(x, y, t) - z\psi_y \\ u_z(x, y, z, t) &= w(x, y, t) \end{aligned} \tag{21}$$

where u, v and w are the reference surface displacements. The governing Mindlin-type equations are given as

$$\begin{aligned} \frac{\partial N_{xx}}{\partial x} + \frac{1}{R}\frac{\partial N_{xy}}{\partial \theta} &= I_0\ddot{u} + I_1\ddot{\psi}_x \\ \frac{\partial N_{xy}}{\partial x} + \frac{1}{R}\frac{\partial N_{yy}}{\partial y} &= I_0\ddot{v} + I_1\ddot{\psi}_y \\ \frac{\partial Q_{xx}}{\partial x} + \frac{\partial Q_{yy}}{\partial y} &= I_0\ddot{w} \\ \frac{\partial M_{xx}}{\partial x} + \frac{\partial M_{xy}}{\partial y} - Q_{xx} &= I_1\ddot{u} + I_2\ddot{\psi}_x \\ \frac{\partial M_{xy}}{\partial x} + \frac{\partial M_{yy}}{\partial y} - Q_{yy} &= I_1\ddot{v} + I_2\ddot{\psi}_y \end{aligned} \tag{22}$$

where N_{xx}, N_{yy}, N_{xy}; Q_{xx}, Q_{yy}; M_{xx}, M_{yy}, M_{xy}; I_0, I_1, I_2 are the components of internal force, the internal moments into which the small-scale effect has been incorporated and mass moments of inertia (Pradhan and Phadikar 2009; Pradhan and Kumar 2010; Ansari et al. 2010a, b). The nonlocal Mindlin plate theory in terms of displacements and rotations is given in Ref. (Arash and Wang 2012).

It has been shown that resonant frequency of GSs obtained from the nonlocal plate model based on CLPT and FSDT are in good agreement with those of MD simulations (Ansari et al. 2010a, b; Arash and Wang 2011). Higher order models for analyzing GSs have not been found to be necessary for analysis of nano-plates so far.

5 Conclusions

CNTs and GSs are increasingly holding many potential applications in the ever-growing nanotechnology industry due to their superior mechanical and physical properties. A detailed understanding of mechanical behaviors of the two materials is crucial. Among different approaches for modeling nanostructures, the nonlocal continuum mechanics theory allows the consideration of the small-scale effects in analysis of nano-materials, which makes the theory as an effective way in simulating the nano-materials. The nonlocal beam and shell models have been widely employed in analysis of the static and dynamic problems of CNTs and GSs.

The determination of the magnitude of the small-scale parameter is the key issue in a successful application of the nonlocal continuum models. However, their validity has been rarely confirmed by atomistic simulation or experimental results. The value of the small-scale parameter depends on boundary condition, chirality, mode shapes, number of walls, and the nature of motions. More studies are needed to fully evaluate the nonlocal continuum models in analysis of the behavior of the nano-materials, especially MWCNTs embedded in an elastic medium with various boundary conditions, dimension and chirality.

High order continuum models providing complicated equations are not practical. Furthermore, there is not any evidence on necessity of using high order continuum models for analysis of CNTs and GSs. In sum, nonlocal Euler-Bernoulli and Timoshenko beam models for long CNTs and elastic shell models based on classical shell theory and FSDT are sufficient to model static and dynamic behavior of short CNTs. Also, plate models based on CLPT and FSDT are adequate to analyze GSs.

Further studies on the nonlocal elastic theory will focus on their applications in modeling of new applications of CNTs and GSs. On example would be the study on vibration characteristic of CNTs and GSs for modeling them as potential mass sensors using the nonlocal continuum theory. SWCNTs have been identified to be able to transport encapsulated atoms and nano-particles via the driving force induced by the vdW interaction between the CNT wall and the filled atoms and nano-particles. Transportation of nano-particles using nonlocal continuum models can be another interesting research area.

Acknowledgments This research was undertaken, in part, thanks to funding from the Canada Research Chairs Program (CRC) and the National Science and Engineering Research Council (NSERC).

References

Adali S (2008) Variational principles for multi-walled carbon nanotubes undergoing buckling based on nonlocal elasticity theory. Phys Lett A 372(35):5701–5705

Amara K, Tounsi A, Mechab I, Adda-Bedia EA (2010) Nonlocal elasticity effect on column buckling of multiwalled carbon nanotubes under temperature field. Appl Math Model 34(12):3933–3942

Ansari R, Arash B (2013) Nonlocal Fl[u-umlaut]gge shell model for vibrations of double-walled carbon nanotubes with different boundary conditions. J Appl Mech 80(2):021006–021012

Ansari R, Rajabiehfard R, Arash B (2010a) Nonlocal finite element model for vibrations of embedded multi-layered graphene sheets. Comput Mater Sci 49(4):831–838

Ansari R, Sahmani S, Arash B (2010b) Nonlocal plate model for free vibrations of single-layered graphene sheets. Phys Lett A 375(1):53–62

Ansari R, Arash B, Rouhi H (2011) Vibration characteristics of embedded multi-layered graphene sheets with different boundary conditions via nonlocal elasticity. Compos Struct 93(9):2419–2429

Antonelli GA, Maris HJ, Malhotra SG, Harper JME (2002) Picosecond ultrasonics study of the vibrational modes of a nanostructure. J Appl Phys 91(5):3261–3267

Arash B, Ansari R (2010) Evaluation of nonlocal parameter in the vibrations of single-walled carbon nanotubes with initial strain. Phys E 42(8):2058–2064
Arash B, Wang Q (2011) Vibration of single- and double-layered graphene sheets. J Nanotechnol Eng Med 2(1):011012–011017
Arash B, Wang Q (2012) A review on the application of nonlocal elastic models in modeling of carbon nanotubes and graphenes. Comput Mater Sci 51(1):303–313
Arash B, Wang Q, Liew KM (2012) Wave propagation in graphene sheets with nonlocal elastic theory via finite element formulation. Comput Methods Appl Mech Eng 223–224:1–9
Aydogdu M (2009a) Axial vibration of the nanorods with the nonlocal continuum rod model. Physica E 41(5):861–864
Aydogdu M (2009b) A general nonlocal beam theory: Its application to nanobeam bending, buckling and vibration. Phys E 41(9):1651–1655
Aydogdu M, Filiz S (2011) Modeling carbon nanotube-based mass sensors using axial vibration and nonlocal elasticity. Physica E 43(6):1229–1234
Behfar K, Naghdabadi R (2005) Nanoscale vibrational analysis of a multi-layered graphene sheet embedded in an elastic medium. Compos Sci Technol 65(7–8):1159–1164
Bodily BH, CTS (2003) Structural and equivalent continuum properties of single-walled car-bon nanotubes. Int J Mater Prod Technol 18(4–6):381–397
Brauns EB, Madaras ML, Coleman RS, Murphy CJ, Berg MA (2002) Complex local dynamics in DNA on the picosecond and nanosecond time scales. Phys Rev Lett 88(15):158101
Bunch JS, van der Zande AM, Verbridge SS, Frank IW, Tanenbaum DM, Parpia JM, Craighead HG, McEuen PL (2007) Electromechanical resonators from graphene sheets. Science 315(5811):490–493. doi:10.1126/science.1136836
ChasteJ EichlerA, MoserJ CeballosG, RuraliR BachtoldA (2012) A nanomechanical mass sensor with yoctogram resolution. Nat Nano 7(5):301–304
Chiu H-Y, Hung P, Postma HWC, Bockrath M (2008) Atomic-scale mass sensing using carbon nanotube resonators. Nano Lett 8(12):4342–4346. doi:10.1021/nl802181c
Duan WH, Wang CM, Zhang YY (2007) Calibration of nonlocal scaling effect parameter for free vibration of carbon nanotubes by molecular dynamics. J Appl Phys 101(2):024305–024307
Duan WH, Wang Q, Wang Q, Liew KM (2010) Modeling the instability of carbon nanotubes: from continuum mechanics to molecular dynamics. J Nanotechnol Eng Med 1(1):011001–011010
Duan WH, Gong K, Wang Q (2011) Controlling the formation of wrinkles in a single layer graphene sheet subjected to in-plane shear. Carbon 49(9):3107–3112
Eringen AC (1976) Nonlocal polar field models. Academic, New York
Eringen AC (1983) On differential equations of nonlocal elasticity and solutions of screw dislocation and surface waves. J Appl Phys 54(9):4703–4710
Falvo MR, Clary GJ, Taylor RM, Chi V, Brooks FP, Washburn S, Superfine R (1997) Bending and buckling of carbon nanotubes under large strain. Nature 389(6651):582–584
Fasolino A, Los JH, Katsnelson MI (2007) Intrinsic ripples in graphene. Nat Mater 6(11):858–861
Filiz S, Aydogdu M (2010) Axial vibration of carbon nanotube heterojunctions using nonlocal elasticity. Comput Mater Sci 49(3):619–627
Gao Y, Hao P (2009) Mechanical properties of monolayer graphene under tensile and compressive loading. Phys E 41(8):1561–1566
Gibson RF, Ayorinde EO, Wen Y-F (2007) Vibrations of carbon nanotubes and their composites: A review. Compos Sci Technol 67(1):1–28
Hao MJ, Guo XM, Wang Q (2010) Small-scale effect on torsional buckling of multi-walled carbon nanotubes. Eur J Mech A Solids 29(1):49–55
He XQ, Kitipornchai S, Liew KM (2005) Resonance analysis of multi-layered graphene sheets used as nanoscale resonators. Nanotechnology 16(10):2086
Heireche H, Tounsi A, Benzair A, Maachou M, Adda Bedia EA (2008) Sound wave propagation in single-walled carbon nanotubes using nonlocal elasticity. Physica E 40(8):2791–2799

Hernández E, Goze C, Bernier P, Rubio A (1998) Elastic properties of C and B_{x}C_{y}N_{z} composite nanotubes. Phys Rev Lett 80(20):4502–4505
Hu Y-G, Liew KM, Wang Q, He XQ, Yakobson BI (2008) Nonlocal shell model for elastic wave propagation in single- and double-walled carbon nanotubes. J Mech Phys Solids 56(12):3475–3485
Iijima S (1991) Helical microtubules of graphitic carbon. Nature 354(6348):56–58
Iijima S, Brabec C, Maiti A, Bernholc J (1996) Structural flexibility of carbon nanotubes. J Chem Phys 104(5):2089–2092
Khademolhosseini F, Rajapakse RKND, Nojeh A (2010) Torsional buckling of carbon nanotubes based on nonlocal elasticity shell models. Comput Mater Sci 48(4):736–742
Kiani K (2010) Longitudinal and transverse vibration of a single-walled carbon nanotube subjected to a moving nanoparticle accounting for both nonlocal and inertial effects. Phys E 42(9):2391–2401
Kiani K, Mehri B (2010) Assessment of nanotube structures under a moving nanoparticle using nonlocal beam theories. J Sound Vib 329(11):2241–2264
Kitipornchai S, He XQ, Liew KM (2005) Continuum model for the vibration of multilayered graphene sheets. Phys Rev B 72(7):075443
Krishnan A, Dujardin E, Ebbesen TW, Yianilos PN, Treacy MMJ (1998) Young's modulus of single-walled nanotubes. Phys Rev B 58(20):14013–14019
Lau K-t GuC, Hui D (2006) A critical review on nanotube and nanotube/nanoclay related polymer composite materials. Compos B Eng 37(6):425–436
Lee H-L, Chang W-J (2009) Vibration analysis of a viscous-fluid-conveying single-walled carbon nanotube embedded in an elastic medium. Phys E 41(4):529–532
Lee H-L, Hsu J-C, Chang W-J (2010) Frequency shift of carbon-nanotube-based mass sensor using nonlocal elasticity theory. Nanoscale Res Lett 5(11):1774–1778. doi:10.1007/s11671-010-9709-8
Li C, Chou T-W (2003a) A structural mechanics approach for the analysis of carbon nanotubes. Int J Solids Struct 40(10):2487–2499
Li C, Chou T-W (2003b) Single-walled carbon nanotubes as ultrahigh frequency nanomechanical resonators. Physical Review B 68(7):073405
Li C, Chou T-W (2006) Elastic wave velocities in single-walled carbon nanotubes. Phys Rev B 73(24):245407
Li R, Kardomateas GA (2007a) Thermal buckling of multi-walled carbon nanotubes by nonlocal elasticity. J Appl Mech 74(3):399–405
Li R, Kardomateas GA (2007b) Vibration characteristics of multiwalled carbon nanotubes embedded in elastic media by a nonlocal elastic shell model. J Appl Mech 74(6):1087–1094
Liew KM, Wang Q (2007) Analysis of wave propagation in carbon nanotubes via elastic shell theories. Int J Eng Sci 45(2–8):227–241
Liew KM, Wong CH, He XQ, Tan MJ, Meguid SA (2004) Nanomechanics of single and multiwalled carbon nanotubes. Phys Rev B 69(11):115429
Liew KM, He XQ, Kitipornchai S (2006) Predicting nanovibration of multi-layered graphene sheets embedded in an elastic matrix. Acta Mater 54(16):4229–4236
Lu Q, Huang R (2009) Nonlinear mechanics of single-atomic-layer graphene sheets. Int J Appl Mech 01(03):443–467
Mohammadimehr M, Saidi AR, Ghorbanpour Arani A, Arefmanesh A, Han Q (2010) Torsional buckling of a DWCNT embedded on winkler and pasternak foundations using nonlocal theory. J Mech Sci Technol 24(6):1289–1299
Murmu T, Adhikari S (2010) Nonlocal effects in the longitudinal vibration of double-nanorod systems. Phys E 43(1):415–422
Murmu T, Pradhan SC (2009a) Buckling analysis of a single-walled carbon nanotube embedded in an elastic medium based on nonlocal elasticity and Timoshenko beam theory and using DQM. Phys E 41(7):1232–1239
Murmu T, Pradhan SC (2009b) Buckling of biaxially compressed orthotropic plates at small scales. Mech Res Commun 36(8):933–938

Murmu T, Pradhan SC (2009c) Thermo-mechanical vibration of a single-walled carbon nanotube embedded in an elastic medium based on nonlocal elasticity theory. Comput Mater Sci 46(4):854–859
Murmu T, Pradhan SC (2009d) Small-scale effect on the free in-plane vibration of nanoplates by nonlocal continuum model. Phys E 41(8):1628–1633
Narendar S, Gopalakrishnan S (2009) Nonlocal scale effects on wave propagation in multi-walled carbon nanotubes. Comput Mater Sci 47(2):526–538
Novoselov KS, Geim AK, Morozov SV, Jiang D, Zhang Y, Dubonos SV, Grigorieva IV, Firsov AA (2004) Electric field effect in atomically thin carbon films. Science 306(5696):666–669. doi:10.1126/science.1102896
Parnes R, Chiskis A (2002) Buckling of nano-fibre reinforced composites: a re-examination of elastic buckling. J Mech Phys Solids 50(4):855–879
Peddieson J, Buchanan GR, McNitt RP (2003) Application of nonlocal continuum models to nanotechnology. Int J Eng Sci 41(3–5):305–312
Pradhan SC (2009) Buckling of single layer graphene sheet based on nonlocal elasticity and higher order shear deformation theory. Phys Lett A 373(45):4182–4188
Pradhan SC, Kumar A (2010) Vibration analysis of orthotropic graphene sheets embedded in Pasternak elastic medium using nonlocal elasticity theory and differential quadrature method. Comput Mater Sci 50(1):239–245
Pradhan SC, Kumar A (2011a) Buckling analysis of single layered graphene sheet under biaxial compression using nonlocal elasticity theory and DQ method. J Comput Theory Nanosci 8(7):1325–1334
Pradhan SC, Kumar A (2011b) Vibration analysis of orthotropic graphene sheets using nonlocal elasticity theory and differential quadrature method. Compos Struct 93(2):774–779
Pradhan SC, Murmu T (2009) Small scale effect on the buckling of single-layered graphene sheets under biaxial compression via nonlocal continuum mechanics. Comput Mater Sci 47(1):268–274
Pradhan SC, Murmu T (2010a) Small scale effect on the buckling analysis of single-layered graphene sheet embedded in an elastic medium based on nonlocal plate theory. Phys E 42(5):1293–1301
Pradhan SC, Murmu T (2010b) Application of nonlocal elasticity and DQM in the flapwise bending vibration of a rotating nanocantilever. Phys E 42(7):1944–1949
Pradhan SC, Phadikar JK (2009) Nonlocal elasticity theory for vibration of nanoplates. J Sound Vib 325(1–2):206–223
Qian D, Wagner GJ, Liu WK, Yu M-F, Ruoff RS (2002) Mechanics of carbon nanotubes. Appl Mech Rev 55(6):495–533
Reddy JN (2007) Nonlocal theories for bending, buckling and vibration of beams. Int J Eng Sci 45(2–8):288–307
Sánchez-Portal D, Artacho E, Soler JM, Rubio A, Ordejón P (1999) Ab initio structural, elastic, and vibrational properties of carbon nanotubes. Phys Rev B 59(19):12678–12688
Schedin F, Geim AK, Morozov SV, Hill EW, Blake P, Katsnelson MI, Novoselov KS (2007) Detection of individual gas molecules adsorbed on graphene. Nat Mater 6(9):652–655
Shen H-S (2010a) Buckling and postbuckling of radially loaded microtubules by nonlocal shear deformable shell model. J Theor Biol 264(2):386–394
Shen H-S (2010b) Nonlocal shear deformable shell model for bending buckling of microtubules embedded in an elastic medium. Phys Lett A 374(39):4030–4039
Shen H-S, Zhang C-L (2010) Torsional buckling and postbuckling of double-walled carbon nanotubes by nonlocal shear deformable shell model. Compos Struct 92(5):1073–1084
Shen L, Shen H-S, Zhang C-L (2010) Nonlocal plate model for nonlinear vibration of single layer graphene sheets in thermal environments. Comput Mater Sci 48(3):680–685
Şimşek M (2010) Vibration analysis of a single-walled carbon nanotube under action of a moving harmonic load based on nonlocal elasticity theory. Physica E 43(1):182–191
Sirtori C (2002) Applied physics: bridge for the terahertz gap. Nature 417(6885):132–133

Soltani P, Taherian MM, Farshidianfar A (2010) Vibration and instability of a viscous-fluid-conveying single-walled carbon nanotube embedded in a visco-elastic medium. J Phys D Appl Phys 43(42):425401

Song J, Shen J, Li XF (2010) Effects of initial axial stress on waves propagating in carbon nanotubes using a generalized nonlocal model. Comput Mater Sci 49(3):518–523

Stankovich S, Dikin DA, Dommett GHB, Kohlhaas KM, Zimney EJ, Stach EA, Piner RD, Nguyen ST, Ruoff RS (2006) Graphene-based composite materials. Nature 442(7100): 282–286

Sudak LJ (2003) Column buckling of multiwalled carbon nanotubes using nonlocal continuum mechanics. J Appl Phys 94(11):7281–7287

Sun C, Liu K (2007) Vibration of multi-walled carbon nanotubes with initial axial loading. Solid State Commun 143(4–5):202–207

Thostenson ET, Ren Z, Chou T-W (2001) Advances in the science and technology of carbon nanotubes and their composites: a review. Compos Sci Technol 61(13):1899–1912

Wagner HD, Lourie O, Feldman Y, Tenne R (1998) Stress-induced fragmentation of multiwall carbon nanotubes in a polymer matrix. Appl Phys Lett 72(2):188–190

Wang Q (2005) Wave propagation in carbon nanotubes via nonlocal continuum mechanics. J Appl Phys 98(12):124301–124306

Wang L (2009) Vibration and instability analysis of tubular nano- and micro-beams conveying fluid using nonlocal elastic theory. Phys E 41(10):1835–1840

Wang L, Hu H (2005) Flexural wave propagation in single-walled carbon nanotubes. Phys Rev B 71(19):195412

Wang Q, Liew KM (2007) Application of nonlocal continuum mechanics to static analysis of micro- and nano-structures. Phys Lett A 363(3):236–242

Wang Q, Varadan VK (2006a) Wave characteristics of carbon nanotubes. Int J Solids Struct 43(2):254–265

Wang Q, Varadan VK (2006b) Vibration of carbon nanotubes studied using nonlocal continuum mechanics. Smart Mater Struct 15(2):659

Wang Q, Varadan VK (2007) Application of nonlocal elastic shell theory in wave propagation analysis of carbon nanotubes. Smart Mater Struct 16(1):178

Wang Q, Wang CM (2007) The constitutive relation and small scale parameter of nonlocal continuum mechanics for modelling carbon nanotubes. Nanotechnology 18(7):075702

Wang X, Yang HK, Dong K (2005) Torsional buckling of multi-walled carbon nanotubes. Mater Sci Eng, A 404(1–2):314–322

Wang CM, Zhang YY, Sai Sudha R, Kitipornchai S (2006a) Buckling analysis of micro- and nano-rods/tubes based on nonlocal Timoshenko beam theory. J Phys D Appl Phys 39(17): 3904

Wang Q, Varadan VK, Quek ST (2006b) Small scale effect on elastic buckling of carbon nanotubes with nonlocal continuum models. Phys Lett A 357(2):130–135

Wang Q, Zhou GY, Lin KC (2006c) Scale effect on wave propagation of double-walled carbon nanotubes. Int J Solids Struct 43(20):6071–6084

Wang CM, Zhang YY, He XQ (2007) Vibration of nonlocal Timoshenko beams. Nanotechnology 18(10):105401

Wang Y-Z, Li F-M, Kishimoto K (2010a) Scale effects on thermal buckling properties of carbon nanotube. Phys Lett A 374(48):4890–4893

Wang Y-Z, Li F-M, Kishimoto K (2010b) Wave propagation characteristics in fluid-conveying double-walled nanotubes with scale effects. Comput Mater Sci 48(2):413–418

Wang Y-Z, Li F-M, Kishimoto K (2010c) Scale effects on the longitudinal wave propagation in nanoplates. Phys E 42(5):1356–1360

Xie GQ, Han X, Liu GR, Long SY (2006) Effect of small size-scale on the radial buckling pressure of a simply supported multi-walled carbon nanotube. Smart Mater Struct 15(4):1143

Yakobson BI, Brabec CJ, Bernholc J (1996) Nanomechanics of carbon tubes: instabilities beyond linear response. Phys Rev Lett 76(14):2511–2514

Yakobson BI, Campbell MP, Brabec CJ, Bernholc J (1997) High strain rate fracture and C-chain unraveling in carbon nanotubes. Comput Mater Sci 8(4):341–348

Yan Y, Wang WQ, Zhang LX (2010) Nonlocal effect on axially compressed buckling of triple-walled carbon nanotubes under temperature field. Appl Math Model 34(11):3422–3429

Yang J, Jia XL, Kitipornchai S (2008) Pull-in instability of nano-switches using nonlocal elasticity theory. J Phys D Appl Phys 41(3):035103

Yang J, Ke LL, Kitipornchai S (2010) Nonlinear free vibration of single-walled carbon nanotubes using nonlocal Timoshenko beam theory. Phys E 42(5):1727–1735

Zhang YQ, Liu GR, Wang JS (2004) Small-scale effects on buckling of multiwalled carbon nanotubes under axial compression. Phys Rev B 70(20):205430

Zhang YQ, Liu GR, Xie XY (2005) Free transverse vibrations of double-walled carbon nanotubes using a theory of nonlocal elasticity. Phys Rev B 71(19):195404

Zhang YQ, Liu GR, Han X (2006) Effect of small length scale on elastic buckling of multi-walled carbon nanotubes under radial pressure. Phys Lett A 349(5):370–376

Zhang YY, Wang CM, Duan WH, Xiang Y, Zong Z (2009a) Assessment of continuum mechanics models in predicting buckling strains of single-walled carbon nanotubes. Nanotechnology 20(39):395707

Zhang YY, Wang CM, Tan VBC (2009b) Assessment of Timoshenko beam models for vibrational behavior of single-walled carbon nanotubes using molecular dynamics. Adv Appl Math Mech 1(1):89–106

Zhang Y, Wang CM, Challamel N (2010) Bending, buckling, and vibration of micro/nanobeams by hybrid nonlocal beam model. J Eng Mech 136(5):562–574

Zhen Y, Fang B (2010) Thermal–mechanical and nonlocal elastic vibration of single-walled carbon nanotubes conveying fluid. Comput Mater Sci 49(2):276–282

A Heterogeneous Discrete Approach of Interfacial Effects on Multi-Scale Modelling of Carbon Nanotube and Graphene Based Composites

S. K. Georgantzinos, G. I. Giannopoulos, K. N. Spanos and N. K. Anifantis

Abstract A multi-scale finite element formulation, combining nanoscopic and macroscopic considerations is presented, for the modelling of the elastic mechanical response of single walled carbon nanotube (single-walled CNT) and graphene based composites. Based on micromechanical theory and adopting appropriate representative volume elements, the carbon nanostructures are modelled according to the molecular mechanics theory via the use of spring elements, while the matrix is modelled as a continuum medium. Here, emphasis is given on interfacial region modelling, where the interactions between the two phases are implemented by utilizing appropriate stiffness variations describing a heterogeneous interfacial region. Using the proposed technique, predictions on mechanical properties and load transfer conditions are performed. The formulation is validated through comparisons with corresponding solutions, obtained from the literature, where possible.

Keywords Carbon nanotube · Graphene · Multi-scale modelling · Finite element method · Interface · Nanocomposite

S. K. Georgantzinos (✉) · K. N. Spanos · N. K. Anifantis
Machine Design Laboratory Mechanical and Aeronautics Engineering Department, University of Patras, 26500 Patras, Greece
e-mail: sgeor@mech.upatras.gr

K. N. Spanos
e-mail: kspanos@mech.upatras.gr

N. K. Anifantis
e-mail: nanif@mech.upatras.gr

G. I. Giannopoulos
Department of Mechanical Engineering, Technological and Educational Institute of Patras, 26334 Patras, Greece
e-mail: g_giann@mech.upatras.gr

K. I. Tserpes and N. Silvestre (eds.), *Modeling of Carbon Nanotubes, Graphene and their Composites*, Springer Series in Materials Science 188,
DOI: 10.1007/978-3-319-01201-8_3,

1 Introduction

Carbon nanotubes (CNTs) and graphene have been proposed as some of the most promising materials for nanoelectromechanical systems due to their extremely high Young's modulus, strength and other properties.

The development and exploitation of novel materials can lead to the growth of new fields of research as well as new solutions to technological problems that could not be resolved up to now. Graphene is one of the latest breakthrough in sciences and technology promising novel applications in different aspects of life. Actually, it is an allotrope of carbon and its structure is one-atom-thick planar sheets of sp2-bonded carbon atoms that are densely packed in a honeycomb crystal lattice. Graphene is the basic structural element of other carbon allotropes including graphite, charcoal, carbon nanotubes and fullerenes. It is most easily visualized as an atomic-scale chicken wire made of carbon atoms and their bonds.

Moreover, CNTs are molecular-scale hollow cylinders composed of carbon atoms arranged in a hexagonal network. For the better understanding of their structure, someone can imagine the well-known geometric structure of the graphene that has to be ideally cut and rolled up to make a seamless cylinder. They may consist of only one layer (single-walled CNTs) or more layers (multi-walled CNTs) of rolled graphene sheets.

The combination of the exceptional mechanical properties, i.e., the outstanding Young's modulus and tensile strength, the small size and the low density of CNTs, make them ideal material components for use as strong reinforcements. Therefore, the study of the mechanical performance of CNT-based composites and the discovery of possible innovative applications has attracted the interest of many researchers. Recently, the use of CNTs as structural reinforcement has resulted in a significant enhancement of the mechanical properties of a variety of materials (Lordi and Yao 2000).

The numerical prediction of the mechanical behavior of nanocomposites is an essential task to enable their efficient production and design because analytical models are difficult to establish and experiments are very expensive due to the nanoscale dimensions involved. MD simulations have accurately predicted the mechanical behavior of individual CNTs, while fewer MD based studies have been performed on CNT-reinforced composites (Frankland et al. 2003; Zou et al. 2006; Han and Elliott 2007), possibly because the MD approach is restricted to small length and time scale problems due to its computational cost. Another possible approach for simulating these systems is by using continuum mechanics based approaches, which seem to be computationally feasible. Continuum mechanics approaches based on either finite element method (FEM) (Chen and Liu 2004; Seidel and Lagoudas 2006; Ashrafi and Hubert 2006) or boundary element method (BEM) (Liu and Chen 2003) have been used to evaluate the elastic properties of CNT-based composites via micromechanical methods. However, in all previous studies, both CNT and matrix materials were modelled as continuum, which

created a noticeable limitation in the accuracy of those simulations since the microstructure of CNTs was not taken into consideration.

The performance of CNT-based composites is greatly influenced by the interface which has different properties from those of the matrix and the CNT. Generally, the three main mechanisms of interfacial load transfer are micromechanical interlocking, chemical bonding, and the van der Waals interactions between the matrix and the reinforcements. Al-Ostaz et al. (2008) investigated single-walled CNT-polymer interface interactions in nanoscale via MD. To represent the CNT-polymer load transfer characteristics and consequently the interface between the CNTs and the polymer, (Frankland et al. 2002) employed just van der Waals forces. Saber-Samadari and Khatibi (2006) considered a continuum interfacial zone with variable elastic modulus to investigate a CNT composite via a unit cell method. However, in the specific study the mechanical response of all phases including CNT were assumed as continuum.

A finite element formulation, based on micromechanical analysis, is proposed for the evaluation of the elastic mechanical behavior of a matrix, filled with short or long CNTs or graphene. Concerning the nanostructured reinforcement modelling, i.e. CNT and graphene modelling, the method is able to utilize the three dimensional atomistic microstructure of the reinforcement, defining nodes at the corresponding atomic positions of carbon atoms. Appropriate spring elements, which interconnect the atoms, incorporate directly the potential energies provided by molecular theory and therefore simulate accurately the interatomic interactions (Rappe et al. 1992). In contrast, the matrix can be considered as a continuum medium. In addition, the load transfer between the reinforcement and the matrix is modelled by special joint elements of variable stiffness. In this way, a heterogenous interface is simulated. The advantage of the proposed hybrid method is that it utilizes macroscopic properties in order to describe the matrix and interface behavior as well as may efficiently couple the nano scaled reinforcement with the macroscale matrix. Detailed representation of the molecular nanostructure is avoided, making the proposed formulation attractive and simultaneously, significant reduction in computational cost and complexity is achieved. Predicted results regarding the nanocomposite mechanical properties are presented and compared to solutions obtained from the literature. The reinforcing ability of nanostructured reinforcements is evaluated.

2 Nano-Reinforcement Modelling

The nanomaterials, which are used to enhance the mechanical behavior of the matrix, are modelled according to their exact atomistic structure, while appropriate potential energy equations are adopted in order to approximate the interatomic interactions observed on them. Small displacement theory is adopted to simulate their elastic response.

2.1 Nanoparticles Geometry

2.1.1 Geometry of Graphene

The honeycomb lattice of graphene, which is assumed to have thickness $t_g = 0.34$ nm (Arroyo and Belytschko 2004) in the present analysis, has a unit cell represented in Fig. 1 by the vectors $\mathbf{r}_1$ and $\mathbf{r}_2$ such that:

$$|\mathbf{r}_1| = |\mathbf{r}_2| = \sqrt{3} r_0 \tag{1}$$

where r_0 is the carbon—carbon distance taken equal to 0.1421 nm in present work. In this basis any lattice vector $\mathbf{r}$ is represented as:

$$\mathbf{r} = n\mathbf{a}_1 + m\mathbf{a}_2 \tag{2}$$

where n, m are integers. In Cartesian coordinates:

$$\mathbf{r}_1 = r_0 \begin{bmatrix} 3/2 & \sqrt{3}/2 & 0 \end{bmatrix}^{\mathrm{T}} \tag{3}$$

$$\mathbf{r}_2 = r_0 \begin{bmatrix} 3/2 & -\sqrt{3}/2 & 0 \end{bmatrix}^{\mathrm{T}} \tag{4}$$

The vectors connecting any atom to its nearest neighbors are:

$$\boldsymbol{\delta}_1 = (\mathbf{r}_1 - 2\mathbf{r}_2)/3 \tag{5}$$

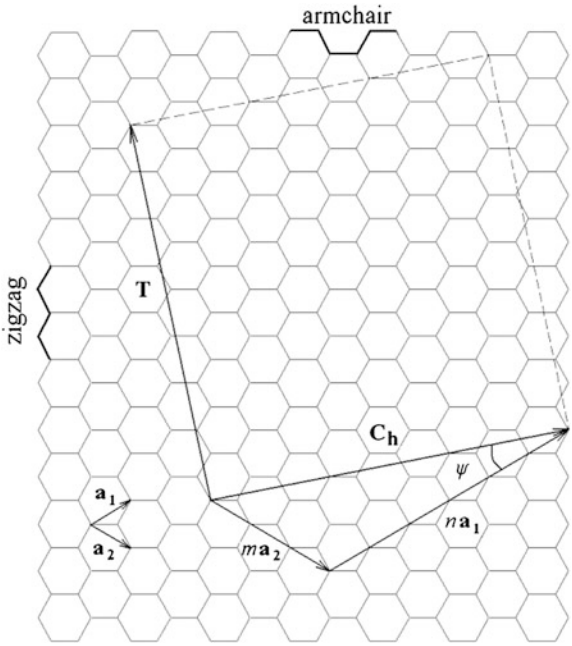

Fig. 1 Generation of a single-walled CNT from a graphene sheet (Giannopoulos et al. 2008)

$$\boldsymbol{\delta}_2 = (\mathbf{r}_2 - 2\mathbf{r}_1)/3 \tag{6}$$

$$\boldsymbol{\delta}_3 = (\mathbf{r}_1 + \mathbf{r}_2)/3 \tag{7}$$

Equations (1)–(7) describe completely the discrete in plane geometry of graphene, essentially defined by the positions of carbon atoms. It becomes evident that the dimensions of width and length of a finite sized graphene, i.e. a GNR may not be integers since they are determined by the positions of edge carbon atoms.

2.1.2 Geometry of CNT

A single-walled CNT can be generated by rolling a graphene sheet, which is ideally cut, to make a cylinder. The graphene sheet must be rolled up in the direction of the chiral vector $\mathbf{C_h}$ defined as (see Fig. 1):

$$\mathbf{C_h} = n\mathbf{a}_1 + m\mathbf{a}_2 \tag{8}$$

where $\mathbf{a}_1$ and $\mathbf{a}_2$ are the basis vectors of the honeycomb lattice and integers (n,m) are the number of steps along the zigzag carbon bonds and generally are used to name a nanotube. A nanotube (n,n) is usually named as armchair while the nanotube $(n,0)$ is usually named zigzag. The chiral angle ψ $(0 \leq \psi \leq 30^{\circ})$ is defined as:

$$\tan\ \psi = \frac{\sqrt{3}m}{(2n+m)} \tag{9}$$

It is obvious that for an armchair nanotube $\psi = 30^{\circ}$ while for a zigzag $\psi = 0^{o}$. The nanotube's diameter D is given by the following equation:

$$D = \frac{r_0\sqrt{3\,(n^2+nm+m^2)}}{\pi} \tag{10}$$

Chiral vector $\mathbf{C_h}$ and the following translational vector $\mathbf{T}$ define the ideal rectangular cutting area of graphene sheet:

$$\mathbf{T} = \left(\frac{2m+n}{W}\right)\mathbf{a}_1 + \left(-\frac{2n+m}{W}\right)\mathbf{a}_2 \tag{11}$$

where W defines the higher common divisor of $2m+n$ and $2n+m$.

In the present work, for simplicity, the original coordinate system of the graphene sheet $(x',\ y')$ is transformed into a new system $(x,\ y,\ z)$ of the nanotube such that $\mathbf{T}$ is along y'-axis. Then, the graphene atomic coordinates are converted to those of the nanotube according to the equation (Kołoczek et al. 2001):

$$(x,\ y,\ z) = \left(R\cos\left(\frac{x'}{R}\right),\ \ r\sin\left(\frac{x'}{R}\right),\ \ y'\right) \tag{12}$$

where R is the nanotube's radius.

The thickness of CNTs investigated here is taken equal to $t_n = 0.34$ nm (Li and Chou 2005).

2.2 Governing Equations

The total potential energy, omitting non-bonded interactions, i.e. the electrostatic energy and the energy due to van der Waals interaction, is a sum of energies caused by the bonded interatomic interactions, which are depicted in Fig. 2a, and may be expressed by the following equation (Rappe et al. 1992):

$$U = \sum U_r + \sum U_\theta + \sum U_\theta + \sum U_\omega \tag{13}$$

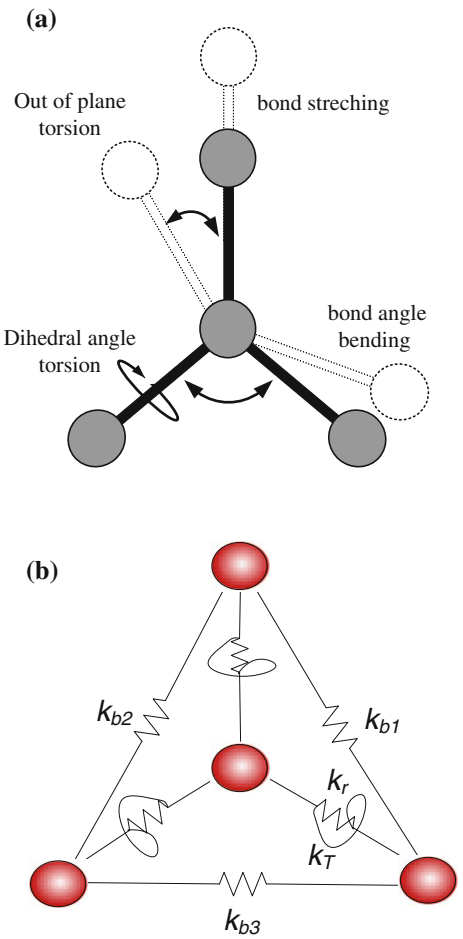

Fig. 2 Force field in neighboring atoms **a** interatomic interactions and **b** spring model (Georgantzinos et al. 2010)

where U_r represents the energy due to bond stretching, U_θ the energy due to bond angle bending, U_ϕ the energy due to dihedral angle torsion and U_ω the energy due to out of plane torsion.

Under the assumption of small deformations, the harmonic approximation is adequate for describing potential energy (Gelin 1994) and therefore the force field. By adopting the simplest harmonic forms and combining the dihedral angle, torsion with the out of plane torsion into a single equivalent term then the following terms can describe the total potential energy (Meo and Rossi 2006):

$$U_r = \frac{1}{2}k_r(\Delta r)^2, \quad \frac{d^2U_r}{d\Delta r^2} = k_r \tag{14}$$

$$U_\theta = \frac{1}{2}k_\theta(\Delta\theta)^2, \quad \frac{d^2U_\theta}{d\Delta\theta^2} = k_\theta \tag{15}$$

$$U_\tau = U_\phi + U_\omega = \frac{1}{2}k_\tau(\Delta\theta)^2, \quad \frac{d^2U_\tau}{d\Delta\tau^2} = k_\tau \tag{16}$$

where k_r, k_θ and k_τ are the bond stretching, bond angle bending, and torsional resistance force constants, respectively, while Δr, $\Delta\theta$ and $\Delta\phi$ represent the bond length, bond angle and twisting bond angle variations, respectively.

The second derivatives of the potential energy terms appearing in Eqs. (14)–(16) with respect to bond stretch, bond angle and twisting bond angle variations, respectively, produce spring stiffness coefficients k_r, k_θ and k_τ. Thus, here, axial and torsional springs that straightforwardly introduce the physical constants are utilized (Fig. 2b) in order to describe the force field. The springs interconnect the nodes that have been extracted from the Eq. (12). The bond angle bending interaction is simulated by axial springs, which have stiffness

$$k_{bi} = \left(\frac{1}{a_{c-c}\cos(90^o - \gamma)}\right)^2 k_\theta \tag{17}$$

as has been described in (Giannopoulos et al. 2008), where $\gamma = 30^o$ in the hexagonal lattice of the graphene. This angle may vary for each C–C–C microstructure in a CNT according to its type and radius due to its cylindrical shape. In the case of chiral nanotubes, three bending springs of different stiffness i.e. $k_{b1} \neq k_{b2} \neq k_{b3}$ appear in the unit cell (Fig. 2b). In the cases of armchair and zigzag nanotubes, two of the three bending spring stiffnesses are equal due to the same angle γ. In the other hand, because of the planar shape of the graphene sheets, all bond angle bending springs have equal stiffness, i.e. $k_{b1} = k_{b2} = k_{b3}$.

On every notional line defined by C–C bonds, a spring-based finite element (a-element) is developed consisting of one axial and one torsion spring. In respect to the local coordinate system of the a-element, the elemental equation for the axial spring has the following form,

$$k_r\mathbf{I_{20}u} = \mathbf{F} \tag{18}$$

where

$$\mathbf{I_{20}} = \begin{bmatrix} 1 & -1 \\ -1 & 1 \end{bmatrix} \tag{19}$$

where vector F contains the forces applied on nodes 1 and 2 of the element, and u is the vector of nodal displacements ($\mathbf{u} = [\, u_1 \quad u_2 \,]^{\mathrm{T}}$, $\mathbf{F} = [\, F_1 \quad F_2 \,]^{\mathrm{T}}$). Similarly, for the torsional spring of the a-element, it can be written that

$$k_\tau \mathbf{I_{20}} \boldsymbol{\theta} = \mathbf{T} \tag{20}$$

where θ is the vector of nodal rotations and T is the vector of the applied torsional moments ($\boldsymbol{\theta} = [\, \theta_1 \quad \theta_2 \,]^{\mathrm{T}}$,$\mathbf{T} = [\, T_1 \quad T_2 \,]^{\mathrm{T}}$). Therefore, the elemental equation for the a-element is

$$\begin{bmatrix} k_r \mathbf{I_{20}} & \mathbf{0} \\ \mathbf{0} & k_\tau \mathbf{I_{20}} \end{bmatrix} \begin{bmatrix} \mathbf{u} \\ \boldsymbol{\theta} \end{bmatrix} = \begin{bmatrix} \mathbf{F} \\ \mathbf{T} \end{bmatrix} \quad \text{or} \quad \mathbf{k_a U} = \mathbf{P} \tag{21}$$

where **U** is the vector of nodal translations and rotations, **P** is the column vector of loads, and finally and ka is the elemental stiffness matrix.

Correspondingly, elements simulating the bond angle bending are also developed ($3.b_i$-element). The equations for these elements are

$$\begin{bmatrix} k_{bi} \mathbf{I_{20}} & \mathbf{0} \\ \mathbf{0} & \mathbf{0} \end{bmatrix} \begin{bmatrix} \mathbf{u} \\ \boldsymbol{\theta} \end{bmatrix} = \begin{bmatrix} \mathbf{F} \\ \mathbf{T} \end{bmatrix} \quad \text{or} \quad \mathbf{k_{bi} U} = \mathbf{P} \tag{22}$$

where k_{bi} is the stiffness coefficient, as previously described.

Hence, the elemental matrices expressed in the global coordinate system are

$$\mathbf{K_a} = \mathbf{T^T k_a T} \tag{23}$$

$$\mathbf{K_{bi}} = \mathbf{T^T k_{bi} T} \tag{24}$$

where **T** is the appropriate transformation matrix, as defined in (Gelin 1994). The displacements and rotations as well as the loads are related by the equation

$$\mathbf{U} = \mathbf{TD} \quad \mathbf{R} = \mathbf{T^T P} \tag{25}$$

where **D** is the vector of displacements and rotations and **R** is the vector of loads with respect to the global coordinates. The superscript T in the above equations denotes matrix transposition. Finally, the elemental equations in the global system become

$$\mathbf{K_a D} = \mathbf{R} \tag{26}$$

$$\mathbf{K_{bi} D} = \mathbf{R} \tag{27}$$

According to the atomistic microstructure of each nanotube or graphene sheet, we assemble the global stiffness matrix K from the above elemental matrices.

After applying the CNT boundary conditions, the mechanical response of nanotube or graphene sheet is evaluated using common finite element procedures. The previous formulation has been algorithmically programmed and can automatically generate discrete spring-based models that are able to simulate the mechanical behavior of any type of single-walled CNTs.

3 Matrix Modelling

The matrix can be modelled discretely, by taking into consideration its molecular structure. However, this would increase significantly the computational cost, as well as the complexity of the whole model. Therefore, the matrix is regarded as a continuum isotropic elastic medium of elastic modulus E_m and Poisson's ratio v_m. Linear three-dimensional hexahedral isoparametric elements are used for the discretization of the matrix (annotated hereafter as s elements). These elements have eight nodes with three degrees of freedom per node (three translations) and a linear strain variation displacement mode (Fig. 3).

4 Interface Modelling

In some multi-scale modelling efforts (Montazeri and Naghdabadi 2010; Shokrieh and Rafiee 2010; Li and Chou 2006), the use of linear spring elements with stiffness obtained by van der Waals interactions is proposed, in order to approach the interfacial mechanical behavior. Specifically, these spring elements connect carbon atoms of the nanostructure with nodes surrounding the inner surface of the continuum matrix. We note that by using such a technique, the stiffness of the interface is strongly dependent on the finite element mesh, since a different mesh gives different number of interfacial springs. In order to avoid this, in this work it is proposed a new technique for the modeling of the interfacial region.

Between the matrix and the nanomaterial, complicated phenomena occur such as chemical bonding and van der Waals interactions which depend on the nature of the interacting atoms and relative distances. Since it is difficult to implement implicitly such phenomena in a numerical model, a computationally efficient formulation capable of representing approximately an overall interfacial mechanical response should be adopted.

Since most modelling difficulties arise when CNT reinforcement is considered, the interfacial formulation will be explained in the following only for this case.

As it was previously mentioned, the nanostructure of a carbon nanotube is developed around a mean diameter, while its thickness is considered indirectly. Therefore, from a physical point of view, it is assumed that the interfacial interactions take place along a radial distance equal to $t_n/2$. Due to the atomistic modelling of nanomaterials, a discrete modelling of the interfacial region is

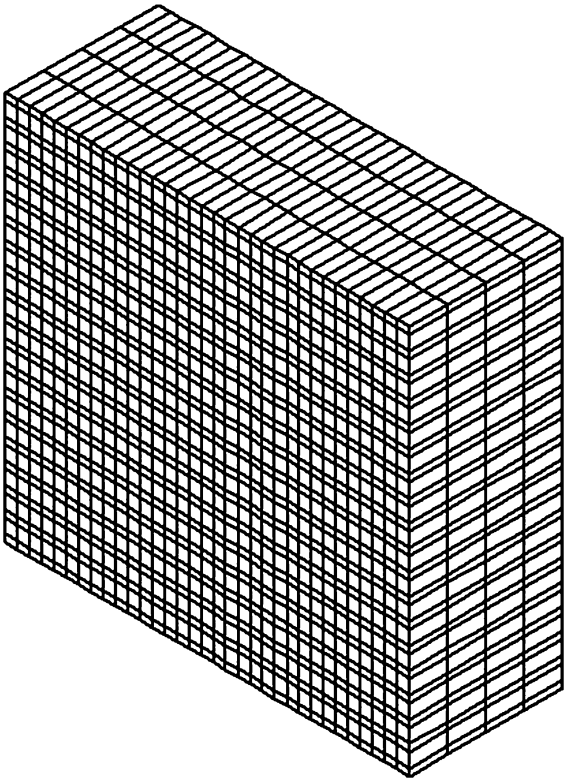

Fig. 3 Example of matrix discretization using linear three-dimensional hexahedral isoparametric elements

adopted. Two-noded interfacial joint elements (3. annotated hereafter as *j* elements), are employed. As Fig. 4 illustrates, these elements interconnect radially the atoms-nodes of the nanomaterial with corresponding nodes, belonging to the inner surface of the matrix.

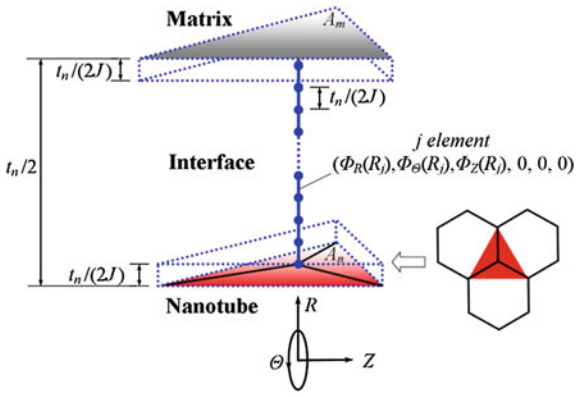

Fig. 4 Finite element model of interfacial interactions (Giannopoulos et al. 2010)

A series of J elements of equal lengths $t_n/(2J)$, is used to span the distance $t_n/2$. The translation stiffnesses, along the three directions of these elements are defined according to a local cylindrical coordinate system (R, Θ, Z), positioned at the center of the CNT perimeter. It is assumed that their values are functions of the radial coordinate R:

$$k_i = \Phi_i(R) \tag{28}$$

where $i = R,\ \Theta,\ \mathrm{Z}$. The following step is to define the lower and upper bounds for functions $\Phi_i(R)$, by taking into consideration their minimum and maximum allowed values. The radial reaction f_R, produced by the joint above the CNT, for a ΔR deformation, is according to Eq. (28):

$$f_R = \Phi_R(R_1)\Delta R \tag{29}$$

where R_1 denotes the radial position of the joint element and is equal to:

$$R_1 = r_n + t_n/(2J) \tag{30}$$

Equation (29) may take the form:

$$\frac{f_R}{A_n} = \frac{\Phi_R(R_1)(t_n/2J)}{A_n}\frac{\Delta R}{(t_n/2J)} \tag{31}$$

where A_n indicates the mean surface area of the nanotube affected by the joint, given by the equation:

$$A_n = \frac{2\pi r_n l_n}{n_\mathrm{c}} \tag{32}$$

where n_c is the total number of carbon atoms of the tube. Equation (31) may be equivalently written as:

$$\sigma_R = \frac{\Phi_R(R_1)t_n n_\mathrm{c}}{4\pi J r_n l_n}\varepsilon_R \tag{33}$$

where σ_R and ε_R denote radial stress and strain, respectively. It is coherent to assume that the radial elastic modulus of the interface, exactly above the reinforcement, is equal to the corresponding radial elastic modulus of the nanotube E_{Rn}. Therefore, from Eq. (33) the following constrained equation is obtained:

$$\Phi_R(R_1) = \frac{4\pi J r_n l_n}{t_n n_\mathrm{c}}E_{Rn} \tag{34}$$

A similar constrain equation can be obtained for function Φ_Θ. The circumferential reaction f_Θ, produced by the joint above the single-walled for a $\Delta\Theta$ deformation, is:

$$f_R = \Phi_R(R_1)\Delta R \tag{35}$$

or

$$\frac{f_\Theta}{A_n} = \frac{\Phi_R(R_1) t_n n_c}{4\pi J r_n l_n} \frac{\Delta\Theta}{(t_n/2J)} \tag{36}$$

For small strains the above equation becomes:

$$\tau_\Theta = \frac{\Phi_R(R_1) t_n n_c}{4\pi J r_n l_n} \gamma_R \tag{37}$$

where τ_Θ and γ_Θ denote circumferential shear stress and strain, respectively. The above equation leads to the following constrain equation:

$$\Phi_\Theta(R_1) = \frac{4\pi J r_n l_n}{t_n n_c} G_{\Theta n} \tag{38}$$

where $G_{\Theta n}$ is the circumferential shear modulus of the single-walled CNT. Accordingly, function Φ_Z becomes:

$$\Phi_Z(R_1) = \frac{4\pi J r_n l_n}{t_n n_c} G_{Z n} \tag{39}$$

where $G_{Z n}$ is the longitudinal shear modulus of the single-walled CNT. In a similar manner and by making the same considerations for the joint element located exactly below the matrix material, the following equations are obtained:

$$\Phi_R(R_2) = \frac{4\pi J (r_n + t_n/2) l_n}{t_n n_c} E_{R m} \tag{40}$$

$$\Phi_\Theta(R_2) = \frac{4\pi J (r_n + t_n/2) l_n}{t_n n_c} G_{\Theta m} \tag{41}$$

$$\Phi_Z(R_2) = \frac{4\pi J (r_n + t_n/2) l_n}{t_n n_c} G_{Z m} \tag{42}$$

where $E_{R m}$, $G_{\Theta m}$ and $G_{Z m}$ are the radial elastic modulus, the circumferential shear modulus and longitudinal shear modulus of the matrix material, respectively. Finally R_2 denotes the radial position of the specific joint element and is given by the following equation:

$$R_2 = r_n + t_n/2 - t_n/(2J) \tag{43}$$

It has to be noted that the above stiffness variations are not appropriate for the capped edges of the tube. Therefore, in order to describe the interface surrounding the capped edges, the above functions are expressed with respect to an appropriate local spherical coordinate system positioned at the centre of the cap.

Summarizing, a heterogeneous interface is modelled in a discrete manner by introducing joint elements of variable stiffness properties. Their mechanical response is prescribed by user-defined functions, along the three dimensions of a

local coordinate system. These functions, from physical point of view, are set to be bounded exclusively by macroscopic parameters of the two phases surrounding the interface.

5 Micromechanical Analysis

In order to treat and investigate the nanocomposite without using a computationally complicated modelling, micromechanical theory is adopted according which a unit cell element is adequate for the analysis of the whole composite volume. Periodic distribution of nanoparticles within matrix is assumed.

5.1 Geometry of the Composite Model

5.1.1 Representative Volume Element for CNT Reinforcement

A composite with homogenously distributed single-walled CNTs is assumed. In such a case, it is considered that all CNTs have the same dimensions and orientation and that their edges are capped. The microstructure of the nanotube is developed around a mean diameter $d_n = 2r_n$. The reinforcement length is ℓ_n. Its thickness is indirectly considered and typically taken equal to $t_n = 0.34$ nm. It is assumed that the longitudinal distances, between neighboring reinforcement ends, are equal to the corresponding transverse distances and equal to d. The last condition in conjunction with the known volume fraction V_{fr}, diameter d_n and length l_n of CNT are sufficient to lead to the complete geometric definition of the problem. Due to the symmetry of the periodic distribution, only the representative repeated unit cell of Fig. 5 is modelled. In this figure, one quarter of the matrix is removed for clarity. An orthogonal Cartesian coordinate system is used as reference with x, y and z axes, aligned with the main dimensions of the unit cell. The longitudinal axis of the reinforcement is aligned with the uniaxial loading direction (Fig. 5).

The volume fraction of the CNT in the composite is:

$$V_{fr} = \frac{V_n}{V_m + V_n} \tag{44}$$

Small volume fractions are considered, so that a negligible interaction between adjacent nanotubes can be assumed. In order to determine the longitudinal and transverse elastic properties of the composite, by using the unit cell model, appropriate boundary conditions must be implemented. For the calculation of the longitudinal elastic modulus $E_L = E_z$ a uniform displacement $u_z = \Delta z$ is applied on the boundary $z = l_n + d$. The symmetry constraint $u_z = 0$ is applied on the boundary $z = 0$, whereas the boundaries $x = \pm(d + r_n + t_n/2)$ and $y = \pm(d + r_n + t_n/2)$ are kept parallel to their original shape by nodal

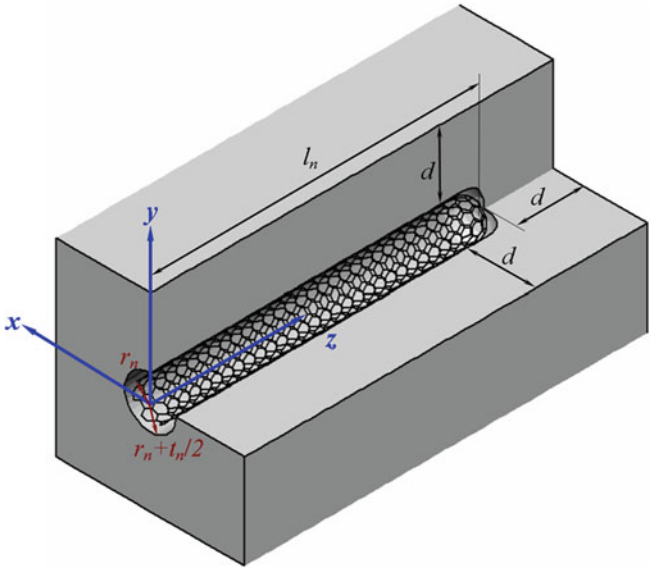

Fig. 5 Representative unit cell of the CNT reinforced nanocomposite (Giannopoulos et al. 2010)

coupling (3. this is required, as shear stresses on these boundaries must be zero due to symmetry). The longitudinal elastic modulus E_L of the composite is computed from average stress σ_z, obtained from the sum of reactions and average strain ε_z on $z = l_n + d$:

$$E_L = \frac{\sigma_z}{\varepsilon_z} = \frac{\frac{\sum_{i=1}^{n}(-{}^{i}f_z)}{(2d+d_n+t_n)^2}}{\frac{\Delta z}{l_n+d}} \tag{45}$$

where ${}^{i}f_z$ is the reaction in the direction z at node i, which belongs on the boundary $z = l_n + d$ and n is the total number of nodes that belong in the specific boundary.

Similarly, in order to compute the transverse elastic modulus $E_T = E_x = E_y$ a uniform displacement $u_x = \Delta x$ is applied on the boundary $x = d + r_n + t_n/2$, while the constraint $u_x = 0$ is imposed on the boundary $x = -(d + r_n + t_n/2)$. In addition, the boundaries $y = \pm(d + r_n + t_n/2)$ and $z = l_n + d$ are constrained to remain parallel to their original configuration. Finally, once more the symmetry constraint $u_z = 0$ is applied on the boundary $z = 0$. The transverse elastic modulus E_T of the composite is calculated from average normal reaction on the face $x = d + r_n + t_n/2$:

$$E_T = \frac{\sigma_x}{\varepsilon_x} = \frac{\frac{\sum_{i=1}^{n}(-{}^{i}f_x)}{(2d+d_n+t_n)(l_n+d)}}{\frac{\Delta x}{(2d+d_n+t_n)}} \tag{46}$$

where ${}^{i}f_x$ denotes the reaction along the direction x at node i, belonging on the face $x = d + r_n + t_n/2$, while n is the sum of the nodes belonging on the corresponding face.

After computing the elastic modulus E_L and E_T, predictions concerning the randomly oriented single-walled CNTs are performed, by using the following Halpin–Tsai relationships for randomly oriented short fiber composites (Mallick 1988):

$$E_{rand} = \frac{3}{8}E_L + \frac{5}{8}E_T \tag{47}$$

$$G_{rand} = \frac{1}{8}E_L + \frac{1}{4}E_T \tag{48}$$

where E_{rand} and $G_{rand}$are the elastic and shear modulus of a composite with randomly distributed short reinforcements, respectively.

5.1.2 Representative Volume Element for Graphene Reinforcement

Similarly, concerning the graphene based composite, we assume a uniformly reinforced matrix with a continuos in length graphene sheet. Here, all the computations are performed in an appropriate rectangular representative volume element (RVE), which is basically consisted by two phases, i.e. Graphene and the matrix material (Fig. 6). The volume fraction, in this case, can be expressed by the following equation:

$$V_g = \frac{W_g \times L_g \times t_g}{(W_g \times L_g \times t_g) + (W_m \times L_m \times t_m)} \tag{49}$$

where W_g, L_g and t_g is the width, length and thickness of the graphene while W_m, L_m and $t_m$is the width, length and thickness of the matrix within the volume element.

Such a model is simple and appropriate for the evaluation of the load transfer in graphene renforced nanocomposites.

5.2 Implementation of the Multi-Scale Technique

Before the implementation of the multiscale teqnique proposed here, for a desired study, the definition of values of specific parameters is required with respect the

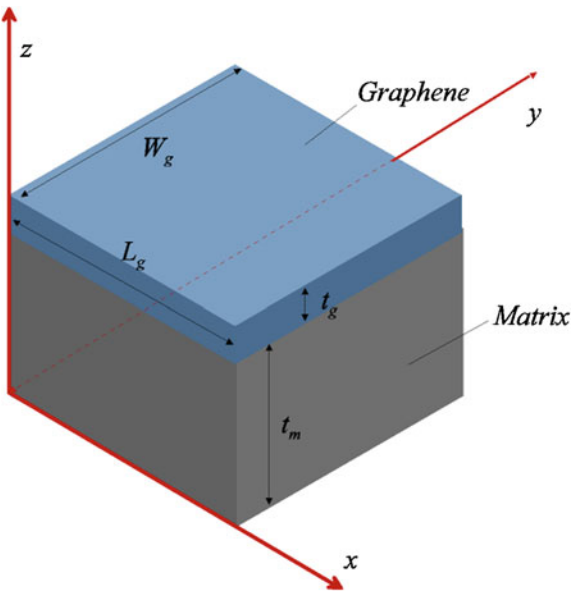

Fig. 6 Representative unit cell of the graphene reinforced nanocomposite

nanoparticle and matrix material. These parameters are significant for the exact description of the heterogeneous interface proposed. Hence, in the next subsection simple formulae utilized to obtain the aforementioned parameters are presented.

5.2.1 Elastic Properties of the Nanostructures Reinforcement

Here, only the parameters regarding the CNT reinforcement are presented. A similar technique could be performed in order to obtain the description of a heterogeneous interface of a graphene based nanocomposite.

In order to represent the mechanical interfacial behavior, as Eqs. (34), (38) and (39) imply, some macroscopic material data i.e. E_{Rn}, $G_{\Theta n}$ and G_{Zn} of the considered single-walled CNT are required. In order to compute the radial elastic modulus of the single-walled CNT E_{Rn}, a radial force f_R is imposed at each one of its nodes. The E_{Rn} can then be calculated via equation:

$$E_{Rn} = \frac{\sigma_R}{\varepsilon_R} = \frac{\frac{n_c f_R}{2\pi r_n l_n}}{\frac{\Delta R}{r_n}} \tag{50}$$

In order to compute the circumferential shear modulus of the single-walled CNT G_{Rn}, the Θ degree of freedom of the nodes at $Z = 0$ is restrained, while a circumferential force f_Θ is applied uniformly on each node that belongs to the $Z = l_n$ plane. The shear module G_{Rn} of the nanotube is computed from the reaction torgue M_Z acting, in the restrained end:

$$G_{Rn} = \frac{\mathrm{M_Z}\, l_n}{S\Delta\Theta} = \frac{n'_{\mathrm{c}} f_\Theta\, r_n l_n}{\frac{\pi}{2}\left(\left(r_n + \frac{t_n}{2}\right)^4 - \left(r_n - \frac{t_n}{2}\right)^4\right)\Delta\Theta} \tag{51}$$

where S is the polar moment of inertia of the cross sectional area of the tube and n'_{c} is the number of edge nodes of the tube.

In order to compute the longitudinal shear modulus of the single-walled CNT G_{Zn}, only half of the tube, from $\Theta = 0$ to $\Theta = \pi$, is modelled. R and Θ degrees of freedom of all nodes an z degree of freedom of nodes belonging to plane $\Theta = \pi$, are constrained. A longitudinal displacement variation $R_i \Delta Z$ is applied to nodes, belonging to planes $Z = 0$ and $Z = l_n$, where R_i is the radial coordinate of node i. The shear module G_{Zn} of the nanotube is computed using the following relationship:

$$G_{Zn} = \frac{\tau_Z}{\gamma_Z} = \frac{\sum_{i=1}^{n''_c} (-{}^i f_Z)}{\frac{l_n t_n}{\frac{\Delta Z}{r_n}}} \tag{52}$$

where ${}^i f_Z$ is the longitudinal reaction of node i, belonging to plane $\Theta = \pi$ and n''_c is the total number of nodes belonging to the same plane.

For an example, the armchair (6,6) single-walled CNTs is considered as reinforcement with a radius equal to $r_n = 0.40709$ nm. For this reason, initially the uncapped (6,6) single-walled CNT is individually modelled. A length equal to $l_n = 10$ nm is selected. The single-walled CNT is analyzed with reference to the local cylindrical coordinate system $(R,\ \Theta,\ \mathrm{Z})$, mentioned earlier. The bond stretching and bond angle bending resistance force constants are taken equal to $k_r = 6.52 \times 10^{-7}$ N nm^{-1}, and $k_\theta = 8.76 \times 10^{-10}$ N nmrad^{-1}, respectively (Cornell et al. 1995).

The obtained values using the above techniques are $E_{Rn} = 1515$ GPa, $G_{\Theta n} = 336.5$ GPa and $G_{Zn} = 547.3$ GPa.

5.2.2 Elastic Properties of the Matrix

Considering an homogenous and isotropic matrix, the shear moduli required for the description of the heterogeneous interface are given by the following equation

$$G_m = G_{\Theta m} = G_{Zm} = \frac{E_m}{2(1 + \nu_m)} = 1.357 \text{ GPa} \tag{53}$$

If someone use the thermoplastic polyamide LaRC-SI (Odegard et al. 2003) as matrix material, the elastic modulus and Poisson's ratio of this material are $E_m = E_{Rm} = 3.8$ GPa and $\nu_m = 0.4$, respectively. The shear moduli of the polymer are $G_m = G_{\Theta m} = G_{Zm} = 1.357$ GPa.

5.2.3 Heterogeneous Interface Evaluation

In order to define the interface properties, a set of linear functions are selected having the form:

$$\Phi_i(R) = \alpha_i R + \beta_i \tag{54}$$

where $i = R$, Θ, Z and α_i, β are constants that must be determined. Since the macroscopic properties E_{Rn}, $G_{\Theta n}$, G_{Zn},E_{Rm}, $G_{\Theta m}$, and G_{Zm} are known, the interfacial stiffness variations, with reference to the local coordinate system (R, Θ, Z), can be fully defined (evaluations of α_i, β_i constants) by substituting Eqs. (34), (38)–(42) and (54). At the capped edge region these variations are transformed with respect to the spherical local coordinate system mentioned previously. A set of $J = 10$ joint elements is used along the radial direction. The selection of this number has been made after convergence tests. During these tests it was proved that for $J > 10$, elastic properties of same magnitude were produced.

5.2.4 Representative Numerical Models

A representative finite element model of the unit cell containing a capped (6,6) single-walled CNT is illustrated in Fig. 7.

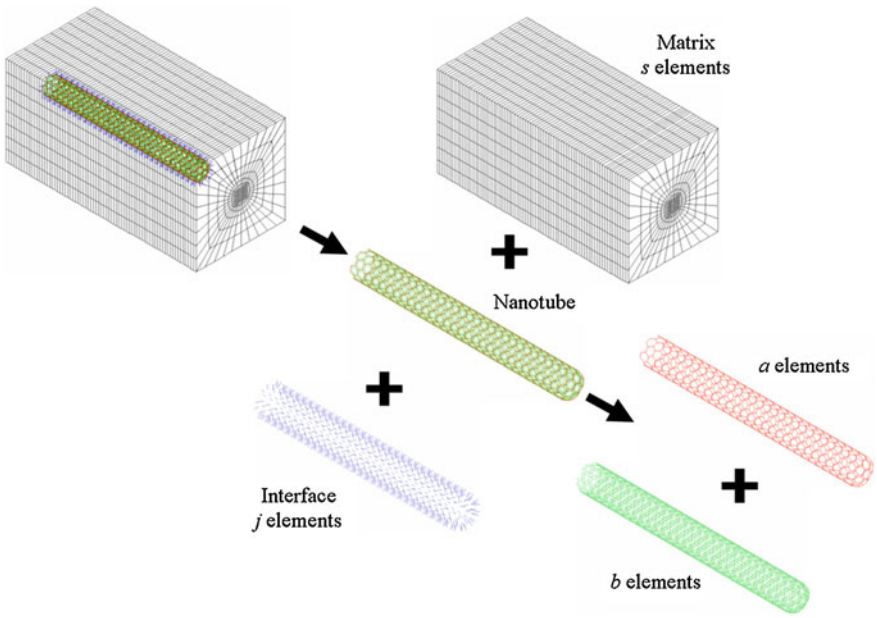

Fig. 7 Finite element model of the unit cell (Giannopoulos et al. 2010)

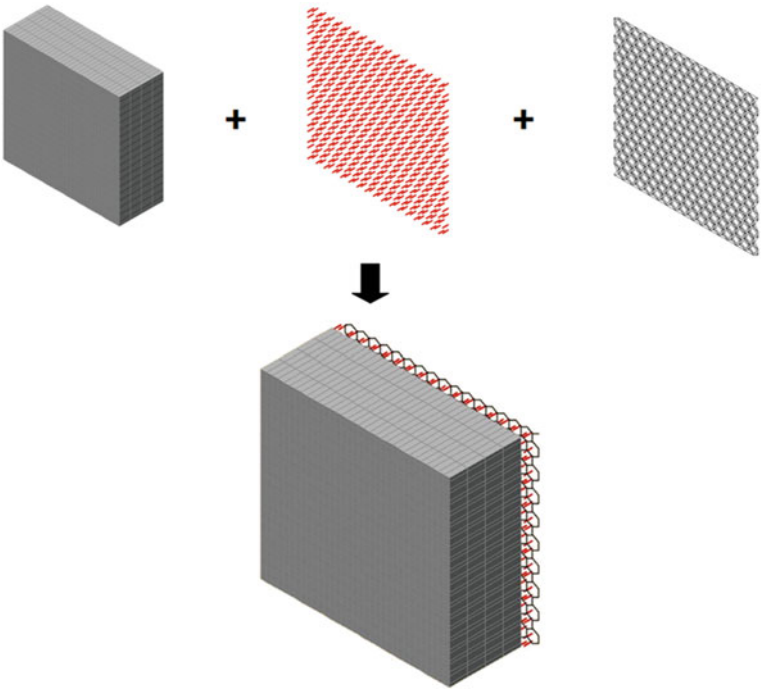

Fig. 8 The nanocomposite: Matrix, interface and Graphene

Before extracting the numerical data, numerous convergence tests have been conducted in order to select the proper mesh density concerning the matrix material.

A representative finite element model for the graphene based nanocomposite analysis is depicted in Fig. 8.

5.3 Static Analysis

In order to examine the elastic mechanical behavior of the nanocomposite, a linear static analysis should be take place. Thus, the system of linear equations is constructed by applying the defined elemental equations of the multiscale model and transformed to the global cartesian (x, y, z) or cylindrical coordinate system (r, θ, z), depending the case. Then all linear equations are assembled according to the requirements of nodal equilibrium and the following system of equations is obtained:

$$\mathbf{KU} = \mathbf{F} \tag{55}$$

where **K**, **U** and **F** are the assembled stiffness matrix, displacement vector and force vector, respectively, of the nanocomposite. Matrix Eq. (55) can be solved via standard numerical techniques such as Gauss elimination or LU decomposition by taking into consideration the imposed boundary conditions.

6 Results

In this section, some representative results are presented utilizing the proposed multi scale modelling technique including the heterogeneous intefacial effects.

6.1 Elastic Behavior of CNT Reinforced Nanocomposites

The variation of longitudinal and transverse elastic moduli versus (6,6) single-walled CNT length, for 1 % volume fraction is given in Fig. 9. The variation of longitudinal and transverse elastic moduli versus volume fraction, for a single-walled CNT length equal to 10 nm, is given in Fig. 10.

The isotropic elastic and shear modulus of a composite, with randomly aligned (6,6) single-walled CNTs, is semi-analytically obtained, by substituting the numerically predicted values of longitudinal and transverse elastic moduli, into Eq. (4) and (5), respectively.

Figure 11 presents the elastic and shear modulus of the composite with randomly aligned tubes, for 1 % volume fraction versus reinforcement length. Figure 12 depicts the elastic and shear modulus of the composite with randomly aligned tubes of 10 nm length versus volume fraction.

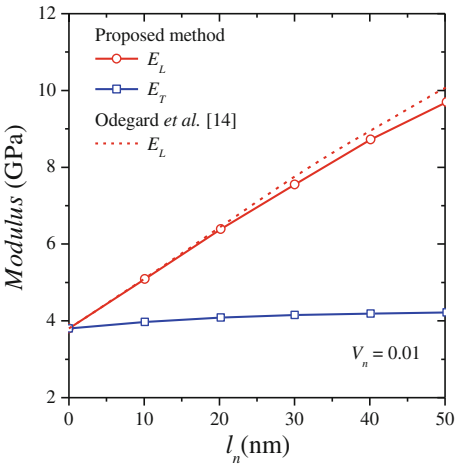

Fig. 9 Longitudinal and transverse moduli of aligned capped (6,6) single-walled CNT/LaRC-SI nanocomposite versus nanotube length, for 1 % volume fraction (Giannopoulos et al. 2010)

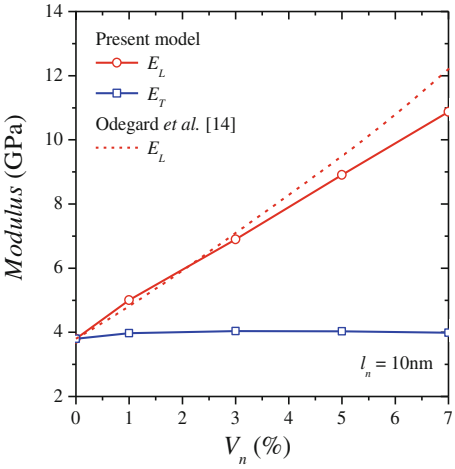

Fig. 10 Longitudinal and transverse moduli of aligned capped (6,6) single-walled CNT/LaRC-SI nanocomposite versus volume fraction, for 1 % volume fraction (Giannopoulos et al. 2010)

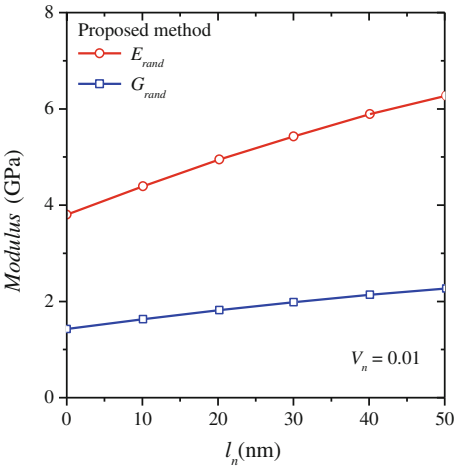

Fig. 11 Elastic and shear moduli of random capped (6,6) single-walled CNT/LaRC-SI nanocomposite versus nanotube length, for 1 % volume fraction (Giannopoulos et al. 2010)

Generally, for the aligned single-walled CNT/LaRC-SI composites, the longitudinal elastic modulus increases significantly, as the reinforcement length and volume fraction increases, while the transverse elastic modulus remains almost constant. For the aligned single-walled CNT/LaRC-SI, the increase of the reinforcement length and volume fraction leads to a less prominent increase of both isotropic elastic and shear moduli. In general, a satifactory agreement is observed between predictions obtained using the proposed method and results presented by Odegard et al. (2003).

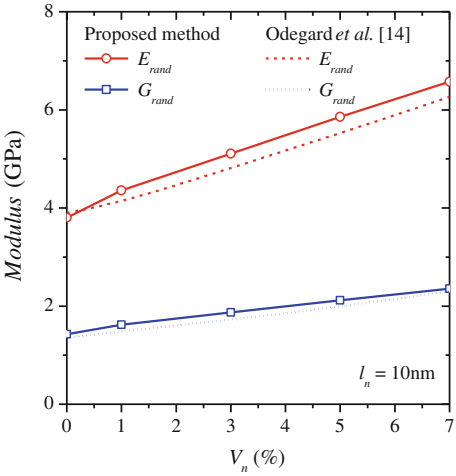

Fig. 12 Elastic and shear moduli of random capped (6,6) single-walled CNT/LaRC-SI nanocomposite versus volume fraction, for 10 nm long nanotubes (Giannopoulos et al. 2010)

6.2 Load Transfer in Graphene Based Nanocomposites

The reinforcement used in the analysis is an armchair square graphene sheet which length is equal to 4.06 nm. Its thickness $t_g$is typically taken equal to 0.34 nm and its width is equal to 9 nm. In the current study the graphene sheet is covered by a matrix material only on its one side. It would be very useful to compare the current RVE with one that the matrix material will cover both sides of the graphene sheet. The axial and shear stress results are shown in Fig. 13.

From this figure it is obvious that for both cases the results are approximately the same either the graphene sheet is both sides covered or not. The proposed RVE (Fig. 13) is deemed appropriate for the current study.

Using the previously presented modeling technique, a parametric study is performed for the graphene-based composite and the results are depicted in Fig. 14. The models are tested in axial and shear stress and results are taken for several positions of the matrix material near the graphene sheet.

Figure 14 depicts the variation of the normalized axial stress (Fig. 14a) and the normalized shear stress (Fig. 14b) in matrix material along the longitudinal direction of the RVE near to the interface region. The normalization was performed via the stress $\sigma_0 = \varepsilon_0 E_m$, where ε_0 is the applied strain on the nanotube. In both cases, the greater stress distribution along the longitudinal direction is observed in the region closer to the interface.

In order to realize the deformations included when a pull out test is performed to the RVE, the displacement ux and the shear strain εrz of a matrix cross section in the center of the RVE are presented in Fig. 15a, b, respectively. The right side corresponds to the region that reaches the interfacial zone. These figures show that the greatest deformations in matrix material exist in the applied load region as expected.

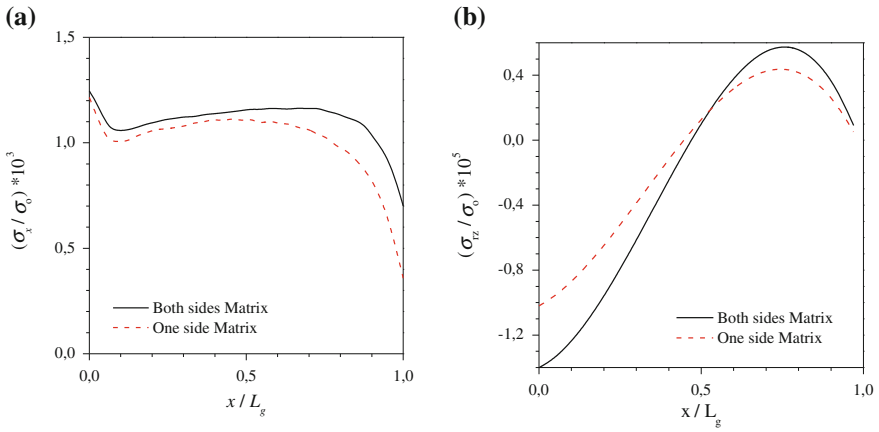

Fig. 13 Stress transfer of graphene reinforced composite for different matrix types: **a** normalized axial stress and **b** normalized shear stress, vs. normalized longitudinal position

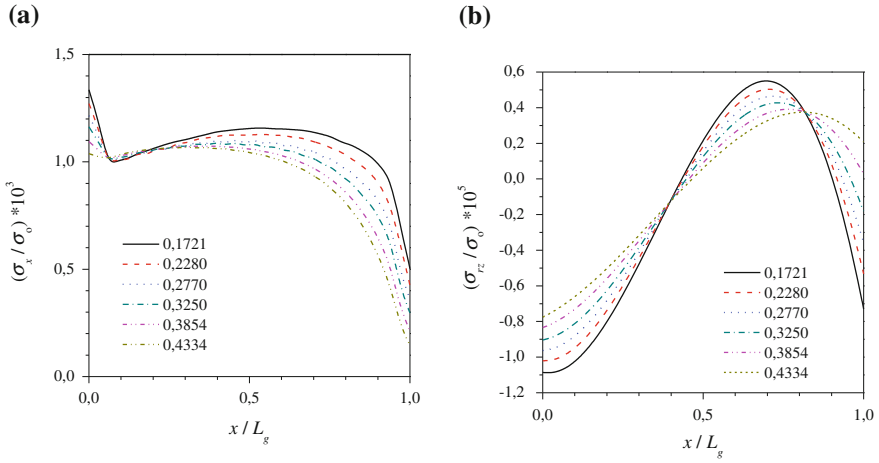

Fig. 14 Stress transfer of graphene reinforced composite for different matrix points: **a** normalized axial stress and **b** normalized shear stress, vs. normalized longitudinal position

A parametric study with different values of the volume fraction of the RVE is performed in order to study its influence on the stress transfer. Fig. 16a illustrates the behavior of normalized axial stress along the longitudinal direction very close to the interfacial zone.

Here, the axial stress seems to be distributed in a similar way for all values of volume fraction, while a slightly different behavior is observed when a different shape of graphene is used (4 × 2 rectangular). On the other hand, the normalized shear stress distribution (Fig. 16b) presents different behavior when a rectangular

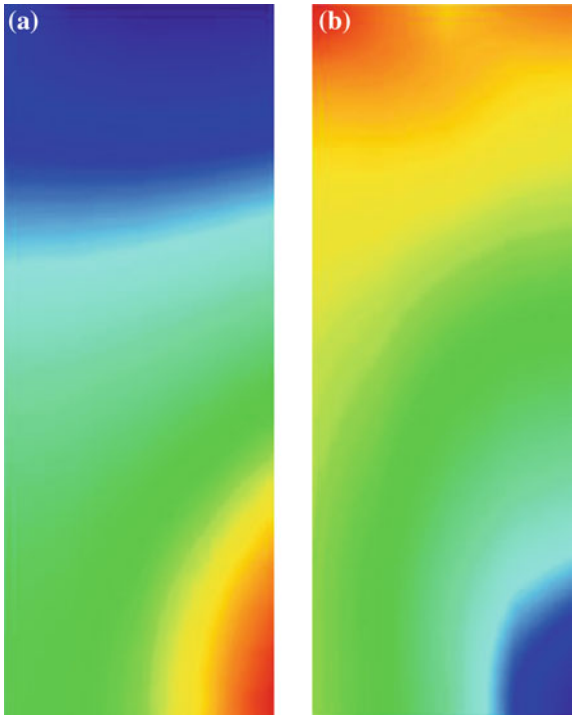

Fig. 15 Contours of **a** axial displacements and **b** shear strains

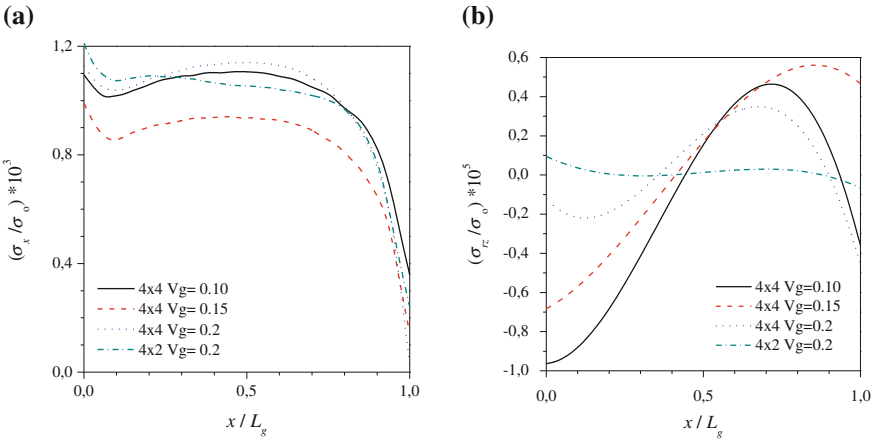

Fig. 16 **a** normalized axial stress and **b** normalized shear stress variations in RVE longitudinal direction for different volume fractions

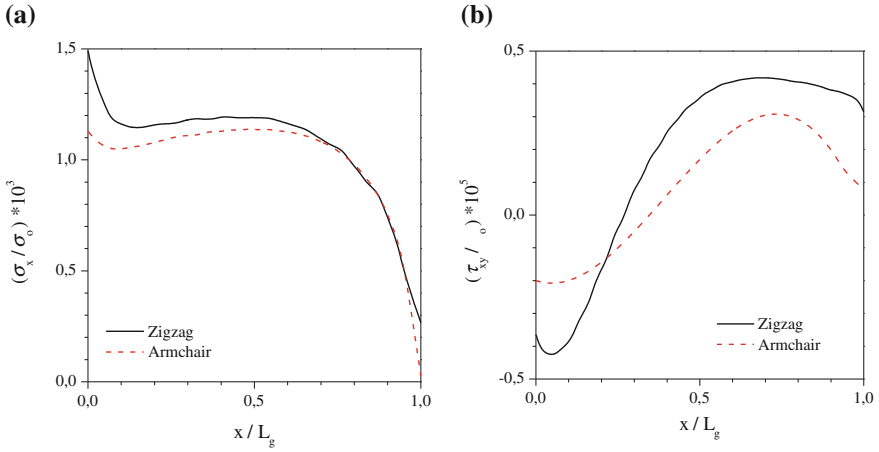

Fig. 17 Zigzag and armchair RVEs comparison of **a** normalized axial stress and **b** normalized shear stress

graphene sheet is used and seems to be reduced when the volume fraction of the RVE is decreased.

In order to examine the behavior of armchair graphene sheet composites compared with the zigzag ones, an axial and shear stress test has taken part. A similar (i.e. same dimensions and volume fraction) zigzag model was used and the results are depicted in Fig. 17.

Here, the axial and shear stress seem to be distributed in a similar way for both RVEs, while it is obvious, especially in the shear stress test, that the armchair values are significantly smaller than these of the zigzag case. It becomes clear that armchair mechanical response seems to be superior than the one observed for zigzags.

7 Conclusions

A numerical scheme has been proposed for the prediction of elastic behavior of both CNT as well as graphene based nanocomposites. The presented method has the efficiency of combining macroscale and nanoscale media via the use of discrete hybrid interface, which is accompliced by the use of special spring like joint elements of variable stiffness along their thickness. Their material properties are functions bounded by the corresponding properties of both matrix and reinforcement. The method has been validated through comparisons with corresponding results arisen by using molecular dynamics modelling of high complexity in terms of molecular representation. This implies the advantage of the proposed approach which utilizes non atomistic modelling for the representation of the matrix, fact

that reduces significantly the computational effort for solving problems involving nanoscaled atomistic structures. The provided numerical tool is expected to reduce the modelling of interactions which occur between two different atomistic mediums. In such interfacial zones, complicated phenomena take place. The atoms may interact via chemical bonding as well as van der Waals interaction forces. Thus, a detailed representation of the interface is required. This fact is overridden by adopting the proposed method.

The effectiveness of the method has been tested using both CNTs and graphene as reinforcing components of the composite. Important composite properties such as elastic moduli seem to increase considerably when the nanoreinforcement volume fraction is also increased.

References

Al-Ostaz A, Pal G, Mantena PR, Cheng A (2008) Molecular dynamics simulation of single-walled CNT-polymer nanocomposite and its constituents. J Mater Sci 43:164–173

Arroyo M, Belytschko T (2004) Finite crystal elasticity of carbon nanotubes based on the exponential Cauchy–Born rule. Phys Rev B 69:115415

Ashrafi B, Hubert P (2006) Modeling the elastic properties of carbon nanotube array/polymer composites. Compos Sci Technol 66:387–396

Chen XL, Liu YJ (2004) Square representative volume elements for evaluating the effective material properties of carbon nanotube-based composites. Comput Mater Sci 29:1–11

Cornell WD, Cieplak P, Bayly CI, Gould IR, Merz KM Jr, Ferguson DM, Spellmeyer DC, Fox T, Caldwell JW, Kollman PA (1995) A second generation force-field for the simulation of proteins, nuclei-acide, and organic-molecules. J Am Chem Soc 117:5179–5197

Frankland SJV, Caglar AD, Brenner WM, Griebel M (2002) Molecular simulation of the influence of chemical cross-links on the shear strength of carbon nanotube-polymer interfaces. J Phys Chem B 106:3046–3048

Frankland SJV, Harik VM, Odegard GM, Brennerc DW, Gates TS (2003) The stress–strain behavior of polymer–nanotube composites from molecular dynamics simulation. Compos Sci Technol 63(11):1655–1661

Gelin BR (1994) Molecular modeling of polymer structures and properties. Hanser/Gardner Publishers, Cincinnati

Georgantzinos SK, Giannopoulos GI, Anifantis NK (2010) On the coupling of axial and shear deformations of single-walled carbon nanotubes and graphene: a numerical study. Proc Inst Mech Eng, Part N: J Nanoeng Nanosystems 224(4):163–172

Giannopoulos GI, Kakavas PA, Anifantis NK (2008) Evaluation of the effective mechanical properties of single walled carbon nanotubes using a spring based finite element approach. Comput Mater Sci 41:561–569

Giannopoulos GI, Georgantzinos SK, Katsareas DE, Anifantis NK (2010) Numerical prediction of Young's and shear moduli of carbon nanotube composites incorporating nanoscale and interfacial effects. CMES-Comput Model Eng Sci 56(3):231–247

Han Y, Elliott J (2007) Molecular dynamics simulations of the elastic properties of polymer/carbon nanotube composites. Comput Mater Sci 39:315–323

Kołoczek J, Young-Kyun K, Burian A (2001) Characterization of spatial correlations in carbon nanotubes-modelling studies. J Alloy Compd 28:222–225

Li C, Chou TW (2005) A structural mechanics approach for the analysis of carbon nanotubes. Int J Solids Struct 40:2487–2499

Li C, Chou TW (2006) Multiscale modeling of compressive behavior of carbon nanotube/polymer composites. Compos Sci Technol 66(14):2409–2414
Liu YJ, Chen XL (2003) Continuum models of carbon nanotube-based composites using the boundary element method. Electron J Boundary Elem 1:316–335
Lordi V, Yao N (2000) Molecular mechanics of binding in carbon-nanotube polymer composites. J Mater Res 15(12):2770–2779
Mallick PK (1988) Fiber-reinforced composites: materials manufacturing and design. Marcel Dekker, New York, p 111
Meo M, Rossi M (2006) Tensile failure prediction of single wall carbon nanotube. Eng Fract Mech 73:2589–2599
Montazeri A, Naghdabadi R (2010) Investigation of the interphase effects on the mechanical behavior of carbon nanotube polymer composites by multiscale modeling. J Appl Polym Sci 117(1):361–367
Odegard GM, Gates TS, Wise KE, Park C, Siochi E (2003) Constitutive modeling of nanotube-reinforced polymer composites. Compos Sci Technol 63(11):1671–1687
Rappe AK, Casewit CJ, Colwell KS, Goddard WA, Skiff WM (1992) UFF, a full periodic table force field for molecular mechanics and molecular dynamics simulations. J Am Chem Soc 114(25):10024–10035
Saber-Samandari S, Khatibi AA (2006) The effect of interphase on the elastic modulus of polymer based nanocomposites. Key Eng Mater 312:199–204
Seidel GD, Lagoudas DC (2006) Micromechanical analysis of the effective elastic properties of carbon nanotube reinforced composites. Mech Mater 38:884–907
Shokrieh MM, Rafiee R (2010) On the tensile behavior of an embedded carbon nanotube in polymer matrix with non-bonded interphase region. Compos Struct 92(3):647–652
Zou J, Ji B, Feng XQ, Gao H (2006) Molecular-dynamic studies of carbon–water–carbon composite nanotubes. Small 2:1348–1355

Effect of Covalent Functionalization on Young's Modulus of a Single-Wall Carbon Nanotube

Priyal H. Shah and Romesh C. Batra

Abstract Effective utilization of carbon nanotubes (CNTs) as reinforcements in composites necessitates good interfacial bonding with the surround matrix material. The covalent functionalization of CNTs is an effective method to enhance this bonding. However, covalent bonds introduced by a functional group may alter the pristine structure of the CNT and lower its mechanical properties. Here we study the effect of hydrogen (–H), hydroxyl (–OH), carboxyl (–COOH), and amine ($–NH_2$) functionalization on Young's modulus of a single-wall CNT (SWCNT) using molecular mechanics (MM) simulations with the MM3 potential and the software TINKER. Both pristine and functionalized SWCNTs have been deformed in simple tension. From the strain energy of deformation vs. the axial strain curves, the value of Young's modulus has been derived as a function of the functionalization group and the amount of functionalization. It is found that Young's modulus decreases by about 30 % with 20 % of functionalization, the reduction is essentially proportional to the increase in the percentage of the functionalization material and is nearly the same for each of the four functional groups studied.

Keywords Carbon nanotubes · Young's modulus · Functionalization · Molecular mechanics · Virtual tension test

P. H. Shah · R. C. Batra (✉)
Department of Engineering Science and Mechanics, Virginia Polytechnic Institute and State University, Blacksburg, VA 24061, USA
e-mail: rbatra@exchange.vt.edu

P. H. Shah
e-mail: spriyal@vt.edu

K. I. Tserpes and N. Silvestre (eds.), *Modeling of Carbon Nanotubes, Graphene and their Composites*, Springer Series in Materials Science 188,
DOI: 10.1007/978-3-319-01201-8_4,

1 Introduction

Researchers have employed experimental, analytical, density functional theory (DFT), molecular dynamics (MD) and molecular mechanics (MM) simulations to predict mechanical properties of carbon nanotubes (CNTs). Assuming that the wall thickness of a single-wall CNT (SWCNT) can be approximated as 0.34 nm, Treacy et al. (1996), Wong et al. (1997), and Krishnan et al. (1998) experimentally determined that Young's modulus of a CNT is in terapascal (TPa) range. Xing et al. (2004) employed MD simulations to predict Young's modulus of a SWCNT. Li and Chou (2003) computed elastic properties of CNTs using a combined structural mechanics and MM approach. Chang and Gao (2003) investigated size dependent elastic properties of SWCNTs through MM simulations. Sears and Batra (2004) determined the wall thickness, Young's modulus, and Poisson's ratio of CNTs using MM simulation with the MM3 potential and the software TINKER. They assumed that the response of a SWCNT in simple tension is energetically equivalent to that of a thin cylinder made of an isotropic and homogeneous material. Furthermore, the wall thickness of the cylinder equals that of the SWCNT. They found the wall thickness and Young's modulus of a SWCNT to be 0.046 nm and 7.26 TPa, respectively. Shen and Li (2004) used MM potential and energy equivalent principle to determine values of five elastic constants of a CNT assuming the CNT as a transversely isotropic material with the centroidal axis of the tube as the axis of transverse isotropy. Batra and Sears (2007) proposed that the axis of transverse isotropy of a CNT is a radial line rather than the centroidal axis. By studying with the MM simulations radial expansion of a SWCNT, they showed that Young's modulus in the radial direction is about 1/4th of that in the axial direction. Gupta and Batra (2008), Batra and Gupta (2008) predicted the wall thickness and the material moduli of a SWCNT by matching frequencies of bending, axial and torsional vibrations as well as that of radial breathing modes of a free–free SWCNT with those of the continuous cylinder of the same length and mean radius as the SWCNT. Wu et al. (2008) developed an atomistic based finite deformation shell theory for a SWCNT and found its stiffness in tension, bending, and torsion.

The SWCNTs due to their cylindrical shape, large length to diameter ratio, and high specific properties are potential candidates as reinforcements in composites. However, the effectiveness of SWCNTs as reinforcements depends on their uniform dispersion in and strong adhesion with the surrounding matrix. It has been very challenging to simultaneously meet these two requirements. The functionalization of SWCNTs appears to be an effective means of achieving good bonding between SWCNTs and the surrounding matrix. The surface properties of CNTs can be modified by either physical or chemical functionalization. The physical functionalization is achieved by attaching noncovalent groups, such as polymer, peptides or surfactants to the nanotubes. It is advantageous since it does not alter the pristine structure of nanotubes hence the mechanical properties of CNTs are not affected. However, these functional groups are attached to nanotubes with weak van der Waals interactions resulting in low load transfer efficiency between

the nanotube and the matrix. In comparison, the chemical functionalization involving the covalent attachment of functional groups to atoms of CNTs provides relatively strong interfacial bonding between CNTs and the surrounding matrix thereby enhancing the load transfer efficiency. Haddon et al. used the nanotube-bound carboxylic acid groups for attaching long alkyl chains to SWCNTs via amide linkages (Chen et al. 1998; Hamon et al. 1999; Niyogi et al. 2001) and via carboxylate-ammonium salt ionic interactions (Chen et al. 2001). Khare et al. (2002) developed hydrogenated CNTs using electric discharge. Sun et al. showed that the esterification of the carboxylic acid groups could also be used to functionalize and solubilize nanotubes of any length (Riggs et al. 2000; Sun et al. 2001; Fu et al. 2001). Wilson et al. illustrated the use of anilines to functionalize nanotubes (Sun et al. 2001). Grujicic et al. (2006) investigated the effect of covalent functionalization of triple-walled CNTs on the efficiency of matrix-nanotube load transfer. Their results reveal that the covalent functionalization improves the load transfer efficiency especially when loads are applied in a direction orthogonal to the axis of the CNT. Experimental works (Cooper et al. 2002; Barber et al. 2003; Shofner et al. 2006; Buffa et al. 2007; Sun et al. 2008) have demonstrated the effectiveness of covalent functionalization in increasing the interfacial bonding strength between CNTs and polymer chains.

Although chemical functionalization is effective in enhancing the binding of CNTs with the surrounding matrix, it may damage the pristine structure of a CNT due to the introduction of covalent bonds, and reduce the mechanical stiffness of the CNT. Much of the research work dealing with the determination of Young's modulus and other elastic properties of CNTs has considered pristine CNTs. Since the covalently functionalized CNTs would be better candidates for reinforcements in a composite than the pristine CNTs, it is important to determine the effect of covalent functionalization on Young's modulus of a CNT. Zhang et al. (2008) used atomistic simulations to analyze mechanical properties of hydrogenated SWCNTs and found a decrease in Young's modulus, strength, and ductility of the CNTs with an increase in the percentage of C–H bonds. Kuang and He (2009) computed Young's moduli of vinyl functionalized SWCNTs using MM simulations with the condense-phase optimized molecular potential for atomistic simulation studies (COMPASS) force field and found that Young's modulus depends on the density of the sp^3 hybridized carbon atoms and chirality of the CNTs. Up to 33 % reduction in Young's modulus was observed in their study with 38 % content of the functionalizing material. Ling et al. (2012) predicted Young's modulus of functionalized CNTs using MM and MD simulations with the COMPASS force field and observed that Young's modulus depends on the type of functionalizing material and the amount of functionalization. Recently, Milowska and Majewski (2013) studied effect of different functional groups on elastic properties of functionalized CNTs using DFT calculations. Their results showed that an increase in amount of covalently bound material to the wall of a CNT decreases Young's, shear and bulk moduli. Here we have considered four functional groups namely, hydrogen (–H), hydroxyl (–OH), carboxyl (–COOH), and amine ($–NH_2$) and compared their effects on the modulus of elasticity of a SWCNT with varying

percentage of functionalization. The study has been carried out using MM simulations with the freely available software TINKER (Ponder 2000).

2 Molecular Mechanics Simulations

2.1 Force-Field

The MM3 potential (Allinger et al. 1989) with higher order expansions and cross-terms has been used to model interatomic interactions. This potential is suitable for studying deformations of CNTs because of similarities between sp^2 bonds in the hexagonal structure of CNTs and the hexagonal structure of aromatic proteins for which the potential was originally developed. This potential describes the energy of the system as summation of the energies due to bonded and non-bonded interactions. The contributions for bonded interactions come from bond stretching (U_s), in-plane angle bending (U_θ), out of plane bending (U_γ), torsion (U_ϕ), and cross-interactions including stretch-bend (U_{sb}), angle–angle $(U_{\theta\theta'})$ and stretch-torsion $(U_{s\phi})$. The non-bonded interactions are van der Waals (U_{vdW}) and dipole–dipole electrostatic $(U_{\mu\mu'})$. Equation (1) gives expressions for these energies.

$$
\begin{aligned}
U_s &= 71.94K_s(r-r_0)^2[1-2.55(r-r_0)+\frac{7}{12}2.55^2(r-r_0)^2] \\
U_\theta &= 0.0219K_\theta(\theta-\theta_0)^2\times[1-0.014(\theta-\theta_0)+5.6(10^{-5})(\theta-\theta_0)^2 \\
&\quad -7.0(10^{-7})(\theta-\theta_0)^3+2.2(10^{-8})(\theta-\theta_0)^4] \\
U_\gamma &= 0.0219K_\gamma\gamma^2\times[1-0.014\gamma+5.6(10^{-5})\gamma^2-7.0(10^{-7})\gamma^3+2.2(10^{-8})\gamma^4] \\
U_\phi &= (V_1/2)(1+\cos\phi)+(V_2/2)(1+\cos 2\phi)\,(V_3/2)(1+\cos 3\phi) \\
U_{s\theta} &= 2.511K_{s\theta}[(r-r_0)+(r'-r'_0)](\theta-\theta_0) \\
U_{\theta\theta'} &= -0.021914K_{\theta\theta'}\,(\theta-\theta_0)\big(\theta'-\theta'_0\big) \\
U_{s\phi} &= -5.9975K_{s\phi}(r-r_0)(1+\cos 3\phi) \\
U_{vdW} &= \varepsilon\Big[-2.25(r_v/r)^6+1.84\big(10^5\big)\exp\{-12.00(r_v/r)\}\Big] \\
U_{\mu\mu'} &= \frac{14.3928[\mu\mu'(\cos\chi-3\cos\alpha\cos\alpha')]}{R^3D}
\end{aligned}
\tag{1}
$$

Parameters r, θ and ϕ in Eq. (1) are shown in Fig. 1. Variable γ is the angle between the plane and one of the bonds. A subscript, 0, on a variable represents its value in the configuration of minimum potential energy. Variables μ and $\mu'$are bond centered dipole moments, χ is the angle between two dipoles, α and α' are angles made by two dipoles with the line connecting their centers, and R is the distance between their centers. The values of constants K_s, K_θ, K_γ, $K'_{\theta\theta}, V_1, V_2, V_3, K_{s\theta}, K_{s\phi}, \varepsilon, r_v$and D given by Ponder (2000) are used in this work.

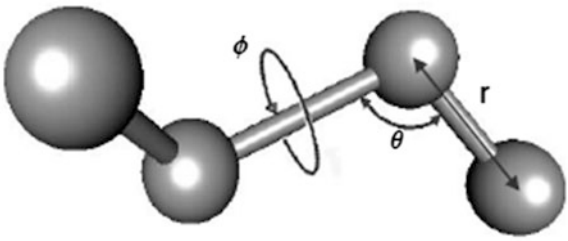

Fig. 1 Definitions of three molecular mechanics variables (Sears and Batra 2004)

2.2 Modeling of Functionalized SWCNTs

Functionalization of a zigzag (10, 0) finite length SWCNT of aspect ratio 12 has been considered as a model problem. The molecular structure of a functionalized SWCNT can be obtained from topologies of the pristine SWCNT and the functional group. In order to obtain the relaxed configuration of the SWCNT we minimize its potential energy by using the steepest decent algorithm with the root mean square (rms) gradient of 0.001. The diameter and the length of the relaxed tube are found to be 7.44 Å and 87.75 Å, respectively. The functional group is then positioned adjacent to a carbon atom of the relaxed CNT and the potential energy of the structure is minimized to obtain the relaxed configuration of the functionalized CNT. Note that the introduction of covalent bonds at the functional sites alters the hybridization of the affected carbon atoms from sp^2 to sp^3. The percentage of functionalization is defined as the ratio of the number of carbon atoms to which atoms of a functional group are attached to the total number of carbon atoms in the CNT. Four different functionalized CNTs have been studied with hydrogen, hydroxyl, carboxyl, and amine as the functionalizing groups. The carbon atoms to which a functional group is attached are randomly selected but the same set of atoms is used in each of the functionalized CNT for maintaining consistency in the numerical experiments. Figure 2 depicts schematics of the functional groups attached to a carbon atom of the CNT. The atoms in white, red, and blue color represent hydrogen, oxygen, and nitrogen atoms, respectively. It should be clear from sketches displayed in the figure that the covalent bond between the carbon atom and a functional group pulls out the carbon atom radially resulting in the distortion of the CNT at the functional site. The SWCNTs functionalized with these groups are schematically shown in Fig. 3.

2.3 Virtual Simple Tension Experiments

While conducting virtual tension tests on the pristine and the functionalized SWCNT, its ends are left open and not saturated with hydrogen atoms which may change the bonding structure at the ends and lead to end effects. Furthermore, carbon atoms one diameter away from each end are fixed during simulations. The

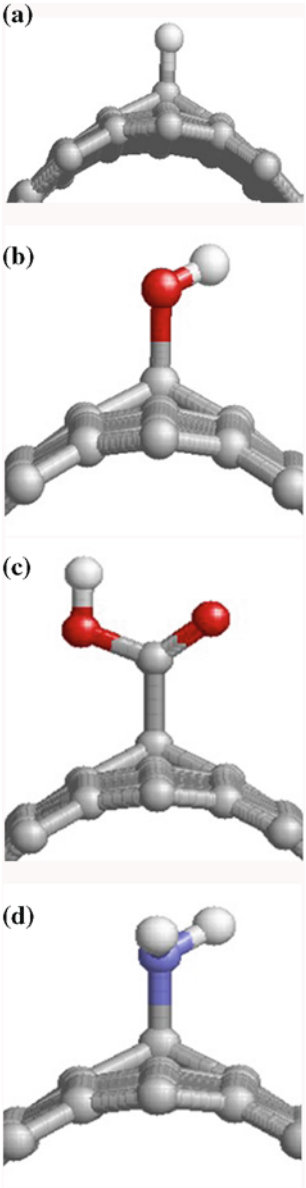

Fig. 2 Schematics of a carbon atom of the CNT attached with **a** hydrogen (–H) **b** hydroxyl (–OH), **c** carboxyl (–COOH), and **d** amine ($–NH_2$) groups

nanotubes are gradually deformed in tension and compression by a total of 3 % axial strain. After each displacement increment applied to atoms near the end faces, the tubes are allowed to equilibrate by minimizing their potential energies. The energy required to deform the tube equals its strain energy. The strain energy density is computed by dividing the strain energy by the volume of the CNT which is taken equal to that of a continuum cylinder of length and diameter equal to those

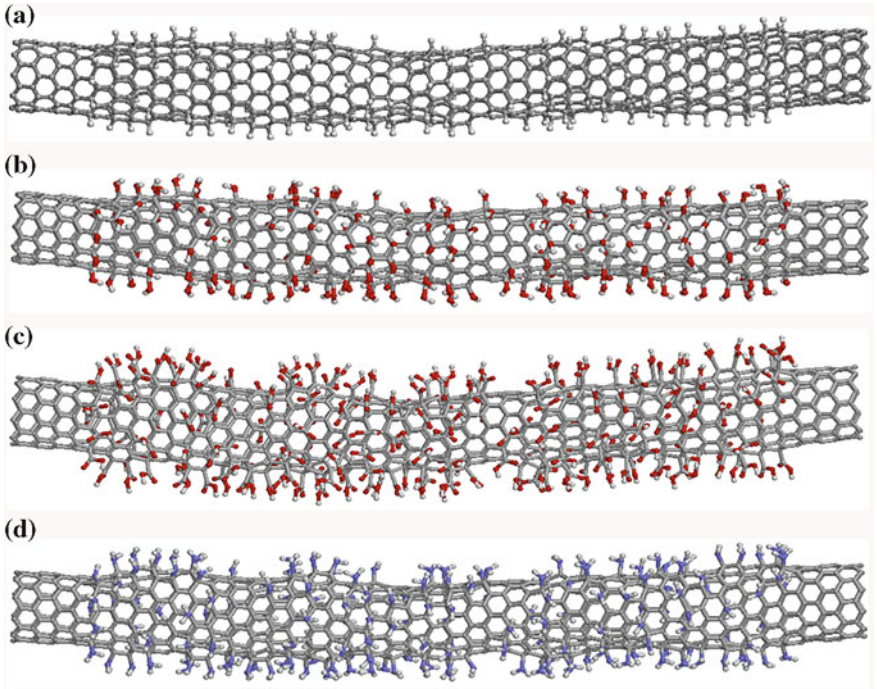

Fig. 3 Schematics of a (10, 0) SWCNT functionalized with 20 % **a** hydrogen (–H), **b** hydroxyl (–OH), **c** carboxyl (–COOH), and **d** amine ($–NH_2$) groups

of the relaxed pristine SWCNT and thickness equal to 0.34 nm. A polynomial through the data points is fitted by the least squares method. The first and the second derivatives of the strain energy density with respect to the axial strain yield the corresponding axial stress and Young's modulus, respectively. This procedure is the same as that used by Sears and Batra (2004) to find Young's modulus of a SWCNT.

3 Numerical Results

3.1 Validation of the Functionalization

In the relaxed configuration of the functionalized CNTs, the equilibrium bond length between the carbon atoms of the CNT and the adjoining atoms of the functional group, if present, has been computed from the equilibrated configurations. The C–H bond length in the hydrogen functionalized CNT is found to be 1.11, which agrees well with that (1.11) in the modified orthogonal tight binding model (Volpe and Cleri 2003) as well as the 1.12 given by the DFT calculations (Letardi et al. 2002). Methanol (CH_3OH), acetic acid (CH_3COOH), and amino

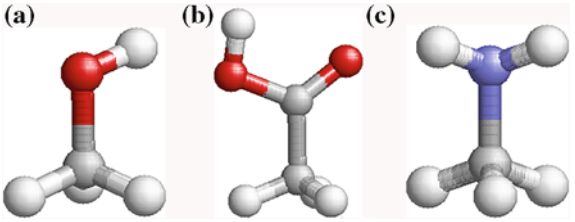

Fig. 4 Structures of **a** methanol, **b** acetic acid, and **c** amino methane generated using SMILES

methane (CH_3NH_2) are simple structures representing covalent bonds between a sp^3 hybridized carbon and hydroxyl, carboxyl, and amine functional group, respectively. These structures can be generated using simplified molecular-input line-entry system (SMILES) specification (Weininger 1988; Weininger et al. 1989) as shown in Fig. 4. In order to validate the functionalization of the CNTs with hydroxyl, carboxyl, and amine groups, the bond angles and bond lengths of the functional groups in the relaxed configuration of the functionalized CNTs have been measured and compared with those in methanol, acetic acid and amino methane. In Tables 1, 2 and 3, we have listed values of these parameters for hydroxyl, carboxyl, and amine groups, respectively. It is evident that there is good agreement between the two sets of values.

3.2 Analysis of Relaxed Configurations

The number of iterations required in the steepest descent method to minimize potential energies of –H, –OH, –COOH and $–NH_2$ functionalized CNTs is plotted

Table 1 Values of geometric parameters in the hydroxyl group

	Methanol	CNT–OH
R–O–H angle (degrees)	108.13	109.18
R–O length (Å)	1.43	1.43
O–H length (Å)	0.95	0.95

Note R denotes sp^3 hybridized carbon atom

Table 2 Values of geometric parameters in the carboxyl group

	Acetic acid	CNT–COOH
C–O–H angle (degrees)	107.39	107.6
R–C–O angle (degrees)	112.04	111.89
R–C = O angle (degrees)	126.04	126.27
C–O length (Å)	1.35	1.35
C = O length (Å)	1.2	1.21
O–H length (Å)	0.97	0.97
R–C length (Å)	1.5	1.53

Note R denotes sp^3 hybridized carbon atom

Table 3 Values of geometric parameters in the amine group

	Amino methane	CNT–NH_2
H–N–H bond angle (degrees)	106.35	106.09
R–N–H bond angle (degrees)	112.35	113.29
Dihedral angle between two R–N–H planes	119.78	121.38
N–H bond length (Å)	1.01	1.01
R–N bond length (Å)	1.46	1.46

Note R denotes sp^3 hybridized carbon atom

in Figs. 5a, b and 6a, b respectively. Note that 0 % functionalization represents the pristine CNT. It can be observed from results depicted in Fig. 5a that when the CNT is functionalized with hydrogen, the potential energy of the relaxed functionalized structure is less than that of the relaxed pristine CNT, and this difference increases with an increase in the percentage of functionalization. It is because the functionalization breaks the pi-bond of the sp^3 hybridized carbon atoms and changes the atom type from alkene to the more stable alkane. Similar characteristics are observed with the hydroxyl and the amine functionalization while the potential energy curves for the carboxyl functionalized CNTs do not exhibit the same behavior due to the presence of double bonds in the –COOH group.

In Fig. 7a we have presented the contribution from each energy term of the MM3 potential to the total potential energies of the pristine CNT for the hydrogen functionalized CNTs in their relaxed configurations. These have been normalized with respect to corresponding energies of the relaxed pristine CNT.

It can be observed from results included in the figure that the sum of the energies associated with the torsional and Van der Waals interactions are about 90 % of the total potential energy of the pristine CNT. The functionalization reduces these components of energies, thereby reducing the total potential energy and the reduction increases with an increase in the percentage of functionalization. Similar results for hydroxyl, carboxyl and amine functionalized CNTs are presented in Figs. 7a, b and 8a, b. Here, small effect of the electrostatic interactions has been observed on the total potential energies of the CNTs because of the presence of dipole moments in these functional groups. For the carboxyl functionalized SWCNT, the potential energy is not a monotonically increasing function of the amount of functionalization.

3.3 Results from Virtual Experiments

In the calculation of Young's modulus, as stated above, the thickness of a SWCNT is assumed to be 0.34 nm. The variation of the computed strain energy density with the axial strain for the pristine CNT is shown in Fig. 9. The third order polynomial fit to the strain energy density of the pristine CNT vs. the axial strain data with the regression coefficient of 1.0 is

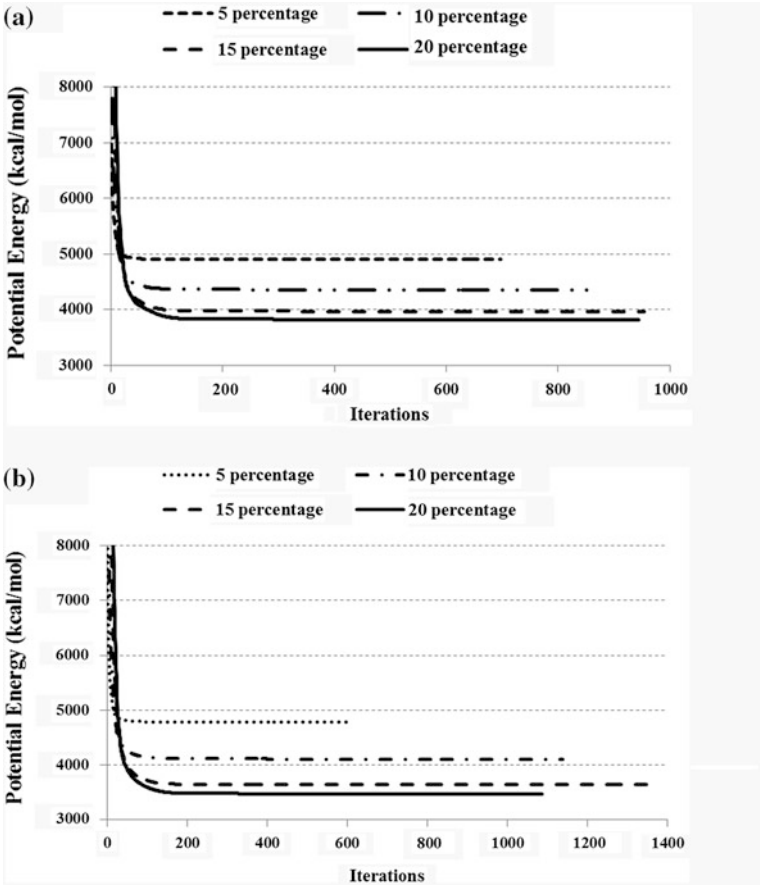

Fig. 5 For four different percentages of functionalization, minimization of the potential energies of a SWCNT functionalized with **a** –H, **b** –OH

$$W_v = -7.46\left(10^{11}\right)\varepsilon^3 + 5.03\left(10^{11}\right)\varepsilon^2 + 5.62\left(10^5\right)\varepsilon \tag{2}$$

where W_v is the strain energy density in J/m^3 and ε is the nominal axial strain. Thus, expressions for the axial stress and the modulus of elasticity E in Pa are

$$\sigma = -2.24\left(10^{12}\right)\varepsilon^2 + 1.101\left(10^{12}\right)\varepsilon + 5.62\left(10^5\right) \tag{3}$$

$$E = -4.48\left(10^{12}\right)\varepsilon + 1.01\left(10^{12}\right) \tag{4}$$

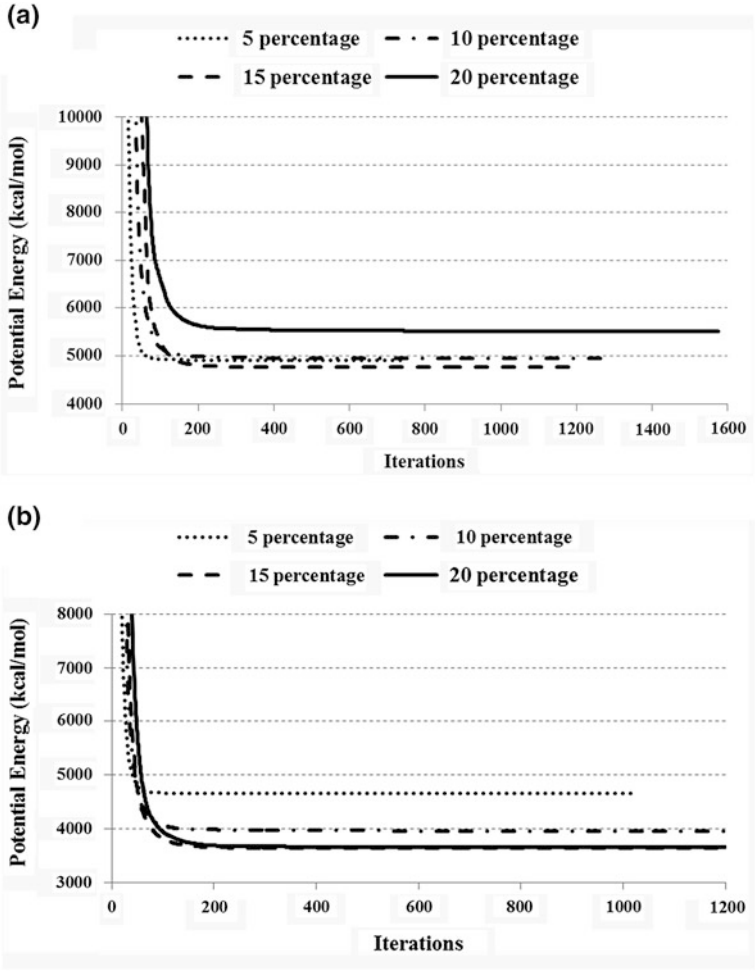

Fig. 6 For four different percentages of functionalization, minimization of the potential energies of a SWCNT the functionalized with **a** –COOH, and **b** $–NH_2$ groups

The modulus of elasticity at zero axial strain equals 1.01 TPa. It compares well with that reported in the literature (Treacy et al. 1996; Wong et al. 1997; Krishnan et al. 1998). For the hydrogen functionalized CNT, the strain energy vs. the axial strain variation and the axial stress-axial strain curves for different percentages of functionalization are shown in Fig. 10a, b, respectively.

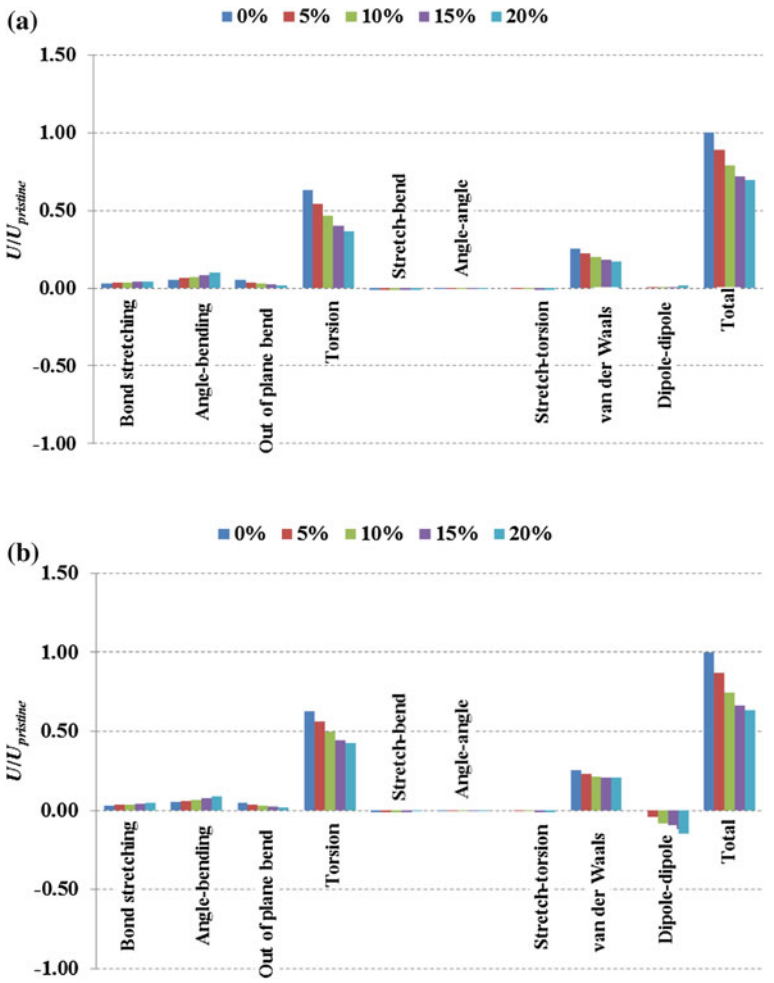

Fig. 7 Break down of total potential energy, U, in the individual energy components for the relaxed configurations of **a** hydrogen, **b** hydroxyl, functionalized CNTs with percentage of functionalization varying from 0 to 20 %

In computing the strain energy density, the volume of the functionalized CNT is taken equal to that of the pristine CNT. These plots reveal that the functionalization reduces the strain energy of deformation, and the slope (hence the modulus of elasticity) of the stress–strain curve for the functionalized tube is less than that

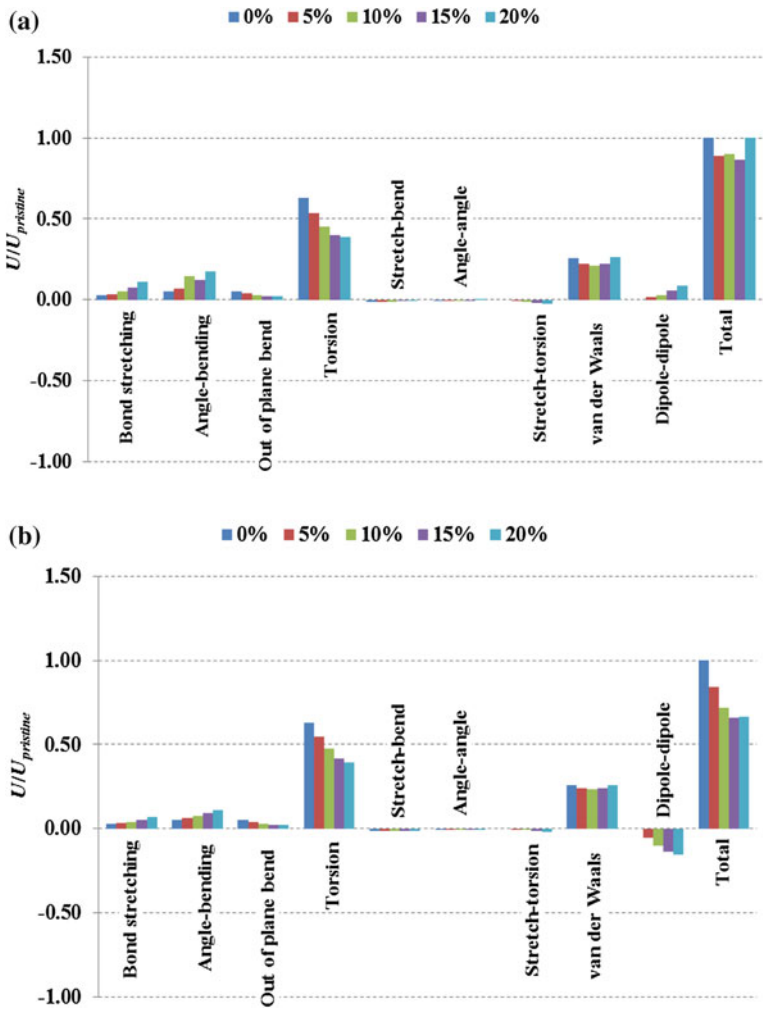

Fig. 8 Break down of total potential energy, U, in the individual energy components for the relaxed configurations of **a** carboxyl, and **b** amine functionalized CNTs with percentage of functionalization varying from 0 to 20 %

of the pristine tube. Moreover, the modulus of elasticity decreases with an increase in the percentage of functionalization. This reduction in the modulus of elasticity could be due to the non-uniformities in the nanotube structure introduced by the

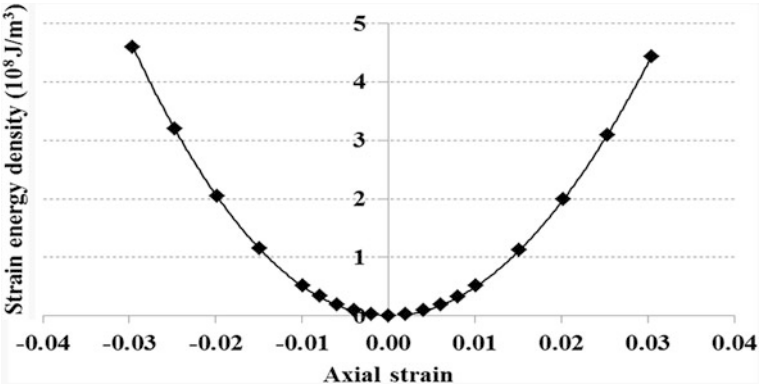

Fig. 9 Strain energy density of the pristine SWCNT vs. the axial strain computed using the MM3 potential

functionalization that lead to localized deformation at the functional sites. Similar results for hydroxyl, carboxyl, and amine groups are exhibited in Figs. 11, 12 and 13, respectively.

Values of Young's modulus of the functionalized CNTs for different percentages of functionalization listed in Table 4 suggest that they do not depend much upon the functionalization agent.

In Table 5, we have summarized similar results reported in the literature obtained using various computational methods and force fields along with the major results of the present study. It should be clear from the summary provided in Table 5 that the present results agree with those of other researchers. To better understand the effect of functionalization on Young's modulus, the strain energies of the deformation in the tension tests of the pristine and the functionalized CNTs have been obtained in terms of their bonded and non-bonded energy components. In Figs. 14a, b and 15a, b we have depicted the contribution of individual energy terms to the total reduction in the strain energy of deformation due to hydrogen, hydroxyl, carboxyl, and amine functionalization, respectively. These values have been normalized with respect to those of the pristine CNT. These results indicate that the functionalization reduces the strain energies associated with bond-stretching and angle bending and increases the strain energies due to torsional, stretch-bend, and van der Waals interactions. The resulting effect is net reduction in strain energy and the reduction is proportional to the amount of functionalizing material attached to the wall of the CNT. Various components of the strain energy for 20 % of functionalization are plotted in Fig. 16. It can be concluded from these results that the type of functional group is found to have significant effect on strain

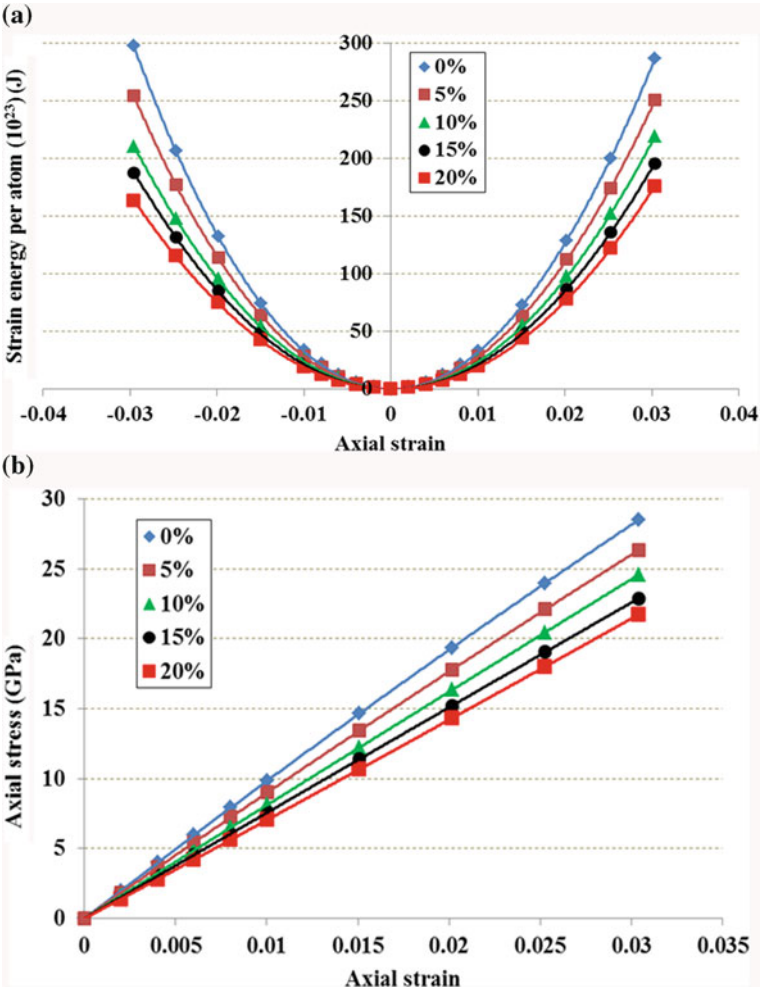

Fig. 10 **a** Variation of the strain energy per atom with axial strain, and **b** axial stress-axial strain curves of –H functionalized SWCNT with the percentage of functionalization varied from 5 to 20 %

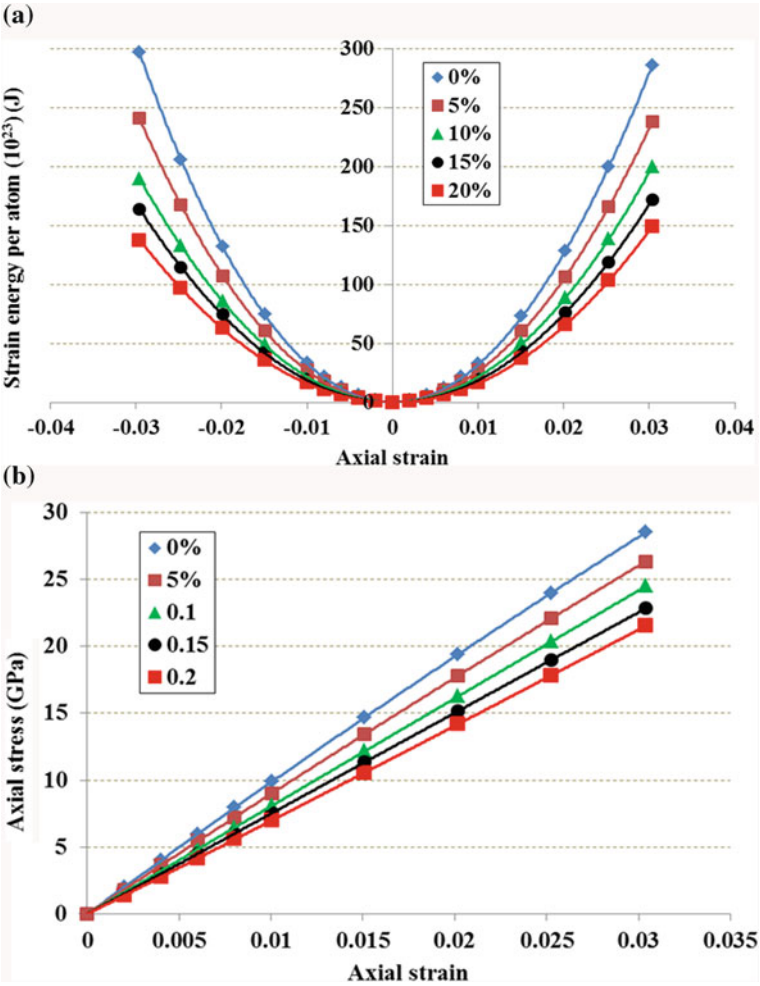

Fig. 11 **a** Variation of the strain energy per atom with axial strain, and **b** axial stress-axial strain curves of –OH functionalized SWCNT with the percentage of functionalization varied from 5 to 20 %

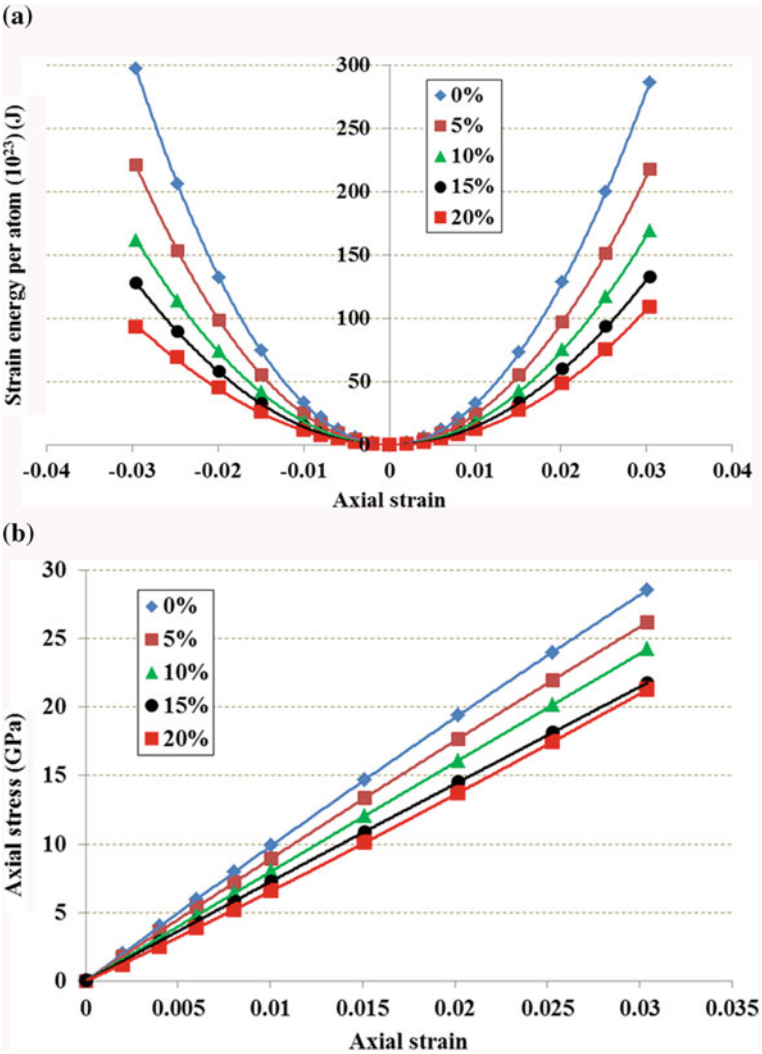

Fig. 12 **a** Variation of the strain energy per atom with axial strain, and **b** axial stress-axial strain curves of –COOH functionalized SWCNT with the percentage of functionalization varied from 5 to 20 %

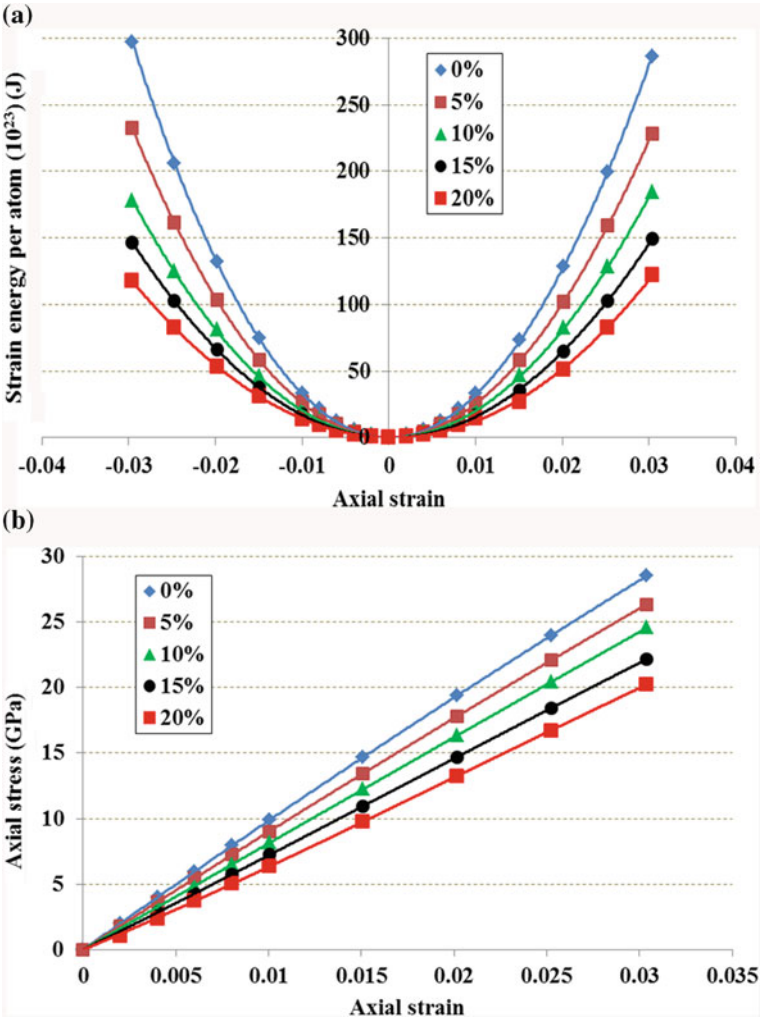

Fig. 13 **a** Variation of the strain energy per atom with axial strain, and **b** axial stress-axial strain curves of $-NH_2$ functionalized SWCNT with the percentage of functionalization varied from 5 to 20 %

Table 4 Young's modulus of the SWCNT functionalized with different groups

	Modulus of elasticity (TPa)			
% of functionalization	With hydrogen	With hydroxyl	With carboxyl	With amine
0	1.01	1.01	1.01	1.01
5	0.91	0.91	0.91	0.91
10	0.82	0.81	0.80	0.82
15	0.76	0.75	0.72	0.74
20	0.70	0.69	0.67	0.66

Note 0 % functionalization represents the pristine CNT

Table 5 Summary of theoretical predictions of reduction in Young's modulus of SWCNTs with covalent functionalization

Analysis method	Potential/force field	CNT	Functional group	Percentage of functionalization	Percentage reduction in Young's modulus	Reference
MM	MM3	(10, 0)	–H	5	10	Present study
				10	19	
			–OH	5	10	
				10	20	
			–COOH	5	10	
				10	21	
			$–NH_2$	5	10	
				10	19	
AFEM	2nd generation interatomic	(9, 0)	–H	10	6	Zhang et al. (2008)
				20	12	
MM	COMPASS	(10, 0)	$–C_2H_3$	8	16	Kuang and He (2009)
				21	31	
MD	COMPASS	(10, 10)	–H	5	11	Ling et al. (2012)
			–OH	5	16	
			–COOH	5	15	
			$–NH_2$	5	14	
DFT	–	(10, 0)	–OH	6	9	Milowska and Majewski (2013)
				10	12	
			–COOH	6	9	
				10	14	
			$–NH_2$	6	9	
				10	12	

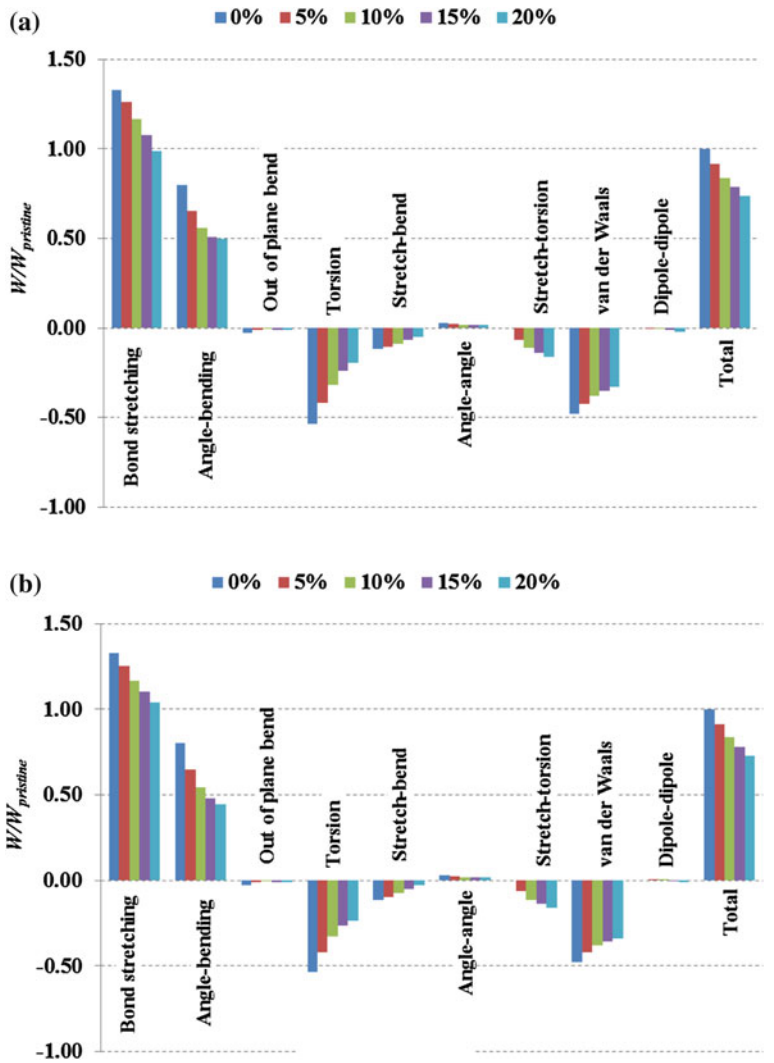

Fig. 14 Break down of the total strain energy of deformation into the individual energy components for **a** hydrogen, **b** hydroxyl, functionalized CNTs with percentage of functionalization varying from 0 to 20 %

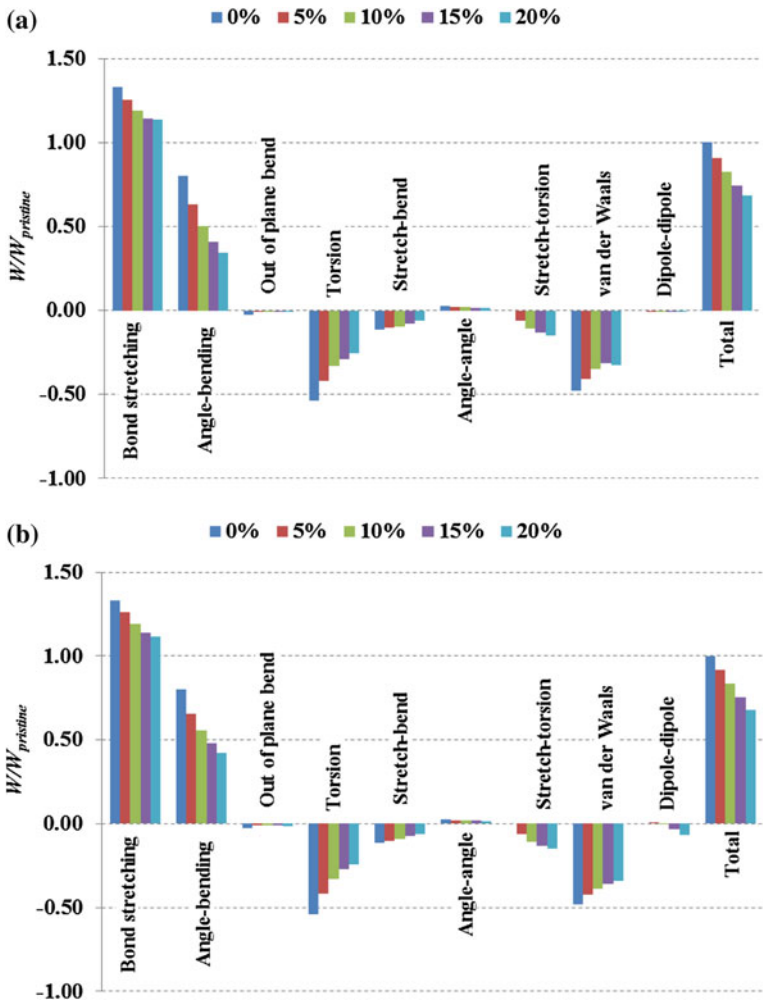

Fig. 15 Break down of the total strain energy of deformation into the individual energy components for **a** carboxyl, and **b** amine functionalized CNTs with percentage of functionalization varying from 0 to 20 %

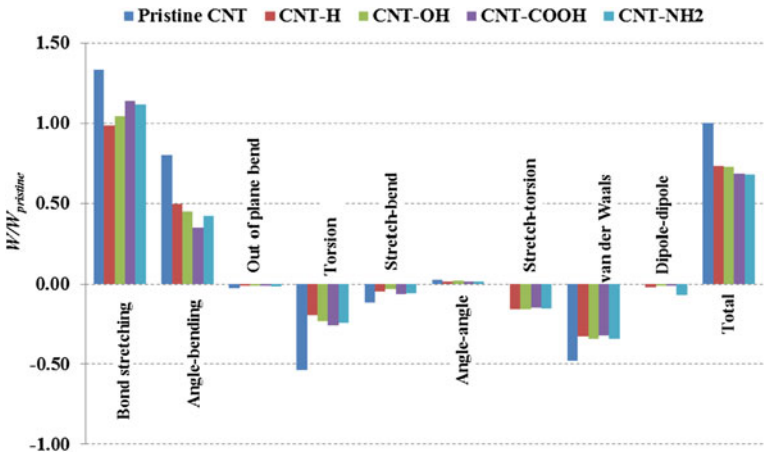

Fig. 16 Break down of the total strain energy of deformation into the individual energy components for the CNTs functionalized (20 %) with different functional groups

energies associated with bond stretching and bond angle bending compared to other energy components but the same net effect is obtained for all functional groups considered here.

4 Conclusions

We have studied the effect of covalent functionalization on Young's modulus of a SWCNT. The functionalization localizes deformations of the CNT at the functionalized sites, which decreases the modulus of elasticity and this reduction increases with an increase in the percentage of functionalization. The type of functional group is found to have negligible effect on the value of Young's modulus of the functionalized SWCNT. Approximately 30 % reduction in the value of Young's modulus of the pristine CNT occurs for 20 % of functionalization.

Acknowledgments This research was sponsored by the Army Research Laboratory and was accomplished under Cooperative Agreement Number W911NF-06-2-0014. The views and conclusions contained in this document are those of the authors and should not be interpreted as representing the official policies, either expressed or implied, of the Army Research Laboratory or the U.S. Government. The U.S. Government is authorized to reproduce and distribute reprints for Government purposes notwithstanding any copyright notation hereon.

References

Treacy MMJ, Ebesen TW, Gibson JM (1996) Exceptionally high Young's modulus observed for individual carbon nanotubes. Nature (London) 381:678–680

Wong EW, Sheehan PE, Lieber CM (1997) Nanobeam mechanics: elasticity, strength and toughness of nanorods and nanotubes. Science 277:1971–1975

Krishnan A, Dujardin E, Ebbesen TW, Yianilos PN, Treacy MMJ (1998) Young's modulus of single-walled nanotubes. Phys Rev B 58:14013–14019

Xing BW, Chun ZC, Zhao CW (2004) Simulation of Young's modulus of single-walled carbon nanotubes by molecular dynamics. Physica B 352:156–163

Li C, Chou TW (2003) A structural mechanics approach for the analysis of carbon nanotubes. Int J Solids Struct 40:2487–2499

Chang T, Gao H (2003) Size-dependent elastic properties of a single-walled carbon nanotube via a molecular mechanics model. J Mech Phys Solids 51:1059–1074

Sears A, Batra RC (2004) Macroscopic properties of carbon nanotubes from molecular mechanics simulations. Phys Rev B 69:Art. No. 235406

Shen L, Li J (2004) Transversely isotropic elastic properties of single-walled carbon nanotubes. Phys Rev B 69:045414

Batra RC, Sears A (2007) Uniform radial expansion/contraction of carbon nanotubes and their transverse elastic moduli. Modell Simul Mater Sci Eng 15:835–844

Gupta SS, Batra RC (2008) Continuum structures equivalent in normal mode vibrations to single-walled carbon nanotubes. Comput Mater Sci 43:715–723

Batra RC, Gupta SS (2008) Wall thickness and radial breathing modes of single-walled carbon nanotubes. ASME J Appl Mech 75:Art. No. 0610101

Wu J, Hwang KC, Huang YJ (2008) An atomistic-based finite-deformation shell theory for single-wall carbon nanotubes. J Mech Phys Solids 56:279–292

Chen J, Hamon MA, Hu H, Chen Y, Rao AM, Eklund PC, Haddon RC (1998) Solution properties of single-walled carbon nanotubes. Science 282:95–98

Hamon MA, Chen J, Hu H, Chen Y, Itkis ME, Rao AM, Eklund PC, Haddon RC (1999) Dissolution of single-walled carbon nanotubes. Adv Mater 11:834–840

Niyogi S, Hu H, Hamon MA, Bhowmik P, Zhao B, Rozenzhak SM, Chen J, Itkis ME, Meier MS, Haddon RC (2001) Chromatographic purification of soluble single walled carbon nanotubes (s-SWNTs). J Am Chem Soc 123:733–734

Chen J, Rao AM, Lyuksyutov S, Itkis ME, Hamon MA, Hu H, Cohn RW, Eklund PC, Colbert DT, Smalley RE, Haddon RC (2001) Dissolution of full-length single-walled carbon nanotubes. J Phys Chem B 105:2525–2528

Khare B, Meyyappan M, Cassell AM, Nguyen CV, Han J (2002) Functionalization of carbon nanotubes with atomic hydrogen from a glow discharge. Nano Lett 2:73–77

Riggs JE, Guo Z, Carroll DL, Sun YP (2000) Strong luminescence of solubilized carbon nanotubes. J Am Chem Soc 122:5879–5880

Sun YP, Huang W, Lin Y, Fu K, Kitaygorodskiy A, Riddle LA, Yu YJ, Carroll DL (2001a) Soluble dendron-functionalized carbon nanotubes: preparation, characterization, and properties. Chem Mater 13:2864–2869

Fu K, Huang W, Lin Y, Riddle LA, Carroll DL, Sun YP (2001) Defunctionalization of functionalized carbon nanotubes. Nano Lett 8:439–441

Sun Y, Wilson SR, Schuster DI (2001b) High dissolution and strong light emission of carbon nanotubes in aromatic amine solvents. J Am Chem Soc 123:5348–5349

Grujicic M, Sun YP, Koudela KL (2006) The effect of covalent functionalization of carbon nanotube reinforcements on the atomic-level mechanical properties of poly-vinyl-ester-epoxy. Appl Surf Sci 253:3009–3021

Cooper CA, Cohen SR, Barber AH, Daniel WH (2002) Detachment of nanotubes from a polymer matrix. Appl Phys Lett 81:3873–3875

Barber AH, Cohen SR, Daniel WH (2003) Measurement of carbon nanotube-polymer interfacial strength. Appl Phys Lett 82:4140–4142

Shofner ML, Khabashesku VN, Barrera EV (2006) Processing and mechanical properties of fluorinated single-wall carbon nanotube–polyethylene composites. Chem Mater 18:906–9013

Buffa F, Abraham GA, Grady BP, Resasco D (2007) Effect of nanotube functionalization on the properties of single-walled carbon nanotube/polyurethane composites. J Polym Sci Part B Polym Phys 45:490–501

Sun L, Warren GL, O'Reilly JY, Everett WN, Lee SM, Davis D, Lagoudas D, Sue HJ et al (2008) Mechanical properties of surface-functionalized SWCNT/epoxy composites. Carbon 46:320–328

Zhang ZQ, Liu B, Chen YL, Jiang H, Hwang KC, Huang Y (2008) Mechanical properties of functionalized carbon nanotubes. Nanotechnology 19:395702

Kuang YD, He XQ (2009) Young's moduli of functionalized single-wall carbon nanotubes under tensile loading. Compos Sci Technol 69:169–175

Ling CC, Xue QZ, Zhou XY (2012) Mechanical properties of functionalized carbon nanotube as reinforcements. Adv Mat Res 583:22–26

Milowska KZ, Majewski JA (2013) Elastic properties of functionalized carbon nanotubes. Phys Chem Ch Ph 15:14303–14309

Ponder JW (2000) Washington University in St. Loius, St. Louis

Allinger NL, Yuh YH, Lii JH (1989) Molecular mechanics. The MM3 force field for hydrocarbons. J Am Chem Soc 111:8551–8566 (and subsequent papers)

Volpe M, Cleri F (2003) Chemisorption of atomic hydrogen in graphite and carbon nanotubes. Surf Sci 544:24–34

Letardi S, Celino M, Cleri F, Rosato V (2002) Atomic hydrogen adsorption on a Stone-Wales defect in graphite. Surf Sci 496:33–38

Weininger D (1988) SMILES, a chemical language and information system. 1. Introduction to methodology and encoding rules. J Chem Inf Comput Sci 28:31–36

Weininger D, Weininger A, Weininger JL (1989) SMILES. 2. Algorithm for generation of unique SMILES notation. J Am Chem Soc 29:97–101

Multiscale Modeling of Multifunctional Fuzzy Fibers Based on Multi-Walled Carbon Nanotubes

Gary Don Seidel, George Chatzigeorgiou, Xiang Ren and Dimitris C. Lagoudas

Abstract This chapter will present an introduction to a novel class of multifunctional scale-bridging materials known as fuzzy fibers, which consist of multi-walled carbon nanotubes grown directly on the surface of structural carbon and glass fibers. The chapter will then identify some of the key challenges in the modeling of the mechanical, electrical, and thermal properties of fuzzy fibers and the composites in which they are embedded, and review some of the recent efforts to model these materials available in the literature. Finally, the description and a demonstration of the application of analytic composite cylinders model and computational homogenization approaches to modeling fuzzy fibers will be provided. A discussion of the potential applications for fuzzy fibers will close the chapter.

Keywords Glass fiber · Polymeric-matrix composites · Carbon nanotubes · Micromechanics · Homogenization · Fuzzy fiber · Composite cylinder method

G. D. Seidel (✉) · X. Ren
Aerospace and Ocean Engineering Department,
Virginia Polytechnic Institute and State University, 228 Randolph Hall (0203),
Blacksburg, VA 24061, USA
e-mail: gary.seidel@vt.edu

X. Ren
e-mail: xiangr7@vt.edu

G. Chatzigeorgiou
Chair of Applied Mechanics, University of Erlangen-Nuremberg, Egerlandstrasse 5,
91058 Erlangen, Germany
e-mail: george.chatzigeorgiou@ltm.uni-erlangen.de

D. C. Lagoudas
Department of Aerospace Engineering, Texas A&M University, 3141 TAMU,
College Station, TX 77843-3141, USA
e-mail: lagoudas@aero.tamu.edu

K. I. Tserpes and N. Silvestre (eds.), *Modeling of Carbon Nanotubes, Graphene and their Composites*, Springer Series in Materials Science 188,
DOI: 10.1007/978-3-319-01201-8_5,

1 Introduction

Since the discovery of carbon nanotubes (CNTs) (Iijima 1991), there has been a significant research effort directed towards understanding the source of their exceptional properties and how to take advantage of those properties in the design of macroscale nanocomposites. A single-walled carbon nanotube can be viewed as a single sheet of graphite (i.e., graphene), which has been rolled into the shape of a tube (Saito et al. 1998). Single and multi walled CNTs have radii on the order of nanometers and lengths on the order of micrometers resulting in large aspect ratios beneficial to their use in composites (Saito et al. 1998; Roche 2000). Carbon nanotubes are reported to have an axial Young's modulus in the range of 300–1000 GPa, up to five times the stiffness and with half the density of SiC fibers, in addition to having a theoretically predicted elongation to break of 30–40 % (Yakobson and Smalley 1997; Yu et al. 2000; Wang et al. 2001; Salvetat-Delmotte and Rubio 2002; Fisher et al. 2002; Popov 2004).

A wide variety of composites containing CNTs have been manufactured (Milo et al. 1999; Peigney et al. 2000; Potschke et al. 2004). Polymer-wrapped and functionalized CNTs, producing distinct interphase regions between matrix and CNTs, are also well documented in the literature (Wagner et al. 1998; Lourie and Wagner 1998; Star et al. 2001; McCarthy et al. 2002; Zhu et al. 2003a). Recent efforts focus on using CNTs in order to enhance the properties of microscale fiber composites. In order to strengthen the interface between the fiber and the matrix, the fibers can be coated with CNTs before being embedded in the matrix. When this coating corresponds to CNTs (in particular, multi-walled carbon nanotubes (MWCNTs)) being grown directly on the fiber surface, the resulting fiber-CNT system is termed a 'fuzzy fiber'. The fuzzy fiber material has a structural fiber core, with dense carbon nanotube 'forest' emanating radially from the fiber surface along the length of the fiber, as observed in Fig. 1. Growth techniques have been developed for carbon fibers (Thostenson et al. 2002; Zhu et al. 2003b; Zhao et al. 2005; Mathur et al. 2008; Sager et al. 2009), ceramic fibers (Ci et al. 2005; Garcia et al. 2008; Yamamoto et al. 2012) and glass fibers (Bower et al. 2000; Wood et al. 2012). The interest in the fuzzy fiber reinforced polymer nanocomposites stems from its multifunctional nanocomposite interphase region (as identified in Fig. 2b), which can provide enhanced load transfer, damage resistance, higher thermal and electrical conductivities, and electromechanical coupling in the form of piezoresistivity. The multi-functionality of the interphase region makes fuzzy fiber reinforced nanocomposites good candidates for multifunctional applications such as structural health monitoring, electromagnetic shielding, fire resisting and deicing.

To date, there has been a significant amount of research focused on developing models for predicting macroscale effective properties of polymer nanocomposites (Lau et al. 2004; Gates et al. 2005; Valaval and Odegard 2005; Fermeglia and Pricl 2007; Zeng et al. 2008; Esteva and Spanos 2009; Haque and Ramasetty 2005). Such models are inherently multiscale in nature, and typically make use of either atomistic simulations (Frankland et al. 2003; Adnan et al. 2007; Zhu et al. 2007;

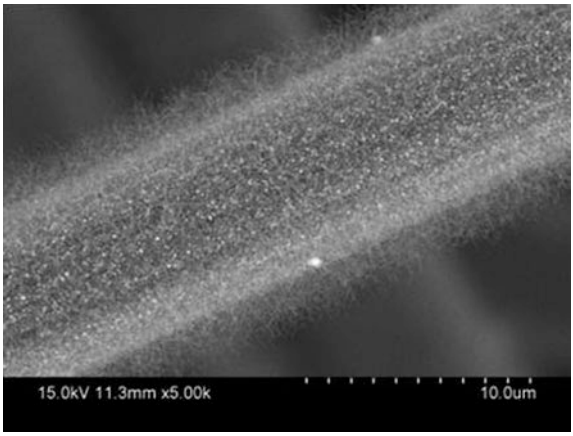

Fig. 1 Fuzzy fiber material: a single fuzzy fiber with densely-packed CNTs on the surface (http://muri18.tamu.edu/)

Awasthi et al. 2009), continuum micromechanics or homogenization techniques (Fisher and Brinson 2001; Fisher et al. 2002, 2003; Bradshaw et al. 2003; Buryachenko and Roy 2005; Liu et al. 2005; Liu and Brinson 2006; Seidel and Lagoudas 2006; Hammerand et al. 2007; Guzman de Villoria and Miravete 2007; Chen et al. 2005; Shenogina et al. 2005; Yan et al. 2007; Seidel and Lagoudas 2008; Seidel and Lagoudas 2009; Seidel and Stephens 2010; Seidel and Puydupin-Jamin 2011; Bonakdar et al. 2012; Oliva-Aviles et al. 2013; Ren and Seidel 2013), or some combination thereof (Li and Chou 2003; Odegard et al. 2003; Odegard et al. 2004; Seidel et al. 2005, 2006; Gao and Li 2005; Seidel and Lagoudas 2008; Li and Seidel 2012). Molecular dynamics simulations have been used to obtain the stress–strain behavior of CNTs embedded in a polymer matrix (Frankland et al. 2003). The mechanical response in tension of a single CNT embedded in polymer was studied via finite element analysis (Liu and Chen 2003). CNT composites have been modeled using the equivalent continuum method in conjunction with the Mori–Tanaka micromechanics method to obtain the effective elastic constants for both aligned and misaligned CNTs (Odegard et al. 2003). Nanocomposite properties have also been obtained via Monte Carlo finite element method (Spanos and Kontsos 2008). The effects of nanotube waviness on the effective composite properties have been studied using finite element analysis in conjunction with the Mori–Tanaka method (Fisher et al. 2002, 2003). Buckling of CNTs within an epoxy matrix has also been considered (Hadjiev et al. 2006). Other efforts have focused on the inclusion of less than ideal CNT adhesion to the matrix in CNT composite modeling (Wagner 2002; Frankland et al. 2003; Griebel and Hamaekers 2004). The clustering of CNTs in the polymer matrix was studied through a micromechanics approach (Seidel and Lagoudas 2006).

In addition to developing models for determining the effective mechanical properties of nanocomposites, there have also been efforts focused on obtaining effective thermal (Chen et al. 2005; Shenogina et al. 2005; Seidel and Lagoudas 2008) and electrical (Yan et al. 2007; Seidel and Lagoudas 2009; Seidel and Puydupin-Jamin 2011) conductivities, coefficients of thermal expansion (Seidel and

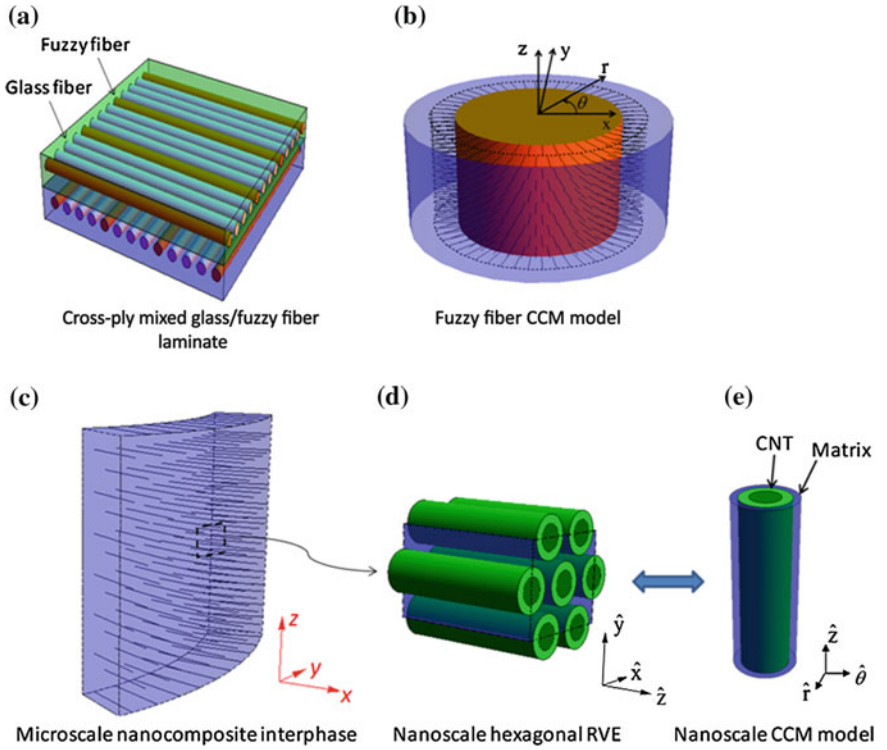

Fig. 2 Schematic of **a** a cross-ply laminate with mixture of non-fuzzy and fuzzy glass fibers, **b** individual fuzzy fiber corresponding to the composite cylinder model (representative of an aligned all fuzzy fiber laminate plies), with the first (innermost) layer being the structural glass fiber, the second layer being the nanocomposite interphase where there are densely packed and radially oriented CNTs, and the third layer being the pure polymer matrix, **c** $\Delta\theta$, Δr, Δz segment of the nanocomposite interphase region, **d** well-dispersed, densely packed CNTs within the interphase corresponding to a hexagonal packing originating at the glass fiber-nanocomposite interface (the *hat* denotes local MWCNT scale), **e** nanocomposite composite cylinder model

Stephens 2010), and piezoresistivity (Oliva-Aviles et al. 2013; Ren and Seidel 2013) of CNT-polymer nanocomposites. For example, Seidel and Lagoudas (Seidel and Lagoudas 2008) developed a hierarchical multiscale model for obtaining nanocomposite effective thermal conductivity which linked MD simulations results to a two scale continuum micromechanics model. In the model, information obtained from MD simulations concerning interfacial thermal resistance was passed to a composite cylinder formulation for obtaining effective nanofiber thermal conductivity. The effective nanofiber conductivity was then used in a Mori–Tanaka averaging approach in order to account for orientation effects in determining the effective thermal conductivity of the CNT-polymer nanocomposite. A similar approach was taken by Seidel and Lagoudas (Seidel and Lagoudas 2009) in determining the effective electrical conductivity of CNT-polymer nanocomposites. In this model, the focus was on accounting for the nanoscale effect of electron

hopping using the composite cylinder approach, and on accounting for the formation of conductive paths and of orientation effects using the Mori–Tanaka method, while in finite element studies (Seidel and Puydupin-Jamin 2011), the combined effects of clustering and electron hopping were considered. However, in all these mechanical, thermal and electrical modeling efforts the composite consists of carbon nanotubes and matrix, and therefore do not address the architecture and associated material symmetry associated with fuzzy fibers.

Herein we examine fuzzy fiber composites where glass fibers, coated with radially aligned carbon nanotubes, are embedded in a matrix. These enhanced glass fibers have the potential to improve not only interface strength, but to provide additional functionality as sensors by taking advantage of the multifunctional properties of CNTs. In the literature the mechanical response of fuzzy fiber composites was investigated using the method of cells (Kundalwal and Ray 2011, 2012). Moreover, a shear lag model was developed for obtaining the behavior of composites reinforced with carbon nanotubes-coated piezoelectric fibers (Ray 2010). Here the investigation of the effective mechanical and electrostatic properties of fuzzy fiber composites is achieved with two different approaches: (a) the generalized self consistent composite cylinders method (Hashin and Rosen 1964; Christensen 1979; Hashin 1990; Seidel and Lagoudas 2006, 2009), modified properly in order to account for the additional interface layer between the fiber and the matrix (Chatzigeorgiou et al. 2012a; Ren and Seidel 2011), and (b) a modified version of the asymptotic expansion homogenization method which accounts for the cylindrical periodicity that the interface layer (carbon nanotubes embedded in matrix) presents as a separate composite (Chatzigeorgiou et al. 2011). These techniques, along with the Mori–Tanaka method (Mori and Tanaka 1973) will be applied in a hierarchical multiscale modeling approach to demonstrate the effective mechanical and electrostatic properties of fuzzy fiber composites consisting of aligned or randomly oriented fuzzy fibers and mixtures of aligned glass and fuzzy fibers having varying concentrations and lengths of MWCNTs in the nanocomposite interphase.

2 Fuzzy Fiber Composites: Micromechanics Approach

A fuzzy fiber composite material system is a fiber composite (Fig. 2a), in which some or all of the structural fibers (glass fibers) are coated with radially aligned microfibers (multi-walled carbon nanotubes (MWCNTs)) (Fig. 2b). For modeling purposes we assume (Chatzigeorgiou et al. 2012a) that the representative volume element (RVE) of the fuzzy fiber contains three layers: the first layer is the cylindrical glass fiber. The second is a reinforced nanocomposite interphase (intermediate cylindrical layer) which consists of cylindrical MWCNTs and matrix. The third layer is the area of the pure matrix (Fig. 2b). The coated glass fibers are arranged to correspond to a unidirectional lamina layer (Fig. 2a), in which the fibers are aligned in the z direction and are well dispersed (randomly distributed) in

the x–y plane. The fibers and the matrix are either isotropic, or transversely isotropic linearly elastic materials with the axis of symmetry parallel to the axis of the fibers. The MWCNTs in the reinforced nanocomposite interphase are assumed to be transversely isotropic with the axis of symmetry parallel with the MWCNT axis (r-direction in Fig. 2b). The idealized RVE of the reinforced interphase is shown in Fig. 2c.

Based on the observations that (a) the diameter of the glass fiber is very large compared to the diameter of the MWCNTs and (b) the MWCNTs are normally densely packed along the glass fiber surface (small $\Delta\theta$ in Fig. 2c), we can assume that the reinforced interphase behaves as a classical unidirectional composite (Fig. 2d), and effectively it is a transversely isotropic medium with the axis of symmetry parallel to the axis of MWCNTs (i.e. in the radial direction of the glass fiber). Hence, we can use micromechanics methods for composites with aligned microfibers in determining the transversely isotropic interphase properties (Seidel and Lagoudas 2006). Kundalwal and Ray (Kundalwal and Ray 2011) present the properties of the reinforced interphase in a Cartesian coordinate system and they assume that the effective behavior is given by averaging over all orientations. This approach alters the anisotropic nature of the reinforced interphase, such that the interphase is identified as transversely isotropic material with axis of symmetry parallel to the axis of the structural fiber (glass fiber) as opposed to the microfiber (MWCNT). In the cylindrical coordinate system shown in Fig. 2b, where z is the glass fiber longitudinal axis, the stress–strain relations of a linearly elastic orthotropic material are written

$$\begin{pmatrix} \sigma_{rr} \\ \sigma_{\theta\theta} \\ \sigma_{zz} \\ \sigma_{z\theta} \\ \sigma_{rz} \\ \sigma_{r\theta} \end{pmatrix} = \begin{pmatrix} C_{11} & C_{12} & C_{13} & 0 & 0 & 0 \\ C_{12} & C_{22} & C_{23} & 0 & 0 & 0 \\ C_{13} & C_{23} & C_{33} & 0 & 0 & 0 \\ 0 & 0 & 0 & C_{44} & 0 & 0 \\ 0 & 0 & 0 & 0 & C_{55} & 0 \\ 0 & 0 & 0 & 0 & 0 & C_{66} \end{pmatrix} \begin{pmatrix} \varepsilon_{rr} \\ \varepsilon_{\theta\theta} \\ \varepsilon_{zz} \\ 2\varepsilon_{z\theta} \\ 2\varepsilon_{rz} \\ 2\varepsilon_{r\theta} \end{pmatrix}, \tag{1}$$

where the indices 1, 2, 3 in the stiffness tensors denote the axes r, θ, z respectively. For the matrix and the glass fiber we have

$$C_{22} = C_{11}, \quad C_{13} = C_{23}, \quad C_{55} = C_{44}, \quad C_{66} = \frac{C_{11} - C_{12}}{2}, \tag{2}$$

while for the intermediate layer (reinforced interphase) holds

$$C_{33} = C_{22}, \quad C_{13} = C_{12}, \quad C_{55} = C_{66}, \quad C_{44} = \frac{C_{22} - C_{23}}{2}. \tag{3}$$

In the case of the unidirectional fuzzy fiber composite, absence of the reinforced interphase (i.e. just fiber in matrix lamina) leads to transversely isotropic effective medium. Moreover we can easily show that, upon arbitrary rotation about the z axis, the stiffness matrix of the reinforced interphase remains the same, which indicates that the quasi-cylindrically orthotropic structure (transversely isotropic

with axis of symmetry parallel to the direction r of Fig. 2b) of the reinforced interphase does not disrupt the overall symmetry of the effective medium. This means that the final composite material will be effectively transversely isotropic, with the axis of symmetry parallel to the axis of the fibers (the z axis). As such, the stress–strain relation of the effective unidirectional lamina in the cylindrical coordinate system is given by (1) and (2) with the superscript "eff" to denote the effective property, e.g. C_{IJ}^{eff} relating σ_I^{eff} and ε_J^{eff}.

The computation of the effective properties requires knowledge of the mechanical response of the fuzzy fiber material system, which ideally consists of concentric cylinders. The elastic response of homogeneous and non-homogeneous thick- or thin-walled tubes under different boundary conditions was studied by many authors (Chatterjee 1970; Horgan and Chan 1999; Chen et al. 2000; Tarn and Wang 2001; Ruhi et al. 2005; Hosseini Kordkheili and Naghdabadi 2007; Chatzigeorgiou et al. 2008; Tsukrov and Drach 2010; Nie and Batra 2010). Our aim is to determine elasticity solutions for a series of boundary value problems (BVPs). These BVPs are used in conjunction with the composite cylinders method in order to identify the effective properties of the composite, as has been successfully implemented in the past in the case of CNT composites (Seidel and Lagoudas 2006).

2.1 Composite Cylinders Method for Mechanical Properties

For the composite cylinders method we use the RVE of Fig. 3a. This 3 layer composite cylinder RVE (fiber, reinforced interphase, matrix) is equivalent to an RVE for a randomly distributed, aligned, fuzzy fiber composite and can be

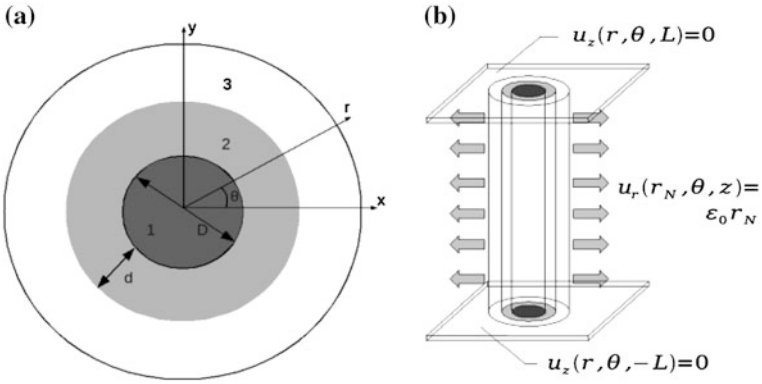

Fig. 3 **a** Identification of layers in composite cylinder method RVE **b** identification of boundary conditions associated with the plane strain (*in-plane*) bulk modulus BVP in the composite cylinder method. (Chatzigeorgiou et al. 2012a)

extended for $N \geq 3$ layers. In the following, we will consider the cylindrical system of the fuzzy fiber RVE as the global coordinate system. In cylindrical coordinates the equilibrium equations are given by

$$\begin{aligned} \frac{\partial \sigma_{rr}^{(i)}}{\partial r} + \frac{1}{r}\frac{\partial \sigma_{r\theta}^{(i)}}{\partial \theta} + \frac{\sigma_{rr}^{(i)} - \sigma_{\theta\theta}^{(i)}}{r} + \frac{\partial \sigma_{rz}^{(i)}}{\partial z} = 0, \\ \frac{\partial \sigma_{r\theta}^{(i)}}{\partial r} + \frac{1}{r}\frac{\partial \sigma_{\theta\theta}^{(i)}}{\partial \theta} + 2\frac{\sigma_{r\theta}^{(i)}}{r} + \frac{\partial \sigma_{z\theta}^{(i)}}{\partial z} = 0, \\ \frac{\partial \sigma_{rz}^{(i)}}{\partial r} + \frac{1}{r}\frac{\partial \sigma_{z\theta}^{(i)}}{\partial \theta} + \frac{\sigma_{rz}^{(i)}}{r} + \frac{\partial \sigma_{zz}^{(i)}}{\partial z} = 0, \end{aligned} \tag{4}$$

where (i) is the material layer (i = 1, 2,…,N). Assuming small deformation gradients, the infinitesimal strains are expressed with respect to the displacements according to the relations

$$\begin{aligned} \varepsilon_{rr}^{(i)} = \frac{\partial u_r^{(i)}}{\partial r}, \quad \varepsilon_{\theta\theta}^{(i)} = \frac{1}{r}\left(\frac{\partial u_\theta^{(i)}}{\partial \theta} + u_r^{(i)}\right), \quad \varepsilon_{zz}^{(i)} = \frac{\partial u_z^{(i)}}{\partial z}, \\ 2\varepsilon_{z\theta}^{(i)} = \frac{\partial u_\theta^{(i)}}{\partial z} + \frac{1}{r}\frac{\partial u_z^{(i)}}{\partial \theta}, \quad 2\varepsilon_{rz}^{(i)} = \frac{\partial u_z^{(i)}}{\partial r} + \frac{\partial u_r^{(i)}}{\partial z}, \\ 2\varepsilon_{r\theta}^{(i)} = \frac{1}{r}\frac{\partial u_r^{(i)}}{\partial \theta} + \frac{\partial u_\theta^{(i)}}{\partial r} - \frac{1}{r}u_\theta^{(i)}. \end{aligned} \tag{5}$$

In order to use the composite cylinders method, we need to determine admissible displacement fields which will satisfy five specific boundary value problems. In order to do this, we have to substitute (5) into the appropriate constitutive relations (1)–(3), and then substitute the resulting equations into (4) to get the equilibrium equations in terms of the displacements. Next we can apply the semi-inverse method to determine the necessary admissible displacement fields. Then, solving the same boundary value problems for the homogenized cylinder we can obtain the effective properties using the direct strain energy equivalency method. The homogenized cylinder is described by the same equations, with the difference that the (i) must be replaced by eff denoting the effective material. Tsukrov and his coworkers (Tsukrov et al. 2009; Tsukrov and Drach 2010) present a similar approach as described above for the case of carbon/carbon composites, where pyrolytic carbon cylindrically orthotropic layers surround a fiber. In their study they present the admissible displacement fields for various loading cases and obtain the effective axial Young's modulus, the transverse bulk modulus and the axial Poisson's ratio. Here we present specific boundary value problems that allow us to obtain all five effective properties (in-plane bulk modulus, axial shear modulus, axial Young's modulus, axial stiffness coefficient, in-plane shear modulus) and the stress concentration tensors for the fuzzy fiber. It is noted that for the in-plane shear modulus we need to use the generalized self consistent composite cylinders method proposed by Christensen (Christensen 1979).

In the following, we denote r_i to be the external radius of each layer, with the inner radius of the solid fiber layer denoted $r_0 = 0$. The length of the composite cylinder is taken as 2L. We also introduce the volume average

$$\langle \varphi \rangle = \frac{1}{V}\int_V \varphi(x,y,z)dxdydz = \frac{1}{V}\int_V r\varphi(r,\theta,z)drd\theta dz, \tag{6}$$

where V is the volume of the RVE. With regard to the stress concentration tensors, it is useful to express the average stresses in Cartesian coordinates, and thus, standard transformation relationships between Cartesian (x, y, z) and cylindrical (r, θ, z) coordinate systems can be applied to obtain the desired integrand in (6).

2.1.1 In-plane Bulk Modulus

The effective in-plane or plane strain bulk modulus, K_{12}^{eff}, is determined from the boundary value problem shown in Fig. 3b, for which the appropriate displacement field is

$$u_r^{(i)} = \sum_{j=1}^{2} D_j^{(i)} r^{n_j^{(i)}}, \quad u_\theta^{(i)} = u_z^{(i)} = 0, \quad i = 1,2,\ldots,N, \tag{7}$$

with $n_1^{(i)} = \sqrt{C_{22}^{(i)}/C_{11}^{(i)}} = -n_2^{(i)}$. For isotropic and transversely isotropic materials with axis of symmetry parallel to the axis of the fiber $n_1^{(i)} = -n_2^{(i)} = 1$ and the displacement field reduces to the expression described in Seidel and Lagoudas (Seidel and Lagoudas 2006). The constants $D_1^{(i)}$ and $D_2^{(i)}$ are computed from the boundary condition $u_r^{(N)}(r_N) = \varepsilon_0 r_N$, the condition $D_2^{(1)} = 0$ (insuring that the displacement is bounded at the origin), and the continuity conditions (considering perfect bonding between layers) $u_r^{(i)}(r_i) = u_r^{(i+1)}(r_i)$ and $\sigma_{rr}^{(i)}(r_i) = \sigma_{rr}^{(i+1)}(r_i)$ for i = 1, 2,…,N−1.

The volume averaged strain energy for the composite cylinder assemblage is given by

$$W^{RVE} = \frac{1}{2}\left\langle \sigma_{rr}^{(i)}\varepsilon_{rr}^{(i)} + \sigma_{\theta\theta}^{(i)}\varepsilon_{\theta\theta}^{(i)} \right\rangle = \frac{1}{r_N^2}\sum_{i=1}^{N}\sum_{j=1}^{2}\left(\frac{C_{22}^{(i)}}{n_j^{(i)}} + C_{12}^{(i)}\right)\left(D_j^{(i)}\right)^2\left(r_i^{2n_j^{(i)}} - r_{i-1}^{2n_j^{(i)}}\right). \tag{8}$$

The homogenized cylinder is described by the same equations, with the difference that the (i) must be replaced by eff and $n_1^{eff} = 1$. For the effective medium we get $D_1^{eff} = \varepsilon_0$. Consequently the strain energy of the effective homogeneous material is written as $W^{eff} = \frac{1}{2}\left\langle \sigma_{rr}^{eff}\varepsilon_{rr}^{eff} + \sigma_{\theta\theta}^{eff}\varepsilon_{\theta\theta}^{eff} \right\rangle = 2K_{12}^{eff}\varepsilon_0^2$. Since $W^{RVE} = W^{eff}$, we get

$$K_{12}^{eff} = \frac{1}{2\varepsilon_0^2 r_N^2} \sum_{i=1}^{N} \sum_{j=1}^{2} \left(\frac{C_{22}^{(i)}}{n_j^{(i)}} + C_{12}^{(i)} \right) \left(D_j^{(i)} \right)^2 \left(r_i^{2n_j^{(i)}} - r_{i-1}^{2n_j^{(i)}} \right). \tag{9}$$

Here we need to mention that the effective in-plane bulk modulus does not depend on the applied strain at the boundary as it can be shown that $D_j^{(i)}$ contains ε_0.

The volume averaged stresses of the entire RVE $\langle \sigma_K^{Total} \rangle$ and the fuzzy fiber $\langle \sigma_K^J \rangle$, expressed in Cartesian coordinates, are given by

$$\begin{aligned} \langle \sigma_K^{Total} \rangle &= \frac{1}{2\pi L r_N} \sum_{i=1}^{N} \int_{-L}^{L} \int_{0}^{2\pi} \int_{r_{i-1}}^{r_i} \sigma_K r dr d\theta dz, \\ \langle \sigma_K^J \rangle &= \frac{1}{2\pi L r_{N-1}} \sum_{i=1}^{N-1} \int_{-L}^{L} \int_{0}^{2\pi} \int_{r_{i-1}}^{r_i} \sigma_K r dr d\theta dz. \end{aligned} \tag{10}$$

Using the displacement field (7), the Eqs. (5), the constitutive law (1) and converting to Cartesian coordinates we obtain the average stresses

$$\begin{aligned} \langle \sigma_1^{Total} \rangle = \langle \sigma_2^{Total} \rangle &= \frac{1}{r_N^2} \sum_{i=1}^{N} \sum_{j=1}^{2} D_j^{(i)} \Omega_j^{(i)} K_j^{(i)}, \langle \sigma_3^{Total} \rangle = \frac{1}{r_N^2} \sum_{i=1}^{N} \sum_{j=1}^{2} D_j^{(i)} \Psi_j^{(i)} K_j^{(i)}, \\ \langle \sigma_1^J \rangle = \langle \sigma_2^J \rangle &= \frac{1}{r_{N-1}^2} \sum_{i=1}^{N-1} \sum_{j=1}^{2} D_j^{(i)} \Omega_j^{(i)} K_j^{(i)}, \langle \sigma_3^J \rangle = \frac{1}{r_{N-1}^2} \sum_{i=1}^{N-1} \sum_{j=1}^{2} D_j^{(i)} \Psi_j^{(i)} K_j^{(i)}, \end{aligned} \tag{11}$$

where

$$\begin{aligned} K_j^{(i)} &= \begin{cases} \frac{r_i^{1+n_j^{(i)}} - r_{i-1}^{1+n_j^{(i)}}}{1+n_j^{(i)}}, & n_j^{(i)} \neq -1, \\ \ln(r_i) - \ln(r_i - 1), & n_j^{(i)} = -1, \end{cases} \\ \Psi_j^{(i)} &= 2n_j^{(i)} C_{13}^{(i)} + 2C_{23}^{(i)}, \quad \Omega_j^{(i)} = n_j^{(i)} \left(C_{11}^{(i)} + C_{12}^{(i)} \right) + C_{12}^{(i)} + C_{22}^{(i)}. \end{aligned} \tag{12}$$

2.1.2 Axial Shear Modulus

The axial shear modulus, $\mu_{23}^{eff} = C_{44}^{eff}$, is determined from the layer displacement field of

$$u_z^{(i)} = \sum_{j=1}^{2} D_j^{(i)} r^{n_j^{(i)}} \cos\theta, \quad u_\theta^{(i)} = u_r^{(i)} = 0, \quad i = 1, 2, ..., N, \tag{13}$$

with $n_1^{(i)} = \sqrt{C_{44}^{(i)}/C_{55}^{(i)}} = -n_2^{(i)}$. For isotropic and transversely isotropic materials with axis of symmetry parallel to the axis of the fiber $n_1^{(i)} = -n_2^{(i)} = 1$ and the displacement field reduces to the expression described in Seidel and Lagoudas (Seidel and Lagoudas 2006). The constants $D_1^{(i)}$ and $D_2^{(i)}$ are computed from the displacement boundary condition $u_z^{(N)}(r_N, \theta) = 2\varepsilon_0 r_N \cos\theta$, the condition $D_2^{(1)} = 0$ (insuring that the displacement is bounded at the origin), and the continuity conditions (considering perfect bonding between layers) $u_z^{(i)}(r_i) = u_z^{(i+1)}(r_i)$and $\sigma_{rz}^{(i)}(r_i) = \sigma_{rz}^{(i+1)}(r_i)$ for i = 1, 2,…,N−1.

The volume averaged strain energy for the composite cylinder assemblage is given by

$$W^{RVE} = \frac{1}{2}\left\langle \sigma_{rz}^{(i)}\varepsilon_{rz}^{(i)} + \sigma_{z\theta}^{(i)}\varepsilon_{z\theta}^{(i)} \right\rangle = \frac{1}{2r_N^2}\sum_{i=1}^{N}\sum_{j=1}^{2}\frac{C_{44}^{(i)}}{n_j^{(i)}}\left(D_j^{(i)}\right)^2\left(r_i^{2n_j^{(i)}} - r_{i-1}^{2n_j^{(i)}}\right). \quad (14)$$

The homogenized cylinder is described by the same equations, with the difference that the (i) must be replaced by eff and $n_1^{eff} = 1$. For the effective medium we get $D_1^{eff} = 2\varepsilon_0$. Consequently the strain energy of the effective homogeneous material is written as $W^{eff} = 2\mu_{23}^{eff}\varepsilon_0^2$. Since $W^{RVE} = W^{eff}$, we get

$$\mu_{23}^{eff} = \frac{1}{4\varepsilon_0^2 r_N^2}\sum_{i=1}^{N}\sum_{j=1}^{2}\frac{C_{44}^{(i)}}{n_j^{(i)}}\left(D_j^{(i)}\right)^2\left(r_i^{2n_j^{(i)}} - r_{i-1}^{2n_j^{(i)}}\right). \quad (15)$$

2.1.3 Axial Young's Modulus and Axial Stiffness Component

The axial Young's modulus, E_3^{eff}, and the axial stiffness coefficient, C_{33}^{eff}, are determined from the same layer displacement field of

$$u_r^{(i)} = \Lambda^{(i)} r + \sum_{j=1}^{2} D_j^{(i)} r^{n_j^{(i)}}, \qquad \Lambda^{(i)} = \begin{cases} \frac{C_{13}^{(i)} - C_{23}^{(i)}}{C_{22}^{(i)} - C_{11}^{(i)}}\varepsilon_0, & C_{11}^{(i)} \neq C_{22}^{(i)}, \\ 0, & C_{11}^{(i)} = C_{22}^{(i)}, \end{cases} \quad (16)$$

$$u_\theta^{(i)} = 0, \qquad u_z^{(i)} = \varepsilon_0, \qquad i = 1, 2, ..., N,$$

with $n_1^{(i)} = \sqrt{C_{22}^{(i)}/C_{11}^{(i)}} = -n_2^{(i)}$. For isotropic and transversely isotropic materials with axis of symmetry parallel to the axis of the fiber $n_1^{(i)} = -n_2^{(i)} = 1$. Relative to an isotropic or transversely isotropic interphase with aligned symmetry axis with the overall symmetry axis (Seidel and Lagoudas 2006), the reinforced interphase behavior introduces a new term, $\Lambda^{(i)} r$, which is needed to satisfy the equilibrium Eqs. (4). $\Lambda^{(i)}$ takes a non-zero value only in the case where the material has different radial and circumferential behavior. It also carries the ε_0 from the

boundary condition which permeates into the solution of the form for $u_r^{(i)}$. The constants $D_1^{(i)}$ and $D_2^{(i)}$ are computed from the condition $D_2^{(1)} = 0$ (insuring that the displacement is bounded at the origin), the continuity conditions (considering perfect bonding between layers) $u_r^{(i)}(r_i) = u_r^{(i+1)}(r_i)$ and $\sigma_{rr}^{(i)}(r_i) = \sigma_{rr}^{(i+1)}(r_i)$ for i = 1,2,…,N−1 and the boundary conditions. The displacement $u_z^{(i)}$ is also trivially enforced. For the axial Young's modulus, the lateral surface is traction free in the tension test ($\sigma_{rr}^{(N)}(r_N) = 0$), while for the axial stiffness component the lateral surface is constrained in the stiffness test ($u_r^{(N)}(r_N) = 0$).

The volume averaged strain energy for the composite cylinder assemblage is given by

$$\begin{aligned} W^{RVE} &= \frac{1}{2}\left\langle \sigma_{rr}^{(i)}\varepsilon_{rr}^{(i)} + \sigma_{\theta\theta}^{(i)}\varepsilon_{\theta\theta}^{(i)} + \sigma_{zz}^{(i)}\varepsilon_{zz}^{(i)} \right\rangle \\ &= \frac{1}{r_N^2}\sum_{i=1}^{N}\left(\Lambda_1^{(i)}\varepsilon_0 + 2\Lambda_2^{(i)}\Lambda^{(i)}\right)\frac{r_i^2 - r_{i-1}^2}{2} + \frac{2\varepsilon_0}{r_N^2}\sum_{i=1}^{N}\sum_{j=1}^{2} D_j^{(i)}\left(C_{23}^{(i)} + n_j^{(i)}C_{13}^{(i)}\right)K_j^{(i)} \\ &\quad + \frac{1}{r_N^2}\sum_{i=1}^{N}\sum_{j=1}^{2}\left(\frac{C_{22}^{(i)}}{n_j^{(i)}} + C_{12}^{(i)}\right)D_j^{(i)}\left(D_j^{(i)}\left(r_i^{2n_j^{(i)}} - r_{i-1}^{2n_j^{(i)}}\right) + 2\Lambda^{(i)}\left(r_i^{1+n_j^{(i)}} - r_{i-1}^{1+n_j^{(i)}}\right)\right), \end{aligned} \tag{17}$$

where $\Lambda_1^{(i)} = C_{13}^{(i)}\Lambda^{(i)} + C_{23}^{(i)}\Lambda^{(i)} + C_{33}^{(i)}\varepsilon_0$, $\Lambda_2^{(i)} = C_{11}^{(i)}\Lambda^{(i)} + C_{12}^{(i)}\Lambda^{(i)} + C_{13}^{(i)}\varepsilon_0$ and $K_j^{(i)}$ is given by (12). The homogenized cylinder is described by the same equations, with the difference that the (i) must be replaced by eff and $n_1^{eff} = 1$.

The boundary conditions for the effective axial Young's modulus lead to $D_1^{eff} = -C_{13}^{eff}\varepsilon_0/(C_{11}^{eff} + C_{12}^{eff})$ and the strain energy of the effective medium is $W^{eff} = \frac{1}{2}E_3^{eff}\varepsilon_0^2$. Since $W^{RVE} = W^{eff}$, we get

$$\begin{aligned} E_3^{eff} &= \frac{2}{r_N^2}\sum_{i=1}^{N}\left(\Lambda_1^{(i)}\varepsilon_0 + 2\Lambda_2^{(i)}\Lambda^{(i)}\right)\frac{r_i^2 - r_{i-1}^2}{2\varepsilon_0^2} + \frac{4}{r_N^2}\sum_{i=1}^{N}\sum_{j=1}^{2} D_j^{(i)}\left(C_{23}^{(i)} + n_j^{(i)}C_{13}^{(i)}\right)\frac{K_j^{(i)}}{\varepsilon_0} \\ &\quad + \frac{2}{\varepsilon_0^2 r_N^2}\sum_{i=1}^{N}\sum_{j=1}^{2}\left(\frac{C_{22}^{(i)}}{n_j^{(i)}} + C_{12}^{(i)}\right)D_j^{(i)}\left(D_j^{(i)}\left(r_i^{2n_j^{(i)}} - r_{i-1}^{2n_j^{(i)}}\right) + 2\Lambda^{(i)}\left(r_i^{1+n_j^{(i)}} - r_{i-1}^{1+n_j^{(i)}}\right)\right). \end{aligned} \tag{18}$$

The boundary conditions for the effective axial stiffness coefficient lead to $D_1^{eff} = 0$, while the strain energy of the effective medium is given by $W^{eff} = \frac{1}{2}C_{33}^{eff}\varepsilon_0^2$. Since $W^{RVE} = W^{eff}$, we get

$$C_{33}^{eff} = \frac{2}{r_N^2}\sum_{i=1}^{N}\left(\Lambda_1^{(i)}\varepsilon_0 + 2\Lambda_2^{(i)}\Lambda^{(i)}\right)\frac{r_i^2 - r_{i-1}^2}{2\varepsilon_0^2} + \frac{4}{r_N^2}\sum_{i=1}^{N}\sum_{j=1}^{2} D_j^{(i)}\left(C_{23}^{(i)} + n_j^{(i)}C_{13}^{(i)}\right)\frac{K_j^{(i)}}{\varepsilon_0}$$
$$+\frac{2}{\varepsilon_0^2 r_N^2}\sum_{i=1}^{N}\sum_{j=1}^{2}\left(\frac{C_{22}^{(i)}}{n_j^{(i)}} + C_{12}^{(i)}\right)D_j^{(i)}\left(D_j^{(i)}\left(r_i^{2n_j^{(i)}} - r_{i-1}^{2n_j^{(i)}}\right) + 2\Lambda^{(i)}\left(r_i^{1+n_j^{(i)}} - r_{i-1}^{1+n_j^{(i)}}\right)\right). \tag{19}$$

We note that the effective properties are independent of the boundary constant ε_0.

2.1.4 In-Plane Shear Modulus

The composite cylinders method (Hashin and Rosen 1964) can provide only bounds for the in-plane shear modulus $\mu_{12}^{eff} = C_{66}^{eff}$. For this reason we will use the generalized self consistent composite cylinders method (Christensen 1979; Christensen and Lo 1979). In this case, an additional layer (layer N + 1) is added, representing the effective medium with external radius $r_{N+1} \to \infty$ (Fig. 4a). The admissible displacement field for this case is described by the equations

$$\begin{aligned}
u_r^{(i)} &= \sum_{j=1}^{4} a_j^{(i)} D_j^{(i)} r^{n_j^{(i)}} \sin(2\theta), \qquad u_\theta^{(i)} = \sum_{j=1}^{4} D_j^{(i)} r^{n_j^{(i)}} \cos(2\theta),\\
u_z^{(i)} &= 0, \qquad\qquad i = 1, 2, ..., N,\\
u_r^{(N+1)} &= \frac{r_N}{4\mu_{12}^{eff}}\left(\frac{2r}{r_N} + D_3^{(N+1)}\frac{r_N^3}{r^3} + 2\left(1 + \frac{\mu_{12}^{eff}}{K_{12}^{eff}}\right)\frac{r_N}{r}\right)\sin(2\theta),\\
u_\theta^{(N+1)} &= \frac{r_N}{4\mu_{12}^{eff}}\left(\frac{2r}{r_N} - D_3^{(N+1)}\frac{r_N^3}{r^3} + \frac{\mu_{12}^{eff}}{K_{12}^{eff}}\frac{r_N}{r}\right)\cos(2\theta),
\end{aligned} \tag{20}$$

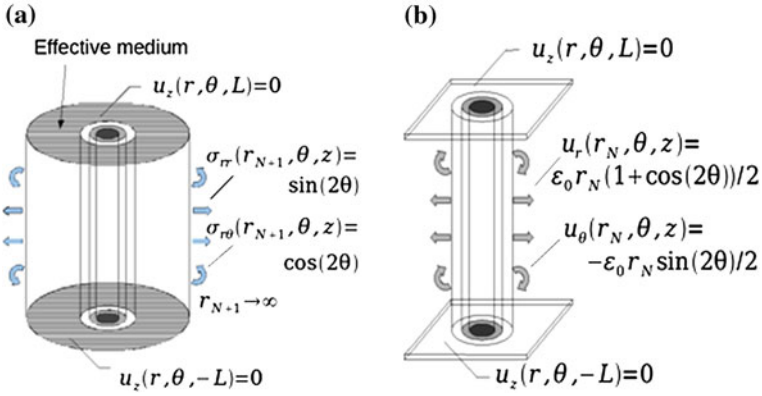

Fig. 4 **a** In-plane shear modulus, **b** transverse extension test (Chatzigeorgiou et al. 2012a)

with

$$a_j^{(i)} = 2\frac{C_{22}^{(i)} + C_{66}^{(i)} - n_j^{(i)}\left(C_{12}^{(i)} + C_{66}^{(i)}\right)}{C_{22}^{(i)} + 4C_{66}^{(i)} - \left(n_j^{(i)}\right)^2 C_{11}^{(i)}}, \quad i = 1, 2, \ldots, N, \quad j = 1, 2, 3, 4, \tag{21}$$

and $n_j^{(i)}$ are the solutions of the polynomial

$$C_{11}^{(i)}C_{66}^{(i)}n^4 - \left(\left(C_{11}^{(i)} + C_{22}^{(i)} - 8C_{12}^{(i)}\right)C_{66}^{(i)} + 4\left(C_{11}^{(i)}C_{22}^{(i)} - \left(C_{12}^{(i)}\right)^2\right)\right)n^2 + 9C_{22}^{(i)}C_{66}^{(i)} = 0. \tag{22}$$

In the above expression, $n_1^{(i)}$ and $n_2^{(i)}$ are the positive and $n_3^{(i)}$ and $n_4^{(i)}$ are the negative solutions. If z is the axis of symmetry for the layer (i.e. the axis of the fiber), these equations reduce to the equations given in Seidel and Lagoudas (Seidel and Lagoudas 2006), therefore the extra complication is directly attributed to the difference in material symmetry orientation of the interphase layer, which is transversely isotropic with axis of symmetry parallel to the radial direction (i.e. the direction of the microfibers).

The external boundary conditions are already included in the displacement field of the N + 1 layer. We also need the conditions ensuring boundness at the origin ($D_3^{(1)} = D_4^{(1)} = 0$) as well as the continuity conditions $u_r^{(i)}(r_i) = u_r^{(i+1)}(r_i)$, $u_\theta^{(i)}(r_i) = u_\theta^{(i+1)}(r_i)$, $\sigma_{rr}^{(i)}(r_i) = \sigma_{rr}^{(i+1)}(r_i)$ and $\sigma_{r\theta}^{(i)}(r_i) = \sigma_{r\theta}^{(i+1)}(r_i)$ for i = 1, 2…,N.

The strain energy equivalency is written

$$\int_0^{2\pi}\left[\sigma_{rr}^{(N+1)}u_r^{eff} + \sigma_{r\theta}^{(N+1)}u_\theta^{eff} - \sigma_{rr}^{eff}u_r^{(N+1)} - \sigma_{r\theta}^{eff}u_\theta^{(N+1)}\right]_{r=r_N} d\theta = 0. \tag{23}$$

Equation (23) is the interaction (surface) energy form converted from the volume averaged form. The surface energy form arises from the strain energy equality between the composite and the homogenized medium (Christensen 1979, pp. 55–56) and it provides easier computations than directly using the stored strain energy equivalency. The displacement field of the effective medium is

$$u_r^{eff} = \frac{r\sin(2\theta)}{2\mu_{12}^{eff}}, \quad u_\theta^{(i)} = \frac{r\cos(2\theta)}{2\mu_{12}^{eff}}, \quad u_z^{(i)} = 0. \tag{24}$$

The strain energy equivalency leads to the final condition that $D_4^{(N+1)} = 0$, from which we solve for μ_{12}^{eff}.

The generalized self consistent composite cylinders method can also be used to obtain the other effective properties (in plane bulk modulus, axial shear modulus, axial Young's modulus and axial stiffness component). In these cases, iterative schemes need to be employed, since the generalized self consistent composite cylinders method leads to nonlinear equations. The values of these properties,

obtained by the later method, are in very good agreement with the values obtained by the composite cylinders method (Seidel 2007), indicating that not using the effective layer in obtaining these properties is an acceptable simplification.

The five boundary value problems that presented so far are sufficient to identify the composite effective behavior for well-dispersed, aligned fiber composites of single type (i.e. all glass or all fuzzy fiber unidirectional laminate plies), and therefore can be used to obtain additional effective properties such as transverse Young's modulus, E_1^{eff}, and axial and transverse Poisson's ratios, v_{32}^{eff} and v_{12}^{eff}, respectively (Chatzigeorgiou et al. 2012a). For mixed fiber types or multiple fiber orientations within a ply, the composite cylinder method can also be used to obtain the components of the stress concentration tensor, B_{ijkl}^J, by connecting the volume average of the stress $\left\langle \sigma_{ij}^{Total} \right\rangle$ over the three material layers (i.e., the fiber, the reinforced interphase and the matrix) with the volume average of the stress $\left\langle \sigma_{ij}^{J} \right\rangle$ (e.g. see (11)) over only the fiber and the reinforced interphase through the relation

$$\left\langle \sigma_{ij}^{J} \right\rangle = B_{ijkl}^{J} \left\langle \sigma_{kl}^{Total} \right\rangle. \tag{25}$$

However, the sets of equations produced by the in-plane bulk modulus test and the axial stiffness component are not linearly independent, and therefore an additional boundary value problem to those described above is needed, i.e. the transverse extension test, to solve the system of equations in (25).

2.1.5 Transverse Extension Test

The transverse extension test boundary value problem is shown in Fig. 4b. The admissible displacement field for this case is described by the equations

$$u_r^{(i)} = \sum_{j=1}^{4} D_j^{(i)} r^{n_j^{(i)}} \cos(2\theta) + \sum_{j=5}^{6} D_j^{(i)} r^{n_j^{(i)}}, \quad u_\theta^{(i)} = \sum_{j=1}^{4} a_j^{(i)} D_j^{(i)} r^{n_j^{(i)}} \sin(2\theta), \quad u_z^{(i)} = 0, \qquad i = 1, 2, ..., N, \tag{26}$$

with

$$a_j^{(i)} = -\frac{1}{2} \frac{C_{22}^{(i)} + 4C_{66}^{(i)} - \left(n_j^{(i)}\right)^2 C_{11}^{(i)}}{C_{22}^{(i)} + C_{66}^{(i)} - n_j^{(i)} \left(C_{12}^{(i)} + C_{66}^{(i)}\right)}, \quad i = 1, 2, \ldots, N, \quad j = 1, 2, 3, 4, \tag{27}$$

$n_j^{(i)}$, j = 1, 2, 3, 4, are the solutions of the polynomial

$$C_{11}^{(i)}C_{66}^{(i)}n^4 - \left(\left(C_{11}^{(i)} + C_{22}^{(i)} - 8C_{12}^{(i)}\right)C_{66}^{(i)} + 4\left(C_{11}^{(i)}C_{22}^{(i)} - \left(C_{12}^{(i)}\right)^2\right)\right)n^2 + 9C_{22}^{(i)}C_{66}^{(i)} = 0, \tag{28}$$

and $n_5^{(i)} = \sqrt{C_{22}^{(i)}/C_{11}^{(i)}} = -n_6^{(i)}$. In Eq. (28), $n_1^{(i)}$ and $n_2^{(i)}$ are the positive and $n_3^{(i)}$ and $n_4^{(i)}$ are the negative solutions.

The external boundary conditions are shown in Fig. 4b. We also need the conditions ensuring boundedness at the origin ($D_3^{(1)} = D_4^{(1)} = D_6^{(1)} = 0$) as well as the continuity conditions $u_r^{(i)}(r_i) = u_r^{(i+1)}(r_i)$, $u_\theta^{(i)}(r_i) = u_\theta^{(i+1)}(r_i)$, $\sigma_{rr}^{(i)}(r_i) = \sigma_{rr}^{(i+1)}(r_i)$ and $\sigma_{r\theta}^{(i)}(r_i) = \sigma_{r\theta}^{(i+1)}(r_i)$ for i = 1,2…,N. Having solved the system of equations, we can then obtain the average of the volume averaged stresses $\left\langle \sigma_{ij}^{Total} \right\rangle$ and $\left\langle \sigma_{ij}^{J} \right\rangle$, thereby providing an additional set of independent equations to be used in (25).

The obtained effective properties of this subsection are related with unidirectional fuzzy fiber composites. In previous work (Seidel and Lagoudas 2006) it was observed that the generalized self consistent composite cylinders and composite cylinders methods yield the same effective properties and concentration tensors for aligned fiber composites. So, for aligned composites, composite cylinders method is a very good approximation of the generalized self consistent composite cylinders concentration tensor components. The method can be extended to consider thermoelastic behavior of aligned fuzzy fiber composites (see Tsukrov et al. 2012 for the case of carbon/carbon composites with pyrolytic carbon cylindrically orthotropic layers).

2.2 Composite Cylinders Method for Electrostatic Properties

The effective electrostatic properties of the aligned fuzzy fiber reinforced polymer nanocomposites can be obtained by likewise using CCM model in which the second layer is the interphase region as was the case for the mechanical properties. In order to simplify the problem, let us likewise assume the CNTs in the interphase region are of the same length, homogeneously distributed, straight and radially oriented, with perfect bounding to the glass fiber and matrix, as illustrated in Fig. 2. For the time-being, we will disregard the effects of electron hopping. The electrostatic properties of the structural fibers and the polymer matrix can be considered as homogeneous and isotropic, but what makes a difference is the interphase region, whose electrostatic properties are of anisotropic symmetry if denoted in rectangle Cartesian coordinate system, such that the analytic solutions are hard to find. However, by observing the CNTs are radially oriented, it is convenient to denote the effective electrical conductivities of the interphase region as cylindrically orthotropic in Cylindrical coordinate system, whose three

components are $\kappa_{rr}^{(2)}$, $\kappa_{\theta\theta}^{(2)}$, and $\kappa_{zz}^{(2)}$[1], in which (2) denotes the conductivities in the second layer. Further, if we introduce a nanoscale RVE to represent a small area of the interphase region (Fig. 2c), we can consider the densely packed CNTs on the glass fiber to have periodic hexagonal pattern in every local nanoscale area (Fig. 2d), which implies that the interphase region in the nanoscale can be regarded as transversely isotropic, with the axial direction in the radial direction relative to the glass fiber. Therefore we can use the nanoscale CCM model to get the effective electrical conductivities of the nanoscale first (Fig. 2e), and then relate the nanoscale effective properties with those of the microscale, such that

$$\kappa_{rr}^{(2)} = \kappa_{zz}^{(2)\text{eff}} \quad \text{and} \quad \kappa_{\theta\theta}^{(2)} = \kappa_{zz}^{(2)} = \kappa_{rr}^{(2)\text{eff}} = \kappa_{\theta\theta}^{(2)\text{eff}} \tag{29}$$

in which '^' denotes material properties in the nanoscale.

Once the electrostatic properties of the second layer are obtained, the electrostatic properties for the three layers as identified in Fig. 2b are all known. Therefore the electrostatic properties of the microscale can be obtained by using the microscale CCM model, which can be used to represent the electrostatic properties of the fuzzy fiber reinforced composites. Section 2.2.1 introduces the governing equations for a general electrostatic CCM model, which can be applied either in the nanoscale or microscale.

2.2.1 The Governing Equations for the Electrostatic CCM Model

For each layer of the multi-layer cylinder, the steady state conservation of charge equation can be denoted in Cylindrical coordinate system as:

$$\frac{\partial J_r^{(k)}}{\partial r} + \frac{1}{r}\frac{\partial J_\theta^{(k)}}{\partial \theta} + \frac{\partial J_z^{(k)}}{\partial z} + \frac{1}{r}J_r^{(k)} = 0 \tag{30}$$

where $J_i^{(k)}(i = r, \theta, z)$ is the current density component with (k) denoting the index of the layer (e.g. $k = 1$ denotes the innermost layer, and so on). Similarly, for the homogenized effective material, the (k) in (30) can be replaced with the superscript 'eff', where $J_i^{eff}(i = r, \theta, z)$ is the current density component of the effective material. For each layer of the multi-layer cylinder, the electric field component $E_i^{(k)}$ can therefore be denoted with

$$E_r^{(k)} = -\frac{\partial \Phi^{(k)}}{\partial r}, \quad E_\theta^{(k)} = -\frac{1}{r}\frac{\partial \Phi^{(k)}}{\partial \theta}, \quad E_z^{(k)} = -\frac{\partial \Phi^{(k)}}{\partial z} \tag{31}$$

[1] In the fuzzy fiber interphase region, due to the curvature of the glass fiber surface, the volume fraction of the CNT is actually radially dependent, with the volume fraction higher close to the glass fiber and lower farther away from it. However, considering the CNTs are densely-packed, the dependency is very weak, which is therefore omitted and the volume fraction of the CNT is kept as the one in the middle of the interphase.

where $\Phi^{(k)}$ is the electric potential for each layer of the multi-layer cylinder, and where the (k) can again be suitably replaced for the effective material equations. The current density is related to electric field by Ohm's law which for the multi-layer cylinder can be written as

$$\begin{Bmatrix} J_r^{(k)} \\ J_\theta^{(k)} \\ J_z^{(k)} \end{Bmatrix} = \begin{bmatrix} \kappa_{rr}^{(k)} & 0 & 0 \\ 0 & \kappa_{\theta\theta}^{(k)} & 0 \\ 0 & 0 & \kappa_{zz}^{(k)} \end{bmatrix} \begin{Bmatrix} E_r^{(k)} \\ E_\theta^{(k)} \\ E_z^{(k)} \end{Bmatrix} \tag{32}$$

where $\kappa_{ij}^{(k)}$ denote components of the second order electrical conductivity tensors for each layer of the multi-layer cylinder, where the layers are generally considered as cylindrically orthotropic such that $\kappa_{rr}^{(k)}$, $\kappa_{\theta\theta}^{(k)}$, and $\kappa_{zz}^{(k)}$ are not necessarily equal. Similarly, for the effective material, Ohm's law can be written as $J_i^{eff} = \kappa_{ij}^{eff} E_j^{eff}$ where κ_{ij}^{eff} denotes the effective conductivities for the effective material, which are obtained by solving electrostatic boundary value problems (BVPs) and constructing electrostatic energy equivalence between the multi-layer cylinder and the effective material. It is noted that, given the cylindrical geometry and cylindrically orthotropic layer conductivities, the effective conductivity should at most maintain the cylindrically orthotropic material symmetry. However, by assuming the fibers are infinitely long and by observing the well-dispersed and aligned fibers have hexagonal symmetry in the transverse plane, the effective electrostatic material properties can be considered as transversely isotropic (Hashin and Rosen, 1964). Therefore, $\kappa_{rr}^{eff} = \kappa_{\theta\theta}^{eff}$, and as such, only two BVPs are then needed (one axial and one transverse) to obtain the two unknown effective electrostatic properties, which are introduced as below.

The in-plane electrostatic BVP

The electric potential for each layer of the multi-layer cylinder is:

$$\Phi^{(k)} = (A^{(k)} r^{\sqrt{\frac{\kappa_{\theta\theta}^{(k)}}{\kappa_{rr}^{(k)}}}} + B^{(k)} r^{-\sqrt{\frac{\kappa_{\theta\theta}^{(k)}}{\kappa_{rr}^{(k)}}}}) \cos(\theta) \tag{33}$$

where $\kappa_{rr}^{(k)}$ and $\kappa_{\theta\theta}^{(k)}$ are known conductivities of each layer, and $A^{(k)}$ are $B^{(k)}$ unknown constants to be solved by using boundary conditions and matching conditions. It is worth noticing that for a layer with in plane isotropic electrostatic properties, i.e. $\kappa_{rr}^{(k)} = \kappa_{\theta\theta}^{(k)}$, the power terms in (33) are reduced to one. This is the case not only for the isotropic glass fiber and matrix materials of the composite cylinder assemblage, but also for the effective homogeneous cylinder which is transversely isotropic with r$-\theta$ isotropy plane. However, for the interphase region of the fuzzy fiber which is cylindrically orthotropic such that $\kappa_{rr}^{(2)} \neq \kappa_{\theta\theta}^{(2)}$, the power terms are not equal to one. As the adjacent layers of the multi-layer cylinder are assumed to be perfectly bounded, the matching conditions between adjacent layers are:

$$\Phi^{(k)}(r = r_k) = \Phi^{(k+1)}(r = r_k),\ k = 1\,to\,N-1 \tag{34a}$$

$$J_r^{(k)}(r = r_k) = J_r^{(k+1)}(r = r_k),\ k = 1\,to\,N-1 \tag{34b}$$

in which N denotes the total number of layers. The boundary conditions for the multi-layer cylinder are:

$$\Phi^{(N)} = E_0 r\cos(\theta)|_{r=r_N,\,0\le z\le L} \tag{35a}$$

$$\Phi^{(1)} = 0|_{r=r_0=0,\,0\le z\le L}\ \ or\ \ J^{(1)} = 0|_{r=r_0\neq 0,\,0\le z\le L} \tag{35b}$$

in which E_0 is a constant electric field component associated with a uniform homogeneous electric field at the macroscale (i.e. here the laminate layer scale), L is the length of the CCM model in z-direction, and r_0 and r_N are the innermost and outermost radius, respectively, of the multi-layer cylinder. Specifically, if $r_0 = 0$, the innermost layer is solid and the first condition of (35b) is applied such that $B^{(1)} = 0$ so that the potential solution remains bounded. In contrast, if $r_0 \neq 0$, there is a hollow region in the innermost layer, and the second condition in (35b) is applied. Similarly, the boundary conditions for the effective homogeneous solid cylinder material are giving (35a) and the first of (35b) with superscripts (N) and (1) replaced by 'eff'.

The axial electrostatic BVP

The electric potential for each layer of the multi-layer cylinder is:

$$\Phi^{(k)} = A^{(k)}z + B^{(k)} \tag{36}$$

where $A^{(k)}$ and $B^{(k)}$ are unknown constants to be solved by using boundary conditions. The boundary conditions of the multi-layer cylinder are provided as

$$\Phi^{(k)}|_{z=0} = \Phi_0\ \ (k = 1\,to\,N) \tag{37a}$$

$$\Phi^{(k)}|_{z=L} = \Phi_1\ \ (k = 1\,to\,N) \tag{37b}$$

in which Φ_0 and Φ_1 are constant potentials as applied at $z = 0$ and $z = L$ respectively. It is noted that, as there is no r- or θ-dependence in the electric potential, then there is no need to enforce matching conditions between the layers. The effective homogeneous solid cylinder is subject to the same form of the potential and boundary conditions as in (36) and (37).

Electrostatic energy equivalence

For each BVP, volume averaged electrostatic energy equivalence is constructed between the multi-layer cylinder and the effective material, such that $W^{RVE} = W^{eff}$ where

$$W^{RVE} = \frac{1}{V}\sum_{k=1}^{N}\int_0^L\int_0^{2\pi}\int_{r_{k-1}}^{r_k}\frac{1}{2}E_i^{(k)}J_i^{(k)}rdrd\theta dz \tag{38a}$$

$$W^{eff} = \frac{1}{V}\int_0^L\int_0^{2\pi}\int_0^{r_N}\frac{1}{2}E_i^{eff}J_i^{eff}rdrd\theta dz \tag{38b}$$

in which V is the whole volume of the model and $V = \pi r_N^2 L$. For the in-plane BVP, $W^{eff} = \frac{1}{2}E_0^2\kappa_{rr}^{eff} = \frac{1}{2}E_0^2\kappa_{\theta\theta}^{eff}$ and for the axial BVP, $W^{eff} = \frac{1}{2}E_0^2\kappa_{zz}^{eff}$. However, it is noted that the effective properties resulting for the equating (38a) and (38b) are independent of the magnitude of the applied electric field as solution of the BVPs reveal that $A^{(k)}$ and $B^{(k)}$depend linearly on E_0.

2.3 *Effective Properties of Composites with Multiple Types of Fuzzy Fibers*

In the previous subsections we dealt with unidirectional fuzzy fiber composites, when only one type of fuzzy fiber is considered. However, in order to consider more complicated structures (for instance, fuzzy fibers with different orientations or different materials for the fibers, fuzzy fibers with various CNT concentrations), the knowledge of the effective properties of the fuzzy fiber itself must be combined with the knowledge of the strain or stress (or by analogy, the electric field or current density) concentration tensors.

2.3.1 General Relations for Composites with Multiple Fuzzy Fiber Types

In the case of multiple fuzzy fiber types, each type defines a different phase in the composite. Assuming $J = 1, 2, \ldots, \Im$ distinct fiber types, with volume fractions c^J and stiffness tensors C_{ijkl}^J, the effective behavior of the final composite is identified by the relation

$$C_{ijkl}^{eff} = C_{ijkl}^m + \sum_{J=1}^{\Im} c^J\left(C_{ijop}^J - C_{ijop}^m\right)A_{opkl}^J, \tag{39}$$

where A_{ijkl}^J is the strain concentration tensor of each phase and the superscript m denotes the matrix phase. It is noted that the volume fraction relation for all phases is given by $c^m + \sum_{J=1}^{\Im} c^J = 1$.

The composite cylinders method introduced in the previous subsection can be used to compute the stress concentration tensors associated with different types of

fuzzy fibers, e.g. different MWCNT concentrations in the nanocomposite interphase or different interphase thicknesses. One can likewise identify the effective properties of various fuzzy fiber types using the described composite cylinders method, by considering almost zero matrix layer (layer with N = 3). This information is necessary if we need the fuzzy fiber properties for use in other methods such as the Mori–Tanaka for addressing composites with multiple inhomogeneity (fuzzy fiber) types or fiber orientations.

It is noted that in four out of five properties, we use the composite cylinders method as opposed to the generalized self consistent composite cylinders method, and as such, the method we propose is termed quasi-dilute in that the interactions between the various types or orientations of fibers are not directly accounted for. When transitioning to a Mori–Tanaka method, we can instead take the computed composite cylinders concentration tensor components to be the dilute concentration tensor components (the difference between the quasi-dilute and the dilute is only on the in-plane shear term). The dilute stress concentration tensor H^J_{ijkl} of a fuzzy fiber composite can be identified using the composite cylinders method and considering very large matrix volume fraction (third layer). The obtained tensor relates the stress in the inhomogeneity to the uniform stress in the far field applied traction. The dilute strain concentration tensor G^J_{ijkl} is computed from the dilute stress concentration tensor H^J_{ijkl}, the fuzzy fiber stiffness tensor C^J_{ijkl} and the matrix stiffness tensor C^m_{ijkl} through the relation

$$G^J_{ijkl} = \left(C^J_{ijop}\right)^{-1} H^J_{opqr} C^m_{qrkl}. \tag{40}$$

The properties C^J_{ijkl} of the fuzzy fiber are computed from the composite cylinders method, imposing essentially the two phase model of glass fiber and reinforced nanocomposite interphase to make an effective layer. The computed dilute strain concentration tensor can be used in a Mori–Tanaka method (in order to allow for indirect interactions between the J phases) to identify the effective properties of a composite with mixed fuzzy fiber types. Especially for composites with "fuzzy fibers" of different orientation, Mori–Tanaka is a very efficient and easily implemented micromechanics method, provided one accounts properly for the interactions of the fibers with different orientation (for further details see Entchev and Lagoudas 2002; Seidel 2007).

According to the Mori–Tanaka method, the strain concentration tensor A^J_{ijkl} for each phase in aligned fiber composites is computed by the relation (Qu and Cherkaoui 2006)

$$A^J_{ijkl} = G^J_{ijmn}\left[c^m I_{mnkl} + \sum_{J=1}^{\mathfrak{I}} c^J G^J_{mnkl}\right]^{-1}. \tag{41}$$

Combining (39) and (41), we obtain the effective stiffness tensor for aligned fuzzy fiber composites,

$$C_{ijkl}^{eff} = C_{ijkl}^{m} + \sum_{J=1}^{\Im} c^{J}\left(C_{ijop}^{J} - C_{ijop}^{m}\right) G_{opmn}^{J}\left[c^{m} I_{mnkl} + \sum_{J=1}^{\Im} c^{J} G_{mnkl}^{J}\right]^{-1}. \quad (42)$$

When the fuzzy fibers have different orientation, the strain concentration tensor $A_{ijkl}^{J}$for each phase is computed by the relation (Entchev and Lagoudas 2002; Seidel 2007)

$$A_{ijkl}^{J} = Q_{ia}^{J} Q_{jb}^{J} Q_{mc}^{J} Q_{nd}^{J} G_{abcd}^{J}\left[c^{m} I_{mnkl} + \sum_{J=1}^{\Im} c^{J} Q_{me}^{J} Q_{nf}^{J} Q_{kg}^{J} Q_{lh}^{J} G_{efgh}^{J}\right]^{-1}, \quad (43)$$

where Q_{ij}^{J} is the direction cosine matrix relating the Jth fiber axis orientation to the global coordinate system (typically through a set of Euler angles). Treating each orientation as a separate phase, (43) can be substituted into (39) to obtain the effective stiffness tensor with mixed orientations.

It is noted that (39) through (43) and the special cases which follow can be appropriately reduced in order from 2nd and 4th order tensors in the mechanical case to vectors and 2nd order tensors in the electrostatic case to obtain the multiphase/multi-orientation Mori–Tanaka expressions for the effective electrical conductivity with the current density, electric field, resistivity, and conductivity analogously replacing the stress, strain, compliance, and stiffness, respectively.

2.3.2 Special Cases of Composites

Based on the relations described previously, we can provide expressions of the effective properties for special cases of composites with fuzzy fibers.

Aligned fiber composites with one fuzzy fiber type

In the case of aligned fiber composites with only one type of fuzzy fibers the effective behavior is directly computed by the proposed composite cylinders method. Alternatively, using the Mori–Tanaka method, the effective stiffness tensor is identified by the relation

$$C_{ijkl}^{eff} = C_{ijkl}^{m} + c^{f}\left(C_{ijop}^{f} - C_{ijop}^{m}\right) G_{opmn}^{f}\left[\left(1 - c^{f}\right) I_{mnkl} + c^{f} G_{mnkl}^{f}\right]^{-1}, \quad (44)$$

where the superscripts f and m denote the fuzzy fiber and the matrix respectively.

Composites with randomly oriented fuzzy fibers

In the case of composites with random orientation of the fibers, the knowledge of the concentration tensors for composites with aligned fibers is sufficient in order to use the Mori–Tanaka method (details are given in Entchev and Lagoudas 2002; Seidel 2007). The actual concentration tensor of the phases is provided through a careful averaging of the dilute concentration tensors for aligned fiber composites

over all possible orientations. The effective stiffness tensor of a composite with randomly oriented fibers is given by (Entchev and Lagoudas 2002)

$$C^{eff}_{ijkl} = C^{m}_{ijkl} + \left(C^{f}_{ijop} - C^{m}_{ijop}\right)\left\{\left\{G^{f}_{opmn}\right\}\right\}\left[(1-c^{f})I_{mnkl} + \left\{\left\{G^{f}_{mnkl}\right\}\right\}\right]^{-1}, \quad (45)$$

where $\{\{\varphi\}\}$ denotes averaging of function φ over all possible orientations and c^f is the fibers volume fraction.

3 Fuzzy Fiber Composites: Periodic Homogenization Approach

The fuzzy fiber composite presented in Fig. 2 deviates significantly from what is called periodic medium. The fibers are generally distributed randomly inside the matrix material, and additionally the CNTs on the reinforced interphase are densely packed in random way. For modeling purposes though we can make several assumptions that allow us to treat it as a composite with periodic or nearly periodic microstructure. We assume that the composite under investigation consists of unidirectional fuzzy fibers, distributed in a hexagonal form inside the matrix (Fig. 5a and b). The hexagonal distribution efficiently represents a random distribution of the fibers in the matrix (Hashin and Rosen 1964). A similar argument holds for the reinforced interface, whose microstructure can be considered to present the cylindrical periodicity of Fig. 5c.

In order to obtain the effective properties of the composite, we are using the asymptotic expansion homogenization (AEH) method, which is a two scale homogenization method. The AEH is a well established method (Sanchez-Palencia 1978; Bensoussan et al. 1978; Kalamkarov and Kolpakov 1997; Chung et al. 2001), in which 2 scales are taken into account, the macroscale and the microscale. In a Cartesian coordinate system framework, the macroscale is described by the

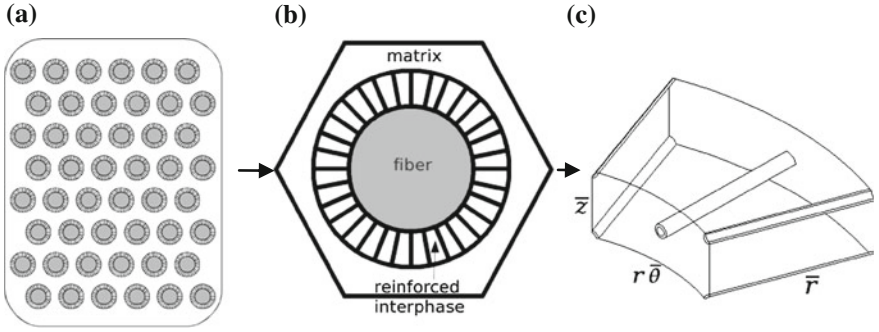

Fig. 5 **a** Fuzzy fiber composite, **b** unit cell of the composite, **c** unit cell of the reinforced interphase (Chatzigeorgiou et al. 2011)

coordinates (x_1, x_2, x_3), while the microscale by the coordinates $\left(\frac{x_1}{e}, \frac{x_2}{e}, \frac{x_3}{e}\right)$, where e is the characteristic length of the periodic cell. The idea of the method is that the displacements are written in an asymptotic series form with respect to e and the expanded forms of the equilibrium equations lead to e^{-1} terms (microequations) and e^0 terms (macroequations). From the microequations we obtain the necessary quantities, whose averages give us the homogenized properties used in the macroequations.

In our composite system, the unit cell of Fig. 5b consists of 3 different material systems, the fiber, the reinforced interphase and the matrix. The interphase itself is also a composite (Fig. 5c), whose periodic cell is represented in a cylindrical coordinate system. Its structure includes MWCNTs in a hexagonal array (Fig. 5c), and thus corresponds to the random distribution of the carbon nanotubes inside the interphase. In this case, in addition to the characteristic length e, we need to introduce the characteristic length of the interphase δ. This leads to three series of coordinates, the macroscale (x_1, x_2, x_3), the mesoscale $\left(\frac{x_1}{e}, \frac{x_2}{e}, \frac{x_3}{e}\right)$ and the microscale $\left(\frac{x_1}{\delta}, \frac{x_2}{\delta}, \frac{x_3}{\delta}\right)$. The characteristic lengths δ and e can be related with one as the square power of the other. Here though we prefer to use two independent characteristic lengths, in order to allow the independency of the two scales. Since the AEH method is based on the idea of e or δ tending to zero, the microscale characteristic length δ and the mesoscale characteristic length e can be seen as independently tending to zero. If one of the two characteristic lengths is not close to zero (for instance, if we have very few CNTs in the reinforced interphase then δ is not close to zero) then the homogenization in this scale is not necessarily accurate.

In order to solve efficiently this 3 scale problem, we split it into two 2 scale problems in a hierarchical fashion. The first problem describes the relation between the microscale and the mesoscale, and focuses on the computation of the effective properties of the reinforced interphase. The interphase effective properties are then used in the second problem which deals with the connection between the mesoscale and the macroscale. We note that, in general, the homogenization of a fuzzy fiber composite can be put into a general framework of homogenization with multiple metrics (for further details, see Chatzigeorgiou et al. 2011).

3.1 Micro-to-Mesoscale Transition on a Fuzzy Fiber Composite

In this subsection we are going to investigate the effective properties of the reinforced interphase. This intermediate layer of the fuzzy fibers composites consists of radially aligned hollow MWCNTs and matrix. The unit cell of the interphase is shown in Fig. 5c. The effective mechanical properties of the interphase will be obtained using the asymptotic expansion homogenization method. In this approach two scales are considered, the mesoscale with characteristic length e and the microscale. In the sequel, for simplicity we omit the mesoscale

characteristic length e. In cylindrical coordinates we have the meso coordinates (r, θ, z) and the micro coordinates $\left(\frac{r}{\delta}, \frac{\theta}{\delta}, \frac{z}{\delta}\right) \to \left(\bar{r}, \bar{\theta}, \bar{z}\right)$. The choice of the cylindrical coordinate system has three main advantages: (a) due to the interphase structure, there is no fast variation in the radial direction, reducing the microscale equations to 2-D, (b) allows us to represent in a rigorous way the homogenization procedure and (c) the periodicity of the microstructure is represented easier with respect to $\bar{\theta}$ and $\bar{z}$. For clarity and simplification, we denote the axes (r, θ, z) as (1, 2, 3) and we use the Einstein summation rule for double indices. Additionally, we introduce the operators L_i for the mesoscale and $\bar{L}_i$ for the microscale, where

$$\begin{aligned} L_1 &= \frac{\partial}{\partial r}, \quad L_2 = \frac{1}{r}\frac{\partial}{\partial \theta}, \quad L_3 = \frac{\partial}{\partial z}, \\ \bar{L}_1 &= \frac{\partial}{\partial \bar{r}}, \quad \bar{L}_2 = \frac{1}{r}\frac{\partial}{\partial \bar{\theta}}, \quad \bar{L}_3 = \frac{\partial}{\partial \bar{z}}. \end{aligned} \tag{46}$$

The aim of the asymptotic expansion homogenization (AEH) method is to identify the behavior of the composite material, when the size of the microstructure becomes infinitesimally small, i.e., $\delta \to 0$. In all the quantities (displacements, strains, stresses, stiffness components) we will use the superscript δ, denoting that we refer to a material point, which can be in the matrix, in the CNT or in the void of the hollow region of the CNT. In the sequel, the hat above a symbol will denote that the specific quantity refers to cylindrical coordinate system. The strain–displacement relation of the material system in cylindrical coordinates reads

$$\begin{aligned} &\hat{\varepsilon}^{\delta}_{11} = L_1 \hat{u}^{\delta}_1, \quad \hat{\varepsilon}^{\delta}_{22} = L_2 \hat{u}^{\delta}_2 + \frac{\hat{u}^{\delta}_1}{r}, \quad \hat{\varepsilon}^{\delta}_{33} = L_3 \hat{u}^{\delta}_3, \\ &\hat{\varepsilon}^{\delta}_{23} = \frac{1}{2}\left(L_2 \hat{u}^{\delta}_3 + L_3 \hat{u}^{\delta}_2\right), \quad \hat{\varepsilon}^{\delta}_{13} = \frac{1}{2}\left(L_1 \hat{u}^{\delta}_3 + L_3 \hat{u}^{\delta}_1\right), \\ &\hat{\varepsilon}^{\delta}_{12} = \frac{1}{2}\left(L_1 \hat{u}^{\delta}_2 + L_2 \hat{u}^{\delta}_1 - \frac{\hat{u}^{\delta}_2}{r}\right). \end{aligned} \tag{47}$$

Ignoring inertia and body forces, the equilibrium equations are written as

$$L_j \hat{\sigma}^{\delta}_{1j} + \frac{\hat{\sigma}^{\delta}_{11} - \hat{\sigma}^{\delta}_{22}}{r} = 0, \quad L_j \hat{\sigma}^{\delta}_{2j} + 2\frac{\hat{\sigma}^{\delta}_{12}}{r} = 0, \quad L_j \hat{\sigma}^{\delta}_{3j} + \frac{\hat{\sigma}^{\delta}_{13}}{r} = 0. \tag{48}$$

Finally, the Hooke's law is written

$$\hat{\sigma}^{\delta}_{ij} = \hat{C}^{\delta}_{ijkl} \hat{\varepsilon}^{\delta}_{kl}. \tag{49}$$

The stiffness components $\hat{C}^{\delta}_{ijkl}$ are generally spatially dependent. At the microscale level it depends on the micro coordinates $\bar{\theta}$ and $\bar{z}$. The material parameters vary very slowly in the radial direction and depend on the meso coordinate r. Due to the geometry of the CNT (only its center is independent on r), the stiffness components present local discontinuity with respect to r. The discontinuity appears only

when we move from the void to the CNT and from the CNT to the matrix. So we can write

$$\hat{C}^{\delta}_{ijkl} = \hat{C}_{ijkl}(r, \bar{\theta}, \bar{z}), \quad \text{slow variation with respect to r.} \tag{50}$$

In the AEH method, the displacements are represented in a series expansion form

$$\hat{u}^{\delta}_i = \hat{u}^{(0)}_i(r, \theta, z) + \delta \hat{u}^{(1)}_i(r, \theta, z, \bar{\theta}, \bar{z}) + \delta^2 \hat{u}^{(2)}_i(r, \theta, z, \bar{\theta}, \bar{z}) + \ldots, \tag{51}$$

where $\hat{u}^{(0)}_i$ denotes the mesodisplacement and $\hat{u}^{(1)}_i$, $\hat{u}^{(2)}_i$ e.t.c. are periodic functions and represent the oscillating terms. The derivatives can be written in the form

$$L_i = L_i + \frac{1}{\delta}\bar{L}_i. \tag{52}$$

Using (51) and (52), the strains in (47) can be written in the form

$$\hat{\varepsilon}^{\delta}_{ij} = \hat{\varepsilon}^{(0)}_{ij} + \delta \hat{\varepsilon}^{(1)}_{ij} + \ldots, \tag{53}$$

where

$$\hat{\varepsilon}^{(q)}_{ij} = \hat{\varepsilon}^{(q*)}_{ij} + \frac{1}{2}\left(\bar{L}_i \hat{u}^{(q+1)}_j + \bar{L}_j \hat{u}^{(q+1)}_i\right), \qquad q = 0, 1, 2, \ldots \tag{54}$$

and $\hat{\varepsilon}^{(q*)}_{ij}$ are given by Eq. (47) by substituting $\hat{u}^{\delta}_i$ with $\hat{u}^{(q)}_i$. From the Hooke's law (49) and Eq. (53) we can write the expanded form of the stresses

$$\hat{\sigma}^{\delta}_{ij} = \hat{\sigma}^{(0)}_{ij} + \delta \hat{\sigma}^{(1)}_{ij} + \ldots, \tag{55}$$

where

$$\hat{\sigma}^{(m)}_{ij} = \hat{C}_{ijkl}\hat{\varepsilon}^{(m*)}_{kl} + \hat{C}_{ijkl}\bar{L}_k \hat{u}^{(m+1)}_l. \tag{56}$$

Using the expanded form of the stresses (55) and Eq. (52) the equilibrium equations take the form

$$\begin{aligned}
&\frac{1}{\delta}\left(\bar{L}_j \hat{\sigma}^{(0)}_{1j}\right) + L_j \hat{\sigma}^{(0)}_{1j} + \frac{\hat{\sigma}^{(0)}_{11} - \hat{\sigma}^{(0)}_{22}}{r} + \bar{L}_j \hat{\sigma}^{(1)}_{1j} + \delta \ldots = 0,\\
&\frac{1}{\delta}\left(\bar{L}_j \hat{\sigma}^{(0)}_{2j}\right) + L_j \hat{\sigma}^{(0)}_{2j} + 2\frac{\hat{\sigma}^{(0)}_{12}}{r} + \bar{L}_j \hat{\sigma}^{(1)}_{2j} + \delta \ldots = 0,\\
&\frac{1}{\delta}\left(\bar{L}_j \hat{\sigma}^{(0)}_{3j}\right) + L_j \hat{\sigma}^{(0)}_{3j} + \frac{\hat{\sigma}^{(0)}_{13}}{r} + \bar{L}_j \hat{\sigma}^{(1)}_{3j} + \delta \ldots = 0.
\end{aligned} \tag{57}$$

According to the classical procedure of the AEH method, the micro-equations are defined from the δ^{-1} terms

$$\bar{L}_j \hat{\sigma}^{(0)}_{ij} = 0, \qquad i = 1, 2, 3, \tag{58}$$

which, using Eq. (56) for m = 0, can be written as

$$\bar{L}_j\left(\hat{C}_{ijkl}\right)\hat{\varepsilon}_{kl}^{(0*)} + \bar{L}_j\left(\hat{C}_{ijkl}\bar{L}_k\hat{u}_l^{(1)}\right) = 0. \tag{59}$$

In Eq. (59) $\hat{\varepsilon}_{kl}^{(0*)}$ depends only on the meso-displacements $\hat{u}_i^{(0)}$. By assuming that

$$\hat{u}_i^{(1)} = \hat{N}_i^{mn}\hat{\varepsilon}_{mn}^{(0*)}, \tag{60}$$

the micro-equations (59) are written

$$\bar{L}_j\left(\hat{C}_{ijmn} + \hat{C}_{ijkl}\bar{L}_k\hat{N}_l^{mn}\right) = 0. \tag{61}$$

The final form of the micro-equations are solved for the unknown functions $\hat{N}_i^{mn}$, which are periodic in the $(\bar{\theta}, \bar{z})$ space. Also, we need to impose the necessary continuity conditions

$$\left[\left[\hat{N}_i^{mn}\right]\right] = 0, \qquad \left[\left[\left(\hat{C}_{ijmn} + \hat{C}_{ijkl}\bar{L}_k\hat{N}_l^{mn}\right)n_j\right]\right] = 0, \tag{62}$$

where n_i is the unit normal vector to the surface of discontinuity and $[\![\varphi]\!] = \varphi^+ - \varphi^-$ denotes the jump of a quantity φ across this surface.

The meso-equations can be obtained from the δ^0 terms of the equilibrium equations. When δ approaches zero, periodic functions attain their weak limit, which is equal to the area integral of the functions in the periodic unit cell. We introduce the area integral symbol on the area A of the 2-D unit cell in $(\bar{\theta}, \bar{z})$,

$$\langle\langle\varphi\rangle\rangle = \frac{r}{\mathrm{A}}\int_{-\bar{z}'/2}^{\bar{z}'/2}\int_{-\bar{\theta}'/2}^{\bar{\theta}'/2}\varphi(r,\bar{\theta},\bar{z})d\bar{\theta}d\bar{z}. \tag{63}$$

By setting ω_i as the outer unit normal vector to the boundary and ∂A the boundary surface of the unit cell, we can use the Gauss theorem and the periodicity of $\hat{\sigma}_{1j}^{(1)}$ to show that

$$\left\langle\left\langle\bar{L}_j\hat{\sigma}_{ij}^{(1)}\right\rangle\right\rangle = \frac{r}{A}\int_{\partial A}\hat{\sigma}_{ij}^{(1)}\omega_j dS = 0. \tag{64}$$

The meso-equations then are obtained from the weak limit of the δ^0 terms of the equilibrium equations

$$\begin{aligned}
&L_j\left\langle\left\langle\hat{\sigma}_{1j}^{(0)}\right\rangle\right\rangle + \frac{\left\langle\left\langle\hat{\sigma}_{11}^{(0)}\right\rangle\right\rangle - \left\langle\left\langle\hat{\sigma}_{22}^{(0)}\right\rangle\right\rangle}{r} = 0,\\
&L_j\left\langle\left\langle\hat{\sigma}_{2j}^{(0)}\right\rangle\right\rangle + 2\frac{\left\langle\left\langle\hat{\sigma}_{12}^{(0)}\right\rangle\right\rangle}{r} = 0, \quad L_j\left\langle\left\langle\hat{\sigma}_{3j}^{(0)}\right\rangle\right\rangle + \frac{\left\langle\left\langle\hat{\sigma}_{13}^{(0)}\right\rangle\right\rangle}{r} = 0,
\end{aligned} \tag{65}$$

where

$$\left\langle\left\langle \hat{\sigma}_{ij}^{(0)} \right\rangle\right\rangle = \left\langle\left\langle \hat{C}_{ijmn} + \hat{C}_{ijkl}\bar{L}_k\hat{N}_l^{mn} \right\rangle\right\rangle \hat{\varepsilon}_{mn}^{(0*)}. \tag{66}$$

From the last equation it becomes obvious that the effective, or homogenized, properties C_{ijmn}^{int} of the reinforced interphase are given by

$$C_{ijmn}^{\text{int}} = \left\langle\left\langle \hat{C}_{ijmn} + \hat{C}_{ijkl}\bar{L}_k\hat{N}_l^{mn} \right\rangle\right\rangle, \tag{67}$$

where the functions $\hat{N}_i^{mn}$ are determined by solving the Eqs. (61). In the microlevel and at a specific radius r, Eqs. (61) represent 2 anti-plane strain problems and 4 plane strain problems. Due to the large difference in $\bar{\theta}$ and $\bar{z}$ scales, it is more preferable to solve the micro-equations in the $r\bar{\theta} - \bar{z}$ space.

A useful characteristic of the AEH method is that it can provides information about the micro-stresses and micro-strains. Using the obtained effective properties of the interphase, the mesoscale problem can be solved and the meso-strains $\hat{\varepsilon}_{mn}^{(0*)}$ can be computed. Then the micro-stresses and micro-strains are obtained from the solution of the unit cell problem (61), using the equations

$$\hat{\sigma}_{ij}^{(0)} = \left(\hat{C}_{ijmn} + \hat{C}_{ijkl}\bar{L}_k\hat{N}_l^{mn}\right)\hat{\varepsilon}_{mn}^{(0*)}, \qquad \hat{\varepsilon}_{ij}^{(0)} = \hat{\varepsilon}_{ij}^{(0*)} + \frac{1}{2}\left(\bar{L}_i\hat{N}_j^{mn} + \bar{L}_j\hat{N}_i^{mn}\right)\hat{\varepsilon}_{mn}^{(0*)}. \tag{68}$$

The proposed methodology can also be extended in the case of thermoelasticity (Chatzigeorgiou et al. 2012b).

3.2 Meso-to-Macroscale Transition on a Fuzzy Fiber Composite

Having defined the effective properties of the reinforced interphase, the macroscopic behavior of the actual composite can be determined using again the AEH method. The actual composite can be described easier in Cartesian coordinates, which necessitates the transfer of the effective properties of the interphase from cylindrical to Cartesian coordinates. The obtained interphase effective properties can be transformed from a cylindrical coordinates form $\mathbf{C}^{\text{int}}(r, \theta, z)$ to a Cartesian coordinates form $\tilde{\mathbf{C}}^{\text{int}}(x_1, x_2, x_3)$ according to the rotation formula for fourth order tensors, $\tilde{C}_{ijkl}^{\text{int}} = R_{im}R_{jn}R_{ko}R_{lp}C_{mnop}^{\text{int}}$, with

$$\mathbf{R} = \begin{pmatrix} \cos\theta & -\sin\theta & 0 \\ \sin\theta & \cos\theta & 0 \\ 0 & 0 & 1 \end{pmatrix}. \tag{69}$$

According to the analysis of the previous subsection, the effective coefficients of the reinforced interphase are functions of the radius r, where $r^2 = x_1^2 + x_2^2$.

The other two material components of the composite, the matrix and the fiber, are generally assumed as homogeneous isotropic or transversely isotropic materials, with the axis of symmetry parallel to the axis of the fiber. Under these conditions, the application of the AEH method for the second periodic problem with characteristic length (Fig. 5b) follows the standard approach (Sanchez-Palencia 1978).

The periodic homogenization approach is a rigorous solution on the three scale problem of a fuzzy fiber composite when a) the CNTs are distributed radially and with periodic fashion in the reinforced interface and b) the fuzzy fibers are distributed periodically inside the matrix material. Under these conditions the method provides information about the effective response of the reinforced interface and the composite, as well as the distribution of stresses and strains in all scales, which is important in case we want to detect possible positions that damage can occur.

4 Examples

In the following examples we consider E glass fibers with radius 5 μm coated with radially aligned hollow carbon nanotubes. The CNTs we study here are considered to be structured with 5 walls of 0.34 nm thickness each. The CNTs have internal radius 0.518 nm and external radius 2.218 nm. The fuzzy fibers are embedded in EPIKOTE 862 resin. The properties of the CNT walls are assumed the same as the properties of the graphene. The mechanical electrostatic properties of the glass fibers, the resin and the graphene are shown in Table 1. It is noted that when the thicknesses of the nanocomposite interphase are 1 μm and 2 μm respectively, the percolation concentrations of fuzzy fiber are 0.69 and 0.51, which are used as upper limits for the volume fraction of glass fiber in the microscale CCM model.

4.1 Fuzzy Fiber Composite Effective Mechanical Properties

In the periodic homogenization approach, the computations are carried out with the finite element program COMSOL Multiphysics. Since the periodic structure of the reinforced interphase depends on the radius, we needed to solve numerically several unit cells. Each unit cell represents a different profile of the interphase with respect to radius and the volume fraction of the CNTs decreases as the radius increases (see Fig. 6) The arrangement of CNTs is exactly hexagonal only at the layer between the carbon fiber and the reinforced interphase. As we move closer to the matrix, the length of the unit cell at the $r\bar{\theta}$ direction elongates, disturbing the hexagonal symmetry. Since the homogenization problem reduces to 2D problem, we use 2D FE meshing for the reinforced interphase (Chatzigeorgiou et al. 2011). The periodicity boundary condition is imposed by applying the same $\hat{N}_i^{mn}$ on opposite sides of the unit cells. For the purposes of the numerical analysis, we use quadratic Lagrange finite elements.

Table 1 Mechanical and electrostatic properties of fuzzy fiber components

E glass fiber		
Axial Young's modulus	78	GPa
Axial Poisson's ratio	0.22	
Electrical conductivity	2.49E−13	S/m
EPIKOTE 862 resin		
Young's modulus	3	GPa
Poisson's ratio	0.3	
Electrical conductivity	6.7E−7	S/m
Graphene		
Young's modulus	1100	GPa
Poisson's ratio	0.14	
Electrical conductivity	1.0E5	S/m

AGY 2006; Resolution Performance Products 2001; Ebbesen et al. 1996; Seidel and Lagoudas 2006, 2009

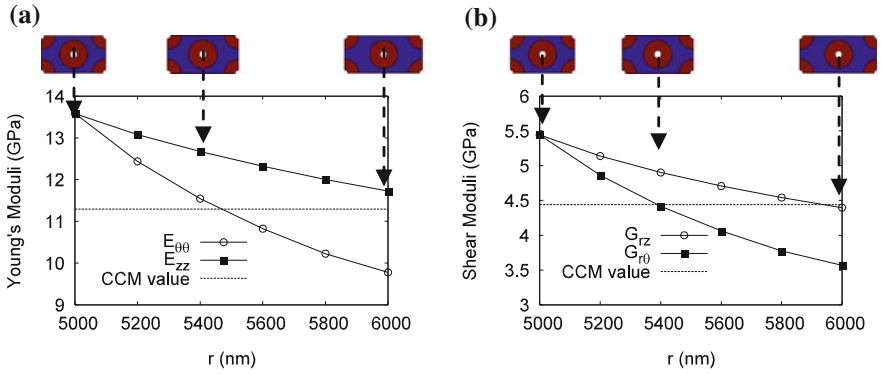

Fig. 6 Effective properties for reinforced interphase with thickness 1 μm: **a** transverse Young's moduli for CNT volume fraction 59.09 %, **b** axial shear moduli for CNT volume fraction 59.09 %. The *dashed line* indicates the average property that is used in the CCM method. In the same figures we show several unit cells of the reinforced interphase as we move from the fiber to the resin

The effective properties of the interphase are obtained in this analysis for 59.09 % CNT volume fraction and some of the results are shown in Fig. 7. This volume fraction has been chosen such as at the connection between the CNTs and the glass fiber the CNT area fraction is 65 %. As it can be seen from these figures, the reinforced interphase becomes more cylindrically orthotropic with the increase of radius. From the results it is clear that the effective properties of the interphase are strongly affected by the radius. This radial dependency can be simulated by assuming that all the mechanical properties can be described with fifth order polynomials with respect to radius. In the same Figures we also present the average value of the properties (under the hypothesis of constant CNT volume fraction over the interphase thickness) that is used in the CCM method and comparison with the results obtained for E-glass fiber composites.

In the second step of the homogenization, the interphase is substituted by the effective medium, which is introduced in the mesoscale unit cell. The program we used for the numerical results is again the COMSOL Multiphysics software. The periodicity in the unit cell is imposed in a similar way as in the case of the microscale. For the purposes of the numerical analysis, we use quadratic Lagrange finite elements. The spatially variable homogenized moduli of the reinforced interphase are introduced in COMSOL as fifth order polynomials in the radial direction.

As it can be seen in Fig. 7, transferring the effective properties from the cylindrical to Cartesian coordinates produces a fully anisotropic behavior for the reinforced interphase. Terms like C_{16} are no longer zero, only the average C_{16} over the whole interphase becomes zero.

In Fig. 8 we present the effective properties of a fuzzy fiber composite with 1 μm reinforced interphase thickness and for 59.09 % CNT volume fraction in the interphase. These plots have been considered for fuzzy fiber volume fractions that vary until the percolation threshold of 69 % (or, equivalently, E-glass volume fraction 47.92 %), i.e. the volume fraction where the nanocomposite interphase regions would be being to touch and interact. We observe that the two approaches, i.e. the composite cylinders method (CCM) and the asymptotic expansion homogenization (AEH) are in a good agreement except in the case of the transverse Young's and transverse shear modulus for very high volume fractions. In the same graphs we present the effective properties of E-glass fiber composites. The results indicate that at E-glass volume fractions above 40 %, the fuzzy fiber provides an increase between 35 and 50 % in the effective properties compared to pure E-glass fibers. It is also interesting to note that, by increasing the interphase thickness from 1 to 2 μm, we obtain 17 and 15 % increase in the transverse Young's and transverse shear modulus respectively.

As it was discussed in the composite cylinders approach, CCM allows, in conjunction with the Mori–Tanaka method, the computation of effective properties for more complicated composites with fuzzy fibers. To demonstrate this ability we perform two case studies.

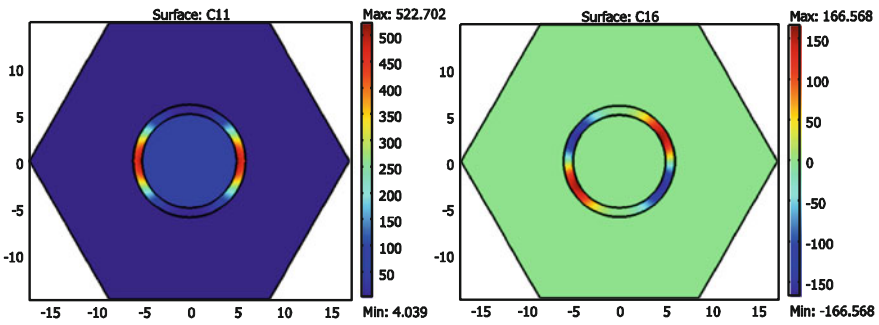

Fig. 7 Distribution of the stiffness coefficients C11 and C16 in the mesoscale unit cell (the units are GPa) for a composite with 15 % fuzzy fiber volume fraction

In the first case we consider mixed type composites where E-glass fibers and fuzzy fibers are present. Table 2 illustrates the transverse composite properties for mixed fiber types with several fractions of E-glass and fuzzy fibers. As we observe, when in each four E-glass fibers two of them are substituted by fuzzy fibers, we have an increase of 13.5 and 11.6 % in the transverse Young's and transverse shear modulus respectively. When in each six E-glass fibers 1 of them is substituted by fuzzy fiber, the same properties increase by 8.6 and 7.4 % respectively.

In the second case we consider E-glass fiber composite and fuzzy fiber composite where the fibers have random orientation. Fig. 9 illustrates the composites effective properties as a function of the E-glass volume fraction. In the fuzzy fiber composite case, the total fiber volume fraction differs from the E-glass volume fraction due to the interphase presence. Thus, for example, 49.72 % E-glass volume fraction leads to 69 % fuzzy fiber volume fraction. The fiber random orientation has the result that the composites behave isotropically. As we observe, for large fiber volume fractions the presence of the CNTs causes significant increase in

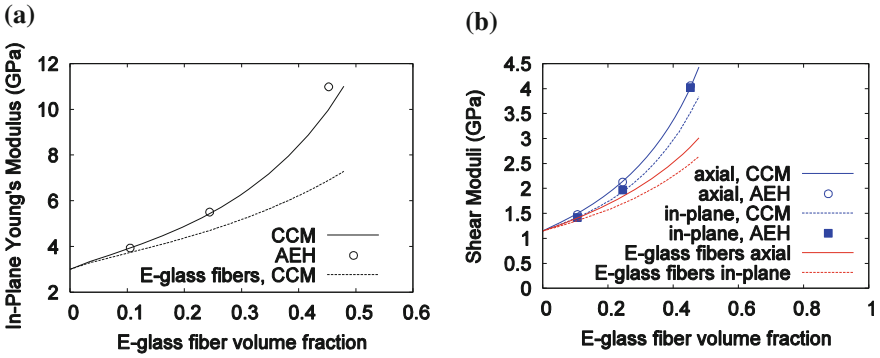

Fig. 8 Effective properties of fuzzy fiber composite with interphase thickness 1 μm: **a** transverse Young's modulus for CNT volume fraction in the interphase 59.09 %, **b** shear moduli for CNT volume fraction in the interphase 59.09 %

Table 2 Effective mechanical properties of mixed E-glass and fuzzy fiber components

Mixed fiber composites			
Fraction of fibers	Volume fraction of fibers	In-plane Young's modulus (GPa)	In-plane shear modulus (GPa)
4 E-glass/0 fuzzy fiber	40 % E-glass/0 % fuzzy fiber	6.22	2.24
2 E-glass/2 fuzzy fiber	20 % E-glass/28.8 % fuzzy fiber	7.06	2.50
0 E-glass/4 fuzzy fiber	0 % E-glass/57.6 % fuzzy fiber	8.10	2.81
6 E-glass/0 fuzzy fiber	60 % E-glass/0 % fuzzy fiber	9.63	3.50
5 E-glass/1 fuzzy fiber	50 % E-glass/14.4 % fuzzy fiber	10.46	3.76
3 E-glass/3 fuzzy fiber	30 % E-glass/43.2 % fuzzy fiber	12.57	4.40
0 E-glass/6 fuzzy fiber	0 % E-glass/86.4 % fuzzy fiber	17.60	5.80

The fuzzy fibers have 1 μm interphase thickness and 59.09 % CNTs in the interphase

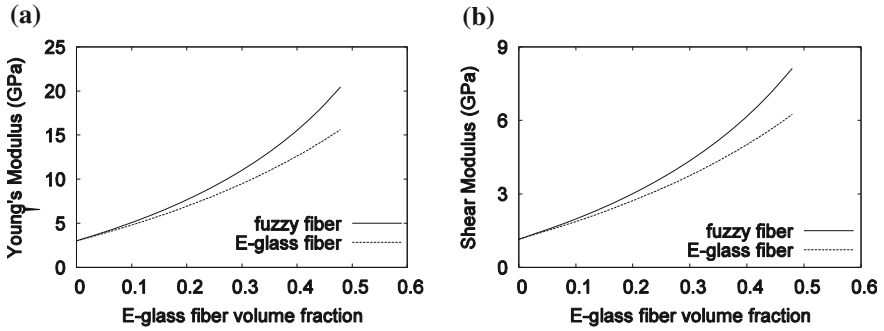

Fig. 9 Effective properties of composites with randomly oriented fuzzy fibers and E-glass fibers: **a** Young's modulus, **b** shear modulus. In the fuzzy fibers the interphase thickness is 1 μm and the CNT volume fraction in the interphase is 59.09 %

the composite mechanical properties. For approximately 50 % E-glass volume fraction, the reinforced interphase provides approximately 30 % increase in both Young's and shear modulus.

4.2 Fuzzy Fiber Composite Effective Electrostatic Properties

The nanoscale CCM model is first used to obtain the effective electrostatic properties of the well-dispersed and aligned CNTs in the polymer matrix, as shown in Table 3. It is observed that with the increase of volume fraction of CNTs in the interphase region, the conductivities $\kappa_{rr}^{(2)}$, $\kappa_{\theta\theta}^{(2)}$, and $\kappa_{zz}^{(2)}$ are all enhanced. It is also noticeable that the radial conductivity $\kappa_{rr}^{(2)}$ is 10 orders higher than the values of the other two directions due to the radial alignment of the CNTs in the interphase region.

By applying the microscale CCM model, the effective conductivities of the aligned fuzzy fiber reinforced nanocomposites can be obtained. When the interphase thickness is 1 μm, the change of effective axial conductivity κ_{zz}^{eff} of the nanocomposites with the change of volume fraction of glass fiber is shown in Fig. 10a. It can be observed that with the increase of volume fraction of glass fiber,

Table 3 The effective conductivities of the fuzzy fiber interphase region as obtained from the nanoscale CCM model

Cases	1 μm & 45.45 %	1 μm & 59.09 %	1 μm & 72.73 %	2 μm & 41.67 %	2 μm & 54.17 %	2 μm & 66.67 %
$\kappa_{rr}^{(2)}$	4.297E4	5.587E4	6.876E4	3.940E4	5.122E4	6.303E4
$\kappa_{\theta\theta}^{(2)} = \kappa_{zz}^{(2)}$	1.778E−6	2.593E−6	4.223E−6	1.619E−6	2.243E−6	3.334E−6

i.e. $\kappa_{rr}^{(2)} = \hat{\kappa}_{zz}^{(2)eff}$ and $\kappa_{\theta\theta}^{(2)} = \kappa_{zz}^{(2)} = \hat{\kappa}_{rr}^{(2)eff} = \hat{\kappa}_{\theta\theta}^{(2)eff}$ (*Unit* S/m)

the effective axial conductivity of the pure glass fiber reinforced nanocomposites become lower due to the glass fiber's low conductivity relative to the matrix. However, with the interphase region added to the surface of glass fiber, the trend is reversed as the axial interphase conductivity begins to exceed that of the matrix with increase in MWCNT concentration. For example, with the volume fraction of glass fiber of 0.51, when the average volume fraction of MWCNTs in the interphase region is increased from 45.45 to 72.73 %, the effective axial conductivities of the fuzzy fiber composites are increased by 76.3, 132, and 244 %, respectively, compared to the pure glass fiber case. Similar increases can be found in the 2 μm thickness interphase cases where, at the volume fraction of glass fiber of 0.51, the effective axial conductivities of the fuzzy fiber composites are increased by 143, 237, and 400 % for interphase average MWCNT volume fractions of increasing from 41.67 to 66.67 %, respectively. These observations are consistent with the three phase rule of mixtures which results from the axial CCM electrostatic BVP. With the thickness of the nanocomposite interphase fixed, as the glass fiber volume fraction increases, so too does the nanocomposite interphase volume fraction, thereby rapidly decreasing the matrix volume fraction. With the axial conductivity of the interphase being an order of magnitude larger than the matrix, the displacement of additional matrix material in moving to the larger interphase thickness leads to substantially larger increases in the effective axial conductivity of the composite.

The change of effective transverse conductivity κ_{rr}^{eff} of the aligned fuzzy fiber composites with the change of volume fraction of glass fiber is shown in Fig. 10b and demonstrates similar trends to those observed in the effective axial conductivity, i.e. increasing conductivity with increasing MWCNT concentration in the nanocomposite interphase. However, despite the transverse conductivity of the nanocomposite interphase, $\kappa_{rr}^{(2)}$, being eight orders of magnitude larger than the axial interphase conductivity, $\kappa_{zz}^{(2)}$ (which is equal to theta transverse conductivity, $\kappa_{\theta\theta}^{(2)}$), the increases in fuzzy fiber composite effective transverse conductivity are much smaller than those observed for the composite axial conductivity.

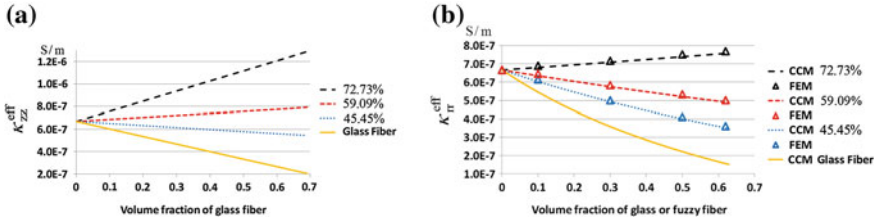

Fig. 10 **a** The axial effective conductivity κ_{zz}^{eff} and **b** comparison of the transverse effective conductivity κ_{rr}^{eff} as obtained from CCM and FEM for aligned fuzzy fiber composites with the change of volume fraction of glass fiber when the interphase thickness is 1 μm

In confirming these observations, a comparison of the hierarchical electrostatic CCM model with a finite element model (FEM) based on the 2D microscale hexagonal representative volume elements (RVE) (Hammerand et al. 2007) is constructed. For the fuzzy fiber's interphase region, the nanoscale electrostatic properties are taken from the nanoscale CCM model and transformed from the Cylindrical coordinate system in the nanoscale to the Cartesian coordinate system in the microscale resulting in θ-dependent interphase conductivities as shown in Fig. 11a. Three electrostatic periodic boundary conditions (PBCs) are independently applied to the microscale RVE, with the energy equivalence method used to obtain the effective electrostatic properties κ_{11}^{eff}, κ_{22}^{eff}, and κ_{12}^{eff} (Ren and Seidel 2013). It is found that κ_{11}^{eff} and κ_{22}^{eff} are equal to each other, and κ_{12}^{eff} is zero, which confirms the accuracy of the transversely isotropic assumption as in the CCM model. As an illustration, the potential, electric field, and current density contours for obtaining κ_{22}^{eff} are shown in Fig. 11b. The transverse effective electrostatic properties as obtained from the FEM model compare well with the CCM model as seen in Fig. 10b, which again confirms the accuracy of the material symmetry assumptions in the hierarchical CCM model.

In contrast to the three-phase rule of mixtures behavior of the axial conductivity, the transverse properties obtained from the CCM and FEM are instead matrix dominated. Yet it is worth noting that relative to the observed changes in the mechanical properties, the increases in both the axial and transverse effective fuzzy fiber electrical conductivity are of sufficient significance to be of practical application in making electrically conductive polymers.

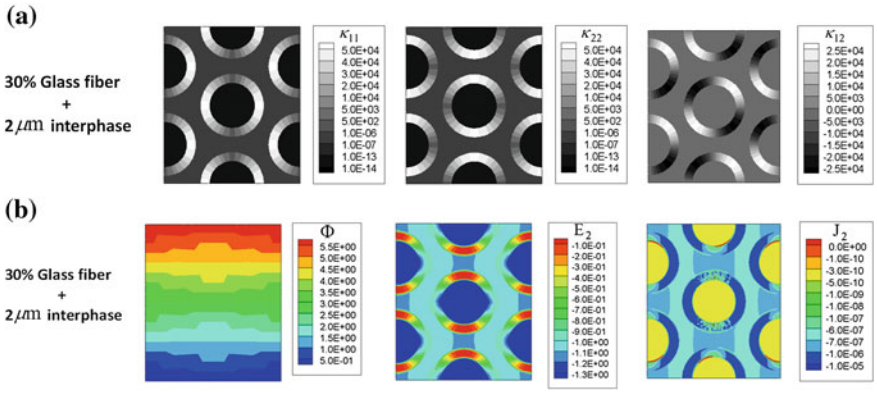

Fig. 11 **a** Distribution of electrical conductivities and **b** distribution of electric potential Φ, electric field E_2, and current density J_2 in the 2D microscale hexagonal RVE when a periodic potential difference of $\Delta\Phi = \widehat{E}_0 \cdot W_2$ is applied in Y direction (*vertical*), in which E_0 is a constant macroscale electric field and W_2 is the width of the 2D microscale RVE in the Y direction. The 2D microscale RVE represents the nanocomposites in which there are 30 % glass fibers with a 2 μm thickness interphase, and the average volume fraction of CNTs within the interphase is 54.17 %

For composites with randomly dispersed glass or fuzzy fibers, the Mori–Tanaka method is used to obtain the effective electrostatic properties. As seen in Fig. 12, for the nanocomposites with randomly dispersed fuzzy fibers, the effective conductivity κ^{eff} of the composites is isotropic, and lies between the axial conductivity κ_{zz}^{eff} and the transverse conductivity κ_{rr}^{eff} of the composites with aligned fibers. For the nanocomposites with random dispersion of fiber orientations, the effective properties are obtained by averaging the fiber response over all the orientations such that the net isotropic symmetry lies between the contributing bounding values of the local orientation axial and transverse conductivities. Also of note in Fig. 12 is that, due dominance of the polymer matrix in the transverse direction, the effective conductivities of the composites with randomly dispersed glass or fuzzy fibers are closer to the effective transverse conductivities as opposed to the effective axial conductivities, thereby indicating the potential importance of controlled placement and alignment of fuzzy fibers in applications.

For the composites with a mixture of aligned glass and fuzzy fibers, as seen in Fig. 13a, even with a small fraction of the glass fibers being fuzzy fibers, the axial effective conductivity κ_{zz}^{eff} of the composite can be significantly increased. However, as seen in Fig. 13b, the transverse effective conductivity κ_{rr}^{eff} of the composites is only marginally influenced by the replacement of pure glass fibers with fuzzy fibers. This indicates not only the importance of controlling alignment of fibers within a composite, but also the level of control over ply properties offered by specifying glass/fuzzy fiber mixture ratios.

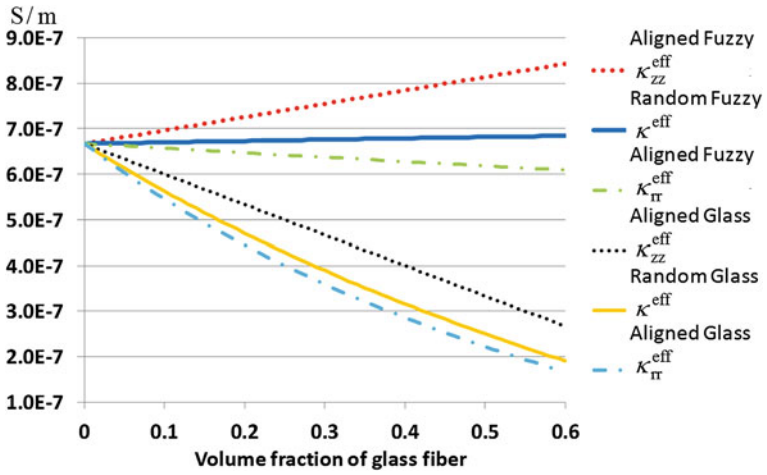

Fig. 12 The change of effective conductivities of the nanocomposites with the change of volume fraction of glass fiber/glass fiber core by using the Mori–Tanaka method

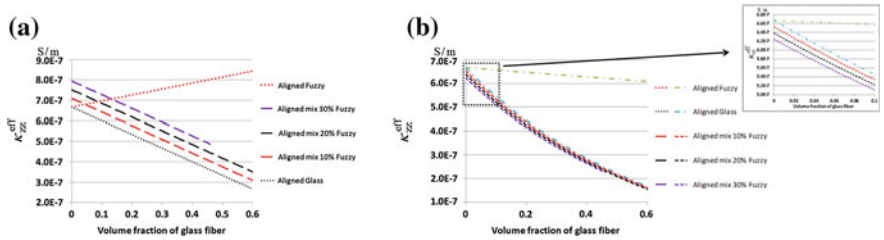

Fig. 13 **a** The change of effective axial conductivity κ_{zz}^{eff} and **b** the change of effective transverse conductivity κ_{rr}^{eff} of composites with volume fraction of glass fiber/glass fiber core. *Note* In the mixture of glass and fuzzy fiber cases, the volume fraction reported for fuzzy fiber is the one of the glass fiber core which is kept constant at 10, 20 and 30 %, respectively, while the volume fraction of the pure glass fibers increases from 0–0.6

5 Conclusion

By taking advantage of the cylindrical orthotropic symmetry, analytic hierarchical mechanical and electrostatic CCM models are developed to obtain the effective mechanical and electrostatic properties of the nanocomposites with well dispersed and aligned fuzzy fibers. As a comparison, an asymptotic expansion homogenization approach for the mechanical and a FEM model for the electrostatic case are developed, which explicitly account for the anisotropic material properties of the fuzzy fiber interphase region to obtain the material response. It is found that the effective mechanical and electrostatic properties as obtained from the CCM models and the numerical methods are in good agreement, which verifies the accuracy of the hierarchical CCM models. In addition, the Mori–Tanaka model is used to obtain the effective mechanical and electrostatic properties of the nanocomposites with randomly dispersed fuzzy fibers or with mixtures of aligned fuzzy fibers and structural fibers. From these cases the importance of controlling alignment is observed in the sensitivity of the aligned direction properties to the presence and properties of the nanocomposite interphase, particularly in terms of effective electrical conductivity. It is further noted that controlling glass/fuzzy fiber mixture ratio can offer a means to achieving desired unidirectional ply properties for stiffening and sensing applications. The analytic hierarchical CCM models therefore show promise as relatively inexpensive preliminary design tools for fuzzy fiber enriched composite laminates.

Acknowledgments The authors would like to acknowledge the financial support provided by NSF, Grant No. DMR-0844082 (International Institute for Multifunctional Materials for Energy Conversion – IIMEC Project), and would also like to acknowledge the financial support provided by AFOSR through MURI-18 Synthesis, Characterization and Modeling of Functionally Graded Hybrid Composites for Extreme Environments Grant FA-9550-09-0686.

References

Adnan A, Sun C, Mahfuz H (2007) A molecular dynamics simulation study to investigate the effect of filler size on elastic properties of polymer nanocomposites. Compos Sci Technol 67:348–356

AGY (2006) High strength glass fibers. Pub. No. LIT-2006-111 R2 (02/06)

Awasthi AP, Lagoudas DC, Hammerand DC (2009) Modeling of graphene–polymer interfacial mechanical behavior using molecular dynamics. Modell Simul Mater Sci Eng 17(1):015002

Bensoussan A, Lions J, Papanicolaou G (1978) Asymptotic methods for periodic structures. North Holland, The Netherlands

Bonakdar M, Seidel GD, Inman DJ (2012) Effect of nanoscale fillers on the viscoelasticity of polymer nanocomposites. In: Proceedings paper for the 53rd AIAA/ASME/ASCE/AHS/ASC structures, structural dynamics and materials conference Honolulu, Hawaii, USA 23–26 April, 2012 (AIAA 2012-1825)

Bower C, Zhu W, Jin S, Zhou O (2000) Plasma-induced alignment of carbon nanotubes. Appl Phys Lett 77(6–7):830–832

Bradshaw R, Fisher F, Brinson L (2003) Fiber waviness in nanotube reinforced polymer composites: II. Modeling via numerical approximation of the dilute strain concentration tensor. Compos Sci Technol 63:1705–1722

Buryachenko V, Roy A (2005) Effective elastic moduli of nanocomposites with prescribed random orientation of nanofibers. Compos B Eng 36:405–416

Chatterjee D (1970) Some problems of plane strain in a non-homogeneous isotropic cylinder. Pure Appl Geophys 82(1):34–40

Chatzigeorgiou G, Charalambakis N, Murat F (2008) Homogenization problems of a hollow cylinder made of elastic materials with discontinuous properties. Int J Solids Struct 45:5165–5180

Chatzigeorgiou G, Efendiev Y, Lagoudas DC (2011) Homogenization of aligned "fuzzy fiber" composites. Int J Solids Struct 48(19):2668–2680

Chatzigeorgiou G, Seidel GD, Lagoudas DC (2012a) Effective mechanical properties of "fuzzy fiber" composites. Composites, B 43:2577–2593

Chatzigeorgiou G, Efendiev Y, Charalambakis N, Lagoudas DC (2012b) Effective thermoelastic properties of composites with periodicity in cylindrical coordinates. Int J Solids Struct 49:2590–2603

Chen T, Chung C-T, Lin W-L (2000) A revisit of a cylindrically anisotropic tube subjected to pressuring, shearing, torsion, extension and a uniform temperature change. Int J Solids Struct 37:5143–5159

Chen T, Weng G, Liu W-C (2005) Effect of kapitza contact and consideration of tube-end transport on the effective conductivity in nanotube-based composites. J Appl Phys 97:104312–1–4

Christensen RM (1979) Mechanics of composite materials. Dover, New York

Christensen RM, Lo K (1979) Solutions for effective shear properties in three phase sphere and cylinder models. J Mech Phys Solids 27:315–330

Chung PW, Tamma KK, Namburu RR (2001) Asymptotic expansion homogenization for heterogenous. media: computational issues and applications. Composites, A 32:1291–1301

Ci L, Zhao Z, Bai J (2005) Direct growth of carbon nanotubes on the surface of ceramic fibers. Carbon 43(4):883–886

Ebbesen T, Lezec H, Hiura H, Bennett J, Ghaemi H, Thio T (1996) Electrical conductivity of individual carbon nanotubes. Nature 382:54–56

Entchev P, Lagoudas D (2002) Modeling porous shape memory alloys using micromechanical averaging techniques. Mech Mater 34:1–24

Esteva M, Spanos PD (2009) Effective elastic properties of nanotube reinforced composites with slightly weakened interfaces. J Mech Mater Struct 4(5):887–900

Fermeglia M, Pricl S (2007) Multiscale modeling for polymer systems of industrial interest. Prog Org Coat 58(2–3):187–199

Fisher F, Brinson L (2001) Viscoelastic interphases in polymer-matrix composites: theoretical models and finite element analysis. Compos Sci Technol 61:731–748

Fisher FT, Bradshaw RD, Brinson LC (2002) Effects of nanotube waviness on the modulus of nanotube-reinforced polymers. Appl Phys Lett 80(24):4647–4649

Fisher FT, Bradshaw RD, Brinson LC (2003) Fiber waviness in nanotube-reinforced polymer composites–I: modulus predictions using effective nanotube properties. Compos Sci Technol 63(11):1689–1703

Frankland S, Harik V, Odegard G, Brenner D, Gates T (2003) The stress–strain behavior of polymer–nanotube composites from molecular dynamics simulation. Compos Sci Technol 63:1655–1661

Garcia E, Wardle B, Hart A, Yamamoto N (2008) Fabrication and multifunctional properties of a hybrid laminate with aligned carbon nanotubes grown in situ. Compos Sci Technol 68:2034–2041

Gao X-L, Li K (2005) A shear-lag model for carbon nanotube-reinforced polymer composites. Int J Solids Struct 42:1649–1667

Gates T, Odegard G, Frankland S, Clancy T (2005) Computational materials: multi-scale modeling and simulation of nanostructured materials. Compos Sci Technol 65:2416–2434

Griebel M, Hamaekers J (2004) Molecular dynamics simulations of the elastic moduli of polymer–carbon nanotube composites. Comput Methods Appl Mech Eng 193:1773–1788

Guzman de Villoria R, Miravete (2007) Mechanical model to evaluate the effect of the dispersion in nanocomposites. Acta Materialia 55(9):3025–3031

Hadjiev VG, Lagoudas DC, Oh E-S, Thakre P, Davis D, Files BS et al (2006) Buckling instabilities of octadecylamine functionalized carbon nanotubes embedded in epoxy. Compos Sci Technol 66:128–136

Hammerand DC, Seidel GD, Lagoudas DC (2007) Computational micromechanics of clustering and interphase effects in carbon nanotube composites. Mech Adv Mater Struct 14(4):277–294

Haque A, Ramasetty A (2005) Theoretical study of stress transfer in carbon nanotube reinforced polymer matrix composites. Compos Struct 71:68–77

Hashin Z, Rosen BW (1964) The elastic moduli of fiber-reinforced materials. J Appl Mech 31:223–232

Hashin Z (1990) Thermoelastic properties of fiber composites with imperfect interface. Mech Mater 8:333–348

Horgan C, Chan A (1999) The pressurized hollow cylinder or disk problem for functionally graded isotropic linearly elastic materials. J Elast 55(1):43–59

Hosseini Kordkheili S, Naghdabadi R (2007) Thermoelastic analysis of a functionally graded rotating disk. Compos Struct 79:508–516

Iijima S (1991) Helical microtubules of graphitic carbon. Nature 354:56–58

Kalamkarov AL, Kolpakov AG (1997). Analysis, design and optimization of composite structures. Wiley, Chichester

Kundalwal SI, Ray MC (2011) Micromechanical analysis of fuzzy fiber reinforced composites. Int J Mech Mater Des 7:149–166

Kundalwal SI, Ray MC (2012) Effective properties of a novel continuous fuzzy-fiber reinforced composite using the method of cells and the finite element method. Eur J Mech–A/Solids 36:191–203

Lau K-T, Chipara M, Ling H-Y, Hui D (2004) On the effective elastic moduli of carbon nanotubes for nanocomposite structures. Compos B Eng 35:95–101

Li C, Chou T-W (2003) Multiscale modeling of carbon nanotube reinforced polymer composites. J Nanosci Nanotechnol 3(6):423–430

Li Y, Seidel GD (2012) Analysis of the interface in CNT-polyethylene nanocomposites using a multiscale modeling method. In: Proceedings paper for the 53rd AIAA/ASME/ASCE/AHS/ASC structures, structural dynamics and materials conference Honolulu, Hawaii, USA 23–26 April, 2012 (AIAA 2012–1819)

Liu H, Brinson L (2006) A hybrid numerical-analytical method for modeling the viscoelastic properties of polymer nanocomposites. J Appl Mech 73:758–768
Liu Y, Chen X (2003) Evaluations of the effective material properties of carbon nanotube-based composites using nanoscale representative volume element. Mech Mater 35:69–81
Liu Y, Nishimura N, Otani Y (2005) Large-scale modeling of carbon-nanotube composites by a fast multipole boundary element method. Comput Mater Sci 34:173–187
Lourie O, Wagner H (1998) Transmission electron microscopy observations of fracture of single-wall carbon nanotubes under axial tension. Appl Phys Lett 73(24):3527–3529
Mathur RB, Chatterjee S, Singh BP (2008) Growth of carbon nanotubes on carbon fibre substrates to produce hybrid/phenolic composites with improved mechanical properties. Compos Sci Technol 68:1608–1615
McCarthy B, Coleman J, Czerw R, Dalton A, in het Panhuis M, Maiti A (2002) A microscopic and spectroscopic study of interactions between carbon nanotubes and a conjugated polymer. J Phys Chem B 106(9):2210–2216
Milo S, Shaffer P, Windle AH (1999) Fabrication and characterization of carbon nanotube/poly(vinyl alcohol) composites. Adv Mater 11(11):937–941
Mori T, Tanaka K (1973) Average stress in matrix and average elastic energy of materials with misfitting inclusions. Acta Metall 21:571–574
Nie G, Batra R (2010) Exact solutions and material tailoring for functionally graded hollow circular cylinders. J Elast 99(2):179–201
Odegard G, Gates T, Wise K, Park C, Siochi E (2003) Constitutive modeling of nanotube-reinforced polymer composites. Compos Sci Technol 63(11):1671–1687
Odegard G, Pipes R, Hubert P (2004) Comparison of two models of swcn polymer composites. Compos Sci Technol 64:1011–1020
Oliva-Aviles AI, Aviles F, Seidel GD, Sosa V (2013) On the contribution of carbon nanotube deformation to piezoresistivity of carbon nanotube/polymer composites. Compos B Eng 47:200–206
Peigney A, Laurent C, Flahaut E, Rousset A (2000) Carbon nanotubes in novel ceramic matrix nanocomposites. Ceram Int 26:677–683
Popov V (2004) Carbon nanotubes: properties and applications. Mater Sci Eng R: Rep 43:61–102
Potschke P, Bhattacharyya AR, Janke A (2004) Carbon nanotube-filled polycarbonate composites produced by melt mixing and their use in blends with polyethylene. Carbon 42:965–969
Qu J, Cherkaoui M (2006) Fundamentals of micromechanics of solids. Wiley, Hoboken
Ray MC (2010) A shear lag model of piezoelectric composite reinforced with carbon nanotubes-coated piezoelectric fibers. Int J Mech Mater Des 6:147–155
Ren X, Seidel GD (2011) Analytic and computational multi-scale micromechanics models for mechanical and electrical properties of fuzzy fiber composites. In: Proceedings paper for the 52nd AIAA/ASME/ASCE/AHS/ASC structures, structural dynamics and materials conference, Denver, Colorado, USA 4–7 April, 2011 (AIAA 2011–1923)
Ren X, Seidel GD (2013) Computational micromechanics modeling of inherent piezoresistivity in carbon nanotube-polymer nanocomposites. J Intell Mater Syst Struct, In press, doi: 10.1177/1045389X12471442
Resolution Performance Products (2001) Product bulletin SC:1183-02
Roche S (2000) Carbon nanotubes: exceptional mechanical and electronic properties. Annales de Chemie Science des Materiaux 25:529–532
Ruhi M, Angoshtari A, Naghdabadi R (2005) Thermoelastic analysis of thick-walled finite-length cylinders of functionally graded materials. J Therm Stresses 28:391–408
Sager RJ, Klein PJ, Lagoudas DC, Zhang Q, Liu J, Dai L et al (2009) Effect of carbon nanotubes on the interfacial shear strength of T650 carbon fiber in an epoxy matrix. Compos Sci Technol 69:898–904
Saito R, Dresselhaus G, Dresselhaus M (1998) Physical properties of carbon nanotubes. Imperial College Press, London
Salvetat-Delmotte J-P, Rubio A (2002) Mechanical properties of carbon nanotubes: a fiber digest for beginners. Carbon 40:1729–1734

Sanchez-Palencia E (1978) Non-homogeneous media and vibration theory. Lecture notes in physics, vol 127. Springer-Verlag, New York

Seidel GD (2007) Micromechanics modeling of the multifunctional nature of carbon nanotube–polymer nanocomposites. Ph.D. Thesis

Seidel GD, Lagoudas DC (2006) Micromechanical analysis of the effective elastic properties of carbon nanotube reinforced composites. Mech Mater 38:884–907

Seidel GD, Lagoudas DC (2008) A micromechanics model for the thermal conductivity of nanotube-polymer nanocomposites. J Appl Mech 75(4) 041025-1-9

Seidel G, Lagoudas D (2009) A micromechanics model for the electrical conductivity of nanotube-polymer nanocomposites. J Compos Mater 43:917–941

Seidel G, Lagoudas D, Frankland S, Gates T (2005) Modeling functionally graded interphase regions in carbon nanotube reinforced composites. In: Proceedings of the 20th ASC technical conference, American Society for Composites, Drexel University, Philadelphia, PA

Seidel G, Lagoudas D, Frankland S, Gates T (2006) Micromechanics modeling of functionally graded interphase regions in carbon nanotube-polymer composites. In: Proceedings paper for the 47th AIAA/ASME/ASCE/AHS/ASC structures, stuctural dynamics, and materials conference, AIAA/ASME/ASCE/AHS/ASC, Newport, Rhode Island, 2006, AIAA 2006–1678

Seidel GD, Puydupin-Jamin A-S (2011) Analysis of clustering, interphase region, and orientation effects on the electrical conductivity of carbon nanotube-polymer nanocomposites via computational micromechanics. Mech Mater 43:755–774

Seidel GD, Stephens SN (2010) Analytical and computational micromechanics analysis of the effects of interphase regions and orientation on the effective coefficient of thermal expansion of carbon nanotube-polymer nanocomposites. In: Proceedings paper for the 51st AIAA/ASME/ASCE/AHS/ASC structures, structural dynamics, and materials conference, Orlando, Florida, April 12–15 2010 (AIAA 2010–2809)

Shenogina N, Shenogin S, Xue L, Keblinski P (2005) On the lack of thermal percolation in carbon nanotube composites. Appl Phys Lett 87:133106–1–3

Spanos PD, Kontsos A (2008) A multiscale Monte Carlo finite element method for determining mechanical properties of polymer nanocomposites. Probab Eng Mech 23(4):456–470

Star A, Stoddart J, Steuerman D, Diehl M, Boukai A, Wong E (2001) Preparation and properties of polymer-wrapped single-walled carbon nanotubes. Angewandte Chemie International Edidion 40(9):1721–1725

Tarn J-Q, Wang Y-M (2001) Laminated composite tubes under extension, torsion, bending, shearing and pressuring: a state space approach. Int J Solids Struct 38:9053–9075

Thostenson ET, Li WZ, Wang DZ, Ren ZF, Chou TW (2002) Carbon nanotube/carbon fiber hybrid multiscale composites. J Appl Phys 91(9):6034–6037

Tsukrov I, Drach B (2010) Elastic deformation of composite cylinders with cylindrically orthotropic layers. Int J Solids Struct 47:25–33

Tsukrov I, Drach B, Gross, TS (2009) Influence of anisotropy of pyrolytic carbon on effective properties of carbon/carbon composites. In: Proceedings of the seventeenth international conference on composite materials, Edinburgh (UK)

Tsukrov I, Drach B, Gross TS (2012) Effective stiffness and thermal expansion coefficients of unidirectional composites with fibers surrounded by cylindrically orthotropic matrix layers. Int J Eng Sci 58:129–143

Valavala P, Odegard G (2005) Modeling techniques for determination of mechanical properties of polymer nanocomposites. Rev Adv Mater Sci 9:34–44

Wagner H (2002) Nanotube–polymer adhesion: a mechanics approach. Chem Phys Lett 361(1–2):57–61

Wagner H, Lourie O, Feldman Y, Tenne R (1998) Stress-induced fragmentation of multiwall carbon nanotubes in a polymer matrix. Appl Phys Lett 72(2):188–190

Wang ZL, Gao RP, Poncharal P, de Heer WA, Dai ZR, Pan ZW (2001) Mechanical and electrostatic properties of carbon nanotubes and nanowires. Mater Sci Eng, C 16:3–10

Wood CD, Palmeri MJ, Putz KW, Ho G, Barto R, Catherine Brinson L (2012). Nanoscale structure and local mechanical properties of fiber-reinforced composites containing mwcnt-grafted hybrid glass fibers. Compos Sci Technol 72:1705–1710

Yakobson B, Smalley R (1997) Fullerene nanotubes: C1,000,000 and beyond. Am Sci 85:324–337

Yamamoto N, Guzman de Villoria R, Wardle BL (2012) Electrical and thermal property enhancement of fiber-reinforced polymer laminate composites through controlled implementation of multi-walled carbon nanotubes. Compos Sci Technol 72:2009–2015

Yan K, Xue Q, Zheng Q, Hao L (2007) The interface effect of the effective electrical conductivity of carbon nanotube composites. Nanotechnology 18:255705–1–6

Yu M-F, Files BS, Arepalli S, Ruoff R (2000) Tensile loading of ropes of single wall carbon nanotubes and their mechanical properties. Phys Rev Lett 84(24):5552–5555

Zeng Q, Yu A, Lu G (2008) Multiscale modeling and simulation of polymer nanocomposites. Prog Polym Sci 33:191–269

Zhao Z-G, Ci L-J, Cheng H-M, Bai J-B (2005) The growth of multi-walled carbon nanotubes with different morphologies on carbon fibers. Carbon 43(3):663–665

Zhu J, Kim J, Peng H, Margrave J, Khabashesku V, Barrera E (2003a) Improving the dispersion and integration of single-walled carbon nanotubes in epoxy composites through functionalization. Nano Lett 3(8):1107–1113

Zhu R, Pan E, Roy A (2007) Molecular dynamics study of the stress-strain behavior of carbon-nanotube reinforced epon 862 composites. Mater Sci Eng, A 447:51–57

Zhu S, Su C, Lehoczky S, Muntele I, Ila D (2003b) Carbon nanotube growth on carbon fibers. Diam Relat Mater 34(12):1825–1828

Geometry–Property Relation in Corrugated Nanocarbon Cylinders

Hiroyuki Shima

Abstract This chapter provides an overview of the geometry–property relation in cylindrical nanocarbon materials. Progressive research in the past years has unveiled an intriguing correlation between geometric modulation and physical properties that were experimentally observed or theoretically predicted for nanocarbon cylinders. The first half of this chapter is devoted to axially corrugated nanocarbon cylinders, so-called peanut-shaped C_{60} polymers, in which axial corrugation induces drastic changes in electronic and optical properties that are distinct from the case of straight, noncorrugated cylinders. In the second half, we will see that the application of hydrostatic pressure to carbon nanotubes yields another class of corrugation, i.e., flower-shaped cross-sectional deformation. Molecular dynamics simulations of such radial corrugation and its consequences to physicochemical properties of multiwall nanotubes are also discussed.

1 Introduction

In the past decade, advanced synthesis techniques have enabled the fabrication of various nanometric materials with complex geometry, especially those made of carbon (Terrones and Terrones (2003); Krasheninnikov and Nordlund (2010); Mao et al. (2011); Gupta and Saxena (2012)). These materials have exhibited unprecedented properties not seen in macroscopic structures, thus triggering the development of next-generation nanodevices. More interestingly, low-dimensional nanocarbon materials provide an experimental platform for exploring the surface curvature effects on the quantum transport of the systems. A better understanding

H. Shima (✉)
Department of Environmental Sciences, University of Yamanashi, 4-4-37, Takeda, Kofu, Yamanashi 400-8510, Japan
e-mail: hshima@yamanashi.ac.jp

K. I. Tserpes and N. Silvestre (eds.), *Modeling of Carbon Nanotubes, Graphene and their Composites*, Springer Series in Materials Science 188,
DOI: 10.1007/978-3-319-01201-8_6,

and more accurate modelling of their basic properties are therefore of significant importance for manufacturing and applying nanodevices.

From quantum aspects, nonzero surface curvature in curved nanocarbons leads to the occurrence of a curvature-induced effective potential field that affects the quantum states of mobile electrons. It was theoretically suggested that an electron moving in a thin curved layer experiences potential energy whose sign and magnitude depend on the local geometric curvature. Such a curvature-induced potential yields dramatic changes in the ballistic electron transport and the collective excitations realized on curved nanocarbon materials. Profound consequences can be seen in a particular class of nanocarbon materials, called peanut-shaped C_{60} polymers, that are endowed with periodically modulated surface curvature. Intensive studies in the past few years have revealed that the C_{60} polymers exhibit a remarkable interplay between the curved geometry and the quantum transport anomaly, as presented in the first half of this chapter. It is also noteworthy that curvature-induced anomalies arise also in classical spin systems (Shima and Sakaniwa (2006); Baek et al. (2009)), which imply untouched properties of quantum counterparts.

The second half deals with the nontrivial mechanics of multiwall carbon nanotubes (MWNTs) under high pressure (Shima and Sato (2013)). An important mechanical feature of carbon nanotubes is their high flexibility in the radial direction. The radial stiffness of an isolated carbon nanotube is much less than its axial stiffness, which results in an elastic deformation of the cross section under hydrostatic pressure (Shima (2012)). Such a pressure-induced radial deformation yields significant changes in electronic and optical properties, indicating the relevance of the deformation in carbon nanotube applications. Intuitively, the multiple-shell structure of MWNTs is thought to enhance the radial stiffness of MWNTs. However, when the number of concentric walls is much greater than unity, the outside walls have to have large diameters, so external pressure may lead to a mechanical instability in the outer walls. This local instability implies a novel cross-sectional shape transition of MWNTs (Shima and Sato (2008); Shima et al. (2010)), as will be demonstrated in the subsequent discussion.

2 Quantum Mechanics on Curved Surfaces

To begin, we briefly survey the theoretical description of quantum mechanics on curved surfaces. Generally, when the motion of a quantum particle is constrained to a curved surface, the surface curvature produces an effective potential field that affects the spatial distribution of the wave function amplitude. Such a geometric curvature effect on quantum states has been debated since the early-stage development of quantum mechanics theory (De Witt (1952, 1957)). In recent years, the effect has received renewed attention in the field of nanoscience (Zhang et al. (2007); Cuoghi et al. (2009); Shima et al. (2009); Szameit et al. (2010); Ortix et al.

(2011)), mainly owing to technological progress that has enabled the fabrication of low-dimensional nanostructures with complex geometry.

The motion of quantum particles constrained to a two-dimensional curved surface is described by one of the two formalisms given below. One is the intrinsic quantization approach (De Witt (1952)), in which the motion is constrained to the surface *a priori*; namely, a classical Hamiltonian is firstly constructed from coordinates and momentum intrinsic to the surface, then the system is quantized canonically. The other approach is the confining-potential approach (Jensen and Koppe (1971); da Costa (1982)), in which the particle is assumed to be confined by a strong force that acts normal to the curved surface. In the latter approach, the quantization of the motion perpendicular to the curved surface results in an effective potential that depends on the local surface curvature. Of the two formalisms, the latter is preferred for considering solid-state physics, since it offers a physically more realistic model of quantum confinement to curved surfaces. In fact, in any real physical system, constrained motion is the result of a strong confining force, not of an ideally zero-thickness (i.e., exactly "two"-dimensional) host material.

Let us consider noninteracting spinless electrons confined to a general two-dimensional curved surface S embedded in a three-dimensional Euclidean space. A point $\boldsymbol{p}$ on S is represented by

$$\boldsymbol{p} = (x(u^1, u^2), y(u^1, u^2), z(u^1, u^2)),$$

where (u^1, u^2) is a curvilinear coordinate spanning the surface and (x, y, z) are the Cartesian coordinates in the embedding space. We now use the notation $\boldsymbol{p}_i \equiv \partial \boldsymbol{p}/\partial u^i$ $(i = 1, 2)$ to introduce the following quantities:

$$g_{ij} = \boldsymbol{p}_i \cdot \boldsymbol{p}_j, \quad h_{ij} = \boldsymbol{p}_{ij} \cdot \boldsymbol{n}, \quad \boldsymbol{n} = \frac{\boldsymbol{p}_i \times \boldsymbol{p}_j}{|\boldsymbol{p}_i \times \boldsymbol{p}_j|}.$$

Here, g_{ij} are (covariant) components of the metric tensor describing the surface, and $\boldsymbol{n}$ is the unit vector normal to the surface. Using the confining-potential approach (Jensen and Koppe (1971); da Costa (1982)), we obtain the Schrödinger equation for noninteracting electron systems on curved surfaces as follows:

$$-\frac{\hbar^2}{2m^*}\left[\frac{1}{\sqrt{g}}\sum_{i,j=1}^{2}\frac{\partial}{\partial u^i}\sqrt{g}g^{ij}\frac{\partial}{\partial u^j} + (H^2 - K)\right]\Psi = E\Psi, \tag{1}$$

where $g = \det(g_{ij})$, $g^{ij} = g_{ij}^{-1}$ (Shima and Nakayama (2009)) and m^* is the effective mass of electrons. The quantities

$$K = \frac{h_{11}h_{22} - h_{12}^2}{g} \quad \textit{and} \quad H = \frac{g_{11}h_{22} + g_{22}h_{11} - 2g_{12}h_{12}}{2g} \tag{2}$$

are the so-called Gaussian curvature and mean curvature, respectively, both of which are functions of (u^1, u^2).

Attention should be paid to the term proportional to $H^2 - K$ in Eq. (1). This term is the effective scalar potential induced by surface curvature. Due to the presence of the effective potential, electrons cannot move around freely on the surface even in the absence of impurities or other interacting entities. This implies that the quantum transport of low-dimensional nanostructures can be controlled by altering the local geometric curvature. In fact, a subtle geometric deformation could induce a drastic change in the ballistic electron transport along nanoscale cylindrical surfaces (Marchi et al. (2005); Taira and Shima (2007)). Furthermore, periodic modulation in surface curvature strongly affects the collective motion of quantum excitations in nanocylindrical systems, as explained in the subsequent three sections.

3 Tomonaga-Luttinger Liquid State of a Peanut-shaped C_{60} Polymer

An important consequence of geometric curvature shows up in the case where the curved nanomaterial forms a quasi-one-dimensional cylindrical shape. It is well known that in a one-dimensional electron system, the conventional Fermi-liquid theory breaks down so that the system is in a Tomonaga-Luttinger liquid (TLL) state (Voit (1994)). In a TLL state, many physical quantities exhibit a power-law dependence stemming from the absence of single-particle excitations near the Fermi energy. This situation naturally raises the question as to how geometric distortion affects the TLL behaviour of quasi-one-dimensional curved systems.

Peanut-shaped C_{60} polymers (Onoe et al. (2003, 2007)) are exemplary materials to be considered for studying TLL behaviour (see Fig. 1). They are synthesized by electron-beam irradiation of pristine two-dimensional C_{60} films, having coalesced structures via the general Stone–Wales rearrangement (Stone and Wales (1986)) between adjacent C_{60} molecules (see Fig. 2). The C_{60} polymer belongs to a class of π-electron conjugated systems, thus exhibiting metallic properties. In addition, they are thin, long, and hollow tubules whose radius is periodically modulated along the tube axis; this implies that the polymer has both positive and negative Gaussian curvatures (see Fig. 3), which thus means it belongs to a novel class of nanocarbon materials distinct from other well-known π-electron systems such as carbon nanotubes (Shima and Sato (2013)) and graphene ribbons (Charlier et al. (2008)). Hence, the periodic surface curvature intrinsic to the systems will produce sizable effects on their TLL properties.

The curvature effect on the TLL nature of the C_{60} polymers can be derived theoretically by using the continuum approximation,[1] wherein the polymer is to be

[1] Mapping the discrete atomic structure of one-dimensional C_{60} polymers to a continuum curved surface is based on the result of first-principles calculations (Beu et al. (2005)), which indicated that π electrons on the polymers are almost free from their atomic configurations.

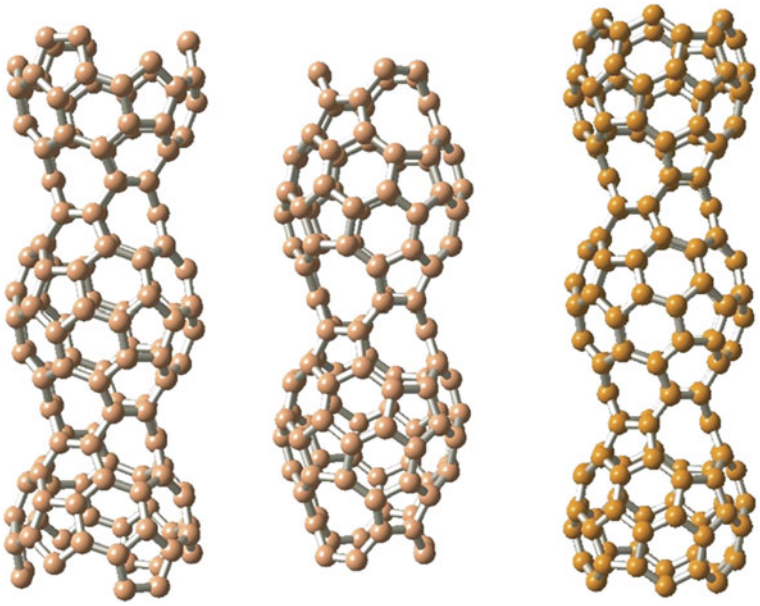

Fig. 1 Structures of three types of peanut-shaped fullerene tubes. After Ref. Nakayama et al. (2007)

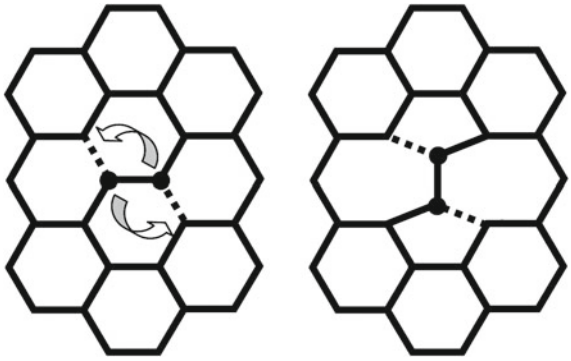

Fig. 2 Diagram of the Stone–Wales transformation that yields a pair of 5–7 defects

regarded as a hollow tube with a periodically varying radius represented by $\boldsymbol{p} = (r(z)\cos\theta, r(z)\sin\theta, z)$ (see Fig. 4). The tube radius $r(z)$ is periodically modulated in the axial z direction as

$$r(z) = r_0 - \frac{\delta r}{2} + \frac{\delta r}{2}\cos\left(\frac{2\pi}{\lambda}z\right), \tag{3}$$

where the parameters r_0 and δr are introduced to express the maximum and minimum of $r(z)$ as r_0 and $r_0 - \delta r$, respectively. Because of rotational symmetry,

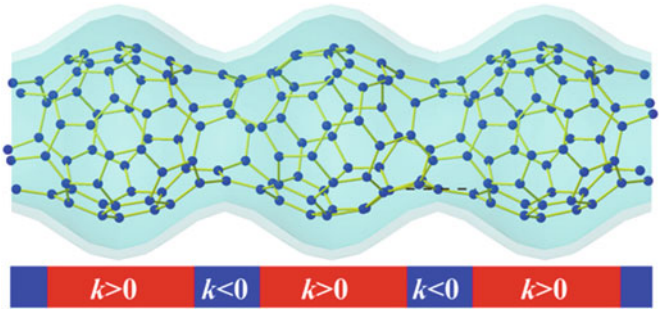

Fig. 3 Hypothesized atomic configuration of a peanut-shaped C_{60} polymer with an uneven peanut-shaped structure. The area coloured in light blue represents a quasi-two-dimensional hollow curved space within which the motion of π electrons is constrained. Alternation in the sign of Gaussian curvature (designated by k in the plot) along the tubular axis is highlighted by a coloured map. After Ref. Onoe et al. (2012)

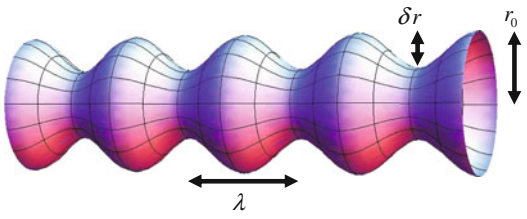

Fig. 4 Schematic illustration of a quantum hollow cylinder with periodic radius modulation. After Ref. Shima et al. (2009)

the eigenfunctions of the system have the form $\Psi(z,\theta) = e^{in\theta}\psi_n(z)$. Thus, the problem reduces to the one-dimensional Schrödinger equation

$$-\frac{\hbar^2}{2m^*}\left[\mathcal{D} - \frac{n^2}{r^2} + (H^2 - K)\right]\psi_n(z) = E\psi_n(z), \tag{4}$$

where

$$\mathcal{D} = \frac{1}{rf}\frac{d}{dz}\frac{r}{f}\frac{d}{dz}, \quad f(z) = \sqrt{1+r'^2}, \quad K = -\frac{r''}{rf^2}, \quad H = \frac{f^2 - rr''}{2rf^3}$$

with $r' \equiv dr/dz$.

Equation (4) can be simplified by using a new variable $\xi = \xi(z) = \int_0^z f(\eta)d\eta$, which corresponds to the line length along the curve on the surface with a fixed θ. Straightforward calculation yields (Shima et al. (2009))

$$\left[-a^2\frac{d^2}{d\xi^2} + U_n(\xi)\right]\psi_n(\xi) = \varepsilon\psi_n(\xi), \quad \varepsilon = \frac{2m^*a^2E}{\hbar^2} \tag{5}$$

with

$$U_n(\xi) = \frac{(n^2 - \frac{1}{4})a^2}{r^2} - \frac{r''^2 a^2}{4f^6},$$

where r, r'', and f are regarded as functions of ξ using the inverse relation $z = z^{-1}(\xi)$. To derive Eq. (5), we introduced the length scale, a, and then multiplied both sides of Eq. (4) by $2m^*a^2/\hbar^2$ to make the units of U_n and ε dimensionless.

Notice that, by the definition of $\xi(z)$, U_n is periodic with a period $\Lambda = \xi(\lambda)$ depending on r_0 and δr (as well as λ). Figure 5 shows the spatial profile of U_n within one period; throughout the present work, we fixed $r_0 = 4.0$ and $\lambda = 8.0$ in units of a by simulating the geometry of actual peanut-shaped C_{60} polymers whose geometry is reproduced by imposing $a = 1$ Å. We found that U_n takes extrema at $\xi = 0$ (or Λ) and $\xi = \Lambda/2$, where r takes the maximum $(r = r_0)$ and the minimum $(r = r_0 - \delta r)$ values, respectively.

We are now ready to evaluate the TLL exponent using a theory based on the confining-potential approach. Consider the Coulombic interactions between spinless electrons. The interactions make the electron–hole pairs share the ground state of the noninteracting electron system, wherein the most strongly affected states are those lying in the vicinity of E_F. As a consequence, the single-particle density of states $n(\omega)$ near E_F exhibits a power-law singularity of the following form (Voit (1994)):

$$n(\omega) \propto |\hbar\omega - E_F|^{\alpha}, \quad \alpha = \frac{\beta + \beta^{-1}}{2} - 1. \tag{6}$$

The explicit form of β is derived by using the bosonization procedure (Voit (1994)) as follows:

$$\beta = \lim_{q \to 0} \sqrt{\frac{2\pi\hbar v_F + g_4(q) - g_2(q)}{2\pi\hbar v_F + g_4(q) + g_2(q)}}. \tag{7}$$

Here, $v_F = \hbar^{-1} dE/dk|_{k=k_F}$ is the Fermi velocity, and $g_4(q) = V(q, m)$ and $g_2(q) = V(q, m) - V(2k_F, m)$ are q-dependent coupling constants. $V(q, m)$ is the Fourier transform of the screened interaction,

$$V(\boldsymbol{r}) = -\frac{e^2}{4\pi\varepsilon|\boldsymbol{r}|} e^{-\kappa|\boldsymbol{r}|}, \tag{8}$$

where ε is the dielectric constant and κ is the screening length. To derive the exponent α, therefore, we need to calculate v_F, g_4, and g_2 under given geometric conditions; see Ref. Shima et al. (2009) for the detailed mathematical manipulation.

Figure 6 shows the δr dependencies of β and α for different k_F values. The interaction-energy scale $e^2/(4\pi\varepsilon a)$ is set to be 1.1 in units of $\hbar^2/(2m^*a^2)$ to mimic those of C_{60}-related materials (Hebard et al. (1991); Oshiyama et al. (1992)). The salient features of Fig. 6 are the significant decrease in β and increase in α with an

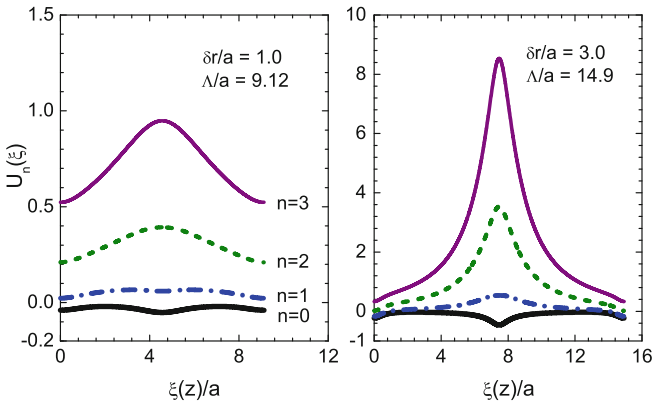

Fig. 5 Profiles of the curvature-induced effective potential $U_n(\xi)$ for one period $[0, \Lambda]$. Geometric parameters $r_0 = 4.0$ and $\lambda = 8.0$ in units of a are fixed. Integers n represent the angular momentum of eigenstates in the circumferential direction of a hollow tube. After Ref. Shima et al. (2009)

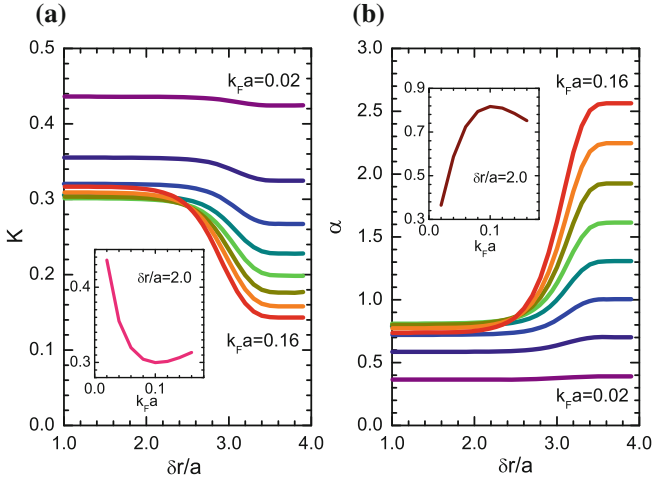

Fig. 6 δr dependencies of β and α defined by Eqs. (6) and (7), respectively. The screening parameter κ is set to be $\kappa a = 1.0 \times 10^{-3}$. *Insets* nonmonotonic behaviours of β and α as a function of k_F at $\delta r/a = 2.0$. After Ref. Shima et al. (2009)

increase in δr for $\delta r/a > 2.5$. Such δr-driven shifts in β and α are attributed to the effects of geometric curvature on the nature of TLL states. In fact, an increase in δr amplifies the curvature-induced effective potential $U_n(\xi)$ (see Fig. 5), thus yielding a monotonic decrease in v_F at $\delta r/a > 2.5$. The decrease in v_F plays a dominant

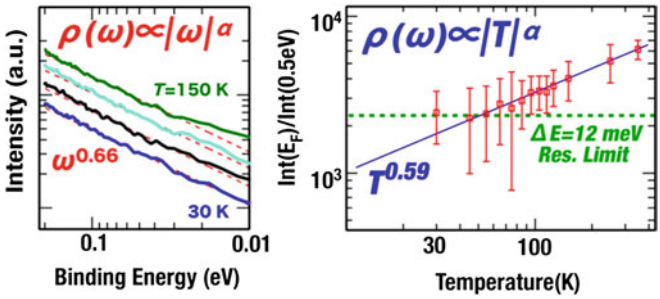

Fig. 7 Photoemission spectra of a peanut-shaped C_{60} polymer in the vicinity of the Fermi level. Power-law dependencies on the binding energy (*left*) and temperature (*right*) are observed. After Ref. Onoe et al. (2012)

role in the numerator of the expression in Eq. (7), and eventually it leads to systematic shifts in β and α.[2]

The aforementioned theory gives a prediction that spatial variation in the surface curvature of C_{60} polymers causes a significant increase in the power-law exponent of the single-particle density of states; the increase in the exponent is thought to originate from a curvature-induced potential that attracts low-energy electrons to regions that have large curvature (Shima et al. (2010)). Eventually, the prediction was verified in a photoemission experiment (Onoe et al. (2012)) three years after the theory was proposed. Figure 7 shows the photoemission spectra $\rho(\omega, T)$ of the peanut-shaped C_{60} polymers in the vicinity of the Fermi level E_F. They exhibit power-law dependencies with respect to both the binding energy (ω) and temperature (T). The TLL exponent, evaluated from the data within the energy range of 18–70 meV in Fig. 7, was found to be $\alpha = 0.65 \pm 0.08$. In contrast, the power-law dependence of $\rho(T)$ on T in the temperature range of 30–350 K led us to the result of $\alpha = 0.59 \pm 0.04$. Hence, it is reasonable to conclude that the TLL exponent α for the one-dimensional, uneven peanut-shaped C_{60} polymer is $\alpha \sim 0.6$, which is significantly larger than $\alpha = 0.5$ for metallic single-walled carbon nanotubes (Ishii et al. (2003)).

It should be emphasized that the curvature-induced shift in the TLL exponent, reported in Ref. Onoe et al. (2012), is the first experimental realization of the curvature–property relation in low-dimensional quantum systems. Furthermore, the remarkable consistency between theory and experiment tells us that the confining-potential approach is effective for exploring the curvature–property relations in C_{60} polymers and possibly other curved nanomaterials.

[2] It is noted that Eq. (5) can formally deal with an uncurved one-dimensional system subject to a periodically electrostatic potential. In a similar manner to the present curved system, therefore, α and β are expected to be shifted even for an uncurved quantum wire by electric-field modulation (Shima et al. (2010)).

4 Electron–Phonon Interaction in C_{60} Polymers

In addition to the shift in the TLL exponent, C_{60} polymers exhibit distinct features that differ greatly from those of conventional nanocarbons. In the case of phononic excitations, infrared spectral measurements evidenced a rapid growth of specific eigenmode peaks with an increase in electron-beam irradiation time (Takashima et al. (2010)). This peak growth is attributed to an anomaly in the phonon density of states peculiar to quasi-one-dimensional systems (Ono and Shima (2011b)).

A more interesting subject is the artificial manipulation of electron–phonon-coupling-induced metal–semiconductor transition (i.e., the Peierls transition) in the C_{60} polymers. Pump–probe spectroscopy measurement has unveiled an energy gap formation in the conduction band of C_{60} polymers below 60 K (Toda et al. (2008)). This energy gap formation suggested the Peierls transition, driven by electron–phonon coupling, though the physical mechanism has not been clarified. For device application, tuning the transition temperature T_c by imposing external conditions can be quite advantageous, because it would enable artificial control of low-temperature conductivity of the C_{60} polymers.

The possibility of such conductivity control has been theoretically proven in Ref. Ono and Shima (2011a). The theory describes the relationship between the electron–phonon coupling strength and the Fermi energy shift resulting from carrier doping. By doping an additional carrier to the pristine C_{60} polymer, the Fermi level is shifted from μ_0 to $\mu \equiv \mu_0 + \Delta\mu$, with $\Delta\mu$ representing the deviation from the initial value μ_0 by doping. For the pristine system, μ_0 is set such that 60 electrons per C_{60} molecule occupy single-particle states from the bottom of the electronic band. The theory states that tuning $\Delta\mu$ via carrier doping gives rise to a significant change in the transition temperature T_c of the C_{60} polymers, allowing for conductivity control at low temperature.

Figure 8 shows the μ dependence of T_c, showing that T_c decreases monotonically as μ increases. This decrease results from a reduction in the commensurate effect (Grüner (1994)) that maximizes T_c at the half-filling state (i.e., $\Delta\mu \sim -50$

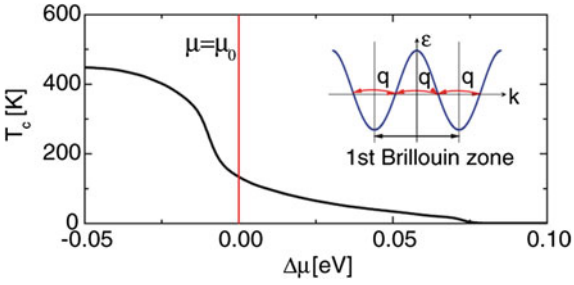

Fig. 8 Transition temperature T_c as a function of the Fermi level shift $\Delta\mu$ because of carrier doping. Without doping, we have $T_c \sim 130$ K, as indicated by a vertical line. Inset: Schematic of the commensurate effect, illustrating the electron band structure and relevant electron–phonon couplings via the phonon wave number q. After Ref. Ono and Shima (2011a)

meV in the present condition; see inset of Fig. 8). The rapid decrease in T_c with the increase in μ is significant in light of controlling the low-temperature electronic conductivity of the C_{60} polymers. For example, an increment $\Delta\mu = 0.3$ eV causes a drastic reduction in T_c from 130 to 1 K; this value of $\Delta\mu$ coincides with the upwards shift in the Fermi level that is observed when one additional alkali atom per C_{60} molecule is inserted into the hollow cavity of the C_{60} polymer. As a result, the metallic nature of the C_{60} polymers can survive even below 60 K, unlike the case of the pristine (undoped) system. This phenomenon provides a new avenue for controlling the low-temperature conductivity of C_{60} polymers by doping, which is highly advantageous in actual device applications.

5 Cross-Sectional Buckling of Carbon Nanotubes

In the remainder of this chapter, we turn to the issue of carbon nanotube buckling observed under hydrostatic pressure. By "buckling" we mean a deformation through which a pressurized material undergoes a sudden failure, exhibiting large displacement in a direction transverse to the load. A typical example of buckling occurs when pressing opposite edges of a long, thin elastic beam towards one another. For small loads, the beam is compressed in the axial direction while keeping its linear shape, and the strain energy is proportional to the square of the axial displacement. Beyond a certain critical load, however, it suddenly bends archwise and the relation between the strain energy and displacements deviates far from the square law. Besides axial compression, bending and torsion give rise to buckling of elastic beams and cylindrical objects, in which the buckled patterns strongly depend on geometric and material parameters.

An interesting class of elastic buckling can be observed in structural pipe-in-pipe cross sections under hydrostatic pressure. Pipe-in-pipe i.e., a pipe inserted inside another pipe) applications are promising for offshore oil and gas production systems in civil engineering. In subsea pipelines in deep water, for instance, buckling resistance to huge external hydrostatic pressure is a key structural design requirement. Pipe-in-pipe systems are a possible efficient design solution to this problem, because their peculiar concentric structures prevent collapse of their cross sections even when the pipes are subjected to high pressure.

The above argument on macroscopic objects raises question as to what buckling sort of behaviour is obtained in nanometric counterparts, i.e., multiwall carbon nanotubes (MWNTs). Because of their nanometric scales, the similarities and differences in buckled patterns compared with their macroscopic counterparts are not at all trivial. This complexity has motivated tremendous efforts towards the buckling analysis of carbon nanotubes under diverse loading conditions: axial compression (Yakobson et al. (1996); Ru (2000b, 2001b); Ni et al. (2002); Waters et al. (2004, 2005); Sears and Batra (2006)), bending (Falvo et al. (1997); Poncharal et al. (1999); Duan et al. (2007); Kutana and Giapis (2006); Wang and Yang (2006); Wang et al. (2007)), torsion (Jeong et al. (2007); Wang (2008,

2009)), and their certain combinations (Wang et al. (2006); Zhang et al. (2007); Jeong et al. (2008)).

It is emphasized that, by applying mechanical deformation, carbon nanotubes show significant changes in their physical and chemical properties. Precise knowledge of their deformation mechanism and available geometry is, therefore, crucial for understanding their structure–property relations and for developing carbon-nanotube-based applications towards the next generation.

6 Uniaxial Collapse of Single-Wall Carbon Nanotubes (SWNTs)

Radial pressure can yield a distinct class of buckling, reflecting the high flexibility of graphene sheets in the normal direction. In fact, the radial stiffness of an isolated carbon nanotube is much less than its axial stiffness (Palaci et al. (2005)), which results in an elastic deformation of the cross section upon application of hydrostatic pressure (Venkateswaran et al. (1999); Tang et al. (2000); Peters et al. (2000); Sharma et al. (2001); Rols et al. (2001); Reich et al. (2002); Sun et al. (2004); Elliott et al. (2004); Tangney et al. (2005); Gadagkar et al. (2006); Zhang et al. (2006); Hasegawa and Nishidate (2006); Yang et al. (2006); Christofilos et al. (2007)) or indentation (Majid and Yu (2008); Barboza et al. (2009); Yang and Li (2011)). Experimental and theoretical studies, focussed on SWNTs and their bundles, revealed flattening and polygonalization in their cross section under pressures on the order of a few gigapascals (Venkateswaran et al. (1999); Sharma et al. (2001)).

The overall scenario of SWNT deformation under hydrostatic pressure is summarized in Fig. 9 (Sun et al. (2004)). With increasing pressure, the cross sections of SWNTs deform continuously from circular to elliptical and finally to peanut-like configurations (Sun et al. (2004); Zhang et al. (2006); Lu et al.

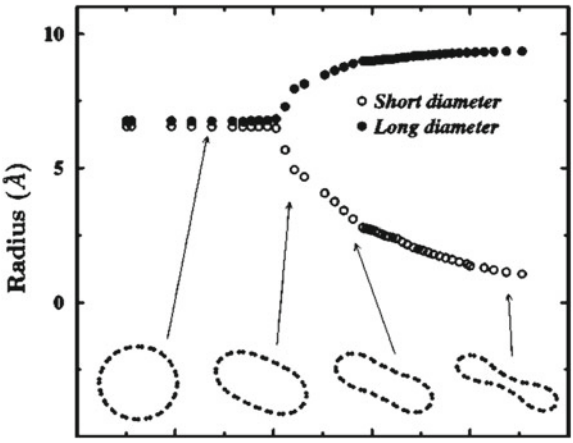

Fig. 9 Long and short diameters of a (10,10) SWNT as a function of applied hydrostatic pressure. The shape of the cross section at some selected pressures is plotted at the bottom of the figure. After Ref. Sun et al. (2004)

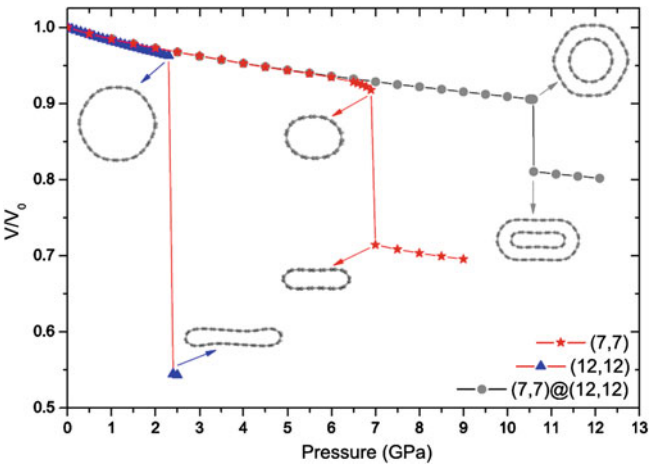

Fig. 10 Change in the relative volume of the (7,7)@(12,12) DWNT bundle and the corresponding SWNT bundles as a function of hydrostatic pressure. After Ref. Yang and Wu (2008)

(2011)).[3] The radial deformation of carbon nanotubes strongly affects their physical and structural properties. For instance, it may cause a semiconductor–metal transition (Barboza et al. (2008); Giusca et al. (2008)), an optical response change (Thirunavukkuarasu et al. (2010)), or magnetic moment quenching (Diniz et al. (2010)) in the nanotubes. From a structural perspective, the radial collapse can give rise to interwall sp^3 bonding between adjacent concentric walls (Fonseca et al. (2010); Sakurai and Saito (2011)), which may increase nanotube stiffness and therefore be effective for high-strength reinforced composites (Xia et al. (2007); Byrne et al. (2009); Filleter et al. (2011); Zhang et al. (2011)).

A bundle of nanotubes (i.e., an ensemble of many nanotubes arranged parallel to each other) can exhibit radial collapse patterns similar to those of an isolated nanotube under hydrostatic pressure. Figure 10 shows (Yang and Wu (2008)) the volume change of a bundle of (7,7) SWNTs and a bundle of (12,12) SWNTs as a function of the applied hydrostatic pressure; the data for a bundle of (7,7)@(12,12) double-walled nanotubes (DWNTs) are also shown on the same plot. The (12,12) SWNT bundle, for instance, collapses spontaneously at a critical pressure of 2.4 GPa, across which the cross section transforms into a peanut-like shape. Two other bundles provide higher critical pressures, as follows from the plot. An interesting observation is that the transition pressure of the (7,7) tube, which is nearly 7.0 GPa when the tube is isolated, becomes higher than 10.5 GPa when it is surrounded by the (12,12) tube. This means that the outer tube acts as a "protection shield" and the inner tube supports the outer one and increases its structural stability; this

[3] For larger radius SWNTs, the peanut-like deformed structure can be transformed to dumbbell-like configurations by van der Waals (vdW) attractions between the opposite walls of the nanotubes. The latter structure is energetically stable even when the applied force is unloaded.

interpretation is consistent with prior optical spectroscopic measurements (Arvanitidis et al. (2005)). This effect, however, is weakened as the tube radius increases owing to the decreasing radial stiffness of SWNTs.

7 Radial Corrugation of MWNTs

In contrast to the intensive studies on SWNTs (and DWNTs), radial deformation of MWNTs has remained largely unexplored till recently. Intuitively, the multilayered structure of MWNTs is expected to enhance the radial stiffness relative to its single-walled counterpart. However, when the number of concentric walls is much greater than unity, the outside walls have to have large diameters, so external pressure may lead to a mechanical instability in the outer walls. This local instability triggers a novel cross-sectional deformation, called radial corrugation (Shima and Sato (2008)), of MWNTs under hydrostatic pressure.

Figure 11a and b illustrate MWNT cross-sectional views of two typical deformation modes: (a) elliptic $(n = 2)$ and (b) corrugation $(n = 5)$ modes. In the elliptic mode, all constituent walls are radially deformed. In contrast, in the corrugation mode, outside walls exhibit significant deformation, whereas the innermost wall maintains its circular shape. Which mode will be obtained under pressure depends on the number of walls, N, and the core tube diameter D of the MWNT considered. In principle, larger N and smaller D favour a corrugation mode with larger n.

Figure 11c shows the critical buckling pressure p_c as a function of N for various values of D, which were derived from the thin-shell theory approach described in Sect. 9. An initial increase in p_c at small N (except for $D = 1.0$ nm) is attributed to the enhancement of radial stiffness of the entire MWNT by encapsulation. This stiffening effect disappears with further increase in N, resulting in decay or convergence of $p_c(N)$. A decay in p_c implies that a relatively low pressure becomes sufficient to produce radial deformation, thus indicating an effective "softening" of the MWNT. The two contrasting types of behaviour, stiffening and softening, are different manifestations of the encapsulation effect of MWNTs. It is noteworthy that practically synthesized MWNTs often show D larger than those presented in Fig. 11c. Hence, $p_c(N)$ of an actual MWNT lies at several hundred megapascals, as estimated from Fig. 11c. Such a degree of pressure applied to MWNTs is easily accessible in high-pressure experiments,[4] supporting the feasibility of our theoretical predictions.

Figure 11d shows the stepwise increases in the corrugation mode index n. For all D, the deformation mode observed just above p_c abruptly increases from $n = 2$ to $n \geq 4$ at a certain value of N, followed by the successive emergence of higher

[4] A radial pressure large enough to cause corrugation can be achieved by electron-beam irradiation (Krasheninnikov and Nordlund (2010)), the self-healing nature of eroded carbon walls gives rise to a spontaneous contraction that exerts a high pressure on the inner walls to yield their radial corrugation (Shima et al. (2010)).

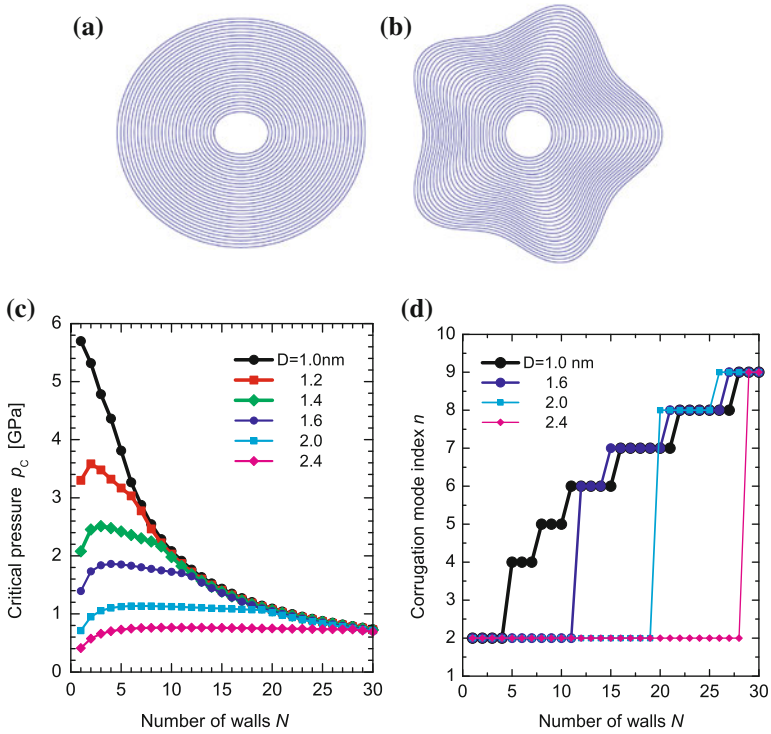

Fig. 11 Cross-sectional views of **a** elliptic $(n = 2)$ and **b** corrugated $(n = 5)$ deformation modes. The mode index n indicates the wave number of the deformation mode along the circumference. **c** Wall-number dependence of critical pressure p_c. Immediately above p_c, the original circular cross section of MWNTs gets radially corrugated. **d** Stepwise increase in the corrugation mode index n. After Refs. Shima and Sato (2008), Shima et al. (2012)

corrugation modes with larger n. These successive transitions in n at $N \gg 1$ originate from the mismatch in the radial stiffness of the innermost and outermost walls. A large discrepancy in the radial stiffness of the inner and outer walls results in a maldistribution of the deformation amplitudes of concentric walls interacting via vdW forces, which consequently produces an abrupt change in the observed deformation mode at a certain value of N.

8 Molecular Dynamics Simulation of Radial Corrugation

The validity of the thin-shell theory prediction has been verified by molecular dynamics (MD) simulations. MD simulations of MWNTs under hydrostatic pressure enable us to deduce the postcorrugated cross-sectional patterns of MWNTs at an atomistic level, as well as to evaluate the critical pressure above

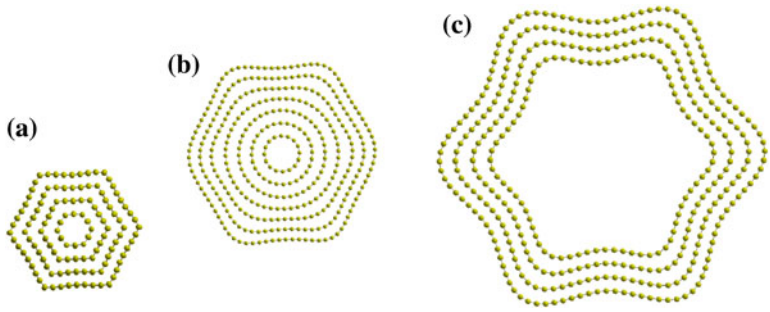

Fig. 12 Cross-sectional view of the radially corrugated MWNTs consisting of concentric zigzag tubes represented by $(n, 0)$: **a** a 4-walled nanotube with $n = 6 + 6(q - 1)$ $[1 \leq q \leq 4]$; **b** a 7-walled nanotube with $n = 8 + 6(q - 1)$ $[1 \leq q \leq 7]$; **c** a 4-walled nanotube with $n = 38 + 6(q - 1)$ $[1 \leq q \leq 4]$. After Ref. Shima et al. (2013)

which the corrugation arises. The predicted morphological variation in the corrugated patterns at the energetically relaxed states, therefore, will facilitate understanding of structure–property relations for MWNTs and the available geometry for developing MWNT-based applications.

The atomistic model simulation performed in Ref. Shima et al. (2013) deals with MWNTs consisting of concentric zigzag nanotubes with chiral vectors of $(n, 0)$. The size of the simulation cells along the tube axis (z axis) is 12.78 Å and a periodic boundary condition is imposed only for the z axis to mimic an isolated (free-standing) MWNT with infinite length. The simulations were based on an in-house code named "MDSPASS2", which carries out classical molecular dynamics calculations using empirical interatomic potentials. The time step was set to 1.0 fs. The pressure exerted on a multiwalled nanotube was mimicked by applying constant forces on the atoms of the outermost wall along the direction perpendicular to the wall. The tangential plane was determined by taking triangles of atoms, each of which consists of an atom and its two nearest-neighbour atoms (i.e., the triangles are isosceles having a 120° angle at initial configuration). The interaction between atoms is calculated by using the Brenner interatomic potential for hydrocarbons (Brenner (1990, 1992)), which has been widely used for deformation of carbon nanotubes.

Figure 12 depicts the cross-sectional view of the radially corrugated MWNTs with isochiral zigzag tubes. The panels correspond to (a) a thin 4-walled nanotube indexed by $(6, 0)/(12, 0)/(18, 0)/(24, 0)$, (b) a 7-walled nanotube with $(8, 0)/(14, 0)/\cdots/(44, 0)$, and (c) a thick 4-walled nanotube with $(38, 0)/(44, 0)/\cdots/(56, 0)$. All the relaxed configurations presented here fall into a hexagonal pattern. although we confirmed that other types of polygonal patterns (pentagonal, octagonal, *etc.*) can be observed depending on the tube chirality, the number of concentric tubes, N, and the innermost tube diameter D.

For a thin 4-walled nanotube (as shown in Fig. 12a), we obtain a hexagonal prism with six well-defined facets at a critical hydrostatic pressure p_c of 297.5 MPa. The graphitic layer at the lateral side of the prism is almost flat, but along the

ridge lines, it suffers from significant penalty in bending energy increase. Whereas this deformation mode involved corrugation in all the nanotube walls but the innermost shell, this multiwalled nanotube exhibited a more "modest" deformation at a much lower pressure, $p_c = 78.0$ MPa, where only the outermost shell made its cross section hexagonal, keeping the other three nanotube walls round. With increasing N or D, the well-defined prism loses stability and the relaxed patterns shift to those having more rounded corners, as illustrated in Fig. 12b and c. The critical pressure p_c for the latter two patterns is 10.5 and 7.5 MPa, respectively; it is surprising that p_c for the 7-walled nanotube is much smaller than p_c for the thin 4-walled one, despite the slight difference in N and D between them. Such morphological evolution in radially corrugated patterns is attributed to the competition of the three relevant energies: in-plane strain energy, vdW interaction energy between adjacent tubes, and out-of-plane bending energy (Shima and Sato (2008); Huang et al. (2011)).

9 Thin-Shell Theory for Radial Corrugation

Although atomistic simulations may provide precise estimations of physical quantities in general, they often demand huge computational resources in systems of interest. Against this background, the thin-shell-theory-based analysis for carbon nanotube mechanics has long been developed (Yakobson et al. (1996); Ru (2000a, 2000b, 2001a, 2001b); Kudin et al. (2011); Pantano et al. (2004); Huang et al. (2006); Chandraseker and Mukherjee (2007)). In the continuum thin-shell method, an MWNT is mapped onto a set of N continuum elastic hollow tubes of radii r_i $(1 \leq i \leq N)$. A point on the circle corresponding to the cross section of the ith tube is described by in terms of polar coordinates, where θ is the circumferential angle around the tube axis. Under pressure p, the point moves to

$$(x^*, y^*) = ([r_i + u_i(\theta, p)] \cos\theta - v_i(\theta, p) \sin\theta, \tag{9}$$

$$[r_i + u_i(\theta, p)] \sin\theta + v_i(\theta, p) \cos\theta \ ). \tag{10}$$

If the deformation amplitudes, u_i and v_i, are sufficiently small, the mechanical energy of the ith tube per unit axial length is given by

$$U_D^{(i)} = \frac{r_i}{2} \left(\frac{\tilde{C}}{1 - \nu^2} \int_0^{2\pi} \epsilon_i^2 d\theta + \tilde{D} \int_0^{2\pi} \kappa_i^2 d\theta \right). \tag{11}$$

Here, ϵ_i and κ_i are, respectively, the in-plane and bending strains of the ith wall, both depending on u_i, v_i and their derivatives with respect to θ (Sanders (1963)). The constant $\tilde{C}$ denotes the in-plane stiffness, $\tilde{D}$ the flexural rigidity, and ν the Poisson ratio of each wall.

For quantitative discussions, the values of $\tilde{C}$ and $\tilde{D}$ must be carefully determined. In the conventional thin-shell theory for macroscopic objects, $\tilde{C}$ and $\tilde{D}$ are related to the Young's modulus E of the wall and its thickness $\tilde{h}$ as

$$\tilde{C} = E\tilde{h}, \quad \tilde{D} = \frac{E\tilde{h}^3}{12(1-\nu^2)} \qquad \text{for macroscopic shells.}$$

However, for carbon nanotubes, the wall is made out of a monoatomic graphitic layer and consequently the notion of wall thickness becomes elusive. Hence, the macroscopic relations for $\tilde{C}$ and $\tilde{D}$ noted above fail since there is no unique way of defining the thickness of the graphene wall (Gupta et al. (2010)). Thus the values of $\tilde{C}$ and $\tilde{D}$ should be evaluated *ab initio* from direct measurements or computations of carbon sheets, without reference to the macroscopic relations. In actual calculations, we substitute

$$\tilde{C} = 345\ nN/nm, \quad \tilde{D} = 0.238\ nN \cdot nm \quad \text{forcarbonnanotubes}$$

and $\nu = 0.149$ along with the prior work (Kudin et al. (2011)) based on density functional theory. It should be noted that the values of $\tilde{C}$ and $\tilde{D}$ are essentially tube-diameter dependent. Nevertheless, such dependencies become negligible when the tube diameter exceeds 1 nm, above which the elastic constants of carbon nanotubes converge to those of a planar graphene sheet (Kudin et al. (2011)). Against this background, we will take into account only the nanotubes whose diameters are larger than 1 nm, which allows us to fix the values of $\tilde{C}$ and $\tilde{D}$ as noted above.

The stable cross sections of MWNTs under p minimize the mechanical energy U of the whole system that is described by (Shima and Sato (2008))

$$U = \sum_{i=1}^{N} U_D^{(i)} + \sum_{i,j=i\pm1} U_I^{(i,j)} + \Omega. \tag{12}$$

Here, $U_I^{(i,j)}$ accounts for the vdW interaction energy of adjacent pairs of walls, whose precise definition will be given in Sect. 10. The term Ω is the negative of the work done by p during cross-sectional deformation, given by

$$\Omega = p\int_0^{2\pi} \left(r_N u_N + \frac{u_N^2 + v_N^2 - u_N{}' v_N + u_N v_N{}'}{2} \right) d\theta, \tag{13}$$

with $u' \equiv du/d\theta$. Note that U is a function of u_i and v_i; therefore, the variational method allows us to obtain the optimal solutions of u_i and v_i that minimize U under a given p.

For $N \gg 1$, the outside walls have large diameters, and consequently they are very flexible and susceptible to mechanical instabilities under radial pressure. The contrast in the radial rigidity between the outermost walls and the innermost ones triggers the nontrivial cross-sectional deformation observed in radially pressurized

MWNTs. In fact, a linearized buckling analysis leads to the conclusion that, immediately above a critical pressure p_c, the circular cross section of MWNTs becomes radially deformed as described by (Shima and Sato (2008))

$$u_i(\theta) = u_i^{(0)}(p_c) + \delta\mu_i(n)\cos n\theta, \quad v_i(\theta) = \delta v_i(n)\sin n\theta. \tag{14}$$

The solution (14) represents a wavy structure of an MWNT's cross section, called radial corrugation with mode index n. The integer n indicates the wave number of the corrugated walls; it is uniquely determined by the one-to-one relation between n and p_c (Shima and Sato (2008)). As seen from Fig. 11, n depends systematically on N and the innermost tube diameter.

10 Wall–Wall Interaction Coefficient

In the radial corrugation of MWNTs, the critical pressure p_c is thought to depend on the strength of vdW interactions; this is the reason why the rigorous formulation of adjacent wall–wall interaction should be addressed.

There exist several continuum models for vdW interactions (He et al. (2005); Lu et al. (2009); Girifalco et al. (2000)). In Ref. He et al. (2005), expressions for the pressure and the vdW interaction coefficients were obtained by integrating the continuum vdW force and its derivative on a curved wall surface, while disregarding the vectorial nature of the force. The significance of the vectorial nature of the force was addressed in Ref. Lu et al. (2009), where analytical expressions for the vdW pressure were obtained by considering only the component of the vdW force normal to the wall. It was emphasized in Ref. Lu et al. (2009) that, for a two-walled carbon nanotube, the pressure exerted on the inner wall is different from the pressure on the outer wall. The pressures on the inner and outer walls for a concentric two-walled tube with radii r_{inn} and r_{out} are (with positive signs for compression)

$$p_{inn} = \alpha\frac{r_{out}}{r_{inn}}f_- \quad and \quad p_{out} = \alpha\frac{r_{inn}}{r_{out}}f_+, \tag{15}$$

where $\alpha = 3\pi\varepsilon\sigma{\rho_c}^2/32$ with $\rho_c = 38.18\ \mathrm{nm}^{-2}$ being the area density of carbon atoms, and

$$f_\pm = 231\beta^{11}(\gamma E_{13} \pm E_{11}) - 160\beta^5(\gamma E_7 \pm E_5), \tag{16}$$

where $\beta = \sigma/(r_{out} + r_{inn})$, $\gamma = h/(r_{out} + r_{inn})$, $h = r_{out} - r_{inn}$, $E_m = \int_0^{\pi/2}(1 - k^2\sin^2\theta)^{-m/2}d\theta$, and $k = 4r_{inn}r_{out}/(r_{inn} + r_{out})^2$.

In the following, we derive analytical expressions for $c_{i,j}$ by linearizing the formula (15) for the pressure. The formula takes into account correctly the normal-to-wall component of vdW forces, and it avoids common assumptions such as $p_{inn} = p_{out}$ (Pantano et al. (2004)) and $p_{inn}r_{inn} = p_{out}r_{out}$ (Ru (2001b)); therefore, the resulting $c_{i,j}$ coefficients will also be free from unnecessary assumptions.

As far as infinitesimal deformation is considered, the linearized pressure is needed for the vdW energy calculation. Note that the vdW energy depends quadratically on the change in spacing between two adjacent walls. Consider two consecutive walls with radii r_i and r_{i+1}, where the subscripts i and $i+1$ correspond to *inn* and *out*, respectively. The vdW energy stored by the symmetric perturbation along the positive direction of pressure is given by

$$U_I^{(i,i+1)} \approx \frac{r_m}{2}\int_0^{2\pi}\left(-p_{i,i+1}\frac{\Delta h}{2} - p_{i,i+1}\frac{\Delta h}{2}\right)d\theta, \tag{17}$$

where $r_m = (r_i + r_{i+1})/2$ is the mean radius and $p_{i,i+1}$ is the vdW pressure on the ith wall. The corresponding linearized pressure is given by $\partial p_{i,i+1}/\partial h\big|_{r_m}$. In Eq. (17), $r_m d\theta$ describes the length of the infinitesimal element on which the pressure is acting. Using the linearized pressure and comparing with Eq. (11), we get the following expressions for the vdW coefficients:

$$c_{i,i+1} = -\frac{1}{4}\left(\frac{\partial p_{i,i+1}}{\partial h} + \frac{\partial p_{i+1,i}}{\partial h}\right), \tag{18}$$

where

$$\begin{aligned}\left.\frac{\partial p_{i,i+1}}{\partial h}\right|_{r_m} &= \frac{2\,\alpha\, r_m}{(r_m - h/2)^2} f_- + \alpha\left(\frac{r_m + h/2}{r_m - h/2}\right)\frac{\partial f_-}{\partial h},\\ \left.\frac{\partial p_{i+1,i}}{\partial h}\right|_{r_m} &= -\frac{2\,\alpha\, r_m}{(r_m + h/2)^2} f_+ + \alpha\left(\frac{r_m - h/2}{r_m + h/2}\right)\frac{\partial f_+}{\partial h}.\end{aligned} \tag{19}$$

Note that the $c_{i,j}$ matrix is symmetric. See Ref. Shima et al. (2012) for the derivatives of $\partial f_\pm/\partial h$. As a result, the vdW interaction energy $U_I^{(i,j)}$ that contributes to the total deformation energy U given in Eq. (12) is defined by Eqs. (17)–(19).

11 Remarks on Radial Deformation

Before closing this chapter, three additional topics warrant remarks. First is the possibility of nanotubes having radial corrugation free from external pressure. Interestingly, cross sections of MWNTs synthesized in the presence of nitrogen have been found to form polygonal shapes rather than circular shapes (Ducati et al. (2006)). It was argued that the polygonization may result from interlayer thermal contraction upon cooling or interwall adhesion energy owing to the increased interwall commensuration (Ducati et al. (2006)). This conjecture implies pressure-free radial corrugation and/or another class of radial deformation that arises when the interwall spacings of MWNTs deviate from the vdW equilibrium distance ($\sim$0.34 nm). These facts motivated the MD-based structural optimization performed in Ref. Huang et al. (2011). In the simulations, the initial cross sections of all the MWNTs are set to be of circular shape and the interwall spacing is 0.359

Fig. 13 Cross-sectional views of relaxed MWNTs indexed by (2,8)/(4,16)/. . ./(2*n*,8*n*). The wall numbers *n* are 5, 10, 15, 20, and 25 from *left* to *right*, and all the MWNTs are 20 nm long. After Ref. Huang et al. (2011)

nm, which is 0.19 nm larger than the equilibrium spacing of two graphene sheets (= 0.34 nm). Figure 13 depicts the cross-sectional configurations of relaxed MWNTs obtained by the simulations. The results showed that the cross sections stabilized at polygonal or water-drop-like shapes, depending on the artificially expanded interwall spacings. It is seen that the 15-walled tube is stabilized at a polygonal cross-sectional configuration with six rounded corners. For the 20- and 25-walled ones, the configuration becomes asymmetric, featuring a water-drop-like morphology. Special localization of surface curvature along the ridge line in the water-drop patterns may be utilized for carbon nanotube functionalization, because large distortion of the bonding angle of three carbon atoms at the severely curved region provides chemical activity high enough to make chemical bonding to other guest atoms or molecules at the outmost graphene layer.

The second topic concerns the nanoengineering perspective associated with the cross-sectional deformation. We insist that the selectivity of the innermost wall geometry by tuning the material parameters may be useful in developing nanotube-based nanofluidic (Majumder et al. (2005); Noy et al. (2007); Whitby and Quirke (2007)) or nanoelectrochemical devices (Frackowiak and Beguin (2002)), because both utilize the hollow cavity within the innermost tube. A very interesting issue from an academic viewpoint is the effect of the core tube deformation on the physical and chemical properties of intercalated molecules confined in the hollow cavity. It has thus far been known that various types of intercalated molecules (diatomic gas, water, organic and transition metal molecules, etc.) can fill the innermost hollow cavities of nanotubes (Noy et al. (2007)) and exhibit intriguing behaviours that are distinct from those of the corresponding bulk systems. (Yang (2003); Maniwa et al. (2007)) These distinct behaviours originate from the fact that the intermolecular spacings become comparable to the linear dimension of the nanoscale confining space. Therefore, the core tube deformation that breaks the cylindrical symmetry of the initial nanoscale compartment will engender unique properties of intercalated molecules that are peculiar to the constrained condition in a radially corrugated space.

The last interesting implication is a pressure-driven change in the quantum transport of π electrons moving along the radially deformed nanotube. We have learned in the previous sections that mobile electrons whose motion is confined to a two-dimensional, curved, thin layer behave differently from those on a conventional flat plane because of an effective electromagnetic field that can affect low-energy

excitations of the electrons. Associated variations in the electron–phonon coupling (Ono and Shima (2011a)) and phononic transport (Ono and Shima (2011b)) through the deformed nanocarbon materials are also interesting and relevant to the physics of radially corrugated MWNTs.

12 Summary

In this chapter, we have had an overview of the progress achieved in the field of "geometry–property relations" that are realized in corrugated nanocarbon cylinders. We focussed on two particular topics: quantum transport in the peanut-shaped C_{60} polymers and radial corrugation of multiwall carbon nantoubes under hydrostatic pressure. In the former materials, the Hamiltonian of a quantum particle involves a curvature-induced effective potential field, which results in the sizable shift in the TLL exponent compared with its straight (noncorrugated) counterpart. In the latter case, we have seen the wide variety of radial corrugation patterns of pressurized nanotubes and theoretical models for them, which imply the potential utility for designing nanotube-based devices. The discussion of the geometry–property relations presented here will hopefully pave the way for the prediction of novel, still uncovered phenomena, particularly those occurring in nanocarbon materials.

References

Arvanitidis J, Christofilos D, Papagelis K, Andrikopoulos KS, Takenobu T, Iwasa Y, Kataura H, Ves S, Kourouklis GA (2005) Phys Rev B 71:125404
Baek SK, Shima H, Kim BJ (2009) Phys Rev E 79:060106
Barboza APM, Gomes AP, Archanjo BS, Araujo PT, Jorio A, Ferlauto AS, Mazzoni MSC, Chacham H, Neves BRA (2008) Phys Rev Lett 100:256804
Barboza APM, Chacham H, Neves BRA (2009) Phys Rev Lett 102:025501
Beu TA, Onoe J, Hida A (2005) Phys Rev B 72:155416
Brenner DW (1990) Phys Rev B 42:9458
Brenner DW (1992) Phys Rev B 46:1948 (Erratum)
Byrne EM, McCarthy MA, Xia Z, Curtin WA (2009) Phys Rev Lett 103:045502
Chandraseker K, Mukherjee S (2007) Comp Mater Sci 40:147
Charlier JC, Eklund PC, Zhu J, Ferrari AC (2008) Electron and phonon properties of graphene: Their relationship with carbon nanotubes. In: Jorio A, Dresselhaus G, Dresselhaus MS (eds) Carbon nanotubes. Advanced topics in the synthesis, structure, properties and applications, vol 111. Springer, Berlin, pp 673–709
Christofilos D, Arvanitidis J, Kourouklis GA, Ves S, Takenobu T, Iwasa Y, Kataura H (2007) Phys Rev B 76:113402
da Costa RCT (1981) Phys Rev A 23:1982
Cuoghi G, Ferrari G, Bertoni A (2009) Phys Rev B 79:073410
De Witt B (1952) Phys Rev 85:635
De Witt B (1957) Rev Mod Phys 29:377
Diniz EM, Nunes RW, Chacham H, Mazzoni MSC (2010) Phys Rev B 81:153413
Duan XJ, Tang C, Zhang J, Guo WL, Liu ZF (2007) Nano Lett 7:143

Ducati C, Koziol K, Friedrichs S, Yates TJV, Shaffer MS, Midgley PA, Windle AH (2006) Small 2:774
Elliott JA, Sandler LKW, Windle AH, Young RJ, Shaffer MSP (2004) Phys Rev Lett 92:095501
Falvo MR, Clary GJ, Taylor RM II, Chi V, Brooks FP Jr, Washburn S, Superfine R (1997) Nature 389:582
Filleter T, Bernal R, Li S, Espinosa HD (2011) Adv Mater 23:2855
Fonseca AF, Borders T, Baughman RH, Cho K (2010) Phys Rev B 81:045429
Frackowiak E, Beguin F (2002) Carbon 40:1775
Gadagkar V, Maiti PK, Lansac Y, Jagota A, Sood AK (2006) Phys Rev B 73:085402
Girifalco LA, Hodak M, Lee RS (2000) Phys Rev B 62:13104
Giusca CE, Tison Y, Silva SRP (2008) Nano Lett 8:3350
Grüner G (1994) Density waves in solids. Addison-Wesley, Reading
Gupta SS, Bosc FG, Batra RC (2010) Comp Mater Sci 47:1049
Gupta S, Saxena A (2012) J Appl Phys 112:114316
Hasegawa M, Nishidate K (2006) Phys Rev B 74:115401
He XQ, Kitipornchai S, Liew KM (2005) J Mech Phys Solids 53:303
Hebard AF, Haddon RC, Fleming RM, Kortan AR (1991) Appl Phys Lett 59:2109
Huang Y, Wu J, Hwang KC (2006) Phys Rev B 74:245413
Huang X, Liang W, Zhang S (2011) Nanoscale Res Lett 6:53
Ishii H, Kataura H, Shiozawa H, Yoshioka H, Otsubo H, Takayama Y, Miyahara T, Suzuki S, Achiba Y, Nakatake M, Narimura T, Higashiguchi M, Shimada K, Namatame H, Taniguchi M (2003) Nature 426:540
Jensen H, Koppe H (1971) Ann Phys 63:586
Jeong BW, Lim JK, Sinnott SB (2007) Appl Phys Lett 91:093102
Jeong BW, Lim JK, Sinnott SB (2008) Appl Phys Lett 92:253114
Krasheninnikov AV, Nordlund K (2010) J Appl Phys 107:071301
Kudin KN, Scuseria GE, Yakobson BI (2001) Phys Rev B 64:235406
Kutana A, Giapis KP (2006) Phys Rev Lett 97:245501
Lu WB, Liu B, Wu J, Xiao J, Hwang KC, Fu SY, Huang Y (2009) Appl Phys Lett 94:101917
Lu W (2011) Tsu-Wei Chou, T.W.; Byung-Sun Kim, B.S. Phys Rev B 83:134113
Majid MJ, Yu MFJ (2008) J Appl Phys 103:073516
Majumder M, Chopra N, Andrews R, Hinds BJ (2005) Nature 438:438
Maniwa Y, Matsuda K, Kyakuno H, Ogasawara S, Hibi T, Kadowaki H, Suzuki S, Achiba Y, Kataura H (2007) Nat Mater 6:135
Mao Y, Wang WL, Wei D, Kaxiras E, Sodroski JG (2011) ACS Nano 5:1395
Marchi A, Reggiani S, Rudan M, Bertoni A (2005) Phys Rev B 72:035403
Nakayama H, Ono T, Goto H, Hirose K (2007) Sci Tech Adv Mater 8:196
Ni B, Sinnott SB, Mikulski PT, Harrison JA (2002) Phys Rev Lett 88:205505
Noy A, Park HG, Fornasiero F, Holt JK, Grigoropoulos CP, Bakajin O (2007) Nano Today 2:22
Ono S, Shima H (2011a) Europhys Lett 96:27011.
Ono S, Shima H (2011b) J Phys Soc Jpn 80:064704
Onoe J, Nakayama T, Aono M, Hara T (2003) Appl Phys Lett 82:595
Onoe J, Ito T, Kimura S, Ohno K, Noguchi Y, Ueda S (2007) Phys Rev B 75(23):233410
Onoe J, Ito T, Shima H, Yoshioka H, Kimura S (2012) EPL 98:27001
Ortix C, Kiravittaya S, Schmidt OG, van den Brink J (2011) Phys Rev B 84:045438
Oshiyama A, Saito S, Hamada N, Miyamoto Y (1992) J Phys Chem Solid 53:1457
Palaci I, Fedrigo S, Brune H, Klinke C, Chen M, Riedo E (2005) Phys Rev Lett 94:175502
Pantano A, Parks DM, Boyce MC (2004) J Mech Phys Solid 52:789
Peters MJ, McNeil LE, Lu JP, Kahn D (2000) Phys Rev B 61:5939
Poncharal P, Wang ZL, Ugarte D, de Heer WA (1999) Science 283:1513
Reich S, Thomsen C, Ordejón P (2003) Phys Rev B 65:153407
Rols S, Gontcharenko IN, Almairac R, Sauvajol JL, Mirebeau I (2001) Phys Rev B 64:153401
Ru CQ (2000a) J Appl Phys 87:7227
Ru CQ (2001a) J Appl Phys 89:3426

Ru CQ (2000b) Phys Rev B 62:16962
Ru CQ (2001b) J Mech Phys Solids 49:1265
Sakurai M, Saito S (2011) Physica E 43:673
Sanders JL Jr (1963) Quart Appl Math 21:21
Sears A, Batra RC (2006) Phys Rev B 73:085410
Sharma SM, Karmakar S, Sikka SK, Teredesai PV, Sood AK, Govindaraj A, Rao CNR (2001) Phys Rev B 63:205417
Shima H, Sakaniwa Y (2006) J Phys A: Math Gen 39:4921
Shima H, Sato M (2008) Nanotechnology 19:495705
Shima H, Sato M, Iiboshi K, Ghosh S, Arroyo M (2010) Phys Rev B 82:085401
Shima H, Ono S, Yoshioka H (2010) Eur Phys J B 71:481
Shima H, Yoshioka H (2011) Chem Phys Lett 513:224
Shima H, Ghosh S, Arroyo M, Iiboshi K, Sato M (2012) Comp Mater Sci 52:90
Shima H (2012) Materials 5:47
Shima H, Sato M (2013) Elastic and plastic buckling of carbon nanotubes, 1st edn. Pan Stanford Publishing, Singapore
Shima H, Nakayama T (2009) Higher mathematics for physics and engineering. Springer, London
Shima H, Umeno Y, Sato M (2013) Mech Adv Mater Str (in press)
Shima H, Yoshioka H, Onoe J (2009) Phys Rev B 79:201401(R)
Stone AJ, Wales DJ (1986) Chem Phys Lett 128:501
Sun DY, Shu DJ, Ji M, Liu F, Wang M, Gong XG (2004) Phys Rev B 70:165417
Szameit A, Dreisow F, Heinrich M, Keil R, Nolte S, Tunnermann A, Longhi S (2010) Phys Rev Lett 104:150403
Taira H, Shima H (2007) Surf Sci 601:5270
Takashima A, Onoe J, Nishii T (2010) J Appl Phys 108:033514
Tang J, Qin JC, Sasaki T, Yudasaka M, Matsushita A, Iijima S (2000) Phys Rev Lett 85:1887
Tangney P, Capaz RB, Spataru CD, Cohen ML, Louie SG (2005) Nano Lett 5:2268
Terrones H, Terrones M (2003) New J Phys 5:126
Thirunavukkuarasu K, Hennrich F, Kamarás K, Kuntscher CA (2010) Phys Rev B 81:045424
Toda Y, Ryuzaki S, Onoe J (2008) Appl Phys Lett 92:094102
Venkateswaran UD, Rao AM, Richter E, Menon M, Rinzler A, Smalley RE, Eklund PC (1999) Phys Rev B 59:10928
Voit J (1994) Rep Prog Phys 57:977
Wang Q (2008) Carbon 46:1172
Wang Q (2009) Carbon 47:1870
Wang X, Yang HK (2006) Phys Rev B 73:085409
Wang X, Sun B, Yang HK (2006) Nanotechnology 17:815
Wang Q, Liew KM, He XQ, Xiang Y (2007) Appl Phys Lett 73:093128
Waters JF, Guduru PR, Jouzi M, Xu JM, Hanlon T, Suresh S (2005) Appl Phys Lett 87:103109
Waters JF, Riester L, Jouzi M, Guduru PR, Xu JM (2004) Appl Phys Lett 85:1787
Whitby M, Quirke N (2007) Nature Nanotechnol. 2:87
Xia ZH, Guduru PR, Curtin WA (2007) Phys Rev Lett 98:245501
Yakobson BI, Brabec CJ, Bernholc J (1996) Phys Rev Lett 76:2511
Yang CK, Zhao J, Lu JP (2003) Phys Rev Lett 90:257203
Yang X, Wu G, Dong J (2006) Appl Phys Lett 89:113101
Yang X, Wu G (2008) EPL 81:47003
Yang YH, Li WZ (2011) Appl Phys Lett 98:041901
Zhang S, Khare R, Belytschko T, Hsia KJ, Mielke SL, Schatz GC (2006) Phys Rev B 73:075423
Zhang E, Zhang S, Wang Q (2007) Phys Rev B 75:085308
Zhang CL, Shen HS (2007) Phys Rev B 75:045408
Zhang YY, Wang CM, Xiang YJ (2011) J Appl Phys 109:083516

Prediction of Mechanical Properties of CNT Based Composites Using Multi-Scale Modeling and Stochastic Analysis

Roham Rafiee and Mahmood M. Shokrieh

Abstract The main goal of this chapter is to predict Young's modulus and Poisson's ratio of carbon nanotube reinforced polymer (CNTRP). Since carbon nanotubes (CNTs) appear at the scale of nano and the mechanical properties of CNTRP are needed to be extracted at the scale of macro, a full-range multi-scale modeling technique covering all scales of nano, micro, meso and macro is developed. The developed technique consists of two phases as top-down scanning and bottom-up modeling. At the first stage, the material region will be scanned from the macro level downward to the nano scale and effective parameters of each and every scale are identified accordingly. In the second stage, a hierarchical multi-scale modeling is developed. This modeling strategy will analyze the material at each scale and obtained results are fed to the upper scale as input information. Due to uncertainties arisen from processing of CNTRP, the full stochastic implementation of modeling is employed treating length, orientation, agglomeration, waviness and volume fraction of CNTs as random parameters. It is revealed that the developed modeling procedure provides a clear insight to the properties of CNTRP.

Keywords Carbon nanotube · Nanocomposites · Mechanical properties Multi-scale modeling · Stochastic analysis

R. Rafiee (✉)
Composites Research Laboratory, Faculty of New Sciences and Technologies, University of Tehran, 1439955941 Tehran, Iran
e-mail: Roham.Rafiee@ut.ac.ir

M. M. Shokrieh
Composites Research Laboratory, Mechanical Engineering Department, Iran University of Science and Technology, 1684613114 Tehran, Iran
e-mail: Shokrieh@iust.ac.ir

K. I. Tserpes and N. Silvestre (eds.), *Modeling of Carbon Nanotubes, Graphene and their Composites*, Springer Series in Materials Science 188,
DOI: 10.1007/978-3-319-01201-8_7,

1 Introduction

Exceptional and supreme mechanical, electrical and thermal properties of carbon nanotubes (CNTs) (Dai 2002; Kang et al. 2006; Salvetat-Delmotte and Rubio 2002; Lau and Gu 2006) as well as their low density and high aspect ratio (Thostenson et al. 2001, 2005) rendered them as a good reinforcing agent candidate for polymer matrix composites. Incorporating CNT into the polymer, new generation of composite materials is evolving and has received extreme attention in recent years. There are some evidences demonstrating significant enhancement in the mechanical properties of polymeric resin by exploiting small portion of CNTs (Qian et al. 2000; Schadler et al. 1998; Zhu et al. 2004). Consequently, an accurate prediction of the mechanical properties of CNTRP plays an important role in understanding their behavior and it is a vital issue to pave the road toward their prospective industrial applications.

While experimental study of CNTRP is a challenging task due to different imposed limitations and obstacles (Spitalsky et al. 2009), theoretical modeling and simulation techniques can provide insight into their properties. Tremendous researches have been carried out to determine mechanical properties of CNTRP both experimentally (Spitalsky et al. 2009) and theoretically (Thostenson et al. 2005; Shokrieh and Rafiee 2010; Gibson 2007; Odegard et al. 2003). It can be inferred from a literature survey on conducted theoretical investigations for predicting Young's/bulk modulus of CNTRP that they are suffering from different drawbacks and/or invalid assumptions (Shokrieh and Rafiee 2010).

Micromechanics rules cannot be directly used to extract mechanical properties of CNTRP, since they have been basically developed for continuum reinforcement phase (Gibson 2007) which is not pertinent to the lattice structure of CNT. It has been shown that direct application of micromechanics equations will result in improper results (Odegard et al. 2003; Ashrafi and Hubert 2006; Han and Elliott 2007; Villoria and Miravete 2007; Tserpes et al. 2008; Frankland et al. 2003; Mokashi et al. 2007; Shokrieh and Rafiee 2009; Selmi et al. 2007; Seidel and Lagoudas 2006; Liu et al. 2005) and they are not able to capture the scale difference between the micro and nano levels. In other word, micromechanics equations cannot take into account the scale of nano, since the first scale of modeling process in those equations is micro.

Direct application of micromechanics equations for CNTRP will simply neglect the lattice structure of CNT and consider CNT as a solid fiber. Moreover, micromechanics equations assume perfect bonding between reinforcing agents and the surrounding polymer (Gibson 2007), which is not pertinent to the interphase between CNT and surrounding polymer interacting naturally through non-bonded van der Waals (vdW) interactions (Lordi and Yao 2000).

Although researches tried to disperse CNT in polymer using sonication techniques to some extent (Mukhopadhyay et al. 2002; Coleman et al. 2006; Tjong 2006; Esawi and Farag 2007), it is extremely difficult to achieve a homogenous medium. Consequently, it is not recommended to use homogenization methods for modeling.

Moreover, the lack of control of their dispersion diminishes the effectiveness of CNT reinforcements in composites due to formation of local aggregates in the form of bundled CNTs. Thus, dispersion of CNTs in different points of the material region does not follow a uniform pattern as a result of agglomeration of CNTs. Therefore, localized homogenous regions should be distinguished at lower scales prior to application of these techniques and they should be employed at those specific regions.

Thanks to the very large aspect ratio and low bending stiffness of CNTs, they are highly experiencing a non-straight shape in the matrix. This also stems from induced uncertainties during the processing of CNTRP. The non-straight shapes of CNTs play a key role in weakening capability of CNT as reinforcement in comparison with straight CNTs. Consequently, neglecting non-straight shapes of CNTs is an important factor resulting in a difference between mechanical properties determined by theoretical models and corresponding experimentally measured ones.

The existence of abovementioned uncertainties consisting of a non-uniform dispersion, agglomeration and non-straight shapes of CNTs necessitates implementation of a stochastic modeling, while deterministic approaches simply overlook them. The main reason of reported discrepancies between experimental observations and theoretical modeling (Lau and Gu 2006) can be routed to the ignorance of uncertainties using deterministic approaches.

Performing a review on the literature (Shokrieh and Rafiee 2010), it can be observed that theoretical investigations on the mechanical properties prediction of CNT reinforced polymers can be divided into three groups as atomistic modeling, continuum modeling (analytical and numerical) and multi-scale methods.

Utilizing the atomistic modeling for composites in order to study their local behavior at nonoscale is inevitable. However, molecular dynamic simulation is limited to small length and short time scales. For instance, all results of molecular simulations for CNT composites are limited to those models comprising one CNT in the polymer matrix. Characterization of a CNT composite requires only the knowledge of its global responses, such as the displacement and stress fields at the boundaries of an RVE. Thus the continuum mechanics approaches may be adequate and sufficient in modeling CNT composites in this regard. Along these methods, the preferred approach for the simulations of CNT composites should be a multi-scale one where the molecular dynamics (MD) and continuum mechanics are integrated in a computing environment that is detailed enough to account for the physics at nanoscale while efficient enough to handle CNT composites at larger length scales (Gates et al. 2005).

2 Framework of the Developed Modeling Technique

In addition to the importance of stochastic modeling to address aforementioned process induced uncertainties in the material region of CNTRP, the wide range of involved scales requires a full-range multi-scale modeling approach covering all

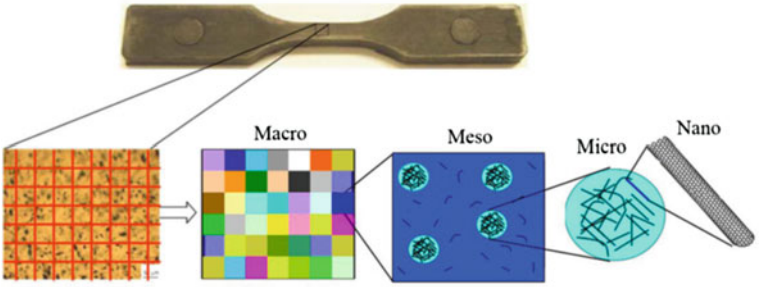

Fig. 1 Involved scales in simulation of CNT-based composites

scales of nano, micro, meso and macro. Subsequently, stochastic multi-scale approach is intended to be developed in this chapter to predict Young's modulus and Poisson's ratio of CNTRP.

In contrast to conventional composite materials wherein reinforcing agent appears at the scale of micro, the starting scale in the modeling of CNT-based composites is shifted to the scale of nano. Young's modulus and Poisson's ratio of a specimen made of CNTRP is characterized at the scale of macro. Different involved length scales are schematically depicted in Fig. 1.

The modeling procedure comprises of three different stages: (i) top-down scanning, (ii) bottom-up modeling and (iii) stochastic implementation.

Different introduced levels associated with the material region of CNTRP demand identification of effective parameters at each and every scale. A top-down scanning is performed to distinguish effective parameters of different involved scales. Namely, involved parameters of modeling and their associated effective scale are required to be recognized via top-down scanning of material region.

As a subsequent, an isolated separate representative volume element (RVE) should be defined for each scale separately to capture corresponding effective parameters, accordingly. The involved parameters categorized by effective scales are presented in Table 1.

It should be noted that a non-uniform dispersion of CNT at meso-scale is different from a non-uniform distribution of inclusions at macro-scale. Distribution

Table 1 Effective parameters for each scale of simulation

Effective scale	Effective length	Parameters
Nano	nm	Molecular interactions, bond configurations, CNT diameter, CNT chirality
Micro	nm/μm	Interaction between CNT and polymer, Stress transfer in interphase, CNT length
Meso	μm	Volume fraction, orientation of CNT, Agglomeration, Dispersion, CNT curvature
Macro	mm	Non-uniform distribution of inclusions, mechanical properties

of CNT at micro-scale addresses the degree to which material region experiences inhomogeneity, however, dispersion of CNT at meso-scale accounts for agglomeration of CNT.

3 *N3M* Multi-scale Modeling

A hierarchical multi-scale modeling will be developed to predict the mechanical properties of CNTRP. Since the developed technique will cover all scales of nano, micro, meso and macro, it will be referred to hereinafter as "N3M" multi-scale modeling. The N3M modeling starts from nano-scale and will last in macro scale passing the in-between scales of micro and meso. The output of each scale will be fed as input data to the very proceeding scale of study. Different stages of proposed modeling procedure at each scale which will be constructed on the basis of bottom-up modeling approach will be outlined in proceeding sections.

3.1 Nanoscale Modeling

As it is reflected in Table 1, a proper RVE at the nano scale should be able to capture molecular interactions of carbon–carbon (C–C) bonds, bond configuration, CNT diameter and its chirality.

Atomistic modeling, continuum modeling and nano-scale continuum modeling are three main approaches to simulate the CNT. Generally, the main drawbacks of atomistic modeling can be summarized as:

1. Limitation of short/small time/length scale on the order of pico-second/nanometer
2. Not being applicable to models including large number of atoms
3. Huge amount of computational efforts
4. Complex formulations.

On the other hand, it is not permissible to treat CNT as a solid/hollow cylinder as mentioned parameters will be neglected and it is vital to keep the lattice structure of CNT in the modeling procedure in order to address the effective parameters of nanoscale. Therefore, those continuum techniques penetrating into smaller length scales with a successful establishment of a linkage between molecular configuration and solid mechanics are known as nano-scale continuum methods and are preferable methods to simulate nanostructure materials (Odegard et al. 2002; Zhang et al. 2002; Gao and Li 2003; Wang 2004). In contrast to continuum modeling of CNTs wherein the whole nano-structure is replaced with a continuum medium, nano-scale continuum modeling provides a rationally acceptable compromise in the modeling process by replacing C–C bond with a

continuum element. In other word, the molecular interactions between C–C bonds are captured using structural members whose properties are adjusted to simulate governing interatomic potentials.

Li and Chou (Li and Chou 2003) developed a molecular structural mechanics approach by establishing an equivalence between the interatomic potential energies of molecular structure and the strain energies of an equivalent beam element representing each C–C bond. Schematic representation of established analogy is demonstrated in Fig. 2.

The illustrated correlation is accomplished by linking the molecular mechanics constants of force fields to frame sectional stiffness parameters using below equations:

$$EA/L = k_r, \quad EI/L = k_\theta, \quad GJ/L = k_\tau \tag{1}$$

where k_r, k_θ and k_τ are the bond stretching force constant, bond angle bending force constant, and torsional resistance. E, A, I, G and J represent Young's modulus, cross section area, moment of inertia, shear modulus and polar moment of inertial of the beam, respectively.

Following the developed analogy by Li and Chou (Li and Chou 2003) stated in Eq. (1) and assuming a circular cross section with diameter d, geometrical parameters and mechanical properties of a load bearing beam element representing C–C bonds can be obtained as below (Tserpes and Papanikos 2005):

$$d = 4\sqrt{\frac{k_\theta}{k_r}}, \quad A = \frac{\pi d^2}{4}, \quad J = 2I = \frac{\pi d^4}{32}, \quad E = \frac{k_r^2 L}{4\pi k_\theta}, \quad G = \frac{k_r^2 k_\tau L}{8\pi k_\theta^2} \tag{2}$$

where L is length of the C–C bond and is chosen as 0.142 nm. The following parameters are utilized using AMBER force filed parameters (Cornell et al. 1991):

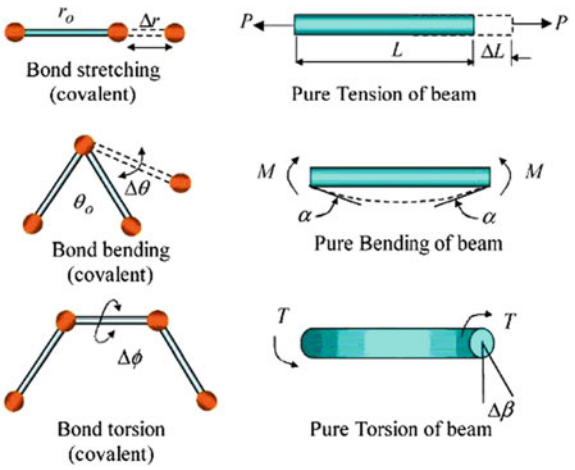

Fig. 2 Energy equivalence between molecular mechanics (*left*) and structural mechanics (*right*) (Kalamkarov et al. 2006)

$$k_r = 6.52 \times 10^{-7}\left[\frac{N}{nm}\right],\ k_\theta = 8.76 \times 10^{-10}\left[\frac{N.nm}{rad^2}\right],\ k_\tau = 2.78 \times 10^{-10}\left[\frac{N.nm}{rad^2}\right] \tag{3}$$

Each C–C bond was replaced with beam element and lattice molecular structure was substituted with equivalent discrete frame structure. The Cartesian coordinates of carbon atoms in a carbon nanotube is produced using developed code in Mathematica platform (Wolfarm 1999) and fed into ANSYS as nodal coordinates of finite element model. Each node is connected to other three adjacent nodes using built-in BEAM4 element (Theory Manual 2003) of ANSYS via developed macro. Different finite element models of single-walled carbon nanotubes (SWCNTS) with various diameters and chiralities are constructed. For instance, the FE model of Armchair CNT with chiral index of (10, 10) is shown in Fig. 3. The models are subjected to uniform tensile axial displacement at one end, while the other end is restricted from the movement in axial direction and it is free to move in radial direction. The length of the CNT along its longitudinal axis is 10 times larger than its radius to prohibit any edge effects.

Two different load cases as axial tension and torsional tension are investigated to extract the longitudinal and shear moduli of the CNT. In order to obtain the longitudinal Young's modulus of SWCNT, the resultant forces on constraint will be read as the output of FEA and below equation is used:

$$E = \frac{FL_{CNT}}{\Delta L A} \tag{4}$$

where, F is resultant force on constraint, L_{CNT} is the length of CNT, $\Delta L$is applied displacement and A is the cross section of CNT. The cross section of CNT is obtained using below equations:

Fig. 3 Finite element model of (10, 10) CNT subjected to axial displacement

$$A = \pi dt, \tag{5}$$

$$d = \frac{\sqrt{3}L}{\pi}\sqrt{(n^2 + m^2 + nm)} \tag{6}$$

where L represents C–C bond length which is taken as 0.142 nm and *(n, m)* resembles of CNT chiral index. Denoted by *t*, thickness of CNT is a challenging value. There is not a consistent value for the thickness of CNT thickness in literature (Robertson et al. 1992; Lu 1997; Yao and Lordi 1998; Hernandez et al. 1999; Jin and Yuan 2003; Yakobson et al. 1996; Arroyo and Belytschko 2004) which is a virtual value. Some researchers employed interlayer spacing between adjacent graphene sheets in graphite (0.34 nm) as the equivalent thickness of graphene sheet (Robertson et al. 1992; Lu 1997; Yao and Lordi 1998; Hernandez et al. 1999; Jin and Yuan 2003), while others obtained different results as 0.066 nm (Yakobson et al. 1996) or 0.68 and 0.57 (Odegard et al. 2002) for this parameter. Chang and Gao (2003) and Arroyo and Belytschko (2004) introduced a new definition of Young's modulus entitled as surface Young's modulus which is a conventional Young's modulus multiplied by the thickness. This definition coincides with the in-plane stiffness of plates and shells in solid mechanics. The widely accepted value of 0.34 nm is employed here in order to be able to compare the results with the published data in the literature.

The calculated mechanical properties of the CNT is summarized in Table 2 and compared with either the published data or experimental observations.

It is worth mentioning that all theoretical results illustrated in Table 2 employed the same magnitude of force fields as mentioned in Eq. (3). The very good agreement between obtained result and published data verifies the proper modeling of isolated CNT.

The present results are lower than predicted results utilizing spring element. The reason is placed behind the different behavior of spring and beam elements. The beam elements can bend while the spring elements cannot bend and stay

Table 2 Comparison between reported results for mechanical properties of SWCNT

Researchers	Employed technique	Young's modulus (TPa)	Shear modulus (TPa)
Li and Chou (2003)	FEM (Beam element)	1.010	0.475
Tserpes and Papakinos (2005)	FEM (Beam element)	1.028	0.410
Giannopoulos et al. (2008)	FEM (Spring element)	1.327	0.416
Shokrieh and Rafiee (2009)	Closed form solution (Beam element)	1.033–1.042	–
Present work[a]	FEM (Beam element)	1.046	0.424
Krishnan et al. (1998)	Thermal vibrations	0.9–1.7	–
Salvetat-Delmotte et al. (1999)	Atomic force microscope	0.8 ± 0.41	–

[a] for the chiral index of (10, 10)

straight. Therefore, the whole applied load will stretch the spring elements while a portion of load will be devoted to the bending of beam elements. Consequently, the obtained global axial deformation of spring-based models is slightly higher than beam-based models.

The results of Young's modulus of CNT show a monotonic increasing trend versus tube diameter and approached to the Young's modulus of a graphene sheet for higher values of tube diameters. This trend was also reported by developed analytical solution (Shokrieh and Rafiee 2009).

3.2 Microscale Modeling

At this level, interaction between the CNT and its surrounding polymer has to be studied accounting for load transferring from the matrix to the CNT. Besides the mechanical properties of isolated CNT, the efficiency of a CNT can be attributed to the load transferring mechanism from the matrix to CNT at nano/micro-scale which accomplishes through interphase region between CNT and surrounding polymer. The RVE of this scale encompasses of an embedded CNT, surrounding polymer and interphase region between the CNT and matrix. The appropriate RVEs of this scale are depicted in Fig. 4.

3.2.1 Finite Element Modeling of RVE at Microscale

The same modeling procedure explained at nanoscale is employed for modeling CNT. An armchair SWCNT with chiral index of (10, 10) is selected for this study. Since the length of the CNT is less than length of surrounding polymer, a capped CNT with a hemispherical section of C_{240} molecules is used. Due to symmetry, the half length of the RVE is constructed as depicted in Fig. 5.

Solid element is used to simulate the surrounding polymer as a continuum medium. The size of each element is selected as small as the length of hexagon rings on the lattice structure of the CNT.

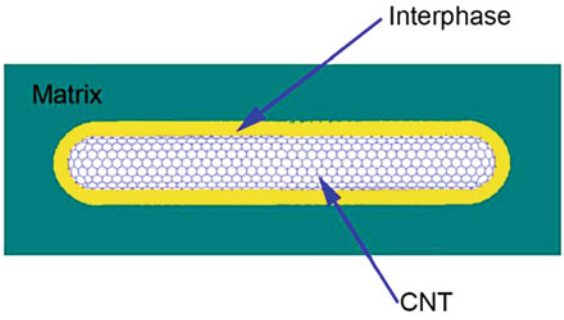

Fig. 4 The RVE at microscale consisting of CNT, interphase and matrix

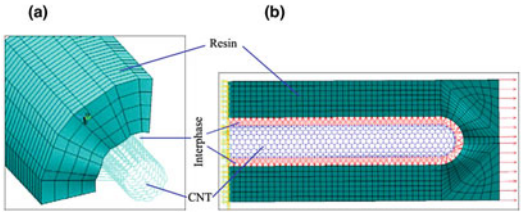

Fig. 5 The FE model of the RVE at microscale (Shokrieh and Rafiee 2009). **a** Cut section of RVE. **b** Side view of RVE with short CNT

Since the volume fraction of CNTs is about 0.1–2 % in composites, subsequently, the volume of polymer matrix is much higher than that of CNTs at molecular scale. It means that simulating the chains of polymer using an atomistic modeling needs a huge amount of atoms and computations at nano scale. Generally, atomistic modeling techniques are limited to model small length scale systems and they are suffering from simulating systems including large number of atoms. On the other hand, the molecular chains of surrounding polymer are considerably tight and provide a high density space in comparison with CNTs. Therefore, as a reasonable compromise, surrounding polymer is taken into account as a continuum medium and solid elements are used to construct the 3D-FEM of the thick resin at the microscale. In other word, a concurrent multi-scale finite element modeling approach is employed wherein CNT is treated at the nano-scale while the resin is modeled at the micro-scale. SOLID95 element was employed for this purpose (Theory Manual 2003) which is a 3-D element with 20 nodes. The element has three degrees of freedom per each node which are translations in x, y and z directions. This brick element has compatible displacement shape and is well suited to model a curved boundary (Theory Manual 2003). Knowing this fact that molecular chain of polymer matrix cannot penetrate into the CNT, the size of this brick element is selected as small as the length of hexagonal rings of CNTs in axial. As a subsequent; it is expected that developed model will address the upper band of estimation for expected results in presence of vdW interactions. The depth of the matrix region is calculated in a manner to reflect the 5 % volume fraction for an embedded CNT. The simulated resin was treated as an isotropic material and corresponding mechanical properties (Young's modulus and Poisson's ratio) are selected in a manner to simulate a typical Epoxy matrix available in the market.

CNTs naturally interact with polymer chains of the matrix through weakly non-bonded van der Waals (vdW) and electrostatic interactions (Lordi and Yao 2000). Mechanical interlocking which is useful to improve the adhesion between fiber and matrix in fibrous composites is not pertinent to carbon nanotube reinforced polymer due to the smooth surface of the CNTs (Hull 1996). Although functionalization can improve load transferring issue from matrix to CNT by providing cross covalent links between carbon atoms of CNTs and molecules of polymer (Sinnott 2002; Bahr and Tour 2002; Frankland et al. 2002; Shofner et al. 2006; Buffa et al. 2007; Cooper et al. 2002; Barber et al. 2003), this procedure has a main drawback in providing defects in the nano-structure of CNTs due to formation of sp^3 hybridized sites. It can significantly reduce the supreme properties of CNTs

(Lordi and Yao 2000; Kuang and He 2008). Electrostatic interactions can be neglected in comparison with vdW interactions, since vdW contributes more considerably in three higher orders of magnitude than the electrostatic energy (Gou et al. 2004). Therefore, interphase region is treated as non-bonded vdW interactions in absence of chemical functionalization.

The vdW forces are most often modeled using famous Lennard-Jones "6–12" potential (Li and Chou 2003). The vdW force is a non-linear force and it can be neglected when the interatomic distance is equal or greater than 0.85 nm as it is shown in Fig. 6. The vdW force in term of interatomic distance is presented by Eq. (7) on the basis of Lennard-Jones "6–12" (Li and Chou 2003):

$$F_{vdW} = 4\frac{\varepsilon}{r}\left[-12\left(\frac{\sigma}{r}\right)^{12} + 6\left(\frac{\sigma}{r}\right)^{6}\right] \tag{7}$$

where ε and σ are the Lennard-Jones parameters and 0.0566 kcal/mol and 0.34 nm, respectively (Chang and Gao 2003). The vdW force is a non-linear force consisting of two distinct regions of repulsion and attraction. Furthermore, the vdW interaction can be neglected when the inter-atomic distance is equal or greater than 0.85 nm.

The vdW interaction between the carbon atoms of CNT and the nodes of resin inner surface is modeled using three dimensional non-linear spring elements. Corresponding data of the non-linear curve of vdW force obtained from Lennard-Jones "6–12" potential is fed into the software to capture the non-linear behavior of vdW interactions. COMBIN39 element is used for this purpose and the parameters are adjusted to obtain translational spring (Theory Manual 2003). A macro is written in APDL of ANSYS to create elements between those nodes whose distance is lower than 0.85 nm.

The thickness of CNT is selected as 0.34 nm and center of the carbon atoms in the CNT are placed at the midsection of the tube thickness. The innermost layer of the resin is assumed to be located at the same position of the outer surface of the CNT. For the sake of better understanding, a schematic top view of the model specifying location of vdW links with respect to carbon atoms of CNT and surrounding polymer is presented in Fig. 7.

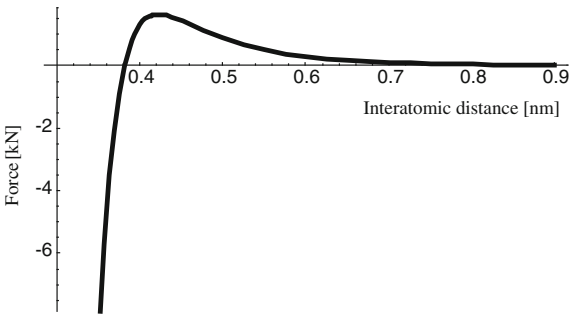

Fig. 6 Variation of vdW force versus interatomic distance

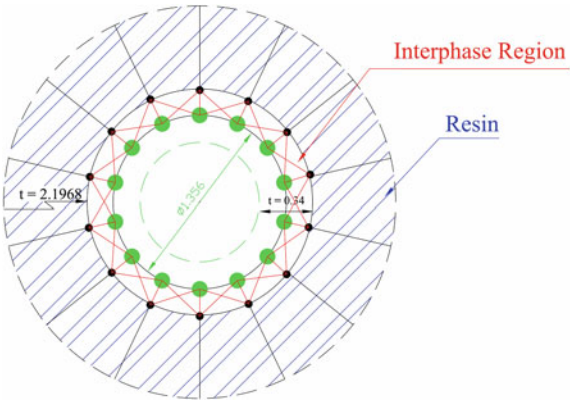

Fig. 7 Schematic *top view* of CNT, interphase and surrounding polymer (Shokrieh and Rafiee 2010)

The model is subjected to three different loadings to obtain longitudinal, transverse and shear moduli.

3.2.2 Longitudinal Young's Modulus of Microscale RVE

A non-linear analysis is performed using full Newton-Raphson iterative method due to the inherently non-linear behavior of the vdW interactions. A progressive analysis entitled as adaptive vdW interactions (AVI) was developed to take into account instantaneous situation of the model in each and every sub-step (Shokrieh and Rafiee 2009). Executing developed AVI technique, the vdW interactions are rearranged and updated based on the new corresponding status of the model. In other word, in each sub-step of the non-linear analysis, some previously active vdW interactions will be deactivated as their distances exceed the cut-off length and cannot transfer load anymore. In the meantime, some new vdW interactions will be formed and activated in accordance with updated situation of the model.

The tensile stress–strain curve of Fig. 8 depicted up to 5 % strain in the present analysis for the CNT length of 432 nm. Different results reported in literature for the strain at failure point of armchair CNT either theoretically or experimentally. It can be seen that all theoretical results are higher than the experimental results which can be attributed to the occurrence of slippage at the attachments for the high-strain cases (Belytschko et al. 2002). The reported theoretical failure strain of armchair CNT varies from 17 % up to 22 % (Tserpes et al. 2006, 2008; Belytschko et al. 2002; Meo and Rossi 2006; Xiao et al. 2005) while the experimental value is reported between 10 and 13 % (Yu et al. 2006). On the other hand, the failure strain of epoxy resin is reported to be about 7 % in literature. It is worth mentioning that according to employed harmonic inter-atomic energies, the present model for isolated CNT behaves linearly, while other authors, who employed Morse potential, reported a non-linear behavior for isolated CNT. Their models also show a linear behavior with a good approximation up to 5 % strain (Tserpes et al. 2006, 2008; Meo and Rossi 2006; Xiao 2005).

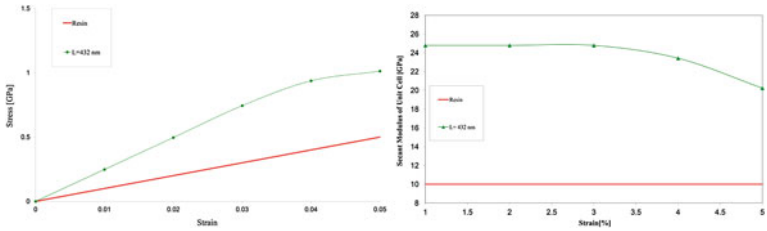

Fig. 8 Tensile stress–strain curve for resin and embedded CNT in resin (*left*), Secant moduli of resin and embedded CNT in resin (*right*)

The predicted results of AVI model show a non-linear behavior for investigated RVE. It should be pointed out that in this study because of linear interatomic potential employment for C–C bonds which has been already explained in the section of nanoscale modeling, the isolated CNT behaves linearly. Therefore, the main source of non-linear behavior of investigated RVE stems from the non-linearity of utilized vdW interactions in the interphase region. When the applied axial strain is increased gradually, more vdW springs will be deactivated and cannot transfer the applied load into the CNT. Frankland et al. (2003) was also reported the same trend of non-linear behavior. In order to quantify the degree of non-linearity, the Secant modulus of the RVE is illustrated in Fig. 8. It can be seen that the RVE is behaving almost linearly up to 2.3 % strain and after that the Secant modulus is decreasing considerably.

It was observed that the length of CNT has an important impact on load transfer efficiency from matrix to CNT (Shokrieh and Rafiee 2009, 2010) due to the dependency of the number of vdW links to the length of CNT. CNTs are commercially available in different lengths ranging from 100 nm to approximately 30 microns in the market based on the employed process of growth (http://www.carbonsolution.com, http://www.fibermax.eu/shop/, http://www.nanoamor.com, www.thomas-swan.co.uk). As a consequent, a parametric study was carried out on different lengths of CNT. The tensile stress–strain curves for different CNT lengths are presented in Fig. 9.

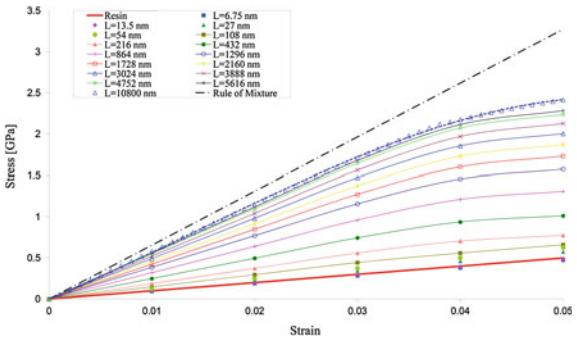

Fig. 9 Tensile stress–strain curves for different lengths of embedded CNT in matrix (Shokrieh 2010)

When the length of CNTs increases, the efficiency of load transfer improves dramatically. The larger the length of CNT, the higher effective longitudinal modulus of the RVE is achieved. Investigating the effect of different lengths of carbon nanotube on reinforcement shows that for the lengths smaller than 100 nm, no tangible reinforcement takes place. Increasing the length of CNTs, the enhancement in tensile modulus becomes more pronounced. It can be understood that the rate of improvement in reinforcement increases very slowly for the lengths larger than 10800 nm. As a case study, if the corresponding instantaneous moduli of the unit cell are drawn in term of nanotube length (Fig. 10), for the strain of 2 %, the obtained trend shows that degree of reinforcement increases rapidly up to CNT with length of 5616 nm and above this length the slope of the curve diminishes dramatically and above 10800 nm (at the order of ten microns) negligible improvement in reinforcement can be seen. It can be seen that for lengths larger than 10800 nm (10.8 μm) the reinforcement in comparison with the very preceding length is not tangible and the stiffness is not influenced considerably.

We have observed that the efficient length of CNT for reinforcement is 9072 nm for the case of (10, 10) by developed method. For efficient and strong load transfer, the required length of the fiber must have a certain value estimated by following equation (MacMillan et al. 1986):

$$L_{EFF} = \frac{\sigma_f d}{2\tau_c} \tag{8}$$

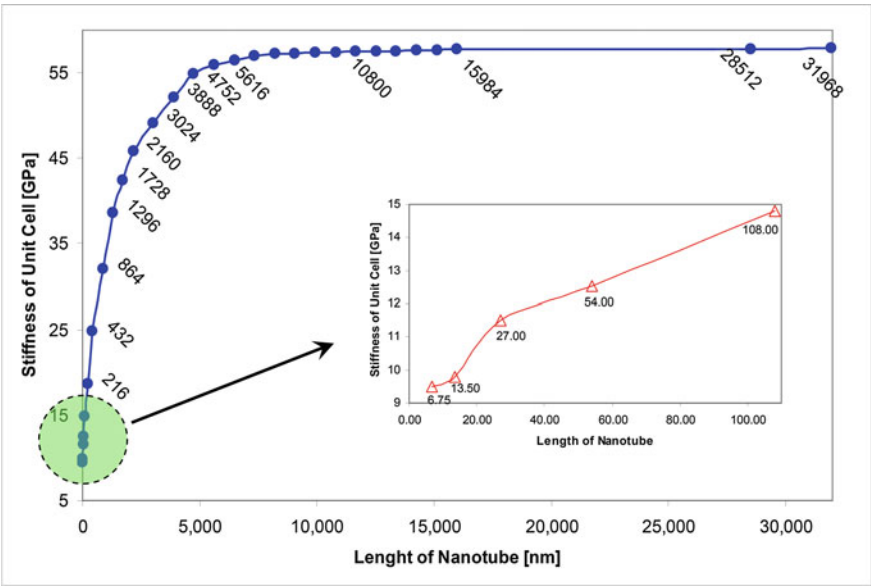

Fig. 10 Modulus of the RVE versus length of CNT (Shokrieh 2010)

where σ_f is tensile strength of the fiber, d is the fiber diameter and $\tau_c$is the fiber-matrix bond strength. Frankland et al. (2002) obtained 2.7 MPa as the interfacial shear strength of SWCNT in the form of (10, 10) in polymer matrix with non-bonded interphase region using molecular dynamics simulation. They also reported that in presence of non-bonded interactions between CNT and polymer matrix, a required length for efficient load transferring issue is about 10 to 100 microns, while this length will be reduced to 1 micron for the case of bonded interphase. Yu et al. (2006) have reported the strength of SWCNT as 11–63 GPa, experimentally. Considering the diameter of SWCNT in the form of (10, 10) as 1.35 nm and aforementioned tensile strength of CNT and interfacial shear strength of SWCNT/polymer, 9250 nm will be obtained as the efficient length using Eq. 8. The results of developed FEM estimate the efficient length as 9072 nm according to the inserted data in Table 3; which is in a very good agreement with obtained value by Eq. 3.

Table 3 Initial stiffness of the unit-cell at microscale and improvement trend

Length of embedded CNT (nm)	Initial stiffness (GPa)	Improvement in stiffness with respect to previous lower length (%)
108	14.8	–
216	18.63	26
432	24.78	33
864	32.03	29.2
1296	38.54	20.3
1728	42.4	10
2160	45.78	8
3024	49.08	7.2
3888	52.08	6.1
4752	54.82	5.3
5616	55.91	2
6480	56.47	1
7344	56.92	0.8
8208	57.21	0.5
9072	57.26	0.1
9936	57.32	0.1
10800	57.38	0.1
11664	57.44	0.1
12528	57.5	0.1
13392	57.55	0.1
14256	57.61	0.1
15120	57.67	0.1
15984	57.72	0.1
28512	57.78	0.1
31968	57.84	0.1

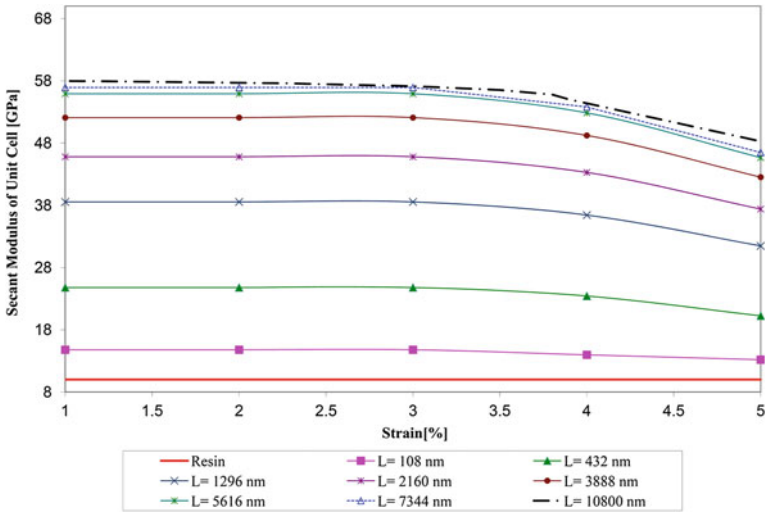

Fig. 11 Secant modulus of the unit cell for different aspect ratios of CNTs

In order to quantify the degree of non-linearity the Secant modulus of the RVE is drawn in Fig. 11. Figures 10 and 11 are providing data for some selected samples of the lengths to avoid messy figures.

3.2.3 Transverse and Shear Moduli of Microscale RVE

It should be pointed out that length of CNT will not affect the transverse and shear modulus of the RVE and it influences the longitudinal modulus.

A uniform angular displacement is applied to one end of the model while the other end is fully constrained. Similar to the preceding section, a non-linear analysis is necessary to obtain the equivalent shear modulus of the RVE. Figure 12 illustrates the obtained results of FEA in comparison with results of the rule of mixture and pure resin. The shear stress–strain curve of adaptive vdW bonded model shows nearly linear trend, since it is expected that a few vdW springs deactivated progressively by increasing torsional displacement.

The FE model is subjected to a uniform internal pressure acting on each node of CNT in radial direction. The results in comparison with predicted values by rule of mixture and pure resin data are shown in Fig. 13. It is worth mentioning that existence of radial stress has to be taken into account carefully, when transverse modulus of AVI model is intended to be extracted. This behavior can be justified using following equation (Sadd 2005):

$$\sigma_{\theta\theta} = E_{\theta}(\varepsilon_{\theta\theta} + \nu\sigma_{RR}/E_R) \tag{9}$$

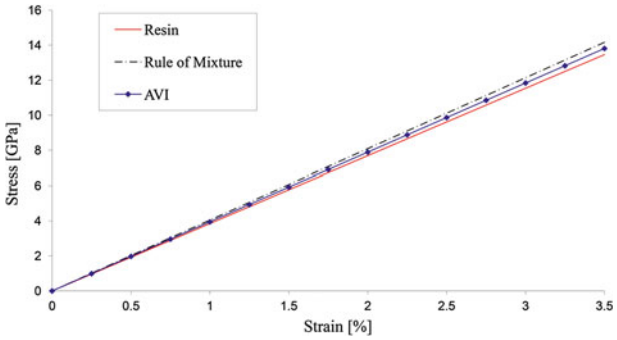

Fig. 12 Shear stress–strain curve for the RVE at miscorscale (Shokrieh and Rafiee 2010)

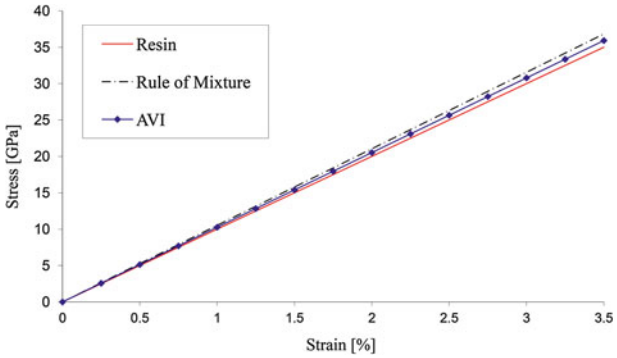

Fig. 13 Stress-strain curves for transverse modulus of the microscale RVE (Shokrieh and Rafiee 2010)

where, E_θ and E_R are circumferential and radial modulus. The corresponding amount of radial modulus is obtained from longitudinal tensile analysis carried out in Sect. 3.2.1.

The radial moduli at trigonometry locations of 0 and 180° are equivalent to the Young's modulus along "x" axis; while circumferential moduli at the same locations are equivalent to the Young's modulus along "y" axis. On the other hand, the radial moduli at trigonometry location of 90 and 270° are equivalent to the Young's modulus along "y" axis and corresponding values of circumferential moduli at the same location are equivalent to the Young's modulus along "x" axis. Since Young's moduli along "x" and "y" axes are the same, as the "z" axis denotes longitudinal axis of the tube, the tangential strain, tangential stress and radial stress components are extracted from the output of FE analysis and substitute into Eq. (9) in one of the trigonometry locations of 0°, 90°, 180° or 270° and then transverse modulus (the Young's modulus along "x" or "y" axis at mentioned locations) will be computed.

3.2.4 Development of Equivalent Fiber

As the output of the microscale analysis, CNT and its inter-phase are converted into the continuum equivalent fiber. The equivalent fiber is a continuum medium which is perfectly bonded to the matrix. The developing strategy is depicted in Fig. 14.

As it was previously stated, direct application of micromechanics rule for predicting mechanical properties of CNTRP is not allowed because it simply neglects the nanoscale by starting simulation from the scale of micro. Developing equivalent fiber, it would be permissible to use micromechanics equations indirectly in upper scales of the study, since the basic assumption of micromechanics rules are valid for the developed equivalent fiber. In other word, instead of developing appropriate equations which can be applied to the case of lattice structure of CNT and its interphase region at nanoscale, CNT and its interphase is converted to equivalent fiber at microscale which can be assumed as a virtual fiber for very well developed micromechanics rules. Moreover, the influence of non-bonded interphase region will be indirectly taken into account in the property of equivalent fiber.

The mechanical properties of the developed equivalent fiber are obtained using developed AVI method. The rule of mixture is utilized inversely for this purpose (Tsai et al. 2003):

$$E_{LEF} = \frac{E_{LRVE}}{V_{EF}} - \frac{E_M V_M}{V_{EF}} \tag{10}$$

$$G_{EF} = \frac{G_{RVE}}{V_{EF}} - \frac{G_M V_M}{V_{EF}} \tag{11}$$

$$E_{TEF} = \frac{E_{TRVE}}{V_{EF}} - \frac{E_M V_M}{V_{EF}} \tag{12}$$

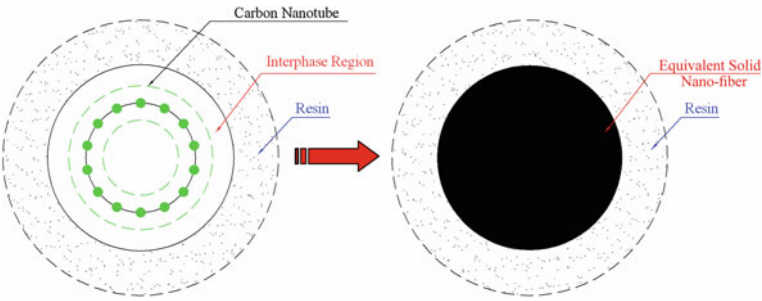

Fig. 14 Illustration of conversion strategy for development of equivalent fiber (Shokrieh and Rafiee 2010)

where E_{LEF}, E_{TEF} and G_{EF}, are longitudinal modulus, transverse modulus and shear modulus of equivalent fiber, respectively. E_{LRVE}, E_{TRVE} and G_{RVE} are representative of longitudinal modulus, transverse modulus and shear modulus of investigated microscale RVE obtained through developed AVI method. E_M, G_M, V_{EF} and V_M stands for Young's modulus modulus of matrix, shear modulus of matrix, volume fraction of the equivalent long fiber and volume fraction of the matrix.

Since the model is subjected to axial strain, the major longitudinal Poisson's ratio can be calculated using following equation:

$$\varepsilon_{\theta\theta} = -\frac{v}{E_Z}\sigma_{ZZ} \tag{13}$$

where circumferential strain ($\varepsilon_{\theta\theta}$) is calculated by dividing the radial displacement by the radius of equivalent long fiber and E_Z is the obtained longitudinal Young's modulus of equivalent long fiber. Following the above mentioned procedure, the Poisson's ratio of the developed equivalent fiber is obtained as 0.284, while the Poisson's ratio of isolated CNT has been reported to be between 0.2 and 0.3 in the literature.

Mechanical properties of developed equivalent fiber are inserted in Tables 4 and 5. Wang et al. (2006) reported that the length of CNTs varies from 50 to 1700 nm when SWCNTs are dispersed in the resin. Since the reinforcement efficiency of CNT highly depends on the length of CNT, longitudinal modulus of developed equivalent fiber is obtained for different lengths of CNTs on mentioned range. As was previously stated, other properties than longitudinal modulus of equivalent fiber are independent of CNT length. It can be seen from Tables 4 and 5 that developed equivalent fiber shows a transversely-isotropic behavior.

Table 4 Effective properties of developed equivalent fiber

E_L (GPa)	E_T (GPa)	E_S (GPa)	v
58–600[a]	11.27	5.13	0.284

[a] See Table 5

Table 5 Longitudinal effective modulus of developed equivalent fiber for different lengths

CNT length (nm)	E_L (GPa)	CNT length (nm)	E_L (GPa)s	CNT length (nm)s	E_L (GPa)
50	58	500	348	1000	504
100	129	550	366	1050	516
150	164	600	384	1100	528
200	203	650	400	1150	540
250	232	700	416	1250	561
300	261	750	432	1300	570
350	287	800	448	1350	578
400	310	850	462	1450	591
450	330	950	490	1550	600

3.3 Mesoscale Modeling

The key factors defining the capability of CNTs in reinforcing of polymers at meso-scale are indicated in Table 1. A schematic presentation of suitable RVE at meso-scale is shown in Fig. 15.

Following to the developed method of simulation at the very lower scale of micro, the RVE at meso-scale consists of developed equivalent fiber instead of CNT. As it is illustrated in Fig. 15, embedded equivalent fibers are oriented in random directions and they can exist in both straight and curved forms. They can be either concentrated in local aggregates or dispersed in some other areas. It is assumed that aggregates will be appeared in the form of spherical regions. All other equivalent fibers located out of the spherical regions are considered to be fully dispersed.

Therefore, a suitable RVE at this scale should account for orientation, agglomeration, non-straight shapes and volume fraction of CNTs.

3.3.1 Agglomeration

It is permissible to utilize micromechanics equations at meso-scale. Using equivalent fiber technique, micromechanics equations will be applied to CNTRP indirectly. Namely, effective stiffness of equivalent fiber not only will be fed into micromechanics equations instead of effective stiffness of CNT, but also micromechanics theories are used at proper scale of meso instead of nano.

Exhibiting isotropic behavior due to random orientations of CNT, Young's modulus and Poisson's ratio of the RVE at meso scale can be calculated using improved Mori-Tanaka model presented by Shi et al. (2004). The improved Mori-Tanaka model considers reinforcement in the form of cylindrical inclusion and it is able to address the random orientations of inclusion and also interaction between them. It can be expanded to consider multiple inclusions. So, it is appropriate for the case of the developed equivalent fiber with different properties. Each and every length of CNT which leads to a different effective stiffness of developed equivalent fiber will be considered as a new phase in multiple-phase Mori-Tanaka equations.

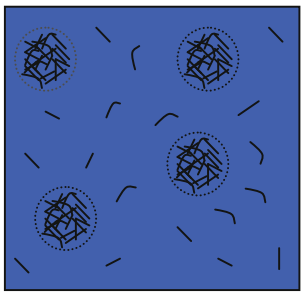

Fig. 15 The RVE of mesoscale containing equivalent fibers

The improved Mori-Tanaka model developed by Shi et al. (2004) evaluates the bulk modulus (K) and shear modulus (G) of mentioned block in Fig. 15 using below equations:

$$\mathrm{K} = \mathrm{K_{out}}\left[1 + \frac{\mu\left(\frac{K_{in}}{K_{out}} - 1\right)}{1 + \alpha(1-\mu)\left(\frac{K_{in}}{K_{out}} - 1\right)}\right] \tag{14}$$

$$\mathrm{G} = \mathrm{G_{out}}\left[1 + \frac{\mu\left(\frac{G_{in}}{G_{out}} - 1\right)}{1 + \beta(1-\mu)\left(\frac{G_{in}}{G_{out}} - 1\right)}\right] \tag{15}$$

where μ accounts for volume fraction of aggregates with respect to the total volume of the block and and κ denotes volume fraction of CNTs inside the aggregates. Therefore, the improved Mori–Tanaka model is a two-parameter model taking into account agglomeration (Shi et al. 2004). When these two parameters are equal, no agglomeration will take place. Other parameters in equations (14) and (15) are calculated using below formulations (Shi et al. 2004):

$$\alpha = \frac{1 + v_{out}}{3(1 - v_{out})} \tag{16}$$

$$\beta = \frac{2(4 - 5v_{out})}{15(1 - v_{out})} \tag{17}$$

$$K_{in} = K_m + \frac{f_r\kappa(\delta_r - 3K_m\alpha_r)}{3[\mu - f_r\kappa + f_r\kappa\alpha_r]} \tag{18}$$

$$K_{out} = K_m + \frac{f_r(1-\kappa)(\delta_r - 3K_m\alpha_r)}{3[1 - \mu - f_r(1-\kappa) + f_r(1-\kappa)\alpha_r]} \tag{19}$$

$$G_{in} = G_m + \frac{f_r\kappa(\eta_r - 2G_m\beta_r)}{2(\mu - f_r\kappa + f_r\kappa\beta_r)} \tag{20}$$

$$G_{out} = G_m + \frac{f_r(1-\kappa)(\eta_r - 2G_m\beta_r)}{2[1 - \mu - f_r(1-\kappa) + f_r(1-\kappa)\beta_r]} \tag{21}$$

$$v_{out} = \frac{3K_{out} - 2G_{out}}{6K_{out} + 2G_{out}} \tag{22}$$

where $\mathrm{K_m}$, $\mathrm{G_m}$ and $\mathrm{f_r}$ are the bulk modulus of matrix, shear modulus of matrix and CNT volume fraction, respectively. α_r and β_r are Hill constants for cylindrical inclusion (Shi et al. 2004).

3.3.2 Waviness

A phenomenological technique is used to consider the non-straight shape of carbon nanotubes. In this approach each arbitrary wavy shape of carbon nanotube will be replaced by a straight equivalent fiber developed with reduced stiffness representing the non-straight shape of CNT.

The stiffness of a unit-cell containing an embedded non-straight fiber in polymer can be bounded between two extreme values dictated by longitudinal and transverse stiffness of the unit-cell. As a subsequent, the effective stiffness of a non-straight fiber is placed between bounding values of longitudinal and transverse effective stiffness of a straight fiber, when it is categorized under the transversely-isotropic material. This phenomenon is shown in Fig. 16.

A mathematical description of this bounding technique is presented in Eqs. (23) and (24) for longitudinal and transverse directions, respectively.

$$E_T^{Straight} \leq E_L^{Wavy} \leq E_L^{Straight} \tag{23}$$

$$E_T^{Straight} \leq E_T^{Wavy} \leq E_L^{Straight} \tag{24}$$

Depending on the length of CNT/equivalent fiber, the corresponding values of $E_L^{Straight}$ are reflected in Table 5; while $E_T^{Straight}$ is 11.27 GPa for all lengths. Therefore, a non-straight equivalent fiber will be replaced by a straight equivalent fiber with reduced effective stiffness. As a result of the developed strategy E_L^{Wavy} and E_T^{Wavy} will be chosen independently. Each case is a representative of an arbitrary non-straight shape and is not limited to any predefined pattern of waviness.

The longitudinal and transverse properties of developed equivalent fiber will be chosen randomly in order to simulate random patterns of waviness.

3.4 Macroscale Modeling

The RVE of the final scale of macro is the investigated material region. As it was reflected in Fig. 1, the material region at macro scale is partitioned into smaller constitutive blocks with different local volume fraction in order to address the material inhomogeneity originated from non-uniform dispersion of CNTs. The mechanical properties (Young's modulus and Poisson's ratio) of each and every constitutive block are evaluated at the lower scale of meso as explained in (3.3)

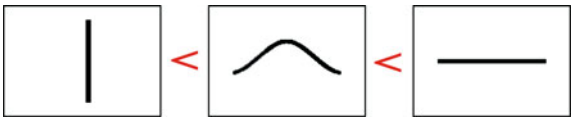

Fig. 16 Illustration of bounding technique for wavy CNT (Rafiee 2013)

section. In order to obtain the overall properties of investigated material region, the average of properties associated with each constitutive block are obtained using Voigt model (Jones 1999):

$$\overline{X} = \frac{\sum_i X_i p_i}{\sum_i p_i} \tag{25}$$

where p_i and X_i stands for portion of constitutive block and mechanical property o associated with i-th block at mescoscale. $\overline{X}$ represents the corresponding mechanical property of the material region at macroscale. Due to the random orientations of CNT in matrix, the material region can be assumed as an isotropic material and two properties out of Elastic modulus, shear modulus and Poisson's ratio can fully describe the material properties.

4 Stochastic Implementation of N3M

Developed "N3M" multi-scale modeling is implemented stochastically to address intrinsically uncertainties in CNTRP. Prior to establishment of stochastic analysis, governing random parameters are identified. Recalling from previous sections, most important parameters behaving randomly are summarized in Table 6.

4.1 Model Preparation

Firstly, the investigated material region at macro-scale is partitioned into smaller constitutive blocks as schematically shown in Fig. 1. Random volume fraction is assigned to each and every single constructive block in order to capture the material inhomogeneity originated from non-uniform dispersion of CNTs. The average of volume fractions in each block is consistent with the overall volume fraction of CNT in investigated material region.

The overall flowchart of stochastic N3M modeling is presented in Fig. 17. As it can be seen from Fig. 17, the model preparation takes place at the scale of macro

Table 6 Random parameters associated with CNTRP

Parameter	Effective scale	Effective length
Length of CNT/Equivalent fiber	Nano/Micro	nm
CNT orientation	Micro/Meso	μm
CNT agglomeration	Meso	μm
CNT curvature	Meso	μm
CNT dispersion	Macro	mm

and then the N3M modeling starts from nano-scale and it continues to the scales of micro, meso and macro, sequentially. Monte Carlo method (Kleiber and Hien 1992) is employed to perform stochastic modeling.

A convergence study is performed to obtain appropriate mesh density for tessellated region and also required number of realizations. For convergence study, Young's modulus of resin is selected as 10 GPa, Poisson's ratio of 0.3 and 3 % CNT volume fraction. Coefficient of variation for mean value of overall Young's modulus of investigated material region is considered less than 0.1 % as a convergence criterion. Therefore, convergence study reveals that the convergence criterion is fulfilled when 500 realizations of stochastic modeling is accomplished on a region with 80 × 80 blocks at macro-scale. For instance, the generated partitioned material region with random volume fraction and 40 × 40 mesh density during convergence study is depicted in Fig. 18. The black color implies on a maximum CNT volume fraction while the white color denoted zero CNT volume fraction. The gray spectrum shows the intermediate values of CNT volume fraction between zero and maximum. The convergence trend is also shown in Fig. 18.

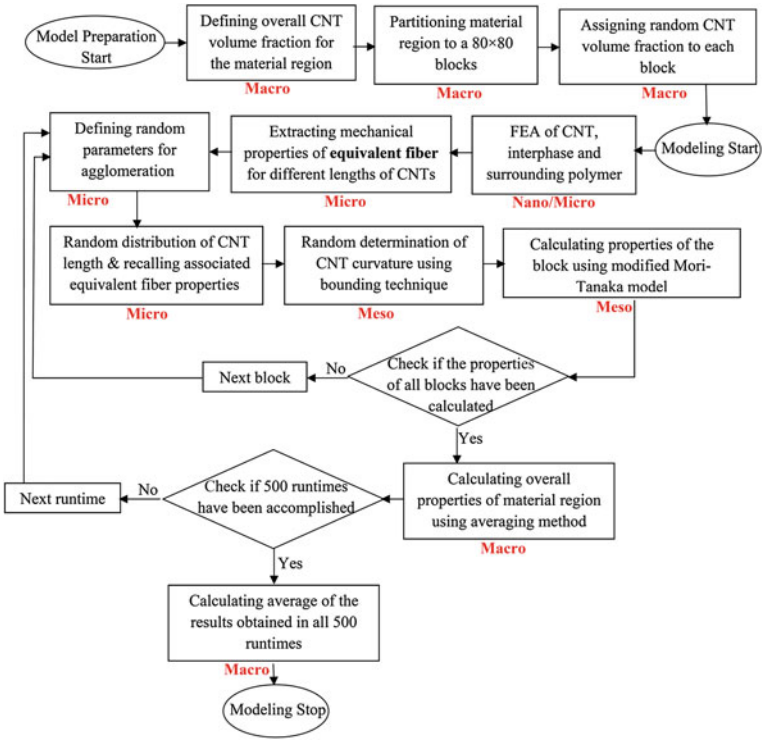

Fig. 17 Flowchart of developed stochastic N3M modeling (Jones 1999)

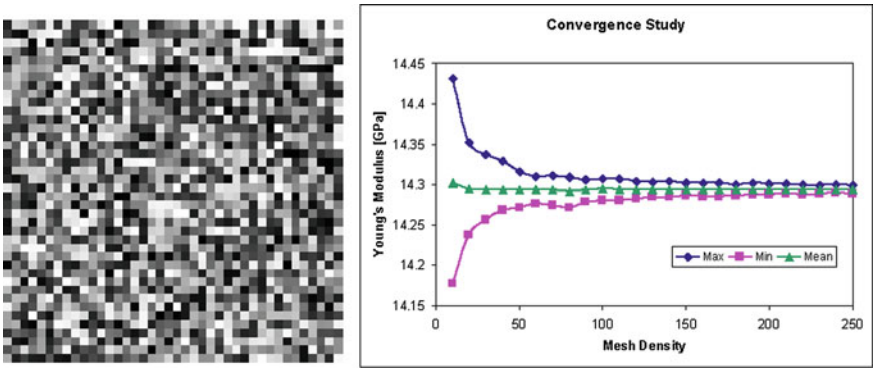

Fig. 18 Sample of partitioned material region for convergence study (*left*) and convergence trend (*right*) (Shokrieh and Rafiee 2012)

4.2 Model Execution

All introduced parameters are considered as random parameters; hence, full stochastic "N3M" modeling is developed. The flowchart of this modeling procedure is presented in Fig. 17. A computer code was established in this research on the platform of Mathematica (Wolfarm 1999). The simulation at nano- and micro-scales has been performed in commercial FE package of ANSYS (Theory Manual 2003) as already explained in Sects. 3.1 and 3.2. It is noteworthy to mention that outcomes of FEA at nano- and micro-scales have been used as a database in developed stochastic analysis.

It is assumed that all CNTs are single-walled CNT (SWCNT) with the same diameter. Due to the very high aspect ratio of CNTs, the length of CNT has a more tangible effect on load transferring than its diameter. A consistent length of CNT cannot be obtained during the processing CNT. Additionally, CNTs are cut into different lengths when CNTRP is exposed to sonication process for better dispersion of CNTs. Wang et al. (2006) statistically characterized the length distribution of SWCNT through an experimental observation. This distribution is used here as a probability density function of CNT lengths. Each and every length of CNT will lead to unique effective stiffness of corresponding equivalent fiber as it is explained in Sect. 3.2.4 and Table 5.

Due to the very small size of CNT, it is almost impossible to align them in one direction and they are oriented in different directions. This phenomenon is taken into account using improved version of Mori–Tanaka equation as it is already explained in Sect. 3.3.

Agglomeration of CNT experiences a non-deterministic pattern in each constitutive block. Therefore, two-parameter model of agglomerations (See Sect. 3.3.) is employed here randomly. Namely, the value of mentioned two parameters in Eqs. (14) and (15), i.e. μ and $\kappa$are chosen randomly. If these two parameters are

accidentally equal, no agglomerations will occur in that block. Consequently, agglomerations of CNTs are considered as random phenomena not only in its occurrence but also in its degree to which it happens, quantitatively.

Following the bounding technique explained in Sect. 3.3.2, E_L^{Wavy} and E_T^{Wavy} will be selected randomly between bounding limits. If it exactly coincides with one of the uppermost values, it will reflect the straight CNT; otherwise it will be a representative of any arbitrary non-straight shape. So, it can be concluded that developed stochastic model treats both occurrence of waviness and its shape as random parameters. It is assumed that CNTs with lengths lower than 100 nm will remain straight in polymer, while other larger lengths will experience non-straight shape randomly.

Gaussian distribution is selected for the volume fractions with mean value of overall volume fraction and different standard deviations are utilized.

4.3 Model Validation

In order to check the accuracy of developed model, developed N3M modeling is evaluated using available experimental results in published data for CNTRP. The comparison of results is inserted in Table 7 wherein the column entitled as chemical treatment refers to functionalization of CNT.

As it was explained in "Sect. 3.2", the interaction between CNT and surrounding polymer is treated as weakly non-bonded vdW interaction. Thus, those experimental observations wherein CNTs have not been chemically treated are selected for comparison purpose, since the developed modeling cannot consider functionalized CNTs.

The percentage of error for estimated results by N3M simulation method is lower than 7 % for the functionalized SWCNT and it is lower than 1.6 % for normal CNTs. This stems from the fact that the developed N3M method treats interphase region between SWCNT and surrounding polymer as non-bonded vdW interactions which is suitable for non-functionalized SWCNT. In addition to the proper percentage of the error, the results of prediction using N3M technique are lower than experimental observations in all cases implying on conservative simulation except on special case reported by Lopez Manchado et al. (2005). In their experimental observation, when the volume fraction of CNT increases from 0.563 to 0.75 the Young's modulus of CNTRP exceptionally decreases from 1.18 to 1.087 GPa. This has led us to −14 % errors in predicting results using developed stochastic N3M. They have justified that this behavior stems from the increased

Table 7 Comparison between predicted results by *N3M* method with experimental published data

Researchers	Constituents' properties			Young's modulus (GPa)		
	E_{Resin} (GPa)	V_F (%)	Chemical treatment	Experimental observation	Mode value (Error [%])	Mean value (Error [%])
Odegard et al. (2003)	0.85	0.1		0.875	0.848–(3)	0.847–(3.2)
		0.5	☑	1.2	1.54–(3.8)	1.152–(4)
		1		1.4	1.33–(5)	1.32–(5.7)
		0.21	☒	1.2	1.2–(0)	1.19–(0.84)
Zhu et al. (2004)	2.026	0.882	☑	2.65 ± 0.125	2.516–(5)	2.514–(5.1)
		3.306		3.44 ± 2.53	3.225–(6.2)	3.223–(6.3)
Paiva et al. (2004)	4	2.28	☑	5.6 ± 0.4	5.28–(5.7)	5.26–(6)
		4.58		6.2 ± 0.1	5.78–(6.7)	5.77–(6.8)
Lopez Manchado et al. (2005)	0.855	0.187		1.02	1.015–(0.5)	1.013–(0.6)
		0.37		1.1	1.1–(0)	1.09–(0.9)
		0.563	☒	1.18	1.17−(0.84)	1.163−(1.4)
		0.75		1.087	1.25–(−15)	1.24–(−14)
Villoria and Miravete (2007)	2.875	0.12	☒	2.909	2.9–(0.3)	2.897–(0.4)
	2.587	0.47		2.659	2.65–(0.3)	2.6s4–(0.7)

local aggregates due to higher level of CNT agglomeration as the higher CNT volume fraction will be resulted in more probability of agglomeration occurrence. The developed N3M modeling treats agglomeration as a random issue and it may not be exactly matches with the realistic situation of investigated CNTRP. In order to investigate this special case in more detail, different random patterns are generated for agglomeration phenomenon. The results are presented in Fig. 20 and it can be observed that the experimentally reported result by Lopez Manchado et al. (2005) can be obtained after modeling when the agglomeration occurrence increases addressing higher level of CNT local concentration. In other word, in all cases depicted in Fig. 19 when the material inhomogeneity becomes more pronounced by formation of more local CNT aggregates, the experimental observation can be met.

Finally, it can be inferred that developed modeling is a reliable modeling procedure, since a very good agreement between experimentally measured data and obtained values by modeling is seen.

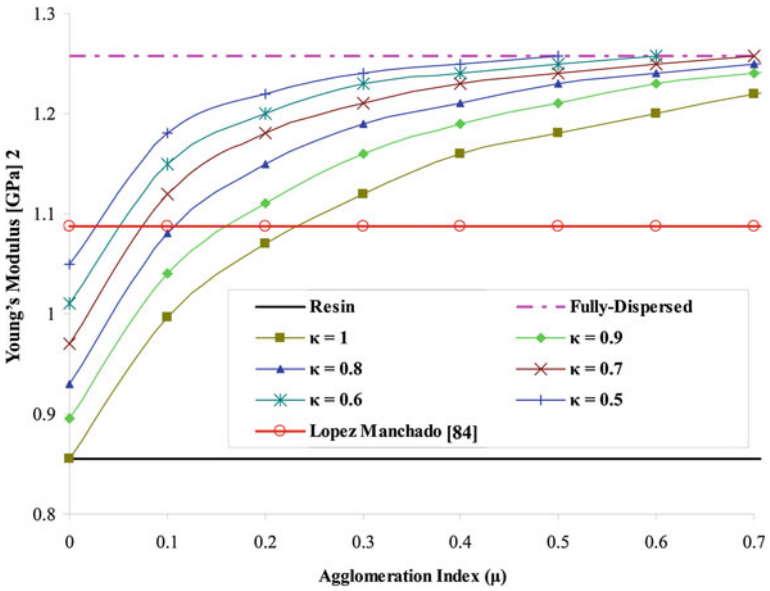

Fig. 19 Parametric study of local CNT aggregate formation and increased level of inhomogeneity

5 Results and Discussion

For the case study, Young's modulus and Poisson's ratio of the matrix are selected as 10 GPa and 0.3, respectively. The simulated resin treated as an elastic and isotropic material. The overall volume fraction of the CNT is selected as 5 %. Different patterns of volume fraction are generated with the same mean values of 5 % and different standard deviations as 0.5, 1.0, 1.5, 2.0 and 2.5 %. Obtained results for Young's modulus and Poisson's ratio are demonstrated in Fig. 20.

The mean values for Poisson's ratio show a negligible fluctuation and it can be considered as 0.293 for all cases with a very good level of accuracy. It can be also figured out from Fig. 20 that the mean values of overall Young's modulus change insignificantly for different patterns of volume fraction.

Mean and mode values for Young's modulus are presented in Table 8 with supplementary information. The range of mean values for overall Young's modulus is also presented in Table 8 on the basis of 95 % confidence level. It can be comprehended from the results that one can simply replace random volume fraction with its deterministic mean value with an acceptable accuracy.

The possibility of replacing random lengths of CNT by its corresponding mean value is also examined. For this case, the mean value of CNT length is obtained

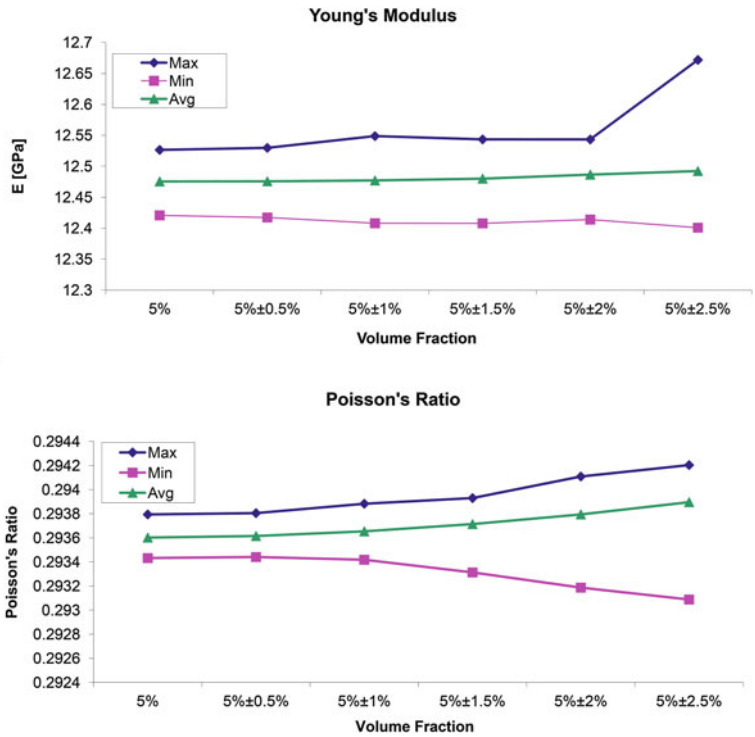

Fig. 20 Overall Young's modulus and Poisson's ratio of investigated material region (Shokrieh and Rafiee 2010

Table 8 Statistical results for Young's modulus of CNTRP

V_{CNT} (%)	Mode value (GPa)	Mean value (GPa)	STD[a] (%)	COV (%)	Limits of mean value (GPa) (Confidence level = 95 %)
5	12.47	12.47	0.12	0.01	12.468–12.471
5 ± 0.5	12.47	12.47	0.25	0.02	12.470–12.474
5 ± 1.0	12.47	12.47	0.50	0.04	12.469–12.472
5 ± 1.5	12.47	12.47	0.74	0.06	12.473–12.477
5 ± 2.0	12.49	12.48	0.87	0.07	12.479–12.483
5 ± 2.5	12.49	12.48	1.12	0.09	12.484–12.489

Note STD Standard Deviation

using probability density function presented by Wang et al. (2006) and then effective stiffness of equivalent fiber with the mean length is obtained using developed AVI technique at micro-scale. It was observed that the results of two different approaches (random lengths versus mean length) are very close. The

maximum difference between these two approaches is about 0.07 %, while the runtime of the modeling process decreases significantly. As a consequent, the length parameter can also be taken into account as a deterministic value using its average value. Therefore, two variables of CNT length and volume fraction out of five introduced parameters in Table 6 can be considered as deterministic values.

Comparing simulation results considering mean values for volume fraction and length of CNT with the case of maximum length of CNT, shows that the former reports Young's modulus 21 % lower than the later. It implies on the important role of CNT length and its subsequent effect on the load transferring efficiency.

The Young's modulus variation of the investigated material region can be described by probability distribution function. It can be seen from Table 4 that for small deviations of volume fraction (0.5, 1.0 and 1.5 %), both mode and mean values of Young's modulus coincide; while for large deviations of volume fraction (2.0 and 2.5 %), mode values are slightly higher than the mean values. Consequently, Gaussian distribution is a proper candidate for the small deviations of volume fraction; while for large deviations Weibull distribution is nominated in order to justify unequal values of mode and mean overall Young's moduli. A comparison between these two probability distribution functions is exemplified in Fig. 21 for the two samples of volume fraction.

In order to study the sensitivity of N3M modeling to the introduced random parameters, the provided code is equipped with a feature that each random parameter can be activated individually; while others are treated deterministically.

It was understood that both CNT length and volume fraction can be treated as deterministic values using their average amounts. On the other side, the random orientation of CNTs renders the CNTRP as an isotropic material. Therefore, the parametric study will concentrate on agglomeration and non-straight shape of CNTs.

Firstly, it is assumed that the investigated material region consists of straight CNTs and the waviness will not be experienced in order to merely concentrate on the influence of agglomeration. A comparison has been done between the results of agglomerated CNTs and fully dispersed CNTs in the matrix and it was shown in Fig. 22. The results show a considerable difference between these two cases for the Young's modulus (about 5 %) implying on importance of agglomeration in stiffness reduction of CNTRP composites. On the other hand, Poisson's ratio can be considered 0.28 for all cases when the accuracy is considered as two orders of magnitude.

Taking into account the waviness of CNT, the model is executed once again. For this purpose, the generated random pattern for all CNT agglomeration and volume fraction in former analysis is exactly used for the current modeling. Reported results in Fig. 23 shows that the overall Young's modulus of the material region reduces 18 % comparing with the results of embedded straight CNTs in matrix. It is interesting to observe that the Poisson's ratio has been increased

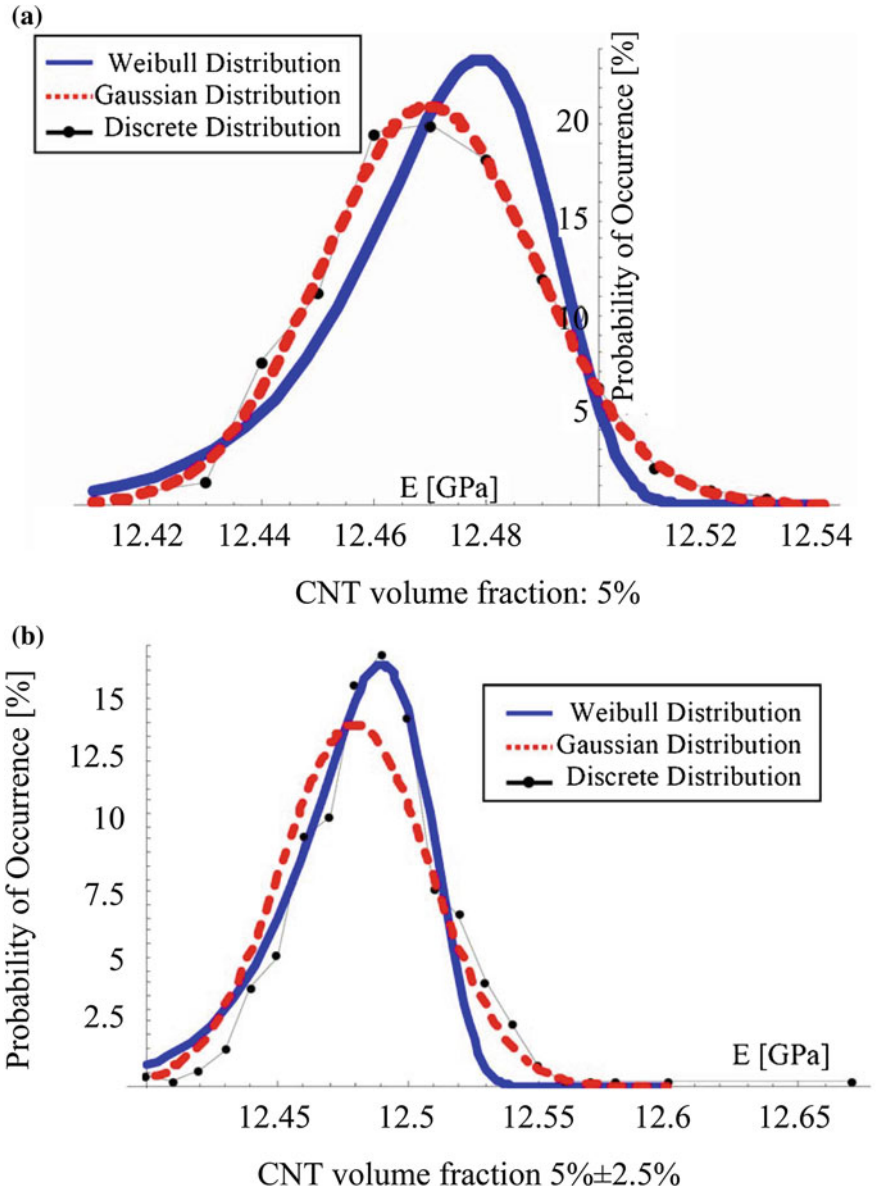

Fig. 21 Discrete distribution versus continuous probability density functions (Shokrieh and Rafiee 2010)

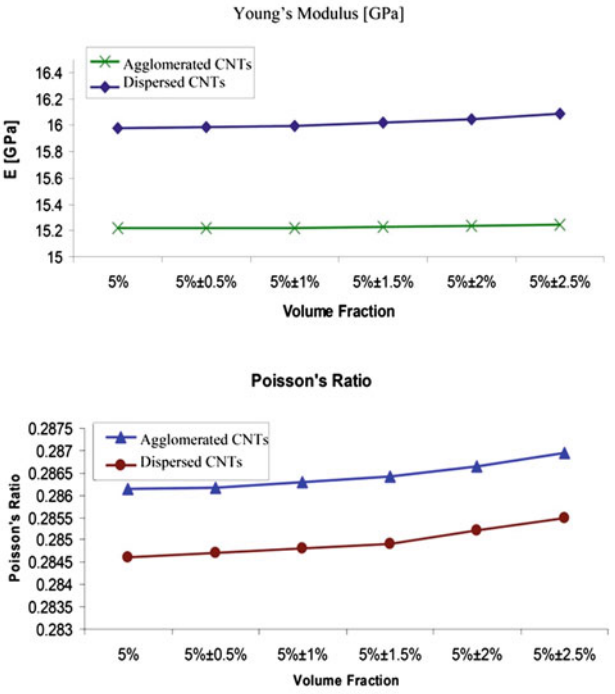

Fig. 22 Comparison between the Young's modulus and Poisson's ratio of agglomerated and fully dispersed CNTs in the matrix (Shokrieh and Rafiee 2012)

slightly in comparison with straight CNTs. It stems from this fact that transverse characteristics of CNTRP is improved due to existence of wavy CNT, therefore the experienced contradiction along transverse direction will be a little bit lower than that of straight CNTs. In other word, the material region resists a little higher against transverse contraction leading to the higher overall Poisson's ratio.

Comparing the results of mentioned parameter study on CNT curvature and agglomeration which are reflected in Figs. 20, 21 and 23, it is realized that the waviness of CNTs reduces Young's modulus of CNTRP more considerably than formation of aggregates. Thus, the developed N3M modeling is severely sensitive to the curvatures of the CNTs. Contributions of agglomerations and orientations of CNTs are moderate with respect to their curvature.

Focusing on the waviness of CNTs, it would be also interesting to study the influence of resin modulus on the properties of CNTRP. For this purpose, the Young's modulus of resin is chosen as 5 GPa; while the Poisson's ratio is kept as 0.3 like pervious sets of analysis. The volume fraction is considered as 2 % for this analysis. The obtained results are presented in Fig. 24. Emphasizing only on the

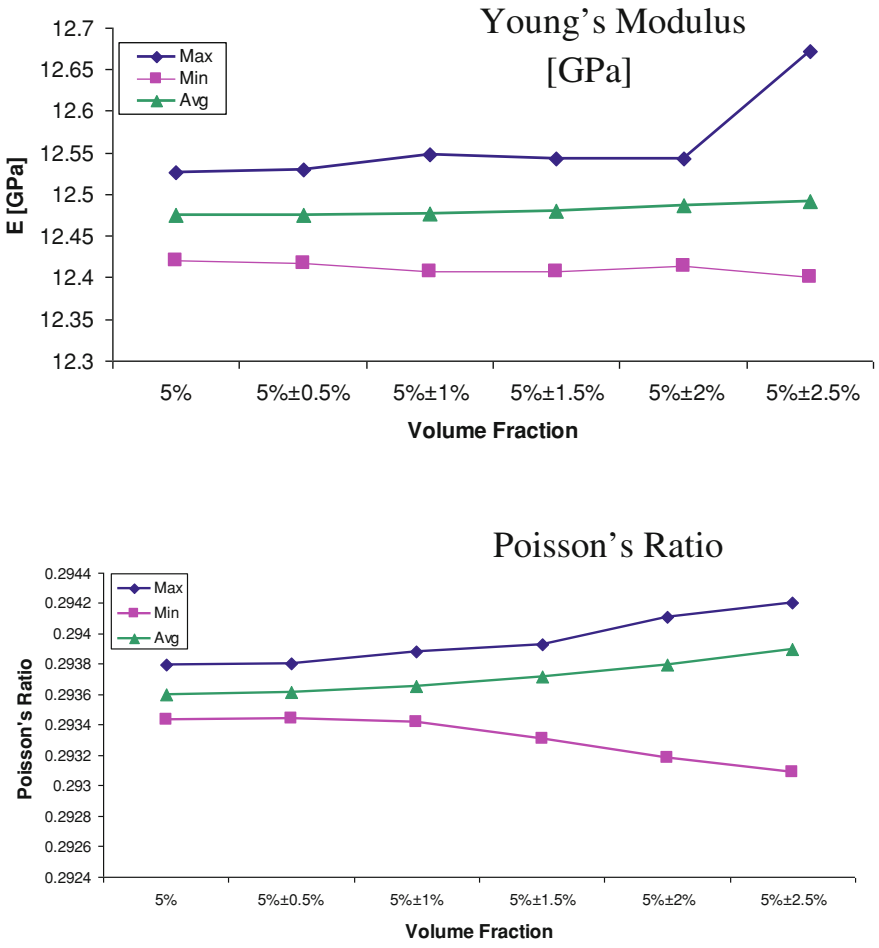

Fig. 23 Overall properties of CNTRP in presence of non-straight CNTs (Rafiee 2013)

waviness effect, the same generated random patterns for CNT curvature and agglomeration are used for all cases reflected in Fig. 24.

It can be seen that non-straight shapes of CNT reduces overall Young's modulus of CNTRP for selected resin, 25 % up to 50 % in comparison with than that of straight CNTs. This reduction becomes more tangible when the CNT volume fraction increases. Furthermore, comparing the results of the current analysis with the obtained results for the matrix with Young's modulus of 10 GPa, it can be comprehended that more stiff matrices will decrease the reduction in the Young's modulus of CNTRP by weakening the level of CNT curvature.

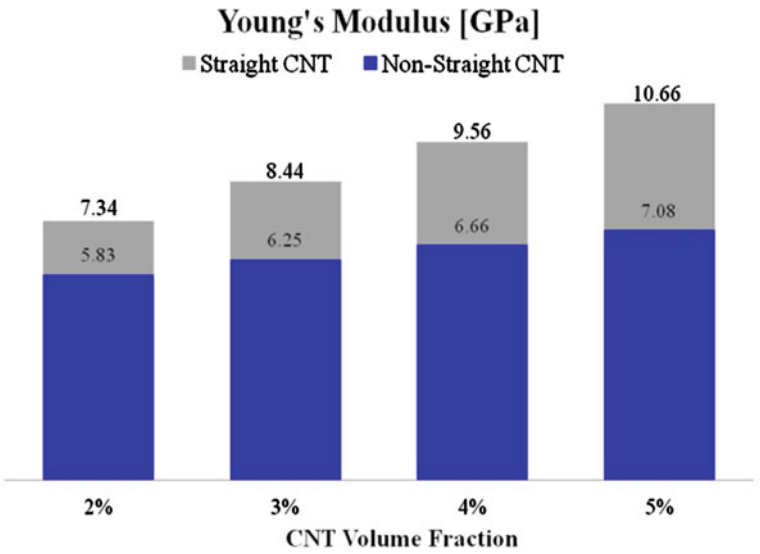

Fig. 24 Comparison of Young's modulus for CNTRP with different CNT volume fraction (Rafiee 2013)

6 Conclusions

Young's modulus and Poisson's ratio of CNTRP are predicted using hierarchical multi-scale simulation approach. Developed multi-scale technique covers the full range of nano, micro, meso and macro scales. The simulation procedure consists of two phases as top-down scanning and bottom-up modeling. Effective parameters of each scale are identified and suitable RVE is defined for each level of simulation.

At nano-scale, each C–C bond of carbon nanotube is replaced with equivalent beam element by a correlation between molecular space and structural mechanics. The lattice structure of CNT is kept by simulating CNT as an equivalent discrete structure.

At micro-scale, a multi-scale FEM is employed which treats CNT as a lattice structure at nano-scale and surrounding resin is simulated as a continuum medium.

Having a crucial influence on load transferring issue, the interphase region was investigated as the non-bonded vdW interactions. Due to non-linear nature of vdW interactions, non-linear FEA has been performed adaptively. In each step of the solution the current status of the model is carefully updated. CNT and its interphase region were replaced with an equivalent fiber. The effective stiffness of the equivalent fibers is fully characterized. Developed equivalent fiber is an appropriate tool for the meso-scale instead of direct application of micromechanics rules to CNTRP.

At meso-scale, appropriate micromechanics model is selected to take into consideration agglomeration and orientation of CNTs. At this scale, existence of non-straight CNT and its effect on reduction of constitutive blocks properties are investigated using phenomenological bounding technique. Overall properties of the investigated material region are obtained using averaging method as Voigt model. Namely, each property of constitutive blocks is averaged at micro-scale as an appropriate alternative approach instead of FEM.

Non-uniform dispersion of CNT leading to an inhomogeneous material region was investigated at a micro-scale. For this purpose, investigated material region was partitioned into different constitutive blocks with different properties.

All four sub-steps of modeling at nano to macro scales are integrated in a unitized modeling procedure. Full stochastic modeling technique is developed to simulate inherent uncertainties associated with manufacturing of CNTRP. Five different parameters as the length, orientation, agglomeration, curvature and dispersion of CNT are treated as random parameters. A case study is performed to verify the developed modeling procedure. It was revealed that length and volume fraction of CNT can be simulated as deterministic parameters using their corresponding mean values. A parametric study is performed and it was understood that CNT curvature affects the result seriously, while CNT agglomeration and orientation have moderate impact on prediction. To validate the developed stochastic modeling procedure, results demonstrate a high level of consistency with experimental observations available in the literature.

References

Ashrafi B, Hubert P (2006) Modeling the elastic properties of carbon nanotube array/polymer composites. Comp Sci Tech 66:387–396

Coleman JN, Khan U, Blau WJ, Gun'ko YK (2006) Small but strong: a review of the mechanical properties of carbon nanotube-polymer composites. Carbon 44:1624–1652

Cornell WD, Cieplak P, Bayly CI, Gould IR, Merz KM, Ferguson DM, Spellmeyer DC, Fox T, Cladwell JW, Kollman PA (1991) A second generation force field for the simulation of proteins, nucleic acids, and organic molecules. J Am Chem Soc 117:5179–5197

Dai H (2002) Carbon nanotubes: opportunities and challenges. Surf Sci 500:218–241

Esawi AMK, Farag MM (2007) Carbon nanotube reinforced composites: potential and current challenges. Mater Des 28:2394–2401

Frankland SJV, Harik VM, Odegard GM, Brenner DW, Gates TS (2003) The stress–strain behavior of polymer–nanotube composites from molecular dynamics simulation. Comp Sci Tech 63:1655–1661

Gao XL, Li K (2003) Finite deformation continuum model for single-walled carbon nanotubes. Int J Sol Struct 40:7329–7337

Gates TS, Odegard GM, Frankland SJV, Clancy TC (2005) Computational materials: multi-scale modeling and simulation of nanostructured materials. Comp Sci Tech 65:2416–2434

Gibson RF (2007) Principles of composite material mechanics, 2nd edn. CRC Press, Boca Raton

Han Y, Elliott J (2007) Molecular dynamics simulations of the elastic properties of polymer/carbon nanotube composites. Comput Mater Sci 39:315–323

Kalamkarov AL, Georgiades AV, Rokkam SK, Veedu VP, Ghasemi-Nejhad MN (2006) Analytical and numerical techniques to predict carbon nanotubes properties. Int J Solids Struct 43:6832–6854

Kang I, Heung YY, Kim JH, Lee JW, Gollapudi R, Subramaniam S et al (2006) Introduction to carbon nanotube and nanofiber smart materials. Compos Part B 37:382–394

Lau KT, Gu C, Hui D (2006) A critical review on nanotube and nanotube/nanoclay related polymer composite materials. Compos Part B 37:425–436

Li C, Chou TW (2003) A structural mechanics approach for the analysis of carbon nanotubes. Int J Solids Struct 40:2487–2499

Liu Y, Nishimura N, Otani Y (2005) Large-scale modeling of carbon-nanotube composites by a fast multipole boundary element method. Comput Mater Sci 34:173–187

Lordi V, Yao N (2000) Molecular mechanics of binding in carbon-nanotube—polymer composites. J Mater Res 15(12):2770–2779

Mokashi VV, Qian D, Liu Y (2007) A study on the tensile response and fracture in carbon nanotube-based composites using molecular mechanics. Comp Sci Tech 67:530–540

Mukhopadhyay K, Dwivedi CD, Mathur GN (2002) Conversion of carbon nanotubes to carbon fibers by sonication. Carbon 40:1373–1376

Odegard GM, Gates TS, Nicholson LM, Wise KE (2002) Equivalent-continuum modeling of nano-structured materials. Comp Sci Tech 62:1869–1880

Odegard GM, Gates TS, Wise KE, Park C, Siochi EJ (2003) Constitutive modeling of nanotube–reinforced polymer composites. Comp Sci Tech 63:1671–1687

Qian D, Dickey E, Andrews R, Rantell T (2000) Load transfer and deformation mechanisms in carbon nanotube-polystyrene composites. Appl Phys Lett 76(20):2868–2870

Salvetat-Delmotte JP, Rubio A (2002) Mechanical properties of carbon nanotubes: a fiber digest for beginners. Carbon 40:1729–1734

Schadler L, Giannaris SC, Ajayan PM (1998) Load transfer in carbon nanotube epoxy composites. Appl Phys Lett 73(26):3842–3844

Seidel GD, Lagoudas DC (2006) Micromechanical analysis of the effective elastic properties of carbon nanotube reinforced composites. Mech Mater 38:884–907

Selmi A, Friebel C, Doghri I, Hassis H (2007) Prediction of the elastic properties of single walled carbon nanotube reinforced polymers: a comparative study of several micromechanical models. Comp Sci Tech 67:2071–2084

Shokrieh MM, Rafiee R (2009) On the tensile behavior of an embedded carbon nanotube in polymer matrix with non-bonded interphase region. J Compos Struct. doi:10.1016/j.compstruct.2009.09.033

Shokrieh MM, Rafiee R (2010) A review of mechanical properties of isolated carbon nanotubes and carbon nanotube composites. J Mech Compos Mater 46(2):155–172

Spitalsky Z, Tasis D, Papagelis K, Galiotis C (2009) Carbon nanotube-polymer composites: Chemistry, processing, mechanical and electrical properties. Prog Polym Sci. doi:10.1016/j.progpolymsci.2009.09.003

Thostenson ET, Ren Z, Chou T-W (2001) Advances in the science and technology of carbon nanotubes and their composites: a review. Compos Sci Technol 61:1899–1912

Thostenson ET, Li CY, Chou T-W (2005) Nanocomposites in context. Compos Sci Technol 65:491–516

Tjong SC (2006) Structural and mechanical properties of polymer nanocomposites. Mater Sci Eng R 53:73–197

Tserpes KI, Papanikos P (2005) Finite element modeling of single-walled carbon nanotubes. Comp B 36:468–477

Tserpes KI, Panikos P, Labeas G, Panterlakis SG (2008) Multi-scale modeling of tensile behavior of carbon nanotube-reinforced composites. Theor Appl Fract Mech 49:51–60

Villoria RG, Miravete A (2007) Mechanical model to evaluate the effect of the dispersion in nanocomposites. Acta Mater 55:3025–3031

Wang Q (2004) Effective in-plane stiffness and bending rigidity of armchair and zigzag carbon nanotubes. Int J Sol Struct 41:5451–5461

Wolfarm S (1999) The mathematica book, 4th edn. Mathematica Version 4, Cambridge University Press, Cambridge
Zhang P, Huang Y, Geubelle PH, Klein PA, Hwang KC (2002) The elastic modulus of single-wall carbon nanotubes: a continuum analysis incorporating interatomic potentials. Int J Sol Struct 39:3893–3906
Zhu J, Peng H, Rodriguez-Macias F, Margrave J, Khabashesku V, Imam A, Lozano K, Barrera E (2004) Reinforcing epoxy polymer composites through covalent integration of functionalized nanotubes. Adv Funct Mater 14(7):643–648
ANSYS Inc. (2003) Theory manual, SAS IP Inc, Houston
Arroyo M, Belytschko T (2004) Finite crystal elasticity of carbon nanotubes based on the exponential Cauchy-Born rule. Phys Rev B 69:115415
Bahr JL, Tour JM (2002) Covalent chemistry of single-wall carbon nanotubes. J Mater Chem 12:1952–1958
Barber AH, Cohen SR, Wagner HD (2003) Measurement of carbon nanotube-polymer interfacial strength, Appl Phys Lett 82(23):4140–4142
Belytschko T, Xiao SP, Schatz GC, Ruoff RS (2002) Atomistic simulations of nanotube fracture. Phys Rev B 65:235–430
Buffa F, Abraham GA, Grady BP, Resasco D (2007) Effect of nanotube functionalization on the properties of single-walled carbon nanotube/polyurethane composites. J Polym Sci Part B: Polym Phys 45:490–501
Chang T, Gao H (2003) Size-dependent elastic properties of a single-walled carbon nanotube via a molecular mechanics model. J Mech Phys Sol 51:1059–1074
Cooper CA, Cohen SR, Barber AH, Wagner HD (2002) Detachment of nanotubes from a polymer matrix. Appl Phys Lett 81(20):3873–3875
Frankland SJV, Caglar A, Brenner DW, Griebel M (2002) Molecular simulation of the influence of chemical cross-links on the shear strength of carbon nanotube-polymer interfaces. J Phys Chem B 106:3046–3048
Frankland SJV, Harik VM, Odegard GM, Brenner DW, Gates TS (2003) The stress–strain behavior of polymer–nanotube composites from molecular dynamics simulation. Comp Sci Tech 63:1655–1661
Giannopoulos GJ, Kakavas PA, Anifantis NK (2008) Evaluation of the effective mechanical properties of single walled carbon nanotubes using a spring based finite element approach. Comput Mater Sci 41:561–569
Gou J, Minaei B, Wang B, Liang Z, Zhang C (2004) Computational and experimental study of interfacial bonding of single-walled nanotube reinforced composites. J Comput Mater Sci 31:225–236
Hernandez E, Goze C, Bernier P, Rubio A (1999) Elastic properties of single-wall nanotubes. Appl Phys A 68:287–292
Hull D (1996) An introduction to composite materials, 2nd edn. Cambridge University Press, Cambridge
Jin Y, Yuan FG (2003) Simulation of elastic properties of single-walled carbon nanotubes. Comp Sci Tech 63:1507–1515
Jones RM (1999) Mechanics of composite materials, 2nd edn. Taylor & Francis, Inc., Philadelphia
Kelly A, MacMillan NH (1986) Strong solids, 3rd edn. Clarendon Press, Oxford
Kleiber M, Hien TD (1992) The stochastic finite element method. John Wiley Publisher Science, New York
Krishnan A, Dujardin E, Ebbesen TW, Yianilos PN, Treacy MMJ (1998) Young's modulus of single-walled nanotubes. Phys Rev Lett B 58(20):14013–14019
Kuang Y, He X (2008) Young's modulus of functionalized single-walled carbon nanotubes under tensile loading. Compos Sci Technol. doi:10.1016/j.compscitech.2008.09.044
Lopez Manchado MA, Valentini L, Biagiotti J, Kenny JM (2005) Thermal and mechanical properties of single-walled carbon nanotubes—polypropylene composites prepared by melt processing. Carbon 43:1499–1505

Lu JP (1997) Elastic properties of carbon nanotubes and nanoropes. Phys Rev Lett 79(7): 1297–1300

Meo M, Rossi M (2006) Tensile failure prediction of single wall carbon nanotube. Eng Fract Mech 73:2589–2599

Paiva MC, Zhou B, Fernando KAS, Lin Y, Kennedy JM, Sun Y-P (2004) Mechanical and morphological characterization of polymer-carbon nanocomposites from functionalized carbon nanotubes. Carbon 42:2849–2854

Rafiee R (2013) Influence of carbon nanotube waviness on the stiffness reduction of CNT/ polymer composites. Compos Struct 97:304–309

Robertson DG, Brenner DW, Mintmire JW (1992) Energies of nanoscale graphitic tubule. Phys Rev B 45(21):12592–12595

Sadd MH (2005) Elasticity, theory application and numerics. Elsevier Butterworth-Heinemann, Oxford

Salvetat-Delmotte JP, Briggs GAD, Bonard JM, Bacsa RR, Kulik AJ (1999) Elastic and shear moduli of single-walled carbon nanotube ropes. Phys Rev Lett 82(5):944–951

Shi DL, Feng XQ, Huang YY, Hwang KC, Gao H (2004) The effect of nanotube waviness and agglomeration on the elastic property of carbon nanotube-reinforced composite. J Eng Mater Technol 126:250–257

Shofner ML, Khabashesku VN, Barrera EV (2006) Processing and mechanical properties of fluorinated single-wall carbon nanotube-polyethylene composites. Chem Mater 18:906–913

Shokrieh MM, Rafiee R (2009) Prediction of Young's modulus of graphene sheets and carbon nanotubes using nanoscale continuum mechanics approach. Mater Des 31:790–795. doi:10.1016/j.matdes.2009.07.058

Shokrieh MM, Rafiee R (2010a) Prediction of mechanical properties of an embedded carbon nanotube in polymer matrix based on developing an equivalent long fiber. Mech Res Commun 37(2):235–240

Shokrieh MM, Rafiee R (2010) Investigation of nanotube length effect on the reinforcement efficiency in carbon nanotube based composites. J Compos Struct (submitted)

Shokrieh MM, Rafiee R (2010c) Stochastic multi-scale modeling of CNT/polymer composites. Comput Mater Sci 50(2):437–446

Shokrieh MM, Rafiee R (2012) Development of a full range multi-scale model to obtain elastic properties of CNT/polymer composites. Iran Polym J 21(6):397–402

Sinnott SB (2002) Chemical functionalization of carbon nanotubes. J Nanosci Nanotechnol 2:113–123

Tsai SW, Hoa CV, Gay D (2003) Composite materials design and applications. CRC Press, Boca Raton

Tserpes KI, Papanikos P, Tsirkas SA (2006) A progressive fracture model for carbon nanotubes. Comp B 37:662–669

Wang S, Liang Z, Wang B, Zhang C (2006) Statistical characterization of single-walled carbon nanotube length distribution. Nanotechnology 17:634–639

Xiao JR, Gama BA, Gillespie Jr JW (2005) An analytical molecular structural mechanics model for the mechanical properties of carbon nanotubes. Int J Solid Struct 42:3075–3092

Yakobson BI, Brabec CJ, Bernholc J (1996) Nanomechanics of carbon tubes: instabilities beyond linear response. Phys Rev Lett 76(14):2511–2514

Yao N, Lordi V (1998) Young's modulus of single-walled carbon nanotubes. J Appl Phys 84(4):1939–1943

Yu MF, Lourie O, Dyer MJ, Moloni K, Kelly TF, Ruo RS (2006) Strength and breaking mechanism of multiwalled carbon nanotubes under tensile load. Science 287(5453):637–640

Molecular Dynamics Simulation and Continuum Shell Model for Buckling Analysis of Carbon Nanotubes

C. M. Wang, A. N. Roy Chowdhury, S. J. A. Koh and Y. Y. Zhang

Abstract Carbon nanotubes (CNTs) have potential applications in various fields of science and engineering due to their extremely high elasticity, strength, and thermal and electrical conductivity. Owing to their hollow and slender nature, these tubes are susceptible to buckling under a compressive axial load. As CNTs can undergo large, reversible post-buckling deformation, one may utilize this post-buckling response of CNT to manufacture mechanical energy storage devices at the nano-scale, or use it as a nano-knife or nano-pump. It is therefore important to understand the buckling behavior of CNTs under a compressive axial load. Experimental investigations on CNT buckling are very expensive and difficult to perform. As such, researchers often rely on molecular dynamics (MD) simulations, or continuum mechanics modeling to study their mechanical behaviors. In order to develop a good continuum mechanics model for buckling analysis of CNTs, one needs to possess adequate experimental or MD simulation data for its calibration. For "short" CNTs with small aspect ratios ($\leq$10), researchers have reported different critical buckling loads/strains for the same CNTs based on MD simulations. Moreover, existing MD simulation data are not sufficiently comprehensive to allow rigorous benchmarking of continuum-based models. This chapter presents

C. M. Wang (✉) · S. J. A. Koh
Engineering Science Programme and Department of Civil and Environmental Engineering, National University of Singapore, Kent Ridge 119260, Singapore
e-mail: ceewcm@nus.edu.sg

S. J. A. Koh
e-mail: ceeksja@nus.edu.sg

A. N. Roy Chowdhury
Department of Civil and Environmental Engineering, National University of Singapore, Kent Ridge 119260, Singapore
e-mail: amar@nus.edu.sg

Y. Y. Zhang
School of Computing, Engineering and Mathematics, University of Western Sydney, Penrith, NSW 2751, Australia
e-mail: yingyan.zhang@uws.edu.au

K. I. Tserpes and N. Silvestre (eds.), *Modeling of Carbon Nanotubes, Graphene and their Composites*, Springer Series in Materials Science 188,
DOI: 10.1007/978-3-319-01201-8_8,

extensive sets of MD critical buckling loads/strains for armchair single-walled CNT (SWCNTs) and double-walled CNTs (DWCNTs), with various aspect ratios less than 10. These results serve to address the discrepancies found in the existing MD simulations, as well as to offer a comprehensive database for the critical buckling loads/strains for various armchair SWCNTs and DWCNTs. The Adaptive Intermolecular Reactive Bond Order (AIREBO) potential was adopted for MD simulations. Based on the MD results, the Young's modulus, Poisson's ratio and thickness for an equivalent continuum cylindrical shell model of CNTs are calibrated. The equivalent continuum shell model may be used to calculate the buckling loads of CNTs, in-lieu of MD simulations.

Keywords Carbon nanotubes · Buckling loads · Molecular dynamics simulations · Thick shell model

1 Introduction

First discovered by Iijima (1991), carbon nanotubes (CNTs) have triggered intense research activities due to their superior properties such as high mechanical strength, excellent thermal and electrical conductivity. CNTs are long and slender cylindrical nanostructures, with diameters of the order of few nanometers, and lengths ranging from several nanometers to several millimeters. CNTs are broadly classified into single-walled carbon nanotubes (SWCNTs) and multi-walled carbon nanotubes (MWCNTs). The ends of the nanotubes may either be open or covered by a surface of similar crystal structure. In pristine SWCNTs, the ends are typically covered with hemispherical fullerene molecule whereas in the case of MWCNTs, the end covers are polyhedral (Saito et al. 1992).

The geometry of a pristine SWCNT may be visualized by wrapping graphene sheet around a cylindrical surface. The direction of wrapping with respect to the crystal structure is known as the chiral vector **C**, which is represented by a pair of integers as shown in Fig. 1a. Based on the wrapping direction, there exist three types of SWCNTs, i.e. armchair, chiral and zigzag (see Fig. 1b). The length of a unit cell of CNT is equal to the magnitude of translational vector **T** as shown in Fig. 1a. Vector **T** is orthogonal to the chiral vector **C** and its magnitude depends on chirality of CNT. MWCNTs consist of multiple nested SWCNTs separated radially by 0.34 nm, which is the equilibrium distance between two parallel graphene sheets. Mechanical strength of MWCNTs can be increased by reducing the intertube spacing below 0.34 nm using neutron irradiation (Xia et al. 2007). These MWCNTs are known as condensed MWCNTs and they have a higher mechanical strength when compared to the normal ones (Zhang et al. 2009).

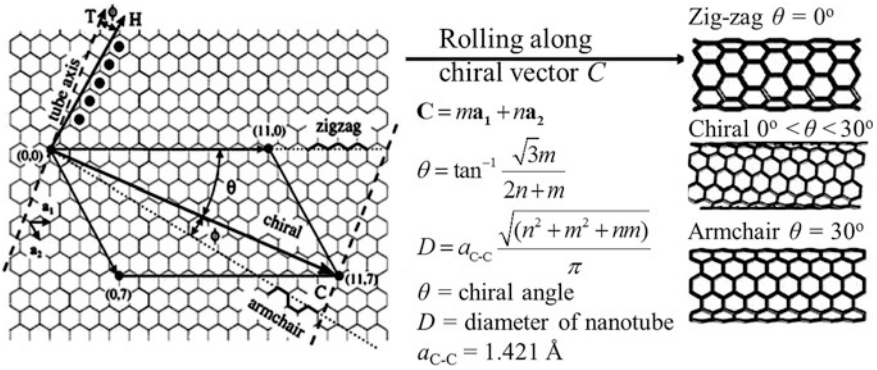

Fig. 1 **a** Translational vector T and chiral vector C **b** Three types of carbon nanotubes

1.1 Special Properties of CNT and Their Applications

CNTs with a very high aspect ratio (length-to-diameter ratio ~1000) can be used as a substitute to conventional fiber materials such as electro-spun (E/S) glass, Kevlar, and polyacrylonitrile (PAN) based carbon fiber. A comparison of mechanical and transport properties between CNTs and conventional fiber materials are given in Tables 1 and 2. The tables show mechanical properties (breaking strain, tensile strength, Young's modulus) of CNTs are not only superior compared to those of conventional fiber materials but these fibers are also lighter and their transport properties (thermal and electrical conductivity) are also comparable to very highly conductive fibers. Although the thermal conductivity of CNT is much less compared to PAN carbon fibers but overall properties of CNT are much superior to PAN carbon fibers.

Owing to their high quality mechanical, electrical, and, thermal properties, CNTs have diverse applications in different fields of engineering and science listed as follows:

Table 1 Mechanical properties of various fiber materials

Fiber material	Specific density	Young's modulus (TPa)	Tensile strength (GPa)	Breaking strain (%)
CNT (Koziol et al. 2007)	1.3–2	0.2–5	10–60	~10.0
HS Steel	7.8	0.2	4.1	<10.0
Carbon fiber–PAN (Liu et al. 2008)	1.7–2	0.2–0.6	1.7–5	0.3–2.4
Carbon fiber–Pitch	2–2.2	0.4–0.96	2.2–3.3	0.27–0.6
E/S–glass	2.5	0.07–0.08	2.4–4.5	~4.8
Kevlar	1.4	0.13	3.6–4.1	2.8

Note http://www.nanocyl.com/CNT-Expertise-Centre/Carbon-Nanotubes (Huang 2009)

Table 2 Transport properties of CNTs and various fiber materials

Material	Thermal conductivity (mK) at 298 K	Electrical conductivity (S/m) at 298 K
CNT (Kim et al. 2001; Li et al. 2007)	25–3000	10^6–10^7
Copper	400	6×10^7
Pitch carbon fiber	1000	2×10^6–8.5×10^6
PAN carbon fiber	8×10^5	6.5×10^6–1.4×10^7

Note http://www.nanocyl.com/CNT-Expertise-Centre/Carbon-Nanotubes

(a) Mechanical, materials and structural systems

(i) Polymer composites (Harris 2004)
(ii) Nano-gears (Endo et al. 2006)
(iii) Artificial muscles (Aliev et al. 2009)
(iv) CNT cement composites (Aliev et al. 2009; Gdoutos et al. 2010; Makar et al. 2005; Zhu et al. 2004)
(v) Atomic force microscopy (AFM) probes (Stevens et al. 2000)
(vi) Nano-cutting tool (Duan et al. 2010)
(vii) Mechanical energy storage devices (Cao et al. 2005; Kozinda et al. 2012)
(viii) High performance composites (De Volder et al. 2013).

(b) Electro-magneto-mechanical systems

(i) Buckypaper (Wang et al. 2008)
(ii) Stretchable and flexible electronic circuits (Sun et al. 2011)
(iii) Electronic motor brushes (Endo et al. 2006)
(iv) Electro-mechanical transducers (Cohen-Karni et al. 2006; Hall et al. 2007).

(c) Green technologies and hydrogen storage

(i) Solar cells (Guangyong and Liming 2011; Klinger et al. 2012)
(ii) Membrane filters (Tanaka 2010)
(iii) Hydrogen storage (Cheng et al. 2001).

1.2 Buckling of CNTs and its Significance

CNTs possess a hollow cylindrical geometry made of one atomic layer of carbon atoms. As such, CNTs are prone to buckle under mechanical loads. Under a compressive axial load, mechanical torque or a bending moment, a CNT experiences localized or global compressive stresses. Compressive stress may result in localized shell-like buckling within the atomic layer of a short CNT, or globalized beam-like buckling for a long and slender CNT. This is usually accompanied by an abrupt change in its transport properties, and a drastic decrease in its mechanical stiffness.

In nano-scale applications such as electro-mechanical transducers, artificial muscles, and AFM probes, buckling often leads to instability and failure of the system. Hence, an optimal design of such CNT-based nano-devices requires a clear knowledge of when and how buckling will occur. That said, buckling of CNT is not always detrimental to the function of nano-devices. One may harness the large deformation, as a result of CNT buckling, to construct a super-compressible spring or structural system (Cao et al. 2005). Such a system of super-compressible CNTs can be squeezed and constrained to store mechanical energy. It is also observed that in bent CNT, localized buckling induces extra curvature at the buckled regions thereby increasing the total strain energy stored in the CNT (Duan et al. 2010). When the bent CNT is released, the stored strain energy are converted into kinetic energy and results in a huge impact load that can be used to cut nano-sized materials.

Therefore the buckling phenomenon of CNT gives CNT intrinsic mechanical properties (e.g. super-compressibility due to elastic buckling under axial load). Hence, an in-depth understanding on the buckling behavior of CNTs allows one to design a CNT-based system that works more effectively and efficiently. This chapter is devoted to the study of buckling behavior of short CNTs under a compressive axial load.

1.3 Atomistic-Based Methods for CNT Buckling Analysis

Buckling analysis of CNT are experimentally conducted using nano-indenters (Waters et al. 2006) which require high precision instruments to measure the buckling load because the buckling loads are usually in the range of 1 nN − 1 μN. These experiments also require expensive instruments like Atomic Force Microscope (Tombler et al. 2000) or optical tweezers etc. (Xu et al. 2009) for picking and aligning the CNTs, and high resolution microscopes such as scanning electron microscope (Tombler et al. 2000) for imaging the CNT. So far, due to difficulty of building an experimental set up at small scale, unavailability of very small nano-indenters and high precision measuring instruments, experimental analysis of CNT buckling has only been possible for MWCNTs longer than 50 nm. The challenge in experiments is evidenced from the fact that relatively few experimental works have been published in the literature. Hence, researchers rely on computational simulations, in particular, atomistic-based or continuum-based methods for the buckling analysis of CNTs.

Atomistic methods are more computationally intensive when compared to continuum-based methods, as it seeks to model the interactions between individual atoms. Consequently, atomistic methods are able to model the physical system accurately as inter-atomic interactions are usually rather well-defined and are grounded upon comparison with first-principle calculations (Sun 1998) or based on experimental results like bond energy and atomization energy (Brenner et al. 2002). We begin by describing three broad classes of atomistic-based

methods, followed by several continuum-based methods, targeted to analyze CNTs under compressive loading.

1.3.1 Molecular Mechanics (MM) and Molecular Dynamics (MD)

In MD/MM, the atomic structure is first defined in accordance to the crystal structure of the CNT. Interactions of carbon atoms in CNT are defined by inter-atomic potential energy function which is either obtained from quantum mechanical calculations (Sun 1998), or from experimental results (Stuart et al. 2000). In general, the inter-atomic potential energy is a function of the position of atoms in the CNT. Force on each atom in the system is derived from the gradient of the total potential energy in CNT.

In MM, thermodynamic equilibrium is achieved by minimizing the total potential energy of the system by changing the atomic coordinates. The governing equation for MM is given by

$$\frac{\partial U(\mathbf{r})}{\partial \mathbf{r}} = 0 \tag{1}$$

where U is the total potential energy of the system and $\mathbf{r}$ is the position vector of atom.

MM does not consider time dependent quantities like velocity, acceleration, and inertia force. Unlike MM, MD is performed by solving Newton's equation of motion for each atom in the system. The governing equations for MD are given by

$$m_i \frac{d^2 \mathbf{r}_i}{dt^2} = \mathbf{F}_i \tag{2}$$

and

$$\mathbf{F}_i = -\frac{\partial U\left(\mathbf{r_1}, \mathbf{r_2}, \ldots, \mathbf{r}_i, \ldots, \mathbf{r}_N\right)}{\partial \mathbf{r_i}} \tag{3}$$

where $\mathbf{r}_i$ is the position vector of atom i, N is the total number of atoms, and $\mathbf{F}_i$ is the force vector acting on atom i, m_i is the mass of ith atom and, t is the time.

Temperature is a continuum parameter, which is related to the total kinetic energy of the system (Frenkel and Smith 2002). Since MM does not consider transient, dynamic quantities, it cannot account for the thermal effect during geometry optimization, unless one introduces a parameter into the inter-atomic potential energy function for thermal change. To do this, MM may adopt a temperature-dependent inter-atomic potential energy function. This type of MM is termed as engineering molecular mechanics (EMM) which was developed by Subramaniyan and Sun (2008). For MD, the temperature is usually controlled using thermostats (Hünenberger 2005).

To perform buckling analysis of CNT using MM/MD method, the CNT is incrementally deformed or loaded. After deforming the CNT, MM/MD is used to compute a state of thermodynamic equilibrium. These steps are repeated until termination. Termination may either be prescribed by the user, or when a state of thermodynamic equilibrium cannot be obtained.

1.3.2 Dissipative Particle Dynamics (DPD)

DPD is commenced by hypothetically dividing the atomic system into small cells that contains more than one atom in each cell (Flekkøy et al. 2000; Fuchslin et al. 2009). Atoms in each of these cells are lumped into a single node which acts as a representative particle during DPD simulations. A collection of these particles are termed dissipative particles. This approximation of a group of atoms as a single representative atom is called coarse-graining. For CNTs, researchers usually take 24 atoms for the coarse-graining procedure (Liba et al. 2008). One may also consider more carbon atoms for coarse-graining but that may induce more approximation errors. By coarse-graining, DPD can simulate much larger atomic systems than MM or MD. However, also due to coarse-graining, DPD is less accurate than MM or MD. Like MD, DPD is also a dynamic method where Newton's equations of motion have to be solved. For each dissipative particle, Newton's equations of motion are collectively given by

$$m_i \frac{d^2 \mathbf{r_i}}{dt^2} = \mathbf{F}_i^{ext} + \sum_{i \neq j} \left(\mathbf{F}_{ij}^{\mathrm{C}} + \mathbf{F}_{ij}^{D} + \mathbf{F}_{ij}^{\mathrm{R}} \right) \tag{4}$$

where $\mathbf{r_i}$ is the position vector of atom *i*. $\mathbf{F}_i^{ext}$ is the external force vector acting on atom *i*, $\mathbf{F}_{ij}^{\mathrm{C}}$ is a conservative force, $\mathbf{F}_{ij}^{\mathrm{D}}$ is a dissipative force, $\mathbf{F}_{ij}^{\mathrm{S}}$ is a stochastic force. Equation (4) is solved to obtain the response of the system.

In DPD, $\mathbf{F}_{ij}^{\mathrm{C}}$ is calculated from a potential energy function and it considers the interaction between dissipative particles. $\mathbf{F}_{ij}^{\mathrm{D}}$ represents a viscous resistance which controls the temperature of the system. The force $\mathbf{F}_{ij}^{\mathrm{S}}$ takes care of the lost degrees of freedom due to coarse-graining.

1.4 Continuum-Based Methods for CNT Buckling Analysis

Since atomistic methods capture the response at the atomic level, these methods are computationally intensive. Hence, researchers resort to continuum-based approaches for buckling analysis of CNT. Continuum-based approaches are less accurate when compared to atomistic methods, but they are far more computationally efficient. There are different continuum-based approximations for establishing a computational model for CNT. After establishing the computational

model using continuum-based methods, buckling analysis can be performed by conventional eigenvalue analysis or nonlinear buckling analysis. There are different types of continuum-based approaches for buckling analysis of CNTs which are briefly described below.

1.4.1 Continuum Shell Models

The geometry of CNT resembles that of a cylindrical shell. Hence, (Yakobson et al. 1996) proposed to homogenize one atomic layer thick cylindrical CNT geometry as a cylindrical shell. There are two types of continuum shell theories used to model CNTs (Wu et al. 2009). In Type I continuum model, conventional shell theories e.g. Donnell shell and Sanders shell with an assumed elastic constitutive relation are used to analyze the CNTs (Batra and Sears 2007; He et al. 2005, 2010; Pantano et al. 2003, 2004a, b Sears and Batra 2006; Wang et al. 2006, 2011; Zhang et al. 2009). Type I continuum shell model requires parameters such as Young's modulus E, Poisson's ratio ν, and shell thickness h; which are usually calibrated from MD simulation results. In Type II shell model, the equilibrium equations are derived by minimizing the total potential energy of the CNT (Ansari and Rouhi 2010; Belytschko et al. 2002; Cheng et al. 2009; Hu et al. 2007; Li and Chou 2003; Lu et al. 2010).

To include the effect of temperature in the buckling analysis of CNT using Type I shell model, one need to calibrate material parameters of CNT at that temperature. In Type II shell model, the effect of temperature can be explicitly incorporated by deriving the equilibrium equations of CNT from the total Helmholtz free energy (Jiang et al. 2005).

Researchers also incorporate a non-local effect in Type I continuum shell models for CNTs. The non-local parameters for CNT are calibrated from MD simulation results (Zhang et al. 2009; Khademolhosseini et al. 2009; Shen 2004). In Type II continuum shell model, the non-local effect is implicitly considered in the formulation. Although Type II shell theory for CNT is more realistic, accurate and general as compared to Type I shell theory, Type I is mostly preferred among researchers because of its ease of implementation.

1.4.2 3D Frame Model

Owing to the resemblance of CNT geometry to a cylindrical frame structure, a 3D frame model is also used among researchers to analyze CNT (Li and Chou 2003; Chen and Cao 2006). In a 3D model, the axial and angular springs are used to model multi-body inter-atomic interactions in CNT. The stiffness of different spring elements is calculated from an inter-atomic potential energy function. Owing to its discrete nature, the grillage model can directly account for chirality in CNT.

1.4.3 Atomic-Scale Finite Element Method

Atomic-scale finite element method (AFEM) resembles the mesh-free finite element method. In AFEM, the atoms of the CNT are treated as finite element nodes and the finite element equations are derived in the same fashion as it is done in Type II continuum shell theory (Liu et al. 2004). Detailed derivation of stiffness and force matrices for AFEM for different inter-atomic potentials can be obtained from the paper by Wackerfuß (2009). Like Type II shell model, AFEM can also consider the nonlinear nature of inter-atomic potential. However, AFEM is more versatile than Type II shell model because AFEM can easily consider the effect of defects and chirality in CNT.

1.4.4 Beam Model for Very Long CNTs

Long CNTs with aspect ratios more than 20 exhibit beam-like buckling mode, with little or no localized shell buckling within the atomic layer. Hence, researchers use conventional beam theories to study the buckling behavior of long CNTs (Hu et al. 2009; Wang et al. 2006; Wong et al. 1997). For the beam model of CNT, the material properties (E, G) and geometrical properties such as h are obtained from MD simulations. The disadvantages of a beam model are that it cannot capture the chirality effect, the effect of defects, and the local deformation mode in CNT. Non-local effect can also be considered in the beam model for CNTs by using a non-local parameter calibrated from MD simulations (Zhang et al. 2009).

1.5 Discrepancies in Existing MD Simulation Data for Buckling Analysis of CNTs

There is a significant number of atomistic-based simulations done to estimate the critical buckling loads (P_{cr})/strains (ε_{cr}) of CNTs. In our literature survey, we observed that the buckling results for armchair CNTs (chirality index: $m = n$) are not comprehensive enough for use in calibrating continuum mechanics models. Moreover, the buckling results of armchair CNTs from MD simulations reported by different researchers have discrepancies. For example

- From Fig. 2 it is observed that for the same SWCNT (5,5), with different interatomic potentials, researchers obtained different critical buckling strain (ε_{cr}) versus aspect ratio (L/D) curves. It is thus unclear which inter-atomic potential predicts the correct buckling behavior of CNTs.
- For the same CNT, reported ε_{cr} values estimated using same REBO^{2nd} + LJ potential are different (see Fig. 3) which varies between 0.06 and 0.047. These differences may be attributed to different MD simulation parameters such as time step size and incremental displacement adopted for the MD simulations.

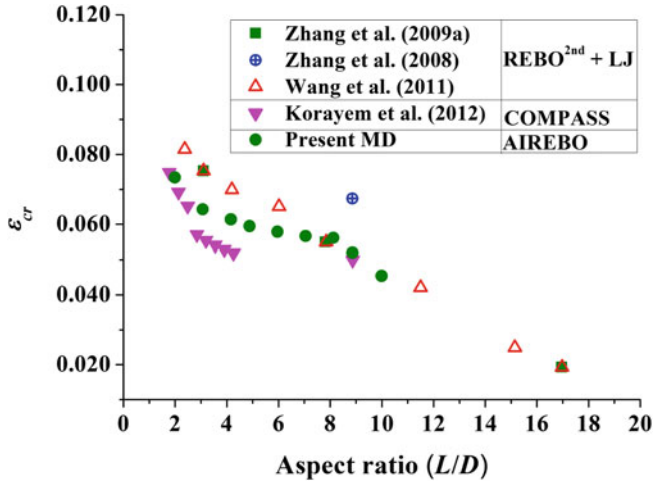

Fig. 2 Comparison of buckling strains for SWCNT(5,5) reported by different researchers

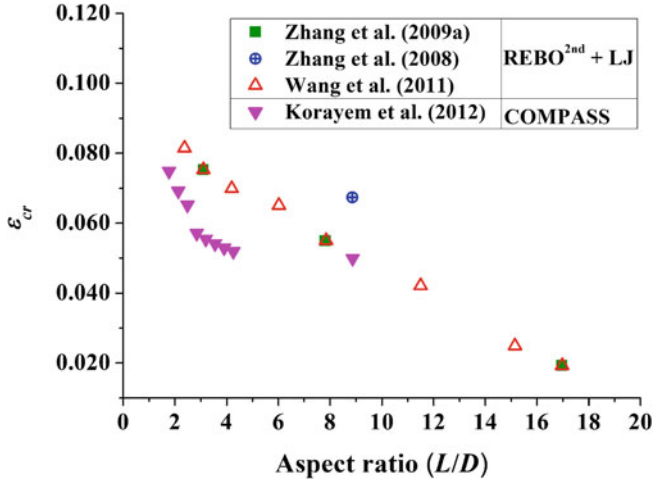

Fig. 3 Comparison of buckling strains for DWCNT((5,5),(10,10)) reported by different researchers

Hence, it is important to know the effect of simulation parameters on buckling strain/load of CNT. It is also necessary to determine a set of simulation parameters suitable to conduct quasi-static buckling analysis of CNT.

- Korayem et al. (2012) using COMPASS potential showed that critical buckling strain of DWCNT((5,5),(10,10)) decreases with increasing aspect ratio and this trend is also supported by conventional cylindrical shell buckling results (Wang et al. 2011). However, by comparing buckling strain results reported by

Korayem et al. (2012) and Kulathunga et al. (2009), it is observed that for a DWCNT((5,5),(10,10)) with an aspect ratio of 12.0 the critical buckling strain is 0.0475, which is higher than 0.0432 for DWCNT((5,5),(10,10)) with smaller aspect ratio of 8.9. These buckling results are contradictory.

1.6 Objectives

The objectives of this chapter are:

- To furnish a comprehensive set of MD buckling results for armchair SWCNTs and DWCNTs which serve as reference to develop continuum based model for CNTs.
- To establish a Type I equivalent cylindrical shell model for buckling analysis of SWCNTs and DWCNTs based on the reference MD buckling results.

2 MD Simulation Results for Buckling of CNTs

MD simulations are carried out using the software package LAMMPS (Plimpton 1995) in a 64-bit machine. For MD simulations, we have selected armchair CNTs with small aspect ratios (i.e. $L/D_i \leq 10$) in order to study shell like deformation behavior of stocky CNTs. The MD simulation results reported in this chapter will be used to develop a robust continuum model for compressive buckling analysis of armchair CNTs with small aspect ratio which will also be applicable for compressive buckling analysis of CNTs with large aspect ratio. A total 49 SWCNTs and 23 DWCNTs are considered. Adaptive Intermolecular Reactive Empirical Bond Order (AIREBO) potential suitable for hydrocarbons (Stuart et al. 2000) is used for all the MD simulations. MD simulation setup and key steps for buckling analysis of CNT are described in the next section.

2.1 MD Simulation Setup and Key Simulation Steps

Geometry of CNT is constructed by mapping a 2-dimensional graphene sheet onto a 3-dimensional circular cylindrical surface. Due to finite curvature on the cylindrical surface, C–C bonds are stretched, resulting in a stressed initial configuration of the CNT. Hence, prior to the MD simulations, the conjugate gradient algorithm is used to minimize the potential energy of the CNT to relax the stresses.

After the minimization process, the CNT achieves a stress-free state and serves as a reference, undeformed configuration for MD simulations. The CNT is heated to 1 K by the velocity rescaling method. Thereafter, MD simulation is carried out by moving one end of the tube with a small incremental displacement $\Delta d = 0.01$ Å

as shown in Fig. 4. The equations of motion are integrated using the velocity-Verlet algorithm for a total period of T_s (termed as relaxation period) = 10.0 ps (11^{-11}s) with a time step size $\Delta t = 1$ fs (10^{-15}s). During the MD simulations, a Nosé-Hoover thermostat (Hünenberger 2005) is used to maintain the system temperature at 1 K. Thermodynamic quantities (temperature, force, and potential energy) are recorded after averaging these quantities for 5000 time steps. The key parameters in MD buckling analysis of CNT are the inter-atomic potential, the incremental displacement Δd, the relaxation period T_s, the time step Δt and the thermostat. In the following sections, we first present the definition of buckling of CNT under compressive load, followed by detailed discussions on the effect of key simulation parameters on MD buckling analysis of CNT.

2.2 Definition of Buckling Load and Buckled Mode Shape

From MD simulation the axial load P versus end shortening Δ plot is obtained as shown in Fig. 5a. The critical buckling state is detected by a sudden drop in the axial load in the plot. As it can be see from Fig. 5a there are two values of axial load at the critical buckling state. The upper value of P at the critical buckling state

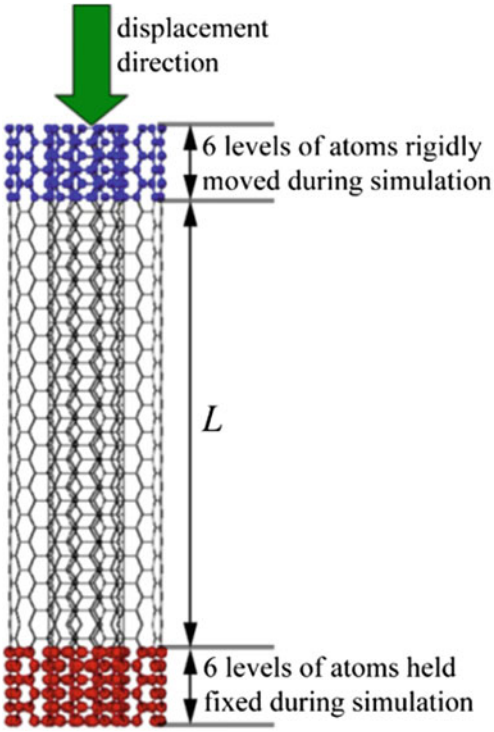

Fig. 4 MD simulation setup

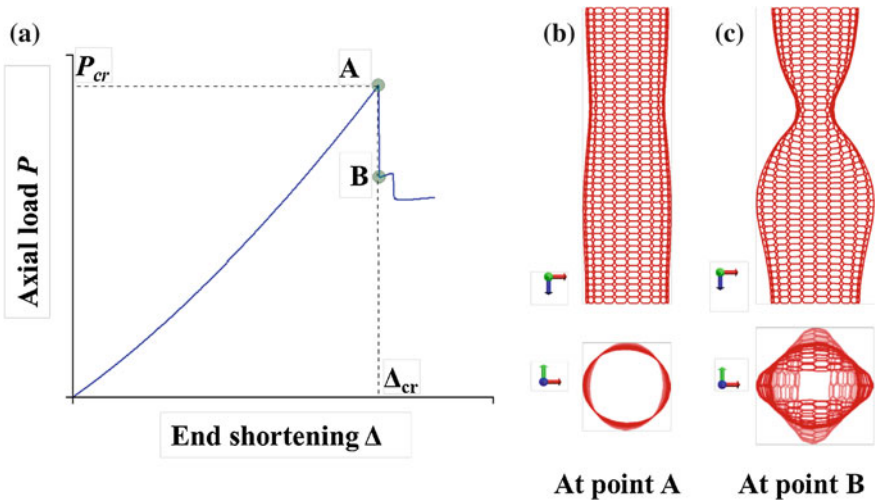

Fig. 5 (**a**) Typical axial load P versus end shortening Δ plot for CNT (**b**) Deformed shape of CNT prior to buckling (**c**) Definition of buckled mode shape of CNT

is defined as the critical buckling load P_{cr} and the corresponding end-shortening is defined as critical end shortening Δ_{cr}. The critical buckling strain ε_{cr} is calculated by dividing Δ_{cr} with the original length L of CNT (please refer to Fig. 4 for the definition of L).

At the critical buckling state, there are two distinct deformed shapes of the CNT. One deformed shape, associated with the P_{cr} (at Point A in Fig. 5a), has slight ripples with the nanotubes section remaining almost circular. The other deformed shape, associated with the lower value of the load (i.e. Point B in Fig. 5a), has flattened portions (sometimes referred to as fins). This observation is similar to the bifurcation buckling of beams and cylindrical shells under axial load where the two equilibrium states are that of an undeformed structural member and that of a grossly deformed shape of the structural member. The buckled mode shape of CNT associated with critical buckling load P_{cr} is defined by the grossly deformed shape at Point B (see Fig. 5a) in the axial load versus end shortening curve.

2.3 Simulation Parameters

For MD analysis of CNT buckling the key parameters are discussed as follows.

2.3.1 Interatomic Potential and Energy Minimization

Xu and Buehler (2010) showed that the AIREBO potential developed by Stuart et al. (2000) can predict wrinkling patterns in graphene sheets that come close to experimental observations. Zheng et al. (2012) also used the AIREBO potential to

study the mechanical strength of graphene and observed that the tensile strength of graphene calculated from their MD simulation agrees well with experimental results. As graphene and CNT possess similar type of sp^2 hybridized C–C covalent bonds, we therefore opine that AIREBO potential should model the interatomic interactions of CNTs rather well. Moreover, deformation induced curvature in CNT changes the hybridization state (Yakobson and Avouris 2001) which can also be captured by the AIREBO potential (Zheng et al. 2012). So, the AIREBO potential is adopted for MD simulations in this study. This potential comprises three terms.

$$U^{AIREBO} = U^{2nd-REBO} + U^{LJ} + U^{Tors} \tag{5}$$

where $U^{2nd-REBO}$ is the second generation REBO potential (Brenner et al. 2002) which accounts for the covalent bond interaction, U^{LJ} is the 12-6 Lennard-Jones' potential (Girifalco and Lad 1956) that accounts for the non-bonded interaction among atoms beyond a distance of 2 Å and, U^{Tors} is the torsional potential term. This potential is discussed in detail in Appendix.

Prior to MD simulations, the minimization of the total potential energy of CNT is necessary to remove excess forces in the initial geometry of the system. A proper energy minimization ensures that there is no resultant force on any atom in the system. To achieve this initial minimum energy state, the absolute maximum force on an atom in the system after energy minimization should be sufficiently small (say $\leq$0.001 eV/Å). Note that this minimization process consumes only a very small percentage ($\sim$2 %) of the total simulation time.

Figure 6 shows the effect of improper energy minimization on axial load P versus end shortening Δ behavior of CNT obtained from MD simulation with different convergence tolerances on absolute maximum force on an atom. For example the line with square symbol represents axial load versus end shortening curve obtained by setting maximum force convergence tolerance 0.001 eV/Å. It can be seen from Fig. 6 that, if the maximum force on an atom in the system after energy minimization is not less than or equal to 0.001 eV/Å, then a non-zero axial load at zero end shortening will be obtained.

2.3.2 Integration Time-Step (Δt)

The time-step Δt is dependent on the numerical integration algorithm; Δt has to be smaller than the lowest period of bond vibration occurring in the CNT (van Gunsteren and Berendsen 1990). In the present MD simulations, the velocity Verlet algorithm (Rapaport 2004) is adopted. A suitable value of the time-step size for all the MD simulations is ascertained by performing a set of MD simulations with different time steps. It is observed that $\Delta t = 10^{-15}$s (1 fs) is appropriate and this time-step has also been used by many researchers to perform MD simulations for buckling analysis of CNTs (Wang et al. 2011; Zhang et al. 2009; Liew et al. 2004).

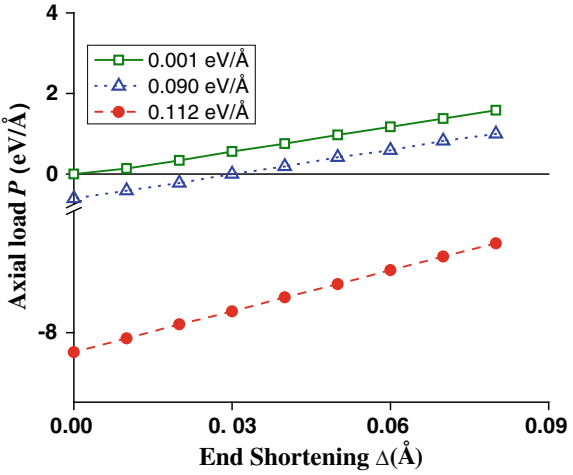

Fig. 6 Effect of energy total potential energy minimization on P versus Δ plot of CNT (square represents force minimization tolerance of 0.001 eV/Å, triangle represents force minimization tolerance of 0.09 eV/Å, filled circles represents force minimization tolerance of 0.112 eV/Å

2.3.3 Relaxation Time (T_s)

In displacement-controlled buckling analysis, one end of CNT is perturbed by small displacement, and during MD simulations, the effect of this perturbation travels through the tube. If the rate of change of displacement is sufficiently slow, such that each displacement perturbation homogeneously affects the entire tube, the simulation is quasi-static. On the other hand, if the displacement rate is too rapid, the effect of each displacement perturbation on the tube may depend on the previous perturbation; the simulation is non-quasi-static. In our simulations, we only consider quasi-static deformation. Hence, for a given perturbation, we compute the total time required for the entire CNT to achieve thermodynamic equilibrium, known as the relaxation time T_s. It is hence obvious that longer T_s are needed for longer tubes. To establish the relaxation period required for quasi-static MD simulation, we have selected the 136Å long DWCNT ((10,10),(15,15)) which is the longest CNT with $L/D_i \leq 10.0$ (D_i is inner diameter). MD analyses were carried out on this DWCNT with different T_s, while keeping the incremental displacement constant at $\Delta d = 0.01$Å. We observe that $T_s = 10$ ps is sufficient to ensure quasi-static deformation. Thus, we adopt this T_s for all MD simulations. Clearly, for shorter CNTs, the adopted relaxation period is also sufficient to ensure quasi-static deformation. We study a 271Å long SWCNT (10,10) as a special case. This tube requires a $T_s = 50$ ps. As a general remark, for tubes longer than those used in the present MD simulations, a longer relaxation period is required.

2.3.4 Incremental Displacement (Δd)

Here we have performed displacement-controlled quasi-static buckling analysis of CNTs. In a displacement-controlled MD scheme, one needs to ascertain Δd based on solution accuracy and computational cost. To determine a suitable Δd value, we

have performed buckling analysis of DWCNT ((5,5),(10,10)) with a length of 60 Å by using three incremental steps 0.1 Å, 0.01 Å, and 0.005 Å but keeping the same relaxation time of 10 ps. The force deformation plots for these three cases are shown in Fig. 7.

Except for the MD simulation with $\Delta d = 0.1$Å, the other two force deformation plots are almost the same. From Fig. 7a, it can be observed that the critical buckling load and critical buckling strain are underestimated using an incremental displacement of 0.1 Å. For the 0.01 Å and 0.005 Å cases, the estimated critical buckling loads are within a tolerance of 0.1 %, and the critical buckling strains are almost the same. MD simulation with $\Delta d = 0.005$ Å is very computationally intensive and therefore, we have adopted $\Delta d = 0.01$ Å for all our MD simulations.

In theory, one may freely choose Δd of any magnitude. Physically, if the prescribed Δd is too large, it will rupture the CNT in just one step. This effect may be understood as an impulsive force impacting on the CNT. This force will cause rupture in the atomic bonds within its vicinity, which is captured by our simulations in LAMMPS. In such a simulation, LAMMPS will terminate with an error, as no thermodynamic equilibrium may be obtained. Nevertheless, the evolution of bond rupture may be observed by varying T_s. As shown in Fig. 7b, for $T_s = 10$ ps, a few bonds at the tip of DWCNT ruptures, whereas for $T_s = 100$ ps, the entire circumference of the CNT has ruptured bonds. To enable quasi-static deformation of a CNT under compression to be analyzed, we need to choose a Δd such that impulsive rupture does not occur. In our simulations, we observed that for Δd close to the C–C bond length of 1.42 Å, impulsive rupture occurs during the first displacement increment. Hence, we conclude that Δd value must be significantly smaller than the smallest bond length in the system.

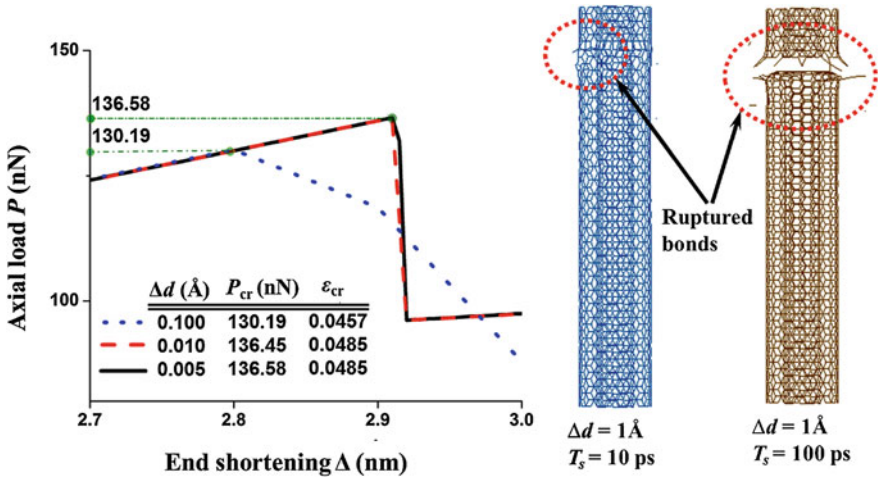

Fig. 7 Effect of large incremental displacement on load deformation plot

2.3.5 Thermostat

Berendsen thermostat, Nosé-Hoover thermostat and velocity rescaling thermostat are the most commonly used thermostats in MD simulations of CNTs (Wang et al. 2010). Researchers observed that the Nosé-Hoover and velocity rescaling thermostat results in reasonable mechanical deformation modes regardless of the percentage of thermostat atoms (Wang et al. 2010; Heo and Sinnott 2007). In Fig. 8, a comparison of the MD simulation results obtained using the Nosé-Hoover thermostat, velocity rescaling thermostat and Berendsen thermostat are made. For the case studies, 60 Å long DWCNT ((5,5),(10,10)) is chosen.

The axial load versus end shortening plots and the variations of temperature during simulation are shown in Fig. 8a, b respectively. It is observed that the axial load versus end shortening curves obtained by using different thermostats are almost indistinguishable and also the critical buckling load of 60 Å long DWCNT ((5, 5), (10,10)) obtained using different thermostats are close. For example, the MD simulation with Velocity rescale thermostat gives a critical buckling load of 136.6 nN which is very close to 136.5 nN obtained from MD simulations with the Nosé-Hoover thermostat. However, unlike the other thermostats, the Nosé-Hoover thermostat can maintain the simulation temperature much closer to 1 K (which is the system temperature for our simulations). Therefore, we have adopted the Nosé-Hoover thermostat for all simulations herein.

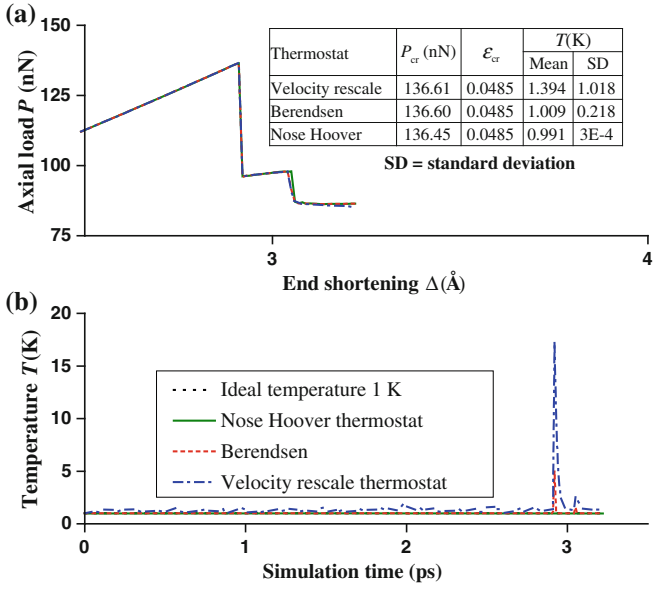

Fig. 8 **a** Effect of thermostat on P versus Δ plot of CNT **b** Variation of system temperature during simulation

In summary, the input parameters recommended for quasi-static MD simulations of buckling of SWCNT and DWCNT with aspect ratios ≤ 10 and $L \leq 136.0$Å using LAMMPS are:

• Inter-atomic potential:	AIREBO
• Thermostat:	Nosé-Hoover thermostat
• Integration scheme:	velocity-Verlet algorithm
• Relaxation time:	10 ps (10^{-11} s)
• Incremental displacement:	0.01 Å
• Time step size:	1 fs (10^{-15} s)

For the 272Å long SWCNT(10,10), the value of relaxation period $T_s = 50$ ps.

2.4 MD Simulation Results and Discussions

Tables 3 and 4 present MD buckling results for armchair SWCNT and DWCNT, respectively. They serve as test results to develop equivalent continuum models. The critical buckling load/strain gradually decreases with respect to increasing tube length. It is observed that DWCNT has a greater buckling load than the sum of the buckling loads of constituent SWCNT due to the strengthening action of van der Waals interaction between the outer and inner tubes of the DWCNT. The critical buckling strain of SWCNT decreases with increasing diameter because the critical buckling strain of a cylindrical shell is inversely proportional to its radius as predicted by Donnell type shell theory (Xiao et al. 2004).

In the case of DWCNT, the outer tube is prone to buckle before the inner tube due to its larger radius. Therefore, the critical buckling strain of a DWCNT is governed more by the outer tube size. For example, the critical buckling strains of 40 Å long SWCNT(5,5), SWCNT(10,10), and, DWCNT((5,5),(10,10)) are 0.0579, 0.0430, and, 0.0508 respectively, which shows that DWCNT((5,5),(10,10)) has a smaller critical buckling strain when compared to that of SWCNT(5,5) but a greater critical buckling strain than that of SWCNT(10,10). The aforementioned CNTs are shaded in Tables 3 and 4.

Figure 9a and b show a comparison of critical buckling strains of SWCNT(5,5) and DWCNT((5,5),(10,10)) predicted by using the AIREBO potential with those reported by other researchers.

Referring to Fig. 9, it can be seen that the use of AIREBO potential furnishes a lower critical buckling strain than that furnished by the (REBO^{2nd} + LJ) potential. When the torsional potential term is switched off in the AIREBO potential, the critical buckling strain of CNTs becomes closer to that obtained using REBO^{2nd} + LJ potential. For instance, the critical buckling strain of a 60 Å DWCNT((5,5),(10,10)) obtained using AIREBO potential without the torsional potential term is 0.0543

Table 3 MD buckling results for armchair SWCNTs

SWCNT (5,5) $D = 0.678$ nm			SWCNT (10,10) $D = 1.356$ nm			SWCNT (15,15) $D = 2.034$ nm			SWCNT (20,20) $D = 2.713$ nm		
L/D	P_{cr} (nN)	ε_{cr}	L/D	P_{cr} (nN)	ε_{cr}	L/D	P_{cr} (nN)	ε_{cr}	L/D	P_{cr} (nN)	ε_{cr}
2.0	76.9	0.0734	1.0	86.8	0.0482	1.0	83.3	0.0336	1.5	79.2	0.0255
3.1	65.1	0.0643	1.5	79.8	0.0450	1.4	77.7	0.0316	1.8	78.1	0.0249
4.2	61.5	0.0614	2.1	79.5	0.0443	1.6	77.6	0.0315	2.0	78.1	0.0249
4.9	59.1	0.0595	2.4	77.2	0.0432	2.0	77.6	0.0314	2.2	78.1	0.0248
6.0	**57.1**	**0.0579**	3.0	76.9	0.0430	2.4	76.7	0.0310	2.6	77.9	0.0248
7.0	55.6	0.0567	3.5	74.8	0.0421	2.7	75.7	0.0306	3.0	77.9	0.0248
8.1	55.1	0.0562	4.1	73.5	0.0402	3.0	75.7	0.0306	3.5	77.8	0.0248
8.9	48.9	0.0520	4.4	70.0	0.0400	3.3	74.5	0.0303	3.8	77.7	0.0247
9.9	41.1	0.0454	5.0	67.8	0.0389	4.0	74.5	0.0302	4.0	76.9	0.0245
			6.1	65.2	0.0376	4.6	74.5	0.0302	4.5	76.2	0.0242
			7.0	62.9	0.0366	5.0	73.9	0.0300			
			7.5	62.1	0.0363	5.4	73.5	0.0298			
			8.0	61.6	0.0359	6.0	73.0	0.0297			
			9.0	60.6	0.0355	6.7	70.6	0.0288			
			10.0	59.8	0.0351						
			20.0	18.6	0.0131						

Note The correspond numbers in bold to CNT with length 40 Å

Table 4 MD buckling results for armchair DWCNTs with $L/D_i \leq 10$

DWCNT (5,5),(10,10) $D_i = 0.678$ nm			DWCNT (10,10),(15,15) $D_i = 1.356$ nm			DWCNT (15,15),(20,20) $D_i = 2.034$ nm		
L/D_i	P_{cr} (nN)	ε_{cr}	L/D_i	P_{cr} (nN)	ε_{cr}	L/D_i	P_{cr} (nN)	ε_{cr}
2.0	164.6	0.0571	2.1	161.2	0.0369	2.0	166.3	0.0287
3.1	155.4	0.0533	3.0	156.8	0.0361	3.0	161.0	0.0279
4.2	149.9	0.0525	4.1	155.7	0.0359	4.0	159.4	0.0278
4.9	146.1	0.0512	4.9	154.8	0.0358	5.0	156.7	0.0274
6.0	**142.8**	**0.0508**	6.1	154.5	0.0357	6.0	153.9	0.0270
7.0	139.2	0.0489	7.0	152.8	0.0354			
8.1	137.3	0.0487	8.0	149.3	0.0348			
8.9	136.5	0.0485	8.9	145.8	0.0339			
9.9	135.0	0.0482	10.0	142.8	0.0335			

Note The correspond numbers in bold to CNT with length 40 Å

which agrees well with 0.0553 obtained by Zhang et al. (2008) who used the REBO^{2nd} + LJ potential. Thus, it is clear that the inclusion of the torsion term in the interatomic potential leads to a significant reduction in the critical buckling strain. Liew et al. (2004) obtained a comparatively higher critical buckling strain of 0.0600

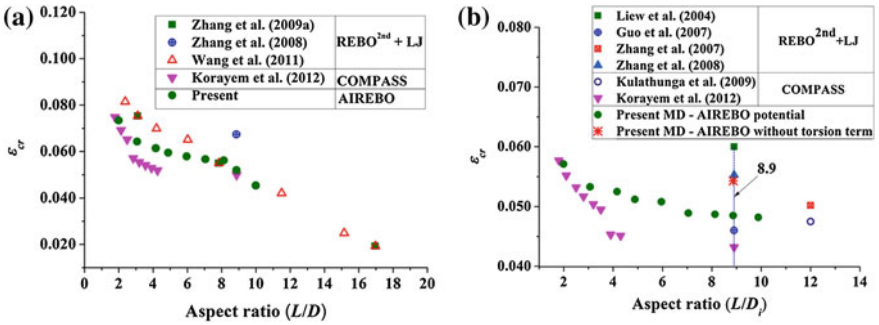

Fig. 9 Comparison of critical buckling strains for (**a**) SWCNT(5,5) and (**b**) DWCNT((5,5),(10,10)) obtained using AIREBO potential with existing results

because they used a much larger displacement rate of $0.1\,\text{Å}/\text{ps}$ which is 100 times higher than $0.001\text{Å}/\text{ps}$ used in the present MD simulations.

Figure 9a and b show that the use of COMPASS potential leads to a lower buckling strain as compared to the strain computed using AIREBO potential. AIREBO and COMPASS potentials follow different approaches in calibrating the parameters in individual potential energy term. For the AIREBO potential, the parameters are calibrated based on experimental data such as bond energy and vacancy formation energy (Stuart et al. 2000). On the other hand, the parameters in the COMPASS potential were initially estimated from ab initio calculations and then they were optimized against experimental data, e.g. heat of vaporization (Sun 1998). So far, no experimental results exist for buckling of CNT with small aspect ratios, and therefore it is difficult to judge which one of these two potentials is better for determining the buckling strain of CNTs. However, Xu and Buehler (2010) have shown that the observed wrinkling patterns in free standing graphene sheets under thermal environment can be predicted well by using the AIREBO potential. This discovery adds credibility to the AIREBO potential for employment in buckling analysis of CNT since CNTs and graphene sheets have similar type of C–C bonds. In computing the buckling strain of DWCNT using an atomic scale finite element method (AFEM), Guo et al. (2007) neglected the van der Waals (vdW) interaction among carbon atoms of the same tube. As a result, Guo et al. (2007) obtained a critical buckling strain that is about 5 % lower than the strain value calculated in present work.

Buckling mode shapes of SWCNT(5,5) with various lengths are shown in Fig. 10 while the modes shapes for DWCNT((5,5),(10,10)) are given in Fig. 11. From Fig. 10, it can be observed that SWCNT(5,5) with an aspect ratio greater than 6 exhibits beam-shell buckling mode (Wang et al. 2010). Apart from these SWCNTs, all other CNTs studied herein show shell buckling modes.

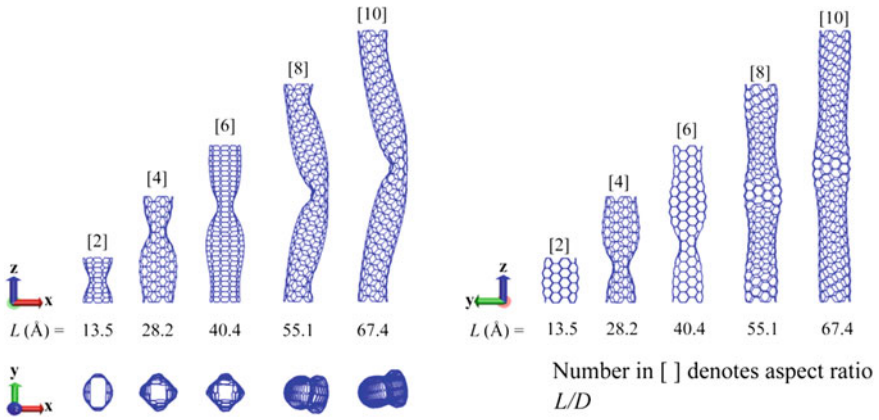

Fig. 10 Buckling mode shapes of SWCNT(5,5) at three different perspectives

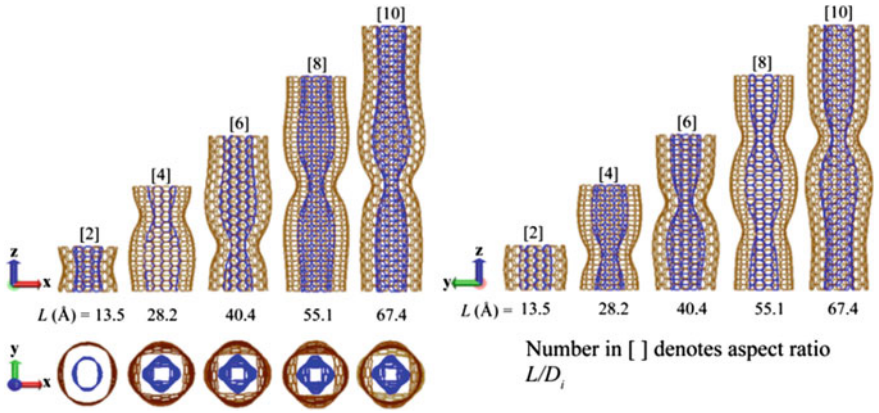

Fig. 11 Buckling mode shapes of DWCNT((5, 5), (10,10)) at three different perspectives

3 Shell Model for Buckling of CNTs

Owing to similarity of CNT geometry and a cylinderical shell, CNT can be modeled as a cylindrical shell. So instead of performing expensive MD simulations, one may use the shell theory for buckling analysis of CNTs. A Type I equivalent shell model for CNT requires the input of the equivalent Young's modulus E, Poisson's ratio v, and the wall thickness h for the CNT. The critical buckling loads P_{cr} and critical buckling strains ε_{cr} estimated using MD simulations are reported in Tables 3 and 4 and these values are used to calibrate the Young's modulus for the proposed equivalent shell model. Based on the proposed equivalent shell model, the buckling loads are estimated for CNTs and compared with MD simulation results in Tables 3 and 4.

3.1 Calibration of Young's Modulus of SWCNTs

For small deformation shell theory (Reddy 2007), the axial stress σ_x may be assumed to be related to the axial strain ε_x in a cylindrical shell as

$$\sigma_x = E\varepsilon_x \quad \Rightarrow \quad \frac{P_x}{A_{eff}} = E\varepsilon_x \quad \Rightarrow \quad \frac{P_x}{\frac{\pi Dh}{1-\nu^2}} = E\varepsilon_x \quad \Rightarrow \quad \frac{P_x}{\pi D} = \frac{Eh}{1-\nu^2}\varepsilon_x \tag{6}$$

where x is the direction along the axis of the tube, D the diameter of tube, h the thickness of shell, P_x is the axial load in cylinder shell.

At the onset of buckling (Point A in Fig. 5a), Eq. (7) is valid for the CNT, as all deformations prior to this is linearly elastic. By substituting P_x with P_{cr} and ε_x with ε_{cr} in Eq. (7), we write:

$$k = \frac{P_{cr}}{\pi D\varepsilon_{cr}} = \frac{Eh}{1-\nu^2} \tag{7}$$

where k is the slope of $P_{cr}/(\pi D)$ versus ε_{cr} curve.

By plotting $P_{cr}/(\pi D)$ versus ε_{cr} curve obtained from MD simulations, it is observed that the slope k of the curve is almost constant and it does not vary with the length of CNT as shown in Fig. 12 (in this figure for a given SWCNT different data points represent different lengths).

By plotting $P_{cr}/(\pi D)$ versus $\varepsilon_{\mathrm{cr}}$ for various dimensions of SWCNTs, it is found that the slope k varies with respect to the diameter D of the SWCNT whereas it is almost unaffected by the length L. Following Yakobson et al. (1996), we assume $\nu = 0.19$ and $h = 0.066\,\mathrm{nm}$ and we seek to determine E from Eq. (7). So far, researchers are able to synthesize SWCNT that has a diameter that varies from 0.4 nm (Hayashi et al. 2003) to 10 nm (Ma et al. 2009). In order to accommodate the full range of SWCNT diameter for developing an empirical relationship

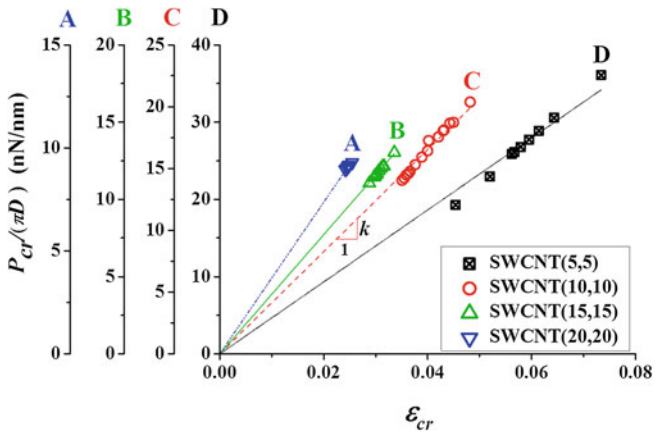

Fig. 12 $P_{\mathrm{cr}}/(\pi D)$ versus ε_{cr} for SWCNT(10,10)

Table 5 Summary of k values for calibration of E

SWCNT	Diameter (nm)	k (TPa-nm)	SWCNT	Diameter (nm)	k (TPa-nm)
(3, 3)	0.407	602.5	(30, 30)	4.069	345.4
(5, 5)	0.678	465.9	(40, 40)	5.425	333.2
(10, 10)	1.356	414.2	(80, 80)	10.850	308.9
(15, 15)	2.034	385.9	(100,100)	13.563	302.8
(20,20)	2.713	368.2			

between Young's modulus and diameter D, we have also performed MD simulations on SWCNT(4,4), SWCNT(30,30), SWCNT(40,40), SWCNT(80,80) and SWCNT(100, 100) to supplement the results report in Table 3. The k values obtained for these SWCNTs are summarized in Table 5.

A power series is fitted with the values reported in Table 5 as shown in Fig. 13. Based on the fitting process an empirical equation relating diameter D (in nm) of armchair SWCNT and its Young's modulus E (in TPa) is given by

$$E = 3.19 + 3.15D^{-0.37} \text{ for } 0.4 \text{ nm} \leq D \leq 14 \text{ nm} \tag{8}$$

Equation (8) furnishes a Young's modulus of 7.6 TPa for SWCNT(3,3), and 4.4 TPa for SWCNT(100,100). A decreasing trend of Young's modulus of CNT with respect to its diameter was also experimentally observed by Lee et al. (2005). This finding validates the credibility of the present MD simulation results to be used as reference results for developing continuum mechanics models. It should be noted that the proposed Young's modulus is a secant modulus evaluated at critical

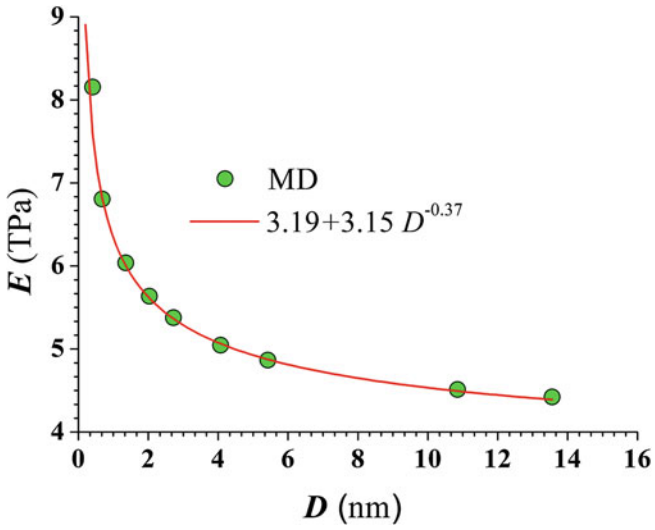

Fig. 13 Variation of E with D for armchair SWCNTs

buckling point and only applicable to buckling of CNT under axial load. Moreover, the Young's modulus of CNT given by Eq. (8) is larger ($\sim$10–40 %) than the tangent Young's modulus of CNT estimated at zero strain.

3.2 Finite Element Model for Buckling Analysis of CNTs

Using the diameter-dependent Young's modulus for SWCNTs as given by Eq. (8), Poisson's ratio of 0.19 and wall thickness of 0.066 nm, we perform the buckling analysis of cylindrical shells (that model armchair SWCNTs) using the commercial finite element software package ABAQUS/Standard and the thick shell element S8R6 (Hibbit and Pawtucket 2005). The finite element model is shown in Fig. 14a. The thick shell element is preferred to the thin shell element since the effect of transverse shear deformation is significant for stocky shells/CNTs (Harik 2002).

The above-mentioned equivalent shell properties are also used to calculate the critical buckling loads for DWCNTs. The Young's moduli of the outer and inner tubes of DWCNTs are calculated from Eq. (7) depending on the diameter of the tube. Here, we use different Young's moduli for both tubes in a DWCNT, a departure from the conventional use of a single Young's modulus for both tubes in a DWCNT. We use a single value for Poisson's ratio and shell thickness of the

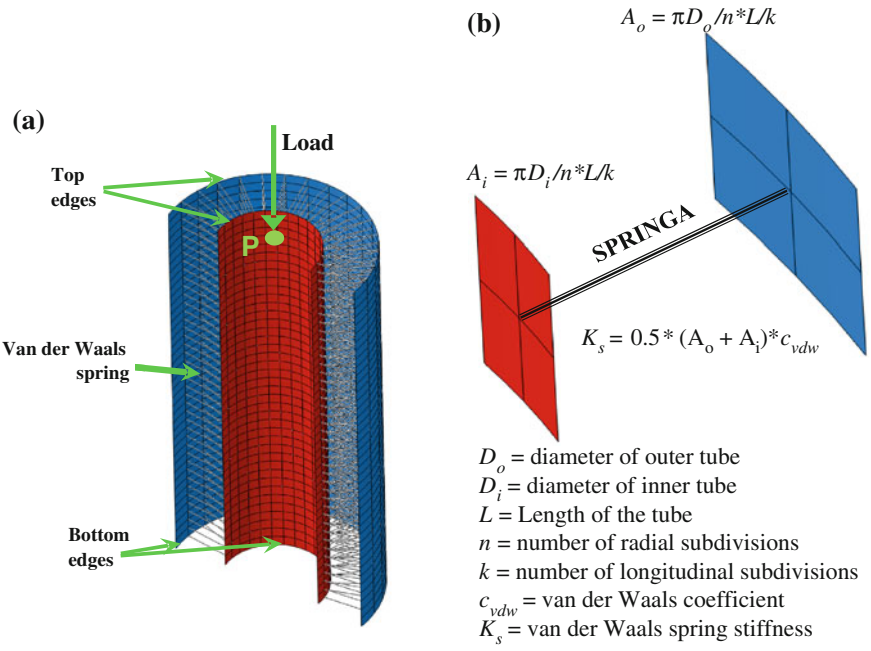

Fig. 14 (**a**) Typical finite element mesh for DWCNT (**b**) Calculation of vdW spring stiffness

outer and inner tubes: 0.19 and 0.066 nm, respectively. In DWCNT, there is van der Waals (vdW) interaction between the outer and inner tubes. The inter-tube vdW interaction is modeled by using linear spring elements SPRINGA in ABAQUS/Standard. The spring stiffness of the linear spring elements is calculated from an assumption of vdW coefficient of $c_{vdw} = 9.919 \times 10^{19}\,\mathrm{N/m^3}$ (Wang et al. 2006; Kulathunga et al. 2009). The van der Waals spring stiffness K_s is the product of c_{vdw} and influence area of spring as shown in Fig. 14b. One may refer to (Wang et al. 2006) for the procedure in calculating the linear spring stiffness.

During the finite element simulations, the bottom edges of DWCNT are kept fixed (i.e. no rotations and displacements). At the top end of the tube, a node (point P in Fig. 14a) is created to connect with the top edges of the tube by using rigid body constraint. This serves the purpose of a rigid indenter for buckling simulation. All the degrees of freedom (DOF) except for the DOF along the axis of tube at node P are restrained. Bifurcation analysis is performed after applying a unit load at point P. In the case of SWCNT, the finite element model is similar that of DWCNT. The only difference is that the vdW spring elements are absent for the SWCNT element model.

3.3 Comparison of Buckling Loads: Equivalent Shell Model and MD Results

Figures 15 and 16 compares the critical buckling loads obtained using the shell finite element S8R6 of ABAQUS/Standard and buckling loads estimated from MD simulations. It is found that critical buckling loads estimated using the finite element shell model are within 10 % difference from those given by MD simulations, except for the cases of few SWCNT (5,5) as shown in Fig. 15.

The critical buckling loads calculated for DWCNTs using the shell finite element model are also compared with those estimated using MD simulations in Fig. 16. The shell model results are in very good agreement with those of MD simulation results (within $\pm$ 5 % difference).

The equivalent shell model can also be used to accurately estimate critical buckling load of CNTs with aspect ratios larger than 10. To substantiate this statement, a SWCNT(10,10) with aspect ratio 20 is selected. The critical buckling load of this SWCNT obtained using the equivalent shell model is 19.8 nN, which is only 6.0 % higher than that obtained by MD simulation. Thus, it can be concluded that the continuum shell model with the proposed E (given by Eq. (8)), v (0.19), and, h (0.066 nm) can be adopted to furnish good prediction of the critical buckling loads for armchair SWCNTs and armchair DWCNTs.

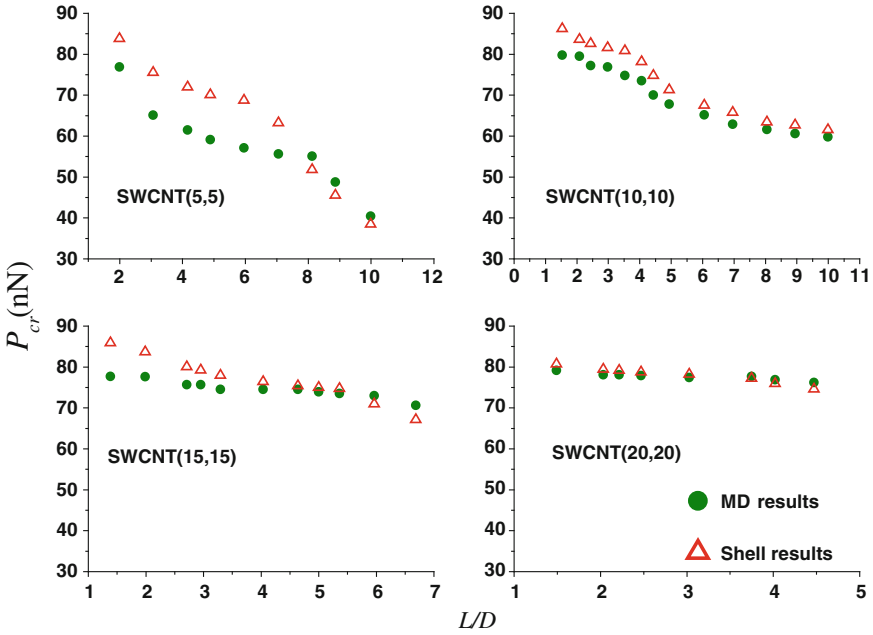

Fig. 15 Comparison of critical buckling loads obtained using equivalent shell model and MD simulations for SWCNTs

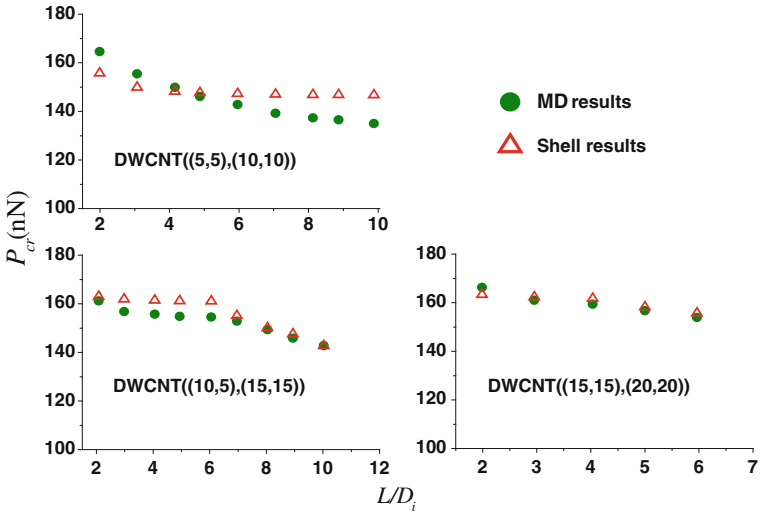

Fig. 16 Comparison of critical buckling loads obtained using equivalent shell model and MD simulations for DWCNTs

4 Conclusions

Presented in this chapter are comprehensive sets of MD buckling strains/loads for armchair SWCNTs and DWCNTs with aspect ratios less than 10. The MD simulations were performed using the software LAMMPS with the AIREBO potential for interatomic forces.

Based on the MD results, an equivalent cylindrical shell model (based on the thick shell theory) is established for the buckling analysis of CNTs. By assuming the Poisson ratio of $\nu = 0.19$ and the shell wall thickness of $h = 0.066$ nm, it was found that the Young's modulus E (in TPa) decreases nonlinearly with respect to diameter D (in nm) of the tube as given by Eq. (8). This implies that the Young's modulus for each tube in an equivalent nested cylindrical shell model for multi-walled CNTs should vary according to the tube diameter. For DWCNT, the inter-wall vdW interaction is modeled using a linear spring element and its stiffness is calculated based on vdW coefficient of $9.919 \times 10^{19}\,\mathrm{N/m^3}$. Using the cylindrical shell model (S8R6 thick shell element of ABAQUS/Standard) with diameter-dependent E given by Eq. (8), $\nu = 0.19$ and $h = 0.066$ nm, we show that the continuum shell model is able to predict critical buckling loads for armchair SWCNTs within 10 % of the MD results, and within 5 % for DWCNTs. The equivalent shell model with diameter-dependent Young's modulus may also be applied to CNTs with larger aspect ratios.Work is underway to refine the continuum model for chiral CNTs as studies have shown that the buckling results are affected by chiral angles Zhang et al. (2006)

Appendix: AIREBO potential

Adaptive Intermolecular Reactive Bond Order Potential (AIREBO) is one of the various interatomic potential available in LAMMPS. AIREBO potential developed by Stuart et al. (2000) is used in the present MD simulations. AIREBO potential comprises the second generation REBO potential $U^{2nd-REBO}$, the torsion potential U^{Tors} and the Lennard-Jones potential U^{LJ}.

Second Generation REBO Potential

The second generation REBO potential $U^{2nd-REBO}$ accounts for covalent bond interaction and its function form is given by

$$U^{2nd-REBO} = \sum_i \sum_{j(>i)} \left[V^R(r_{ij}) - b_{ij} V^A(r_{ij}) \right] \tag{A1}$$

where, V^R is the repulsive term, V^A is the attractive term and b_{ij} is bond order term. The repulsive term is given by

$$V^R(r_{ij}) = w_{ij}(r_{ij})A_{ij}(1 + Q_{ij}/r_{ij})e^{-\alpha_{ij}r_{ij}} \tag{A2}$$

The function form of the attractive term is given by

$$V^A(r_{ij}) = w_{ij}(r_{ij})\left[B_1 e^{-\beta_1 r_{ij}} + B_2 e^{-\beta_2 r_{ij}} + B_3 e^{-\beta_3 r_{ij}}\right] \tag{A3}$$

In Eqs. (A1)–(A3), $w_{ij}\left(r_{ij}\right)$ is a switching function which automatically dictates whether covalent interaction needs to be considered between any two atoms. The switching function $w_{ij}\left(r_{ij}\right)$ is given by

$$w_{ij}(r_{ij}) = \Theta(-t) + \Theta(t)\Theta(1-t)[1 + \cos \pi t]/2,\ t = \frac{r_{ij} - r_{ij}^{\min}}{r_{ij}^{\max} - r_{ij}^{\min}} \tag{A4}$$

where $\Theta(t)$is the Heaviside step function.

Values of the parameters for carbon–carbon (C–C) bond in Eqs. (A1)–(A4) are summarized in Table A.1.

In the 2nd generation REBO potential, the influence of neighboring atoms on the considered atom is incorporated by using bond order function b_{ij} in Eq. (A1). The term b_{ij} adjusts attraction force between atoms based on the position of other neighboring atoms and thus considers multi-body interactions.

The bond order term b_{ij} for a bond *i-j*, depends on the neighborhood bond angles θ and dihedral angles φ. Function form of the bond order term is given by

$$b_{ij} \approx \frac{1}{2}\left[p_{ij}^{\sigma\pi} + p_{ij}^{\pi\sigma}\right] + \Pi_{ij}^{DH} + \Pi_{ij}^{RC} \tag{A5}$$

where

$$p_{ij}^{\sigma\pi} = \left[1 + \sum_{\alpha \neq i,j} w_{i\alpha}(r_{i\alpha})g_C(\cos(\theta_{ji\alpha})) + P_{CC}(N_i^C, N_i^H)\right]^{-1/2} \tag{A6}$$

and $p_{ji}^{\sigma\pi}$ is similar to Eq. (A6) except the indices *i* and *j* are interchanged. The pair-angle cross interaction is incorporated by function $g_c\left(\cos\left(\theta_{ji\alpha}\right)\right)$ which depends on the angle between bond *i-j* and neighboring atom α. In a pristine CNT, $g_c\left(\cos\left(\theta_{ji\alpha}\right)\right)$ is a function of two angles$\theta_{ji\alpha}$, where $\alpha = k, m$ (see Fig. A.1a).

Table A.1 Parameters in AIREBO potential for C–C bond

$B_1 = 12{,}388.792$ eV	$\beta_1 = 4.720$ Å-1	$Q_{ij} = 0.313$ Å
$B_2 = 17.567$ eV	$\beta_2 = 1.433$ Å-1	$A_{ij} = 10953.544$ eV
$B_3 = 30.715$ eV	$\beta_3 = 1.383$ Å-1	$\alpha_{ij} = 4.747$ Å-1
$r_{ij}^{\max} = 2.0$Å	$r_{ij}^{\min} = 1.7$Å	

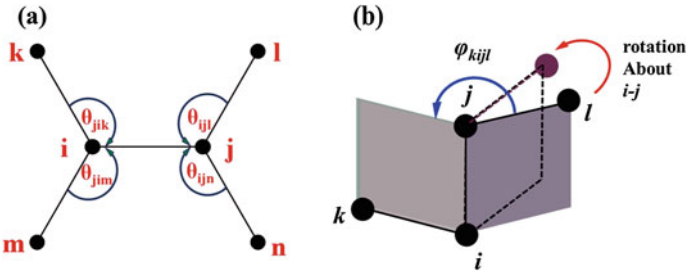

Fig. A.1 (**a**) Typical C–C bond in a CNT and its neighborhood (**b**) Definition of dihedral angle

Table A.2 Interpolation points for quintic spline $y(x) = \sum_{m=0}^{5} C_m (x - x_k)^m$ Stuart et al. (2000)

Function	$\cos\theta$	$g_i(\cos\theta)$	$\frac{dg_i}{d\cos\theta}$	$\frac{d^2 g_i}{d(\cos\theta)^2}$
$g_C(\cos(\theta_{ji\alpha}))$	−1	−0.010	0.104	0.000
	−2/3	0.028	0.131	0.140
	−1/2	0.053	0.170	0.370
	−1/3	0.097	0.400	1.980
	1	1.000	2.835	10.265

The function $g_c\left(\cos\left(\theta_{ji\alpha}\right)\right)$ in Eq. (A6) is fitted to a quintic spline. The coefficients of the quintic spline function are evaluated by LAMMPS using the values given in Table A.2.

In each interval of $\cos(\theta)$, six values of interpolation points are reported in Table A.2. These six values are used to derive the coefficients of the quintic spline. For pristine CNT $P_{\mathrm{CC}}(N_i^C, N_i^H)$ in Eq. (A6) is −0.027603.

The function Π_{ij}^{DH} in Eq. (A5) represents the cross interaction between pair *i-j* and dihedral angle $\varphi_{\alpha ij\beta}$. In a pristine CNT, a bond pair *i-j* is affected by four dihedral angles. These four dihedral angles can be represented as $\varphi_{\alpha ij\beta}$ where $\alpha = k, m$ and $\beta = l, n$ (please refer to Fig. A.1a). Function Π_{ij}^{DH} is equal to the expression given by Eq. (A7).

$$T_{ij}(N_i^t, N_j^t, N_{ij}^{conj}) \sum_{\alpha \neq i,j} \sum_{\beta \neq i,j} \left(1 - \cos^2(\varphi)\right) w_{i\alpha} w_{j\beta} \Theta(\sin(\theta_{ji\alpha} - s^{\min})) \Theta(\sin(\theta_{ij\beta} - s^{\min})) \tag{A7}$$

where $w_{\alpha\beta}$ is the switching function to be calculated as per Eq. (A4). In a pristine CNT, $T_{ij}(N_{ij}, N_{ji}, N_{ij}^{\mathrm{conj}}) = -0.004048$. The radical term Π_{ij}^{RC}in Equation (A5) does not contribute to force on an atom in CNT.

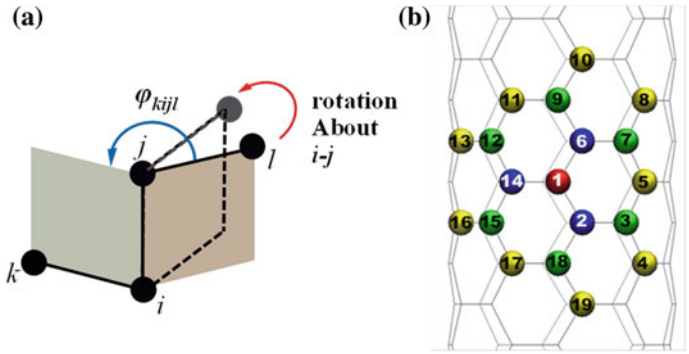

Fig. A.2 (**a**) Dihedral bond rotation, (**b**) Typical neighborhood of an atom with id 1 in pristine carbon nanotube

Torsion Term

The torsion term U^{Tors} in AIREBO potential is a valence term which adds stiffness to the dihedral rotation about a bond pair *i-j* as shown in Fig. A.2a.

The torsion potential U^{Tors} is given by

$$U_{\alpha ij\beta}^{tors} = w_{\alpha i}(r_{\alpha i}) w_{ij}(r_{ij}) w_{j\beta}(r_{j\beta}) V^{tors}(\omega_{\alpha ij\beta}) \tag{A8}$$

$$V^{tors} = \frac{256}{405}\varepsilon_{\alpha ij\beta}\cos^{10}(\omega_{\alpha ij\beta}/2) - \frac{1}{10}\varepsilon_{\alpha ij\beta} \tag{A9}$$

The value of $\varepsilon_{\alpha ij\beta}$ for CNT is 0.3079. The number of dihedral angles in CNT which contribute to the forces on an atom *i* depends on the neighborhood of that atom. There are 25 dihedral angles in a pristine CNT, which contribute to the forces on atom 1 shown in Fig. A.2b. The switching functions $w(r)$ in Eq. (A8) is used by the MD code to determine all the dihedral angles contributing to force on an atom. Switching function $w(r)$ in Eq. (A8) are calculated by using Eq. (A4).

Non-bonded Potential

The non-bonded potential U^{LJ} given by Eq. (A10), takes into account a pair type interaction between atoms which have interatomic distances $\geq$2 Å. In LAMMPS, one needs to specify a cutoff distance beyond which the non-bonded potential does not contribute to interatomic forces. In the case of C–C bond, this cutoff is taken as 10.2 Å but the user may set a longer cutoff distance at an expense of more computational time. The non-bonded potential is given by

$$U_{ij}^{LJ} = S(t_r(r_{ij}))S(t_b(b_{ij}^*))C_{ij}V^{LJ}(r_{ij}) + \left[1 - S(t_r(r_{ij}))\right]C_{ij}V^{LJ}(r_{ij})$$
$$w_{ij}(r_{ij}) = S^{'}(t_c(r_{ij})),\ t_c(r_{ij}) = \frac{r_{ij} - r_{ij}^{LJ\min}}{r_{ij}^{LJ\max} - r_{ij}^{LJ\min}} \tag{A10}$$

where $S^{'}(t) = \Theta(-t) + \Theta(t)\Theta(1-t)\frac{1}{2}[1 + \cos \pi t]$

$$t_b(b_{ij}^*) = \frac{b_{ij}^* - b_{ij}^{\min}}{b_{ij}^{\max} - b_{ij}^{\min}}$$

In Eq. (A10), b_{ij}^* is a hypothetical bond-order term which is evaluated at $r_{ij}^{\min}$. To understand the previous statement, let us consider the non-bonded interaction between atom i and j. Since the distance between these two atoms typically exceeds the covalent bonding distance $r_{ij}^{\max}$(for C–C bond $r_{ij}^{\max} = 2.0$ Å), there is no actual bond-order term b_{ij} (Eq. A5). Consequently a hypothetical bond order term b_{ij}^* is evaluated by assuming the distance between atoms i and j to be 1.7 Å. In Eq. (A10), V^{LJ} is a 12-6 Lennard-Jones potential which is given by Eq. (A11).

$$V_{ij}^{LJ} = 4\varepsilon_{ij}\left[\left(\frac{\sigma}{r_{ij}}\right)^{12} - \left(\frac{\sigma}{r_{ij}}\right)^{6}\right] \tag{A11}$$

The parameters required to evaluate the non-bonded interaction in CNT are $\sigma = 3.4$Å, $\varepsilon_{ij} = 0.00284$ eV, $r_{ij}^{LJ\max} = \sigma$, $r_{ij}^{LJ\min} = 2^{1/6}\sigma$, $b_{ij}^{\max} = 0.81$ and $b_{ij}^{\min} = 0.77$.

References

ABAQUS/Standard User's Manual, v.6.9.

Aliev AE, Oh J, Kozlov ME, Kuznetsov AA, Fang S, Fonseca AF, Ovalle R, Lima MD, Haque MH, Gartstein YN, Zhang M, Zakhidov AA, Baughman RH (2009) Giant-stroke superelastic carbon nanotube aerogel muscles. Science 323:1575–1578

Ansari R, Rouhi S (2010) Atomistic finite element model for axial buckling of single-walled carbon nanotubes. Phys E 43:58–69

Batra RC, Sears A (2007) Continuum models of multi-walled carbon nanotubes. Int J Solids Struct 44:7577–7596

Belytschko T, Xiao S, Schatz G, Ruoff R (2002) Atomistic simulations of nanotube fracture. Phys Rev B 65:235430

Brenner DW, Shenderova OA, Harrison JA, Stuart SJ, Ni B, Sinnott SB (2002) A second-generation reactive empirical bond order (REBO) potential energy expression for hydrocarbons. J Phys: Condens Matter 14:783–802

Cao A, Dickrell PL, Sawyer WG, Ghasemi-Nejhad MN, Ajayan PM (2005) Super-compressible foamlike carbon nanotube films. Science 310:1307–1310

Chen X, Cao G (2006) A structural mechanics study of single-walled carbon nanotubes generalized from atomistic simulation. Nanotechnology 17:1004–1015

Cheng HM, Yang QH, Liu C (2001) Hydrogen storage in carbon nanotubes. Carbon 39:1447–1454

Cheng HC, Liu YL, Hsu YC, Chen WH (2009) Atomistic-continuum modeling for mechanical properties of single-walled carbon nanotubes. Int J Solids Struct 46:1695–1704
Cohen-Karni T, Segev L, Srur-Lavi O, Cohen SR, Joselevich E (2006) Torsional electromechanical quantum oscillations in carbon nanotubes. Nat Nanotechnol 1:36–41
De Volder MF, Tawfick SH, Baughman RH, Hart AJ (2013) Carbon nanotubes: present and future commercial applications. Science 339:535–539
Duan WH, Wang CM, Tang WX (2010) Collision of a suddenly released bent carbon nanotube with a circular graphene sheet. J Appl Phys 107:074303
Endo M, Hayashi T, Kim YA (2006a) Large-scale production of carbon nanotubes and their applications. Pure Appl Chem 78:1703–1713
Endo M, Hayashi T, Kim YA, Muramatsu H (2006b) Development and application of carbon nanotubes. Jpn J Appl Phys 45:4883–4892
Flekkøy EG, Coveney PV, De Fabritiis G (2000) Foundations of dissipative particle dynamics. Phys Rev E 62:2140–2157
Frenkel D, Smith B (2002) Understanding molecular simulation: From alogorithms to applications, 2nd edn. Academic Press, USA
Fuchslin RM, Fellermann H, Eriksson A, Ziock HJ (2009) Coarse graining and scaling in dissipative particle dynamics. J Chem Phys 130:214102
Gdoutos MSK, Metaxa ZS, Shah SP (2010) Multi-scale mechanical and fracture characteristics and early-age strain capacity of high performance carbon nanotube/cement nanocomposites. Cement Concr Compos 32:110–115
Girifalco LA, Lad RA (1956) Energy of cohesion, compressibility, and the potential energy functions of the graphite system. J Chem Phys 25:693–697
Guangyong L, Liming L (2011) Carbon nanotubes for organic solar cells. Nanotechnology Magazine, IEEE 5:18–24
Guo X, Leung AYT, Jiang H, He XQ, Huang Y (2007) Critical strain of carbon nanotubes: An atomic-scale finite element study. J Appl Mech 74:347–351
Hall AR, Falvo MR, Superfine R, Washburn S (2007) Electromechanical response of single-walled carbon nanotubes to torsional strain in a self-contained device. Nat Nanotechnol 2:413–416
Harik VM (2002) Mechanics of carbon nanotubes applicability of continuum-beam models. Comput Mater Sci 24:328–342
Harris PJF (2004) Carbon nanotube composites. Int Mater Rev 49:31–43
Hayashi T, Kim YA, Matoba T, Esaka M, Nishimura K, Tsukada T, Endo M, Dresselhaus MS (2003) Smallest freestanding single-walled carbon nanotube. Nano Lett 3:887–889
He XQ, Kitipornchai S, Liew KM (2005) Buckling analysis of multi-walled carbon nanotubes: a continuum model accounting for van der waals interaction. J Mech Phys Solids 53:303–326
He XQ, Kitipornchai S, Wang CM, Xiang Y, Zhou Q (2010) A nonlinear van der waals force model for multiwalled carbon nanotubes modeled by a nested system of cylindrical shells. J Appl Mech 77:061006
Heo SJ, Sinnott SB (2007) Investigation of influence of thermostat configurations on the mechanical properties of carbon nanotubes in molecular dynamics simulations. J Nanosci Nanotechnol 7:1518–1524
Hu N, Nunoya K, Pan D, Okabe T, Fukunaga H (2007) Prediction of buckling characteristics of carbon nanotubes. Int J Solids Struct 44:6535–6550
Hu YG, Liew KM, Wang Q (2009) Nonlocal elastic beam models for flexural wave propagation in double-walled carbon nanotubes. J Appl Phys 106:044301
Huang X (2009) Fabrication and properties of carbon fibers. Materials 2:2369–2403
Hünenberger PH (2005) Thermostat algorithms for molecular dynamics simulations. Adv Polym Sci 173:105–147
Iijima S (1991) Helical microtubules of graphitic carbon. Nature 354:56–58
Jiang H, Huang Y, Hwang KC (2005) A finite-temperature continuum theory based on interatomic potentials. J Eng Mater Technol 127:408–416

Khademolhosseini F, Rajapakse N, Nojeh A (2009) Application of nonlocal elasticity shell model for axial buckling of single-walled carbon nanotubes. Sens Trans 7:88–100
Kim P, Shi L, Majumdar A, McEuen PL (2001) Thermal transport measurements of individual multiwalled nanotubes. Phys Rev Lett 87:215502
Klinger C, Patel Y, Postma HWC (2012) Carbon nanotube solar cells. PLoS ONE 7:37806
Korayem AH, Duan WH, Zhao XL, Wang CM (2012) Buckling behaviour of short multi-walled carbon nanotubes under axial compression loads. Int J Struct Stab Dyn 12:1250045
Kozinda A, Jiang Y, Lin L (2012) Flexible energy storage devices based on lift-off of cnt films, Micro Electro Mechanical Systems (MEMS), 2012 IEEE 25th International Conference on, 1233–1236
Koziol K, Vilatela J, Moisala A, Motta M, Cunniff P, Sennett M, Windle A (2007) High-performance carbon nanotube fiber. Science 318:1892–1895
Kulathunga DD, Ang KK, Reddy JN (2009) Accurate modeling of buckling of single- and double-walled carbon nanotubes based on shell theories. J Phys: Condens Matter 21:435301
Lee K, Lukic B, Magrez A, Seo JW, Kulik A (2005) Diameter dependence of the elastic modulus of cvd-grown carbon nanotubes. XIX International winterschool/euroconference on electronic properties of novel materials, Austria, Electronic properties of novel nanostructures, pp 143–145
Li C, Chou TW (2003) A structural mechanics approach for the analysis of carbon nanotubes. Int J Solids Struct 40:2487–2499
Li QW, Li Y, Zhang XF, Chikkannanavar SB, Zhao YH, Dangelewicz AM, Zheng LX, Doorn SK, Jia QX, Peterson DE, Arendt PN, Zhu YT (2007) Structure-dependent electrical properties of carbon nanotube fibers. Adv Mater 19:3358–3363
Liba O, Kauzlarić D, Abrams ZR, Hanein Y, Greiner A, Korvink JG (2008) A dissipative particle dynamics model of carbon nanotubes. Mol Simul 34:737–748
Liew KM, Wong CH, He XQ, Tan MJ, Meguid SA (2004) Nanomechanics of single and multiwalled carbon nanotubes. Phys Rev B 69:115429
Liu B, Huang Y, Jiang H, Qu S, Hwang KC (2004) The atomic-scale finite element method. Comput Method Appl Mech Eng 193:1849–1864
Liu F, Wang H, Xue L, Fan L, Zhu Z (2008) Effect of microstructure on the mechanical properties of pan-based carbon fibers during high-temperature graphitization. J Mater Sci 43:4316–4322
Lu WB, Wu J, Feng X, Hwang KC, Huang Y (2010) Buckling analyses of double-wall carbon nanotubes: A shell theory based on the interatomic potential. J Appl Mech 77:061016
Ma J, Wang JN, Wang XX (2009) Large-diameter and water-dispersible single-walled carbon nanotubes: Synthesis, characterization and applications. J Mater Chem 19:3033–3041
Makar JM, Margeson J, Luh J (2005) Carbon nanotube/cement composites—early results and potential applications. In: The 3rd international conference on construction materials: performance, innovations and structural implications, Vancouver, B.C., Canada
Pantano A, Boyce M, Parks D (2003) Nonlinear structural mechanics based modeling of carbon nanotube deformation. Phys Rev Lett 91:145504
Pantano A, Boyce MC, Parks DM (2004a) Mechanics of axial compression of single and multi-wall carbon nanotubes. J Eng Mater Technol 126:279–284
Pantano A, Parks DM, Boyce MC (2004b) Mechanics of deformation of single- and multi-wall carbon nanotubes. J Mech Phys Solid 52:789–821
Plimpton S (1995) Fast parallel algorithms for short-range molecular dynamics. J Comput Phys 117:1–19
Rapaport DC (2004) The art of molecular dynamics simulation, 2nd edn. Cambridge University Press, Cambridge
Reddy JN (2007) Theory and analysis of elastic plates and shells, 2nd edn. CRC Press, London
Saito R, Fujita M, Dresselhaus G, Dresselhaus MS (1992) Electronic structure of chiral graphene tubules. Appl Phys Lett 60:2204–2206
Sears A, Batra R (2006) Buckling of multiwalled carbon nanotubes under axial compression. Phys Rev B 73:085410

Shen HS (2004) Postbuckling prediction of double-walled carbon nanotubes under hydrostatic pressure. Int J Solids Struct 41:2643–2657
Stevens RMD, Frederick NA, Smith BL, Morse DE, Stucky GD, Hansma PK (2000) Carbon nanotubes as probes for atomic force microscopy. Nanotechnology 11:1–5
Stuart SJ, Tutein AB, Harrison JA (2000) A reactive potential for hydrocarbons with intermolecular interactions. J Chem Phys 112:6472–6486
Subramaniyan AK, Sun CT (2008) Engineering molecular mechanics: An efficient static high temperature molecular simulation technique. Nanotechnology 19:285706
Sun H (1998) COMPASS: An ab initio force-field optimized for condensed-phase applications overview with details on alkane and benzene compounds. J Phys Chem B 102:7338–7364
Sun DM, Timmermans MY, Tian Y, Nasibulin AG, Kauppinen EI, Kishimoto S, Mizutani T, Ohno Y (2011) Flexible high-performance carbon nanotube integrated circuits. Nat Nanotechnol 6:156–161
Tanaka T (2010) Filtration characteristics of carbon nanotubes and preparation of buckypapers. Desalination and Water Treatment, 17:193–198
Tombler TW, Zhou C, Alexseyev L, Kong J, Dai H, Liu L, Jayanthi CS, Tang M, Wu S-Y (2000) Reversible electromechanical characteristics of carbon nanotubes under local-probe manipulation. Lett Nat 405:769–772
van Gunsteren WF, Berendsen HJC (1990) Computer simulation of molecular dynamics:Methodology, applications, and perspectives in chemistry. Angew Chem, Int Ed Engl 29:992–1023
Wackerfuß J (2009) Molecular mechanics in the context of the finite element method. Int J Numer Meth Eng 77:969–997
Wang CM, Ma YQ, Zhang YY, Ang KK (2006a) Buckling of double-walled carbon nanotubes modeled by solid shell elements. J Appl Phys 99:114317
Wang CM, Tan VBC, Zhang YY (2006b) Timoshenko beam model for vibration analysis of multi-walled carbon nanotubes. J Sound Vib 294:1060–1072
Wang D, Song P, Liu C, Wu W, Fan S (2008) Highly oriented carbon nanotube papers made of aligned carbon nanotubes. Nanotechnology 19:075609
Wang CM, Zhang YY, Xiang Y, Reddy JN (2010) Recent studies on buckling of carbon nanotubes. Appl Mech Rev 63:030804
Wang CM, Tay ZY, Chowdhuary ANR, Duan WH, Zhang YY, Silvestre N (2011) Examination of cylindrical shell theories for buckling of carbon nanotubes. Int J Struct Stab Dyn 11:1035–1058
Waters JF, Guduru PR, Xu JM (2006) Nanotube mechanics—recent progress in shell buckling mechanics and quantum electromechanical coupling. Compos Sci Technol 66:1141–1150
Wong EW, Sheehan PE, Lieber CM (1997) Nanobeam mechanics: Elasticity, strength, and toughness of nanorods and nanotubes. Science 277:1971–1975
Wu J, Hwang KC, Huang Y (2009) Chapter 1 a shell theory for carbon nanotubes based on the interatomic potential and atomic structure, Advances in Applied Mechanics. Elsevier, p 1–68
Xia Z, Guduru P, Curtin W (2007) Enhancing mechanical properties of multiwall carbon nanotubes via sp^3 interwall bridging. Phys Rev Lett, 98:245501
Xiao T, Xu X, Liao K (2004) Characterization of nonlinear elasticity and elastic instability in single-walled carbon nanotubes. J Appl Phys 95:8145–8148
Xu Z, Buehler MJ (2010) Geometry controls conformation of graphene sheets: Membranes, ribbons, and scrolls. ACS Nano 4:3869–3876
Xu YQ, Barnard A, McEuen PL (2009) Bending and twisting of suspended single-walled carbon nanotubes in solution. Nano Lett 9:1609–1614
Yakobson BI, Avouris P (2001) Mechanical properties of carbon nanotubes, Topics in applied physics. Springer–Verlag, Heidelberg, Germany, 287–329
Yakobson BI, Brabec CJ, Bernholc J (1996) Nanomechanics of carbon tubes: instabilities beyond linear response. Phys Rev Lett 76:2511–2514
Zhang YY, Tan VBC, Wang CM (2006) Effect of chirality on buckling behavior of single-walled carbon nanotubes. J Appl Phy 100:074304

Zhang YY, Wang CM, Tan VBC (2008) Examining the effects of wall numbers on buckling behavior and mechanical properties of multiwalled carbon nanotubes via molecular dynamics simulations. J Appl Phys 103:053505

Zhang YY, Wang CM, Tan VBC (2009a) Mechanical properties and buckling behaviors of condensed double-walled carbon nanotubes. J Nanosci Nanotechnol 9:4870–4879

Zhang YY, Wang CM, Duan WH, Xiang Y, Zong Z (2009b) Assessment of continuum mechanics models in predicting buckling strains of single-walled carbon nanotubes. Nanotechnology 20:395707

Zheng Y, Lanqing X, Zheyong F, Wei N, Lu Y, Huang Z (2012) Mechanical properties of graphene nanobuds: a molecular dynamics study. Curr Nanosci 8:89–96

Zhu W, Bartos PJM, Porro A (2004) Application of nanotechnology in construction—summary of a state-of-the-art report. Mater Struct 37:649–658

Influence of Bond Kinematics on the Rupture of Non-Chiral CNTs under Stretching–Twisting

Bruno Faria, Nuno Silvestre and José N. Canongia Lopes

Abstract This chapter focuses on the role played by bond kinematics in the collapse behaviour of armchair and zig-zag CNTs under combined stretching-twisting. The analyses are performed through MD simulations, using LAMMPS code with the built-in potential AIREBO for C–C bonds. Incremental combinations of stretching displacements and twisting rotations are imposed to the CNT end atoms. The results are first analyzed in the form of diagrams of energy at rupture versus the twisting-to-stretching rate and diagrams of interaction between the axial stretching displacement at rupture and the angle of twist at rupture. A detailed study on the variation of bond length and angle amplitude with the imposed stretching and twisting deformations is shown. The case of pure stretching is first described, as a reference case. Two combined twisting-stretching cases and the pure twisting case are dealt with separately for zig-zag and armchair CNTs. It is concluded that two kinematic mechanisms influence the rupture of CNTs: one is the bond elongation for low twisting-to-stretching rate and other is the hexagonal cell distortion for moderate to high twisting-to-stretching rate.

Keywords Carbon nanotube · Tension · Torsion · Collapse · Kinematics

B. Faria
Department of Civil Engineering and Architecture, ICIST, Instituto Superior Tùcnico, University of Lisbon, Av. Rovisco Pais 1049-001 Lisboa, Portugal
e-mail: bmsfaria@gmail.com

J. N. C. Lopes
Department of Chemical and Biological Engineering, CQE, Instituto Superior Tùcnico, University of Lisbon, Av. Rovisco Pais 1049-001 Lisboa, Portugal
e-mail: jnlopes@ist.utl.pt

N. Silvestre (✉)
Department of Mechanical Engineering, IDMEC, Instituto Superior Tùcnico, University of Lisbon, Av. Rovisco Pais 1049-001 Lisboa, Portugal
e-mail: nsilvestre@ist.utl.pt

K. I. Tserpes and N. Silvestre (eds.), *Modeling of Carbon Nanotubes, Graphene and their Composites*, Springer Series in Materials Science 188,
DOI: 10.1007/978-3-319-01201-8_9,

1 Introduction

Carbon nanotubes (CNTs) are known for their unique mechanical, thermal and electrical properties. In the past two decades these properties were extensively studied with promising results (Wang and Liew 2008; Wang et al. 2010; Wernik and Meguid 2010; Byrne et al. 2010; Zhao and Luo 2011). The potential application of CNTs as basic elements in nano-devices such as nano-drive systems, nano-actuators or nano-oscillators, for instance as spring elements in torsional paddle oscillators or twisting bearings in nano-electric motors, prompted research on CNT mechanical behaviour under different directional loads (Williams et al. 2002; Fennimore et al. 2003; Hall et al. 2012). The research on the stiffness and strength of CNTs under different loading can be accomplished with either experiments or molecular dynamics (MD) simulations. Owing to the complexity in setting up rigorous test arrangements to make measurements at the nanoscale, experimental investigations are scarce (Hall et al. 2006, 2010; Xu et al. 2009; Sun et al. 2012). On the other hand, MD simulations have been widely used to study the mechanical behaviour of CNTs. Both the pure axial (tensile and compressive) and the pure twisting mechanical behaviours of armchair, zigzag and chiral CNTs were investigated (Yakobson et al. 1996; Sears and Batra 2004; Bao et al. 2004; Tserpes et al. 2006; Batra and Sears 2007; Chang 2007; Agrawal et al. 2008; Georgantzinos and Anifantis 2009; Arash and Wang 2012; Shima 2012). However, pure loading actions are difficult to occur at nanoscale level due to support imperfections, load eccentricities and geometrical inaccuracies of fixing CNTs in nano-devices. Thus, combinations of individual (pure) loadings are expected to occur. Understanding the CNTs mechanical response to combined loading is crucial to the design and optimization of CNT-based devices.

Regarding the use of MD to simulate CNTs under combined twisting-stretching, few works have been published (Jeong et al. 2007a, b; Talukdar and Mitra 2010). Jeong et al. (2007a) concluded that armchair and zig-zag CNTs under combined tension-twisting have decreasing tensile strength with linearly increasing twist. Talukdar and Mitra (2010) concluded that the defects change significantly the mechanical properties of armchair CNTs as well as their failure stresses and failure strains. Jeong et al. (2007b) developed failure criteria for the strength of armchair CNTs under tension-twisting and indicated that yielding or fracture behaviour of CNTs "*should be described by detailed atomistic observations involving chemical bond breaking, and therefore cannot be described with only macroscopic or continuum modeling that lack these atomistic details*". This is the main reason for using MD simulations in the present study, instead of either molecular mechanics or continuum models. In recent papers, Faria et al. (2013a, b) studied the twist-induced elastic anisotropic behaviour of chiral CNTs under pure twisting and moderate-to-high twist-to-stretching rates, as well as their stifness, strength and fracture toughness. We showed that the addition of axial tension (stretching) plays a key role in the chiral CNT linear and post-buckling stiffness. We also studied the continuous evolution of (i) chiral CNTs strength and fracture

toughness and (ii) the type of failure mechanism, under different twist-tension rate regimes (either low, moderate or high).

In this chapter, a study on the influence of bond kinematics and hexagonal lattice deformation on the CNTs mechanical behaviour is performed, in particular their rupture (1st failure). With this purpose, zig-zag and armchair CNTs are selected since the bond kinematics of chiral CNTs have already been investigated by Faria et al. (2013a, b). The CNT is subjected to tensile and torsional loads by imposing specific combinations of stretching and twisting displacements to the CNT boundary atoms. Using LAMMPS classical molecular dynamics simulator (Plimpton 1995), the carbon–carbon interaction parameters are modelled by the latest version of the AIREBO potential proposed by Stuart et al. (2000) and based on the well-known Brenner's second generation bond order potential. Bond lengths and angle amplitudes were measured after each simulation using the tools built-in VMD visualization software.

2 Molecular Dynamics Simulation

Molecular dynamics (MD) simulations were performed using the Large Scale Atomic/Molecular Massively Parallel Simulator (LAMMPS) (Plimpton 1995). The Adaptive Intermolecular Reactive Empirical Bond Order Potential (AIREBO), included in the LAMMPS software package, was used to model the inter-atomic forces present in the covalent binding of carbon in the CNT structure. The AIREBO potential is an improved version of Brenner's well-known second generation Reactive Empirical Bond Order Potential (REBO) that includes a Lenhard-Jones potential form to describe the Van-der-Waals long-range interactions and a torsional term for the σ-bond torsion. The general form of the AIREBO potential is

$$E = \frac{1}{2}\sum_i \sum_{j\neq i} \left[E_{ij}^{REBO} + \sum_{k\neq i,j} \sum_{l\neq i,j,k} E_{k,i,j,l}^{Tors} + E_{i,j}^{LJ} \right] \quad (1)$$

More detailed expressions can be found in Stuart et al. (2000). For a given CNT with radius R and length L, both end sections are located at $x = \pm L/2$ (x is the tube axis). For pure tensile loads, incremental axial displacements are imposed in opposite directions, $u = -0.025$ Å for atoms located at $x = -L/2$ and $u = +0.025$ Å for atoms at located $x = +L/2$. These imposed displacements stretch the CNT by 0.050 Å in each increment. For pure torsional loads, a twisting deformation is imposed to the atoms located in both ends of the CNT. The end sections rotate an angle ϕ about the x axis in opposite directions. The rotation angle per simulation is $\phi = +0.5° = +\pi/360°$ rad for the atoms at located $x = -L/2$ and $\phi = -0.5° = -\pi/360°$ rad for the atoms located at $x = +L/2$. With these rotations imposed to the CNT boundary atoms, the CNT twists by $\Delta\phi_0 = 1.0° = \pi/180°$ rad. During the simulation the CNT is allowed to relax, reaching a new equilibrium state while maintaining the prescribed displacement and rotation. The "0" subscripts mean either "pure stretching" (no twisting) or "pure twisting" (no stretching). In

order to impose combinations between tensile and twisting deformations, the following relationship is adopted between the combined Δu and $\Delta\phi$,

$$\left(\frac{\Delta u}{\Delta u_0}\right)^2+\left(\frac{\Delta \phi}{\Delta \phi_0}\right)^2=1 \tag{2}$$

$$\Delta u=\Delta u_0 \cos\beta, \quad \Delta\phi=\Delta\phi_0 \sin\beta \tag{3}$$

where the parameter β varies from 0 to 90°, as depicted in Fig. 1a. For $\beta = 0^\circ$, it is obtained $\Delta u = \Delta u_0$ and $\Delta\phi = 0$, i.e., pure stretching behaviour (no twisting). For $\beta = 90°$, it is obtained $\Delta\phi = \Delta\phi_0$ and $\Delta u = 0$, i.e., pure twisting behaviour (no stretching). Table 1 shows the correspondence between the angle β and the twisting-to-stretching rate ϕ/u.

All simulations were performed at a temperature of 300 K using the canonical NVT ensemble and Nose–Hoover thermostat. The newtonian equations of motion were integrated using the velocity-Verlet algorithm. A timestep of 0.8 fs was used and all simulations comprised 10,000 time-steps. The configurational (or strain) energy V of the CNT calculated in the end of each simulation corresponds to the average value of the energy within the last 4,000 time-steps. Four-hundred simulations were performed for each β, in the case of pure stretching ($\beta = 0°$), combined stretching-twisting and pure twisting ($\beta = 90°$). In order to study the mechanical behaviour of CNTs under pure and combined tensile and torsional loads, we have considered the following zig-zag and armchair CNT structures[1]:

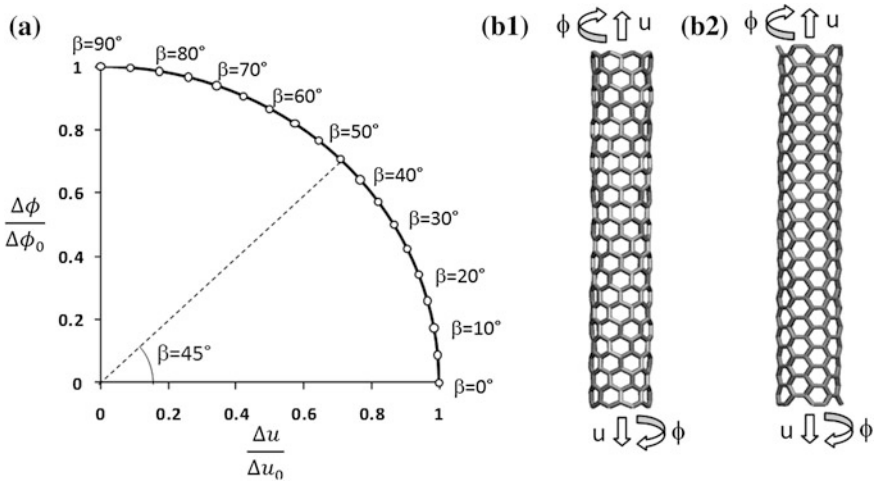

Fig. 1 **a** Stretching-twisting combinations, **b** zig-zag (8, 0) CNT, **c** armchair (5, 5) CNT

[1] The chiral vector (n, m) represents the way grapheme sheet is wrapped. The pair of indices n and m denote the number of unit vectors along two directions in the honeycomb crystal lattice of graphene. If $m = 0$, the CNTs are called zig-zag. If $n = m$, the CNTs are called armchair. If $m \neq 0$ and $m \neq n$, the CNTs are called chiral.

Table 1 Correspondence between angle β and the twisting-to-stretching rate ϕ/u

β																		
0°	5°	10°	15°	20°	25°	30°	35°	40°	45°	50°	55°	60°	65°	70°	75°	80°	85°	90°
ϕ/u (rad/Å)																		
0	0.03	0.06	0.09	0.13	0.16	0.20	0.24	0.29	0.35	0.42	0.50	0.60	0.75	0.96	1.30	1.98	3.99	∞

zig-zag (8, 0) with L = 46.3 Å and R = 3.1 Å, having an aspect ratio L/D = 7.4 and 352 atoms; armchair (5, 5) with L = 47.3 Å and R = 3.4 Å, having an aspect ratio L/D = 7.0 and 380 atoms. These are depicted in Fig. 1b, c. A similar study was performed by the authors for the case of chiral CNTs. The interested reader is referred to Faria et al. (2013a, b). The MD simulation results concerning the zig-zag and armchair CNTS are presented and discussed in the following sections.

3 Interaction Diagrams

MD simulations were performed on the CNTs (5, 5) and (8, 0), for pure stretching, combined stretching-twisting and pure twisting. This was achieved by adopting the relation defined in Eq. (2). Results were obtained for β from 0 (pure stretching) to 90° (pure twisting) using a stepwise increase of 5°. The results shown in Fig. 2 depict the variation of the deformation energy per atom, V, as a function of the angle of twist per length, $\alpha = \phi/\mathrm{L}$, for both CNTs.

Figure 2 shows clear differences between both CNTs in terms of energy of deformation achieved at rupture—here, "rupture" means the equilibrium state of the CNT at which the first failure of a C–C bond is reached. For pure stretching ($\beta = 0°$), the armchair tube reaches a higher energy of deformation (more than twice) of that of the zig-zag tube. This difference persists even in combined behaviour, as the twisting increases from $\beta = 5$ to 15°. For $\beta = 20°$ (twisting-to-stretching rate of 0.12 rad/Å) the deformation energy sharply drops to almost half, indicating the beginning of the twisting effects over the stretching ones. From then on, the deformation energy steadily decreases for increasing β and it seems to be more or less stabilized for $\beta \geq 50°$. It is also clear from Fig. 2a that the $V(\alpha)$ curves become less steep with increasing β, clearly showing that the deformation energy derives mainly from stretching the CNT rather than twisting it. Figure 2b differs significantly from Fig. 2a. In fact, the structural rupture takes place at a lower deformation energy for the zig-zag CNT when pure stretching ($\beta = 0°$) is involved, comparing to the armchair tube. However, as the twisting-to-stretching rate increases we see that the rupture deformation energy does not change much, implying that twisting does not affect the CNT rupture, which seems to be only affected by stretching. For $\beta = 45°$ (twisting-to-stretching rate of 0.35 rad/Å—Table 1), we see a small drop in the deformation energy. From $\beta = 45$ to 90°, previous trend is resumed and a steady slight increase in the rupture deformation energy occurs.

Note that, for the armchair CNT, the rupture points do not always correspond to the maximum energy achieved (remind that rupture is defined as the breaking of the first bond). This means that even when bonds break and 7–5 Stone-Waals defects start to appear the structure does not immediately break apart, but the CNT continues to stretch, reaching higher deformation energies and showing some resilience. This is seen mainly after $\beta > 30°$. On the other hand, zig-zag shows the

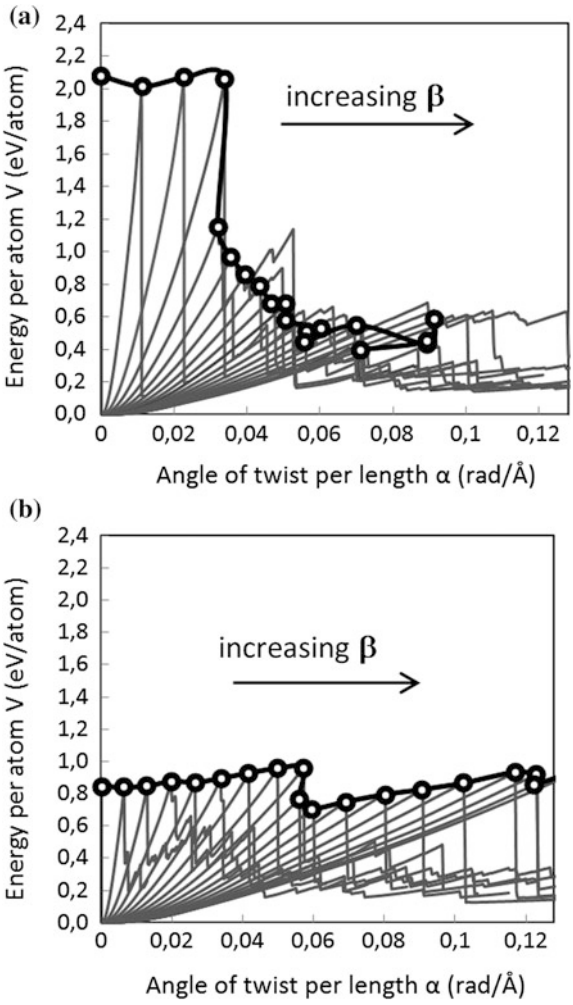

Fig. 2 Variation of the deformation energy, V, with angle of twist per length, α, for different values of β (rupture points are denoted by *circles*): **a** CNT (5, 5), **b** CNT (8, 0)

opposite behaviour. As soon as the first bond breaks, energy starts to sharply decrease, meaning that the structure collapsed or that it triggered a wide rupture.

Diagrams of interaction between the axial stretching u and the angle of twist ϕ at rupture are shown in Fig. 3a, b for the zig-zag and armchair CNTs, respectively. The (8, 0) zig-zag tube (Fig. 3a) has a maximum stretching displacement of roughly 10.0 Å if no twisting is applied. This CNT is able to augment its length from L = 46.3 to 56.3 Å without breaking. Furthermore, it is capable of maintaining the critical length of nearly 55–56 Å for low twisting-to-stretching rates (up to 0.29 rad/Å, i.e. $\beta = 40°$—see Table 1), denoting a clear non dependence on the twisting-to-stretching rate. A significant drop in u occurs for $\beta = 45°$, from 10 to 6.62 Å, which seems to indicate a clear interference of twist on the rupture

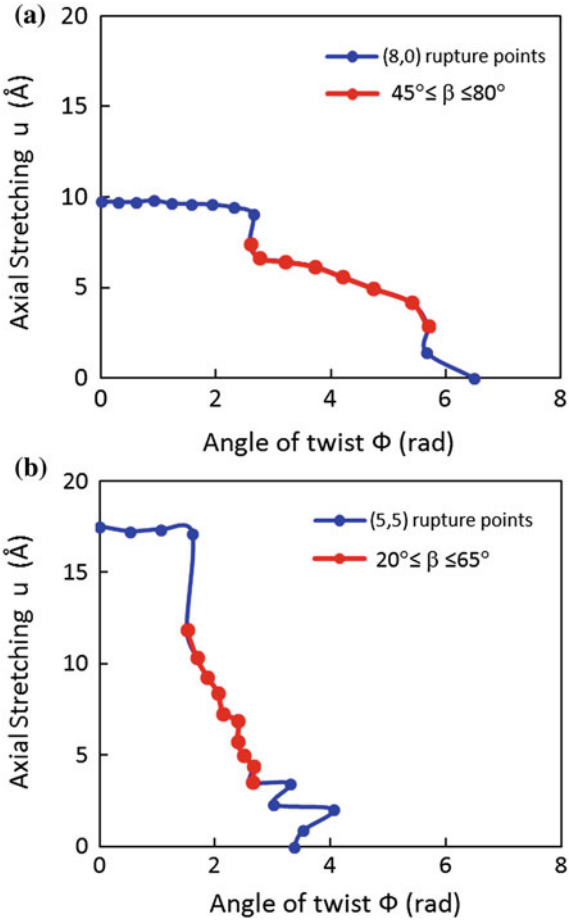

Fig. 3 Interaction diagrams between the axial stretching u (Å) and angle of twist ϕ (rad) for **a** zig-zag (8, 0) CNT and **b** armchair (5, 5) CNT

process. Increasing twisting-to-stretching rates (from $\beta = 45$ to 80°), denoted in Fig. 3a by the red dots and lines, imply a steady (almost linear) reduction of the maximum axial stretching, which is reduced to 2.88 Å for $\beta = 80°$. This means more or less 0.1 Å reduction per 5° increase in β. Pure twisting ($\beta = 90°$) induces rupture at an angle of twist of 6.5 rad (slightly more than a full 2π turn). Comparing Figs. 2b and 3a it can be concluded that although the deformation energy is derived mainly from bond stretching, the fact that the decrease in axial stretching from $\beta = 45$ to 80° is opposing a slight increase in deformation energy suggests that twisted CNTs can also increase their potential energy due to bond angle variation.

The armchair (5, 5) interaction diagram is shown in Fig. 3b. In pure stretching, the armchair CNT extends 17.5 Å without rupture. This means that the armchair CNT length increases from L = 47.3 to 64.8 Å without breaking. But when combined torsional-tensile displacements are applied, the armchair CNT can keep

this length only to a twisting-to-stretching rate of 0.10 rad/Å ($\beta = 15°$—see Table 1). If a twisting-to-stretching rate of 0.12 rad/Å is applied, the maximum stretching length is reduced 32 %, indicating that this twisting-to-stretching rate forces the CNT to break apart sooner than expected. After this major drop, the axial stretching at rupture continues to drop in an almost linear trend. This stage steeply descendent branch of the interaction curve is shown in Fig. 3b. For $\beta \geq 65°$, there is no clear trend besides a clear drop in axial stretching maximum length.

For pure loading, some differences between the two CNTs deserve to be mentioned, namely that:

- the armchair CNT reaches almost twice the maximum elongation achieved by the zig-zag CNT: $u = 17.5$ Å for the armchair CNT and $u = 10.0$ Å for the zig-zag CNT. The armchair CNT resists much better (without bond break) to pure stretching than the zig-zag CNT.
- the zig-zag CNT reaches almost twice the maximum twist achieved by the armchair CNT: $\phi = 6.5$ rad for the zig-zag CNT and $\phi = 3.36$ rad for the armchair CNT. The zig-zag CNT resist much better (without bond break) to pure twisting than the armchair CNT.

For combined stretching-twisting loading, it is concluded that interaction diagrams involve two different branches:

- For low twisting-to-stretching rate, a horizontal branch exists in which the axial stretching does not vary much with the low amount of twist. The width of this branch is distinct for armchair and zig-zag CNTs. The zig-zag CNT withstands combined stretching-twisting to a higher extent than the armchair CNT: this corresponds to $\beta = 40^{\circ}$ for zig-zag CNT and $\beta = 15^{\circ}$ for the armchair CNT.
- For moderate to high twisting-to-stretching rate, an almost (with some scatter) linear descending branch exists in both interaction u-ϕ diagrams. This "linear" branch is much steepest for the armchair CNT than for the zig-zag CNT, which means that the strength of the armchair CNT is much more affected by the twisting-to-stretching rate than the zig-zag one.

4 Bond Kinematics

The interaction diagrams corresponding to CNT rupture (1st bond failure) presented in the previous section state that both (5, 5) and (8, 0) CNTs break apart for distinct maximum stretching displacements and strains. Furthermore, if twisting deformations are imposed in combination with stretching deformations, both CNTs behave differently in order to accommodate these deformations. As a consequence, their rupture behaviour follows dissimilar trends. Albeit rupture can be seen as a global phenomenon, it may depend on CNT diameter and length. In the cases studied herein, these two variables are made very similar. Thus, the major factor contributing to that dissimilar behaviour is chirality. In order to

understand why CNT rupture occurs at different stretching displacements and different twisting angles, it is mandatory to assess how the hexagonal lattice of armchair and zig-zag configurations accommodates the imposed deformations. To achieve this goal, the kinematics of the hexagonal lattice is analyzed, which comprises the assessment of bond length variations and angle amplitude variations with the prescribed displacements. For both CNTs the hexagonal cell in which rupture first occurs is selected and the bond length and angle variations are measured against the initial equilibrium values, i.e. before any displacements are imposed. Figure 4a presents a scheme with (i) the bond labels x, y and z and (ii) the angle labels a, b and c. Figure 4b depicts both CNTs in initial equilibrium state and fully tensioned state.

In the following sections, results regarding bond length variations and angle amplitude variations are presented. Firstly, pure stretching is established as the reference case. The results for combined stretching-twisting deformations (including pure twisting) are then presented and compared with the reference case, i.e. pure stretching deformations.

4.1 Pure Tensile Behaviour

Figure 5a gives clear evidence that bonds **y** and **z** are responsible for the high stretching displacement (17.5 Å) and high strain ($\varepsilon = 17.5/47.3 = 37$ %) achieved by (5, 5) CNT before rupture is attained. As the stretching deformation is imposed to the (5, 5) CNT, bonds **y** and **z** increase their length simultaneously and with equal variation ($\sim$23 %), meaning that they give equivalent response to the deformation imposed.

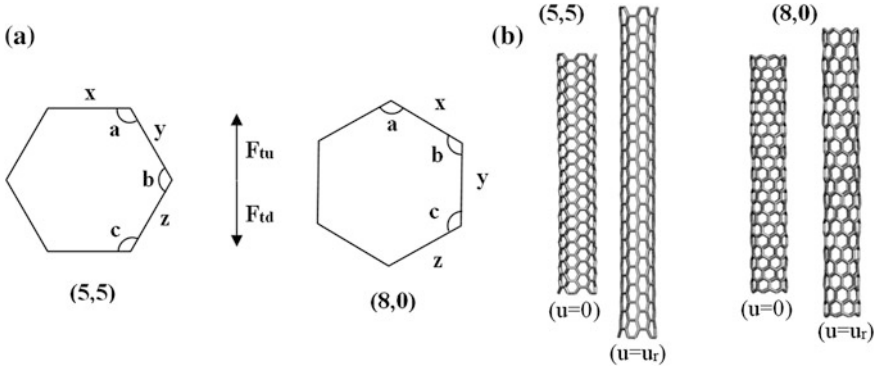

Fig. 4 **a** Scheme representing the adopted nomenclature. In this scheme, the *hexagon* cells are aligned with the tube axis, for which the tensile loads, F_{tu} and F_{td}, are applied. x, y and z represent bonds while a, b and c represent angles. **b** Representation of the two CNTs, each one with two representations, the initial equilibrium state (*left*) and the pre-rupture state for pure stretching (*right*)

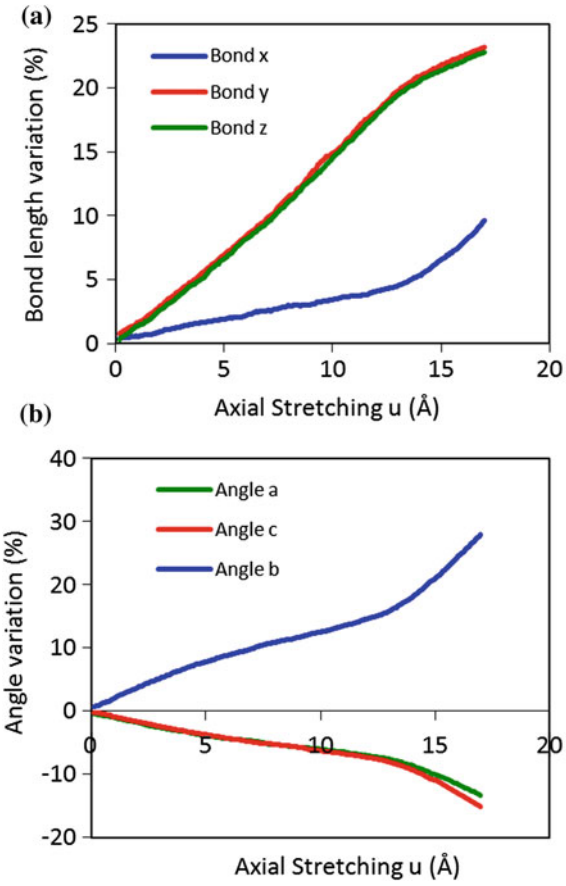

Fig. 5 CNT (5, 5): Variation, with the axial stretching u (Å), of **a** bond length variation and **b** angle amplitude variation

Bond **x**, positioned transversally to the tube axis (see Fig. 4a), also presents some positive length variation (increase of $\sim$10 %) but to a lesser extent than the other two bonds. The axial stretching imposed to the (5, 5) CNT also implies a $\sim$28 % increase of amplitude of angle **b,** forcing angles **a** and **c** to close (see Fig. 4b). For a stretching displacement up to 13.0 Å, there is a linear trend between the bond variation and the imposed axial stretching u (Fig. 4a). Similar linear trend also exists for between the angle variation and imposed axial stretching u (Fig. 4b). For stretching displacement greater than 13.0 Å, there is a clear change of the curves' slopes. The data suggests that around $u = 13.0$ Å both bonds **y** and **z** reach their maximum length. In order to accommodate further stretching without rupture, the hexagonal lattice starts to open angle **b** at a faster rate: it rapidly increases from 15 % variation at $u = 13.0$ Å to 28 % variation at $u = 17.5$ Å. Consequently, bond **x** has to increase faster also. If these changes are uniform throughout the CNT structure, it is expected that a diameter reduction occurs because bond **x** increase of 10 % variation cannot compensate a 28 % variation of angle **b**.

Figure 7 depicts the variation of diameter reduction with u, for the (5, 5) CNT. The red curve shown in Fig. 7 proves that assumption. It is clear that a 2 % reduction of CNT diameter is achieved for $u < 13.0$ Å. But for $u > 13.0$ Å, the curve slope increases and the diameter reduction rapidly achieves 7 %, which is a rather significant value since the CNT diameter decreases about 0.5 Å.

The (8, 0) CNT behaves very differently because it has a bond that is perfectly aligned with the direction in which the stretching is imposed. That is bond **y**. As we can see in Fig. 6a, bond **y** increases its length up to 21 % of its initial value and then breaks, inducing the CNT global failure. Bonds **x** and **z** show minor variations of about 6 % and are not so affected as bond **y**, mostly because their initial directions are far from the axial direction, although their are not fully orthogonal either. Angle **a** decreases its amplitude as a consequence of being pulled, forcing a small increase in the amplitudes of angles **b** and **c**. Notice that the same phenomenon found in (5, 5) CNT is also present to a lesser extent in (8, 0) CNT. From $u = 7.0$ to 9.75 Å, there is a sudden decrease of the amplitude of angle **a** (the slope

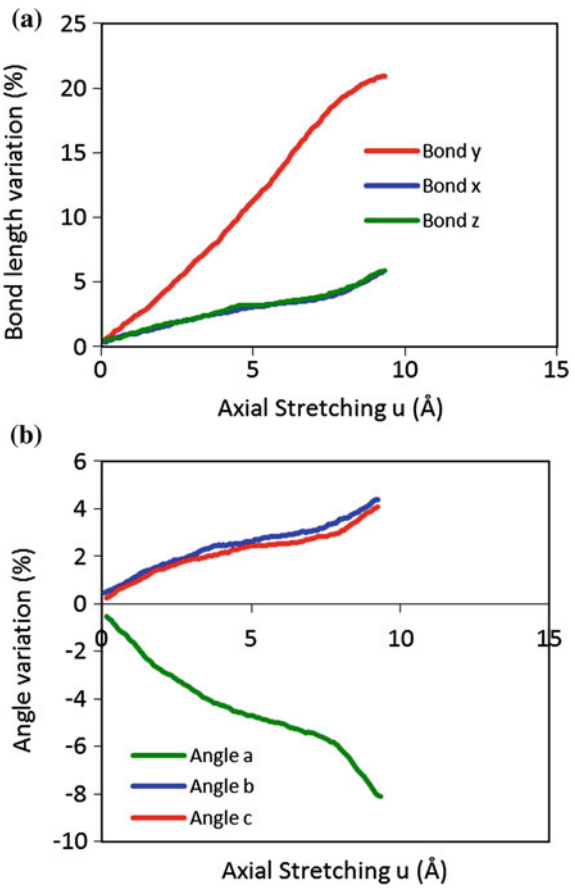

Fig. 6 CNT (8, 0): Variation, with the axial stretching u (Å), of **a** bond length variation and **b** angle amplitude variation

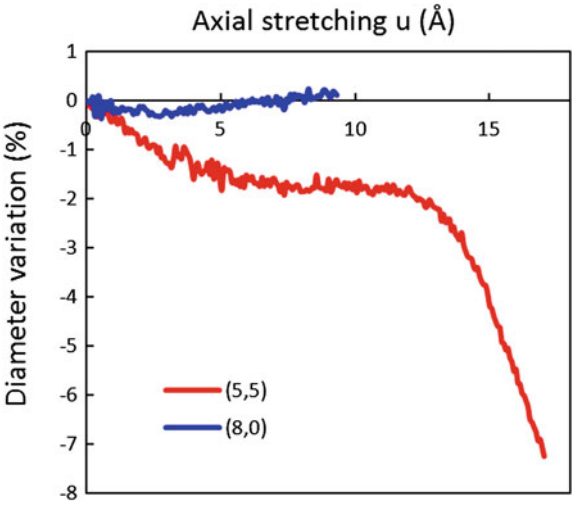

Fig. 7 Variation, with the axial stretching u (Å), of diameter variation

of angle **a** is the steepest in Fig. 6b. This enforces some increase in the amplitudes of angles **c** and **b**, but not very prominent variations of length of bonds **x** and **z**. Thus, some diameter reduction would be expected. However, the opposite scenario is obtained, as depicted in Fig. 7, in which there is a slight increase of CNT diameter.

In fact, a decrease of (8, 0) CNT diameter really happens, as we can see from Fig. 8. However, this diameter decrease is purely local and is localized in the CNT

Fig. 8 Localised diameter reduction in the region where the CNT (8, 0) rupture occurs

section where rupture will then occur. This diameter reduction is not reflected in the blue curve of Fig. 7 because the diameter variation depicted in this figure is the average value measured in several cross-sections of the CNT, in a given instant. The reason why the diameter reduction has a global nature in armchair CNTs and local nature in zig-zag CNTs is not clear. Yet, we suggest that it is a consequence of the process of axial load transfer throughout the whole CNT. If we notice Fig. 4b, the (5, 5) CNT lattice orientation is such that only bonds **y** and **z** have projection in the axial direction (x is orthogonal to it) but are not fully aligned to it. The **y** and **z** bonds form a "zig-zag" chain along the axial direction that behaves like an elastic spring and enhances the axial load transfer. This is the reason behind the very high failure strain of (5, 5) CNT, reaching 37 %! In case of (8, 0) CNT, **x** and **z** bonds are almost perpendicular to the axial direction and bond **y** is the one that is mostly responsible for the CNT elongation. The "armchair" chain formed by **y** and **x** (or **z**) bonds is less flexible and the load transfer between bonds **y** and **x** (or **z**) is harder to achieve, giving rise to local necking phenomena.

4.2 Twisting and Combined Stretching-Twisting Behaviour

In this section, it is considered the behaviour of the CNTs under combined stretching-twisting and pure twisting. Three β values are considered (see Fig. 1a):

- $\beta = 45°$ corresponding to a twisting-to-stretching rate $\phi/\mathrm{u} = 0.35$ rad/Å (Table 1). It means that the CNT is twisted 0.35 radians for each angstrom that it is stretched.
- $\beta = 60°$ corresponding to a twisting-to-stretching rate $\phi/\mathrm{u} = 0.60$ rad/Å (Table 1). This means that, for each angstrom of stretching displacement, the CNT is twisted 0.60 rad.
- $\beta = 90°$ corresponding to a twisting-to-stretching rate $\phi/\mathrm{u} = \infty$ (Table 1) or a stretching-to-twisting rate $\mathrm{u}/\phi = 0$. It means that the CNT is not stretched but only twisted. This situation corresponds to pure twisting.

4.2.1 Armchair CNT

For the (5, 5) CNT, Figs. 9 and 10 depict the bond length variations and angle amplitude variations with respect to the angle of twist ϕ, respectively. Each curve corresponds to a given β value and to a given ϕ/u rate. Thus, and given a ϕ value, it is always possible to obtain the u value using one of the adopted ϕ/u rates. From Fig. 3b and for these β values (45 and 60°), it becomes understandable that the rupture points are placed in the red region of the interaction diagram, for which rupture is mostly influenced by twisting. Figures 9 and 10 are easier to interpret if the CNT MD simulations are visualized while the ϕ/u rate is imposed to the CNT.

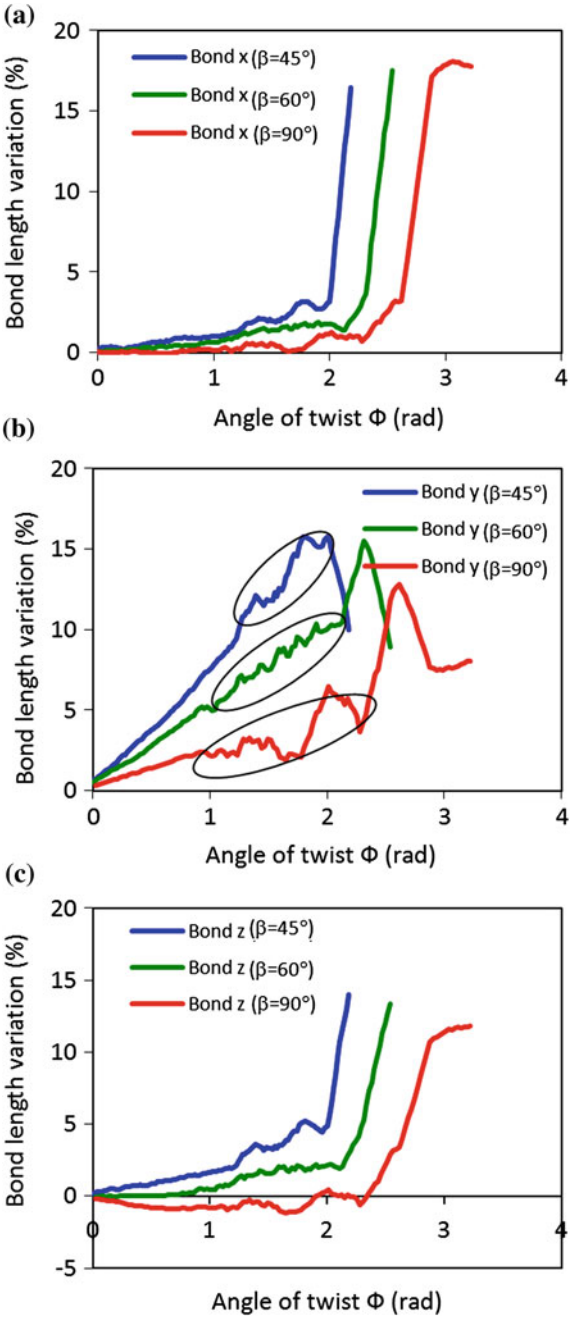

Fig. 9 CNT (5, 5): Variation, with the angle of twist ϕ (rad), of **a** bond x length variation, **b** bond y length variation, and **c** bond z length variation

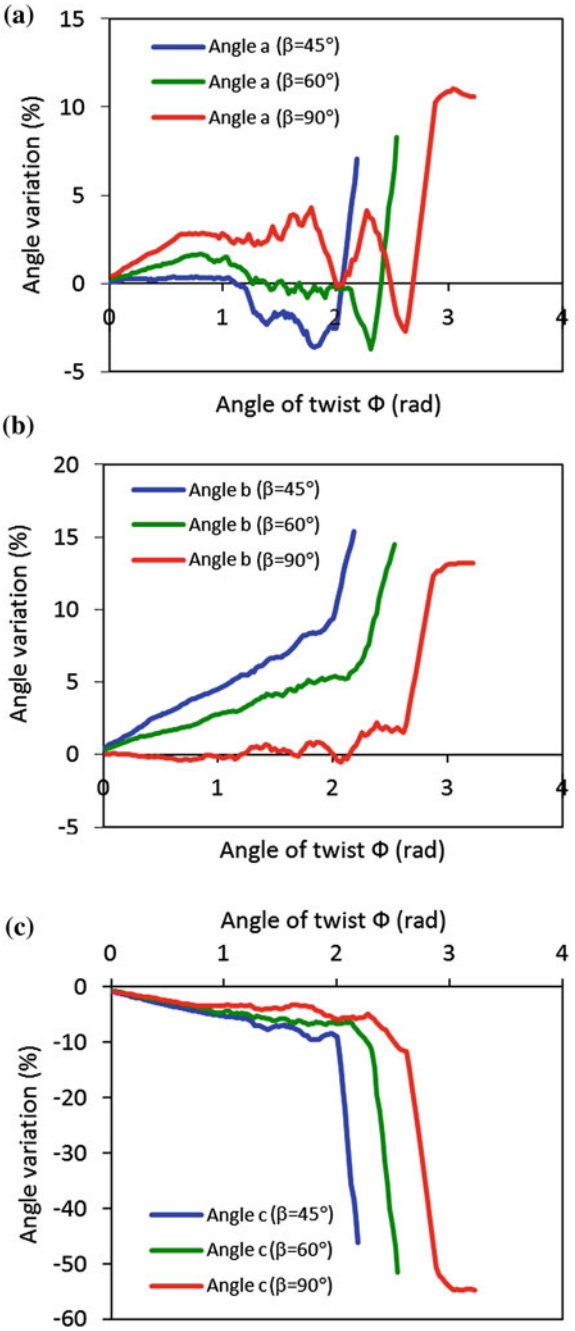

Fig. 10 CNT (5, 5): Variation, with the angle of twist ϕ (rad), of **a** angle *a* variation, **b** angle *b* variation, and **c** angle *c* variation

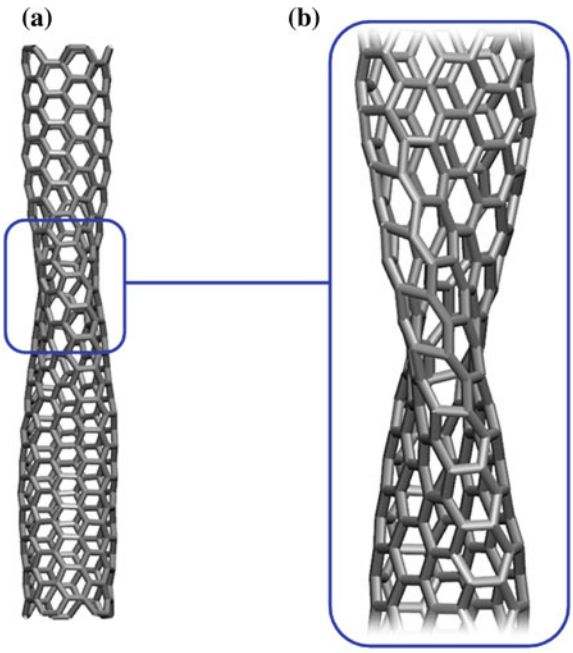

Fig. 11 CNT (5,5): **a** Visualization of the *helix shaped* configuration and **b** Zoom-in of the distorted *hexagonal* cells

Three different events might occur. Firstly, at a certain instant, the CNT buckles from a circular cylindrical shape into an oval helix shape, as depicted in Fig. 11a. This shape appears to rotate but, in fact, it's an illusion caused by the surface waves. This movement induces atomic oscillations in the radial direction. This helix shape configuration permits the CNT to relax local tensions arising from twisting. However, because part of the oval section surface is strongly curved, it also imposes local tensions in the mostly bent zones of CNT wall. As a result, bond lengths and angle amplitudes measured in a fixed hexagonal cell oscillate and the results show some scatter. The regions with oscillations due to the "rotating" helix shape are denoted in Fig. 9b. Secondly, and for a given ϕ value, the helix shape stops oscillating because the angle of twist and stretching displacement are high enough to stiffen the helix-shaped surfaces of the CNT. At this point, the CNT has two accentuated surface curvatures due the high ovalization. This gives rise to local tensions and impedes further oscillations. Beyond this stage, bond lengths and angle amplitude change rapidly as the CNT continues to twist. Thirdly, two regions of heavily distorted hexagonal cells are formed in the axial direction (Fig. 11b). These regions are situated in the mid section of the CNT. These hexagonal cells are forced to distort because of the torque. The twisting rotations imposed in opposite directions to the CNT top and bottom ends, tend to concentrate strain in its mid section, especially in the curved surfaces of the helix-shaped CNT. The increasing strains existing in hexagon cells require now the increase of bond lengths beyond the breaking instant.

Bond length variation can naturally be separated in three stages, considering the events just described. Bond **x** length variation depicted in Fig. 9a holds the same trend for the three β values. The length of bond **x** increases marginally, below 4 %, before reaching the stage in which the hexagonal cell is distorted. After that, it shows a very high length increase. The length increase in the first and second stages is small and almost inversely proportional to the twisting-to-stretching rate ϕ/u. For instance, it is seen that length increase is higher for $\beta = 45°$ (blue curve) than for $\beta = 90°$ (red curve). Although bond **x** does not show a variation exceeding 20 %, it is expected that this bond is responsible for the CNT rupture. We must be aware that a bond breaks for $\sim$23 % extension and that the bond length variation corresponds to average values. Thus, it is possible to have some bonds elongated by 23 % and still have average values below 20 %.

The length variation of bond **y** shows a higher increase than the other two bonds (**x** and **z**), during the first two stages and for the three β values considered. It is known that a continuum tube under torsion exhibits shear stresses in the contour direction (arising from torque) but also in the axial direction (arising from equilibrium). This shear stress state is characterized by principal stress directions oriented at 45° with respect to the contour and axial directions. These principal stresses correspond to tensile stresses in one direction but compressive stresses in the other (orthogonal) direction. Similar behaviour exists in CNT under twisting and the alignment of bond **y** is closer to the direction of tensile stresses. Therefore, the bond **y** increases its length the most. When the oscillations stop, increasing tensions stretch the bond even further, a fact that is visible for $\beta = 60°$ and $\beta = 90°$. The hexagonal cell distortions that follow relief this bond and decrease its length by closing angle **c** and opening angles **a** and **b** (see Fig. 11b).

Bond **z** (Fig. 9c) presents a length variation very close to that of bond **x**. Comparing the curves in Fig. 9c with the variations it showed when there was no twisting (Figs. 5b,6b), it is clear that the twisting direction misaligns the bond with the stretching direction. In fact, the bonds extend much less, even to $\beta = 45°$, showing poor load transfer. Once again, when severe deformation occurs in the hexagonal cell before rupture, the bond **z** (like bond **x**) increases its length.

Amplitude variations for angles **a, b** and **c** are shown in Fig. 10. Hexagonal cell deformation explains fairly well the very high slopes of the last portion of the curves. The hexagonal cell deformation consists mainly in the abrupt closing of angle **c.** As a consequence angles **b** and **a** have to open. This phenomenon occurs regardless of β value, and might indicate a possible cause for CNT rupture.

The amplitude variation of angles **b** and **c** is predictable. Angle **b** opens proportionally to the imposed stretching and inversely to the imposed twisting. Therefore, the curve slope is higher for lower β values. For $\beta = 90°$ (red curve), note that the variation of angle **b** is negligible while it is meaningful for $\beta = 45°$ (blue curve). On the other hand, angle **c** always closes: first because of stretching and then, for high twisting-to-stretching rates, because the twisting forces the amplitude to decrease. Angle **a** also exhibits these two opposed effects: stretching make it close while twisting make it open. For $\beta = 45°$, it is visible that these two effects cancelled each other prior to the CNT buckling into a helix shape tube.

Thus, angle **a** amplitude showed null variation. For $\beta = 60$ and 90°, it is clear that twisting component is predominant because the angle **a** opens. The oscillations of the helix shaped tube tend to close angle **a**. In fact, Fig. 10 shows that angle **a** closes in order to compensate an equal increase of angle **b** amplitude. Angle **a** amplitude variation also shows one negative peak for $\beta = 60°$ (green curve) and a positive peak beside two negative peaks for $\beta = 90°$ (red curve). These peaks are correlated with the length variation of bond **y** (Fig. 9b). Before cell distortion takes place, increasing local tensions tend to enlarge the length of bond **y** and force the closing of angle **a**. From the comparison between Figs. 9b and 10a, we see that the variations in these regions are complementary.

The rupture process can now be explained resorting to the observation of Fig. 12, which depicts the rupture mechanism and its sequence of steps. The last stage previously defined in curves shown in Figs. 9 and 10 was characterized by a severe distortion of the hexagonal cells situated in curved surface regions. This distortion was explained by the extreme closing of angle **c** and opening of angles **a** and **b,** while bond lengths abruptly increased. Rupture occurred at the end of this stage. Based on the visual representation of MD results, we suggest that rupture is triggered by the formation of a new bond, as depicted in Fig. 12, involving sp3 hybridization of the two carbon atoms that were brought into bond length distance by the closing of angle **c**. These two carbon atoms then return to sp2 hybridization due to the break of bond **z**, because this new state is energetically more favourable—recall that tension is released, not only by breaking of a tensioned bond but also by angular relaxation. This configuration originates a 7–5 Stone-Waals defect that spreads as the imposed stretching-twisting combination continues. Figure 12 shows this process for $\beta = 45°$. This failure mechanism was equally observed for all $\beta > 15°$, showing that rupture occurs in twisted (5, 5) CNTs in an identical process regardless of the twisting-to-stretching rate ($\beta > 15°$).

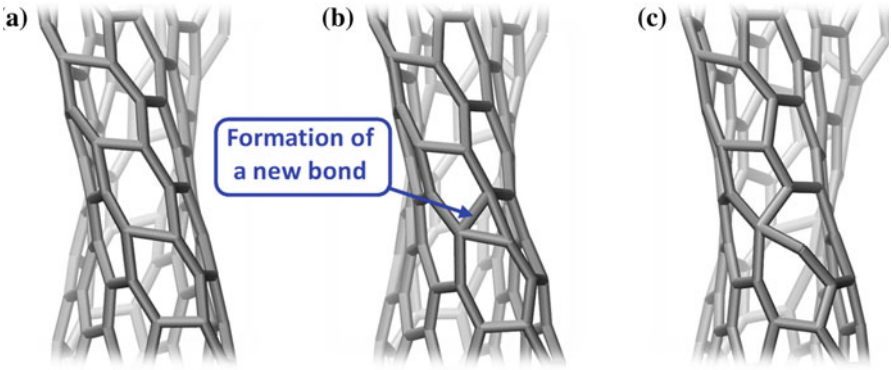

Fig. 12 (5, 5) CNT: sequential views showing the beginning of the rupture process for $\beta = 45°$

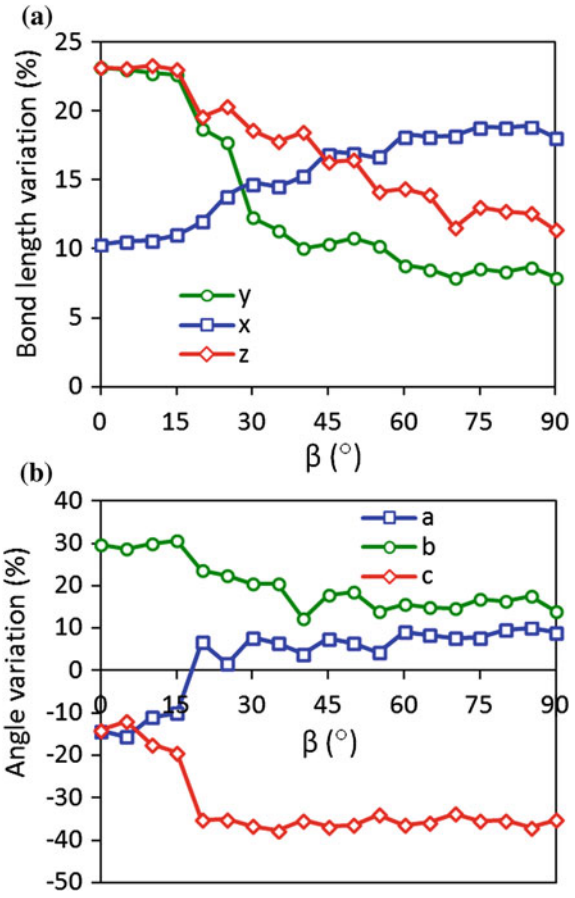

Fig. 13 CNT (5, 5): **a** bond length variation at rupture vs. β and **b** angle amplitude variation at rupture vs. β

Figure 13 depicts the variation, with β, of bond length and angle amplitude at rupture. These variables are scaled to their initial values and they correspond to the average value of the last 100 steps before rupture.

Firstly, it is seen that the influence of twisting-to-stretching rate ϕ/u (or β) on the kinematics of CNT rupture is relevant. The bond length increase remains almost unchanged from $\beta = 0$ to 15°. In this case, bonds **y** and **z** reach their maximum length ($\sim$23 %) and force bond **x** to stretch also. Angle **b** opens widely and obliges the other angles to decrease their amplitude. The CNT reaches its maximum length ($\sim$17.5 Å) for $0° \leq \beta \leq 15°$, meaning twisting effects are negligible in this range. CNT rupture is achieved by breaking of bonds **y** or **z**. From $\beta = 15$ to 20°, the angle amplitudes at rupture change a lot. The angle **b** amplitude drops but the angle still opens, while the amplitude of angle **a** is now positive (angle opens). The amplitude of angle **c** decreases the most and closes. For $\beta = 20°$, the amplitude of angles at rupture become characteristic of a distorted cell. From $\beta = 20$ to 90°, the amplitudes of the angles show some scatter but small

variation. In this range, the length of bond **y** shows a high decrease, bond **z** exhibits a smaller drop in its length, and bond **x** increases its length. However, none of these bonds achieve their maximum elongation ($\sim$23 %) in the range $20° \leq \beta \leq 90°$. Thus, we conclude that the rupture mechanism involves the deformation (distortion) of the hexagonal cell with abrupt closing of angle **c**. This leads to the formation of a new bond through sp3 hybridization of two carbon atoms, followed by breaking of a tensioned adjacent bond and new hybridization to sp2.

4.2.2 Zig-Zag CNT

The first fact to notice when comparing the (8, 0) CNT with (5, 5) CNT is that the former withstands much less axial stretching than the latter. Although it maintains similar axial stretching at failure in spite of increasing twisting-to-stretching rate, it also endures more twisting without rupture. The request is to explain the reason why it can endure more twisting when compared with (5, 5) CNT. The explanation clearly lies in the differences presented in the chiral matrix. Figures 14 and 15 depict the bond length variations and angle amplitude variations of (8, 0) CNT with respect to the angle of twist ϕ: recall the bond and angle nomenclature of (8, 0) CNT shown in Fig. 4a. The results shown in Fig. 6a (pure stretching) demonstrated that bond **y** length variation was responsible for much of the CNT elongation without rupture.

Firstly, let us discuss the $\beta = 45°$ case (blue curves in Fig. 14). We see that all bonds increase their length in a linear trend with the twist ϕ: bond **y** is the most elongated (achieving a maximum of 15.9 %) while the elongations of bonds **x** and **z** are fair and marginal, respectively. However, this linear path is abruptly changed for $\phi > 2.3$ rad as the length of bonds **x** and **z** increase sharply and the length bond **y** decreases steeply, indicating the occurrence of extreme deformation (distortion) of the hexagonal cell. This fact is confirmed by angle amplitude analysis (Fig. 15). Initially, there is a linear variation of all angles with the twist ϕ: angle **b** increases the most (achieving a maximum of 12.0 %) while the amplitudes of angles **a** and **c** decrease to a lesser extent.

As mentioned before, this linear path changes suddenly for $\phi > 2.3$ rad, and a sudden rise is observed in the amplitudes of angles **b** and **c** (Figs. 15b, c) while an abrupt decay of angle **a** occurs (Fig. 15a). This change of angle amplitudes is associated with a distortion of the hexagonal cell that leads to rupture, similarly to that observed for (5, 5) CNT—in this case, angle **a** closes instead. Notice that, for $\beta = 45°$, oscillations of helix shape rotations were not observed. Visual MD data confirms that a helix shape forms, similar to the one observed in Fig. 11a. From Fig. 3, we are able to mention that hexagonal cell distortion occurs in (8, 0) CNT for $\beta \geq 45°$ ($\phi = 2.6$ rad and u = 7.4 Å, Fig. 3a) while in (5, 5) CNT it takes place for $\beta \geq 20°$ ($\phi = 1.5$ rad and u = 11.9 Å, Fig. 3b). Comparing both CNTs, we see that (8, 0) CNT requires much larger twist ϕ and lower stretch u to collapse than the (5, 5) CNT.

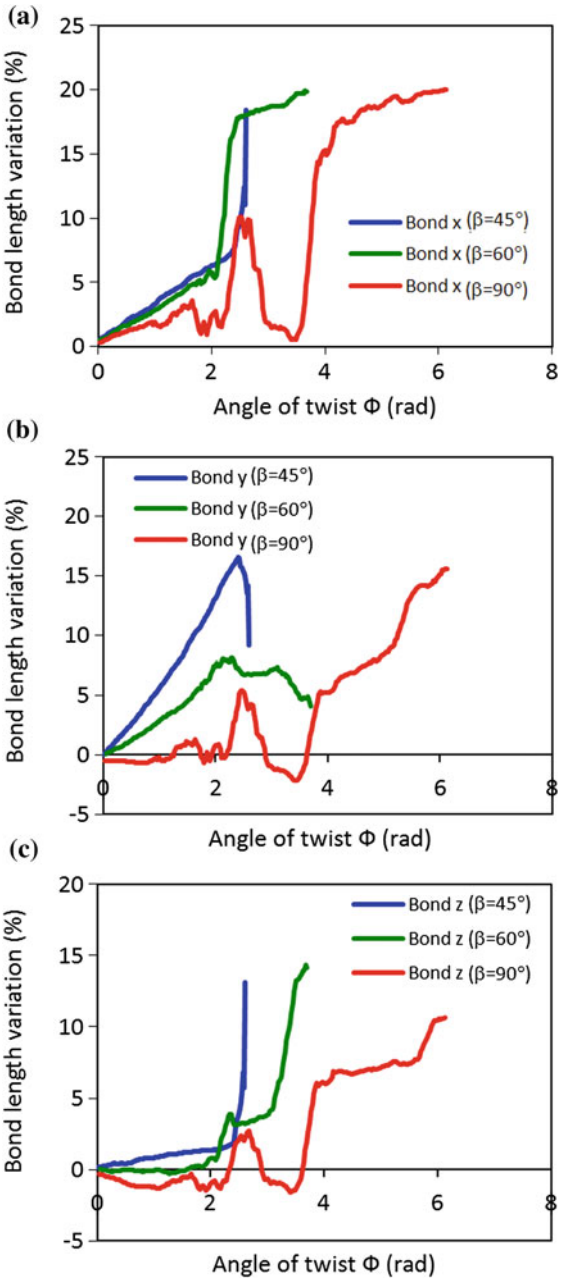

Fig. 14 CNT (8, 0): Variation, with the angle of twist ϕ (rad), of **a** bond x length variation, **b** bond y length variation, and **c** bond z length variation

For $\beta = 60°$, the bond length and angle amplitude variation curves do not exhibit a clear trend, but it is possible to discern four stages. Initially ($\phi < 2.0$ rad), there is a linear trend similar to that observed for $\beta = 45°$. For

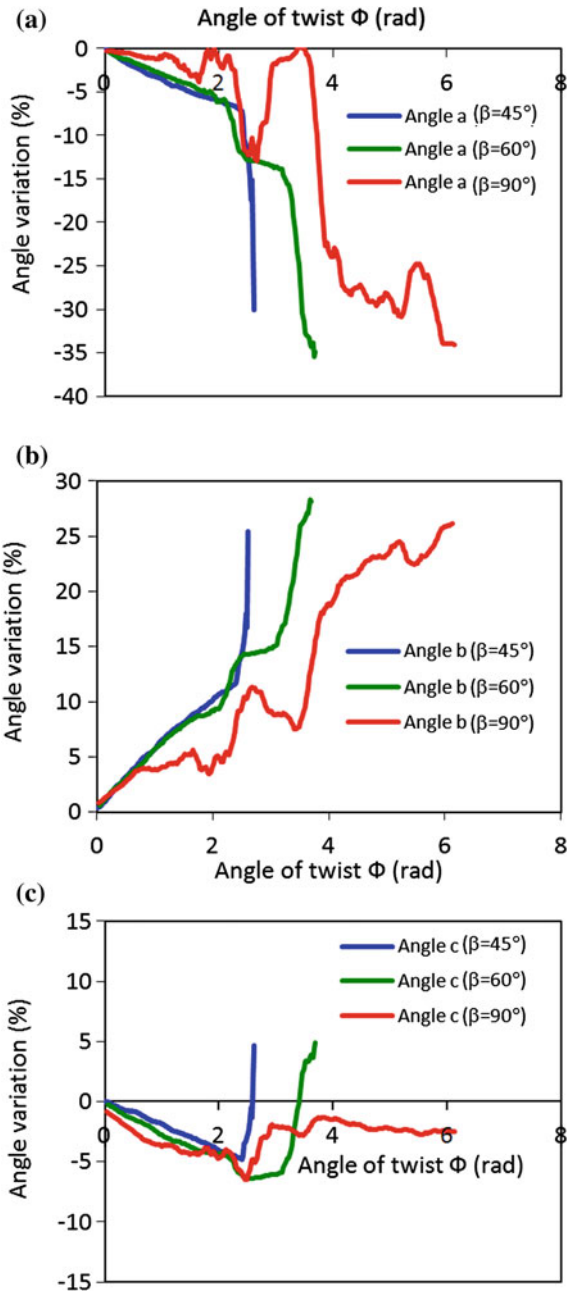

Fig. 15 CNT (8, 0): Variation, with the angle of twist ϕ (rad), of **a** angle a variation, **b** angle b variation, and **c** angle c variation

$2.0 < \phi < 2.33$ rad, the CNT buckles into a helix shape that oscillates about the CNT axis. The bonds **x** and **z** increase their length, especially bond **x** because it is oriented towards the stretching direction, while bond **y** maintains its length. Angles

a and **c** decrease their amplitude while angle **b** opens. These fluctuations reflect the consecutive reversible deformations of the lattice cell when the helix shape oscillates. These oscillations tend to redistribute and homogenize the bond and angle tensions throughout the CNT. This explains the huge increase of bond **x** length. These oscillations enable the load transfer from cell to cell in the axial directions. For $2.33 < \phi < 3.0$ rad, the helix shape oscillations almost stop. As twisting progresses beyond $\phi = 3.0$ rad, the helix shape is so twisted that the hexagonal cell distorts and CNT fails by the process depicted in Fig. 16. Deformation of the lattice cell consists mainly of the quick closing of angle **a** and opening of angles **b** and **c**. Notice that angle **c** was closing in previous stages, but this cell deformation increases the length of bond **z**, forcing angle **c** to open. The lengths of bonds **x** and **y** do not show much change because they were already stretched.

For $\beta = 90°$ (pure twisting), torsional buckling occurs very soon (at $\phi = 0.94$ rad) and, from then on, the helix shape oscillations alternate between high and low rotations. This gives rise to the red curves depicted in Figs. 14 and 15, in which the bond length and angle amplitude variations show a high scatter. For $\phi > 4.0$ rad, bond **x** increases its length almost 20 %, very close to the rupture length ($\sim$23 %), proving very good alignment with the stretching direction (CNT axis). The bonds **y** and **z** also increase length, as expected. A major difference to the combined twisting-stretching behaviour ($\beta = 45$ and 60°) is that the distortion of the hexagonal cell is not abrupt as it was for $\beta = 45$ and 60°. Angles show the same trend variations as before ($\beta = 60°$), but now are more gradual. The exception is that angle **c** no longer shows positive variation in this final stage before rupture (see Fig. 15c). This is a direct consequence of the length increase of bond **y**, which did not happen for $\beta = 60°$. This kinematic behaviour of bond

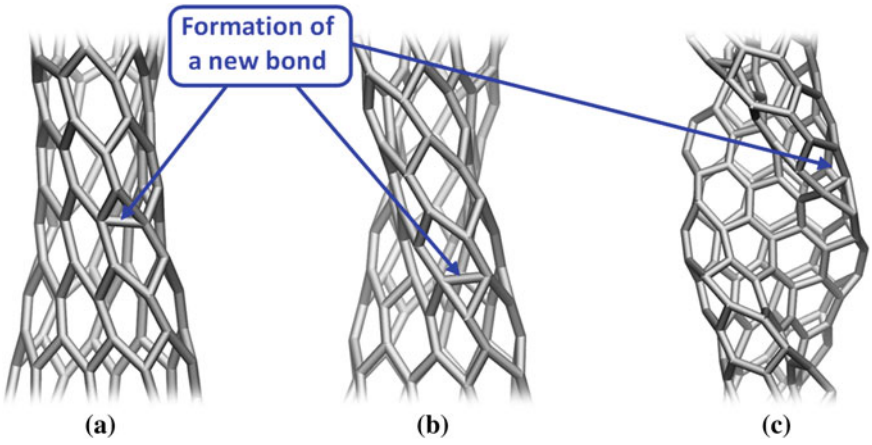

Fig. 16 (8, 0) CNT: views showing the formation of a new bond and beginning of the rupture process for **a** $\beta = 45°$, **b** $\beta = 60°$ and **c** $\beta = 90°$

y could be the result of the slow deformation of the hexagon cell, contrasting with the sudden deformation registered before ($\beta = 60°$).

For $\beta = 45$, 60 and 90°, Fig. 16 shows zoom-in views of new bond formation that consequently leads to CNT rupture. The distortion of hexagonal cell is clearly visible in Figs. 16a, b and c. It is also visible that cell deformation always occurs in the mostly bent and strained region of the buckled CNT. For $\beta = 45°$, it is interesting to notice that the closing of angle **a** is directly responsible for the creation of a new bond. However, for $\beta = 60$ and 90°, it is the closing of its symmetrical. Comparing Figs. 12 ((5, 5) CNT) and Fig. 16 ((8, 0) CNT), we conclude that the deformed shape of the cell is very similar.

Figure 17 depicts the variation of bond length and angle amplitude at rupture with β—recall that bond lengths and angle amplitudes are scaled to their initial values and they are the average value of the last 100 steps before rupture. From Fig. 17, it is seen that the influence of twisting-to-stretching rate ϕ/u (or β) on the kinematics of CNT rupture is deemed relevant. The bond **y** achieves the maximum

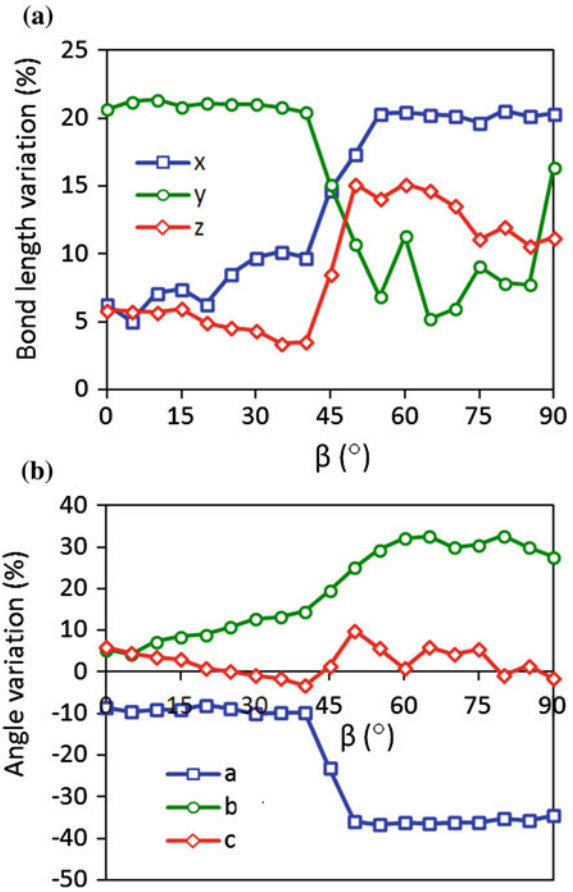

Fig. 17 CNT (8, 0): **a** bond length variation at rupture vs. β and **b** angle amplitude variation at rupture vs. β

elongation ($\sim$23 %) from $\beta = 0$ to 40° and the breaking of this bond initiates the CNT rupture. In this β range, bond **x** increases slightly its length because it becomes more align with the CNT axis due to the amount of twist. Oppositely, the bond **z** decreases its length. For the range $0° \leq \beta \leq 40°$, the amplitudes of the angles remain almost unchanged (Fig. 17b). For $45° \leq \beta \leq 90°$, there is a combination of angles typical of a distorted cell, with a sudden decline of angle **a** (even more closed) and increase of angle **b.** The combination of bond lengths also changes in this interval of β. From $\beta = 40$ to 50°, the lengths of bonds **x** and **z** increase while there is a major decline of the length of bond **y**. Although bond **x** achieves a maximum extension of 20 %, the rupture mechanism is not due to direct bond breaking but rather due to cell distortion. It is similar to the one described earlier for the (5, 5) CNT and $\beta \geq 20^{\circ}$.

5 Conclusion

This chapter presented a study on the kinematics of bonds and their influence on the collapse behaviour of armchair and zig-zag CNTs under combined stretching-twisting. MD simulations were used to achieve this goal and prescribed axial displacements (stretching) and twisting rotations (torsion) were imposed to both CNT ends (supports). The results were extensively analyzed, mainly in the form of (i) diagrams of energy at rupture versus the twisting-to-stretching rate and (ii) diagrams of interaction between the axial stretching displacement at rupture and the angle of twist at rupture. Then, a detailed study on the variation of bond length and angle amplitude with the imposed stretching and twisting deformations was shown. Firstly, the case of pure stretching was described as a reference. After that, the cases of combined twisting-stretching and pure twisting were dealt with separately for zig-zag (8, 0) CNT and armchair (5, 5) CNT.

From the remarks drawn before, we are now able to answer the question: why can (8, 0) CNT undergo more twisting compared with the (5, 5) CNT? The differences between the two CNTs (zig-zag and armchair) lie in the orientation of hexagonal cells, i.e. their chirality. With a meaningless amount of twist, the extension of the (5, 5) CNT is much higher (almost twice) than that of (8, 0) CNT because this CNT has only one bond (**y**) aligned with the axial direction while the armchair has two bonds (**y** and **z**) fairly aligned with the axial direction. For moderate to high twisting, the CNT rupture follows a different mechanism. Twisting deforms the matrix cells and brings carbon atoms into bond forming distances in order to promote the formation of new bonds and breaking more strained bonds. This mechanism relies on cell distortion. For the same twisting angle, the hexagonal cell of (5, 5) CNT deforms much more than that of (8, 0) CNT, meaning that rupture will occur sooner for the armchair CNT than for zig-zag one. Other factors may attenuate or contribute to cell deformation and may turn this dependence less clear, like load transfer, localized strain and rotational oscillations.

Acknowledgments The authors gratefully acknowledged the financial support given by FCT, in the context of the project "Modelling and Analysis of Nanostructures: Carbon Nanotubes and Nanocomposites" (PTDC/ECM/103490/2008).

References

Agrawal PM, Sudalayandi BS, Raff LM, Komanduri R (2008) Molecular dynamics (MD) simulations of the dependence of C–C bond lengths and bond angles on the tensile strain in single-wall carbon nanotubes (SWCNT). Comput Mater Sci 41:450–456

Arash B, Wang Q (2012) A review on the application of nonlocal elastic models in modeling of carbon nanotubes and graphenes. Comput Mater Sci 51(1):303–313

Bao WX, Zhu CC, Cui WZ (2004) Simulation of Young's modulus of single-walled carbon nanotubes by molecular dynamics. Phys B 352:156–163

Batra RC, Sears A (2007) Continuum models of multi-walled carbon nanotubes. Int J Solids Struct 44(22–23):7577–7596

Byrne EM, Letertre A, McCarthy MA, Curtin WA, Xia Z (2010) Optimizing load transfer in multiwall nanotubes through interwall coupling: theory and simulation. Acta Mater 58(19):6324–6333

Chang T (2007) Torsional behavior of chiral single-walled carbon nanotubes is loading direction dependent. Appl Phys Lett 90(20):201910

Faria B, Silvestre N, Canongia Lopes JN (2013a) Induced anisotropy of chiral carbon nanotubes under combined tension-twisting. Mech Mater 58:97–109

Faria B, Silvestre N, Canongia Lopes JN (2013b) Tension-twisting dependent kinematics of chiral CNTs. Compos Sci Technol 74:211–220

Fennimore AM, Yuzvinsky TD, Han WQ, Fuhrer MS, Cumings J, Zettl A (2003) Rotational actuators based on carbon nanotubes. Nature 424:408–410

Georgantzinos SK, Anifantis NK (2009) Vibration analysis of multi-walled carbon nanotubes using a spring-mass based finite element model. Comput Mater Sci 47(1):168–177

Hall AR, An L, Liu J, Vicci L, Falvo MR, Superfine R, Washburn S (2006) Experimental measurement of single-wall carbon nanotube torsional properties. Phys Rev Lett 96:256102

Hall AR, An L, Liu J, Vicci L, Falvo MR, Superfine R, Washburn S (2010) Erratum: Experimental measurement of single-wall carbon nanotube torsional properties [Phys Rev Lett 96 256102 (2006)]. Phys Rev Lett 105:069904

Hall AR, Paulson S, Cui T, Lu JP, Qin LC, Washburn S (2012) Torsional electromechanical systems based on carbon nanotubes. Rep Prog Phys 75(11):116501

Jeong BW, Lim JK, Sinnott SB (2007a) Tensile mechanical behavior of hollow and filled carbon nanotubes under tension or combined tension-torsion. Appl Phys Lett 90:023102

Jeong BW, Lim JK, Sinnott SB (2007b) Multiscale-failure criteria of carbon nanotube systems under biaxial tension-torsion. Nanotechnology 18:485715

Plimpton S (1995) Fast parallel algorithms for short-range molecular dynamics. J Comput Phys 117:1–19

Sears A, Batra RC (2004) Macroscopic properties of carbon nanotubes from molecular-mechanics simulations. Phys Rev B 69(23):235406

Shima H (2012) Buckling of carbon nanotubes: a state of the art review. Materials 5(1):47–84

Stuart SJ, Tutein AB, Harrison JA (2000) A reactive potential for hydrocarbons with intermolecular interactions. J Chem Phys 112:6472–6486

Sun J, Xu F, Sun LT (2012) In situ investigation of the mechanical properties of nanomaterials by transmission electron microscopy. Acta Mech Sin 28(6):1513–1527

Talukdar K, Mitra AK (2010) Influence of odd and even number of stone-wales defects on the fracture behaviour of an armchair single-walled carbon nanotube under axial and torsional strain. Mol Simul 36:409–417

Tserpes KI, Papanikos P, Tsirkas SA (2006) A progressive fracture model for carbon nanotubes. Compos B Eng 37(7–8):662–669

Wang Q, Liew KM (2008) Molecular mechanics modeling for properties of carbon nanotubes. J Appl Phys 103(4):046103

Wang CM, Zhang YY, Xiang Y, Reddy JN (2010) Recent studies on buckling of carbon nanotubes. Appl Mech Rev 63:030804

Wernik JM, Meguid SA (2010) Atomistic-based continuum modeling of the nonlinear behavior of carbon nanotubes. Acta Mech 212(1–2):167–179

Williams PA, Papadakis SJ, Patel AM, Falvo MR, Washburn S, Superfine R (2002) Torsional response and stiffening of individual multiwalled carbon nanotubes. Phys Rev Lett 89:255502

Xu YQ, Barnard A, McEuen PL (2009) Bending and twisting of suspended single-walled carbon nanotubes in solution. Nano Lett 9(4):1609–1614

Yakobson BI, Brabec CJ, Bernholc J (1996) Nanomechanics of carbon tubes: Instabilities beyond linear response. Phys Rev Lett 76:2511–2514

Zhao R, Luo CL (2011) Torsion-induced mechanical couplings of single-walled carbon nanotubes. Appl Phys Lett 99:231904

Finite Element Modeling of the Tensile Behavior of Carbon Nanotubes, Graphene and Their Composites

Konstantinos I. Tserpes and Paraskevas Papanikos

Abstract Due to their extraordinary mechanical properties, carbon nanotubes and graphene serve as ideal reinforcements. However, the effectiveness of reinforcement may be counterbalanced by the presence of defects, which degrades significantly the mechanical properties of nanomaterials, and the negative influence of several material-related and geometrical factors on the effective elastic properties of nano-reinforced composites. This chapter reviews the continuum models that were developed by the authors in order to predict the elastic properties of isolated defect-free carbon nanotubes, to simulate the tensile behavior of defected carbon nanotubes and graphene and to evaluate parametrically the effective elastic properties of nano-reinforced polymers.

Keywords Carbon nanotubes · Graphene · Nanocomposites · Finite element analysis

1 Introduction

Graphene is not only the thinnest material ever but also the strongest. Recently, Lee et al. (2008) have measured, by nanoidentation in an atomic force microscope, the Young's modulus and intrinsic strength of defect-free graphene monolayer to be 1.0 TPa and 130 GPa, respectively. This finding gave strong support to the

K. I. Tserpes (✉)
Laboratory of Technology and Strength of Materials, Department of Mechanical Engineering and Aeronautics, University of Patras, 26500 Patras, Greece
e-mail: kit2005@mech.upatras.gr

P. Papanikos
Department of Product and Systems Design Engineering, University of the Aegean, Ermoupolis, 84100 Syros, Greece
e-mail: ppap@aegean.gr

K. I. Tserpes and N. Silvestre (eds.), *Modeling of Carbon Nanotubes, Graphene and their Composites*, Springer Series in Materials Science 188,
DOI: 10.1007/978-3-319-01201-8_10,

investigation currently being evolved for establishing carbon nanotubes (CNTs) and graphene as reinforcements since it was the first time the suspected extraordinary mechanical properties of these materials were experimentally verified. In the past, similar values were also reported for the mechanical properties of CNTs [e.g. Belytschko et al. 2002; Duan et al. 2007; Mielke et al. 2004] but only by simulations; the mechanical properties of defect-free CNTs have not been measured yet. Contrary to simulations, experiments give a Young's modulus of 0.45 TPa and a strength of 40 GPa for CNTs (Yu et al. 2002). The large deviation between simulations and experiments is attributed to the presence of defects in the nanotube structure. The deviation between predicted and measured mechanical properties of CNTs as well as the need for predicting the mechanical properties of defected graphene, given the difficulties in performing experiments at the nano-scale, has enhanced the need for developing reliable models capable of predicting the mechanical properties and simulating the mechanical behavior of isolated CNTs and graphene.

Combining extraordinary mechanical properties and fiber-like structure, CNTs offer unique potential for reinforcing polymers either as replacements of conventional fibers or as fillers to enhance the properties of existing advanced composites. After the recent achievement of obtaining graphene in a crystalline form (Geim and Novolesov 2007; Hashimoto et al. 2004), research on the usage of graphene as a reinforcement was also initiated. Graphene is more promising than CNTs in this role since it offers reinforcement in two directions instead of one. The first efforts to manufacture CNT- and graphene-reinforced composites revealed several technological problems as well as the influence of several material-related and geometrical factors on the reinforcement efficiency of the nano-reinforced composites. To understand and to overcome the negative effect of the above factors on the macroscopic properties of nano-reinforced composites an exhausting experimental research is needed. However, the experimental effort can be disburdened by using efficient models that perform virtual design and optimization of the nano-reinforced composites.

Virtual design and optimization of nano-reinforced composites cannot be performed by pure atomistic models since they are limited in both time and scale and require large computational effort even for the analysis of an isolated CNT or graphene. On the contrary, continuum methods are computationally efficient, can be extended in different scales and also can incorporate data from the nano-scale for the sake of accuracy.

This chapter reviews the continuum models developed by the authors in order to predict the elastic properties of isolated defect-free CNTs (Tserpes and Papanikos 2005), simulate the tensile behavior of defected CNTs (Tserpes et al. 2006; Tserpes and Papanikos 2007) and graphene (Tserpes 2012) and parametrically evaluate the effective elastic properties of CNT-reinforced (Tserpes and Chanteli 2013) and graphene-reinforced polymers. All models are based on the FE method and wherever necessary they incorporate data from the nano-scale.

2 FE Modeling of CNTs and Graphene

Carbon atoms in CNTs and graphene are bonded together with covalent bonds forming a hexagonal 2D lattice. These bonds have a characteristic bond length and bond angle. The displacement of the individual atoms under an external force is constrained by the bonds. Therefore, the total deformation of CNTs and graphene is the result of the interactions between the bonds. By considering the bonds as connecting load-carrying elements, and atoms as joints of the connecting elements, the hexagonal lattice may be simulated as a frame structure. By treating CNTs as a space-frame structure and graphene as a plane-frame structure, their mechanical behavior can be analyzed using classical structural mechanics methods such as the FE method.

Based on the concept described above, 3D FE models representing the exact atomic lattice of CNTs and graphene were developed in (Tserpes and Papanikos 2005) and (Tserpes 2012), respectively, using the ANSYS commercial FE code. For the modeling of the carbon–carbon (C–C) bonds, the 3D elastic BEAM4 ANSYS element was used. Figure 1 depicts how the hexagon, which is the constitutional element of CNTs and graphene, is simulated as structural element of a frame. In the same way the entire lattice is simulated. The simulation leads to the correspondence of bond length to the element length as well as the wall thickness to the element thickness. By assuming a circular cross-sectional area for the element, as in Fig. 1, wall thickness corresponds to element diameter. Typical FE meshes of CNTs and graphene are illustrated in Fig. 2.

The FE models depicted in Fig. 2 were used for predicting the elastic properties and simulating the tensile behavior of pristine and defected CNTs and graphene. They predominate over atomistic models, such as the molecular mechanics and molecular dynamics models, in the handling and required computational effort.

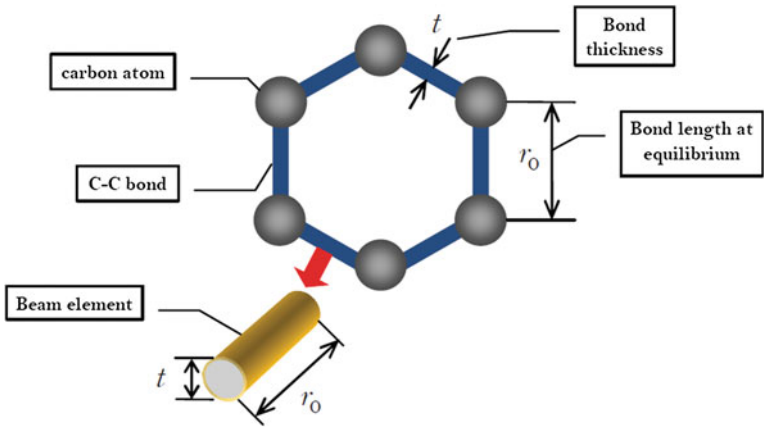

Fig. 1 Beam FE modeling of the hexagonal cell composed of C–C bonds

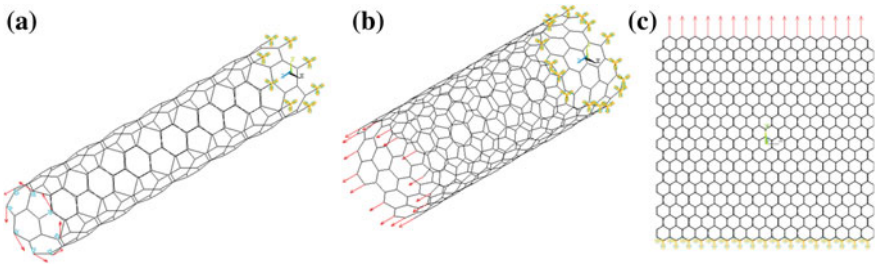

Fig. 2 Typical FE mesh of **a** the armchair (10,10) nanotube, **b** the zigzag (8,0) nanotube and **c** the graphene

Moreover, these FE models can incorporate data from atomistic methods, as it will be described in a forthcoming section, for the sake of accuracy of the analysis.

3 Modeling of the Behavior of C–C Bonds

There are two options for modeling the behavior of C–C bonds: assume a linear behavior or a non-linear behavior. Assuming a linear behavior for the C–C bonds is the easiest approach to model the behavior of carbon-based nanomaterials. However, the efficiency of this approach is limited to problems where very small deformations take place such as the evaluation of the elastic moduli. In order to model the behavior of CNTs and graphene under large deformation, the actual non-linear behavior of the C–C bonds should be simulated through the use of an interatomic potential. In this section, both modeling approaches will be described.

3.1 Linear behavior of C–C Bonds

In this case, the elastic moduli of beam elements, representing the C–C bonds, are derived using a linkage between molecular and structural mechanics (Tserpes and Papanikos 2005; Odegard et al. 2002). According to this linkage, the following molecular mechanics expressions of stretching energy U_r, bending energy U_θ and combined torsion energy U_τ

$$U_r = \frac{1}{2}k_r(r - r_0)^2 = \frac{1}{2}k_r(\Delta r)^2, \tag{1}$$

$$U_\theta = \frac{1}{2}k_\theta(\theta - \theta_0)^2 = \frac{1}{2}k_r(\Delta\theta)^2, \tag{2}$$

$$U_\tau = U_\phi + U_\omega = \frac{1}{2} k_\tau (\Delta\phi)^2, \tag{3}$$

where U_ϕ is the energy due to dihedral angle torsion, k_r, k_θ and k_τ are the force constants and r, θ and τ the corresponding deflections, are combined with the corresponding following classical mechanics expressions of tension U_A, bending U_M and torsion U_T

$$U_A = \frac{1}{2} \frac{E_b A_b}{L_b} (\Delta L_b)^2, \tag{4}$$

$$U_M = \frac{1}{2} \frac{E_b I_b}{L_b} (2\alpha)^2, \tag{5}$$

$$U_T = \frac{1}{2} \frac{G_b J_b}{L_b} (\Delta\beta)^2, \tag{6}$$

where E_b and G_b are the bond's Young's modulus and shear modulus, respectively, I_b and I_b are the secondary moment of inertia and polar moment of inertia, respectively, ΔL_b, 2α and $\Delta\beta$ are the corresponding macro-deflections and A_b and L_b are the cross-sectional area and bond length, respectively, to get the following relations between beam rigidities and force constants

$$\frac{E_b A_b}{L_b} = k_r, \tag{7}$$

$$\frac{E_b I_b}{L_b} = k_\theta, \tag{8}$$

$$\frac{G_b J_b}{L_b} = k_\tau. \tag{9}$$

By assuming a circular cross-section of diameter d_b for the beams, Eqs. (7)–(9) give

$$d_b = 4\sqrt{\frac{k_\theta}{k_r}}, \tag{10}$$

$$E_b = \frac{k_r^2 L_b}{4\pi k_\theta}, \tag{11}$$

$$G_b = \frac{k_r^2 k_\tau L_b}{8\pi k_\theta^2}, \tag{12}$$

which fully define the beam element. Thus, given the length of the bond, which is defined by the type of the bond and the values of force constants, one can derive through Eqs. (10)–(12) the elastic moduli and diameter of the beam element required by the FE method.

3.2 Non-linear Behavior of C–C Bonds

The non-linear behavior of C–C bonds was simulated using the modified Morse interatomic potential (Belytschko et al. 2002). This potential seems not appropriate for describing the behavior of CNTs and graphene when bonds are broken, since it does not allow for reconfiguration of bonds. However, as shown in (Belytschko et al. 2002), the fracture strength of CNTs depends primarily on the inflection point of the interatomic energy and is almost independent of dissociation energy. Therefore, since the inflection strain occurs substantially before the strain associated with bond breaking, where the formation of other bonds is expected, the independence of fracture strength to the dissociation energy provides some confidence that the modified Morse potential can give a correct picture of CNT and graphene fracture in cases of moderate temperatures (0–500 K). Such were the cases in (Tserpes et al. 2006; Tserpes and Papanikos 2007; Tserpes 2012) where the specific potential was used to simulate the tensile behavior, including fracture, of pristine and defected CNTs and graphene.

According to the modified Morse potential, the potential energy of the nanotube system is expressed as

$$E = E_{stretch} + E_{angle}, \tag{13}$$

$$E_{stretch} = D_e\left\{1 - e^{-\beta(r-r_0)}\right]^2 - 1\right\}, \tag{14}$$

$$E_{angle} = \frac{1}{2}k_\theta(\theta - \theta_0)^2\left[1 + k_{sextic}(\theta - \theta_0)^4\right], \tag{15}$$

where $E_{stretch}$ is the bond energy due to bond stretching and E_{angle} the bond energy due to bond angle-bending, r is the current bond length and θ is the current angle of the adjacent bond. The parameters of the potential are (Belytschko et al. 2002):

$r_0 = 1.421 \times 10^{-10}$ m, $D_e = 6.03105 \times 10^{-19}$ Nm,

$\beta = 2.625 \times 10^{10}$ m^{-1}, $\theta_0 = 2.094$ rad, $k_\theta = 0.9 \times 10^{-18}$ Nm/rad^{-2}, $k_{sextic} = 0.754$ rad^{-4}.

As bond stretching dominates tensile behavior of CNTs and graphene and the effect of angle-bending potential is very small, only the bond stretching potential was considered.

By differentiating Eq. (14), the stretching force of atomic bonds is obtained in the molecular force-field as

$$F = 2\beta D_e\left(1 - e^{\beta(r-r_0)}\right)e^{-\beta(r-r_0)} \tag{16}$$

Figure 3 plots the relationship between force F and bond strain $\varepsilon_b = (r - r_0)/r_0$ for the C–C bonds. As may be seen, the force-strain relation is highly non-linear at the attraction region especially at large strains. The inflection point (peak force) occurs at 19 % strain.

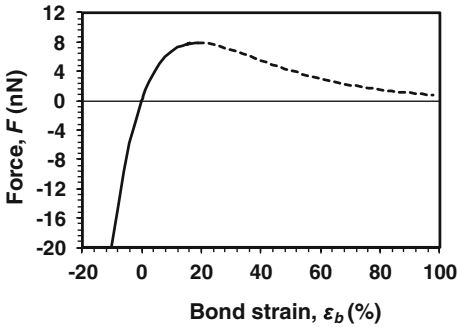

Fig. 3 The force-strain *curve* of the modified Morse potential

3.2.1 Algorithm

The non-linear behavior of the C–C bonds, as described by the interatomic potential, was assigned to the beam elements using the stepwise procedure of progressive fracture modeling, which is briefly described in the following lines. Initially, the stiffness of the beam elements is evaluated from the initial slope of the force-strain curve of the modified Morse potential (Fig. 3) using the element's cross sectional area A_b. The nanomaterial is loaded by an incremental displacement at one end with the other end fixed. At each load step, the stiffness of each element is set equal to $F/A_b\varepsilon_b$, where ε_b is the axial strain of the element as evaluated from the FE model and F is the interatomic force calculated using Eq. (16) given the r. The next displacement increment is then applied to the graphene and this iterative procedure goes on until catastrophic failure of the nanomaterial takes place.

4 Elastic Moduli of Pristine CNTs

Using the linear modeling approach for the C–C bonds, the effect of diameter on the elastic moduli of pristine CNTs was examined in (Tserpes and Papanikos 2005). Figure 4 shows the variation of Young's modulus of armchair, zigzag and chiral single-walled CNTs with nanotube diameter. The Young's modulus was derived by loading the nanotubes in axial tension as shown in Fig. 2a. Contrary to chiral CNTs, there is an evident effect of diameter on the Young's modulus of armchair and zigzag CNTs, especially for small diameters. With increasing nanotube diameter, the Young's modulus of CNTs increases but not with the same trend for all CNTs. The increase is due to the effect of nanotube curvature. A small nanotube diameter results in high curvature of the nanotube which causes large distortion of C–C bonds and therefore, large elongations. As diameter increases, the effect of curvature diminishes. For a variation of nanotube diameter between 0.4 and 2.714 nm for the armchair SWCNTs, between 0.391 and 2.35 nm for the

zigzag SWCNTs and between 0.5 and 2.57 nm for the chiral SWCNTs, the Young's moduli vary from 0.97 to 1.03 TPa, from 0.952 to 1.038 TPa and from 1.023 to 1.066 TPa, respectively.

Similar to Figs. 4, 5 displays the variation of shear modulus of armchair, zigzag and chiral single-walled CNTs with nanotube diameter. The shear modulus was derived by loading the nanotubes in torsion as shown in Fig. 2b. As may be seen, the shear modulus is sensitive to both diameter and chirality, especially at small diameters (less than 1.5 nm). As explained in the previous section, this sensitivity is due to the effect of curvature, which is a function of nanotube diameter. With increasing the diameter, the shear moduli of all CNTs increase with the same trend. The effect diminishes for values of diameter larger than 1.1 nm. For a diameter variation between 0.678 and 2.443 nm for the armchair CNTs, between 0.391 and 2.354 nm for the zigzag SWCNTs, between 0.489 and 2.57 nm for the 5-series chiral SWCNTs and 0.565 and 2.54 nm for the 6-series of chiral CNTs, the shear moduli vary from 0.351 to 0.485 TPa, from 0.283 to 0.487 TPa, from 0.312 to 0.491 TPa and 0.242 to 0.504 TPa, respectively.

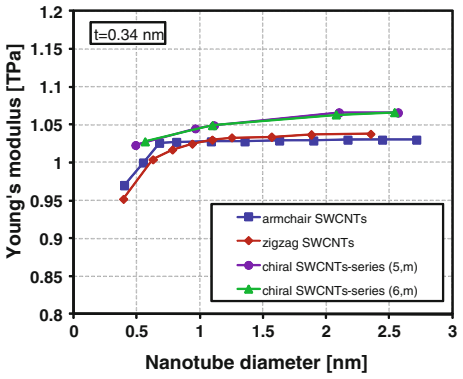

Fig. 4 Variation of nanotube's Young's modulus with diameter and chirality

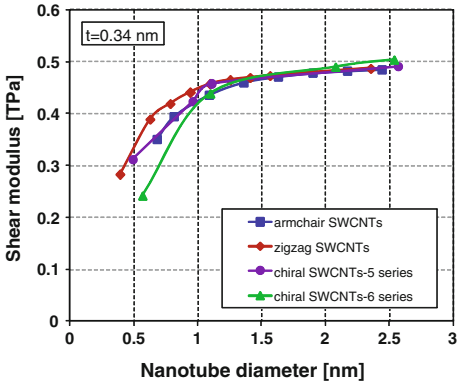

Fig. 5 Variation of nanotube's shear modulus with diameter and chirality

5 Tensile Behavior of Pristine and Defected CNTs

Using the non-linear modeling approach for the C–C bonds, as applied through the progressive fracture model developed in (Tserpes et al. 2006), the tensile behavior of pristine and defected CNTs was simulated in (Tserpes et al. 2006; Tserpes and Papanikos 2007). Three types of defects were considered: weakening of bonds, vacancies (1 missing atom corresponding to three missing bonds) and Stone–Wales (SW) defect. Vacancies and SW defects are very common in CNTs and were found to significantly decrease the mechanical properties of the nanomaterials (Mielke et al. 2004; Khare et al. 2007; Zhang et al. 2005; Xiao et al. 2010).

5.1 Vacancy-defected CNTs

Figure 6 compares the stress–strain curves predicted by the progressive fracture model for the (20,0) tube with those obtained by the molecular mechanics simulations of (Belytschko et al. 2002) and the experiments of (Yu et al. 2002). In (Yu et al. 2002) several tests were performed. The stress–strain curves of the tests show very large dispersion. As comparison with the whole number of the curves would be valueless, three of those, which show the best correlation between them, were included in Fig. 6. In the analyses of the progressive fracture model and the molecular mechanics model, two types of initial defects were considered: 10 % weakening of a bond (type I) and 1 missing atom (type II). As may be seen in Fig. 6, both theoretical models significantly overestimate the Young's modulus and strength of CNTs. The most possible cause for this deviation is the presence defects in the nanotubes tested by Yu et al. (2002) and not considered by the two models. Mielke et al. (2004) found that large approximately circular holes, which would be consistent with damage resulting from harsh oxidative purification processes, may substantially reduce the failure stresses and failure strains of CNTs providing a

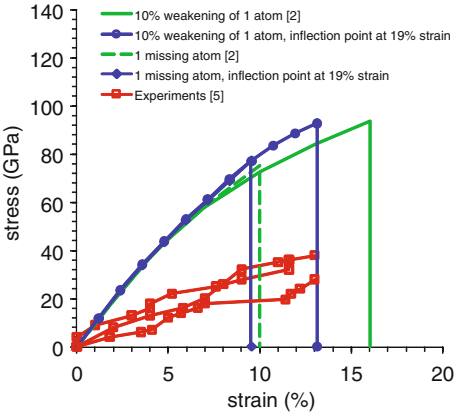

Fig. 6 Comparison of predicted tensile stress–strain curves (Tserpes et al. 2006) for the (20,0) tube with theoretical and experimental curves from the literature

likely explanation for the discrepancy. Another possible cause, as stated in (Mielke et al. 2004), is the slippage that possibly occurred at the attachments for the high strain cases reported in (Yu et al. 2002) resulting in a decrease of the measured values of nanotube Young's modulus. This kind of slippage would also imply that the failure strains are actually smaller than reported.

Concerning the comparison between the progressive fracture model (Tserpes et al. 2006) and the molecular mechanics simulations of (Belytschko et al. 2002), a very good agreement is achieved regarding the Young's modulus and tensile strength of the nanotubes. The curves obtained by the two methods for both types of initial defects coincide up to 8 % strain giving the same Young's modulus for the nanotubes. From this strain and on, the progressive fracture model predicts higher Young's modulus than the molecular mechanics simulations. This difference is much smaller in the case of type II defect, since the analyses of both models stop at around 9.5–10 % strain. The tensile strength predicted by the model is 92.7 GPa for the case of type I defect and 77 GPa for the case of type II. The corresponding tensile strengths reported by Belytschko et al. (2002) were 93.5 and 75 GPa. It is obvious that a very good agreement is achieved. Regarding failure strain, in the case of type II defect, the fracture strain predicted by the model agree very well with the one reported by Belytschko et al. (2002) (9.54 % against 10 %), while in the case of type I defect, it shows a considerable difference (13.12 % against 16 %). Nevertheless, the fracture strain predicted by the model in this case (13.12 %) was equal to the one obtained by two different experiments of Yu et al. (2002).

The evolution of fracture after the first bond fracture depends on the type of initial defect considered. Figure 7 shows the evolution of fracture as function of the nanotube elongation in the (20,0) tubes in which the type I initial defect was modeled. In Fig. 7a, the state of first bond fracture in the (20,0) nanotube is displayed. As expected, fracture initiated in the area close to the weakened bond. The two longitudinal bonds, in which the additional load from the weakened bond was transferred, were failed simultaneously. Increasing the load, fracture is propagated circumferentially spreading at the same time in more than two rows of bonds. In Fig. 7c, fracture has propagated to the other half of the nanotube. At this stage, some bonds at the bottom nanotube end have also failed due to the stress raising caused in this area by the application of boundary conditions. From this point and on, the circumferential propagation of fracture in the middle of the nanotube stopped and fracture of the bonds at the bottom end of the nanotube started to progress. Figure 7d shows the final state of fracture in the nanotube in which all bonds of the bottom end have failed.

5.2 SW-defected CNTs

Beyond a critical value of tension, a CNT releases its excess tension via formation of topological defects. Such a defect is the SW defect. In the case of armchair nanotubes under axial tension, where a transverse tension takes place (the applied

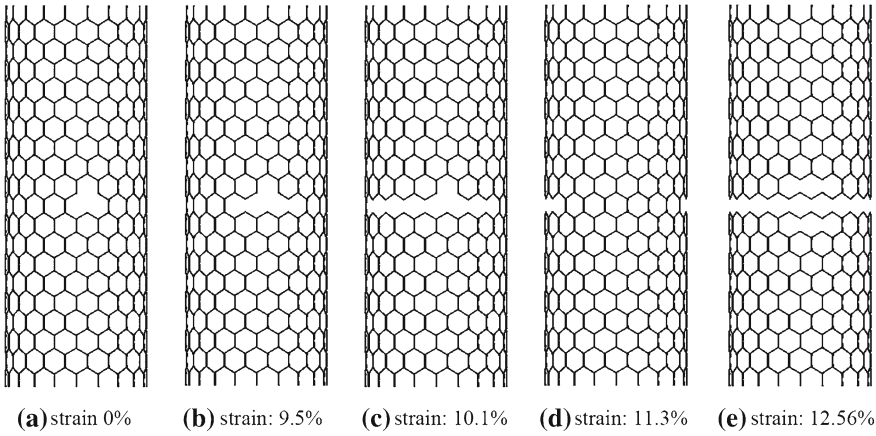

Fig. 7 Predicted fracture evolution in the (20,0) tube containing type II defect. Parts (**a**), (**b**) and (**c**) of the figure show the evolution of fracture in the front half of the nanotube, while parts (**d**) and (**e**), in the back half

load is perpendicular to the C–C bonds), the excess strain is released via the 90° rotation of the perpendicular bond as schematically described in Fig. 8. On the contrary, in the case of zigzag nanotubes under axial tension, the C–C bonds are parallel to the applied load, which is already the minimum energy configuration for the strained bonds. Therefore, the formation of SW defect in zigzag nanotubes is limited to the rotation of the bonds oriented 120° with respect to the tube axis. In zigzag nanotubes, two types of SW defects may be created as indicated in Fig. 9. It was established from simulations that in armchair CNTs SW defects are formed at around 5–6 % applied tensile strain and in zigzag SWCNTs at around 12 %. For the chiral CNTs, no relative information was reported. In (Tserpes and Papanikos 2007), as a strain barrier for the formation of the SW defect the value of 5 % was adopted for the armchair and chiral CNTs, and the value of 12 % for the zigzag SWCNTs.

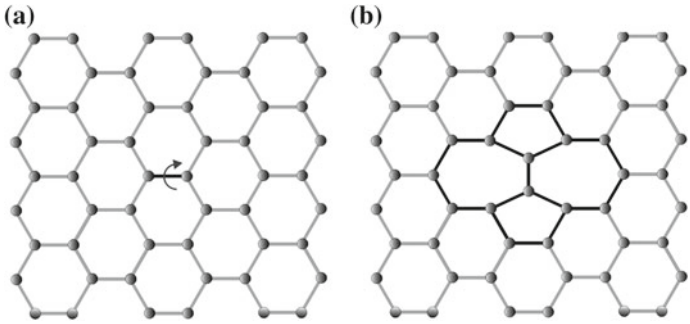

Fig. 8 Schematic of the SW formation in the hexagonal lattice of CNTs: **a** pristine lattice, and **b** SW-defected lattice

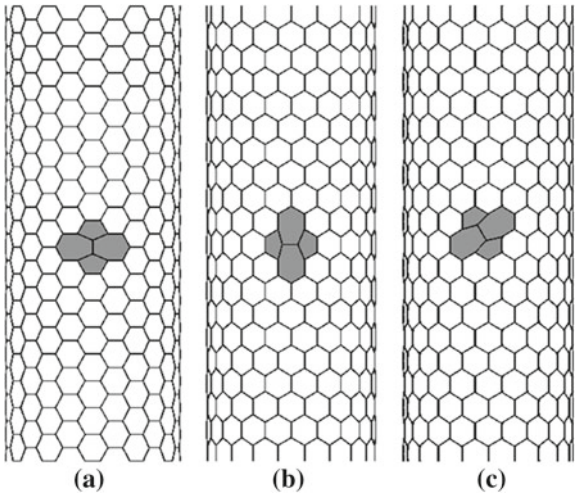

Fig. 9 FE meshes of the SW-defected CNTs. The areas enclosed to the pentagons and heptagons of the defects were colored dark gray. (**a**) (10,10) nanotube, (**b**) (20,0) nanotube: SW-type I and (**c**) (20,0) nanotube: SW-type II

The transformation of 4 hexagons to 2 pentagons and 2 heptagons leads to the elongation of the structure along the axis connecting the pentagons and shrinkage along the perpendicular direction. Thus, the rotation of a bond from a predominately circumferential to a predominately axial orientation lengthens the tube but not to such a degree to change the load distribution between the bonds in the nanotube. In the simulations conducted in (Tserpes and Papanikos 2007), for the sake of simplicity, it was assumed that after the creation of SW defect the dimensions of the nanotubes remained unchanged.

In Fig. 10, the predicted stress–strain curves of the SW-defected (12,12) and (20,0) CNTs are depicted and compared with the curves of the pristine CNTs. When the SW defect is formed, the bonds of the nanotube are already strained. To account for this feature, a combination of the stress–strain curve of the pristine nanotube with that of the defected nanotube was adopted. Up to the defect formation strain (5 or 12 % according to nanotube chirality), the stress–strain curve of the pristine nanotube was used. For strains greater than the defect formation strain, the stress–strain curve of the defected nanotube was used. In the analysis of the defected nanotube, the first applied strain was equal to the defect formation strain. For the nanotubes included in Fig. 10, the stiffness remained unaffected by the presence of the SW defect. A marginal decrease in the nanotube stiffness was predicted only in cases where the fraction of defected area to the nanotube area was high such as the (5,5) tube. This conclusion is supported from results of analyses performed using aggregation of SW defects in the (5,5) tube. The results showed that with increasing number of aggregated defects, the decrease in nanotube stiffness enlarges. In any case, the decrease in stiffness remained marginal.

Computed results show that CNTs containing SW defects exhibit a non-linear (plastic) tensile behavior. The presence of SW defects decreases the nanotubes'

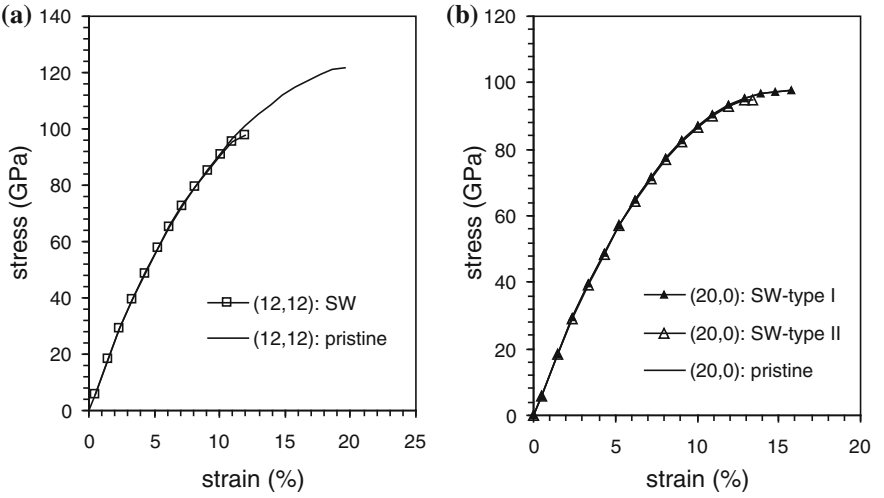

Fig. 10 Predicted stress–strain curves of the SW-defected CNTs. **a** (12,12) nanotube and **b** (20,0) nanotube

failure stress and failure strain but not the stiffness. Table 1 lists the predicted failure stresses and strains for all defected nanotubes analyzed in (Tserpes et al. 2006). Failure stresses correspond to peak stresses in the stress–strain curves, while failure strains to the applied strains at which the peak stresses occur. The case of the SW-defected (12,12) tube was also considered in (Belytschko et al. 2002). Using molecular dynamic simulations they calculated the failure stress and failure strain to be as high as 97.5 GPa and 14.3 %, respectively. These values are in good agreement with the current predicted values of 100 GPa and 12 %, respectively. By comparing the failure stresses and strains of pristine and defected (12,12) (20,0) and (16,8) tubes, which are of the same size, it becomes evident that

Table 1 Predicted failure stresses and strains of SW-defected SWCNTs

Nanotube	Failure stress (GPa)	Failure strain (%)
(12,12): pristine	121.86	19.61
(12,12): SW	100	11.96
(20,0): pristine	97.68	15.75
(20,0): SW-type I	97.68	15.75
(20,0): SW-type II	94.86	13.36
(16,8): pristine	114.18	17.9
(16,8): SW	96.85	12.1
(5,5): pristine	122.54	19.64
(5,5): SW	92.44	11.51
(18,18): pristine	120.63	18.96
(18,18): SW	100	12.2

reduction of these quantities depends on nanotube chirality. There is a significant reduction in the failure stress and failure strain of the armchair (12,12) and chiral (16,8) tubes and an insignificant one in the zigzag (20,0) tube under the presence of both types of SW defects. This alteration is attributed to the bond rearrangement imposed by the SW defects as explained in detail in (Tserpes et al. 2006).

6 Tensile Strength of Defected Graphene

In (Tserpes 2012), tensile strength of graphene containing randomly dispersed vacancies was predicted using the progressive fracture model developed in (Tserpes et al. 2006) and described briefly in Sect. 3.2 of the present chapter. Randomly dispersed vacancies (1 missing atom) were introduced into graphene using a random numbers algorithm. Graphene was subjected to incremental uniaxial tension. The effects of defect-density and defect-topology on the Young's modulus, strength and failure strain of graphene were examined.

Creation of random vacancies in graphene structure was done using a random numbers algorithm. A set of random numbers equal to the number of defects were created using a Random Integer Generator (http://www.random.org) in which randomness comes from atmospheric noise, which for many purposes is better than the pseudo-random number algorithms typically used in computer programs. Random numbers correspond to carbon atoms or nodes in the FE model which are removed from graphene together with the three adjacent bonds. The procedure is illustrated in Fig. 11 for the creation of 10 defects at a graphene with 217 atoms.

The effect of defects is measured in terms of defect-density defined as

$$D_d = \frac{D_n}{A_n} \tag{17}$$

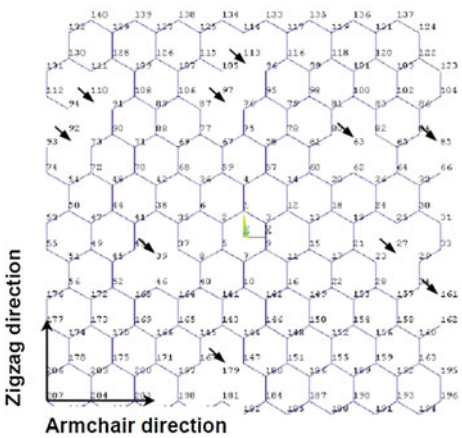

Fig. 11 Graphene with 10 missing atoms indicated by arrows. Numbers of the deleted nodes were given by the random number generator. Zigzag and armchair directions are also indicated

where $D_n$is the number of defects andA_n is the total number of atoms in graphene.

Analyses of the 14.52 nm × 12.20 nm graphene containing different number of vacancies were performed. Figures 12 and 13 plot the predicted tensile stress–strain curves of the defected zigzag and armchair graphene, respectively. It is shown that the presence of defects dramatically degrade the mechanical performance of graphenes by reducing their Young's modulus, tensile strength and failure strain

The variation of Young's modulus and tensile strength of defected graphenes are plotted against defect density in Fig. 14. A similar linear reduction is observed for the Young's modulus for both loading directions. The tensile strength reduces in a bi-linear way: the reduction rate is larger in small defect densities. For a defect density of 4.5 %, a 50 % reduction in Young's modulus and tensile strength in both types of graphenes occurs. This is a very important finding because it reveals that vacancy defects, appearing in considerable densities in graphenes, may counterbalance the extraordinary mechanical properties of the materials.

The obtained effect of vacancies on the strength of graphenes was more or less expected since this type of defects act as holes, thus seriously degrading the load-carrying capability of the material. However, the importance of the finding is the extent of the effect as a function of defect-density. As defect-density increases, a multi-site damage state is developed in graphene. Moreover, the possibility for the creation of holes due to defect aggregation prior to loading and early defect interaction during loading increases dramatically. Figure 15a shows the 14.52 nm × 12.20 nm graphene containing defects of a 3.3 % density. As can be

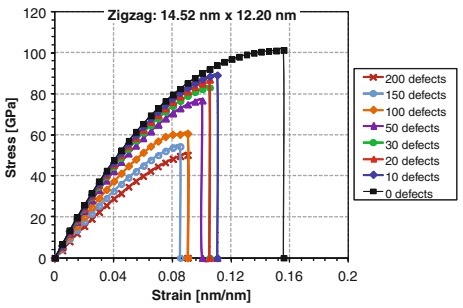

Fig. 12 Predicted tensile stress–strain curves of defected zigzag graphene

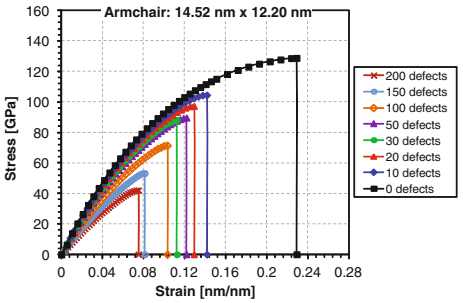

Fig. 13 Predicted tensile stress–strain curves of defected armchair graphene

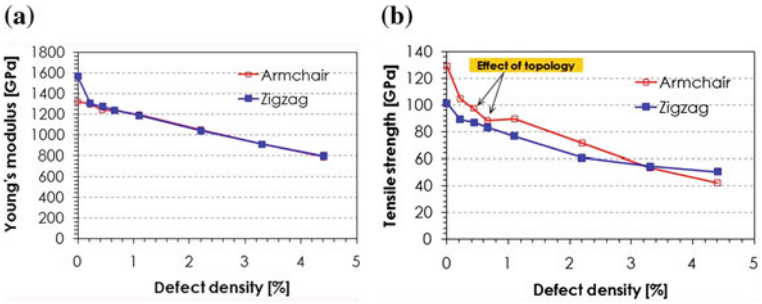

Fig. 14 Variation of **a** the Young's modulus and **b** the tensile strength of defected graphenes as functions of defect-density

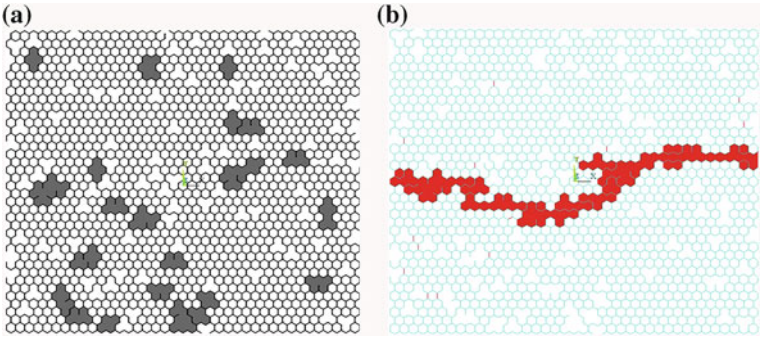

Fig. 15 **a** Formation of holes (*gray areas*) due to defect aggregation prior to loading at the 14.52 nm × 12.20 nm with a 3.3 % defect-density, **b** Early failure of graphene due to the formation of a large crack (*red area*)

seen, the presence of this amount of defects has created several large holes (gray areas) in the structure due to defect aggregation. These holes propagate very quickly during loading to interact and form cracks perpendicular to the loading direction which extends through the width of the structure leading to an early failure, as can be seen in Fig. 15b.

7 Parametric Evaluation of the Effective Elastic Properties of CNT-Reinforced Polymers

The effective elastic properties of CNT-reinforced polymers were evaluated as functions of material and geometrical parameters using a multi-scale approach based on a homogenized RVE presented in (Tserpes and Chanteli 2013). The RVE was also used to predict the tensile modulus of a polystyrene specimen reinforced by randomly aligned MWCNTs for which experimental data exist in the literature.

In this Section, the methodology and basic findings of both applications will be described.

7.1 The RVE

The RVE has a square cross-section. It consists of the polymer matrix, an embedded MWCNT and the interface between them. MWCNT consists of seven hollow single-walled CNTs all gathered to the outer diameter. The outer diameter of the MWCNT is 9.5 nm and the thickness of each tube is 0.34 nm. For the interface, a hollow capped configuration is used in order to consider the entire actual interfacial area between the nanotube and the polymer. The outer dimensions of the RVE are defined according to the desired nanotube volume fraction V_f taken as the ratio of nanotube's volume to RVE's volume. Nanotube length L_{cnt} is determined according to the desired V_f and nanotube aspect ratio taken as the ratio of L_{cnt} to nanotube diameter D_{cnt}. The interface thickness, considered to be equal between the cylindrical part and the capped part, varies within the range of 0 and 2.72 nm (Liu and Chen 2003; Chen and Liu 2004; Haque and Ramasetty 2005; Bhuiyan et al. 2013; Hernández-Pérez and Avilés 2010; Bhuiyan et al. 2011; Delale and Shen 2005; Peng et al. 2012). As an independent parameter considered also is the ratio L_{cnt}/L_{rve} which from preliminary analyses conducted in (Papanikos and Tserpes 2011) was found to affect the computed elastic properties of the RVE.

7.1.1 Materials

The polymer matrix considered in the study was the M21. This is a very tough epoxy matrix that exhibits excellent damage tolerance especially at high energy impact. M21 epoxy resin was extensively used in primary aircraft structures and Formula 1 applications. An isotropic linear elastic behavior was considered for the matrix since the load applied in the RVE is very small. The Young's modulus and Poisson's ratio of the M21 epoxy are 3.5 GPa and 0.3, respectively. The nanotube/polymer interface was found to play an important role in the load transfer between the two constituents (Liu and Chen 2003; Peng et al. 2012; Frankland et al. 2002). In (Tserpes and Chanteli 2013), isotropic material properties were assumed for the interface. For the interface stiffnessE_{int}, three cases were considered, namely$E_{\text{int}} = 0.25 \times E_m$,$E_{\text{int}} = 0.5 \times E_m$ and $E_{\text{int}} = 10 \times E_m$to study the possible effect.

7.1.2 FEA of the RVE

The analyses were conducted by means of a 3D FE model of the RVE developed using the ANSYS commercial FE code. All constituents were represented using

the ANSYS 3D SOLID185 element. Different views of a typical FE mesh of the RVE are shown in Fig. 16. The mesh adopted was selected from a parametric study conducted on the effect of mesh density on the evaluated effective elastic properties. The selected mesh is not very dense as the analyses conducted are linear elastic and the geometry of the RVE has not any geometrical non-linearities.

To derive its elastic moduli, the RVE was loaded in axial tension in the three directions by applying a small normal displacement at one side and fully restraining the other side. Similarly, to derive the shear moduli, the three planes were loaded in shear by applying a shear displacement at one face and fully restraining the opposite face. The elastic moduli were simply derived by using the Hooke's law and the Poisson's ratio using the negative ratio between longitudinal and transverse strains. In order to obtain the homogenized engineering behavior of the RVE, reflecting the macroscopic behavior of the material, periodic boundary conditions were applied in the RVE using constraint equations in opposite faces.

7.2 Parametric Study

In this section, the numerical results from the parametric study conducted are presented. The complete list of the parameters considered as well as the range of variation of each parameter is given in Table 2.

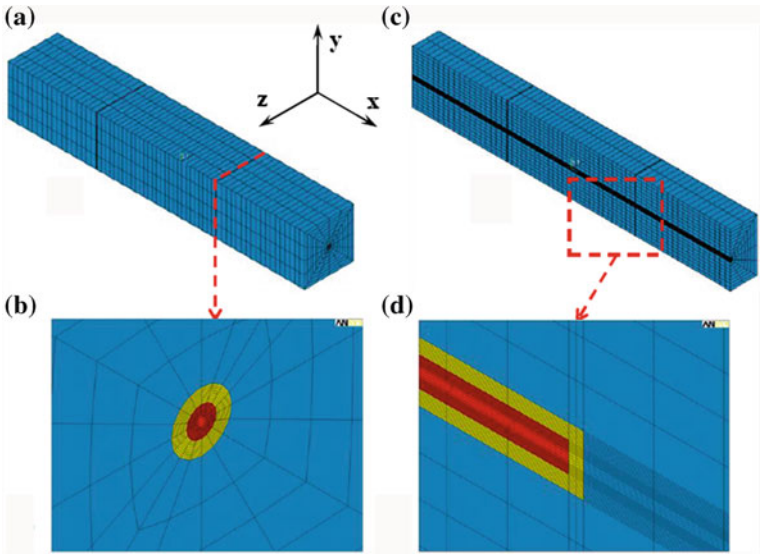

Fig. 16 Views of a typical FE mesh of the RVE: **a** Iso-view of the RVE, **b** Close-view of the cross-sectional area at the nanotube end, **c** Iso-view of half of the RVE and **d** Close-view of half RVE at the nanotube end

7.2.1 Effect of Interface Stiffness and Thickness

The effects of interface stiffness and thickness were studied first in order to decide whether it is necessary to consider an interface in the model and with which stiffness. Figures 17a, b show the variation of E_x and E_y, respectively, with regard to E_{int} for $V_f = 20\%$. The first conclusion and most important is that E_x is not affected by E_{int} for both values of V_f. Consequently, in the models aiming to evaluate E_x the nanotube/polymer interface can be neglected for simplification reasons. On the other hand, E_{int} affects E_y and all other matrix-dominated properties at large values of V_f. Another important conclusion, arising from Fig. 17, is that the elastic moduli depend highly on the L_{cnt}/L_{rve} ratio. An explanation about the effect of L_{cnt}/L_{rve} will be given in a forthcoming Section. Contrary to interface stiffness E_{int}, interface thickness t_{int} was found, as can be seen in Fig. 18, to mainly affect E_x and secondarily the matrix-dominated elastic properties. The effect increases with the L_{cnt}/L_{rve}.

7.2.2 Effect of Nanotube Aspect Ratio

Figure 19 plots the predicted E_x with respect to nanotube aspect ratio L_{cnt}/D_{cnt} for different values ofV_f. As can be seen, for$L_{cnt}/D_{cnt} < 20$ with increasing$L_{cnt}/D_{cnt}$the $E_x$increases for all cases ofV_f. However, for values of $L_{cnt}/D_{cnt} > 20$ the effect almost diminishes for all cases ofV_f. The same effect of L_{cnt}/D_{cnt} was found for all effective elastic properties. Based on this finding, in order to exclude the effect ofL_{cnt}/D_{cnt}, hereafter, the value of 20 was considered in all subsequent analyses. This choice is realistic since CNTs used in real applications have very large aspect rations as they posses a length in the range of μm and a diameter in the range of nm.

7.2.3 Effect of Nanotube Volume Fraction

The nanotube volume fraction V_f is probably the parameter affecting most the effective elastic properties of CNT-polymer composites. It is obvious that large values of V_f leads to large values for the effective elastic moduli. However, it is not always easy, from the practical viewpoint, to implement large values of V_f in

Table 2 List of parameters and their range of variation

Parameter	Range of variation
Nanotube length to RVE length ratio, L_{cnt}/L_{rve}	0.4–0.8
Interface thickness, t_{int}	0.17–2.72 nm
Interface stiffness, E_{int}	0.875–35 GPa
Nanotube volume fraction, V_f	5–20 %
Nanotube aspect ratio, D_{cnt}/L_{cnt}	6–70

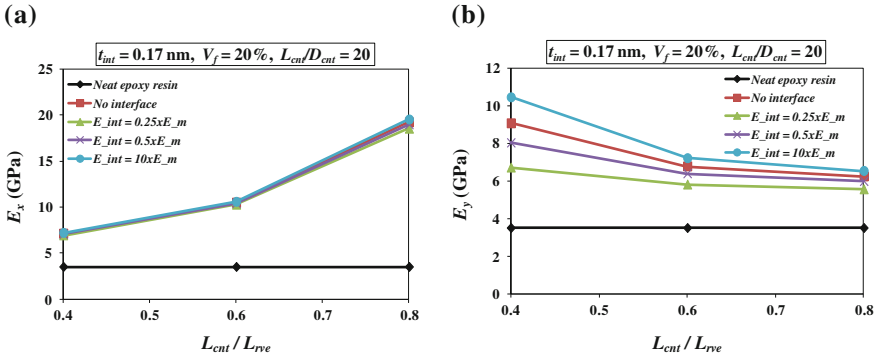

Fig. 17 **a** Predicted variation of **a** E_x and **b** E_y with respect to L_{cnt}/L_{rve} for different values of interface stiffness E_{int} for the case of$V_f = 20\%$

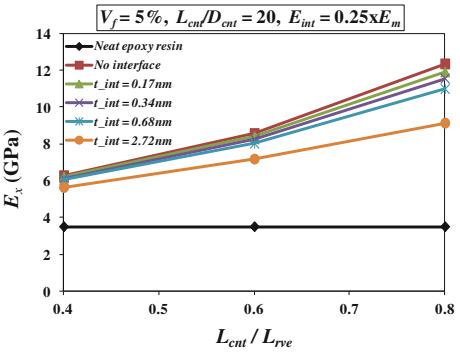

Fig. 18 Predicted variation of E_x with respect to L_{cnt}/L_{rve} for different values of t_{int}

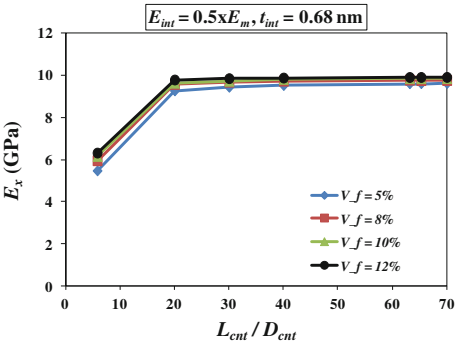

Fig. 19 Predicted variation of E_x with respect to nanotube aspect ratio L_{cnt}/D_{cnt} for different values of V_f

CNT-polymer composites due to problems associated with treatment and processing of the composite material. In Fig. 20, E_x is plotted with respect to L_{cnt}/L_{rve} for four different values of V_f, namely 5, 10, 15 and 20 %. In the graph, the Young's modulus of the M21 matrix is also depicted for comparison reasons. From

Fig. 20, a clear enhancement in E_x is observed. The enhancement stands for all elastic moduli, however, is greater for is larger for E_x; for $V_f = 5\%$ the increase in E_x is 77 % at $L_{cnt}/L_{rve} = 0.4$ reaching 240 % at $L_{cnt}/L_{rve} = 0.8$.

From Fig. 20, it is also obvious the dependence of computed E_x on the L_{cnt}/L_{rve} ratio. This is because as L_{cnt}/L_{rve} increases the nanotube gets closer to the loaded end of the RVE. Thus, a larger amount of the applied load is carried by the stiffer nanotube causing an increase in E_x. At the extreme case of $L_{cnt}/L_{rve} = 1$, the nanotube spans through length of the RVE, thus being loaded directly. This is the case with the maximum effective E_x. This phenomenon is illustrated in Fig. 21 in which the contour of longitudinal stress in the RVE is shown for the cases of $L_{cnt}/L_{rve} = 0.4$ and $L_{cnt}/L_{rve} = 0.8$ for an axial strain of 1 %. At $L_{cnt}/L_{rve} = 0.8$, the stress in the nanotube is 3.3 times the stress at $L_{cnt}/L_{rve} = 0.4$. It is a fact that the dependence of the model computations on the L_{cnt}/L_{rve} ratio limits the applicability and predictability of the model. However, this is regular for RVEs containing stress concentrations due to geometrical non-linearities or stiffness gradients. This restriction can be overcome by adjusting the RVE's dimensions using experimental results. This is not an easy task for materials of complex and unknown architecture incorporating constituents lying at the nano-scale. After adjustment, the predicted RVE's effective elastic properties belong to the properties of the CNT-polymer composite and the RVE can be used to predict the elastic properties of any specimen made from the specific CNT-polymer composite.

7.3 Modeling of a MWCNT-Polystyrene Specimen

By homogenizing the elastic properties of the RVE at the nano-level, an estimation of the elastic properties of the CNT-polymer composite at the micro/meso-level was achieved. In order to check the accuracy of this estimation and also demonstrate the usage of the RVE in the modeling of CNT-polymer specimens lying at the meso-level, a polystyrene specimen reinforced by randomly aligned

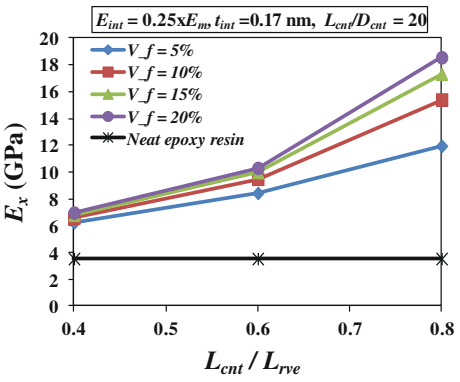

Fig. 20 Predicted variation of E_x with respect to L_{cnt}/L_{rve} for different values of V_f

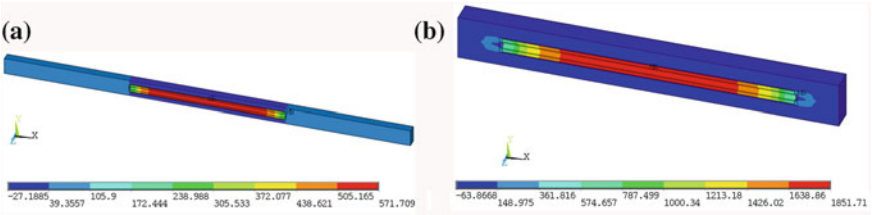

Fig. 21 Contour of longitudinal stress (MPa) in the RVE in the cases of **a** $L_{cnt}/L_{rve} = 0.4$ and **b** $L_{cnt}/L_{rve} = 0.8$for an applied longitudinal strain of 1 %

MWCNTs, for which experimental results exist in (Thostenson and Chou 2003), was modeled. In this section, the modeling procedure and the predicted tensile moduli of the specimen are described.

First, the homogenized effective elastic properties of the MWCNT-polystyrene composite were evaluated using the RVE analysis described in the previous sections. The nanotube diameter in the RVE was chosen based on experimental observations made in (Thostenson and Chou 2003). Figure 22 shows the Lorentzian and Gaussian probability distributions of nanotube diameter obtained in (Thostenson and Chou 2003) from high resolution TEM micrographs and image analysis. From Fig. 22 it is observed that the nanotube diameter with the greater distribution is 18 nm; this value was used in the RVE. For the L_{cnt}/L_{rve} ratio, the value of 0.4 was used. This choice will be explained later. The nanotube aspect ration was taken equal to 20.

The second step is to model the polystyrene specimen containing MWCNTs by 5 % wt. This analysis lies from the meso- to the macro-scale. The specimen dimensions are: 50 mm × 10 mm × 2 mm. A 2D FE model of the specimen was developed using the ANSYS 2D SHELL63 element. Fundamental for this modeling task is the efficient modeling of nanotube orientation with regard to loading axis. Again, this was based on experimental observations from (Thostenson and

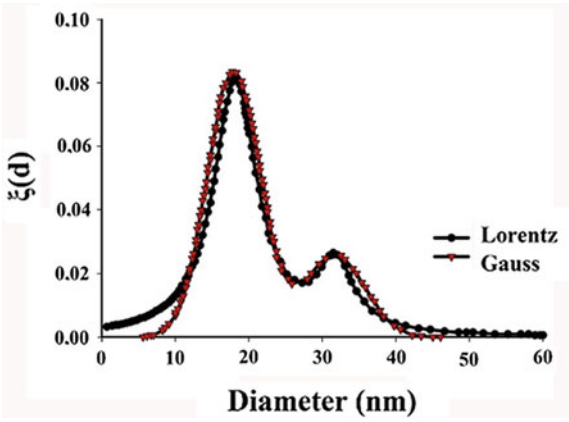

Fig. 22 Diameter distribution of CNTs in the polystyrene specimen taken from (Thostenson and Chou 2003)

Chou 2003). Using image analysis of TEM micrographs taken from a 5 % wt nanocomposite film with a large-scale dispersion Thostenson and Chou (2003) derived the distribution of nanotube alignment described by the histogram shown in Fig. 23.

Based on the histogram of Fig. 23, the nanotube orientation in the FE model of the specimen was modeled using the following procedure:

1. All orientation-frequency pairs were recorded.
2. The range of orientation angle from −60 to 100° was divided into 32 intervals of 5°. For each interval, the mean frequency was derived. The sum of all mean frequencies is 100 %. The orientation interval-frequency pairs were stored.
3. Assuming uniform nanotube dispersion in the specimen, which means that every element is an RVE, the number of elements having a specific orientation was found by multiplying the frequency of this orientation by the total number of elements in the model.
4. Assuming random nanotube alignment, the elements having a specific orientation were selected randomly from the total set of the elements using a pseudorandom function. Every time, the selected elements were removed from the total sample to avoid duplications.
5. The different nanotube orientation θ was implied at each element by transforming the coordinate system of the element by an angle equals to the orientation angle θ. Figure 24 shows a part of the FE mesh of the specimen in which the reoriented coordinate systems of the elements are also plotted.

The tensile modulus of the specimen was derived through the application of an axial strain of 0.01 %. In the histogram of Fig. 25, the predicted tensile modulus is compared with the experimental modulus of (Thostenson and Chou 2003). As can be seen, a very good agreement between the two approaches is achieved. This agreement leads to the conclusion that the capacity of the RVE to estimate the effective elastic moduli of CNT-polymer composites and its usage in the modeling

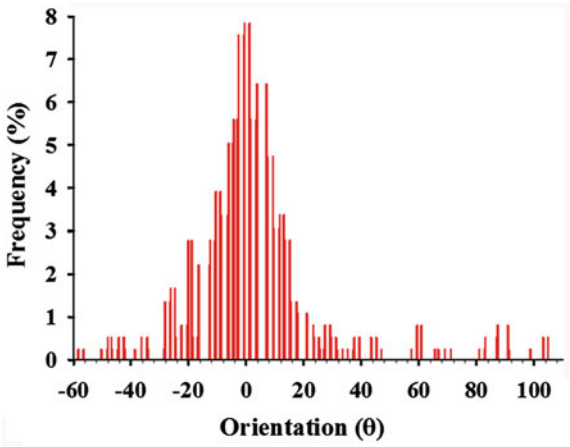

Fig. 23 Distribution of nanotube alignment taken from (Thostenson and Chou 2003)

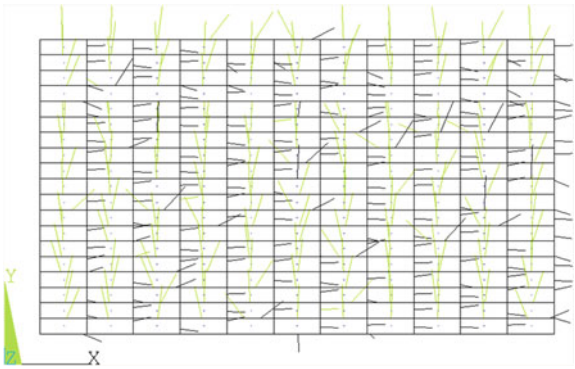

Fig. 24 Part of the specimen's FE mesh. Plotted also are the reoriented coordinate specimens of the elements

of CNT-polymer specimens lying at the macro-scale are validated. Moreover, the simple approach used to model the different nanotube orientation in the specimen has proved effective. For the ratio L_{cnt}/L_{rve}, the value of 0.4 was chosen because it gives the best prediction for the tensile modulus of the specimen with respect to the experimental value. The values of 0.6 and 0.8 gave larger L_{cnt}/L_{rve} for the RVE which led to larger predictions for the modulus of the specimen. This way of selecting the L_{cnt}/L_{rve} ratio suggests an adjustment of the RVE's dimensions from experimental data. After the adjustment, the RVE with the specific L_{cnt}/L_{rve} ratio can be used for the modeling of any structural part made from the same material under the same manufacturing conditions.

Using the 2D FE model of the specimen, the effect of nanotube orientation on the tensile modulus of the CNT-polymer was further studied. In the study, it was assumed that all nanotubes have the same orientation. The orientation angles considered are: 0, 15, 30 and 45°. The model predictions for these four cases as well as the modulus of the neat polystyrene specimen are also included in Fig. 25. As expected, the higher modulus is predicted for the case of perfect nanotube alignment $(\theta = 0°)$. With increasing θ, the modulus decreases dramatically and at $(\theta = 45°)$ almost no reinforcement is found at the longitudinal direction.

7.4 Modeling of a Graphene-Polystyrene Specimen

Using the methodology described in Sects. 5.1, 5.2 and 5.3, the tensile modulus of a graphene-polystyrene specimen was derived. In this application, for comparison reasons, the same volume fraction and alignment as in for the MWCNT-polystyrene specimen were assumed. First, the homogenized effective elastic properties of the graphene-polystyrene composite were evaluated using a RVE analysis and then, the graphene-polystyrene specimen was modeled.

The computed effective tensile moduli of the graphene-polystyrene specimen are compared in Fig. 26 with the ones of the MWCNT-polystyrene specimen for

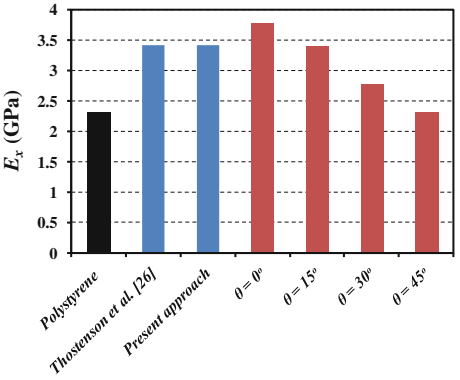

Fig. 25 Comparison between the predicted tensile moduli of the MWCNT-polystyrene specimen for the cases of random nanotube alignment and for different specific nanotube orientations with the experimental measurements of Thostenson and Chou (Thostenson and Chou 2003)

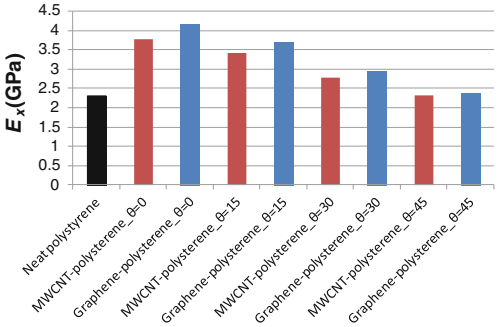

Fig. 26 Comparison between the predicted tensile moduli of the MWCNT-polystyrene specimen and the graphene-polystyrene specimen

all orientation cases considered in Fig. 25. As can be seen, for orientation angles, the Young's modulus of the graphene-polystyrene specimen is larger than the one of the MWCNT-polystyrene specimen which is attributed to the fact that graphene offers reinforcement in two directions.

8 Summary and Conclusions

This chapter reviews the continuum models that were developed by the authors from 2005 until today to predict the elastic properties and simulate tensile behavior of pristine and defected CNTs and graphene as well as CNT- and graphene-reinforced polymers. The models are based on the FE method. Thus, they incorporate all advantages of continuum modeling and FE modeling and they predominate over atomistic models in the handling and required computational effort. A quasi-static FE solution of CNTs and graphene, consisting of several thousands of atoms, requires only a few minutes in a conventional computer whereas the same solution using molecular dynamic simulations can be treated

only by powerful workstations in a few hours. However, perhaps the most important advantage of continuum modeling methods over atomistic simulation methods is the capability of performing without limit in time and length scale, thus enabling the modeling of materials with constituents in different scales and allowing the study of the effect of parameters lying in the nano-scale on the mechanical properties of the macro-scale.

The FE model of the single-walled CNTs developed in (Tserpes and Papanikos 2005) represents the first attempt to model CNTs using the FE method. In the model, a linear behavior of the C–C bonds was assumed. By applying small deformations in the nanotube, the effect of diameter on the nanotube's elastic moduli was evaluated and found considerable at small nanotube diameters.

Having as a basis the FE model of (Tserpes and Papanikos 2005), a progressive fracture model capable of simulating the tensile behavior and predict fracture of CNTs was developed in (Tserpes et al. 2006). The model was implemented to predict the effect of defects on the tensile behavior of CNTs in (Tserpes and Papanikos 2007) and graphene (Tserpes 2012). The simulations showed that both topological defects and vacancies in large densities degrade significantly the mechanical properties of the nanomaterials, thus counterbalancing their reinforcing effectiveness.

Moving one scale upwards, the effective elastic properties of CNT-polymers and graphene-polymers were evaluated as functions of material-related and geometrical parameters. The analysis was done using a FE model of a homogenized RVE. The results from this study maybe proved useful in the design and manufacturing processes of nano-reinforced composites. Using the results from the RVE, two polystyrene specimens reinforced by MWCNTs and graphene, respectively, were modeled and their tensile modulus was evaluated as a function of alignment of the nano-material.

Concluding this chapter, it can be stated that the methodologies and results presented herein verify that continuum modeling was proved efficient and effective in the modeling of nanomaterials and can be considered as a very strong alternative to atomistic simulation methods.

References

Belytschko T, Xiao SP, Schatz GC, Ruoff RS (2002) Atomistic simulations of nanotube fracture. Phys. Rev. B 65:235430

Bhuiyan MA, Pucha RV, Karevan M, Kalaitzidou K (2011) Tensile modulus of carbon nanotube/polypropylene composites: a computational study based on experimental characterization. Comput Mater Sci 50:2347–2353

Bhuiyan MA, Pucha RV, Worthy J, Karevan M, Kalaitzidou K (2013) Defining the lower and upper limit of the effective modulus of CNT/polypropylene composites through integration of modeling and experiments. Compos Struct 95:80–87

Chen XL, Liu YJ (2004) Square representative volume elements for evaluating the effective material properties of carbon nanotube-based composites. Comput Mater Sci 29:1–11

Delale HWF, Shen L (2005) Effect of CNT length and CNT-matrix interface in carbon nanotube (CNT) reinforced composites. Mech Res Commun 32:481–489

Duan WH, Wang Q, Liew KM, He XQ (2007) Molecular mechanics modeling of carbon nanotube fracture. Carbon 45:1769–1776

Frankland SJV, Caglar A, Brenner DW, Griebel M (2002) Molecular simulation of the influence of chemical cross-links on the shear strength of carbon nanotube-polymer interfaces. J Phys Chem B 106:3046–3048

Geim AK, Novolesov KS (2007) The rise of graphene. Nature Mater 6:183–191

Haque A, Ramasetty A (2005) Theoretical study of stress transfer in carbon nanotube reinforced polymer matrix composites. Compos Struct 71:68–77

Hashimoto A, Suenaga K, Gloter A, Urita K, Iijima S (2004) Direct evidence for atomic defects in graphene layers. Nature 430:870–873

Hernández-Pérez A, Avilés F (2010) Modeling the influence of interphase on the elastic properties of carbon nanotube composites. Comput Mater Sci 47:926–933

Khare R, Mielke SL, Paci JT, Zhang S, Ballarini R, Schatz GC, Belytschko T (2007) Coupled quantum mechanical/molecular mechanical modeling of the fracture of defective carbon nanotubes and graphene sheets. Phys. Rev. B. 75:075412

Lee C, Wei X, Kysar JW, Hone J (2008) Measurement of the elastic properties and intrinsic strength of monolayer graphene. Science 321:385–388

Liu YJ, Chen XL (2003) Evaluations of the effective material properties of carbon nanotube-based composites using a nanoscale representative volume element. Mech Mater 35:69–81

Mielke SL, Troya D, Zhang S, Li J-L, Xiao S, Car R, Ruoff RS, Schatz GC, Belytschko T (2004) The role of vacanciess and holes in the fracture of carbon nanotubes. Chem Phys Lett 390:413–420

Odegard GM, Gates TS, Nicholson LM, Wise KE (2002) Equivalent-continuum modeling of nano-structured materials. Compos Sci Technol 62:1869–1880

Papanikos P, Tserpes KI (2011) Stiffness evaluation of polymers reinforced by specifically or randomly distributed carbon nanotubes. In: Proceedings of the 16th international conference on composite structures, Porto, 28–30 June 2011

Peng RD, Wang HW, Mishnaesky L Jr (2012) Modeling of nano-reinforced polymer-composites: microstructure effect on Young's modulus. Comput Mater Sci 60:19–31

Thostenson ET, Chou T-W (2003) On the elastic properties of carbon nanotube—based composites modeling and characterization. J Phys D Appl Phys 36:573–582

Tserpes KI (2012) Strength of graphenes containing randomly dispersed vacancies. Acta Mech 223:669–678

Tserpes KI, Chanteli A (2013) Parametric numerical evaluation of the elastic properties of carbon nanotube-reinforced polymers. Compos Struct 99:366–374

Tserpes KI, Papanikos P (2005) Finite element modeling of single-walled carbon nanotubes. Compos B Eng 36:468–477

Tserpes KI, Papanikos P (2007) The effect of Stone-Wales defect on the tensile behavior and fracture of single-walled carbon nanotubes. Compos Struct 79:581–589

Tserpes KI, Papanikos P, Tsirkas SA (2006) A progressive fracture model for carbon nanotubes. Compos B Eng 37:662–669

Xiao JR, Staniszewski J, Gillespie JW Jr, (2010) Tensile behaviors of graphene sheets and carbon nanotubes with multiple Stone–Wales defects. Mater Sci Eng A 527:715–723

Yu MF, Lourie O, Dyer MJ, Moloni K, Kelly TF, Ruoff RS (2002) Strength and breaking mechanism of multiwalled carbon nanotubes under tensile load. Science 200:287

Zhang S, Mielke SL, Khare R, Troya D, Ruoff RS, Schatz GC, Belytschko T (2005) Mechanics of defects in carbon nanotubes: atomistic and multiscale simulations. Phys. Rev. B 71:115403

About the Editors

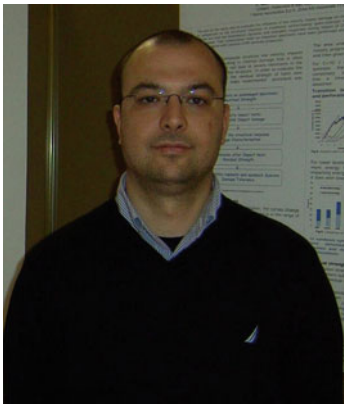

Dr. Konstantinos I. Tserpes is a Mechanical Engineer with a Ph.D. in Strength Prediction of Composite Materials. Currently, he is a Lecturer of Strength of Materials at the Department of Mechanical Engineering & Aeronautics, University of Patras, Greece. His research interests are in the areas of Strength of Composite Materials, Strength of Bonded and Bolted Joints, Mechanical Behavior of Carbon Nanotubes, Graphene and Nano-Reinforced Composites, Multi-scale Analysis of Materials and Structural Parts, Development of Methodologies for Relating Data from Non-destructive Testing with Numerical Strength Prediction Models as well as Strength Prediction of Corroded Aluminum Parts. He has published 1 chapter in a book, more than 30 papers in journals and more than 40 papers in Conference proceedings. He has 14 years of research experience in the area of aeronautical structures gathered through participation in national and international research projects.

Nuno Silvestre is Associate Professor at the Department of Mechanical Engineering of IST – University of Lisbon, Portugal. He holds a PhD degree in Civil Engineering and has more than 20 years of experience in teaching, researching and consulting. His research interests include Nanomechanics, Simulation at Nanoscale, Behaviour of Thin-walled Structures, Nonlinear Solid Mechanics and Numerical Analysis of Structures, Structural Stability and Dynamics, and Design of Steel and FRP Composite

K. I. Tserpes and N. Silvestre (eds.), *Modeling of Carbon Nanotubes, Graphene and their Composites*, Springer Series in Materials Science 188,
DOI: 10.1007/978-3-319-01201-8, © Springer International Publishing Switzerland 2014

Structures. He has more than 70 journal publications in peer reviewed journals and about 200 communications in international conferences. Professor Silvestre participated in several funded R&D projects, supervised various PhD and MSc students and received many awards from international and national institutions in recognition for his scientific achievements. He is also an esteemed member of several scientific and management committees, member of 7 editorial boards of international journals, and also a referee to more than 40 journals.
https://fenix.ist.utl.pt/homepage/ist13506
http://www.researcherid.com/rid/A-5644-2010
http://scholar.google.pt/citations?user=mgXXcU0AAAAJ&hl=pt-PT